

**Evaluation of Progressive Collapse Resistance of RC Framed Buildings Using Alternate Path
Method**

Omar El Kafrawy

A Thesis

in the Department of

Building, Civil and Environmental Engineering

Presented in Partial Fulfillment of the Requirements

for the Degree of

Doctor of Philosophy (Civil Engineering)

at Concordia University

Montréal, Québec, Canada

August 2025

© Omar El Kafrawy, 2025

**CONCORDIA UNIVERSITY
SCHOOL OF GRADUATE STUDIES**

This is to certify that the thesis prepared

By Omar El Kafrawy

Entitled Evaluation of Progressive Collapse Resistance of RC Framed Buildings Using Alternate Path Method

and submitted in partial fulfillment of the requirements for the degree of

DOCTOR OF PHILOSOPHY (Civil Engineering)

complies with the regulations of the University and meets the accepted standards with respect to originality and quality.

Signed by the final examining committee:

_____ Chair
Dr. Thomas Fevens

_____ External Examiner
Dr. Ayan Sadhu

_____ Arm's Length Examiner
Dr. Muthukumaran Packirisamy

_____ Examiner
Dr. Anjan Bhowmick

_____ Examiner
Dr. Lucia Tirca

_____ Thesis Supervisor
Dr. Ashutosh Bagchi

Approved by

Dr. Po-Han Chen, Graduate Program Director

April 24, 2025

Dr. Mourad Debbabi, Dean

ABSTRACT

Evaluation of Progressive Collapse Resistance of RC Framed Buildings Using Alternate Path Method

Omar El Kafrawy, Ph.D.

Concordia University, 2025

This thesis presents a comprehensive investigation into the progressive collapse resistance of reinforced concrete (RC) framed structures using the Alternate Path Method (APM), a widely used threat-independent approach aimed at ensuring building stability after localized structural damage. Progressive collapse, characterized by disproportionate structural failure following the loss of one or more critical components, is often triggered by extreme events like explosions, impacts, or material degradation. The primary objective of this research is to evaluate the ability of RC frames to withstand progressive collapse under various column loss scenarios, while examining the effects of structural simplifications and modeling reductions on analysis accuracy.

The study investigates the behavior of full-frame and bare-frame models under the sudden removal of interior and corner columns. Nonlinear static and dynamic analyses were conducted using finite element modeling. Analytical models were validated against experimental data to ensure the reliability of numerical results, followed by the design and analysis of a multi-story case study building. Dynamic Increase Factors (DIFs) were calculated to account for the increased demands on structural elements due to the dynamic nature of column removal scenarios. Average values of approximately 1.33 and 1.67 were observed for full-frames and bare-frames, respectively. These results were more critical compared to the average DIF of 1.17 prescribed by the General Services Administration (GSA) and Unified Facilities Criteria (UFC) guidelines.

The influence of floor slabs on structural robustness was quantified, revealing enhancements ranging from 87% to 114% under quasi-static analysis and from 160% to 187% under dynamic analysis, further highlighting their contribution to resisting inertial forces. Model reduction techniques focusing on interior column loss showed that simplified models could predict load capacity within 2% error, offering significant computational savings without compromising reliability.

Finally, a simplified approximate method was developed to evaluate progressive collapse, estimating peak flexural/arch capacity with average errors of 5.6% for peak load and 17% for corresponding displacement

compared to experimental results. This method, validated against experimental data, offers a practical tool for early-stage design evaluations, balancing accuracy and efficiency in progressive collapse assessment.

ACKNOWLEDGMENTS

I would like to express my deepest gratitude to my supervisor, Dr. Ashutosh Bagchi, for his ongoing support and guidance throughout the course of my Ph.D. His insights and expertise are invaluable in shaping this research, and I am truly grateful for the opportunity to work under his mentorship.

I would also like to thank my mom and dad for their endless love, unwavering support and belief in me throughout this journey. For that, I am eternally grateful. I am equally grateful to my wife, whose encouragement, understanding and patience serve as my foundation during the most challenging times.

This thesis is dedicated to the loving memory of my brother, Hesham, who passed away during this program. I miss him dearly every day. His memory is a source of motivation for me to continue and complete this work. Rest in peace, my dear brother. You will always be in my heart.

CONTENTS

FIGURES	XI
TABLES	XXIII
1. INTRODUCTION	1
1.1 BACKGROUND	1
1.2 DESIGN APPROACHES.....	2
1.2.1 <i>Indirect Design Approach</i>	2
1.2.1.1 Tie Force Method (TF).....	2
1.2.1.2 Enhanced Local Resistance (ELR) Method.....	2
1.2.2 <i>Direct Design Approach</i>	2
1.2.2.1 Specific Load Resistance (SLR) Method.....	3
1.2.2.2 Alternate Path Method (APM)	3
1.3 GUIDELINES.....	4
1.3.1 <i>United Facilities Criteria (UFC)</i>	4
1.3.2 <i>General Service Administration (GSA)</i>	4
1.4 ANALYSIS & DESIGN PROCEDURES.....	5
1.4.1 <i>Analysis Procedures</i>	5
1.4.1.1 Linear Static Analysis (LSA).....	6
1.4.1.2 Nonlinear Static Analysis (NSA).....	6
1.4.1.3 Nonlinear Dynamic Analysis (NDA)	6
1.4.2 <i>Design Criteria</i>	6
1.5 MOTIVATION & APPROACH.....	7
1.6 RESEARCH OBJECTIVES	8
2. LITERATURE REVIEW	10
2.1 INTRODUCTION	10
2.2 EXPERIMENTAL WORK.....	10
2.2.1 <i>Quasi-Static Experiments</i>	11
2.2.2 <i>Dynamic Column Loss Experiments</i>	11
2.3 MODELING	12
2.4 ANALYSIS METHODS	14
2.4.1 <i>Finite Element Method (FEM)</i>	14
2.4.1.1 Load-Control Method.....	15
2.4.1.2 Displacement-Control Method	17

2.4.2	<i>Discrete Element Method (DEM)</i>	17
2.4.3	<i>Applied Element Method (AEM)</i>	18
2.5	STRUCTURAL ROBUSTNESS	19
2.5.1	<i>Redundancy</i>	21
2.5.2	<i>Ductility & Residual Strength</i>	22
2.5.3	<i>Reserve Strength</i>	22
2.5.4	<i>Energy Absorption Capacity</i>	23
2.6	RESISTANCE MECHANISMS	23
2.6.1	<i>Flexural Resistance</i>	24
2.6.2	<i>Compressive Arch Action</i>	24
2.6.3	<i>Catenary Action</i>	25
2.6.4	<i>Membrane Action</i>	26
2.6.5	<i>Vierendeel Action</i>	26
2.6.6	<i>Non-Structural Elements</i>	26
2.7	SUMMARY & CONCLUSIONS	27
2.7.1	<i>Experimental & Numerical Research on Progressive Collapse</i>	27
2.7.2	<i>Identified Gaps and Research Needs</i>	27
2.7.3	<i>Focus of This Study</i>	28
3.	RESEARCH METHODOLOGY	29
3.1	INTRODUCTION	29
3.2	METHODOLOGY	29
3.2.1	<i>Choice of Analysis Software</i>	29
3.2.2	<i>First Experimental Study Example</i>	30
3.2.3	<i>Second Experimental Study Example</i>	33
3.2.4	<i>Third Experimental Study Example</i>	34
3.2.5	<i>Fourth Experimental Study Example</i>	35
3.2.6	<i>Case Study</i>	36
3.2.7	<i>Simplified Approximate Method</i>	39
3.3	SUMMARY & CONCLUSIONS	40
4.	ANALYSIS SOFTWARE VALIDATION	41
4.1	INTRODUCTION	41
4.2	FIRST EXPERIMENTAL STUDY EXAMPLE	41
4.2.1	<i>Model Description</i>	41

4.2.1.1	Choice of Structural Elements	41
4.2.1.2	Modeling of Concrete Behavior	42
4.2.1.3	Modeling of Reinforcing Steel Behavior.....	45
4.2.2	<i>Validation of Results</i>	47
4.3	SECOND EXPERIMENTAL STUDY EXAMPLE	48
4.3.1	<i>Model Description</i>	48
4.3.2	<i>Validation of Results</i>	51
4.4	THIRD EXPERIMENTAL STUDY EXAMPLE	52
4.4.1	<i>Model Description</i>	52
4.4.1.1	Modeling of Elements & Materials	52
4.4.1.2	Column Removal Simulation	54
4.4.2	<i>Validation of Results</i>	55
4.5	FOURTH EXPERIMENTAL STUDY EXAMPLE	56
4.5.1	<i>Model Description</i>	56
4.5.2	<i>Validation of Results</i>	58
4.6	SUMMARY & CONCLUSIONS	60
5.	PROGRESSIVE COLLAPSE ANALYSIS OF A MULTI-STORY CASE STUDY BUILDING	62
5.1	INTRODUCTION	62
5.2	DESIGN	62
5.2.1	<i>Design Input</i>	62
5.2.1.1	Material Properties	62
5.2.1.2	Input Loads.....	63
5.2.1.3	Analysis & Design	66
5.3	NONLINEAR ANALYSIS	70
5.3.1	<i>Models</i>	70
5.3.2	<i>Modal Analysis</i>	72
5.3.3	<i>Gravity Analysis</i>	73
5.3.4	<i>Pushdown Analysis</i>	73
5.3.4.1	Full-Frame Corner Column Removal Results	74
5.3.4.2	Bare-Frame Corner Column Removal Results	80
5.3.4.3	Full-Frame Interior Column Removal Results.....	86
5.3.4.4	Bare-Frame Interior Column Removal Results	92
5.3.5	<i>Column Loss Analysis</i>	98
5.3.5.1	Full-Frame Corner Column Removal Results	98
5.3.5.2	Bare-Frame Corner Column Removal Results	107
5.3.5.3	Full-Frame Interior Column Removal Results.....	115

5.3.5.4	Bare-Frame Interior Column Removal Results	124
5.4	INTERPRETATION OF RESULTS	132
5.4.1	<i>Dynamic Increase Factors</i>	132
5.4.2	<i>Slab Effect</i>	138
5.4.3	<i>Column Location Effect</i>	145
5.5	MODEL REDUCTION	145
5.6	DISPLACEMENT-CONTROL PUSHDOWN CURVES	150
5.6.1	<i>Reduced System Pushdown</i>	150
5.6.2	<i>Energy Balance Approach</i>	152
5.6.3	<i>Reverse Energy Balance Approach</i>	155
5.6.4	<i>Method Implementation on Case Study</i>	156
5.7	SUMMARY & CONCLUSIONS	162
6.	SIMPLIFIED METHOD FOR FLEXURAL/ARCH CAPACITY ESTIMATION UNDER COLUMN LOSS	166
6.1	INTRODUCTION	166
6.2	METHOD DEVELOPMENT	166
6.2.1	<i>Assumptions</i>	166
6.2.2	<i>Description of Method</i>	168
6.2.3	<i>Moment-Rotation Curves</i>	174
6.2.4	<i>D Calibration</i>	176
6.3	RESULTS	178
6.4	CLOSED-FORM SOLUTION	184
6.5	TRIANGULAR DISTRIBUTED LOAD	190
6.5.1.1	Method Adaptation	190
6.5.1.2	Case Study Results Comparison	192
6.6	SUMMARY & CONCLUSIONS	193
7.	CONCLUSIONS	194
7.1	SUMMARY	194
7.2	RESEARCH CONTRIBUTIONS	194
7.3	KEY FINDINGS OF THE THESIS	195
7.3.1	<i>Key Findings from the Case Study Analyses</i>	195
7.3.1.1	Load-Carrying Capacity & Failure Mechanism	195
7.3.1.2	Influence of Column Removal Floor & Vierendeel Action	195
7.3.1.3	Contribution of Floor Slabs & Membrane Action	196
7.3.1.4	Effect of Removed Column Location	196

7.3.1.5	Influence of Load Type	197
7.3.1.6	Dynamic Increase Factors	197
7.3.1.7	Displacements at Peak Capacity & Failure	198
7.3.2	<i>Key Findings from the Simplified Analytical Method</i>	198
7.4	LIMITATIONS & FUTURE RESEARCH	198
7.4.1	<i>Building Configuration & Properties</i>	199
7.4.2	<i>Structural Response Evaluation Criterion</i>	199
7.4.3	<i>DIF Limitation</i>	199
7.4.4	<i>Bond Slip</i>	199
7.4.5	<i>Non-Structural Elements</i>	200
7.4.6	<i>APM Limitation</i>	200
7.4.7	<i>Simplified Method Improvement</i>	200
7.4.8	<i>The Need for More Experimental Studies</i>	200
REFERENCES	201
APPENDIX A.	SOFTWARE VALIDATION INPUT & RESULTS	A-1
APPENDIX B.	RESULTS OF ANALYSIS & DESIGN OF BUILDING IN SAP2000	B-1
APPENDIX C.	CASE STUDY DAMAGED MODELS	C-1

FIGURES

Figure 1-1: The Partial Collapse of the Ronan Point Building (Left) [2] & The Alfred P. Murrah Building (Right) [3]	1
Figure 1-2: Progressive Collapse Design Applicability Chart Flow According to the GSA Guidelines [6].....	5
Figure 2-1: Number of Experimental Research Papers by Specimen & Threat Dependency [14]	10
Figure 2-2: GSA-Prescribed Nonlinear Static Analysis DAF	13
Figure 2-3: Limit Points under Load-Control (Left) & Displacement-Control (Right) [34]	15
Figure 2-4: Arc-Length Procedure with Newton-Raphson Equilibrium Iterations [35]	16
Figure 2-5: Full Newton-Raphson Method (Left) & Modified Newton-Raphson Method (Right) [36].....	17
Figure 2-6: Deactivation of FEM Element & Creation of DEM Elements [38]	18
Figure 2-7: Element Connectivity & Deformation in FEM vs. AEM [41].....	18
Figure 2-8: Actual (Left) [47] vs. Simulated (Right) [41] Collapse of the Alfred P. Murrah Building	19
Figure 2-9: Top Grid Retrofit System [48]	20
Figure 2-10: Design Alternatives for Improving the Progressive Collapse Response of the Murrah Building [41]	21
Figure 2-11: Generic Load-Displacement Curve for Horizontally-Restrained Beam-Column Systems Under Static Pushdown	24
Figure 2-12: Compressive Arch Resistance Mechanism [54]	25
Figure 2-13: Tensile Catenary Resistance Mechanism [55]	25
Figure 2-14: Membrane Action in Slabs at Large Displacements [56]	26
Figure 2-15: Vierendeel Truss	26
Figure 3-1: Test Configuration & Selected Instrumentation [16].....	31
Figure 3-2: Structural Details of IMF Specimen (a) & SMF Specimen (b) [16].....	32
Figure 3-3: Concrete Dimensions & Rebar Details of S1 [25].....	33
Figure 3-4: Layout & Reinforcement Details of DF1 & DF2 (Dimensions Are in mm) [28]	34
Figure 3-5: Steel Assembly Details [28].....	35
Figure 3-6: Typical Layout & Reinforcement Details of the Specimens [30]	36
Figure 3-7: Building Plan	37
Figure 3-8: Interior Frame (Section A-A) Concrete Dimensions	38
Figure 3-9: Exterior Frame (Section B-B) Concrete Dimensions.....	38
Figure 3-10: Analysis Plan Chart	39

Figure 4-1: Abaqus Model for IMF Showing Meshed Solid Elements with Restraints (Left) & Embedded Rebar (Right)	41
Figure 4-2: Abaqus Model for SMF Showing Meshed Solid Elements with Restraints (Left) & Embedded Rebar (Right)	42
Figure 4-3: Response of Concrete to Uniaxial Loading in Compression (Left) & Tension (Right) [73]	43
Figure 4-4: Input Compression (Left) & Tension (Right) Stress-Strain Curves for Concrete in IMF.....	44
Figure 4-5: Input Compression (Left) & Tension (Right) Stress-Strain Curves for Concrete in SMF	44
Figure 4-6: Idealized Tension Stiffening Model for Concrete [80]	45
Figure 4-7: Input Stress-Strain Curves for Steel Rebar Sizes 8 (Left) & 9 (Right) in IMF.....	46
Figure 4-8: Input Stress-Strain Curves for Steel Rebar Size 8 in IMF & SMF	46
Figure 4-9: Input Stress-Strain Curves for Steel Rebar Sizes 4 (Left) & 10 (Right) in SMF.....	47
Figure 4-10: Force-Displacement Curves for IMF (Left) & SMF (Right)	48
Figure 4-11: Abaqus Model for T1 Showing Meshed Solid Elements with Restraints (Left) & Embedded Rebar (Right)	49
Figure 4-12: Abaqus Model for S1 Showing Meshed Solid Elements with Restraints (Left) & Embedded Rebar (Right)	49
Figure 4-13: Input Compression (Left) & Tension (Right) Stress-Strain Curves for Concrete in T1	50
Figure 4-14: Input Compression (Left) & Tension (Right) Stress-Strain Curves for Concrete in S1	50
Figure 4-15: Input Stress-Strain Curves for Steel Rebar Sizes R6 (Top Left), T10 (Top Right), T13 (Bottom Left) & T16 (Bottom Right) in T1 & S1	51
Figure 4-16: Force-Displacement Curves for T1 (Left) & S1 (Right)	52
Figure 4-17: Abaqus Model for DF2 Showing Meshed Solid Elements with Restraints (Left) & Embedded Rebar (Right)	53
Figure 4-18: Input Compression (Left) & Tension (Right) Stress-Strain Curves for Concrete in DF2.....	53
Figure 4-19: Input Stress-Strain Curves for Steel Rebar Sizes R6 (Top Left), T10 (Top Right), T13 (Bottom Left) & T16 (Bottom Right) in DF2	54
Figure 4-20: Generic Time-History for Column Loss Simulation	55
Figure 4-21: Vertical Displacement of the Corner Joint of DF2.....	56
Figure 4-22: Abaqus Model for D-0.91 Showing Meshed Solid Elements with Restraints (Left) & Embedded Rebar (Right)	57
Figure 4-23: Input Compression (Left) & Tension (Right) Stress-Strain Curves for Concrete in D-0.91	57
Figure 4-24: Input Stress-Strain Curves for Steel Rebar Sizes R3 (Top Left), R6 (Top Right), R8 (Middle Left), T10 (Middle Right) & T13 (Bottom) in D-0.91	58
Figure 4-25: Vertical Displacement at the Removed Column in D-0.91.....	60
Figure 5-1: Input Compression (Left) & Tension (Right) Stress-Strain Curves for Concrete.....	63

Figure 5-2: Input Stress-Strain Curves for Steel Rebar	63
Figure 5-3: Design 5% Damped Spectral Response Acceleration in Calgary	64
Figure 5-4: Lateral Force Distribution on SFRS.....	65
Figure 5-5: Rebar Plan.....	67
Figure 5-6: Interior Frame (Section A-A) Rebar Details.....	67
Figure 5-7: Exterior Frame (Section B-B) Rebar Details	68
Figure 5-8: Column Sections	68
Figure 5-9: Beam Sections	69
Figure 5-10: Abaqus Model for FF Showing Meshed Solid Elements with Restraints (Left) & Embedded Rebar (Right)	71
Figure 5-11: Closeup of FF Model Showing Meshed Solid Elements with Restraints (Left) & Embedded Rebar (Right)	71
Figure 5-12: Abaqus Model for BF Showing Meshed Solid Elements with Restraints (Left) & Embedded Rebar (Right)	72
Figure 5-13: Closeup of BF Model Showing Meshed Solid Elements with Restraints (Left) & Embedded Rebar (Right).....	72
Figure 5-14: Pushdown Curves for FF-CC Models	76
Figure 5-15: Von Mises Stresses (Left) & Total Displacement (Right) in Solid Elements for FF-CC-C1 Under Pushdown Analysis at 282% Design Load at First Fracture (Full Model Shown).....	76
Figure 5-16: Von Mises Stresses (Left) & Total Displacement (Right) in Solid Elements for FF-CC-C6 Under Pushdown Analysis at 259% Design Load at First Fracture (Full Model Shown).....	77
Figure 5-17: S11 Stresses in Truss Elements for FF-CC-C1 Under Pushdown Analysis at 282% Design Load at First Fracture, Full Model (Left) & Closeup on Plastic Hinge (Right).....	77
Figure 5-18: S11 Stresses in Truss Elements for FF-CC-C6 Under Pushdown Analysis at 259% Design Load at First Fracture, Full Model (Left) & Closeup on Plastic Hinge (Right).....	78
Figure 5-19: Logarithmic Strains in Truss Elements for FF-CC-C1 Under Pushdown Analysis at 282% Design Load at First Fracture, Full Model (Left) & Closeup on Plastic Hinge (Right)	78
Figure 5-20: Logarithmic Strains in Truss Elements for FF-CC-C6 Under Pushdown Analysis at 259% Design Load at First Fracture, Full Model (Left) & Closeup on Plastic Hinge (Right)	79
Figure 5-21: Von Mises Stresses in Solid Elements (Left) & S11 Stresses in Truss Elements (Right) for FF-CC-C1 Under Pushdown Analysis After Damage Propagation (Full Model Shown)	79
Figure 5-22: Von Mises Stresses in Solid Elements (Left) & S11 Stresses in Truss Elements (Right) for FF-CC-C6 Under Pushdown Analysis After Damage Propagation (Full Model Shown)	80
Figure 5-23: Pushdown Curves for BF-CC Models.....	81

Figure 5-24: Von Mises Stresses (Left) & Total Displacement (Right) in Solid Elements for BF-CC-C1 Under Pushdown Analysis at 155% Design Load at First Fracture (Full Model Shown)	82
Figure 5-25: Von Mises Stresses (Left) & Total Displacement (Right) in Solid Elements for BF-CC-C6 Under Pushdown Analysis at 113% Design Load at First Fracture (Full Model Shown)	82
Figure 5-26: S11 Stresses in Truss Elements for BF-CC-C1 Under Pushdown Analysis at 155% Design Load at First Fracture, Full Model (Left) & Closeup on Plastic Hinge (Right)	83
Figure 5-27: S11 Stresses in Truss Elements for BF-CC-C6 Under Pushdown Analysis at 113% Design Load at First Fracture, Full Model (Left) & Closeup on Plastic Hinge (Right)	83
Figure 5-28: Logarithmic Strains in Truss Elements for BF-CC-C1 Under Pushdown Analysis at 155% Design Load at First Fracture, Full Model (Left) & Closeup on Plastic Hinge (Right)	84
Figure 5-29: Logarithmic Strains in Truss Elements for BF-CC-C6 Under Pushdown Analysis at 113% Design Load at First Fracture, Full Model (Left) & Closeup on Plastic Hinge (Right)	84
Figure 5-30: Von Mises Stresses in Solid Elements (Left) & S11 Stresses in Truss Elements (Right) for BF-CC-C1 Under Pushdown Analysis After Damage Propagation (Full Model Shown)	85
Figure 5-31: Von Mises Stresses in Solid Elements (Left) & S11 Stresses in Truss Elements (Right) for BF-CC-C6 Under Pushdown Analysis After Damage Propagation (Full Model Shown)	85
Figure 5-32: Pushdown Curves for FF-IC Models	87
Figure 5-33: Von Mises Stresses (Left) & Total Displacement (Right) in Solid Elements for FF-IC-C1 Under Pushdown Analysis at 328% Design Load at First Fracture (Quarter Model Shown)	88
Figure 5-34: Von Mises Stresses (Left) & Total Displacement (Right) in Solid Elements for FF-IC-C6 Under Pushdown Analysis at 350% Design Load at First Fracture (Quarter Model Shown)	88
Figure 5-35: S11 Stresses in Truss Elements for FF-IC-C1 Under Pushdown Analysis at 328% Design Load at First Fracture, Quarter Model (Left) & Closeup on Plastic Hinge (Right)	89
Figure 5-36: S11 Stresses in Truss Elements for FF-IC-C6 Under Pushdown Analysis at 350% Design Load at First Fracture, Quarter Model (Left) & Closeup on Plastic Hinge (Right)	89
Figure 5-37: Logarithmic Strains in Truss Elements for FF-IC-C1 Under Pushdown Analysis at 328% Design Load at First Fracture, Quarter Model (Left) & Closeup on Plastic Hinge (Right)	90
Figure 5-38: Logarithmic Strains in Truss Elements for FF-IC-C6 Under Pushdown Analysis at 350% Design Load at First Fracture, Quarter Model (Left) & Closeup on Plastic Hinge (Right)	90
Figure 5-39: Von Mises Stresses in Solid Elements (Left) & S11 Stresses in Truss Elements (Right) for FF-IC-C1 Under Pushdown Analysis After Damage Propagation (Quarter Model Shown)	91
Figure 5-40: Von Mises Stresses in Solid Elements (Left) & S11 Stresses in Truss Elements (Right) for FF-IC-C6 Under Pushdown Analysis After Damage Propagation (Quarter Model Shown)	91

Figure 5-41: Pushdown Curves for BF-IC Models.....	93
Figure 5-42: Von Mises Stresses (Left) & Total Displacement (Right) in Solid Elements for BF-IC-C1 Under Pushdown Analysis at 141% Design Load at First Fracture (Quarter Model Shown).....	94
Figure 5-43: Von Mises Stresses (Left) & Total Displacement (Right) in Solid Elements for BF-IC-C6 Under Pushdown Analysis at 155% Design Load at First Fracture (Quarter Model Shown).....	94
Figure 5-44: S11 Stresses in Truss Elements for BF-IC-C1 Under Pushdown Analysis at 141% Design Load at First Fracture, Quarter Model (Left) & Closeup on Plastic Hinge (Right)	95
Figure 5-45: S11 Stresses in Truss Elements for BF-IC-C6 Under Pushdown Analysis at 155% Design Load at First Fracture, Quarter Model (Left) & Closeup on Plastic Hinge (Right)	95
Figure 5-46: Logarithmic Strains in Truss Elements for BF-IC-C1 Under Pushdown Analysis at 141% Design Load at First Fracture, Quarter Model (Left) & Closeup on Plastic Hinge (Right).....	96
Figure 5-47: Logarithmic Strains in Truss Elements for BF-IC-C6 Under Pushdown Analysis at 155% Design Load at First Fracture, Quarter Model (Left) & Closeup on Plastic Hinge (Right).....	96
Figure 5-48: Von Mises Stresses in Solid Elements (Left) & S11 Stresses in Truss Elements (Right) for BF-IC-C1 Under Pushdown Analysis After Damage Propagation (Quarter Model Shown)	97
Figure 5-49: Von Mises Stresses in Solid Elements (Left) & S11 Stresses in Truss Elements (Right) for BF-IC-C6 Under Pushdown Analysis After Damage Propagation (Quarter Model Shown)	97
Figure 5-50: Joint Displacements for FF-CC-C1 Subjected to Sudden Column Loss Under Different Load Values.....	99
Figure 5-51: Joint Displacements for FF-CC-C2 Subjected to Sudden Column Loss Under Different Load Values.....	100
Figure 5-52: Joint Displacements for FF-CC-C3 Subjected to Sudden Column Loss Under Different Load Values.....	100
Figure 5-53: Joint Displacements for FF-CC-C4 Subjected to Sudden Column Loss Under Different Load Values.....	101
Figure 5-54: Joint Displacements for FF-CC-C5 Subjected to Sudden Column Loss Under Different Load Values.....	101
Figure 5-55: Joint Displacements for FF-CC-C6 Subjected to Sudden Column Loss Under Different Load Values.....	102
Figure 5-56: Pseudo-Static Curves for FF Due to the Sudden Loss of CC at Each Floor	102
Figure 5-57: Von Mises Stresses (Left) & Total Displacement (Right) in Solid Elements for FF-CC-C1 Under Sudden Column Loss at 180% Design Load at First Fracture (Full Model Shown)	103
Figure 5-58: Von Mises Stresses (Left) & Total Displacement (Right) in Solid Elements for FF-CC-C6 Under Sudden Column Loss at 160% Design Load at First Fracture (Full Model Shown)	103
Figure 5-59: S11 Stresses in Truss Elements for FF-CC-C1 Under Sudden Column Loss at 180% Design Load at First Fracture, Full Model (Left) & Closeup on Plastic Hinge (Right).....	104
Figure 5-60: S11 Stresses in Truss Elements for FF-CC-C6 Under Sudden Column Loss at 160% Design Load at First Fracture, Full Model (Left) & Closeup on Plastic Hinge (Right).....	104

Figure 5-61: Logarithmic Strains in Truss Elements for FF-CC-C1 Under Sudden Column Loss at 180% Design Load at First Fracture, Full Model (Left) & Closeup on Plastic Hinge (Right)	105
Figure 5-62: Logarithmic Strains in Truss Elements for FF-CC-C6 Under Sudden Column Loss at 160% Design Load at First Fracture, Full Model (Left) & Closeup on Plastic Hinge (Right)	105
Figure 5-63: Von Mises Stresses in Solid Elements (Left) & S11 Stresses in Truss Elements (Right) for FF-CC-C1 Under Sudden Column Loss at 180% Design Load After Damage Propagation (Full Model Shown)	106
Figure 5-64: Von Mises Stresses in Solid Elements (Left) & S11 Stresses in Truss Elements (Right) for FF-CC-C6 Under Sudden Column Loss at 160% Design Load After Damage Propagation (Full Model Shown)	106
Figure 5-65: Joint Displacements for BF-CC-C1 Subjected to Sudden Column Loss Under Different Load Values	108
Figure 5-66: Joint Displacements for BF-CC-C2 Subjected to Sudden Column Loss Under Different Load Values	108
Figure 5-67: Joint Displacements for BF-CC-C3 Subjected to Sudden Column Loss Under Different Load Values	109
Figure 5-68: Joint Displacements for BF-CC-C4 Subjected to Sudden Column Loss Under Different Load Values	109
Figure 5-69: Joint Displacements for BF-CC-C5 Subjected to Sudden Column Loss Under Different Load Values	110
Figure 5-70: Joint Displacements for BF-CC-C6 Subjected to Sudden Column Loss Under Different Load Values	110
Figure 5-71: Pseudo-Static Curves for BF Due to the Sudden Loss of CC at Each Floor	111
Figure 5-72: Von Mises Stresses (Left) & Total Displacement (Right) in Solid Elements for BF-CC-C1 Under Sudden Column Loss at 100% Design Load at First Fracture (Full Model Shown)	111
Figure 5-73: Von Mises Stresses (Left) & Total Displacement (Right) in Solid Elements for BF-CC-C6 Under Sudden Column Loss at 60% Design Load at First Fracture (Full Model Shown)	112
Figure 5-74: S11 Stresses in Truss Elements for BF-CC-C1 Under Sudden Column Loss at 100% Design Load at First Fracture, Full Model (Left) & Closeup on Plastic Hinge (Right)	112
Figure 5-75: S11 Stresses in Truss Elements for BF-CC-C6 Under Sudden Column Loss at 60% Design Load at First Fracture, Full Model (Left) & Closeup on Plastic Hinge (Right)	113
Figure 5-76: Logarithmic Strains in Truss Elements for BF-CC-C1 Under Sudden Column Loss at 100% Design Load at First Fracture, Full Model (Left) & Closeup on Plastic Hinge (Right)	113
Figure 5-77: Logarithmic Strains in Truss Elements for BF-CC-C6 Under Sudden Column Loss at 60% Design Load at First Fracture, Full Model (Left) & Closeup on Plastic Hinge (Right)	114
Figure 5-78: Von Mises Stresses in Solid Elements (Left) & S11 Stresses in Truss Elements (Right) for BF-CC-C1 Under Sudden Column Loss at 100% Design Load After Damage Propagation (Full Model Shown)	114
Figure 5-79: Von Mises Stresses in Solid Elements (Left) & S11 Stresses in Truss Elements (Right) for BF-CC-C6 Under Sudden Column Loss at 60% Design Load After Damage Propagation (Full Model Shown)	115
Figure 5-80: Joint Displacements for FF-IC-C1 Subjected to Sudden Column Loss Under Different Load Values	116

Figure 5-81: Joint Displacements for FF-IC-C2 Subjected to Sudden Column Loss Under Different Load Values	117
Figure 5-82: Joint Displacements for FF-IC-C3 Subjected to Sudden Column Loss Under Different Load Values	117
Figure 5-83: Joint Displacements for FF-IC-C4 Subjected to Sudden Column Loss Under Different Load Values	118
Figure 5-84: Joint Displacements for FF-IC-C5 Subjected to Sudden Column Loss Under Different Load Values	118
Figure 5-85: Joint Displacements for FF-IC-C6 Subjected to Sudden Column Loss Under Different Load Values	119
Figure 5-86: Pseudo-Static Curves for FF Due to the Sudden Loss of IC at Each Floor	119
Figure 5-87: Von Mises Stresses (Left) & Total Displacement (Right) in Solid Elements for FF-IC-C1 Under Sudden Column Loss at 280% Design Load at First Fracture (Quarter Model Shown)	120
Figure 5-88: Von Mises Stresses (Left) & Total Displacement (Right) in Solid Elements for FF-IC-C6 Under Sudden Column Loss at 320% Design Load at First Fracture (Quarter Model Shown)	120
Figure 5-89: S11 Stresses in Truss Elements for FF-IC-C1 Under Sudden Column Loss at 280% Design Load at First Fracture, Quarter Model (Left) & Closeup on Plastic Hinge (Right)	121
Figure 5-90: S11 Stresses in Truss Elements for FF-IC-C6 Under Sudden Column Loss at 320% Design Load at First Fracture, Quarter Model (Left) & Closeup on Plastic Hinge (Right)	121
Figure 5-91: Logarithmic Strains in Truss Elements for FF-IC-C1 Under Sudden Column Loss at 280% Design Load at First Fracture, Quarter Model (Left) & Closeup on Plastic Hinge (Right)	122
Figure 5-92: Logarithmic Strains in Truss Elements for FF-IC-C6 Under Sudden Column Loss at 320% Design Load at First Fracture, Quarter Model (Left) & Closeup on Plastic Hinge (Right)	122
Figure 5-93: Von Mises Stresses in Solid Elements (Left) & S11 Stresses in Truss Elements (Right) for FF-IC-C1 Under Sudden Column Loss at 280% Design Load After Damage Propagation (Quarter Model Shown)	123
Figure 5-94: Von Mises Stresses in Solid Elements (Left) & S11 Stresses in Truss Elements (Right) for FF-IC-C6 Under Sudden Column Loss at 320% Design Load After Damage Propagation (Quarter Model Shown)	123
Figure 5-95: Joint Displacements for BF-IC-C1 Subjected to Sudden Column Loss Under Different Load Values	124
Figure 5-96: Joint Displacements for BF-IC-C2 Subjected to Sudden Column Loss Under Different Load Values	125
Figure 5-97: Joint Displacements for BF-IC-C3 Subjected to Sudden Column Loss Under Different Load Values	125
Figure 5-98: Joint Displacements for BF-IC-C4 Subjected to Sudden Column Loss Under Different Load Values	126
Figure 5-99: Joint Displacements for BF-IC-C5 Subjected to Sudden Column Loss Under Different Load Values	126
Figure 5-100: Joint Displacements for BF-IC-C6 Subjected to Sudden Column Loss Under Different Load Values	127
Figure 5-101: Pseudo-Static Curves for BF Due to the Sudden Loss of IC at Each Floor	127
Figure 5-102: Von Mises Stresses (Left) & Total Displacement (Right) in Solid Elements for BF-IC-C1 Under Sudden Column Loss at 100% Design Load at First Fracture (Quarter Model Shown)	128

Figure 5-103: Von Mises Stresses (Left) & Total Displacement (Right) in Solid Elements for BF-IC-C6 Under Sudden Column Loss at 100% Design Load at First Fracture (Quarter Model Shown)	128
Figure 5-104: S11 Stresses in Truss Elements for BF-IC-C1 Under Sudden Column Loss at 100% Design Load at First Fracture, Quarter Model (Left) & Closeup on Plastic Hinge (Right)	129
Figure 5-105: S11 Stresses in Truss Elements for BF-IC-C6 Under Sudden Column Loss at 100% Design Load at First Fracture, Quarter Model (Left) & Closeup on Plastic Hinge (Right)	129
Figure 5-106: Logarithmic Strains in Truss Elements for BF-IC-C1 Under Sudden Column Loss at 100% Design Load at First Fracture, Quarter Model (Left) & Closeup on Plastic Hinge (Right)	130
Figure 5-107: Logarithmic Strains in Truss Elements for BF-IC-C6 Under Sudden Column Loss at 100% Design Load at First Fracture, Quarter Model (Left) & Closeup on Plastic Hinge (Right)	130
Figure 5-108: Von Mises Stresses in Solid Elements (Left) & S11 Stresses in Truss Elements (Right) for BF-IC-C1 Under Sudden Column Loss at 100% Design Load After Damage Propagation (Quarter Model Shown)	131
Figure 5-109: Von Mises Stresses in Solid Elements (Left) & S11 Stresses in Truss Elements (Right) for BF-IC-C6 Under Sudden Column Loss at 100% Design Load After Damage Propagation (Quarter Model Shown)	131
Figure 5-110: Normalized Applied Load vs. Slope for FF-CC Models	134
Figure 5-111: Dynamic Increase Factor for FF-CC Models	134
Figure 5-112: Normalized Applied Load vs. Slope for BF-CC Models	135
Figure 5-113: Dynamic Increase Factor for BF-CC Models	135
Figure 5-114: Normalized Applied Load vs. Slope for FF-IC Models	136
Figure 5-115: Dynamic Increase Factor for FF-IC Models	136
Figure 5-116: Normalized Applied Load vs. Slope for BF-IC Models	137
Figure 5-117: Dynamic Increase Factor for BF-IC Models	137
Figure 5-118: Normalized Applied Load vs. Slope for PD-CC Models	139
Figure 5-119: Slab Effect Factor for PD-CC Models	139
Figure 5-120: Normalized Applied Load vs. Slope for CL-CC Models	140
Figure 5-121: Slab Effect Factor for CL-CC Models	140
Figure 5-122: Normalized Applied Load vs. Slope for PD-IC Models	141
Figure 5-123: Slab Effect Factor for PD-IC Models	141
Figure 5-124: Normalized Applied Load vs. Slope for CL-IC Models	142
Figure 5-125: Slab Effect Factor for CL-IC Models	142

Figure 5-126: Single-Story Reduced BF-IC Abaqus Quarter Model Showing Meshed Solid Elements (Left) & Embedded Rebar (Right)	146
Figure 5-127: Single-Frame Reduced BF-IC Abaqus Quarter Model Showing Meshed Solid Elements (Left) & Embedded Rebar (Right) ...	147
Figure 5-128: Pushdown Curves for BF-PD-IC-C6 & Reduced BF-IC Models	147
Figure 5-129: Von Mises Stresses (Left) & Total Displacement (Right) in Solid Elements for Single-Story Reduced BF-IC Model Under Pushdown Analysis at 152% Design Load at First Fracture (Quarter Model Shown)	148
Figure 5-130: S11 Stresses (Left) & Logarithmic Strains (Right) in Truss Elements for the Single-Story Reduced BF-IC Model Under Pushdown Analysis at 152% Design Load at First Fracture	148
Figure 5-131: Von Mises Stresses in Solid Elements (Left) & S11 Stresses in Truss Elements (Right) for the Single-Story Reduced BF-IC Model Under Pushdown Analysis After Damage Propagation (Quarter Model Shown).....	148
Figure 5-132: Von Mises Stresses (Left) & Total Displacement (Right) in Solid Elements for Single-Frame Reduced BF-IC Model Under Pushdown Analysis at 152% Design Load at First Fracture (Quarter Model Shown)	149
Figure 5-133: S11 Stresses (Left) & Logarithmic Strains (Right) in Truss Elements for the Single-Frame Reduced BF-IC Model Under Pushdown Analysis at 152% Design Load at First Fracture	149
Figure 5-134: Von Mises Stresses in Solid Elements (Left) & S11 Stresses in Truss Elements (Right) for the Single-Frame Reduced BF-IC Model Under Pushdown Analysis After Damage Propagation (Quarter Model Shown).....	149
Figure 5-135: Pushdown Curves for Single-Frame Reduced BF-IC Horizontally Unrestrained & Restrained Models Subjected to Concentrated Monotonic Downward Displacement	150
Figure 5-136: Pushdown Curves for Single-Frame Reduced BF-IC Horizontally Restrained Model Subjected to Load-Control & Displacement-Control Loading	152
Figure 5-137: Dynamic Response at Two Various Levels of Suddenly Applied Gravity Loading [13]	153
Figure 5-138: Pseudo-Static Response [13]	154
Figure 5-139: Actual vs. Generated Pseudo Static Curves for Single-Frame Reduced BF-IC Horizontally Restrained Model	155
Figure 5-140: Pushdown Curve Generated from Reverse Energy Balance Method vs. Displacement-Control Pushdown Curve for Single-Frame Reduced BF-IC Horizontally Restrained Model	156
Figure 5-141: Refined Pseudo-Static Curves	157
Figure 5-142: Load-Control vs. Displacement-Control (Projected) Pushdown Curves for FF-CC-C3	158
Figure 5-143: Load-Control vs. Displacement-Control (Projected) Pushdown Curves for FF-CC-C6	158
Figure 5-144: Load-Control vs. Displacement-Control (Projected) Pushdown Curves for BF-CC-C3	159
Figure 5-145: Load-Control vs. Displacement-Control (Projected) Pushdown Curves for BF-CC-C6	159
Figure 5-146: Load-Control vs. Displacement-Control (Projected) Pushdown Curves for FF-IC-C3	160
Figure 5-147: Load-Control vs. Displacement-Control (Projected) Pushdown Curves for FF-IC-C6	160

Figure 5-148: Load-Control vs. Displacement-Control (Projected) Pushdown Curves for BF-IC-C3.....	161
Figure 5-149: Load-Control vs. Displacement-Control (Projected) Pushdown Curves for BF-IC-C6.....	161
Figure 5-150: Average Normalized Load-Displacement Curves for All Models.....	162
Figure 5-151: Joint Displacements for C1 Models Under Sudden Column Loss at 40% Design Load	164
Figure 6-1: Idealization of the Structural System at the Beginning of the Flexural/Arch Phase	167
Figure 6-2: Procedure for Predicting the Initial Flexural/Arch Response.....	173
Figure 6-3: Maximum Load Sensitivity to Increment Size for IMF	174
Figure 6-4: Idealized Moment-Rotation Curve at Beam Ends.....	175
Figure 6-5: Stresses & Strains on Beam Cross Section	176
Figure 6-6: Relationship between D/h and L/h.....	177
Figure 6-7: Correlation Curve for D/h Values.....	177
Figure 6-8: Correlation Curves for P_{anal} Values (Left) & $y_{2,anal}$ Values (Right).....	180
Figure 6-9: Correlation Curve for $k_{p,anal}$ Values.....	180
Figure 6-10: Error Percentage in P_{anal} Values	181
Figure 6-11: Error Percentage in $y_{2,anal}$ Values	181
Figure 6-12: Comparison between Experimental & Analytical Load-Displacement Curves for Specimens IMF & SMF [16]	182
Figure 6-13: Comparison between Experimental & Analytical Load-Displacement Curves for Specimens P1 & P2 [24]	182
Figure 6-14: Comparison between Experimental & Analytical Load-Displacement Curves for Specimens S1 & S2 [20].....	182
Figure 6-15: Comparison between Experimental & Analytical Load-Displacement Curves for Specimens S3 to S8 [21]	183
Figure 6-16: Comparison between Experimental & Analytical Load-Displacement Curves for Specimens A1 to A6 [22]	184
Figure 6-17: Relationship between $y_{2,anal}/L$ & h/L	185
Figure 6-18: Relationship between $k_{F,anal}$ & $k_{p,anal}$	186
Figure 6-19: Correlation Curves for P_{ECFS} Values (Left) & $y_{2,ECFS}$ Values (Right).....	188
Figure 6-20: Correlation Curve for $k_{p,ECFS}$ Values.....	188
Figure 6-21: Error Percentage in P_{ECFS} Values	189
Figure 6-22: Error Percentage in $y_{2,ECFS}$ Values	189
Figure 6-23: Slab Load Distribution on Beams (Partial Floor Plan Shown).....	190
Figure 6-24: Modified Structural System & Free Body Diagram	191

Figure 6-25: Comparison between Numerical & Analytical Load-Displacement Curves for Models BF-IC-C3 and BF-IC-C6	192
Figure A-1: Normal Stresses in Concrete in X-Direction (Left) & Rebar (Right) for IMF During Rising Arch Action, Declining Arch Action & Catenary Action	A-1
Figure A-2: Normal Stresses in Concrete in X-Direction (Left) & Rebar (Right) for SMF During Rising Arch Action, Declining Arch Action & Catenary Action	A-2
Figure A-3: Normal Stresses in Concrete in X-Direction (Left) & Rebar (Right) for T1 During Rising Arch Action, Declining Arch Action & Catenary Action	A-3
Figure A-4: Normal Stresses in Concrete in X-Direction (Left) & Rebar (Right) for S1 During Rising Arch Action, Declining Arch Action & Catenary Action	A-4
Figure A-5: Total Displacement in Solid Elements (Left) & Truss Elements (Right) in DF2 at the End of the Analysis	A-5
Figure A-6: Von Mises Stresses in Solid Elements (Left) & S11 Stresses in Truss Elements (Right) in DF2 at the End of the Analysis	A-5
Figure A-7: Total Displacement in Solid Elements (Left) & Truss Elements (Right) in D-0.91 at the End of the Analysis	A-6
Figure A-8: Von Mises Stresses in Solid Elements (Left) & S11 Stresses in Truss Elements (Right) in D-0.91 at the End of the Analysis	A-6
Figure B-1: Deformed Shape (Scale Factor = 50) Due to Service Loads (mm)	B-1
Figure B-2: Bending Moments in X-Direction in Typical Slab Due to Combo 1 (kN.mm)	B-2
Figure B-3: Axial Forces in Interior Frames Due to Combo 1 (kN)	B-3
Figure B-4: In-Plane Shear Forces in Interior Frames Due to Combo 1 (kN)	B-4
Figure B-5: In-Plane Bending Moments in Interior Frames Due to Combo 1 (kN.mm)	B-5
Figure B-6: Required Reinforcing Area in Interior Frames According to CSA A23.3-14 [69] (mm ²)	B-6
Figure B-7: Axial Forces in Exterior Frames Due to Combo 1 (kN)	B-7
Figure B-8: Axial Forces in Exterior Frames Due to Combo 2 (kN)	B-8
Figure B-9: In-Plane Shear Forces in Exterior Frames Due to Combo 1 (kN)	B-9
Figure B-10: In-Plane Shear Forces in Exterior Frames Due to Combo 2 (kN)	B-10
Figure B-11: In-Plane Bending Moments in Exterior Frames Due to Combo 1 (kN.mm)	B-11
Figure B-12: In-Plane Bending Moments in Exterior Frames Due to Combo 2 (kN.mm)	B-12
Figure B-13: Reinforcing Area in Exterior Frames According to CSA A23.3-14 [69] (mm ²)	B-13
Figure C-1: Abaqus Model for FF-CC-C1 Showing Meshed Solid Elements with Restraints (Left) & Embedded Rebar (Right)	C-1
Figure C-2: Abaqus Model for FF-CC-C2 Showing Meshed Solid Elements with Restraints (Left) & Embedded Rebar (Right)	C-1
Figure C-3: Abaqus Model for FF-CC-C3 Showing Meshed Solid Elements with Restraints (Left) & Embedded Rebar (Right)	C-2

Figure C-4: Abaqus Model for FF-CC-C4 Showing Meshed Solid Elements with Restraints (Left) & Embedded Rebar (Right).....C-2

Figure C-5: Abaqus Model for FF-CC-C5 Showing Meshed Solid Elements with Restraints (Left) & Embedded Rebar (Right).....C-3

Figure C-6: Abaqus Model for FF-CC-C6 Showing Meshed Solid Elements with Restraints (Left) & Embedded Rebar (Right).....C-3

Figure C-7: Abaqus Model for BF-CC-C1 Showing Meshed Solid Elements with Restraints (Left) & Embedded Rebar (Right)C-4

Figure C-8: Abaqus Model for BF-CC-C2 Showing Meshed Solid Elements with Restraints (Left) & Embedded Rebar (Right)C-4

Figure C-9: Abaqus Model for BF-CC-C3 Showing Meshed Solid Elements with Restraints (Left) & Embedded Rebar (Right)C-5

Figure C-10: Abaqus Model for BF-CC-C4 Showing Meshed Solid Elements with Restraints (Left) & Embedded Rebar (Right)C-5

Figure C-11: Abaqus Model for BF-CC-C5 Showing Meshed Solid Elements with Restraints (Left) & Embedded Rebar (Right)C-6

Figure C-12: Abaqus Model for BF-CC-C6 Showing Meshed Solid Elements with Restraints (Left) & Embedded Rebar (Right)C-6

Figure C-13: Abaqus Model for FF-IC-C1 Showing Meshed Solid Elements with Restraints (Left) & Embedded Rebar (Right).....C-7

Figure C-14: Abaqus Model for FF-IC-C2 Showing Meshed Solid Elements with Restraints (Left) & Embedded Rebar (Right).....C-7

Figure C-15: Abaqus Model for FF-IC-C3 Showing Meshed Solid Elements with Restraints (Left) & Embedded Rebar (Right).....C-8

Figure C-16: Abaqus Model for FF-IC-C4 Showing Meshed Solid Elements with Restraints (Left) & Embedded Rebar (Right).....C-8

Figure C-17: Abaqus Model for FF-IC-C5 Showing Meshed Solid Elements with Restraints (Left) & Embedded Rebar (Right).....C-9

Figure C-18: Abaqus Model for FF-IC-C6 Showing Meshed Solid Elements with Restraints (Left) & Embedded Rebar (Right).....C-9

Figure C-19: Abaqus Model for BF-IC-C1 Showing Meshed Solid Elements with Restraints (Left) & Embedded Rebar (Right)C-10

Figure C-20: Abaqus Model for BF-IC-C2 Showing Meshed Solid Elements with Restraints (Left) & Embedded Rebar (Right)C-10

Figure C-21: Abaqus Model for BF-IC-C3 Showing Meshed Solid Elements with Restraints (Left) & Embedded Rebar (Right)C-11

Figure C-22: Abaqus Model for BF-IC-C4 Showing Meshed Solid Elements with Restraints (Left) & Embedded Rebar (Right)C-11

Figure C-23: Abaqus Model for BF-IC-C5 Showing Meshed Solid Elements with Restraints (Left) & Embedded Rebar (Right)C-12

Figure C-24: Abaqus Model for BF-IC-C6 Showing Meshed Solid Elements with Restraints (Left) & Embedded Rebar (Right)C-12

TABLES

Table 1-1: Risk Categories & Design Requirements According to the UFC Guidelines [7]	4
Table 3-1: Summary of Chosen Experiments	30
Table 3-2: Average Compressive & Tensile Strength of 152x305 mm Concrete Cylinders [16]	31
Table 3-3: Average Mechanical Properties of Reinforcing Bars [16]	31
Table 4-1: Abaqus CDP Plasticity Parameters	45
Table 5-1: Critical Design Load Combinations	66
Table 5-2: Case Study Models	70
Table 5-3: Period of Vibration of the Building Models	73
Table 5-4: Maximum Pushdown Analysis Values for FF-CC Models	74
Table 5-5: Maximum Pushdown Analysis Values for BF-CC Models	80
Table 5-6: Maximum Pushdown Analysis Values for FF-IC Models	86
Table 5-7: Maximum Pushdown Analysis Values for BF-IC Models	92
Table 5-8: Maximum Column Loss Analysis Values for FF-CC Models	98
Table 5-9: Maximum Column Loss Analysis Values for BF-CC Models	107
Table 5-10: Maximum Column Loss Analysis Values for FF-IC Models	115
Table 5-11: Maximum Column Loss Analysis Values for BF-IC Models	124
Table 5-12: Dynamic Increase Factors for Nonlinear Static analysis [6], [7]	132
Table 5-13: Calculation of Dynamic Increase Factors According to the GSA & UFC Guidelines	133
Table 5-14: Comparison of DIF Values Obtained from the Analysis with Guideline-Prescribed Values	133
Table 5-15: Average Slab Effect Factor Values	143
Table 5-16: Average Simplified Slab Effect Factor Values	144
Table 5-17: Average CLE Values	145
Table 5-18: Maximum Pushdown Analysis Values for Original & Reduced BF-IC Models	147
Table 5-19: Comparison of DIF Values	162
Table 5-20: Average Load Capacities & Corresponding Displacements	163
Table 6-1: Maximum Load & Corresponding Displacement for Different Increment Sizes for IMF	174
Table 6-2: Comparison between Experimental & Analytical Results at Peak Flexural/Arch Resistance	179

Table 6-3: Comparison of Empirical Results with Experimental & Analytical Results 187

1. INTRODUCTION

1.1 BACKGROUND

In 1968, in East London, Mrs. Ivy Hodge, who lived on the eighteenth floor of the Ronan Point Tower, unaware of a gas leak, lit up a match to light the stove, and an explosion occurred. The blast took down the concrete bearing walls of her kitchen which in turn triggered the collapse of an entire corner of the building (Figure 1-1), killing five people in the process and injuring seventeen others. The disproportionate nature of the Ronan Point collapse became a subject of interest for researchers and engineers. As a result, changes in the British Standards as well as the American and Canadian codes of practice were implemented to ensure a minimum level of structural integrity [1]. However, these new provisions dealt with progressive collapse resistance in an indirect way by providing adequate ductility, continuity and redundancy to ensure that the structure was robust enough to resist extreme loading conditions.



Figure 1-1: The Partial Collapse of the Ronan Point Building (Left) [2] & The Alfred P. Murrah Building (Right) [3]

The need for a more direct analysis procedure became more evident after the partial collapse of the Alfred P. Murrah federal building in Oklahoma City. On Wednesday, April 19th, 1995, a bomb placed in a truck was detonated in front of the building, bringing almost half the structure to the ground (Figure 1-1) and killing 168 people in the process. This partial collapse can be attributed to the failure of the third floor's transfer girder after the complete damage of one of its supporting columns [4].

CHAPTER 1. INTRODUCTION

The Oklahoma bombing followed by the collapse of the Twin Towers on September 11th, 2001, influenced the introduction of progressive collapse assessment and design guidelines by the US General Service Administration (GSA) and by the US Department of Defense (DOD).

1.2 DESIGN APPROACHES

Progressive collapse is a low probability/high consequence (LPHC) event [5] defined as “an extent of damage or collapse that is disproportionate to the magnitude of the initiating event” [6] and is therefore sometimes referred to as disproportionate collapse. The design of buildings to resist this type of collapse is not as straight forward as designing for gravity or lateral loads. The ambiguity associated with events that could cause progressive collapse poses a lot of difficulties in developing an efficient and effective design methodology. In general, progressive collapse design can be divided into two distinct approaches.

1.2.1 INDIRECT DESIGN APPROACH

Indirect design methods are similar to the early guidelines formulated in the aftermath of the Ronan Point building collapse. With this approach, progressive collapse is only accounted for implicitly by ensuring that the building possesses minimum levels of strength, continuity and ductility [7]. The following two indirect methods are prescribed by the United Facilities Criteria (UFC), released by the DOD.

1.2.1.1 TIE FORCE METHOD (TF)

The TF ensures that the structural elements (slabs, beams and columns) possess a minimum amount of tensile strength to transfer the load from any damaged portion of the structure through axial forces and catenary behavior.

1.2.1.2 ENHANCED LOCAL RESISTANCE (ELR) METHOD

The ELR ensures that a ductile failure occurs when vertical support members (columns and walls) are laterally loaded by increasing their flexural and shear strengths. To ensure a non-brittle failure, the shear strength of these elements must be higher than the shear demand associated with their flexural strength.

1.2.2 DIRECT DESIGN APPROACH

Direct design methods can be further classified into threat-dependent and threat-independent methods. In the former, the building is designed to withstand a specific extreme loading case while in the latter, the building is designed to remain stable after suffering local damage regardless of its cause.

CHAPTER 1. INTRODUCTION

1.2.2.1 SPECIFIC LOAD RESISTANCE (SLR) METHOD

The SLR is a threat-dependent method used to test whether a structure is capable of resisting a specific extreme load without progressive collapse. The problem with this method is that, due to the inherent uncertain nature of abnormal events, it is hard to define and quantify the design threat, which may lead to either an uneconomic or an unconservative design. However, the use of SLR in progressive collapse analysis and design can be found in many literatures. Some researchers studying the subject of progressive collapse have examined the effects of fire and blast loads on structures. In [8], a multi-story building is analyzed in the event of a terrorist attack. The building is subjected to a specific blast load, which is defined by the type, weight and stand-off distance of the bomb. The analysis was carried out in two stages, local and global. The local analysis was performed on a single column to examine the minimum stand-off distance, below which the column would be severely damaged and therefore removed from the global model. The global model was then conducted for the whole structure, and the columns close enough to the bomb to be severely damaged were removed from the analysis. A similar approach was also used in [9], and the results were validated with experimental data.

1.2.2.2 ALTERNATE PATH METHOD (APM)

The APM is a threat-independent method that examines the ability of the structure to bridge over a removed structural element without damage propagation (i.e., damage is localized). In this method, the extreme event that caused the local damage is not considered. The resulting local failure, however, is what's important, and the building should be able to remain stable after the removal of a specific structural element. One of the limitations of this method lies in the oversimplified post-event damage. The likelihood of an extreme event occurring that causes the complete failure of only one element is very low, as argued in [10]. Instead, a partially distributed damage method was proposed, in which extreme event damage is distributed between two columns using damage indices. The results of the study were then compared with those obtained from the APM, and show that the latter, in most cases, can be unconservative. Two partially damaged columns can generally be more critical than one completely damaged (removed) column. Nevertheless, it is this very simplicity and threat-independence that make the APM both flexible and, consequently, the primary method recommended by progressive collapse guidelines.

1.3 GUIDELINES

1.3.1 UNITED FACILITIES CRITERIA (UFC)

The DoD first issued the UFC guidelines for the “Design of Buildings to Resist Progressive Collapse” [7] in 2005. A more refined edition was published in 2009, with subsequent updates through Change 4, released in 2024. Three design methods were provided, the TF, ELR and APM, to be followed according to the building’s risk category which is defined according to Table 2-2 of UFC 4-023-03 [7], reproduced as Table 1-1 in this thesis, and Table 2-2 of UFC 3-301-01 [11].

The applicability criteria for progressive collapse design under the UFC guidelines are outlined in Section 1-2 of UFC 4-023-03 [7], which defines the scope of buildings subject to these requirements based on factors such as height, occupancy and operational characteristics, including whether the building involves new construction, major renovation or leasing. Compliance is mandatory for new construction of buildings three or more stories high, while application to existing buildings is determined by the project authority or jurisdiction.

Table 1-1: Risk Categories & Design Requirements According to the UFC Guidelines [7]

Risk Category	Design Requirement
I	No specific requirements
II	Option 1: Tie Forces (TF) for the entire structure and Enhanced Local Resistance (ELR) for the corner and penultimate columns or walls at the first story OR Option 2: Alternate Path (AP) for specified column and wall removal locations
III	Alternate Path (AP) for specified column and wall removal locations and Enhanced Local Resistance (ELR) for all perimeter first story columns or walls
IV	Tie Forces (TF) and Alternate Path (AP) for specified column and wall removal locations and Enhanced Local Resistance (ELR) for all perimeter first story columns or walls

1.3.2 GENERAL SERVICE ADMINISTRATION (GSA)

The GSA released its first progressive collapse design guidelines in 2003 where the same methods mentioned in the previous section and prescribed by the DOD’s UFC were employed. However, in its latest release [6], in 2013, the GSA eliminated the TF and ELR and left the APM as the only method allowed to be used in the design of buildings to resist progressive collapse. The load combination factors were changed to match those used in the more modern UFC in an effort to unify the progressive collapse design guidelines and make use of the latest observations and research in the subject. The applicability of the GSA guidelines is summarized in the flow chart presented in Figure 1-2, which outlines the conditions under which progressive collapse design is required.

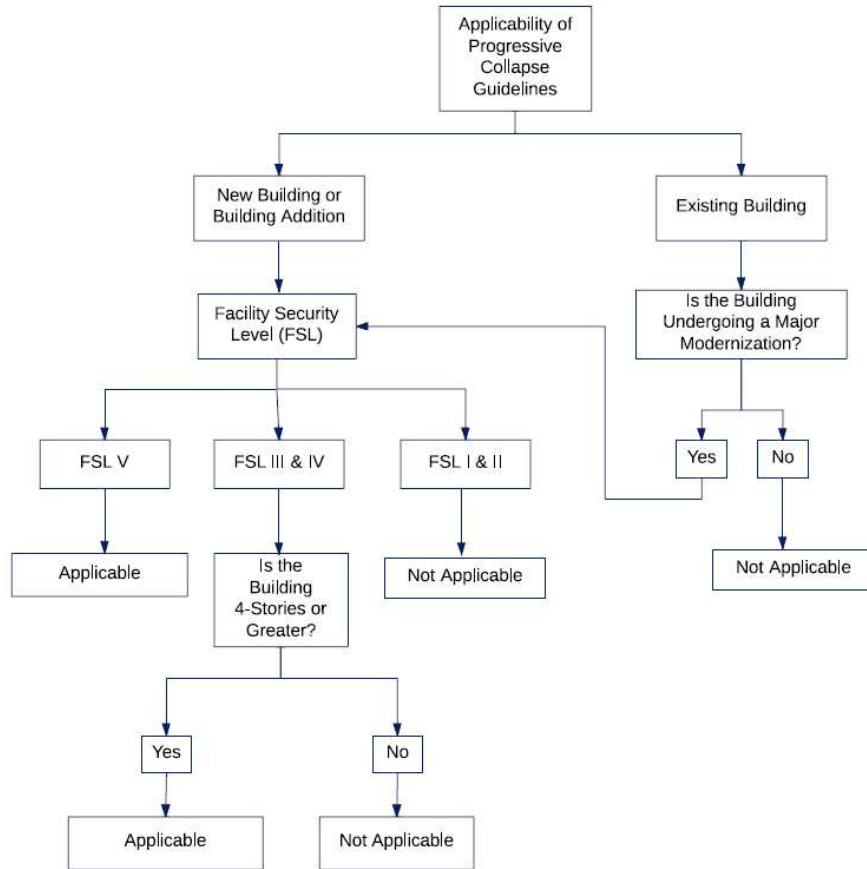


Figure 1-2: Progressive Collapse Design Applicability Chart Flow According to the GSA Guidelines [6]

1.4 ANALYSIS & DESIGN PROCEDURES

1.4.1 ANALYSIS PROCEDURES

Essentially, progressive collapse is a structurally nonlinear dynamic problem, usually caused by extreme loading events such as vehicle collisions, accidental explosions, terrorist bombings [12] or simply the sudden failure of a structural member due to material degradation, fatigue, steel corrosion, etc. However, the GSA does not require the use of any specific analysis procedure, and instead allows the use of “alternative rational analysis” procedures as long as they are based on fundamental principles of engineering [6]. Acceptable analysis may include the use of Finite Element Method (FEM), Applied Element Method (AEM) as well as hand calculations. This flexibility in the analysis procedure also means that 2D models can be used instead of 3D models, as long as they comply with the performance objectives and fulfill the acceptance criteria of the guidelines. Also, due to the complexity and time-consuming nature of nonlinear dynamic analysis (NDA), static methods may be used in combination with dynamic amplification factors (DAF) as well as linear methods with demand modifiers to account for plastic

CHAPTER 1. INTRODUCTION

behavior. The latest GSA guidelines allow the use of the following three types of analysis in progressive collapse design.

1.4.1.1 LINEAR STATIC ANALYSIS (LSA)

LSA is the simplest method of analysis where loads are applied once in a linear static analysis. In order to account for the dynamic nature of the extreme event a DAF is applied to the gravity loads. Furthermore, a demand modifier (m-factor) is applied to the expected capacity of the structural element in deformation-controlled actions to account for the ductility and plastic behavior of the member. The m-factor can be regarded as the maximum allowable demand-capacity ratio (DCR). The GSA allows the use of LSA for regular buildings up to ten stories.

1.4.1.2 NONLINEAR STATIC ANALYSIS (NSA)

Also allowed by the GSA is NSA which accounts for the nonlinearity of the structure by incrementally applying the gravity loads and calculating the response of the structure. Usually referred to as pushdown analysis, this procedure resembles the pushover analysis used in lateral load design. A DAF, however, is still required to account for the dynamic effects of the structural response. Another NSA method, not included in the GSA guidelines, developed in [13], does not require the use of a DAF. In this method, the potential energy released by the column's removal is balanced with the internal strain energy, and the deformation capacity required to stabilize the structure is evaluated [1].

1.4.1.3 NONLINEAR DYNAMIC ANALYSIS (NDA)

NDA is the most accurate analysis procedure as it takes into account inertial effects as well as material and geometric nonlinearities [6], and therefore, no DAFs or m-factors are needed. Using a time integration procedure, the response of the structure can be determined as a function of time.

1.4.2 DESIGN CRITERIA

In general, the design methodology for any analysis method is more or less the same. After the analysis, the actions and/or deformations are checked against, and should not exceed, the allowable capacities of any element at any cross section. First, the loads are combined using the following general gravity load combination prescribed by the GSA:

$$G = \Omega [1.2 D + (0.5 L \text{ or } 0.2 S)]$$

where G = Design gravity loads,

CHAPTER 1. INTRODUCTION

Ω = Load increase factor, dynamic amplification factor or dynamic increase factor in case of LSA and NSA, respectively, for bays immediately adjacent to the removed element and all floors above it = 1 for all other bays and floors and in case of NDA,

D = Dead load including façade loads,

L = Live load including live load reduction, not to exceed 2.4 kN/m²,

S = Snow load.

Then, the safety of the structure is checked using the following general acceptance criteria:

$$\Phi m Q_{L/E} \geq Q_U$$

where Φ = Strength reduction factor in case of force-controlled actions and LSA-deformation-controlled actions = 1 in case of NSA- and NDA-deformation-controlled actions,

m = m-factor (demand modifier) in case of LSA-deformation-controlled actions = 1 in all other cases,

$Q_{L/E}$ = Lower-bound strength in case of LSA-force-controlled actions, NSA and NSP = expected strength in case of LSA-deformation-controlled actions = expected deformation capacity in case of NSA- and NDA-deformation-controlled actions,

Q_U = LSA action, NSA-force-controlled action and NDA-force-controlled action = NSA and NDA deformation in case of deformation-controlled actions.

1.5 MOTIVATION & APPROACH

The study of progressive collapse of structures is one that is still constantly evolving. More research is still needed to advance our knowledge in the subject and create a more coherent framework for the design of buildings against such phenomenon. Unfortunately, while full-scale testing of whole structures is definitely the best way to examine the behavior of structures under extreme loading conditions, it is usually not the most practical and feasible way. However, experimental studies on sub-assemblages and scaled structural systems may still provide valuable insight into the response and resistance of structures to disproportionate collapse. These results can be used to calibrate numerical models capable of accurately simulating the nonlinear behavior of RC structures under extreme conditions. Such validated models, in turn, support the development of simplified tools that make progressive collapse assessment more practical for everyday design.

In this research, a numerical study is conducted with the main focus being on the APM since it is the primary method prescribed in the progressive collapse design guidelines. A case study building is considered and analyzed extensively for progressive collapse using the APM. First, however, data produced from experiments available in

the literature were used to validate the chosen software for creating reliable structural analysis models. This validation was essential to ensure the credibility of the modeling approach and the subsequent analytical results.

1.6 RESEARCH OBJECTIVES

The ability of a structure to resist progressive collapse in column loss scenarios begins with the robustness of the structural members directly supported by the removed column. If these immediate members are able to withstand the load redistribution as well as the dynamic impact caused by the extreme event, the likelihood of a disproportionate collapse reduces significantly. It is, therefore, more computationally economic to study the progressive collapse behavior of sub-systems without sacrificing too much accuracy and relevance. A large portion of progressive collapse research is focused on the behavior of single-story sub-assemblages, where only part of the structure is taken from one floor and examined.

Furthermore, numerous numerical studies have been conducted on bare structures where floor slabs were not included in the model, for simplicity and time saving. However, as of late, there has been a noticeable increase in research exploring the role of slabs in progressive collapse scenarios. While this growing interest has undoubtedly enriched our understanding of slab contribution, there still remains a need to reinforce and consolidate these findings, especially through comprehensive comparisons between full-frame and bare-frame behavior under different column loss scenarios.

Another common approximation is to use nonlinear quasi-static analysis in place of nonlinear dynamic analysis, given its lower computational cost and simpler implementation. While the use of dynamic analysis has become more widespread in recent studies, particularly as computing power improves, there is still a need for deeper investigation, especially in terms of how different modeling assumptions, structural configurations and loading conditions affect the dynamic response.

In this research, focusing on regular RC framed structures, the main objectives are as follows:

1. **Investigate the Influence of Floor Slabs on Progressive Collapse Resistance**

Floor slabs play a crucial role in redistributing loads and enhancing structural resilience during column loss scenarios. This research aims to quantify the contribution of floor slabs by comparing the progressive collapse response of bare frames (without slabs) and full frames (with slabs) under different column removal scenarios.

2. **Examine the Effect of Column Location on Progressive Collapse Resistance**

The structural response to column loss varies depending on whether the removed column is an interior or corner column. This study will assess the differences in load redistribution, deformation and load capacities,

and failure mechanisms associated with each case to better understand the role of column location in progressive collapse resistance. Additionally, the effect of removing a column from different floors will be investigated to determine how the building's response varies across its height.

3. Compare Nonlinear Static and Nonlinear Dynamic Analyses for Predicting Progressive Collapse Response

Due to the computational cost of nonlinear dynamic analysis, many studies rely on nonlinear static analysis as a more practical alternative. This research will compare both approaches to evaluate their relative accuracy in predicting structural behavior under sudden column loss conditions. By performing both nonlinear static and nonlinear dynamic analyses, the dynamic increase factor (DIF) will be determined as the ratio of dynamic to static response values. The obtained DIFs will then be compared with the values prescribed by progressive collapse guidelines to assess their accuracy and applicability.

4. Evaluate the Accuracy of Model Reduction Approaches

Many progressive collapse studies utilize model reduction techniques, such as single-story sub-assemblages or single-frame models, to reduce computational effort. This study will systematically assess the accuracy of these simplifications by comparing their results with those obtained from full models.

5. Develop a Simplified Method for Evaluating Progressive Collapse Response

Given the complexity of high-fidelity numerical models, there is a need for a simplified yet reliable method to estimate progressive collapse behavior. This research aims to develop such a method based on analytical approximations while validating its accuracy against both numerical and experimental results. By ensuring a balance between computational efficiency and predictive reliability, the proposed method will provide a practical tool for assessing progressive collapse resistance.

2. LITERATURE REVIEW

2.1 INTRODUCTION

This chapter presents a review of the existing research related to the progressive collapse of reinforced concrete framed structures. It covers key experimental investigations on quasi-static and dynamic column loss scenarios, different numerical modeling approaches and various structural analysis methods used to simulate collapse behavior. Additionally, concepts related to structural robustness and the main resistance mechanisms activated during progressive collapse are discussed. The chapter concludes by summarizing previous work and identifying key challenges and gaps that motivate the focus of this study.

2.2 EXPERIMENTAL WORK

Due to the extreme nature of progressive collapse, data from actual events remain scarce. Therefore, experimental studies are fundamental to our understanding of progressive collapse resistance [14]. In the last couple of decades, interest in progressive collapse research has significantly risen, spurring an increase in experimental studies of the subject. In [14], a summary of the experimental research in the field is presented, where 158 papers are found and categorized by specimen type and threat dependency (Figure 2-1). The majority of the studies found here were conducted on sub-assemblages. Possibly, this is not only due to practical and economic reasons, but also because the damage caused by single column removal is usually localized and does not spread outside of the vicinity of the column [15]. The summary chart, taken from a 2021 publication [14], provides a valuable snapshot of experimental efforts up to that point. Though it excludes more recent developments, it remains useful for understanding the focus areas and methodological trends that shaped earlier work. More recent research, though not captured in this figure, has continued to evolve toward more complex and diversified investigations.

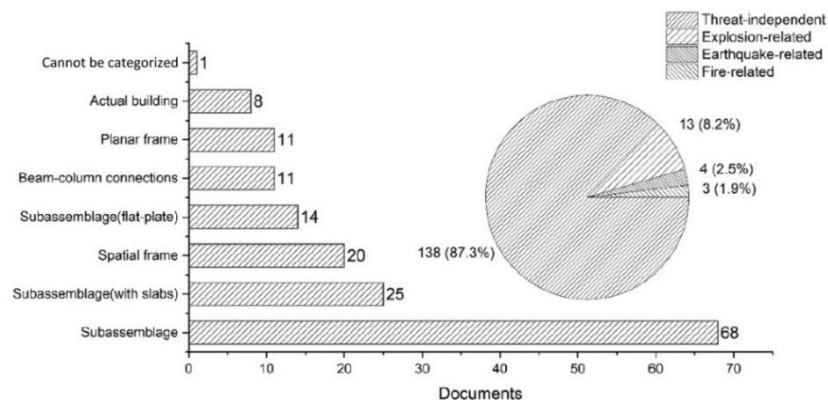


Figure 2-1: Number of Experimental Research Papers by Specimen & Threat Dependency [14]

2.2.1 QUASI-STATIC EXPERIMENTS

A common way to study the progressive collapse resistance of systems and sub-systems is to conduct monotonic quasi-static loading tests. These kinds of tests are a bit easier to conduct as they don't require the simulation of column removal. The specimen is usually slowly loaded up to large deformations until it fails, and by means of load cells, strain gauges and other sensors, the response is recorded. In [16], two full-scale reinforced concrete beam-column sub-assemblages were subjected to monotonic pushdown loading at their middle columns up to their full collapse. One specimen was of an intermediate moment frame (IMF) and the other of a special moment frame (SMF). The study highlighted the effect of stiffness and reinforcement on the nonlinear response of the system. The same experiment was replicated on a three-tenths-scale model of the IMF in [17]. The results of the scaled specimen were compared with the full-scale model and showed similar overall behavior and response. More beam-column sub-assembly pushdown tests were conducted on the middle column in [18], [19], [20], [21], [22]. Another recent big study was conducted and summarized in [23], where twelve one-quarter-scale precast concrete specimens were tested under quasi-static loading. The specimens had different types of beam-columns, eight of which were wet, and four were dry. Moreover, the effect of flanges, transverse beams and slabs were also examined in the study. In [24] and [25], the out-of-plane effect of secondary beams as well as the effect of the membrane action provided by the slab was studied when six one-quarter-scale specimens were subjected to monotonic displacement at a middle joint. Two specimens were two-dimensional beam-column sub-systems, two were three-dimensional beam-column sub-systems and, finally, two were slab-beam-column sub-systems. The effect of slab aspect ratio was also examined in the study. While the majority of experimental research has been concerned with the removal of middle or interior columns, some studies examined the effect of corner column removal on the system. For instance, in [26], a comparison was made between the response of the sub-assembly to the removal of the corner column and the removal of the exterior column. The effect of slabs was also investigated here.

2.2.2 DYNAMIC COLUMN LOSS EXPERIMENTS

As discussed, reproducing a column loss scenario on a full-scale structure may not be practically or economically feasible. This explains the shortage of experiments such as [27], where a full-scale two-story flat slab structure was subjected to the sudden removal of one of its corner columns. The structure did not suffer any extensive damage as the building was able to bridge over the damaged element and redistribute its loads safely to the adjacent members. However, it is a bit easier to simulate the column removal in a lab experiment as done in [28], where six one-third-scale specimens were tested for the sudden loss of their corner column. The models were

beam-column sub-assemblages with varying designs to study the effects of seismic detailing, span length, aspect ratio and other factors on the behavior of the system. In [29] and [30], two one-quarter-scale specimens were tested under dynamic column loss. The results were compared with each other and with a third control specimen subjected to pushdown loading. Similar experiments are further needed to enhance our understanding of the building's response to column removal and to improve our numerical models and simplified methods used to design for extreme loading cases such as progressive collapse.

2.3 **MODELING**

The most fundamental principles of structural analysis and mechanics are built on assumptions and idealizations, without which, it would be almost impossible to predict the structural behavior of buildings under any type of loading. Although approximations are commonplace in structural engineering, simplified methods should be carefully selected, especially when dealing with progressive collapse. For instance, although 2D analysis is widely accepted in gravity load design, it is not recommended in the case of progressive collapse, especially in the case of irregular buildings. Even though the GSA allows it in special cases, 2D analysis fails to account for out-of-plane resistance mechanisms such as flexural, membrane, arching and catenary actions of slabs and secondary beams. Generally, in progressive collapse, load redistribution paths and resisting elements often include secondary members. For example, joists, struts, non-structural walls or infill panels can act as primary members [12]. It is argued in [1] that the observed robustness of framed buildings during World War II can be attributed to the use of solid masonry infill panel walls in facades as well as internal partitions, contrasted with today's light weight partitions such as those used in the Alfred P. Murrah building. Therefore, skeletal 2D analysis might lead to the underestimation or, in some cases, overestimation of a building's strength and redundancy under extreme loading events.

Similarly, guidelines-prescribed DAFs used with linear and static methods may over- or underestimate the dynamic response of a structure. The latest GSA guidelines prescribe a DAF value dependent on the allowable plastic and yield rotations, in case of framed structures using NSA (Figure 2-2), as opposed to the previous fixed value of 2. As for LSA and other brittle structures that behave practically linearly, a DAF value of 2 is still used. However, due to the complexity of the dynamic response, which depends on many factors such as the strength and ductility of the structure, the intensity of the gravity loads, etc., this oversimplification may not always be accurate.

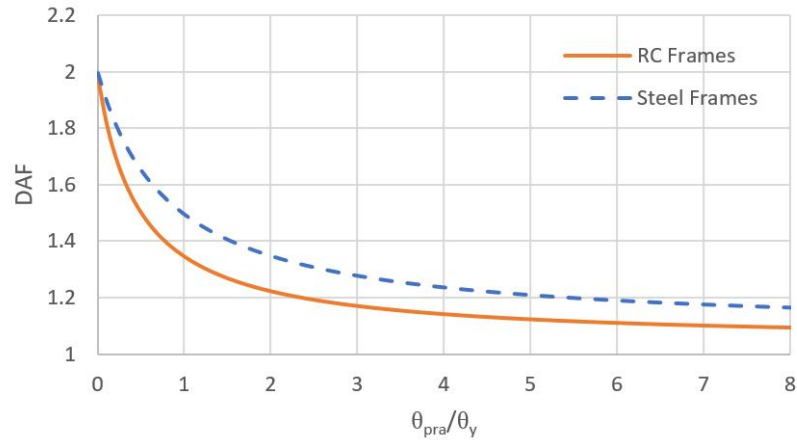


Figure 2-2: GSA-Prescribed Nonlinear Static Analysis DAF

In [12], it is shown that a four-story steel structure checked for progressive collapse safety according to the UFC's APM, is found safe when performing a detailed NDA accounting for all primary and secondary members. While the same structure is found unsafe when running skeletal LSA and NDA. Furthermore, the deformation of the structure decreased significantly (by almost 90%) when using partially restrained connections as opposed to fully hinged connections.

Of course, this is not to say that efforts for simplification and optimization shouldn't be made to deal with the tediousness of running a detailed NDA, not to mention the complexities of modeling the behavior of every single element, especially with the lack of sufficient experimental data. For example, the reinforcement contact function provided in Ansys Workbench to reduce the number of elements involved in the nonlinear dynamic reenactment of the Alfred P. Murrah building collapse, was implemented in [31] with a good degree of accuracy.

Another common approach for effective and computationally efficient progressive collapse analysis is the use of macro-modeling. Due to the complexity of the analysis, which involves material and geometric nonlinearities as well as dynamic effects [32], a comprehensive progressive collapse analysis can be time-consuming and cumbersome. Building on existing models and/or experimental results, the structural behavior of certain elements can be approximated in large scale simulations using macro-models. This approach is often used to represent the structural contribution of infill panels, usually, in lateral load analysis. In [33], an experimental shake-table test was performed on a one-story structure, and the results were used to create an FEM model, where the infill panels were modelled using two-strut compression-only macro-models, and the slabs were modelled using two-diagonal-truss-element models to account for their in-plane shear stiffness. A multi-spring macro-model based on the multi-vertical-line-element model (MVLEM), was used in [32] to represent the structural response of RC shear walls due to partial wall loss. Due to the lack of experimental data, the behavior of the macro-model was calibrated with an

FEM model. The simplified shear wall model was then included in two multi-story frame-wall structures, and the interaction of the frames and walls was examined under the assumed partial wall loss scenarios.

2.4 ANALYSIS METHODS

2.4.1 FINITE ELEMENT METHOD (FEM)

The most widely used method in modern structural analysis is FEM as it is used in the overwhelming majority of structural analysis software. However, the study of progressive collapse, by definition, should involve the post-peak response of the structure. The collapse of an element that might trigger a chain reaction and lead to the total or partial collapse of a building should be examined and accounted for. Unfortunately, the simulation of progressive collapse is not easy to conduct using traditional structural analysis methods such as FEM. Because FEM is used to approximate the response of a continuum, the cracking, separation and collision of elements is difficult to simulate without encountering numerical issues and stress singularities. So, predefining the plastic hinge zones, as well as crack locations and propagation directions, may sometimes be required to accurately simulate post-failure analysis. Nevertheless, most progressive collapse research is carried out using FEM. Moreover, since the GSA guidelines do not allow the failure of any structural element beside the removed element, the analysis is generally not concerned with post-failure behavior.

FEM is a stiffness method of structural analysis, also known as a displacement method, in which the main unknowns in the system are the displacements. The number of equilibrium equations (n) to be solved is equal to the number of available degrees of freedom. The structure is said to be kinematically indeterminate to the n^{th} degree. The equilibrium equations may be written in matrix form as:

$$[K]_{n \times n} \{U\}_{n \times 1} = \{F\}_{n \times 1}$$

where $[K]$ = Global stiffness matrix,

$\{U\}$ = Nodal displacement vector,

$\{F\}$ = Nodal force vector.

In general, under a given set of applied forces, the equations are solved for the displacements. Then, the local stiffness matrices of the members are used in conjunction with the nodal displacements to obtain the internal forces in the system using equilibrium equations.

When dealing with nonlinear structures, whether it is geometric or material nonlinearity, the system is solved by means of a linear incremental procedure, where the response is divided into small linear problems superposed

together to produce the final cumulative nonlinear behavior. Solution methods for these kinds of problems may be divided into two main methods: the load-control (or force-control) method and the displacement-control method.

2.4.1.1 LOAD-CONTROL METHOD

The most widely used method is definitely the load-control method as it is more flexible and robust. A problem that the load-control method encounters, though, is a phenomenon called snap-through. This occurs when the actual load-carrying capacity of the system decreases beyond a specific (limit) point. Since the solution technique is based on the incremental application of the load, it fails to account for the response when the load capacity is declining and jumps or “snaps through” to the closest equilibrium point with higher load, if any, skipping the whole softening phase in the process. This is depicted in Figure 2-3 which also shows that limit points under load-control may not only be peaks but minimum points as well. Basically, limit points are points where the actual load reverses in the opposite direction to the incremental loading direction. One way to overcome this problem is to impose a constraint on the distance between consecutive solution points on the load-displacement curve. The system is then subjected to an incremental load that is constrained with the displacement along an arc with a prescribed radius as depicted in Figure 2-4. This way, it is guaranteed that no sudden large jumps will occur and that the loading direction may indeed change beyond limit points. This technique is called the arc-length method.

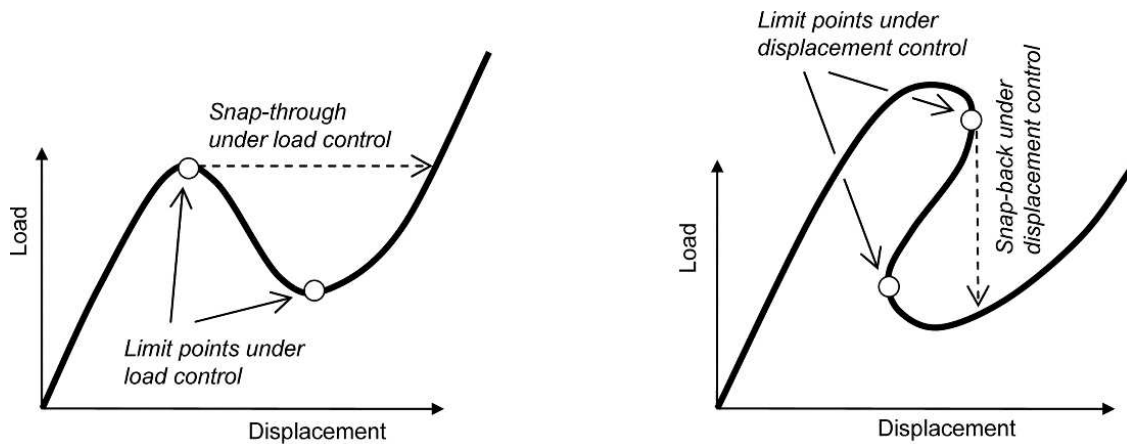


Figure 2-3: Limit Points under Load-Control (Left) & Displacement-Control (Right) [34]

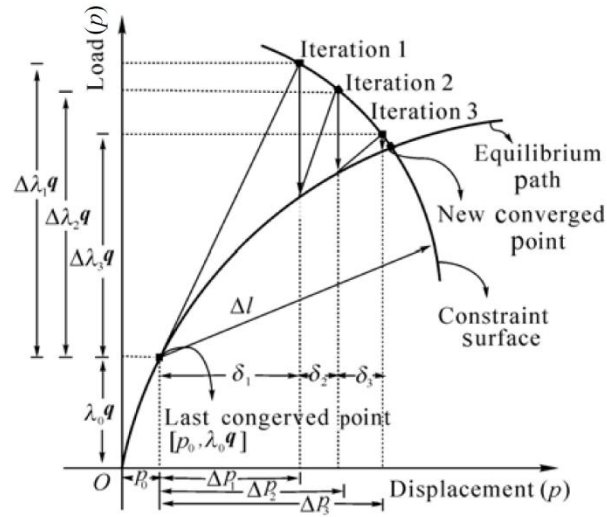


Figure 2-4: Arc-Length Procedure with Newton-Raphson Equilibrium Iterations [35]

Another problem that is not just exclusive to the load-control method but to nonlinear numerical methods in general, is the fact that the response is treated as a piecewise linear function. This approximation causes the results to drift from the actual solution with every step, especially under large load/displacement increments [36]. These drift-off errors create unbalanced forces between the external loads and the internal forces. A solution to this problem is to use iterative methods, where these residual forces are minimized as much as possible. One of the most popular iterative techniques for solving nonlinear equilibrium equations is the Newton-Raphson method. It has a few variations, two of which are the full Newton-Raphson and modified Newton-Raphson which are graphically represented here in Figure 2-5. This technique is normally used with the load-control method, where the residual forces are calculated at each load increment, and then, using the equilibrium equations, the corresponding displacements are solved, producing lower residual forces, and the additional displacements are added to the displacements of the previous iteration. This process is repeated until the desired level of accuracy is achieved. The difference between the two method variations previously mentioned is that in the full Newton-Raphson method, the global stiffness matrix of the system is recalculated at each iteration, while in the modified Newton-Raphson method, the global stiffness matrix is only calculated once at the beginning of the increment at the first iteration and is used in all subsequent iterations. This means that the full Newton-Raphson method requires less iterations to converge, however, each iteration takes longer than in the modified Newton-Raphson method. Finally, it should be mentioned that the Newton-Raphson technique may also be implemented in the arc-length method as depicted in Figure 2-4, in order to minimize the residual forces.

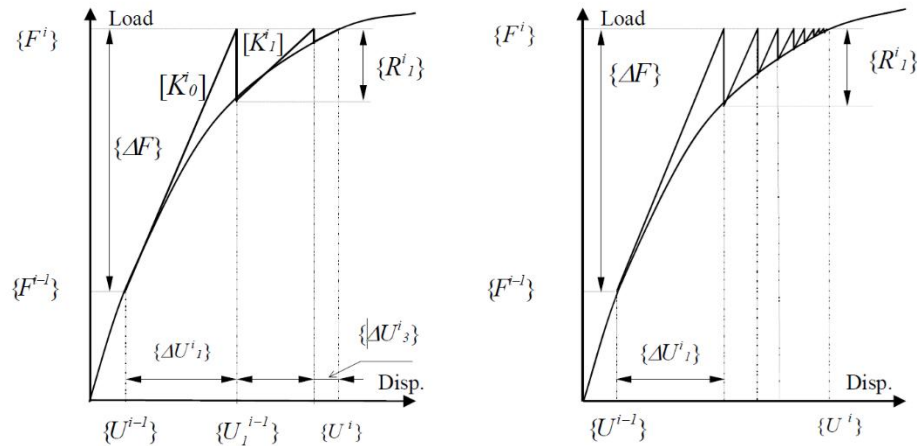


Figure 2-5: Full Newton-Raphson Method (Left) & Modified Newton-Raphson Method (Right) [36]

2.4.1.2 DISPLACEMENT-CONTROL METHOD

The displacement-control method can be a very useful tool in capturing complex behavior such as load drops, softening and post-peak responses. It involves applying incremental displacement steps to a structure at a specific degree of freedom, called the control displacement, then observing the resulting forces. However, as illustrated in Figure 2-3, the method undergoes snap-back at displacement limit points where the actual displacement response changes direction. The displacement-control method is suitable when the response is governed by a single displacement such as in the case of an applied concentrated force. As the loading and geometry of the system become more complicated, the method becomes unsuitable for the analysis.

2.4.2 DISCRETE ELEMENT METHOD (DEM)

To tackle this issue, some researchers have implemented the Discrete Element Method (DEM) in order to simulate the response of the structure after failure of an element has occurred. DEM is usually used to analyze the motion of discontinuous materials composed of a large number of small particles such as granular materials. In [37], using Euler-Bernoulli beam elements along with spherical discrete elements, the progressive collapse of a number of elements was examined by means of column removal. In [38], coupled FEM and DEM (F/DEM) which is a combination of FEM with DEM was used to simulate the progressive collapse of a multi-story building. FEM was used to analyze the structure until the failure of a finite element occurs, after which the element was replaced with a number of discrete elements with the total mass, displacement, velocity and acceleration of the original element (Figure 2-6). This way, not only was the nonlinear post-failure behavior simulated, but also the impact and stack load of fragments were predicted. The results of the F/DEM model were compared with the results of

the same FEM model and showed that the impact and stack load can affect the response of the structure and, therefore, should be accounted for in simulation.

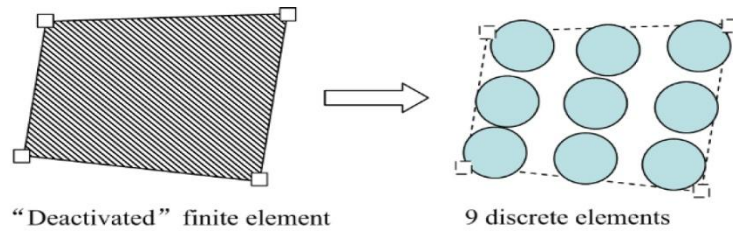


Figure 2-6: Deactivation of FEM Element & Creation of DEM Elements [38]

2.4.3 APPLIED ELEMENT METHOD (AEM)

Another method, developed in [39] and used for failure analysis, is the AEM. Similar to FEM, the structure is divided into small elements connected together. However, instead of being connected together through nodes, the elements are connected through a number of normal and shear springs (Figure 2-7). In AEM, the elements are considered as rigid bodies that do not deform, while the connecting springs deform according to their respective stiffnesses. The stresses and strains in the structure are therefore a function of the deformation in the springs. The springs are assigned a maximum allowable deformation which corresponds to a separation strain, above which the spring is removed and its internal forces are redistributed [4]. This way, the crack initiation and propagation in a structure can be predicted without preassigning the location of the cracks and the direction of their propagation as done in FEM [39]. Generally, AEM is less time consuming than FEM since there are only three degrees of freedom for each spring as opposed to six per finite element node [40].

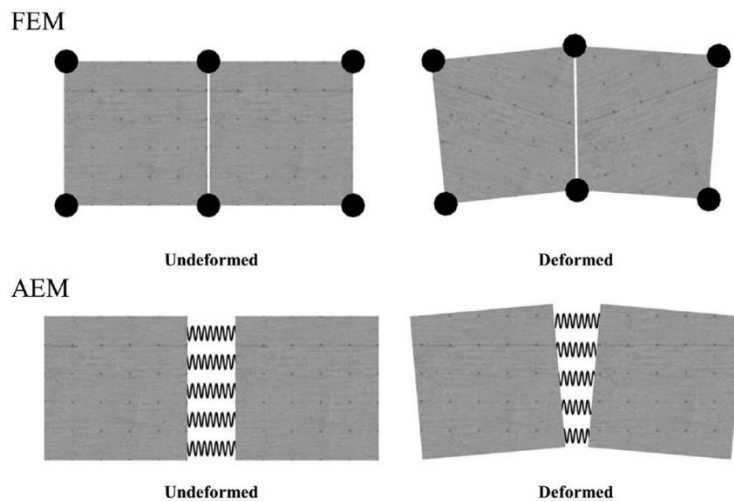


Figure 2-7: Element Connectivity & Deformation in FEM vs. AEM [41]

To validate the results obtained by the AEM, a comparison is made for a two-story RC frame in [39], between the experimental results and the AEM results. The deformed shape and crack locations obtained by the AEM are in good agreement with the actual results. A Brazilian test is also simulated in [42] and loaded models are analyzed using square elements for different orientations. The analysis shows that the crack location and propagation are independent of the shape and arrangement of the elements. The results confirm that element edges need not be parallel to the crack direction and that there is no need to pre-guess the location and propagation direction of the crack. A sensitivity analysis is also conducted in [43] by varying the size of the elements as well as the number of springs for a laterally loaded 2D portal frame. The results are compared with those obtained from FEM and show that using a large number of elements (i.e., smaller element size) with a lesser number of springs gives a better approximation than using a smaller number of elements with a large number of springs. Similar findings were also obtained in [44]. Crack development and propagation are also examined in [45] under the effect of cyclic loading, and the results are in good agreement with the experimental ones.

AEM is a relatively simple numerical technique, which offers the ability to predict the structural behavior under large displacements and account for buckling and p-delta effects [46]. It is, therefore, a nonlinear dynamic analysis tool that can be used in progressive collapse simulation as demonstrated in [41] in simulating the partial collapse of the Alfred P. Murrah building (Figure 2-8).

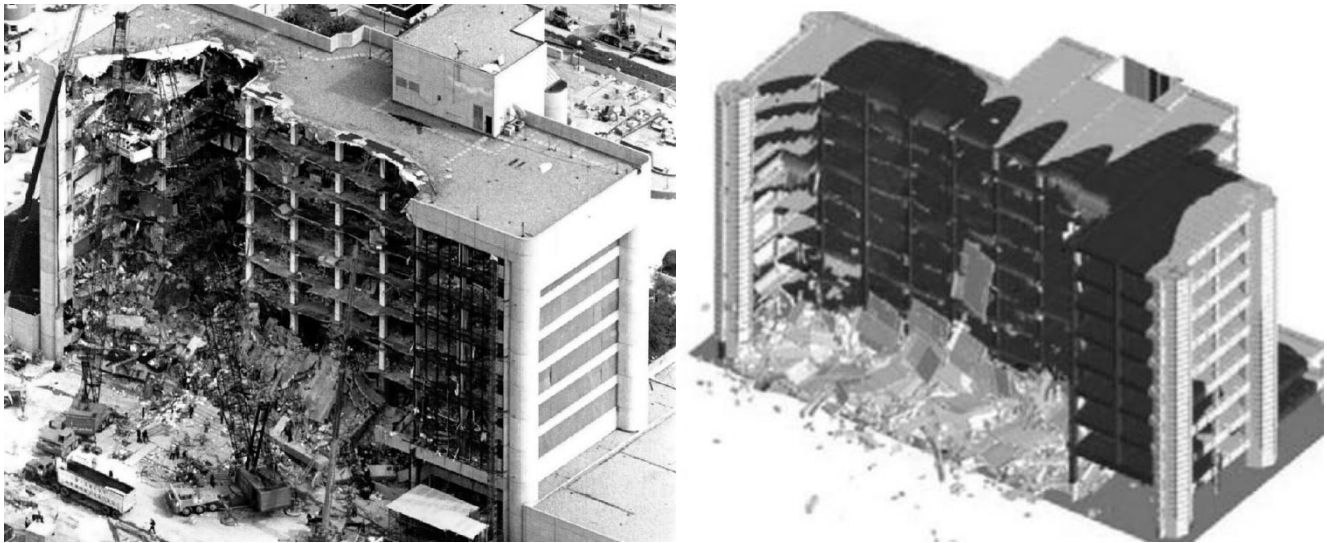


Figure 2-8: Actual (Left) [47] vs. Simulated (Right) [41] Collapse of the Alfred P. Murrah Building

2.5 STRUCTURAL ROBUSTNESS

Structures capable of withstanding extreme loading events are often referred to as being robust. Terms such as structural integrity and resilience are frequently encountered in progressive collapse literature and are practically

interchangeable with robustness. Although there is no standard definition or quantitative measure to describe it yet, robustness encompasses many structural properties such as redundancy, ductility and reserve strength. Progressive collapse design and retrofit methods are based on increasing these structural characteristics in order to improve the structural integrity and resilience of the building.

A retrofit method to improve the robustness and progressive collapse resistance of existing structures designed for low seismicity is suggested in [48] and consists of adding a grid of beams or trusses at the top of the structure (Figure 2-9). The grid acts as additional confinement to the building, tying the columns together and offering more redistribution paths, thereby increasing the redundancy of the system.

A similar approach was followed in [41] to simulate the Alfred P. Murrah building collapse using AEM. After finding the appropriate separation strain for reinforced concrete to mimic the collapse of the building, an additional transfer girder was added to the top of the building, and the building's response to the blast was reexamined (Figure 2-10 (right)). The new transfer girder added more in-plane bracing to the system and more support to the columns below. Another design alternative was tested, where all the columns started at the ground-floor level and none were supported on the lower transfer girder (Figure 2-10 (left)), although this option might not be architecturally desirable. As expected, both alternatives drastically improved the building's robustness by increasing its redundancy. The amount of damage was decreased from 27% in the case of the original design, to 12% and 9% in the case of the first (Figure 2-10 (right)) and second (Figure 2-10 (left)) alternatives, respectively.

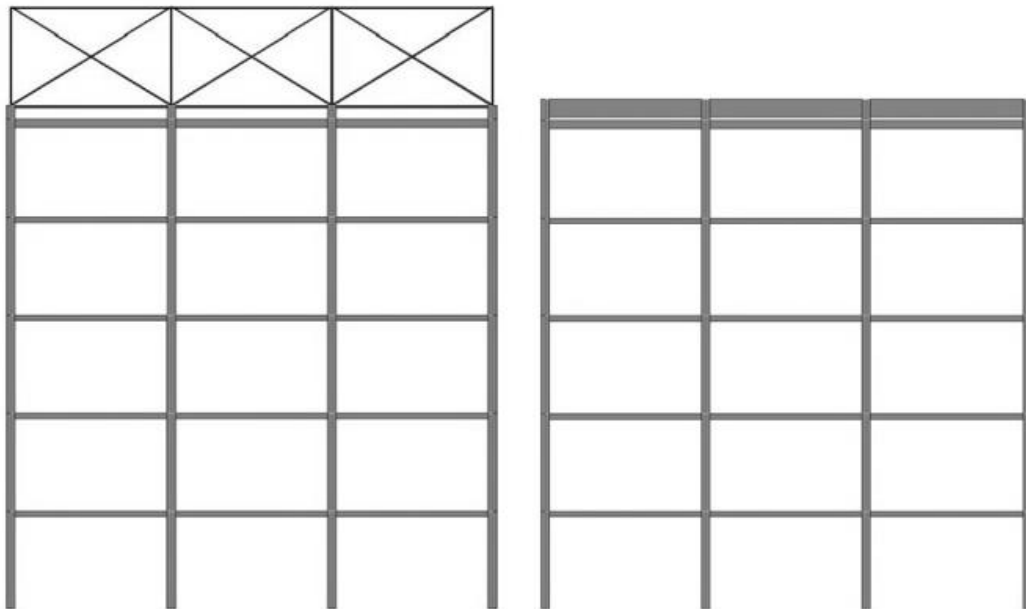


Figure 2-9: Top Grid Retrofit System [48]

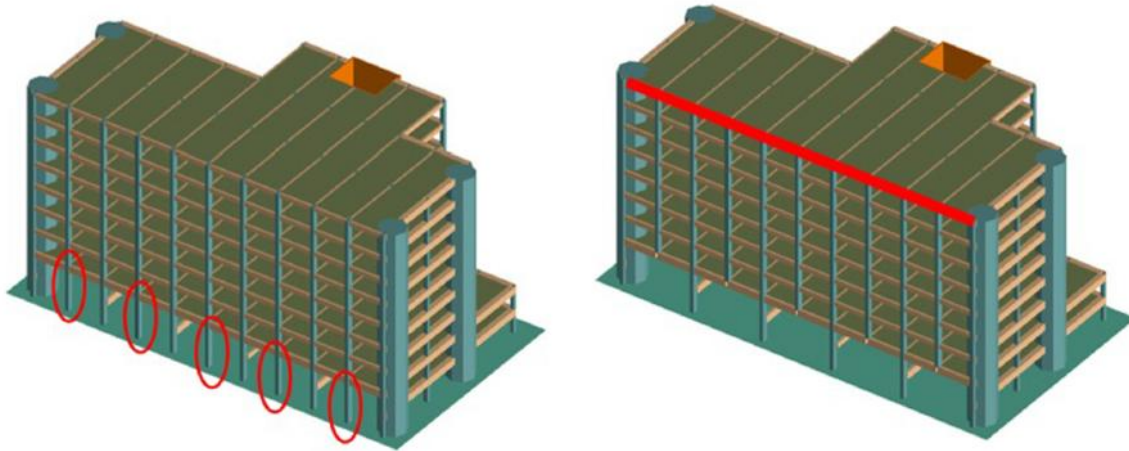


Figure 2-10: Design Alternatives for Improving the Progressive Collapse Response of the Murrah Building [41]

2.5.1 REDUNDANCY

One of the main structural attributes that contributes to a building's robustness is its redundancy. Redundancy highlights a structure's ability to redistribute among its members and connections loads which can no longer be supported by other damaged portions [49]. Although not exactly synonymous with static indeterminacy, redundancy is certainly associated with the level of restraints in a system. As known in classical structural analysis, static determinacy describes a structure that has the exact number of restraints needed to achieve equilibrium, provided that the geometric configuration of the members and supports does not allow the formation of a mechanism or instability. In other words, the number of restraints should equal the number of equilibrium equations, and the support reactions should neither be parallel nor concurrent in order to restrain any possible displacement or rotation. Statically indeterminate structures, on the other hand, are those that possess more than the minimum number of restraints needed for equilibrium. In general, the degree of indeterminacy i_e measures the number of redundant restraints in a structure. It can be calculated as the difference between the number of support reactions and the number of equilibrium and condition equations or by using the following formula in cases where closed loops are present in the structure:

$$i_e = (6m + r) - (6j + e_c) \text{ for 3D structures,}$$

$$i_e = (3m + r) - (3j + e_c) \text{ for 2D structures,}$$

where i_e = Degree of indeterminacy,

m = Number of members,

j = Number of joints,

e_c = Number of equations of condition.

CHAPTER 2. LITERATURE REVIEW

In general, a building with more structural members, supports, rigid connections, closed loops and continuity will have more alternative load redistribution paths. For example, a statically determinate frame will become unstable as soon as one of its columns fails, while a statically indeterminate frame will likely remain stable. The question remains, though, whether the other remaining members will be able to resist the redistributed loads for which they were not originally designed.

However, it is noteworthy that static indeterminacy, especially continuity, may not always be favorable and can, in some rare cases, contribute to the propagation of damage throughout the structure. This is why segmentation of a building is sometimes a recommended design solution in order to isolate the damaged parts of the structure and keep the damage localized to a limited area.

2.5.2 DUCTILITY & RESIDUAL STRENGTH

Another key property that contributes to a building's robustness is its ductility. Ductile structures are able to undergo larger deformations without collapsing. Unlike brittle members and connections, ductile elements may be able to remain in function after reaching their peak response by means of residual strength or plastic hinges. This ability may allow the structure to redistribute its loads and form a new partially damaged yet stable structural system. For instance, a mechanism such as catenary actions, is unlikely to form in brittle structures as it requires large deflections and rotations to develop. In studying the moment-rotation curves of beam-column assemblies where one column has been removed for a group of RC frame buildings, it is shown in [50] that the progressive collapse resistance of plastic hinges in ductile frames is higher than those in conventional frames. In general, ductile members allow more plastic rotation and, therefore, better progressive collapse resistance than less ductile ones [51].

Similar to continuity, ductility, in rare cases, may be unfavorable to the structure in extreme loading events. It is argued in [37], that damage is usually compartmentalized in buildings with small plastic capacity while there's a higher probability of damage propagation in buildings with high plastic capacity. Furthermore, collapsed fragments are more massive in ductile structures which increases the collision impact loads on the structure. In such cases, segmentation is also a viable option to localize any structural damage and stop it from spreading to the rest of the structure.

2.5.3 RESERVE STRENGTH

The robustness of a structure is also affected by the amount of reserve strength present in a structure. For instance, factors of safety accounted for in the design and construction processes may be advantageous to the

structural behavior and resistance to progressive collapse. In RC structures, compression-side steel reinforcement which otherwise serves as stirrup hangers, can play a key role in the progressive collapse resistance of a building, especially in cases of load/moment reversals. Shrinkage bars can also contribute to the response of the structure as well as any excess in steel rebar area and cross-sectional dimensions. Essentially, any reserve strength may add to the robustness of the structure. For instance, buildings designed in high seismic zones and, therefore, for high peak ground accelerations (PGA) are shown to be more robust than those designed in lower seismic zones or seismically deficient buildings [5], [52], [48], [50], [51]. Of course, this may be attributed to their higher strength capacity as well as their higher ductility.

2.5.4 ENERGY ABSORPTION CAPACITY

When a structural member suddenly fails, the strain energy stored within the member is released to the remaining structure. This dynamic loading causes the structure to vibrate, and the ability to absorb this energy and transform it into strain energy contributes to reaching a new equilibrium position and hence increases the structure's robustness. The energy absorption capacity of a structure is related to its strength and ductility as it is a function of the area of the stress-strain curve. However, the increased capacity to dissipate plastic energy does not always lead to improved structural robustness, as argued in [13].

2.6 RESISTANCE MECHANISMS

Under extreme loading cases and after suffering local failure, a building will begin to redistribute its loads among its remaining members. Depending on the load and the robustness of the system, different resistance mechanisms may develop. In the case of a single column failure, the horizontal members, whether beams or slabs, will begin to resist the additional load and attempt to redistribute it to the adjacent vertical members. If a horizontal member is free to move in the normal direction, that is to say it is axially unrestrained, then it shall experience additional flexural stresses following the removal of one of its columns. However, if the adjacent spans provide full or even partial axial restraint, then mechanisms such as compressive arching action followed by tensile catenary action may develop in the beam as the deflection at the failed column increases. Similarly, in the case of slabs, compressive membrane action followed by tensile membrane action may develop under increased vertical deformation. A typical load-displacement response curve is shown in Figure 2-11 in order to help visualize the extreme loading process leading to the failure of the system.

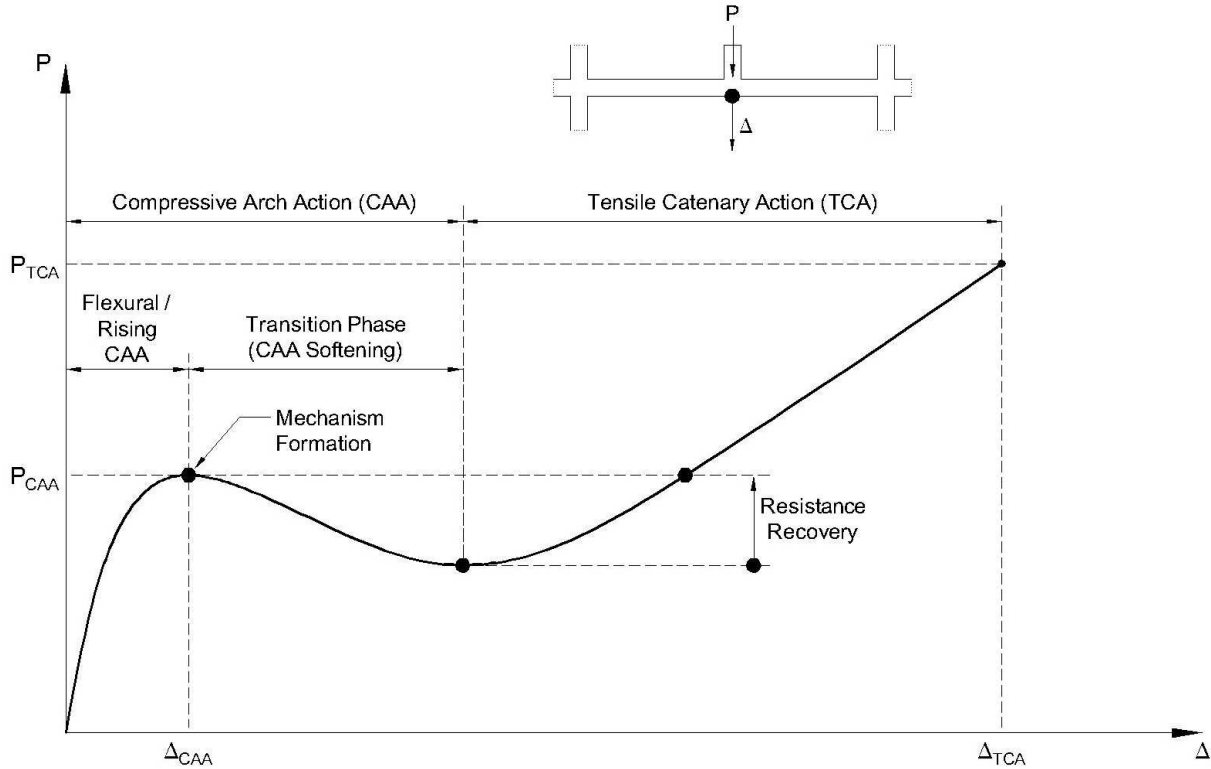


Figure 2-11: Generic Load-Displacement Curve for Horizontally-Restrained Beam-Column Systems Under Static Pushdown

2.6.1 FLEXURAL RESISTANCE

The most basic form of resistance mechanism in conventional structural design is through flexural behavior. Therefore, the bending capacity of a beam and/or slab is the first thing to be tested after the loss of a column. In most column loss scenarios, the bending moment reverses, and the section’s compression side becomes its tension side. Sections designed for such reversals as those designed for lateral loads, will be more robust in resisting the redistributed loads. If the capacity of the horizontal members directly above the damaged column is much higher than the demand, then flexural action may be sufficient to transfer the excess loads to the neighboring columns and the remaining structure. In slabs, at the ultimate stage of flexural resistance, plastic strain concentrations develop forming yield line patterns in what is also known as yield line mechanism [53].

2.6.2 COMPRESSIVE ARCH ACTION

The more axially-restrained the horizontal members are, the more compressive arch action that develops. Technically, compressive arch action (Figure 2-12) develops at the beginning of the loading period. However, its effect becomes more pronounced as deformations increase and the flexural stiffness reduces. This usually occurs at higher deformations such as those experienced during sudden column loss scenarios. The contribution of

compressive arch action can drastically increase the section’s capacity and, therefore, increase the member’s strength and ductility as well as the system’s robustness. As shown in Figure 2-11, the system reaches its peak flexural/arching resistance where the bending moment and compressive axial force are at their maximum, at which point a plastic hinge develops, and the system begins to lose some of its load-carrying capacity. In this transition phase, the system exhibits an overall negative stiffness, and the compression force begins dropping in value. This softening phenomenon continues until the system reaches the end of the compressive arching action.

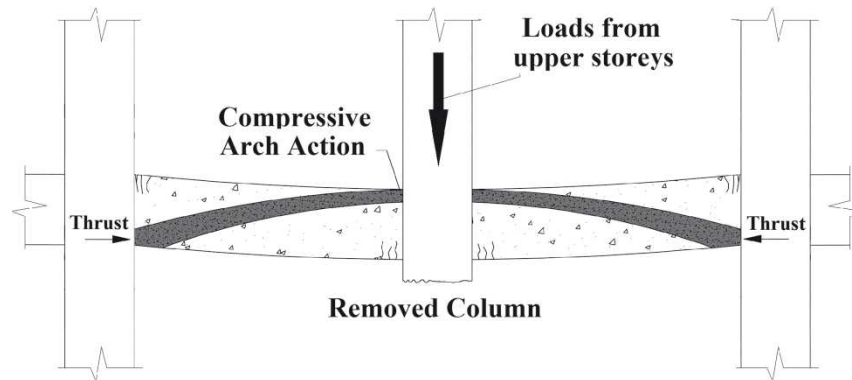


Figure 2-12: Compressive Arch Resistance Mechanism [54]

2.6.3 CATENARY ACTION

As deformation continues to increase, plastic hinges, cracks, crushing and ruptures occur. The compressive arching force that once held the system together decreases and turns into a tensile force. The catenary tensile force (Figure 2-13), which can be considered as the last line of defense, continues to increase until reaching its maximum capacity beyond which the horizontal member continues to deform until reaching its failure strain. Similar to compressive arching forces, catenary forces can grossly increase the section’s load-carrying and deformation capacity.

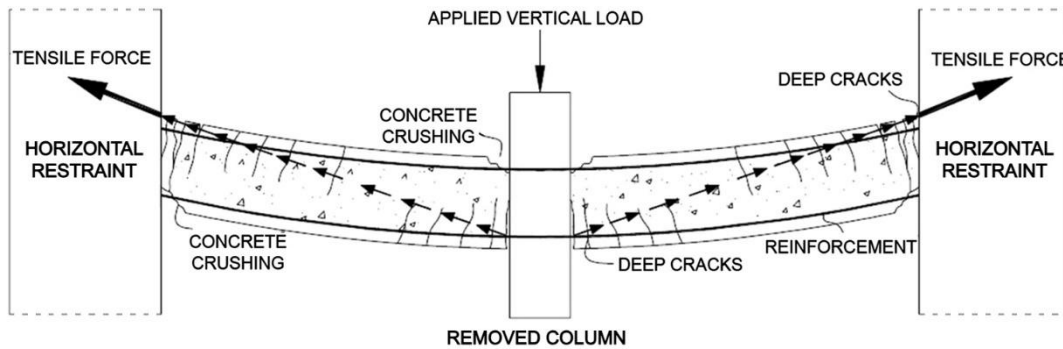


Figure 2-13: Tensile Catenary Resistance Mechanism [55]

2.6.4 MEMBRANE ACTION

While compressive arching action and catenary action mainly develop in beams after flexural action, membrane action is the main resistance mechanism in slabs following the flexural resistance and yield line mechanism stage. At relatively low displacements, compression membrane forces arise and help increase the load-bearing capacity of the slab, similar to the effect of compressive arching action on the behavior of beams. On the other hand, tensile membrane forces may develop in the center of the slab at large displacements, while compressive membrane forces may occur forming a ring near the perimeter of the slab [56] as shown in Figure 2-14.

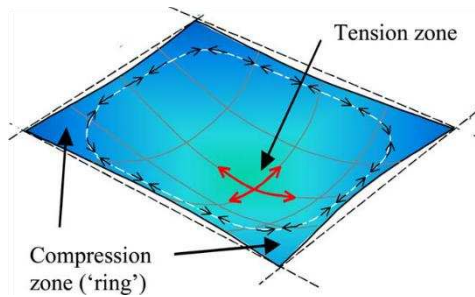


Figure 2-14: Membrane Action in Slabs at Large Displacements [56]

2.6.5 VIERENDEEL ACTION

Another resistance mechanism, not often mentioned in literature, is the Vierendeel action or diaphragm effect. As the name suggests, this form of mechanism is similar to the behavior of Vierendeel trusses, which are trusses with only vertical members between the top and bottom chords (Figure 2-15). In the case of column loss, the structure may function as a Vierendeel truss in order to transfer its loads to the surrounding columns.

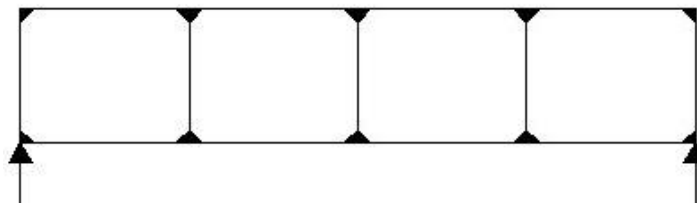


Figure 2-15: Vierendeel Truss

2.6.6 NON-STRUCTURAL ELEMENTS

Finally, the effect of non-structural elements such as infill panels on the progressive collapse behavior should not be overlooked. Infill panels placed between columns and beams can carry part of the redistributed load and, in turn, affect the alternate load path in a positive manner. In addition to adding vertical stiffness, wall panels can also contribute to the lateral stiffness of the system, which could also benefit the load and moment redistribution.

2.7 SUMMARY & CONCLUSIONS

2.7.1 EXPERIMENTAL & NUMERICAL RESEARCH ON PROGRESSIVE COLLAPSE

The literature on progressive collapse of RC framed structures has expanded significantly over the past two decades, driven by the increasing need for structural resilience against extreme events. Experimental research has played a crucial role in understanding progressive collapse mechanisms, yet many studies have been limited to sub-assemblages rather than full-scale structures due to practical and economic constraints. Additionally, while quasi-static column loss experiments have provided valuable insights, there remains a shortage of dynamic column loss experimental data, particularly for multi-story buildings.

From a numerical modeling perspective, various approaches have been employed to simulate progressive collapse, including finite element modeling (FEM), discrete element modeling (DEM), and applied element modeling (AEM). However, each method has its limitations. While FEM remains the most widely used method, it struggles to simulate element separation, debris impact and collapse propagation, requiring additional modeling techniques. On the other hand, AEM is better suited for post-failure analysis but is generally less accurate in predicting overall structural behavior before failure.

2.7.2 IDENTIFIED GAPS AND RESEARCH NEEDS

In recent years, several studies have explored the contribution of slabs to progressive collapse resistance, primarily through experimental investigations on scaled specimens and substructures. While works such as those in [57], [58], [59] and [60] have advanced our understanding, particularly in single-story configurations, a notable gap remains in the literature regarding the behavior of multi-story buildings. Owing to the high computational cost, detailed numerical studies remain scarce. In [61] for instance, a fully detailed substructure with explicitly modeled concrete and reinforcement was analyzed under quasi-static loading. However, there is a clear lack of studies extending this level of detail to complete multi-story structures subjected to both quasi-static and dynamic analysis. Furthermore, most existing studies do not explicitly quantify the contribution of the slab and direct comparisons between bare-frame and full-frame configurations, essential for isolating slab effects, are rarely conducted. This research addresses these limitations by numerically evaluating a fully detailed multi-story RC frame building with and without slabs under both interior and corner column removal scenarios and by explicitly quantifying the slab's contribution under both quasi-static and dynamic loading conditions.

Another key challenge lies in the accuracy of commonly used analysis methods. Nonlinear static analysis (NSA) and nonlinear dynamic analysis (NDA) are frequently adopted with guidelines recommending dynamic increase

factors (DIFs) to approximate dynamic effects within static frameworks. However, these prescribed factors often fall short of capturing the full complexity of structural response, particularly in scenarios involving sudden column loss. Several studies have examined and calculated DIF values through numerical simulations, offering valuable insights into dynamic behavior. Nonetheless, these investigations were often based on simplified models. In [62], the slab was not modeled, while in [63], a one-way slab was represented using frame elements in the transverse direction. To further enhance the reliability and applicability of DIF values, there remains a need for studies based on complete multi-story RC buildings with fully detailed components, such as the approach adopted in the present research.

2.7.3 FOCUS OF THIS STUDY

This research aims to address these gaps by:

- Investigating the role of floor slabs in progressive collapse resistance by comparing bare-frame and full-frame responses.
- Examining the effect of column location and floor level by conducting column removal analyses at different positions within the structure.
- Comparing nonlinear static and nonlinear dynamic analyses, calculating DIFs from the numerical results and evaluating their accuracy against guideline values.
- Assessing the validity of model reduction techniques, particularly the accuracy of single-story and single-frame models in capturing realistic structural behavior.
- Developing a simplified predictive method that balances computational efficiency with accuracy and validating it against both experimental and numerical results.

By tackling these challenges, this study contributes to a more comprehensive understanding of progressive collapse mechanisms and enhances the reliability of numerical and analytical approaches in structural engineering.

3. RESEARCH METHODOLOGY

3.1 INTRODUCTION

As mentioned in Chapter 1 of this thesis, the main objective of the research is to study the progressive collapse response of regular RC framed buildings subjected to column loss using the APM. The effect of floor slabs, the type of analysis carried out and the location of the damaged column are among the main points on which this research is focused. These factors significantly affect load redistribution mechanisms and the ability of the structure to resist collapse. Therefore, a rigorous methodology is required to capture these behaviors accurately.

This chapter outlines the methodology adopted in this study, detailing the software selection, experimental validation, case study development, and analytical approach. By establishing a clear research framework, this methodology provides a structured basis for the analyses presented in the subsequent chapters.

3.2 METHODOLOGY

3.2.1 CHOICE OF ANALYSIS SOFTWARE

In progressive collapse analysis, the building is subjected to excessive deformation that pushes it way beyond its linear elastic range. However, most commercial structural analysis software might not be able to simulate the nonlinear response of the building under extreme loading conditions. In this research, Abaqus was chosen as the main analysis tool for its advanced capabilities in capturing the nonlinear response of structural systems. It is one of the most widely used software programs by structural engineers and researchers.

Due to the complex and sensitive nature of nonlinear analysis, the first step was to validate the results obtained by the chosen structural analysis software used in the research. In the next chapter (Chapter 4), four experimental studies found in literature were replicated using the analysis software to ensure that it produced reliable results. The experimental studies were selected to cover a range of structural configurations and systems, as well as different loading and column removal scenarios, as summarized in Table 3-1. The software models were calibrated by varying input parameters until sufficient confidence in the results was achieved.

Table 3-1: Summary of Chosen Experiments

Experiment	Scale	Number of Modeled Specimens	Type of Modeled Specimen	Removed Column Location	Type of Loading
Experiment 1 [16]	1/1 (full-scale)	2	2D bare-frame sub-assembly	Interior column	Quasi-static pushdown
Experiment 2 [24], [25]	1/4 (quarter-scale)	2	3D bare-floor system (without slab) and 3D full-floor system (with slab)	Interior column	Quasi-static pushdown
Experiment 3 [28]	1/3 (third-scale)	1	3D bare-floor system (without slab)	Corner column	Dynamic column loss
Experiment 4 [29], [30]	1/4 (quarter-scale)	1	3D full-floor system (with slab)	Edge column	Dynamic column loss

3.2.2 FIRST EXPERIMENTAL STUDY EXAMPLE

The first chosen example was of an experiment conducted in [16] which was briefly mentioned in Section 2.2.1. The experiment led by the authors was aimed at examining the progressive collapse resistance of RC framed structures due to column loss. Two buildings were designed according to the 2003 IBC [64], the SEI/ASCE 7-02 [65] and the ACI 318-02 [66]. To observe the difference in behavior resulting from stiffness and reinforcement, one building was seismically designed using intermediate moment frames (IMF) and the other using special moment frames (SMF). The test was performed on two full-scale RC beam-column sub-assemblages taken from each building, loaded at the intermediate joint and subjected to monotonic downward displacement. The test specimens were equipped with strain gauges among other sensors to capture the performance at different locations. Figure 3-1 shows the test configuration and layout of the sensory equipment, while Figure 3-2 shows the structural details of both test specimens. The nominal compressive strength of concrete used in the design of beams and columns was 27.6 MPa while the used rebar was ASTM A706 Grade 60 with a minimum yield strength of 413.7 MPa. Table 3-2 and Table 3-3 show the average compressive and tensile strength of concrete and the mechanical properties of steel reinforcing bars at the time of testing, respectively. The modulus of elasticity of steel was taken as 210 GPa while that of concrete was calculated using the following ACI [67] formula in MPa:

$$E_c = 4700 \sqrt{f'_c}$$

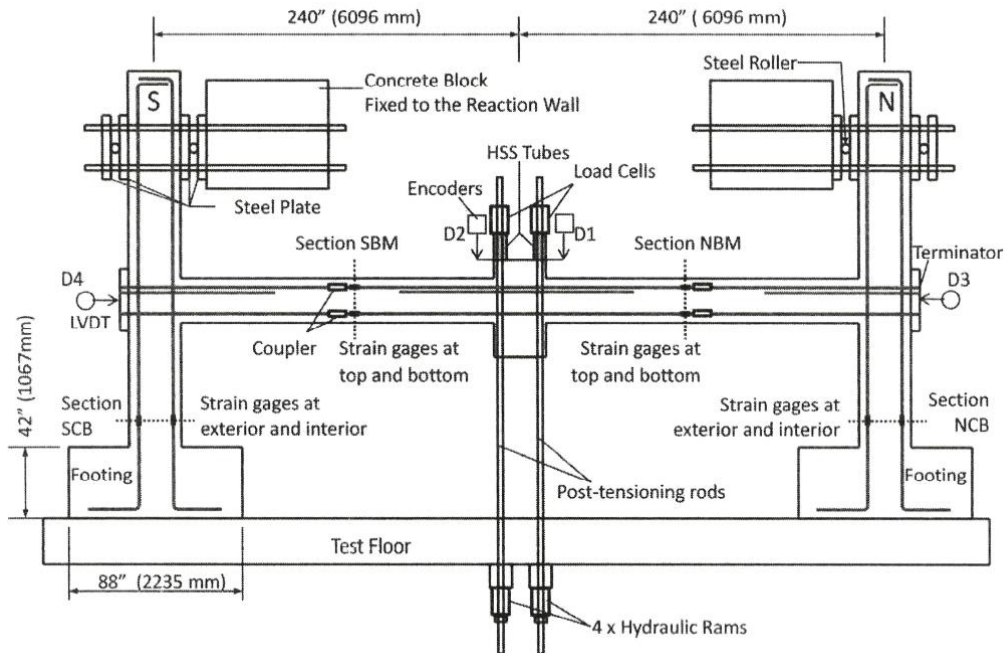


Figure 3-1: Test Configuration & Selected Instrumentation [16]

Table 3-2: Average Compressive & Tensile Strength of 152x305 mm Concrete Cylinders [16]

Specimen	Compressive Strength (MPa)		Split-Cylinder Tensile
	Footings	Beams & Columns	Beams & Columns
IMF	39	32	3.1
SMF	37	36	2.9

Table 3-3: Average Mechanical Properties of Reinforcing Bars [16]

Bar Size	Yield Strength (MPa)	Ultimate Strength (MPa)	Rupture Strain (%)
8	476	94	21
9 (Bottom Bars in IMF Beams)	462	93	18
9 (Vertical Bars in IMF Columns)	483	100	17
10	503	106	16
4 (Ties & Stirrups in IMF)	524	103	14
4 (Ties & Stirrups in SMF)	545	98	15

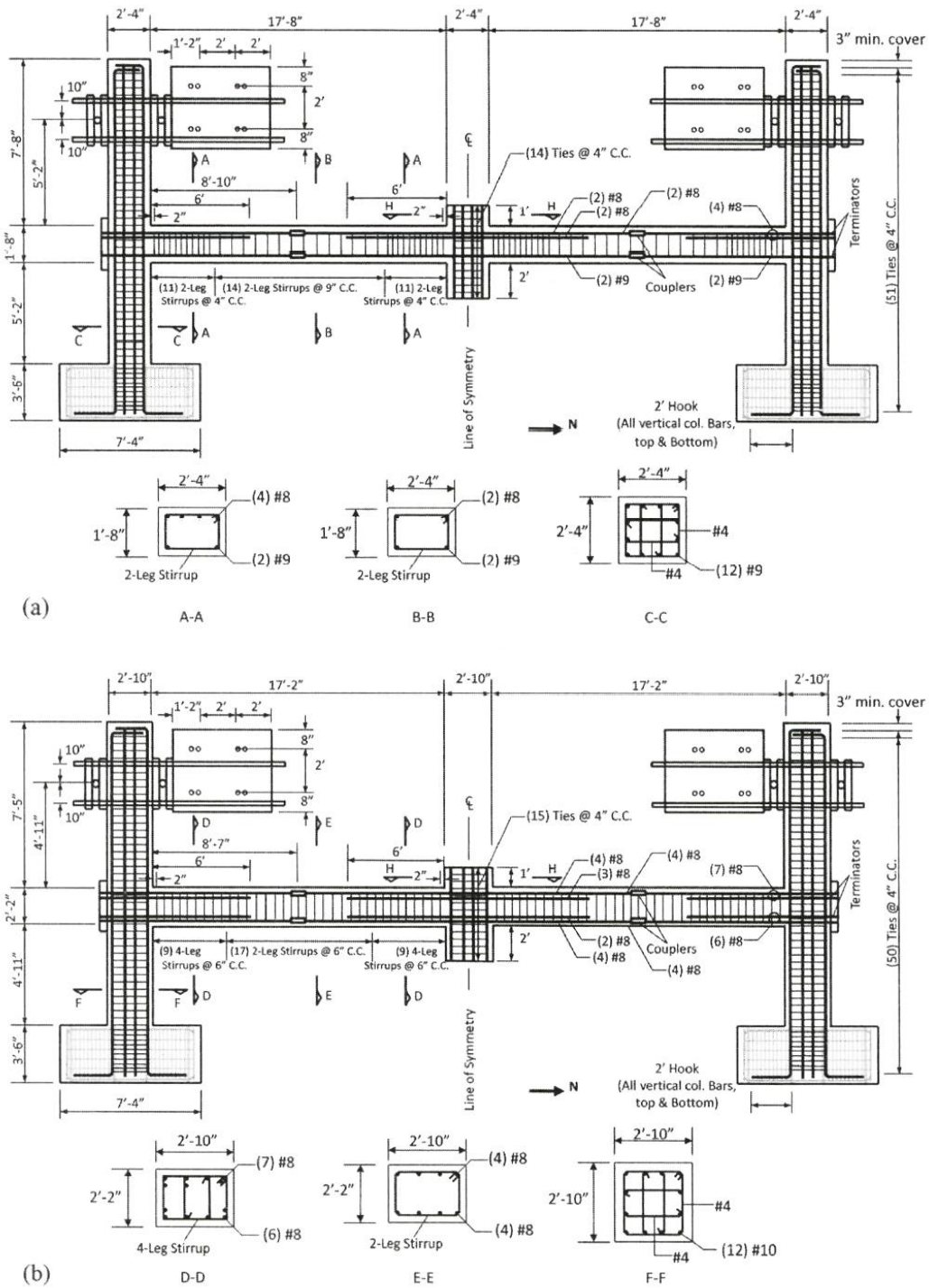


Figure 3-2: Structural Details of IMF Specimen (a) & SMF Specimen (b) [16]

3.2.3 SECOND EXPERIMENTAL STUDY EXAMPLE

The second chosen experiment published in [24] and [25], examined the 3D effect of transversal beams as well as slabs on the progressive collapse of RC sub-systems. Two prototype buildings with different slab aspect ratios were seismically designed according to the ACI 318-08 [24]. Then, a sub-system of each building was considered in the study. Six one-quarter-scale specimens were tested, representing 2D beam-column sub-assemblages (P1 and P2), 3D beam-column sub-assemblages (T1 and T2) and 3D slab-beam-column sub-assemblages (S1 and S2) for each building. The specimens were then subjected to monotonic downward displacement at the middle joint of each system. Figure 3-3 shows the concrete dimensions and reinforcing steel details for specimen S1.

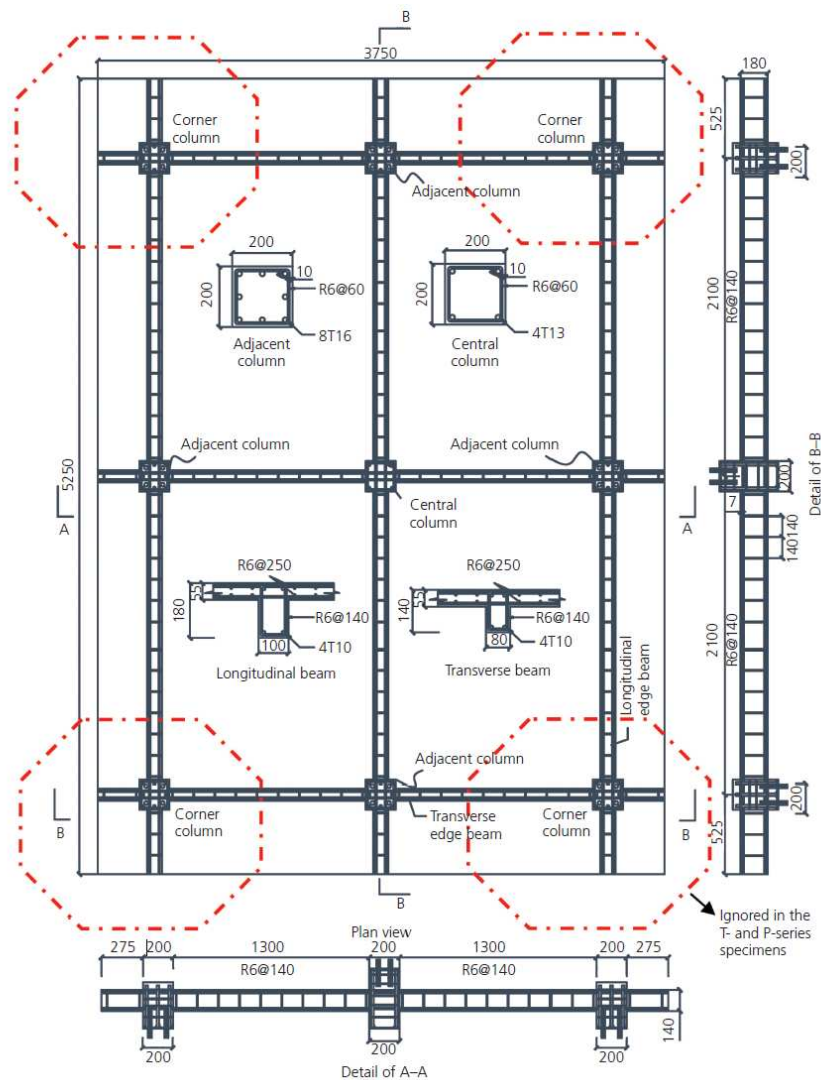


Figure 3-3: Concrete Dimensions & Rebar Details of S1 [25]

3.2.4 THIRD EXPERIMENTAL STUDY EXAMPLE

Unlike the first two experiments, the third chosen experiment examined the dynamic response of RC framed structures to sudden column loss. In [28], the authors tested six one-third-scale sub-systems (DF1 to DF6) representing the external bays of RC frame floor systems. Each specimen was designed according to different criteria to study the influence of seismic detailing, high service load, span variations, etc., on the progressive collapse behavior of the system. Figure 3-4 shows the structural layout and details of specimens DF1 and DF2. To simulate the loss of the corner column, an apparatus composed of a steel column, pin support and a load cell was designed and installed in each specimen at the corner joint. Furthermore, the steel assembly shown in Figure 3-5 was designed to provide partial rotation and horizontal displacement at the corner joint to account for the effect of the floors above. Horizontal and vertical double action load cells were applied at the other end of each beam to account for the boundary conditions imposed by the adjacent interior panels.

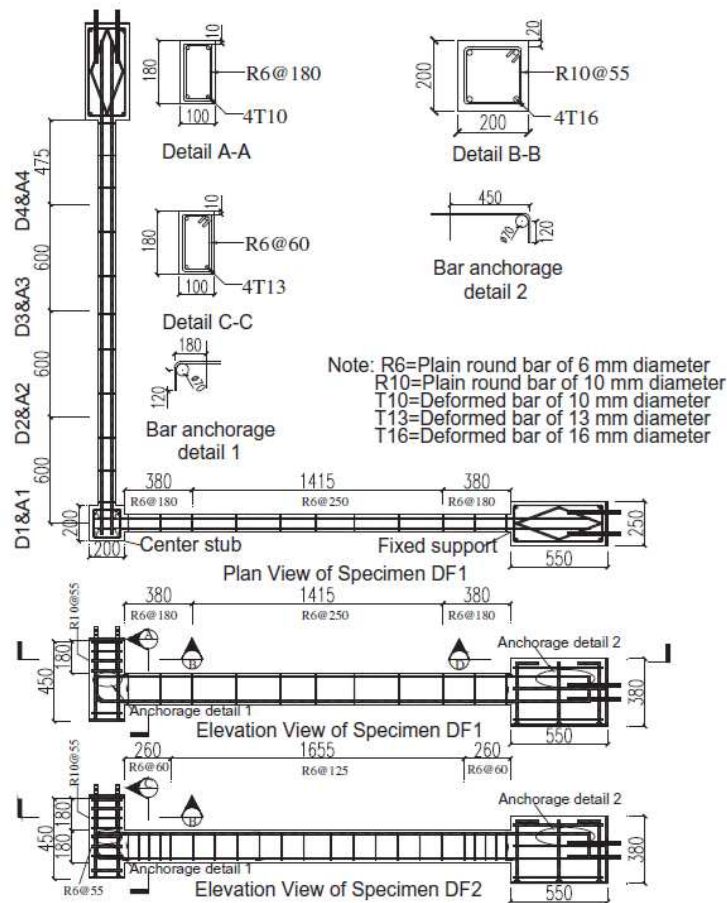


Figure 3-4: Layout & Reinforcement Details of DF1 & DF2 (Dimensions Are in mm) [28]

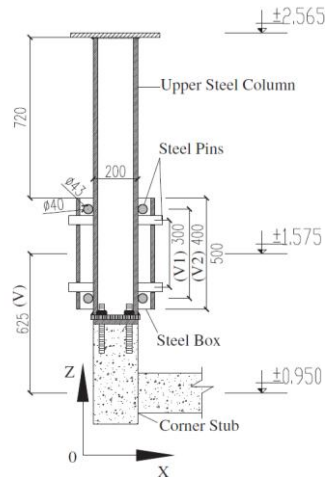


Figure 3-5: Steel Assembly Details [28]

3.2.5 FOURTH EXPERIMENTAL STUDY EXAMPLE

Similar to the third experiment, this fourth and final chosen experiment examined the dynamic behavior of the RC system to the sudden removal of one of its columns. However, in this experiment, the sub-system was composed of columns, beams and slabs, unlike the previous experiment where the slab was omitted from the specimen. Another difference between both experiments was that in this experiment, the removed column was an edge column not a corner column like in the third experiment.

In [29] and [30], three identical one-quarter-scale RC slab-beam-column specimens were experimentally tested. The control specimen was subjected to pushdown loading, and the other two (D-0.91 and D-1.16) were subjected to dynamic column loss scenarios under two different sets of gravity loads. Figure 3-6 shows the typical structural drawings for the specimens. It should be noted that the appropriate boundary conditions were applied to the columns by fixing them on steel column supports, which in turn were clamped to the floor.

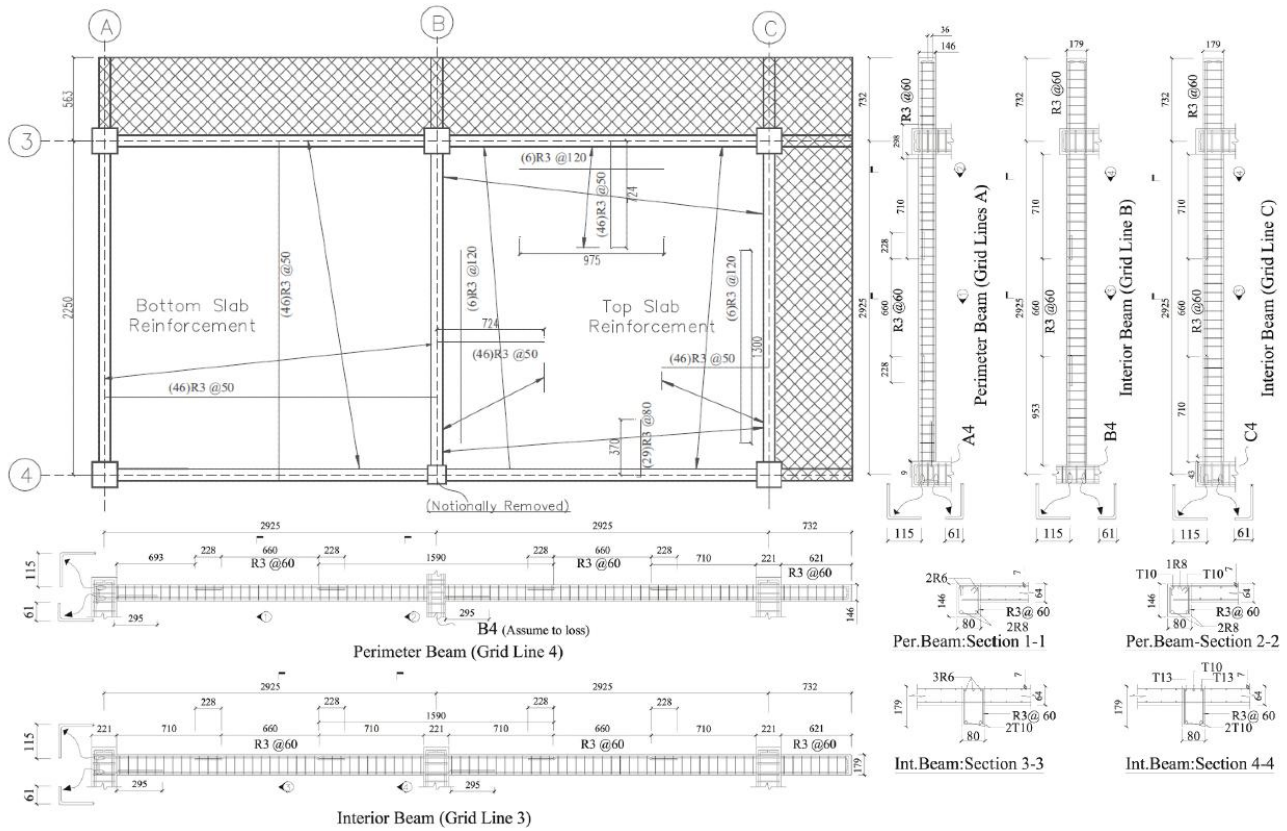


Figure 3-6: Typical Layout & Reinforcement Details of the Specimens [30]

3.2.6 CASE STUDY

Chapter 5 presents the main step where the case study building was designed according to the NBCC 2015 [68], CSA A23.3-14 [69] and CAC Concrete Design Handbook [70]. The building was a six-story reinforced concrete structure (Figure 3-7, Figure 3-8 and Figure 3-9) designed according to the NBCC 2015 [68], CSA A23.3-14 [69] and CAC Concrete Design Handbook [70]. The building was assumed to be residential and located in downtown Calgary, Alberta. The building was 20 m long, 20 m wide and 19 m high. It was composed of four 5 m bays in each horizontal direction. The height of all typical stories was 3 m while the ground floor was 4 m high. Gravity loads were supported by solid slab floor systems, while lateral loads were resisted by moment resisting frames located on axes 1, 5, A and E. For the sake of simplicity, staircases and elevator shafts were not considered in this study.

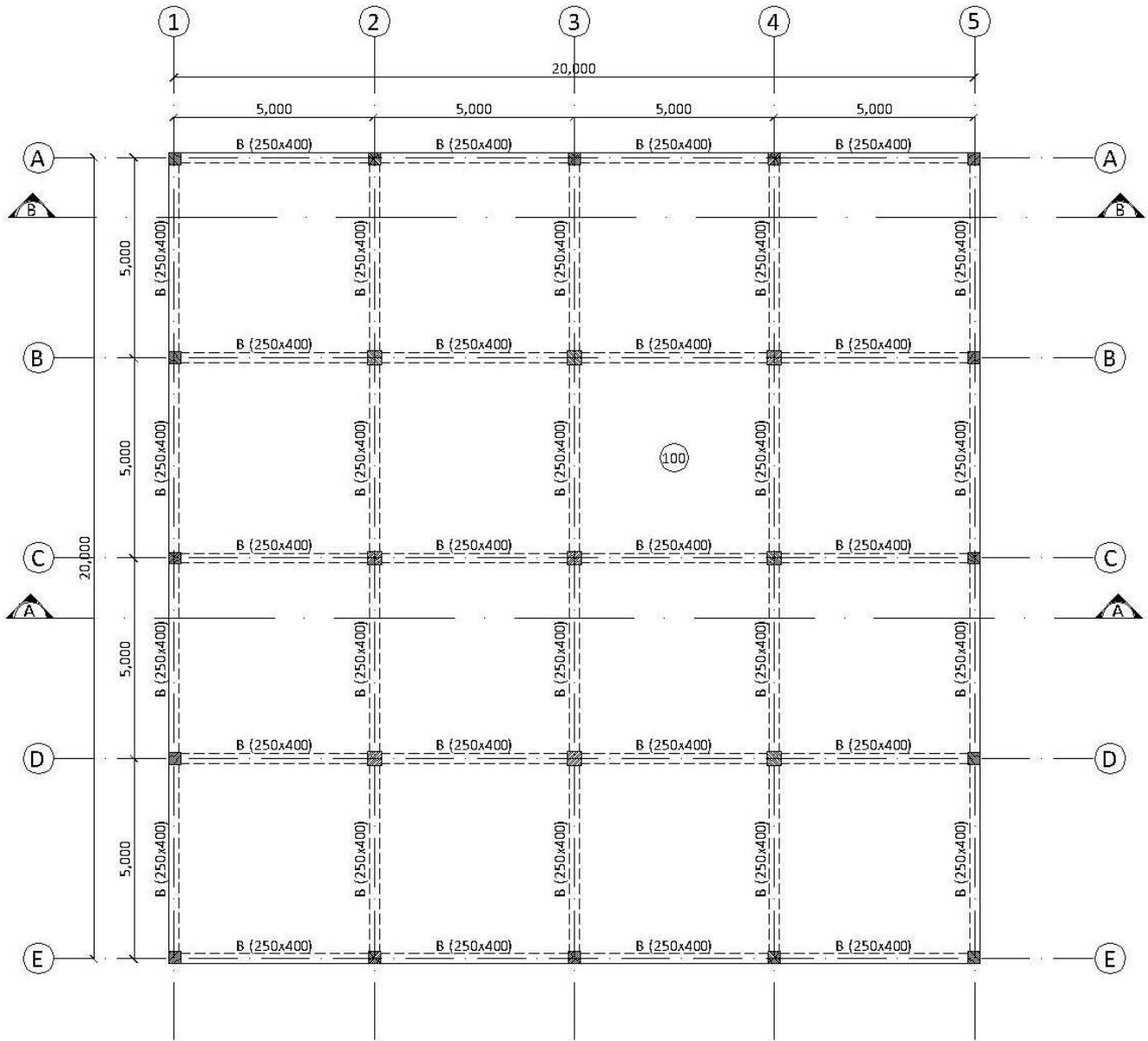


Figure 3-7: Building Plan

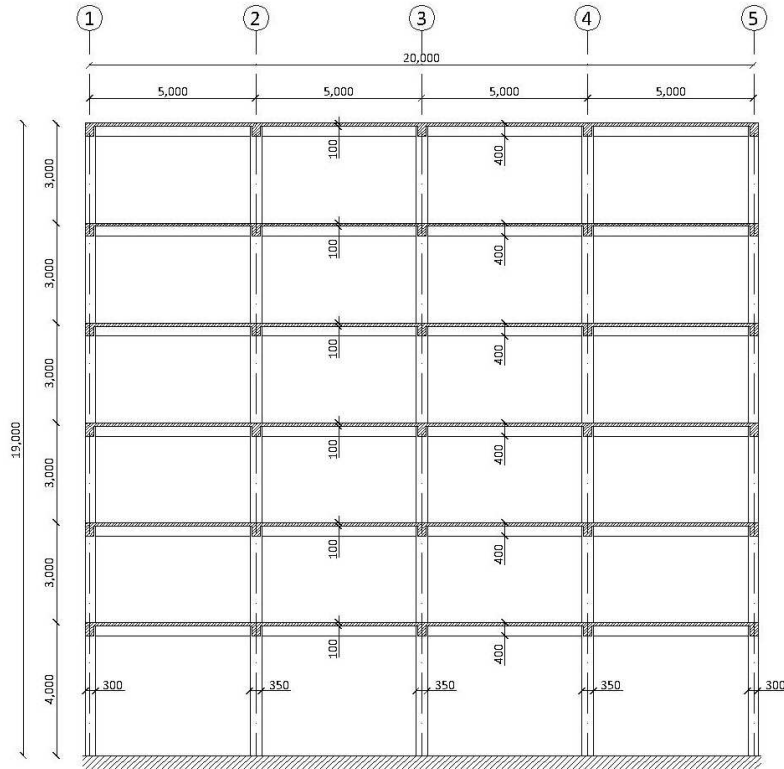


Figure 3-8: Interior Frame (Section A-A) Concrete Dimensions

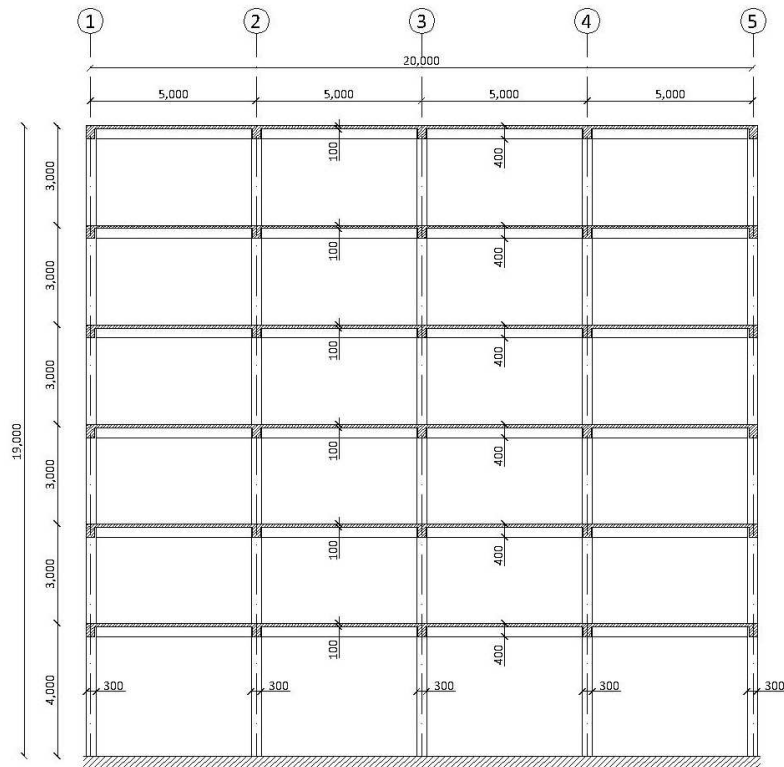


Figure 3-9: Exterior Frame (Section B-B) Concrete Dimensions

Two models of the building were considered in the analysis, the full-frame and bare-frame models. The full-frame model was composed of columns, beams and slabs, while the bare-frame model was composed of only columns and beams. This comparison was made to assess and quantify the effect of the slab on the progressive collapse behavior of the structure. Due to the complexity of nonlinear analysis, many studies have been conducted on bare frames where the effect of floor slabs has been discarded for simplicity. While there exists a number of studies where the full frame is accounted for, more research is definitely needed to measure the membrane action contribution to the system’s response and resilience.

As mentioned in Chapter 1, a comparison was made between the results obtained from nonlinear static and nonlinear dynamic analyses. This comparison was used to calculate the dynamic increase factors and assess their alignment with the values prescribed in the GSA and UFC guidelines. Additionally, the effect of column position on the structural response was investigated by comparing the removal of an interior column with that of a corner column. The analysis plan is summarized in Figure 3-10, which illustrates the models, and the types of analysis conducted. Each full-frame and bare-frame model was subjected to nonlinear static (pushdown) and nonlinear dynamic (column loss) analyses. Both analyses were performed for cases of interior and corner column removal. Furthermore, for each case, the analysis was repeated for different floors of the building to evaluate the influence of column removal at various heights.

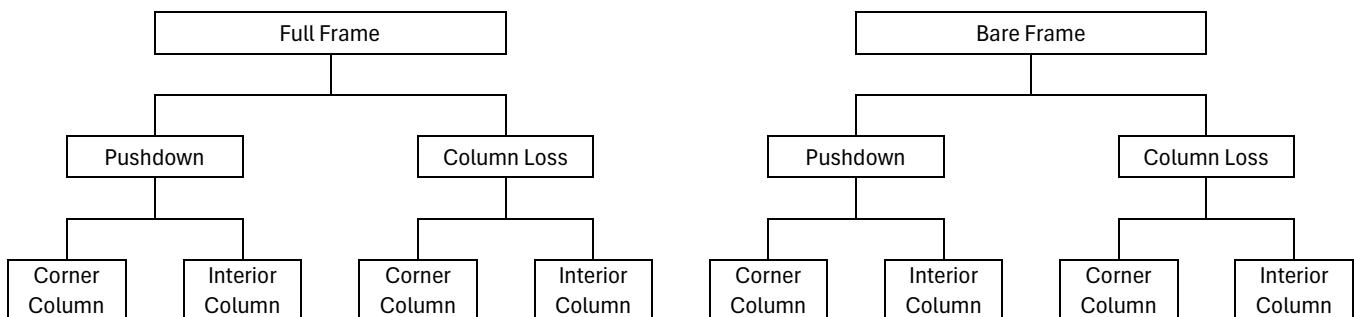


Figure 3-10: Analysis Plan Chart

3.2.7 SIMPLIFIED APPROXIMATE METHOD

Finally, in Chapter 1 using experimental data obtained from literature, a simplified analytical method was developed to predict the peak flexural/arch response of 2D bare single-story sub-assemblages. The method provides a quick alternative to nonlinear numerical analysis to calculate the force capacity of systems under quasi-static pushdown.

3.3 SUMMARY & CONCLUSIONS

Following the methodology explained in this chapter, this research aims to take a further step into examining the response of regular RC framed structures and quantifying the effects of slab membrane action, type of analysis, and removed column position on the progressive collapse behavior of buildings. The methodology adopted in this study was structured to ensure a comprehensive and reliable evaluation of the nonlinear response of RC frames to extreme loading conditions.

To achieve this, a validated numerical modeling approach was established using Abaqus, ensuring that the analysis accurately reflects real structural behavior. The selection of experimental studies from the literature allowed for model verification and calibration, confirming the software's ability to capture critical collapse mechanisms, including flexural response, as well as compressive arching, catenary and membrane actions.

The case study of a six-story RC building was developed to systematically investigate progressive collapse resistance under different column removal scenarios. By comparing full-frame and bare-frame models, this research aimed to isolate and quantify the contribution of slab membrane action to structural robustness. The analysis was performed under both static pushdown and dynamic column loss conditions to evaluate differences in structural response and determine appropriate dynamic increase factors in accordance with existing guidelines.

Additionally, a simplified approximate method was developed based on experimental data to provide a practical and computationally efficient alternative for estimating structural capacity in progressive collapse scenarios. This method offers a bridge between complex numerical simulations and simplified engineering assessments, making it a valuable tool for future research and practical applications.

In summary, the methodology outlined in this chapter provides a structured and multi-faceted approach to studying progressive collapse in RC frames. By integrating experimental validation, numerical analysis, and simplified modeling techniques, this research enhances the current understanding of progressive collapse resistance and contributes to the development of more effective assessment methods for structural safety.

4. ANALYSIS SOFTWARE VALIDATION

4.1 INTRODUCTION

Before analyzing the case study building, it was necessary to validate the ability of the chosen software (Abaqus) and modeling techniques to simulate the nonlinear response of reinforced concrete structures under column loss. Four experimental studies from the literature were selected to replicate and verify key aspects of structural behavior across a range of configurations, boundary conditions, and loading scenarios. This chapter outlines the process, including modeling assumptions, material properties, analysis steps, and comparisons with experimental results. The goal is to ensure that the software setup, element types, material models, and analysis methods produce reliable predictions of progressive collapse behavior.

4.2 FIRST EXPERIMENTAL STUDY EXAMPLE

4.2.1 MODEL DESCRIPTION

4.2.1.1 CHOICE OF STRUCTURAL ELEMENTS

Three-dimensional 8-node deformable solid brick elements C3D8R were used to model the concrete members, while 3-dimensional 2-node truss elements T3D2 were used to model the steel reinforcement. By embedding the rebar elements in the concrete, the interaction between steel and concrete was better represented compared to other types of elements. Due to the geometric and loading symmetry, only half of the system was modeled (Figure 4-1 and Figure 4-2) by fixing the rotations about the Z-Axis and Y-Axis and the displacement in the X-Direction at all the nodes on the plane of symmetry. Furthermore, according to [71] and [72], mesh sizes within 30 mm to 76 mm (1.2 in. to 3 in.) were observed to give accurate results. Therefore, a mesh size of 50 mm was chosen for the solid and truss elements used in the analysis.

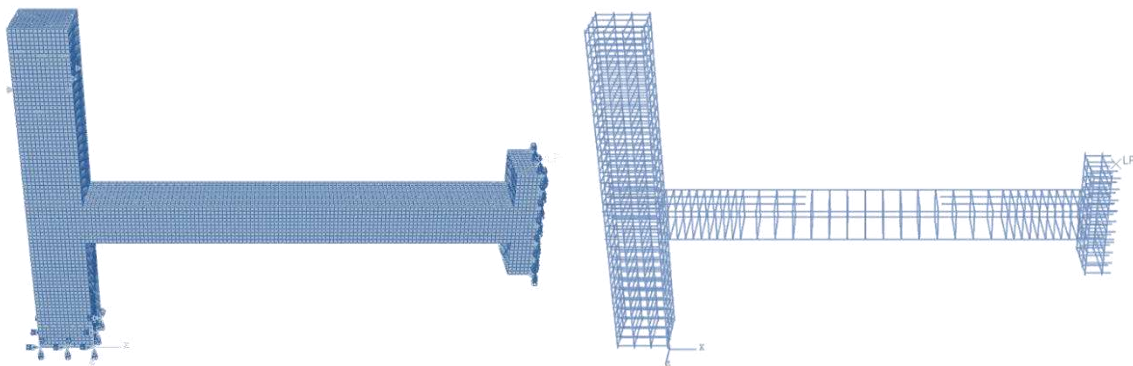


Figure 4-1: Abaqus Model for IMF Showing Meshed Solid Elements with Restraints (Left) & Embedded Rebar (Right)

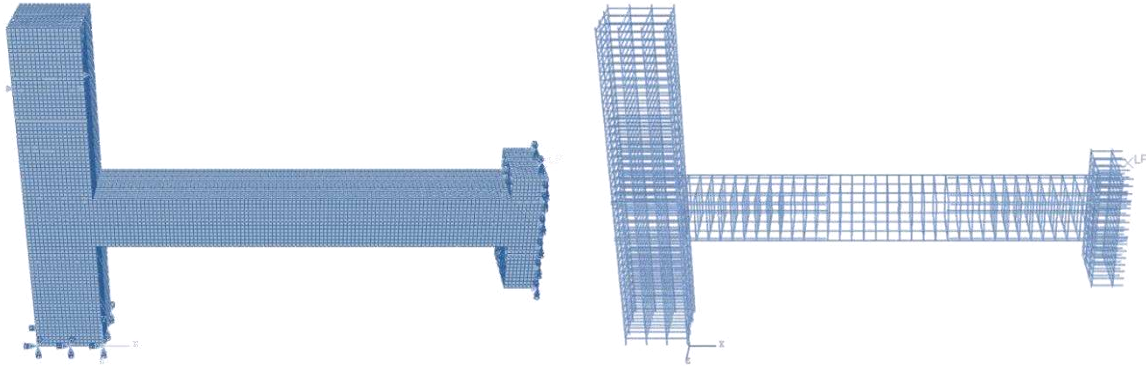


Figure 4-2: Abaqus Model for SMF Showing Meshed Solid Elements with Restraints (Left) & Embedded Rebar (Right)

4.2.1.2 MODELING OF CONCRETE BEHAVIOR

To describe the inelastic nonlinear behavior of concrete in both tension and compression, the Concrete Damaged Plasticity Model (CDP) available in Abaqus was chosen. Two stress-strain curves are needed to define the plastic behavior of the concrete. The stress-strain data to be provided should be true stress versus inelastic strain which may be obtained from the engineering stress-strain data using the following formulas:

$$\sigma_{\text{true}} = \sigma_{\text{eng}} (1 + \epsilon_{\text{eng}})$$

$$\epsilon_{\text{true}} = \ln (1 + \epsilon_{\text{eng}})$$

$$\epsilon_{\text{inelastic}} = \epsilon_{\text{true}} - \sigma_{\text{true}}/E_0$$

where σ_{eng} = Engineering stress,

ϵ_{eng} = Engineering strain,

σ_{true} = True stress,

ϵ_{true} = True strain,

$\epsilon_{\text{inelastic}}$ = Inelastic strain,

E_0 = Elastic Young's modulus.

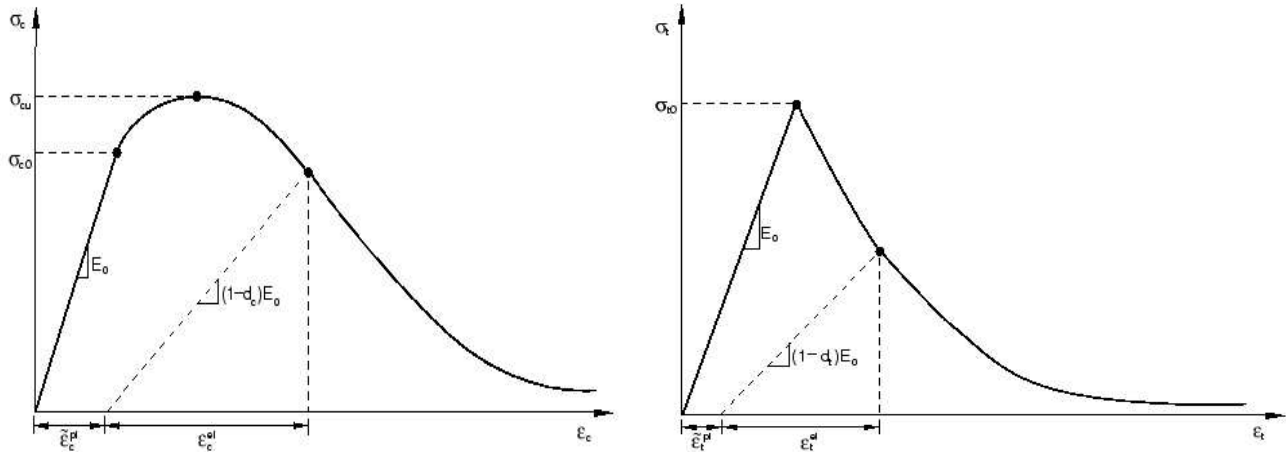


Figure 4-3: Response of Concrete to Uniaxial Loading in Compression (Left) & Tension (Right) [73]

The model also incorporates two damage variables d_c and d_t to be defined for the compression and tension post-peak behavior, respectively. These parameters are useful in defining the (elastic) stiffness degradation that occurs after the peak stress is reached when the concrete specimen is unloaded at any point on the strain softening branch (Figure 4-3). Different approaches and formulas to calculate the damage parameters can be found in literature. Some are simple and straightforward as in [74], while others are a bit more elaborate and complex as in [75]. A comparative study was conducted to choose the most suitable formula that produces results similar to the experimental ones. The following expression mentioned in [76] and [77] was found to be the most consistent:

$$d_c = 1 - \frac{\sigma_c}{f'_c}$$

where d_c = Concrete damage parameter in compression,

σ_c = Compressive stress of concrete (on the descending branch),

f'_c = Peak compressive stress of concrete.

The damage is assumed to occur after the peak stress is reached, so only plasticity is responsible for the nonlinearity of the material before this point. Similarly, for tensile stresses, the damage parameter can be expressed as:

$$d_t = 1 - \frac{\sigma_t}{f_t}$$

where d_t = Concrete damage parameter in tension,

σ_t = Tensile stress of concrete (on the descending branch),

f_t = Peak tensile stress of concrete.

However, these damage parameters are mainly useful in cyclic loading where the structural elements are loaded and unloaded several times. In monotonic loading, on the other hand, the omission of these parameters was found to be acceptable, and indeed the results obtained without using the damage parameters were in general the closest to the experimental ones. Therefore, for simplicity, the damage parameters were not used.

The input stress-strain curves for the IMF and SMF specimens are shown in Figure 4-4 and Figure 4-5. In compression, the material was assumed to obey Hooke's law up to 40% of the ultimate compressive strength (i.e., the behavior is linear), after which the numerical model proposed by Hsu and Hsu in [78] was used to generate the nonlinear part of the stress strain curve as per the following equation:

$$\frac{\sigma_c}{f_c'} = \frac{\beta (\epsilon/\epsilon_c')}{\beta - 1 + (\epsilon/\epsilon_c')^\beta}$$

where $\beta = \frac{1}{1 - \frac{f_c'}{\epsilon_c' E_0}}$

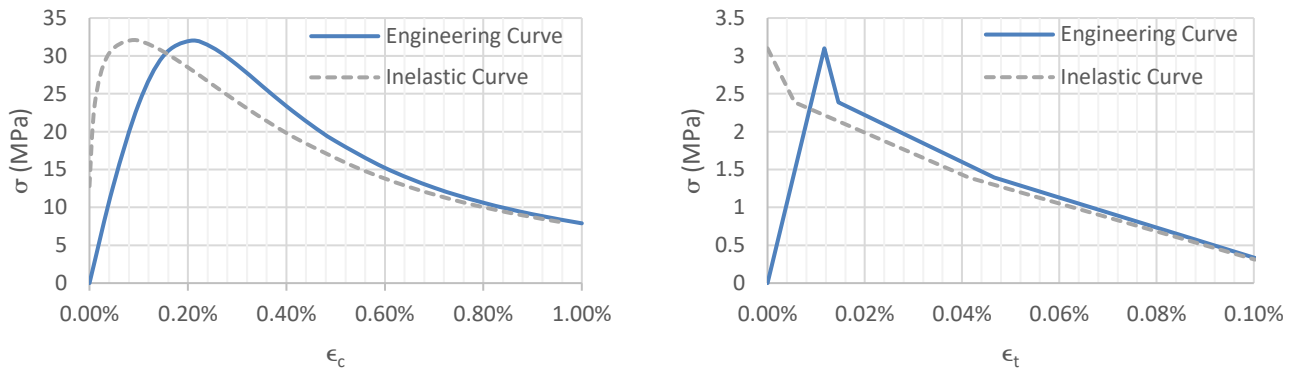


Figure 4-4: Input Compression (Left) & Tension (Right) Stress-Strain Curves for Concrete in IMF

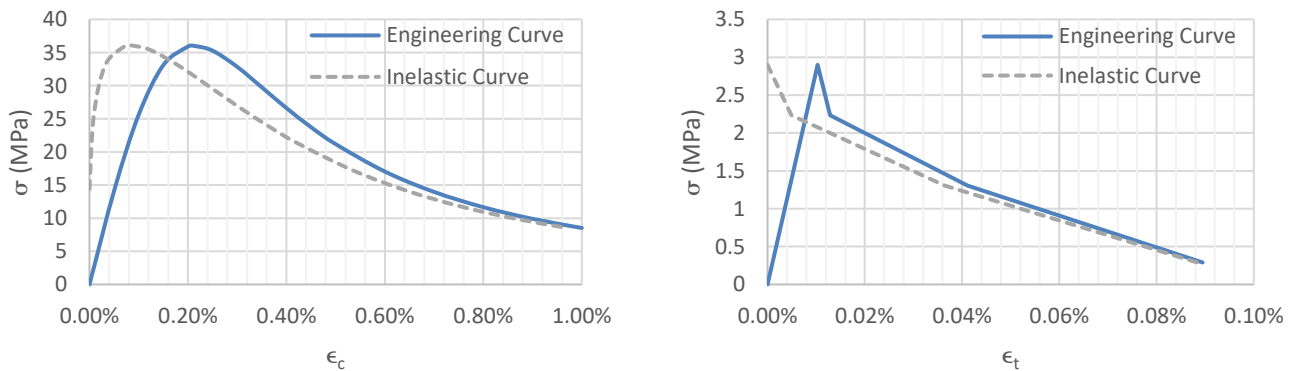


Figure 4-5: Input Compression (Left) & Tension (Right) Stress-Strain Curves for Concrete in SMF

In tension, on the other hand, the tension stiffening model developed in [79] and modified in [80] for Abaqus was adopted in this study and shown in Figure 4-6.

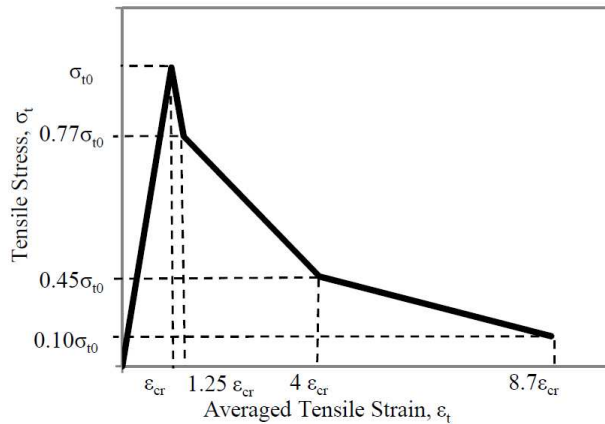


Figure 4-6: Idealized Tension Stiffening Model for Concrete [80]

Finally, the CDP parameters required to define the plastic behavior are shown in Table 4-1. The values of these parameters are discussed in abundance in literature, as in [76] and [81].

Table 4-1: Abaqus CDP Plasticity Parameters

Dilation Angle	Eccentricity	f_{b0}/f_{c0}	K	Viscosity Parameter
30	0.1	1.16	0.667	0.0005

4.2.1.3 MODELING OF REINFORCING STEEL BEHAVIOR

The plastic behavior of steel in Abaqus is defined using a true stress vs plastic strain curve valid for both tensile and compressive stresses. The following formula developed in [82] was used to describe the stress strain curve:

$$\epsilon = \frac{\sigma}{E} + 0.002 \left(\frac{\sigma}{\sigma_y} \right)^{1/n}$$

where n = Strain hardening exponent of the material = $\frac{\log(\sigma_u/\sigma_y)}{\log(\epsilon_f/0.002)}$,

ϵ = Total strain (elastic and plastic) at any given point,

ϵ_f = Elongation strain = $\epsilon_u - \sigma_u/E$,

ϵ_u = Ultimate strain (elastic and plastic),

σ = Stress at any given point,

σ_y = Yield stress of the material,

σ_u = Ultimate stress of the material,

E = Elastic Young's modulus.

Plastic strain represents the permanent, non-recoverable component of material deformation. It is calculated as the difference between the inelastic strain and the strain associated with material stiffness degradation (damage), as expressed by:

$$\epsilon_{\text{plastic}} = \epsilon_{\text{inelastic}} - \frac{d}{(1-d)} \frac{\sigma}{E_0}$$

When damage effects are neglected (i.e., $d = 0$), the plastic strain becomes equal to the inelastic strain. Consequently, the same material modeling approach used for concrete can be directly applied to steel without introducing additional damage parameters.

Figure 4-7, Figure 4-8 and Figure 4-9 show the characteristic data for the used rebar in both IMF and SMF models.

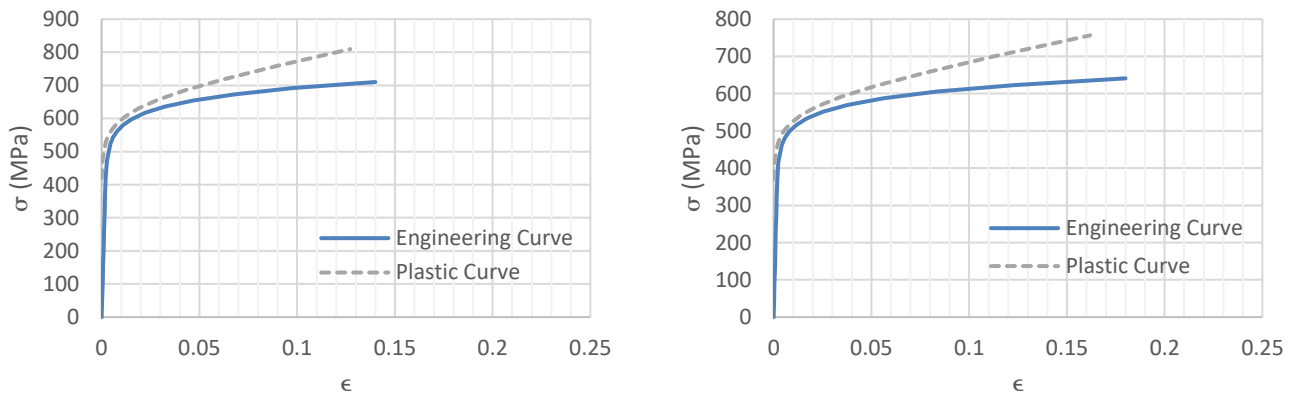


Figure 4-7: Input Stress-Strain Curves for Steel Rebar Sizes 8 (Left) & 9 (Right) in IMF

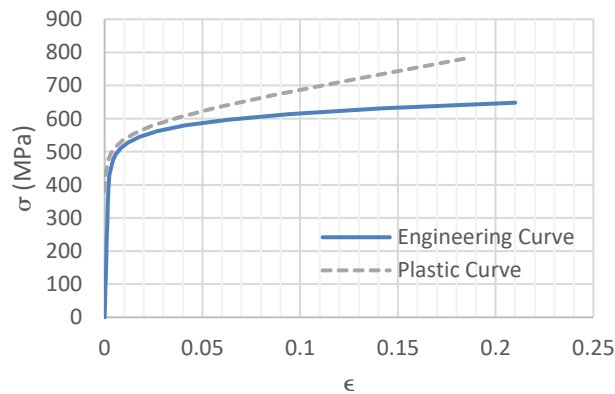


Figure 4-8: Input Stress-Strain Curves for Steel Rebar Size 8 in IMF & SMF

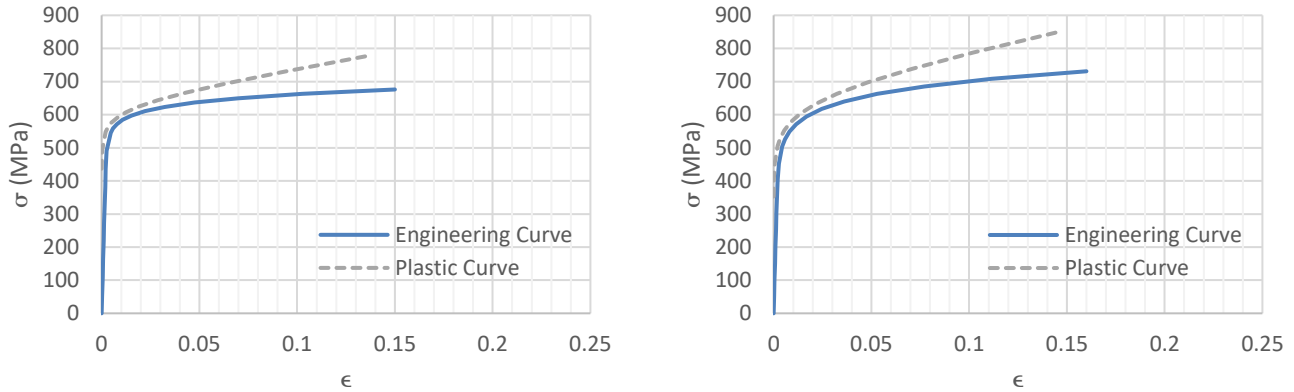


Figure 4-9: Input Stress-Strain Curves for Steel Rebar Sizes 4 (Left) & 10 (Right) in SMF

4.2.2 VALIDATION OF RESULTS

Because of the high nonlinearity and large deformations of the problem, explicit analysis was chosen over implicit analysis due to its much lower computational cost. Implicit analysis was carried out once, though, for the IMF and compared with the explicit analysis. The results were very close, and therefore, explicit analysis was used in the remainder of this research. To simulate the monotonic displacement control analysis that matches the experimental tests, a displacement was applied at the middle joint of each model using the pre-built smooth amplitude in Abaqus. In order for the analysis to be considered as quasi-static, most of the external work must be converted into internal energy with a minimal part converted into kinetic energy. Therefore, an energy balance check was made after the conclusion of the analysis, and the kinetic energy was checked to make sure it did not exceed 10% of the internal energy [83]. After this condition was satisfied, the resulting force-displacement curves were then plotted along with the experimental ones, for both IMF and SMF (Figure 4-10). The error in predicting the behavior of the system is obtained by calculating the difference between the analytical and experimental applied force values at each displacement ordinate. This is done up to the point of rebar fracture and serves as a simple and approximate guide to the accuracy of the analysis and, therefore, the similarity between the numerical and experimental curves. However, it should be noted that if two curves are quite similar but are slightly shifted from each other, the value of the error increases and might imply more dissimilarity than there actually is. Nevertheless, the average error was found to be respectively 23.07% and 14.84% for the IMF and SMF. Generally, due to the nonlinearity of the problem, the analysis was considered acceptable and showed satisfactory agreement with the experimental tests. One thing to be mentioned, though, is that the analytical model was found to moderately overestimate the resistance of the sub-assembly.

The main resistance mechanisms exhibited by the sub-assemblages can be seen in the force-displacement curves. Initially, the resistance was provided by the flexural strength and the rising compressive arch action in the beam. At this stage, the load-bearing capacity increased until reaching its peak. This usually occurs when the bending moment and compressive axial force are almost at their maximum. In the second stage, both bending moment and compressive axial force began to drop while the displacement continued to increase, and so the system’s load-bearing capacity decreased. Due to the ductility of the structural elements, the decrease in bending moment and axial force began to slow down, and the negative slope of the load-displacement curve began to increase before completely reversing when the axial force in the beam turned into tension and the load-bearing capacity of the system started to improve. During this final stage, most of the concrete was either crushed or cracked, and the main resistance was provided by the steel rebar until the rupture occurred. Three points are highlighted in Figure 4-10 for each model, corresponding to the initial peak resistance of the system, the turning point at the end of the arching phase when the beam capacity began to increase again and the fracture point of the rebar at the end of the catenary stage. Figure A-1 and Figure A-2 show the internal normal stresses of the systems at the three points. Stresses in concrete are shown on the left, while stresses in rebar are displayed on the right.

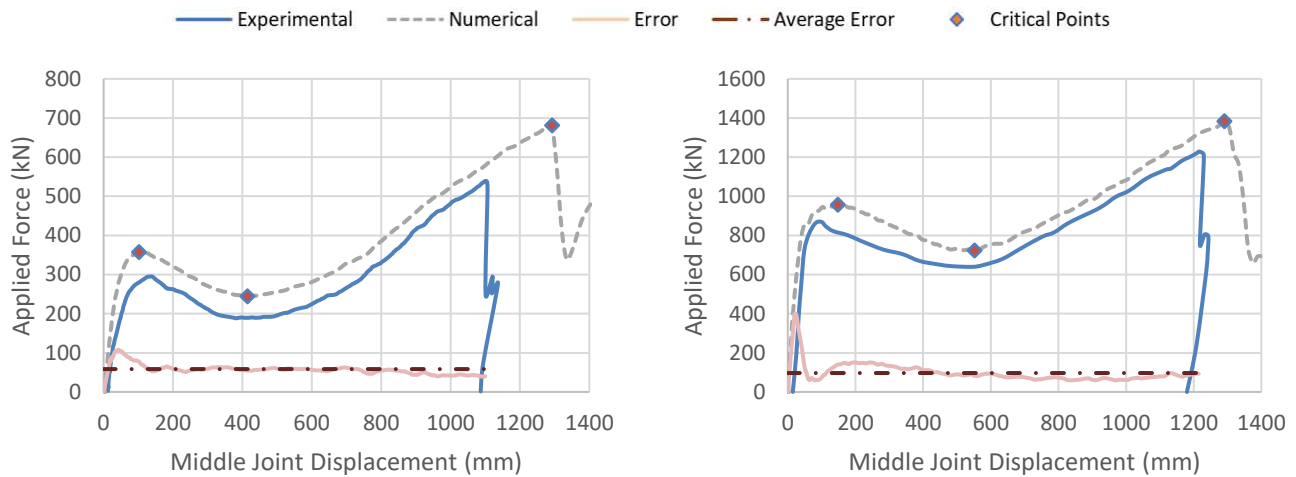


Figure 4-10: Force-Displacement Curves for IMF (Left) & SMF (Right)

4.3 SECOND EXPERIMENTAL STUDY EXAMPLE

4.3.1 MODEL DESCRIPTION

Two specimens, T1 and S1 (Figure 4-11 and Figure 4-12, respectively), were modeled in Abaqus to test and validate the software’s ability to predict the response of 3D systems with transversal beams and slabs. Similar to the first study, concrete was modeled using C3D8R solid elements, while rebar was modeled using T3D2 truss elements.

CHAPTER 4. ANALYSIS SOFTWARE VALIDATION

The embedded region constraint was used to define the interaction between the rebar truss elements and the concrete brick elements. The concrete material was modeled using the Concrete Damaged Plasticity Model (CDP). Figure 4-13 and Figure 4-14 show the input stress-strain curves for concrete in compression and tension, while Figure 4-15 shows the stress-strain curves for the used reinforcing steel.

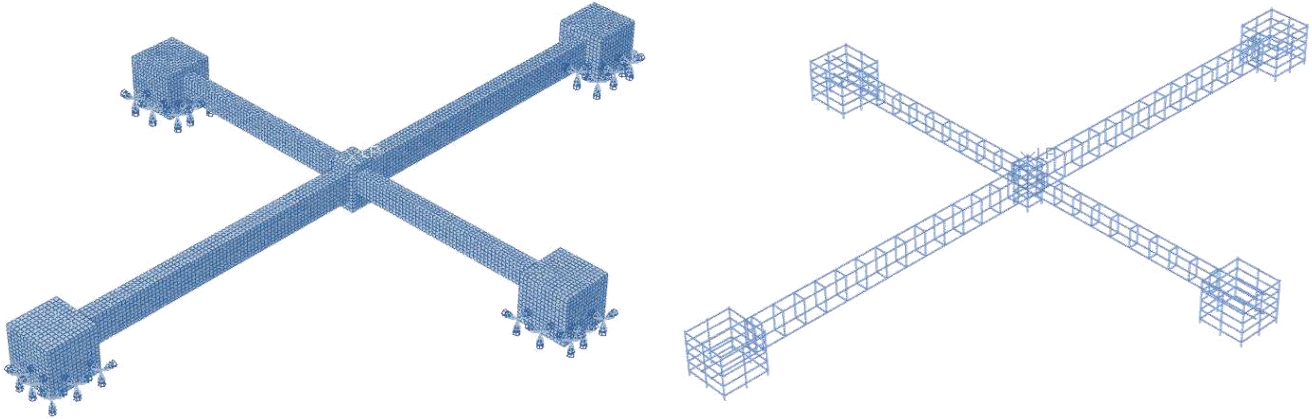


Figure 4-11: Abaqus Model for T1 Showing Meshed Solid Elements with Restraints (Left) & Embedded Rebar (Right)

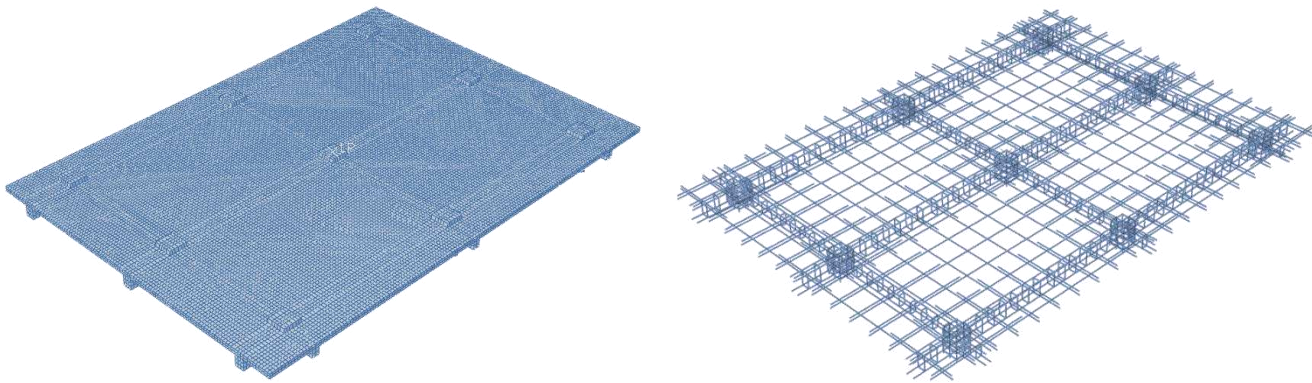


Figure 4-12: Abaqus Model for S1 Showing Meshed Solid Elements with Restraints (Left) & Embedded Rebar (Right)

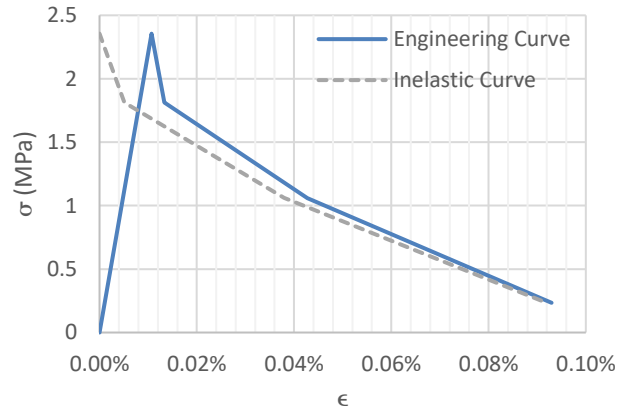
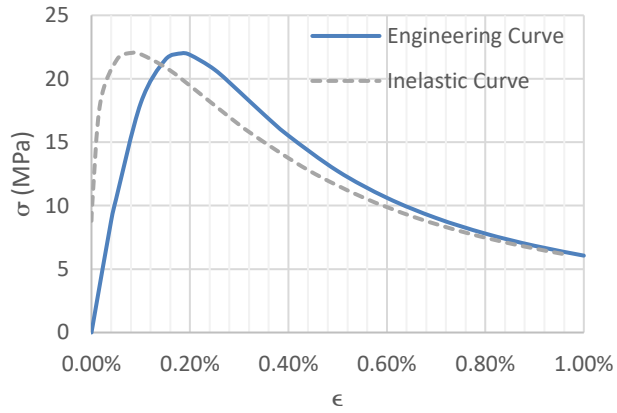


Figure 4-13: Input Compression (Left) & Tension (Right) Stress-Strain Curves for Concrete in T1

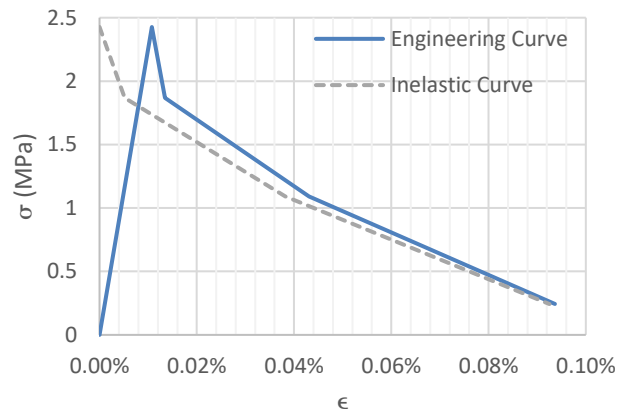
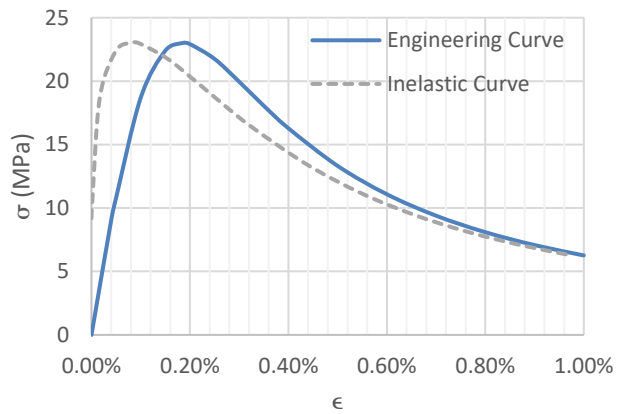


Figure 4-14: Input Compression (Left) & Tension (Right) Stress-Strain Curves for Concrete in S1

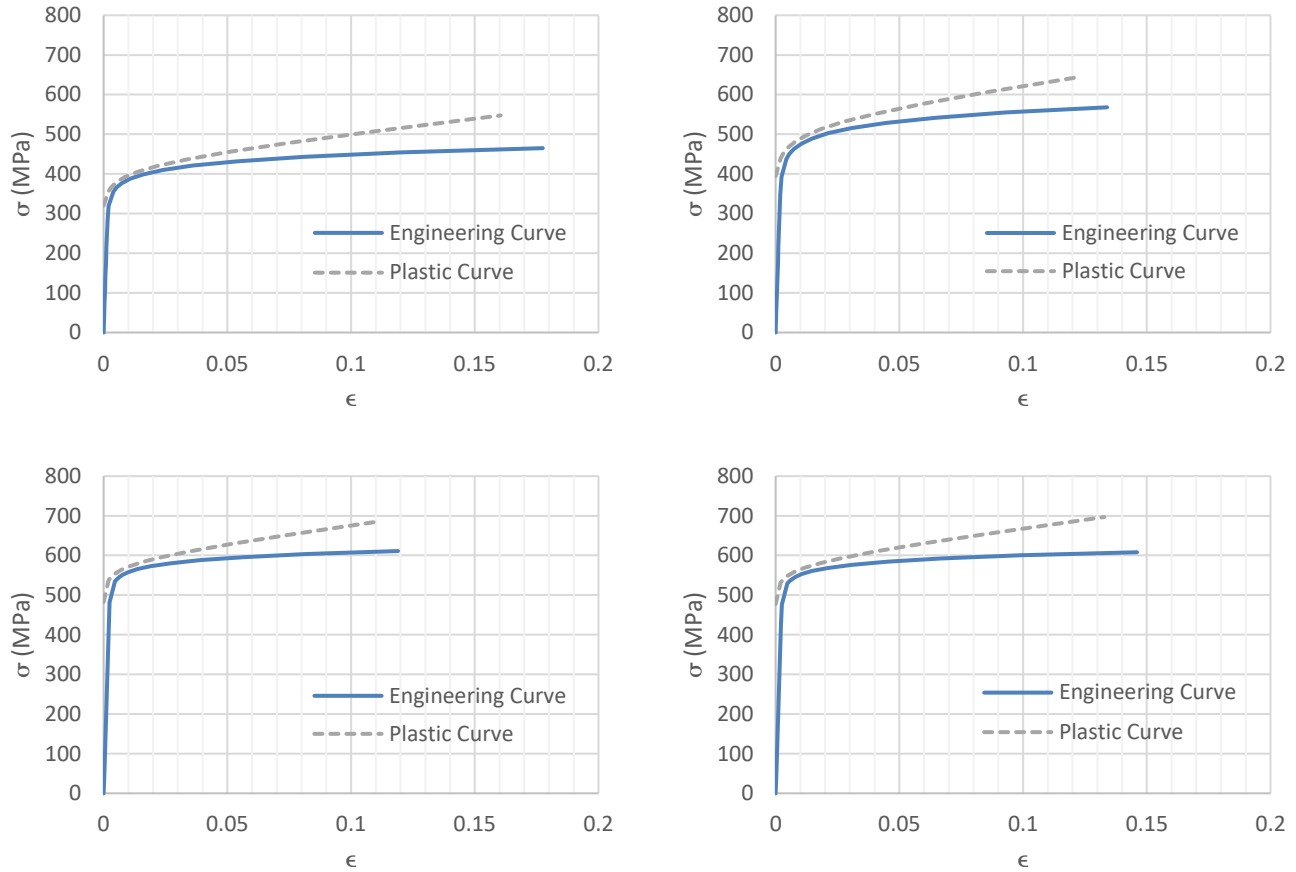


Figure 4-15: Input Stress-Strain Curves for Steel Rebar Sizes R6 (Top Left), T10 (Top Right), T13 (Bottom Left) & T16 (Bottom Right) in T1 & S1

4.3.2 VALIDATION OF RESULTS

Similar to the first experiment, explicit analysis was carried out for time-saving purposes. An energy balance check was made, and the kinetic energy was found to be negligible in relation to the internal energy. The load-displacement curves of the analytical models were plotted against the experimental ones (Figure 4-16). The average error was found to be 16.95% and 11.54% for T1 and S1, respectively. The results were found to be acceptable and in agreement, especially at the beginning of the response at lower displacements. However, as the deformation of the system increases, the discrepancies between the results were found to slightly increase. It is also worth mentioning that the system's load capacity is overestimated in the case of T1.

The normal stresses in the concrete and rebar were examined at three critical points. The first point is when the system reached its peak response during the flexural and compressive arch/membrane actions. The second point was when the system's load-bearing capacity, after dropping, began to rise again at the end of the compressive arch/membrane actions phase and right before the start of the tensile catenary/membrane actions. The last point

is at the end of the tensile catenary/membrane actions phase and right before the first rebar fracture. The internal normal stresses in concrete (left) and steel reinforcement (right) at the three points are shown in Figure A-3 and Figure A-4 for T1 and S1, respectively.

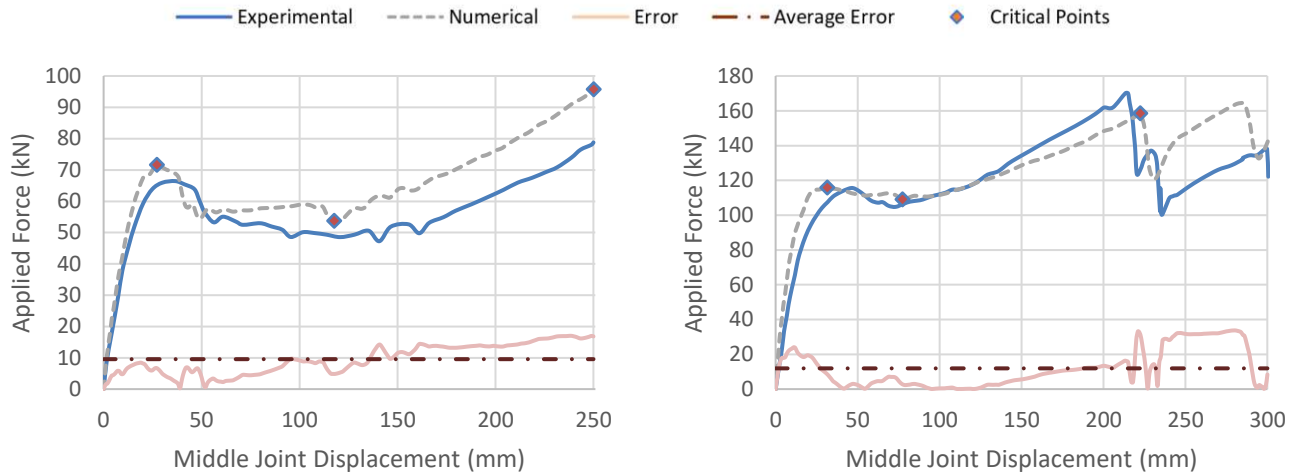


Figure 4-16: Force-Displacement Curves for T1 (Left) & S1 (Right)

4.4 THIRD EXPERIMENTAL STUDY EXAMPLE

4.4.1 MODEL DESCRIPTION

4.4.1.1 MODELING OF ELEMENTS & MATERIALS

Specimen DF2, which was seismically detailed, was modeled in Abaqus using C3D8R solid elements to represent concrete elements as well as structural steel members such as the steel assembly described herein and steel pipes used at the end of the beams to approximate the actual boundary conditions (i.e., the contribution of the rest of the structure). Steel rebar was modeled using T3D2 truss elements which were embedded in the concrete solid elements to simulate the bond between them. Figure 4-17 shows the concrete and rebar elements as well as the steel members used in the experiment to provide adequate boundary conditions to the system. The concrete material was modeled using the Concrete Damaged Plasticity Model (CDP), and the input stress-strain curves for concrete in compression and tension are shown in Figure 4-18, while the stress-strain curves for the used reinforcing steel materials is shown in Figure 4-19. It should be noted, though, that mechanical properties and input data for the double action load cell pipes at the other end of each beam were not provided in the available literature and were, therefore, iteratively assumed.

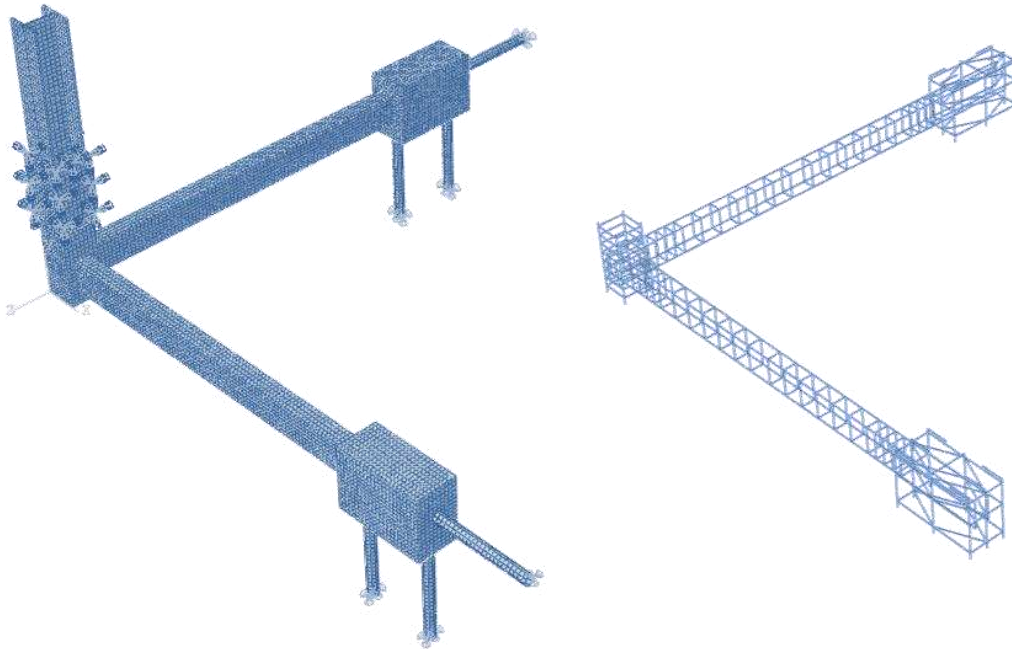


Figure 4-17: Abaqus Model for DF2 Showing Meshed Solid Elements with Restraints (Left) & Embedded Rebar (Right)

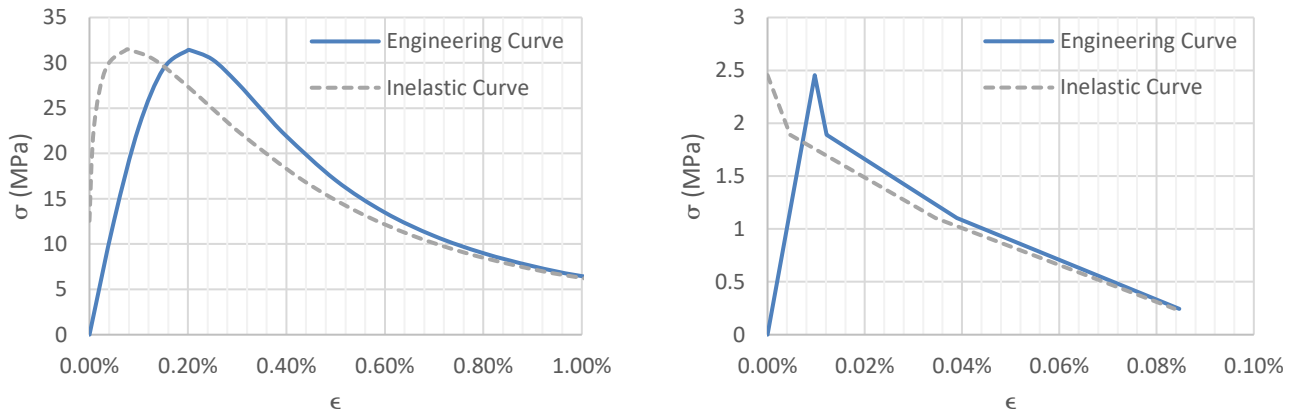


Figure 4-18: Input Compression (Left) & Tension (Right) Stress-Strain Curves for Concrete in DF2

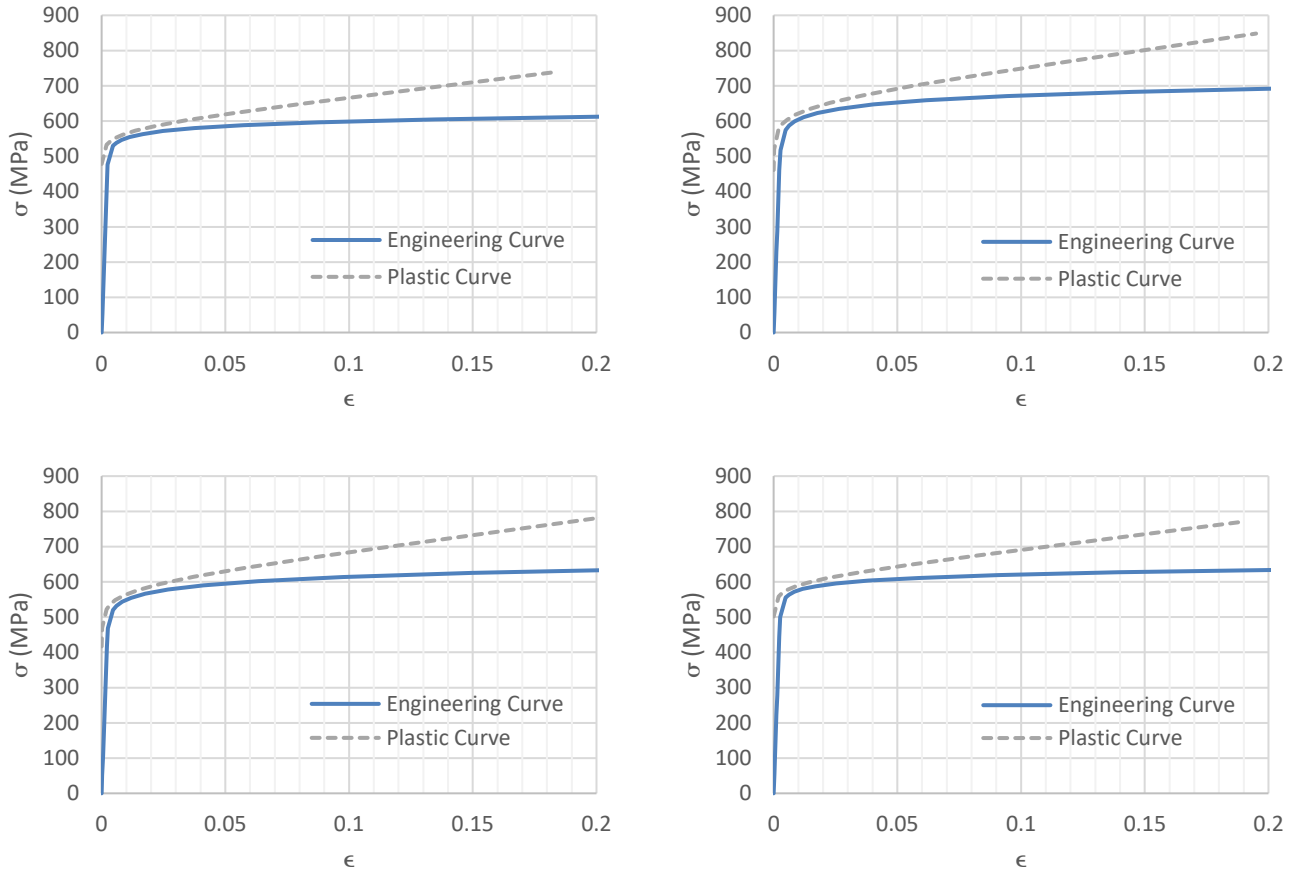


Figure 4-19: Input Stress-Strain Curves for Steel Rebar Sizes R6 (Top Left), T10 (Top Right), T13 (Bottom Left) & T16 (Bottom Right) in DF2

4.4.1.2 COLUMN REMOVAL SIMULATION

To simulate column loss analytically, two models in Abaqus were analyzed. The first was the undamaged model where all columns and supports were present and intact. The undamaged model was solved quasi-statically under the effect of the dead loads, ensuring that no significant inertial effects arose, in order to obtain the values of the column reactions. The second was the damaged model where the column/support in question was removed from the system. First, the dead loads were applied to the system along with the removed column reactions which were applied at the location of the removed column to account for the column's presence before removal. Then, these reactions were reapplied at the same location but in the opposite direction within a very small duration, less than $1/10$ of the period of vibration [30], to simulate the almost sudden column loss. This procedure is summarized in Figure 4-20 where the time-history of the loading is shown. It should be noted that after the system is fully loaded, there is a stabilization period where no loads are applied in order to provide some time for any transient vibrations to peter out before suddenly removing the column.

Another method for the simulation of the column loss is the sudden application of the gravity loads to the damaged model. Unlike the first technique, this procedure does not require the knowledge of the internal forces of the removed column [84] and is, therefore, a more approximate method. Both methods were used in the analysis, and their results were compared together.

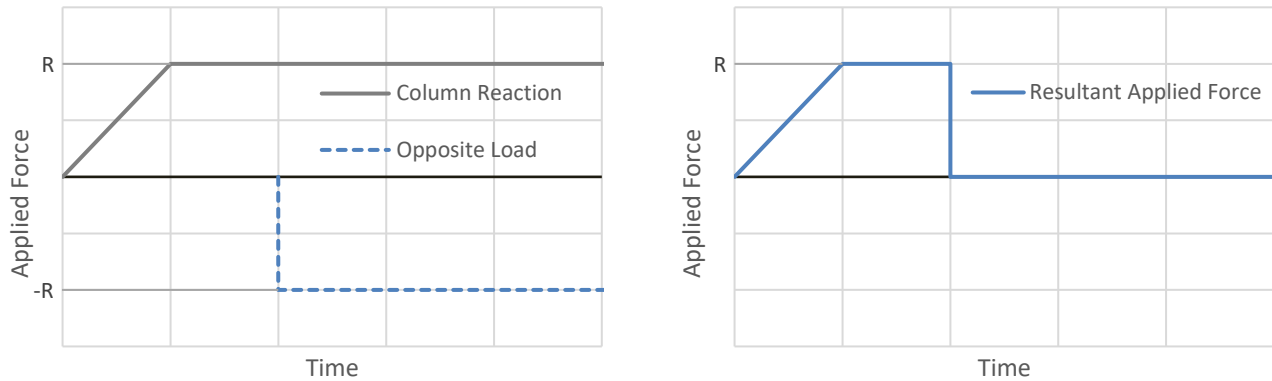


Figure 4-20: Generic Time-History for Column Loss Simulation

4.4.2 VALIDATION OF RESULTS

The vertical displacement of the corner joint produced by the column loss simulation method, referred to as Numerical (CL), as well as the displacement produced by the second method, referred to as Numerical (SL), were plotted in Figure 4-21 along with the experimental results. The graph shows that the numerical results are almost identical, though shifted. Of course, this shift is due to the fact that in the second method, the gravity loads were suddenly applied to the system from the beginning of the analysis, unlike the first method where the system was initially quasi-statically loaded before the internal forces and moments of the column were removed. However, both methods produced virtually the same displacement and vibration. A snapshot of the final point of the “Numerical (CL)” analysis where most of the dynamic vibrations had ceased and static equilibrium had almost completely been achieved is shown in Figure A-5 and Figure A-6, where the total displacement and the stresses, respectively, are illustrated for solid elements as well as rebar elements.

Compared to the experimental results, the numerical methods were able to predict the displacement to a high degree of accuracy. The maximum displacement was found to be 28.96 mm and 28.54 mm respectively in the case of the column loss (CL) and the sudden application of the gravity loads (SL), while the corresponding experimental value was found to be about 29 mm. However, there is a significant difference in the vibrational properties of the system between the experimental specimen and the numerical model. The period of vibration of the actual system appears to be noticeably higher than that of the numerical model. This indicates that the numerical model is stiffer

than the experimental one. This difference may be attributed to idealized modeling assumptions, such as perfect boundary conditions and perfect bond between steel and concrete, as bond slip is not modeled. Furthermore, the previously mentioned lack of available data regarding the end conditions of the beams likely contributes to the discrepancy between the numerical and experimental results. It should, therefore, be emphasized that the behavior of the model and the results of the analysis are highly sensitive to any missing input parameters.

Another observation is that the numerical model failed under the effect of column removal when the CDP damage parameters, previously described in Section 4.2.1.2, were considered in the analysis. Therefore, the results shown herein are of when the damage parameters were not taken into account in the CDP model.

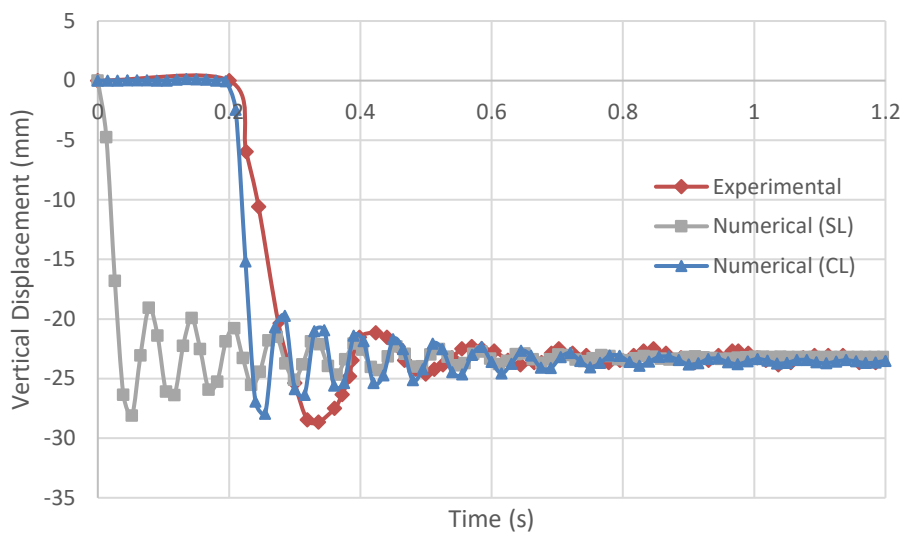


Figure 4-21: Vertical Displacement of the Corner Joint of DF2

4.5 FOURTH EXPERIMENTAL STUDY EXAMPLE

4.5.1 MODEL DESCRIPTION

Specimen D-0.91, which was subjected to 91% of the total applied design loads, was modeled in Abaqus using the same type of elements used in the previous experiments. C3D8R solid elements were used to model the concrete and structural steel columns, while T3D2 truss elements were used to represent the reinforcing steel bars. Although equivalent weights were used in the actual experiment to simulate the applied loads, uniformly distributed surface loads were used in the analysis instead. This is mainly due to the lack of data provided by the authors regarding the used dead weights. Figure 4-22 shows the solid elements as well as the truss elements of the Abaqus model. Again, the CDP model was used to model the concrete behavior. However, as discovered with the previous model, the damage parameters were omitted as they produced unrealistic results and premature

failure. The stress-strain curves for the used concrete material are shown in Figure 4-23, and those of the used steel material are shown in Figure 4-24.

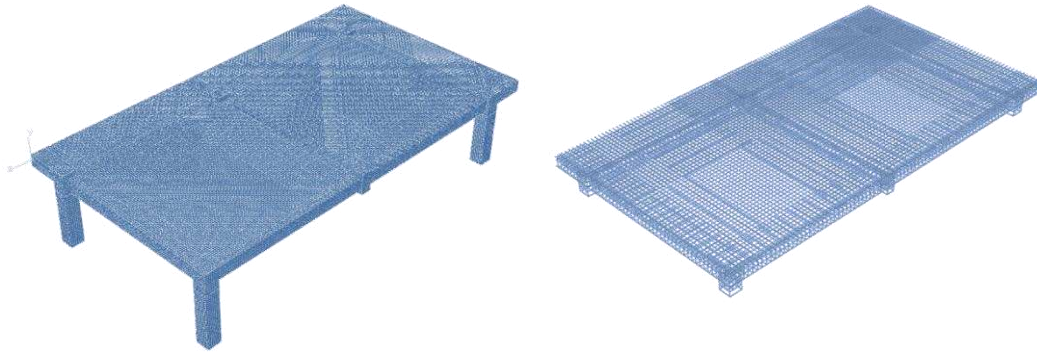


Figure 4-22: Abaqus Model for D-0.91 Showing Meshed Solid Elements with Restraints (Left) & Embedded Rebar (Right)

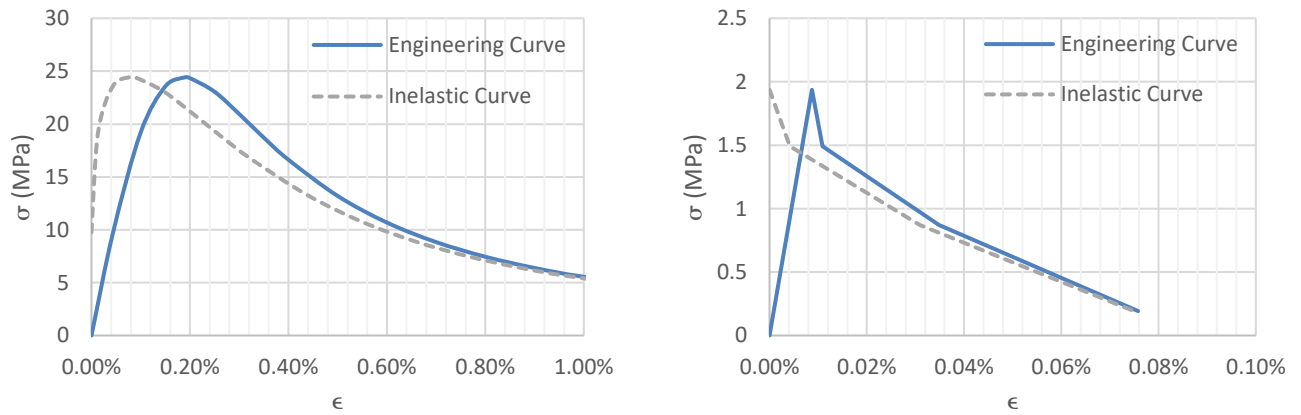


Figure 4-23: Input Compression (Left) & Tension (Right) Stress-Strain Curves for Concrete in D-0.91

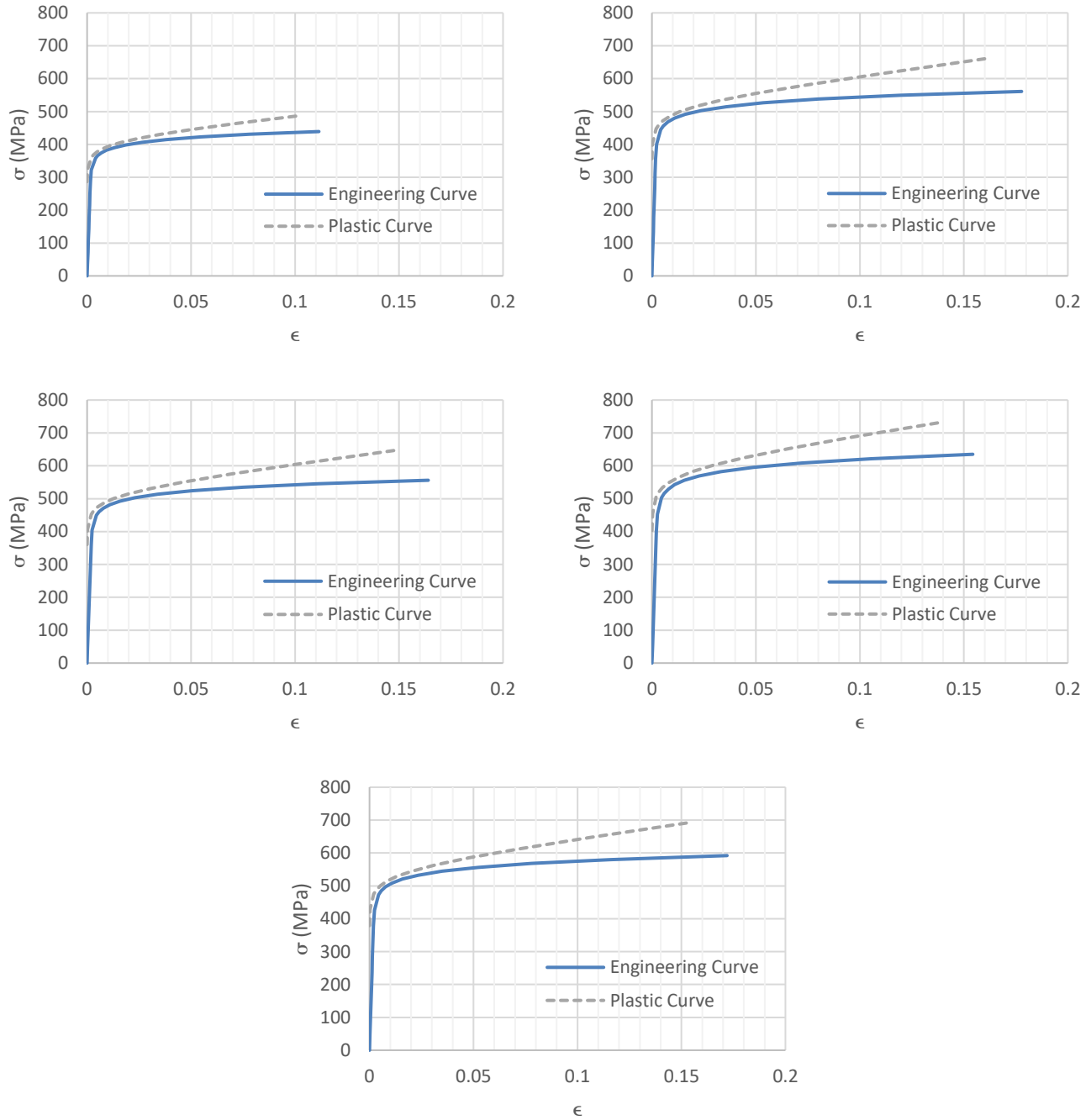


Figure 4-24: Input Stress-Strain Curves for Steel Rebar Sizes R3 (Top Left), R6 (Top Right), R8 (Middle Left), T10 (Middle Right) & T13 (Bottom) in D-0.91

4.5.2 VALIDATION OF RESULTS

The maximum vertical displacement obtained in the actual experiment was found to be 42.5 mm, while the permanent displacement at the end of the vibration was 40.1 mm. As was performed with the preceding

experiment, the column loss analysis was conducted using the two previously mentioned methods, and their results were compared with the experimental ones. As can be seen in Figure 4-25, the first (CL) and second (SL) numerical methods produced maximum displacements of 37.6 mm and 43.2 mm and permanent displacements of 36.2 mm and 41.9 mm, respectively. Therefore, there is a difference of 14.9% in the maximum displacement values between the two methods and a difference of 15.6% in the final displacement. The second method produces higher values, and this could be mainly attributed to the fact that all gravity loads are suddenly applied to the system. In the first method, only the column reaction is suddenly removed, which means that only part of the gravity loads is dynamically applied, while the remaining portion is statically applied. It is quite curious, though, that both methods produced virtually the same results in the previous experiment. This may be explained by the fact that most of the applied gravity loads were supported by the removed corner column.

Another thing worth mentioning is that the analysis was found to be very sensitive to input parameters. For instance, no data regarding the supporting steel columns were provided by the authors, and therefore, these parameters were iteratively assumed, and their values were found to notably affect the results. Therefore, it cannot be stated that one method produced better results, when compared to the experimental values, than the other one. Although it may seem that the second method (SL) was more accurate, a slight change, for example, in the assumed thickness of the steel columns, could shift the results in the other direction. Furthermore, as previously explained, the first method (CL) is the more accurate one, as it replicates the loss of the column by removing its internal forces and, therefore, its existence in the system.

Another remark is that the numerical system again showed more stiffness which in turn affected its response and dynamic properties. However, it can be said that the overall behavior of the system was acceptably similar to the actual response of the specimen. Most importantly, the system did not fail and produced comparable displacements and results. Figure A-7 and Figure A-8 show the displacements and the stresses in the concrete and rebar at the end of the analysis.

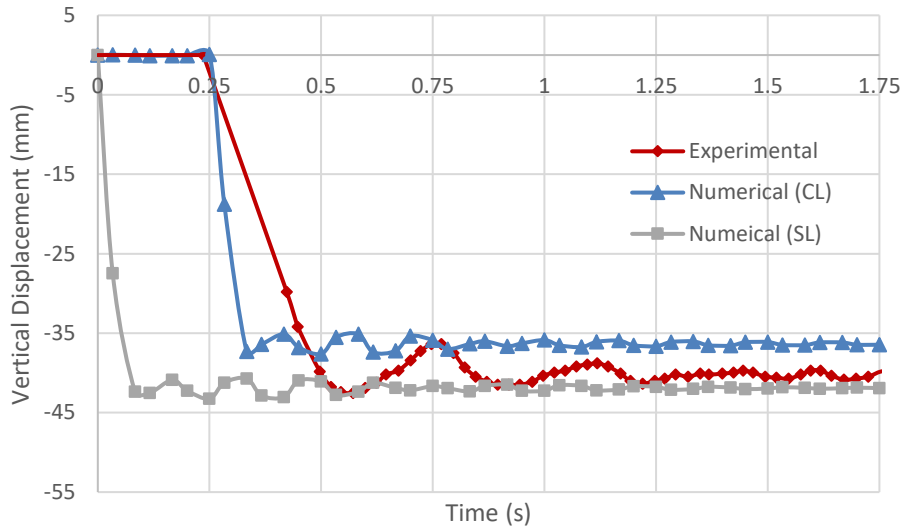


Figure 4-25: Vertical Displacement at the Removed Column in D-0.91

4.6 SUMMARY & CONCLUSIONS

At the end of the validation phase, four experimental studies covering different structural configurations, boundary conditions and loading scenarios were successfully modeled and replicated. Based on the results, the following key observations were made:

- In general, the numerical models exhibited greater stiffness than the experimental specimens. This resulted in higher vibration frequencies and faster loading and unloading rates under dynamic conditions.
- The numerical models typically produced slightly higher load-carrying capacities or lower deformations compared to experimental results.
- The damage parameters of the Concrete Damaged Plasticity (CDP) model tended to induce premature failure during dynamic column removal simulations and were, therefore, omitted.
- The analysis results were highly sensitive to input parameters, particularly material properties and boundary conditions, especially at advanced nonlinear stages.
- Overall, the program produced acceptable and reliable results and was deemed suitable for application to the case study analyses presented in the following chapters.

These observations confirmed that the modeling strategies adopted, including the selection of elements, material models and analysis procedures were appropriate for simulating the progressive collapse behavior of RC structures. Although minor discrepancies between numerical and experimental results were observed, they were

CHAPTER 4. ANALYSIS SOFTWARE VALIDATION

within acceptable limits considering the complexity of the problem. The validation results provided a sound basis for applying the finite element models to the subsequent case study analyses.

5. PROGRESSIVE COLLAPSE ANALYSIS OF A MULTI-STORY CASE STUDY BUILDING

5.1 INTRODUCTION

This chapter presents the application of the validated analysis methodology to a reinforced concrete multi-story case study building. The objective is to evaluate the structure's resistance to progressive collapse following sudden column removal scenarios. The chapter begins by describing the building design process, including assumptions, material properties, loading conditions and structural modeling choices. Nonlinear static and dynamic analyses are then conducted to simulate different column loss scenarios and assess the resulting load capacities, deformation and collapse mechanisms. Dynamic Increase Factors are computed to quantify the amplified structural demands under dynamic conditions and are compared to code-based estimates. The results are interpreted to assess the influence of structural features such as floor slabs, column location and frame type on progressive collapse resistance. Finally, model reduction techniques are introduced to simplify the structural system while preserving its essential collapse behavior. An approximate transformation method, based on the principle of energy conservation, is then proposed to convert pseudo-static curves into equivalent displacement-controlled quasi-static responses. This approach captures the post-peak softening behavior associated with arch action as well as the onset of catenary behavior, enabling a more realistic assessment of the structure's full progressive collapse capacity.

5.2 DESIGN

5.2.1 DESIGN INPUT

5.2.1.1 MATERIAL PROPERTIES

The compressive strength of the used concrete was assumed to be 30 MPa with a specific weight of 24 kN/m³. Its response was linear up to 12 MPa (40% of ultimate strength). The yielding strength of the reinforcing steel was taken as 400 MPa while its ultimate strength was taken as 600 MPa. The modulus of elasticity of concrete was calculated using the following expression taken from CSA, while that of steel was taken as 210 GPa.

$$E_c = 4500 \sqrt{f'_c}$$

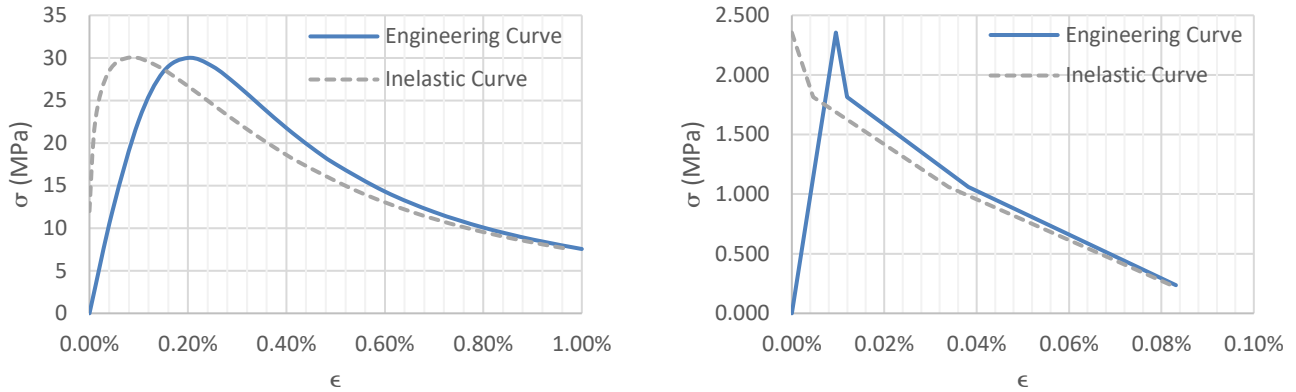


Figure 5-1: Input Compression (Left) & Tension (Right) Stress-Strain Curves for Concrete

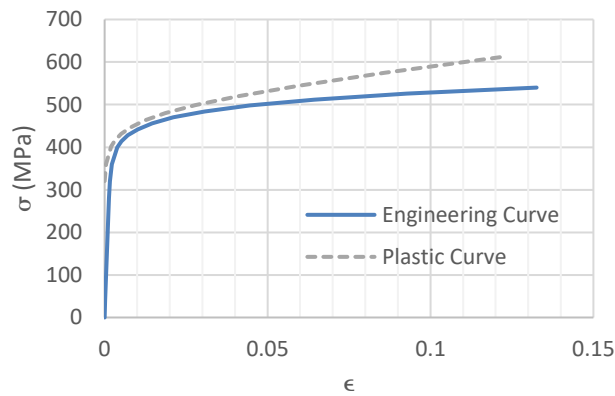


Figure 5-2: Input Stress-Strain Curves for Steel Rebar

The ultimate strain of steel was assumed to be 13%. The stress-strain curves were generated according to the same equations adopted in Sections 4.2.1.2 and 4.2.1.3 for modeling concrete and reinforcing steel, respectively. These curves are presented in Figure 5-1 and Figure 5-2.

5.2.1.2 INPUT LOADS

Since the building was assumed to be residential, the live load was taken to be 1.9 kPa as prescribed by Table 4.1.5.3. of the NBCC [68]. The snow load acting on the final roof was taken to be 2.23 kPa, and the finishing load on each floor was assumed to be 1.5 kPa. The façade walls were assumed to be brick with a thickness of 100 mm and net weight of 3.25 kN/m including plaster and windows.

As for the seismic design load, it was calculated according to Section 4.1.8. of the NBCC [68]. First, a modal analysis was conducted in SAP2000 on the whole building, and the lateral period of vibration was found to be 1.53 s. However, according to Sentence 4.1.8.11.(3), the design period (T_a) was taken as 1.02 s. Since the structure was

regular and less than 60 m in height, and had a period lower than 2 s, the Equivalent Static Force Procedure (ESFP) was allowed to be used in the design. Alternatively, because the value of $I_E F_a S_a(0.2)$ was found to be 0.19 which was less than 0.35, the ESFP was also allowed to be used. Therefore, the value of the base shear (V) was calculated using the following equation:

$$V = S(T_a) M_v I_E W / (R_d R_o)$$

where $S(T_a)$ = Design spectral response acceleration, expressed as a ratio to gravitational acceleration, for a period of T_a ,

M_v = Factor to account for higher mode effect on base shear,

I_E = Earthquake importance factor of the structure,

W = Dead weight of the building, plus 25% of the snow load,

R_d = Ductility-related force modification factor,

R_o = Overstrength-related force modification factor.

The supporting soil was assumed to be very dense and was, therefore, Class C. The building’s importance category was considered normal, and therefore, the importance factor was equal to 1.0. The seismic force resisting system (SFERS) was ductile moment resisting frames, and therefore, R_d and R_o were 4.0 and 1.7, respectively. The 5% damped spectral response acceleration $S_a(T)$ is equal to $S(T)$ in the case of Class C soil and is plotted against the period of vibration in Figure 5-3.

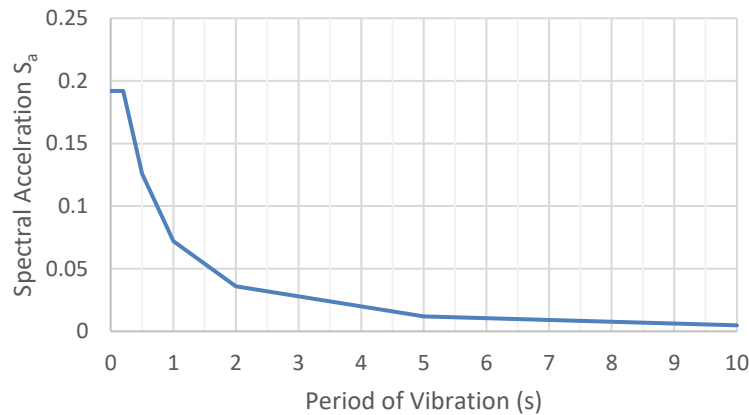


Figure 5-3: Design 5% Damped Spectral Response Acceleration in Calgary

The base shear V was found to be 158.24 kN and was then distributed over the height of the building with a portion F_t equal to 11.34 kN concentrated at the top. Due to the symmetry in both directions, only 5% accidental torsion

was considered in the design. The total lateral force applied per SFRS, including torsional effects, was 83.07 kN distributed as shown in Figure 5-4.

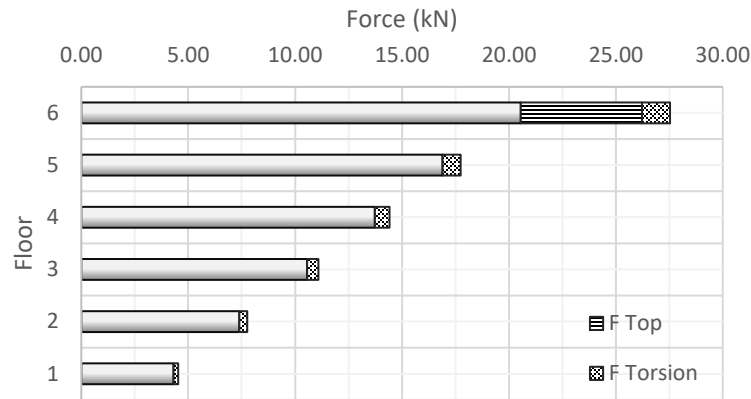


Figure 5-4: Lateral Force Distribution on SFRS

Finally, the wind loads were calculated according to Section 4.1.7. of the NBCC [68]. The external design pressure or suction (p) exerted by wind on a portion or the entirety of a building's surface was determined using the following equation:

$$p = I_w q C_e C_t C_g C_p$$

where I_w = Importance factor for wind load,

q = reference velocity pressure,

C_e = Exposure factor,

C_t = Topographic factor,

C_g = Gust effect factor,

C_p = External pressure coefficient.

Similar to the earthquake force calculations, the importance factor for wind load (I_w) was taken as 1.0, as the building was classified as a normal-importance structure. The reference wind pressure (q) was obtained from Table C-2 of the NBCC [68], yielding 0.48 kPa for Calgary, based on a return period of 1 in 50 years. The exposure factor (C_e) was determined to be 0.8, as the building is assumed to be located in a dense urban area downtown. The topographic factor (C_t) was taken as 1.0, as the site is assumed to be relatively flat, lacking significant topographic variations that could influence wind flow. Finally, the product of $C_g C_p$ was obtained from Figure

4.1.7.6.-A of the NBCC [68]. The resulting wind pressure distribution was then applied to the structure accordingly for further analysis.

Load combinations used in the design were taken from Table 4.1.3.2.-A of the NBCC [68]. Two combinations, shown in Table 5-1, were found to be the most critical to the design. The slabs and interior frames were designed according to Combo 1, while the exterior frames were designed according to Combo 2.

Table 5-1: Critical Design Load Combinations

Combo	Case	Principle Loads	Companion Loads
1	2	1.25D + 1.5L	S
2	5	D + E	0.5L + 0.25S

5.2.1.3 ANALYSIS & DESIGN

Manual calculations were used to choose the preliminary concrete dimensions. Then linear static analysis was conducted using SAP2000, and the reinforcement was chosen according to CSA A23.3-14 [69]. Also, section modifiers mentioned in Section 10.14.1.2 of the CSA A23.3-14 [69] were adopted in the design to account for reduced stiffness due to concrete cracking. The foundation of the building was assumed to be stiff enough for the columns to be considered clamped to the ground. Although the building analyzed in this study is located in Calgary, Alberta, the reinforcement bars were selected based on U.S. standards with imperial units (#3 [9.5 mm], #4 [12.7 mm], #5 [15.9 mm], and #6 [19.1 mm]) rather than the metric units prescribed by CSA G30.18. This decision was made to maintain consistency with comparative studies and simplify referencing external datasets. For real-world construction, equivalent metric bars such as 10M, 15M, and 20M would be used, with minor adjustments to reinforcement areas to comply fully with Canadian code requirements. Given the small differences in bar dimensions, the overall behavior trends, findings, and conclusions of the study remain unaffected. The results of the analysis and required reinforcing areas are displayed in Appendix B. A bottom mesh of #3 bars every 250 mm was chosen for the bottom reinforcement of the slabs. The same reinforcing area was also supplied as top reinforcement at the supports (i.e., beams and columns). The mid-span deflections of the slabs were checked against the limits specified in the CSA A23.3-14 [69], and while the immediate live load deflection was well within range, the long-term deflection exceeded the allowable limit, and therefore, a camber of 15 mm was to be implemented at the mid-span of each slab. It is worth noting that the interior columns of the sixth floor of the (exterior) moment resisting frames were supplied with additional rebar to fulfill the “Strong Column – Weak Beam” criterion. The final design plan, details and sections are shown in Figure 5-5 to Figure 5-9.

CHAPTER 5. PROGRESSIVE COLLAPSE ANALYSIS OF A MULTI-STORY CASE STUDY BUILDING

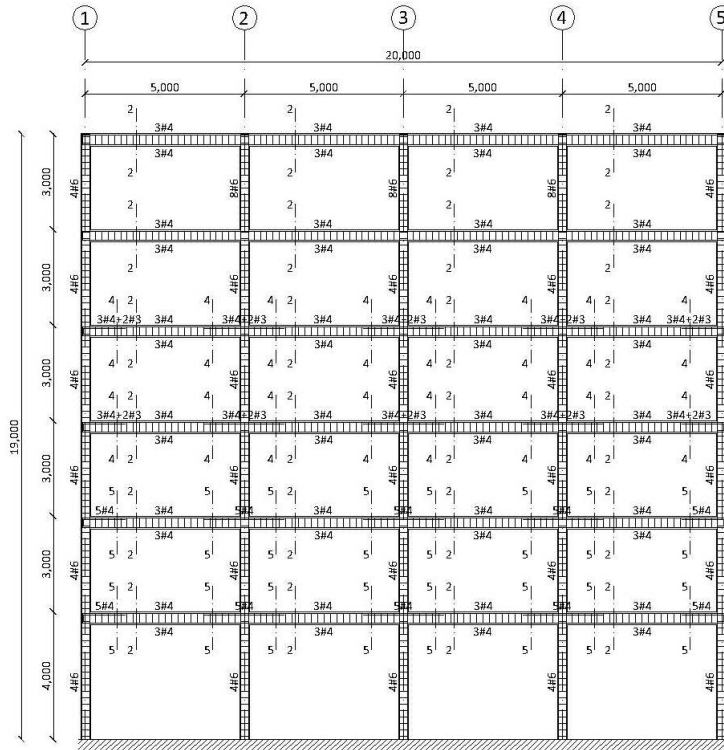


Figure 5-7: Exterior Frame (Section B-B) Rebar Details

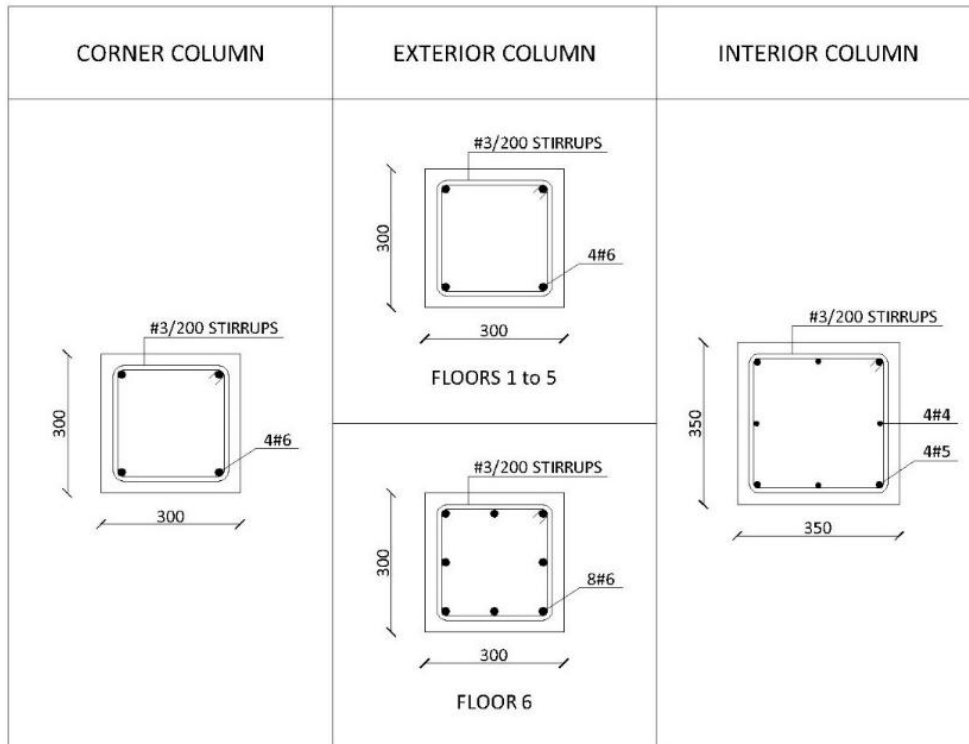


Figure 5-8: Column Sections

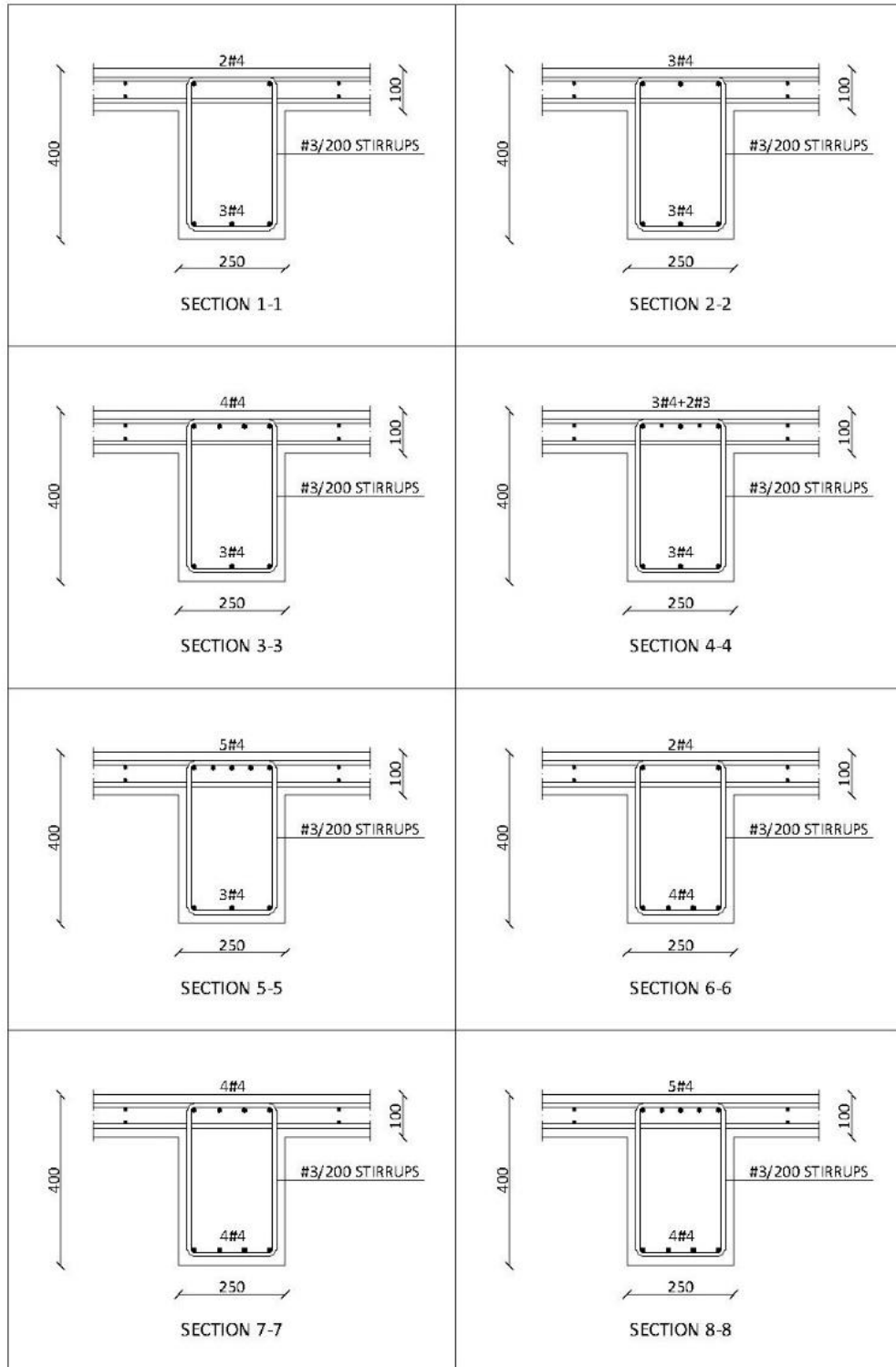


Figure 5-9: Beam Sections

5.3 NONLINEAR ANALYSIS

5.3.1 MODELS

As discussed in previous chapters of this thesis, one of the main objectives of this study is to examine the influence of the RC slab on the progressive collapse behavior of the structure. Therefore, referring to Figure 3-10, two main models were created. The “Full-Frame” model (FF) represents the entire structure, while the “Bare-Frame” model (BF) includes only beams and columns, with slabs omitted. Figure 5-10 and Figure 5-12 show the complete FF and BF models, respectively, while Figure 5-11 and Figure 5-13 show a zoomed-in portion of each model. Similar to the experimental studies previously discussed in Chapter 4, C3D8R solid brick elements were used to model the concrete members, while T3D2 truss elements were used to model the steel reinforcement. Using the “embedded region” constraint in Abaqus, the rebar elements were embedded in the concrete elements. An equal mesh size of 100 mm was used for both solid and truss elements. As previously mentioned, the columns were assumed to be fixed at their bottom.

As planned, two types of columns were considered in the column removal scenarios. The first is the corner column (CC) and the second is the interior column (IC) taken as the exact middle column of the building. Figure C-1 to Figure C-24 show the damaged models considered in the analyses. The corner column (CC) was removed from both FF and BF models at each floor, producing twelve CC models in total. Similarly, the interior (middle) column was removed from both models at each floor, resulting in a total of twelve IC models. Therefore, twenty-four models overall, as summarized in Table 5-2, were evaluated using nonlinear dynamic column loss analysis and nonlinear quasi-static pushdown analysis. Due to symmetry, only a quarter of the structure was represented in the case of the IC models by restricting the degrees of freedom of all nodes located on both symmetry planes. These imposed boundary conditions are shown in Figure C-13 to Figure C-24.

Table 5-2: Case Study Models

Type of Column		Corner Column (CC)		Interior Column (IC)	
Type of Frame		Full Frame (FF)	Bare Frame (BF)	Full Frame (FF)	Bare Frame (BF)
Floor from Which the Column Is Removed	1 st Floor	FF-CC-C1	BF-CC-C1	FF-IC-C1	BF-IC-C1
	2 nd Floor	FF-CC-C2	BF-CC-C2	FF-IC-C2	BF-IC-C2
	3 rd Floor	FF-CC-C3	BF-CC-C3	FF-IC-C3	BF-IC-C3
	4 th Floor	FF-CC-C4	BF-CC-C4	FF-IC-C4	BF-IC-C4
	5 th Floor	FF-CC-C5	BF-CC-C5	FF-IC-C5	BF-IC-C5
	6 th Floor	FF-CC-C6	BF-CC-C6	FF-IC-C6	BF-IC-C6

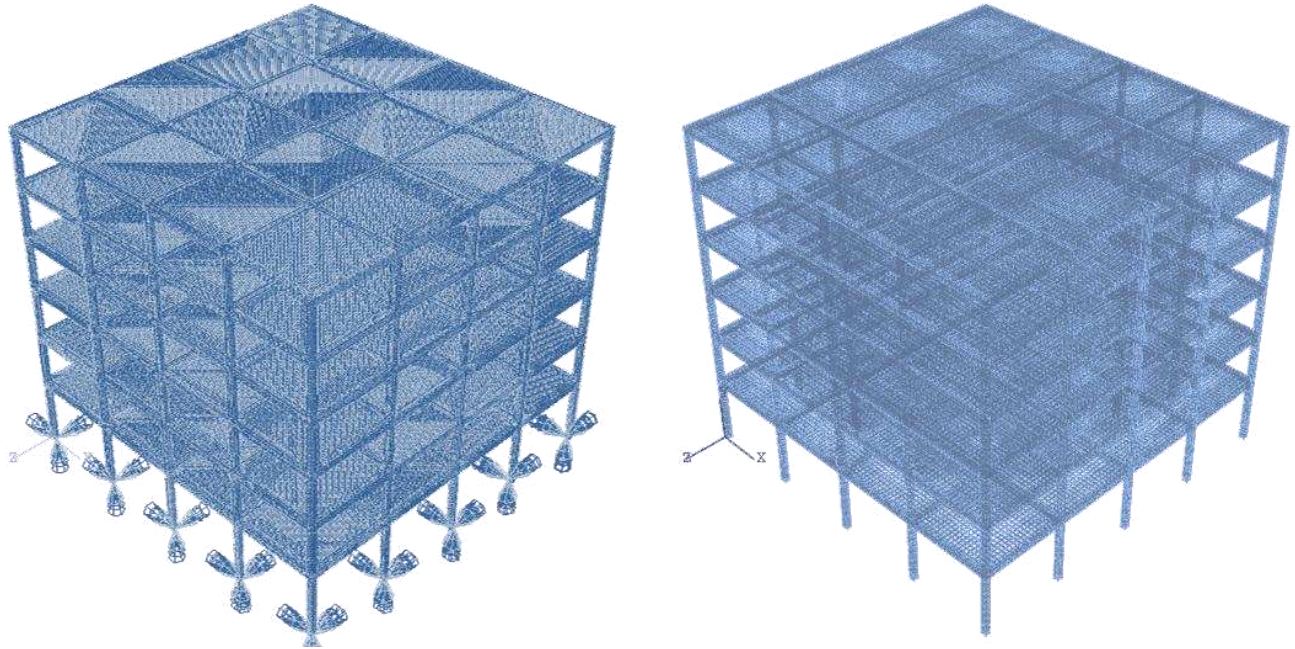


Figure 5-10: Abaqus Model for FF Showing Meshed Solid Elements with Restraints (Left) & Embedded Rebar (Right)

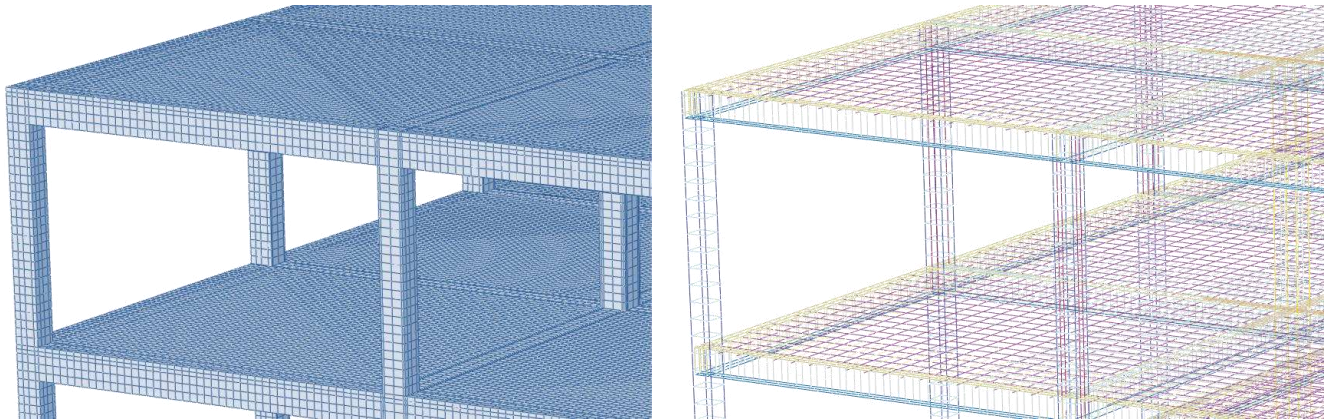


Figure 5-11: Closeup of FF Model Showing Meshed Solid Elements with Restraints (Left) & Embedded Rebar (Right)

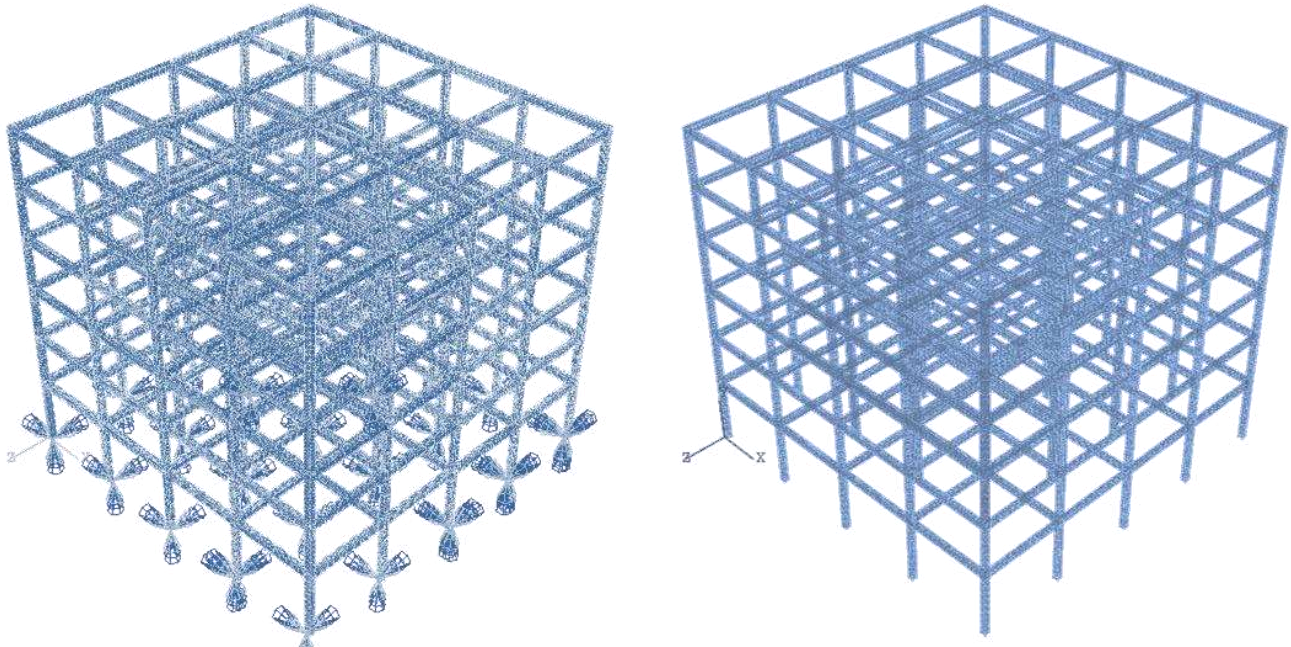


Figure 5-12: Abaqus Model for BF Showing Meshed Solid Elements with Restraints (Left) & Embedded Rebar (Right)

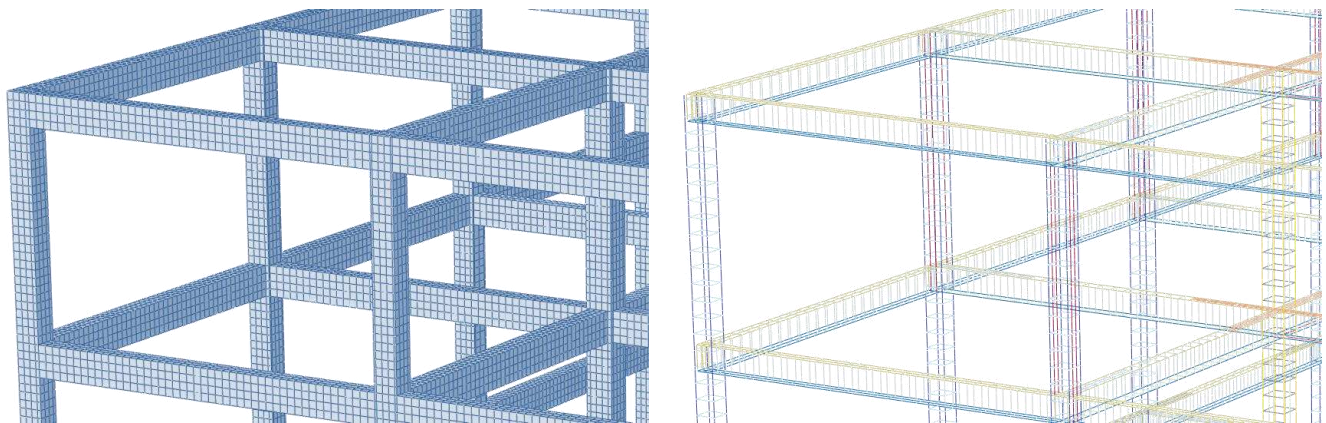


Figure 5-13: Closeup of BF Model Showing Meshed Solid Elements with Restraints (Left) & Embedded Rebar (Right)

5.3.2 MODAL ANALYSIS

The first step, after creating the models, was to obtain the fundamental periods of vibration of the models. These periods were used to determine the damping of the systems using Rayleigh damping. Also, they were used to check that the column removal duration was short enough as it should not exceed $1/10$ of the fundamental period of vibration of the structure, as mentioned in Section 04.4.1.2. The modal analysis showed that the difference in vibrational properties when the same column is removed from different floors is minor and could be neglected. For instance, the variation in the periods of vibration of the FF-IC-C1 up to FF-IC-C6 models was found to be less

than 5.1%. Table 5-3 shows the values of the fundamental period of vibration considered in the analysis for each of the four model divisions.

Table 5-3: Period of Vibration of the Building Models

Model	FF-CC	BF-CC	FF-IC	BF-IC
Period of Vibration (s)	0.125	0.114	0.117	0.094

5.3.3 GRAVITY ANALYSIS

The next step, before running the nonlinear analysis, was to conduct a gravity load analysis under the progressive collapse design load combination (1.2 D + 0.5 L) prescribed in the GSA and UFC guidelines, to obtain the internal forces of the columns in order to carry out the column removal analysis.

5.3.4 PUSHDOWN ANALYSIS

As discussed before, perhaps the most common way to assess the progressive collapse resistance of a building is through nonlinear quasi-static analysis. In this study, each (damaged) model was subjected to a pushdown analysis where the applied loads were monotonically increased as fractions/multiples of the progressive collapse design load (1.2 D + 0.5 L), up to the system’s failure. In the case of the FF models, the loads were uniformly distributed on each floor. On the other hand, in the case of the BF models, the slab loads have been applied directly to the beams as triangular distributed loads.

In each case, the normalized applied loads were plotted against the vertical displacement at the top of the removed column. One thing to note is that since the building is multi-story and the applied loads are distributed, a displacement-controlled pushdown as conducted in Chapter 4 was not possible, and therefore, the described load-controlled analysis was instead executed. This meant that the analysis wouldn’t be able to capture the softening response beyond the limit points, if any, and would snap-through to the next equilibrium point with higher load capacity as previously discussed in Section 2.4.1.1. However, this problem will be addressed at a later stage in this thesis.

To better assess the impact of column removal on the load-bearing capacity of the structure, a nonlinear static analysis, where the applied gravity loads were incrementally (quasi-statically) applied until failure, was conducted on both the undamaged full frame and the undamaged bare frame as baseline comparisons against the damaged systems. In the full-frame model, compression failure initiated at the top of the bottom-floor (first-floor) intermediate columns at a normalized applied load of 365%. Similarly, in the bare frame, compression failure was also observed, however, this time, it was at the bottom of the second-floor intermediate columns at a load of

345%. This 5.8% difference in load capacity, may be partially attributed to the fact that the slab loads were represented as triangular loads of equal magnitudes applied on each beam, which, of course, is an approximation of the actual load distribution. Moreover, the exclusion of slabs from the bare frame also alters the load distribution and affects the failure mechanism. The damage in both cases rapidly propagated and eventually led to the complete progressive collapse of the structure.

5.3.4.1 FULL-FRAME CORNER COLUMN REMOVAL RESULTS

The pushdown curves for the FF-CC models are shown in Figure 5-14. The curves show the applied loads normalized with respect to the progressive collapse design load versus the vertical displacement up to the first point of rebar fracture for each model. Beyond these fracture points, damage propagated, and partial collapse occurred. Table 5-4 shows the values of the applied load (P), displacement (u) and slope (s) at the fracture points. The slope (s) is simply calculated by dividing the absolute displacement (u) by the center-to-center span, which in this case study is equal to 5 m for all models. It should be noted that after examining the vertical displacements of the columns, they were found too small with respect to the deflections at the removed columns. Consequently, and for simplicity, the total displacements have been used in the results assessment since their values are very close to the relative ones.

Table 5-4: Maximum Pushdown Analysis Values for FF-CC Models

Model	FF-CC-C1	FF-CC-C2	FF-CC-C3	FF-CC-C4	FF-CC-C5	FF-CC-C6	Undamaged
P_{max}	282%	273%	273%	273%	273%	259%	365%
U_{max} (mm)	779	714	679	746	799	1,019	NA
S_{max}	15.57%	14.27%	13.57%	14.93%	15.98%	20.37%	NA

By examining the results, it can be seen that the responses of Model FF-CC-C1 to Model FF-CC-C5 were almost identical at lower deformation values while still reasonably close at higher values. The maximum normalized load-carrying capacity of the system was found to be 282% for Model FF-CC-C1 and 273% for Model FF-CC-C2 to Model FF-CC-C5. The corresponding vertical displacement decreased from 779 mm for Model FF-CC-C1 to 679 mm for Model FF-CC-C3, and then started to increase again up to 799 mm for Model FF-CC-C5. On the other hand, the response of Model FF-CC-C6 was different in terms of load capacity as well as maximum deformation. The normalized fracture load for FF-CC-C6 was found to be 259% while the average load for the other five models was 275%. The corresponding vertical displacement was found to be 1,019 mm while the average vertical displacement for the rest of the models was 743 mm. This discrepancy may be attributed to the multi-story Vierendeel action or diaphragm effect, mentioned in Section 2.6.5, present in Model FF-CC-C1 to Model FF-CC-C5. Model FF-CC-C6 behaves as a single-story cantilever and, therefore, exhibited more deformation and less load-bearing capacity than multi-story cantilevers. In fact, the diaphragm effect increased the load capacity of the system by 6% and

decreased the maximum vertical displacement by 27%. In general, the results imply that the load capacity of the system increases as the number of floors above the removed column increases. In other words, as the number of vertically stacked closed loops increased, the system's load-carrying capacity increased. Of course, it should be noted, though, that in this case, the amount of damage was higher since more floors got damaged. However, the evaluation in this study is based on comparing the displacements of the joints above the removed columns as well as the load-bearing capacity of the system, not the total amount of damage in the structure.

To shed more light on the nonlinear response of the systems, two models were chosen since they represented the two extremes of the response, Model FF-CC-C1 and Model FF-CC-C6. Two points in the analysis timeline were further examined. The first point corresponded to the first rebar fracture after which the damage started to propagate, while the second point was after the damage had progressed into partial collapse. The von Mises stresses in the RC elements at first fracture along with the total displacement are shown in Figure 5-15 and Figure 5-16 respectively for FF-CC-C1 and FF-CC-C6. The normal stresses and strains in the rebar elements, at the same point, as well as the fractured rebar zones are shown in Figure 5-17 to Figure 5-20. The first rebar fracture happened in the top longitudinal reinforcement steel bars of the fourth floor's beam for FF-CC-C1 while it happened in the top bars of the sixth floor's beam for FF-CC-C6. The rebar failed after reaching the ultimate plastic strain of 0.12 which corresponds to a true stress of 612 MPa. This initial fracture triggered a series of subsequent fractures as the redistributed loads were too much to resist by the adjacent rebar. The damage also spread to the rest of the floors above the removed column. The stresses in RC solid and rebar truss elements after damage propagation are shown in Figure 5-21 and Figure 5-22. The system suffered a localized/partial progressive collapse of all floors above the removed column, confined to the external corner bay.

Finally, comparing the obtained results of the damaged models with those of the undamaged model, it can be concluded that the removal of a corner column changed the failure mechanism and caused a minimum of 23% reduction in the load-bearing capacity of the system.

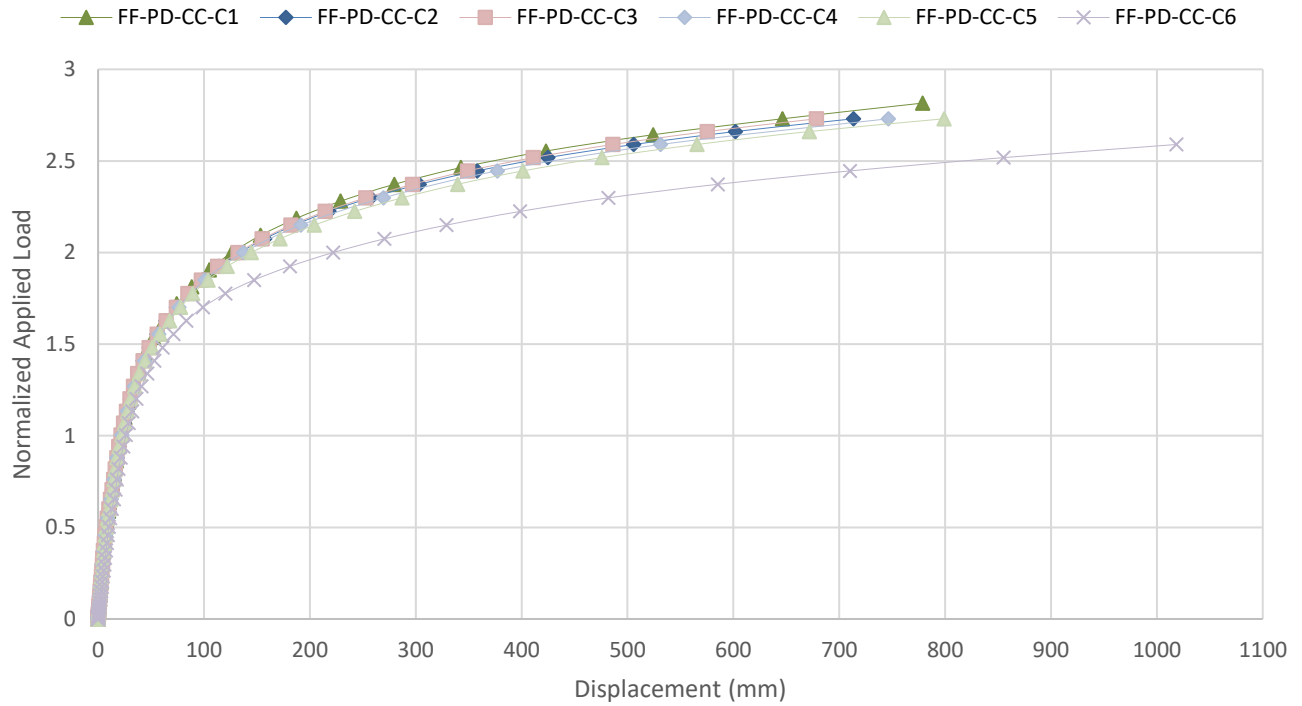


Figure 5-14: Pushdown Curves for FF-CC Models

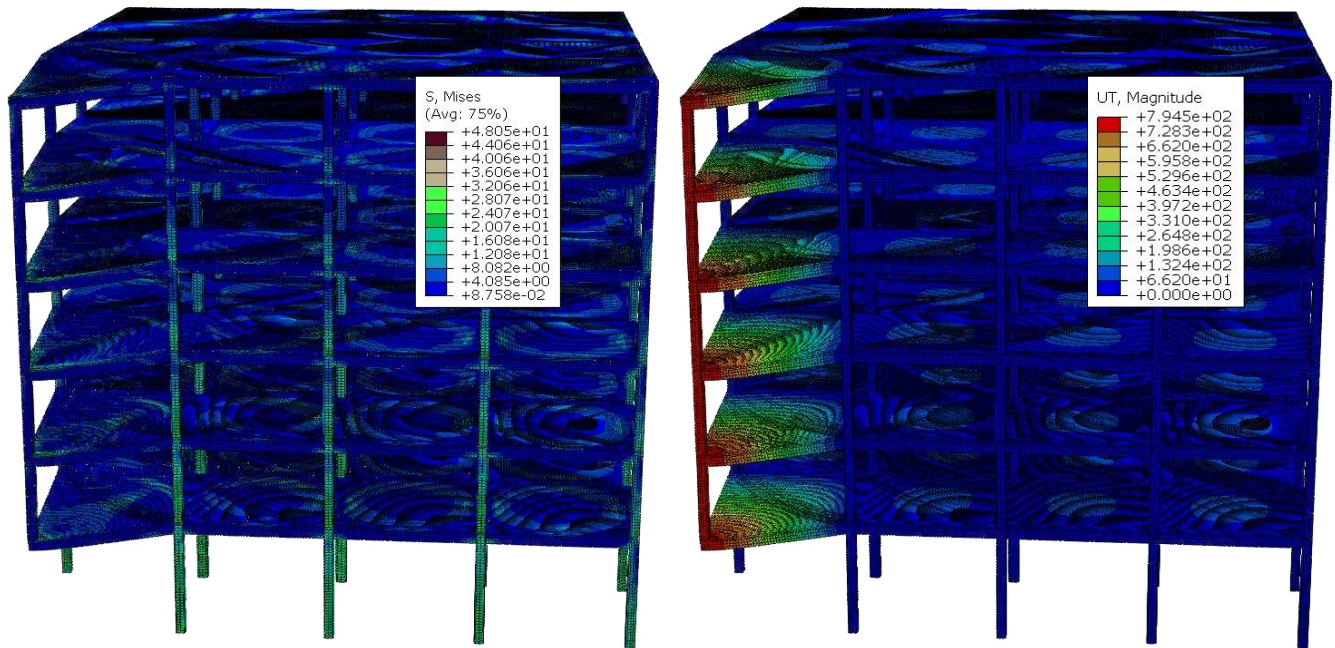


Figure 5-15: Von Mises Stresses (Left) & Total Displacement (Right) in Solid Elements for FF-CC-C1 Under Pushdown Analysis at 282% Design Load at First Fracture (Full Model Shown)

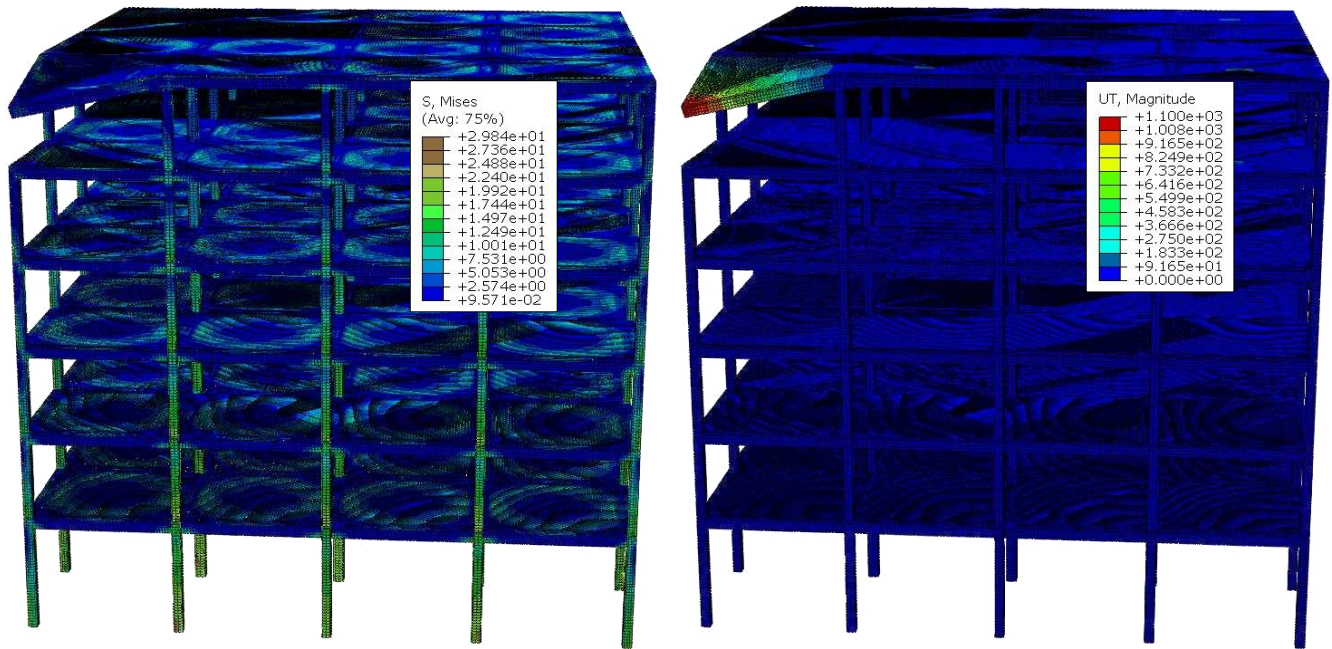


Figure 5-16: Von Mises Stresses (Left) & Total Displacement (Right) in Solid Elements for FF-CC-C6 Under Pushdown Analysis at 259% Design Load at First Fracture (Full Model Shown)

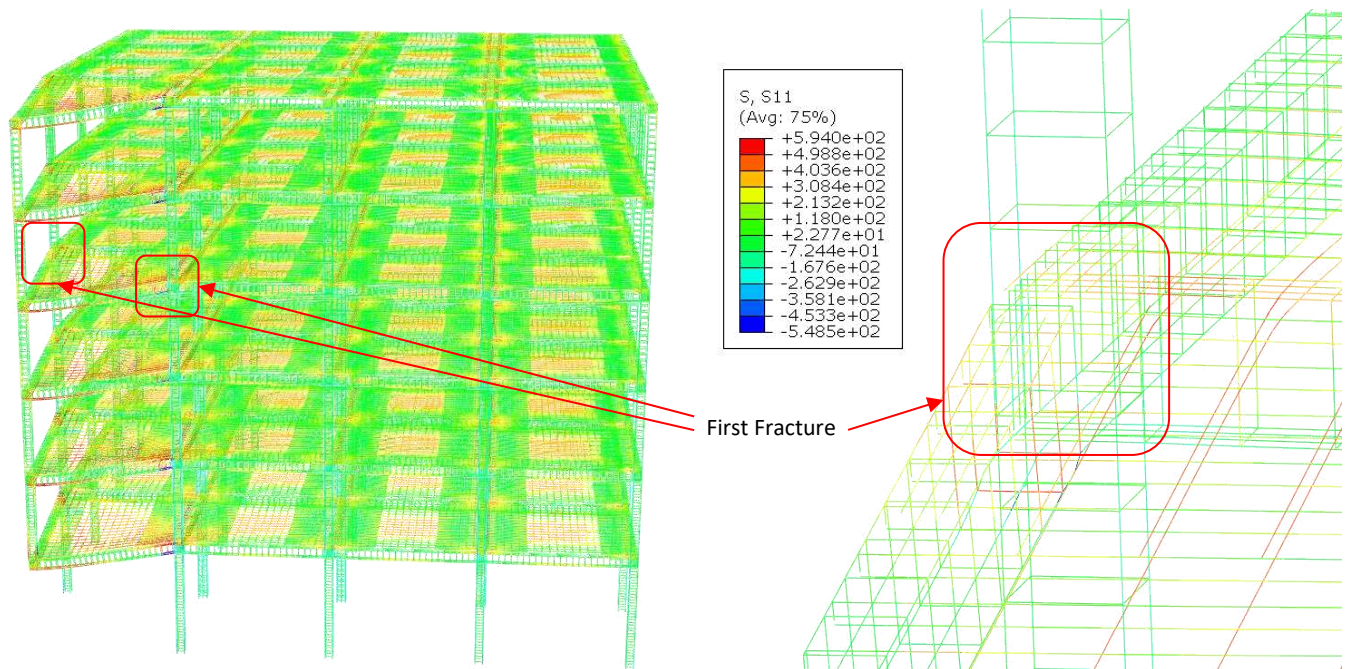


Figure 5-17: S11 Stresses in Truss Elements for FF-CC-C1 Under Pushdown Analysis at 282% Design Load at First Fracture, Full Model (Left) & Closeup on Plastic Hinge (Right)

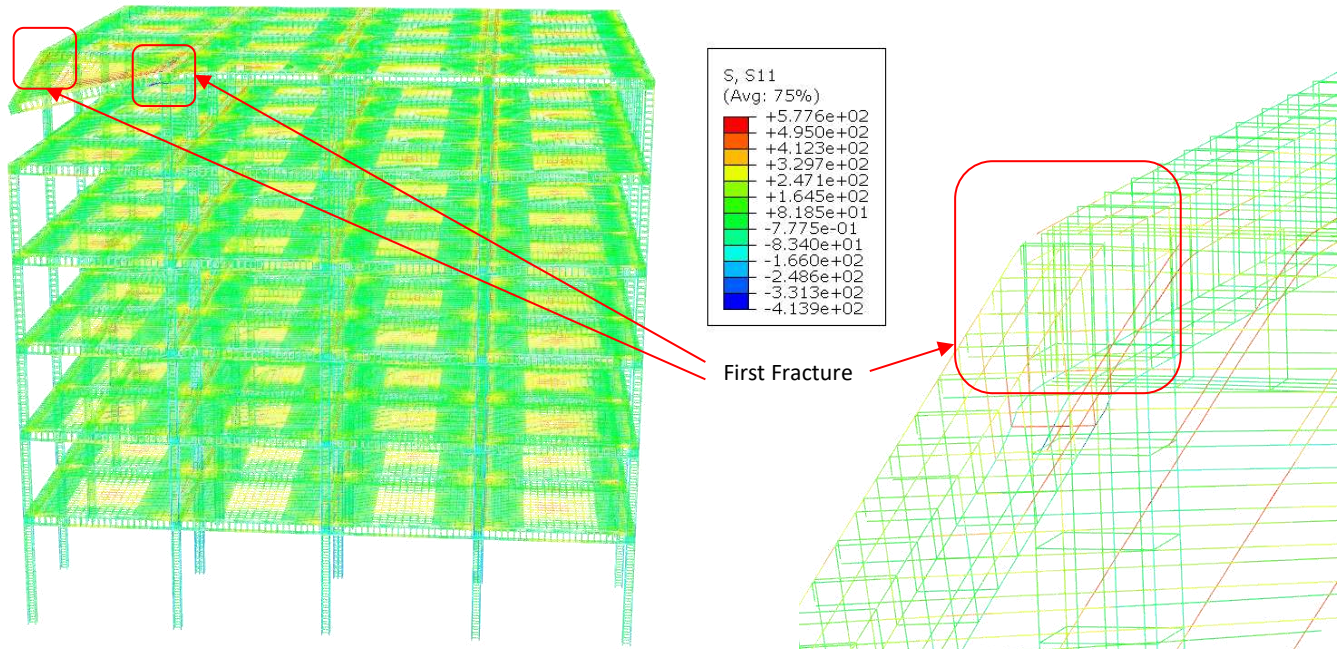


Figure 5-18: S11 Stresses in Truss Elements for FF-CC-C6 Under Pushdown Analysis at 259% Design Load at First Fracture, Full Model (Left) & Closeup on Plastic Hinge (Right)

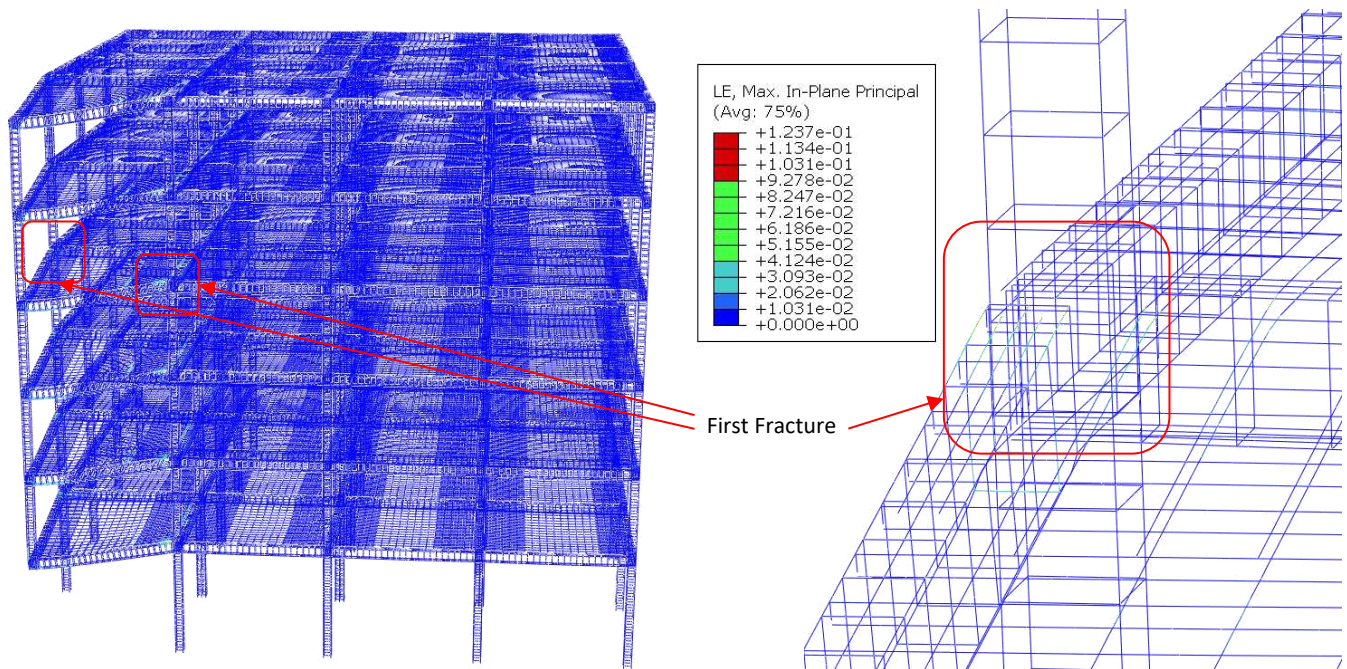


Figure 5-19: Logarithmic Strains in Truss Elements for FF-CC-C1 Under Pushdown Analysis at 282% Design Load at First Fracture, Full Model (Left) & Closeup on Plastic Hinge (Right)

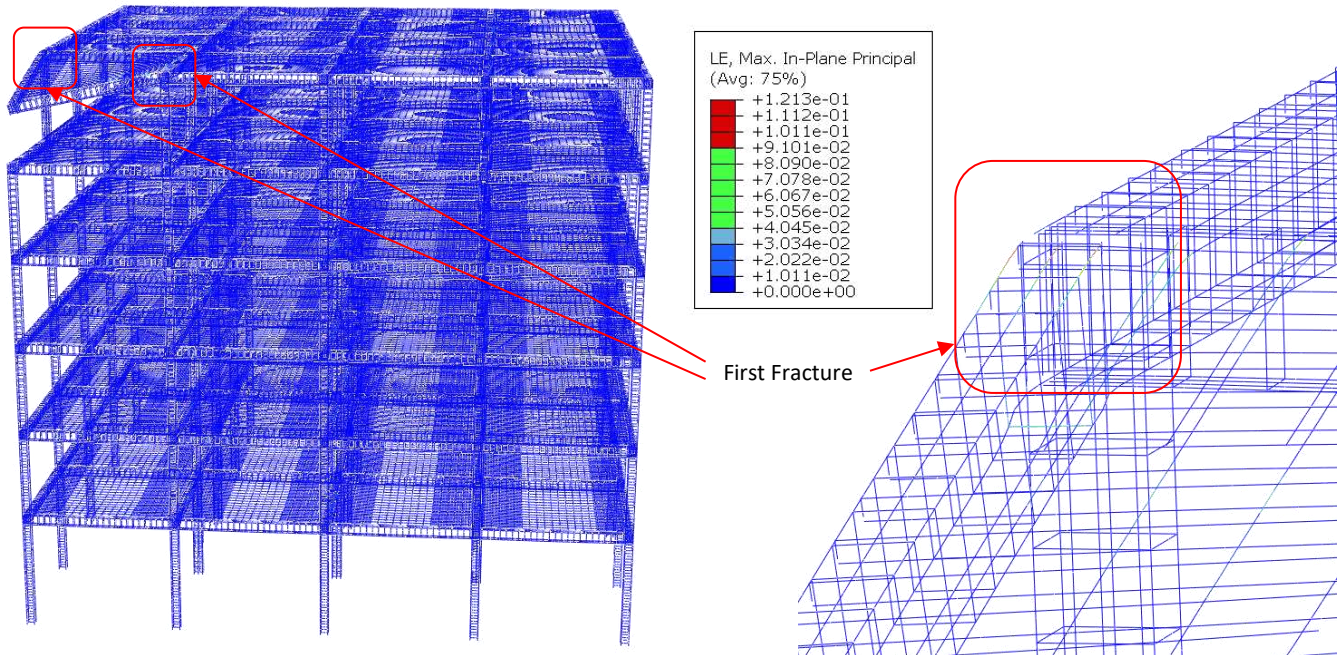


Figure 5-20: Logarithmic Strains in Truss Elements for FF-CC-C6 Under Pushdown Analysis at 259% Design Load at First Fracture, Full Model (Left) & Closeup on Plastic Hinge (Right)

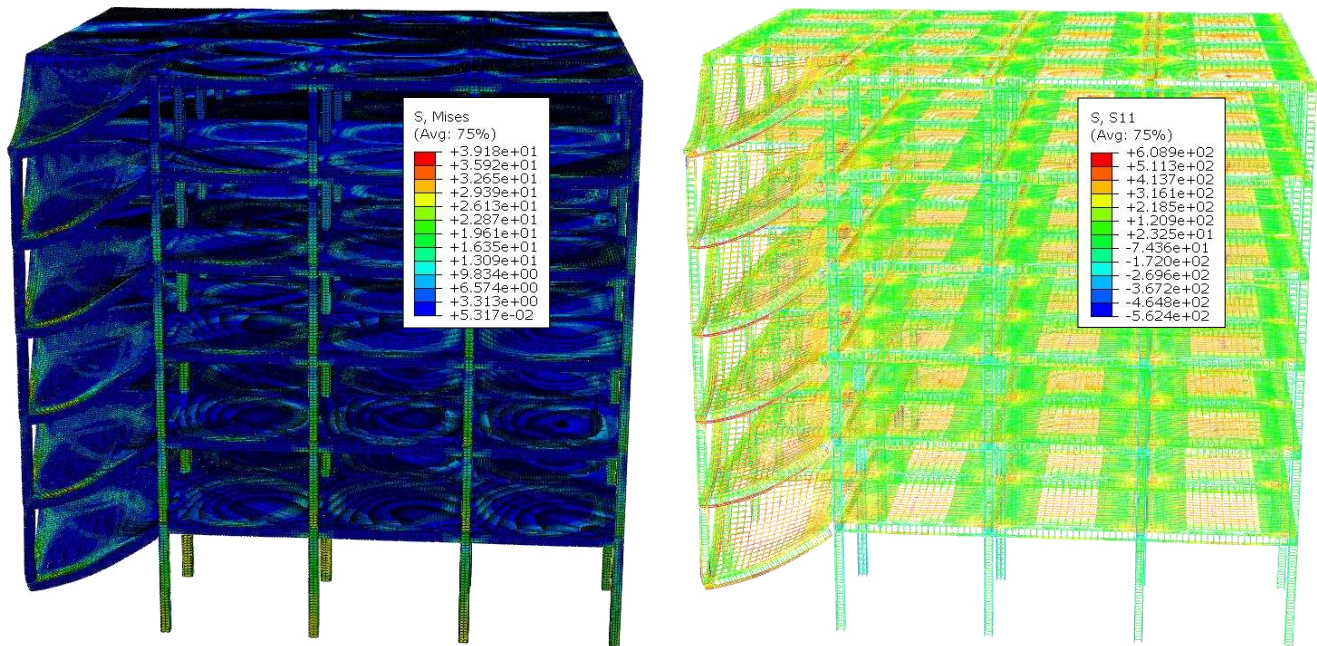


Figure 5-21: Von Mises Stresses in Solid Elements (Left) & S11 Stresses in Truss Elements (Right) for FF-CC-C1 Under Pushdown Analysis After Damage Propagation (Full Model Shown)

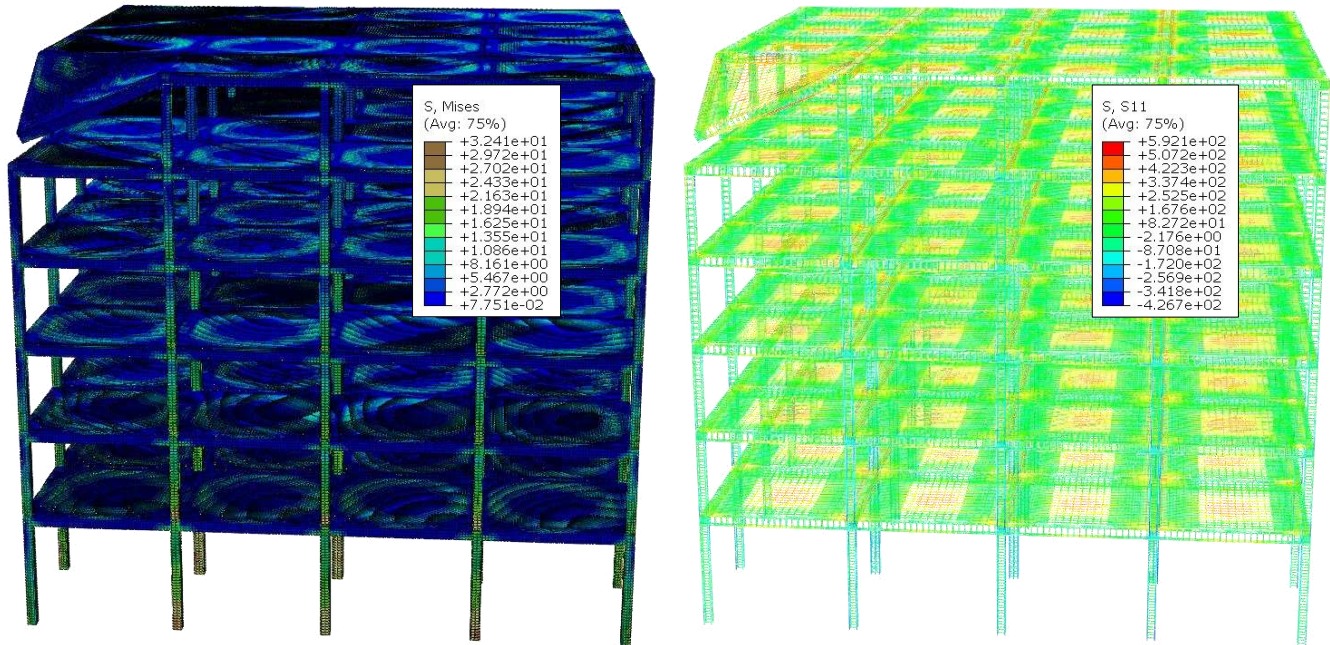


Figure 5-22: Von Mises Stresses in Solid Elements (Left) & S11 Stresses in Truss Elements (Right) for FF-CC-C6 Under Pushdown Analysis After Damage Propagation (Full Model Shown)

5.3.4.2 BARE-FRAME CORNER COLUMN REMOVAL RESULTS

The pushdown curves for the BF-CC models are shown in Figure 5-23, and the values of the applied load (P), displacement (u) and slope (s) at the fracture points are shown in Table 5-5.

Table 5-5: Maximum Pushdown Analysis Values for BF-CC Models

Model	BF-CC-C1	BF-CC-C2	BF-CC-C3	BF-CC-C4	BF-CC-C5	BF-CC-C6	Undamaged
P_{max}	155%	155%	148%	148%	141%	113%	345%
u_{max} (mm)	462	485	453	493	483	608	NA
s_{max}	9.24%	9.69%	9.06%	9.86%	9.66%	12.15%	NA

Similar to the FF-CC results, the responses of Model BF-CC-C1 to Model BF-CC-C5 were very close, especially at lower deformation values. The maximum normalized force capacity up to the first rebar fracture point varied from 141% to 155%, again increasing as the number of vertically stacked closed loops increased in the system. On the other hand, the corresponding vertical displacements varied from 453 mm to 493 mm but did not seem to follow a specific pattern or trend. The response of Model BF-CC-C6 was significantly different than the rest of the models. Again, this may be attributed to the fact that it behaves as a single-story cantilever lacking the Vierendeel action or diaphragm effect present in the other models. The normalized load capacity of Model BF-CC-C6 was found to be 113% while the average load capacity of the other models was 150%. The corresponding deformation was found to be 608 mm while the average displacement exhibited by the other models was 475 mm. This means that the diaphragm effect increased the load capacity by 33% and decreased the displacement by 22%.

Model BF-CC-C1 and Model BF-CC-C6 were chosen for further examination. Two points in the analysis timeline were considered in this assessment. The first point represented the first rebar fracture while the second point was taken after partial collapse had progressed. The von Mises stresses and total displacement in RC elements at first fracture are shown in Figure 5-24 and Figure 5-25 respectively for BF-CC-C1 and BF-CC-C6. Figure 5-26 to Figure 5-29 show the normal stresses and strains in the rebar elements at the same point. The first rebar fracture happened in the top longitudinal reinforcement steel bars of the sixth floor’s beam for BF-CC-C1 and BF-CC-C6 after reaching the ultimate plastic strain of 0.12 and its corresponding true stress of 612 MPa. Following the initial fracture, damage progressed, and the structure suffered a localized/partial progressive collapse above the removed column, confined to the external corner bay. The stresses in RC solid and rebar truss elements after damage propagation are shown in Figure 5-30 and Figure 5-31.

In conclusion, a comparison between the results of the damaged models and the undamaged model indicates that the removal of a corner column altered the failure mechanism and led to at least a 55% reduction in the system's load-bearing capacity.

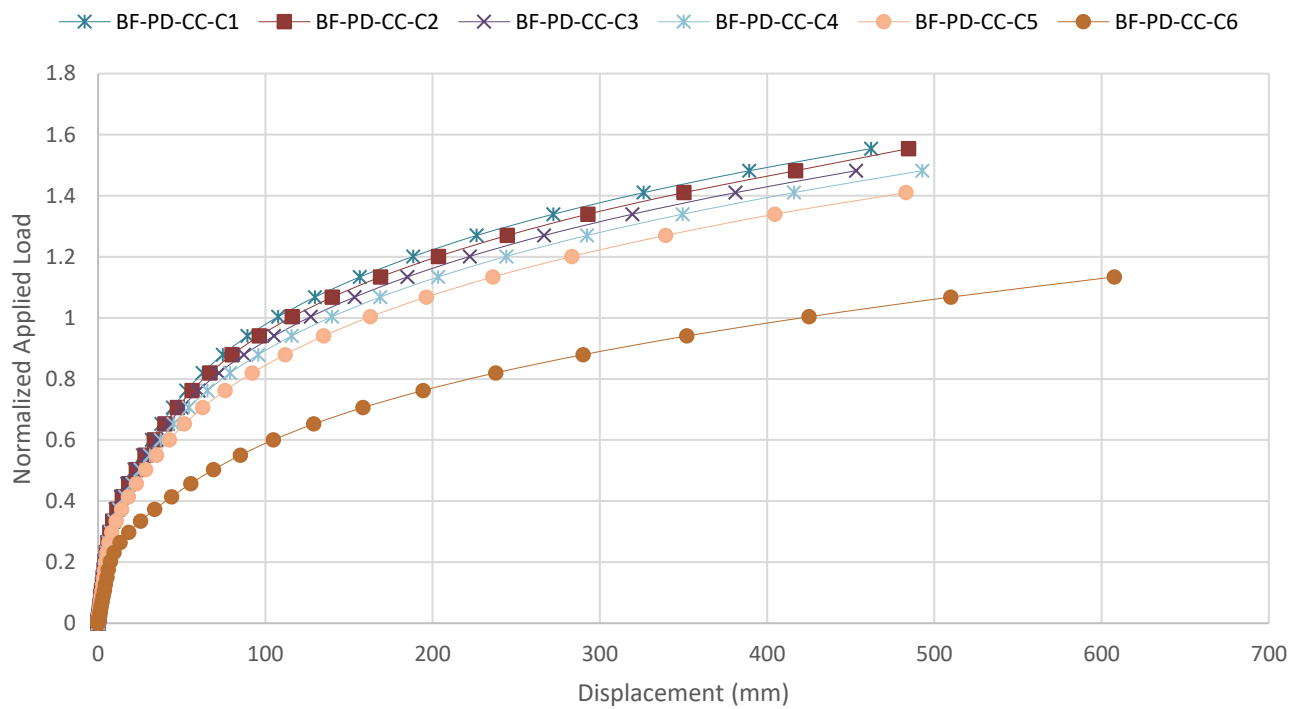


Figure 5-23: Pushdown Curves for BF-CC Models



Figure 5-24: Von Mises Stresses (Left) & Total Displacement (Right) in Solid Elements for BF-CC-C1 Under Pushdown Analysis at 155% Design Load at First Fracture (Full Model Shown)



Figure 5-25: Von Mises Stresses (Left) & Total Displacement (Right) in Solid Elements for BF-CC-C6 Under Pushdown Analysis at 113% Design Load at First Fracture (Full Model Shown)

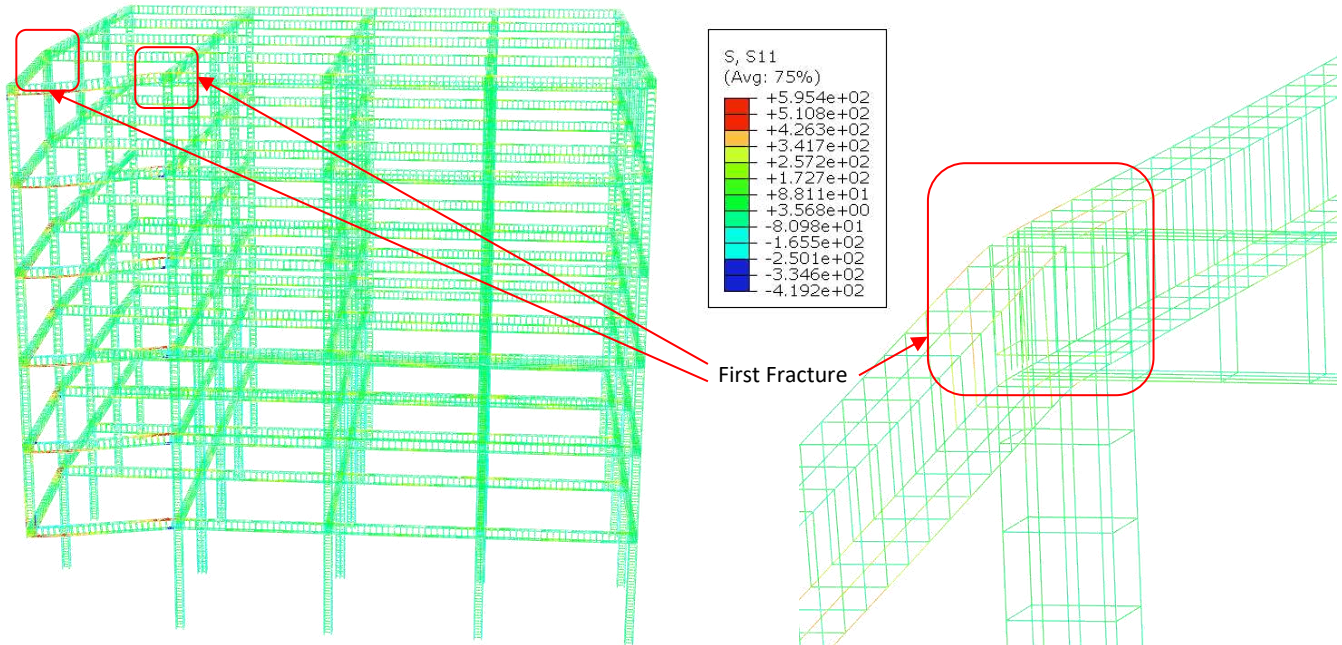


Figure 5-26: S11 Stresses in Truss Elements for BF-CC-C1 Under Pushdown Analysis at 155% Design Load at First Fracture, Full Model (Left) & Closeup on Plastic Hinge (Right)

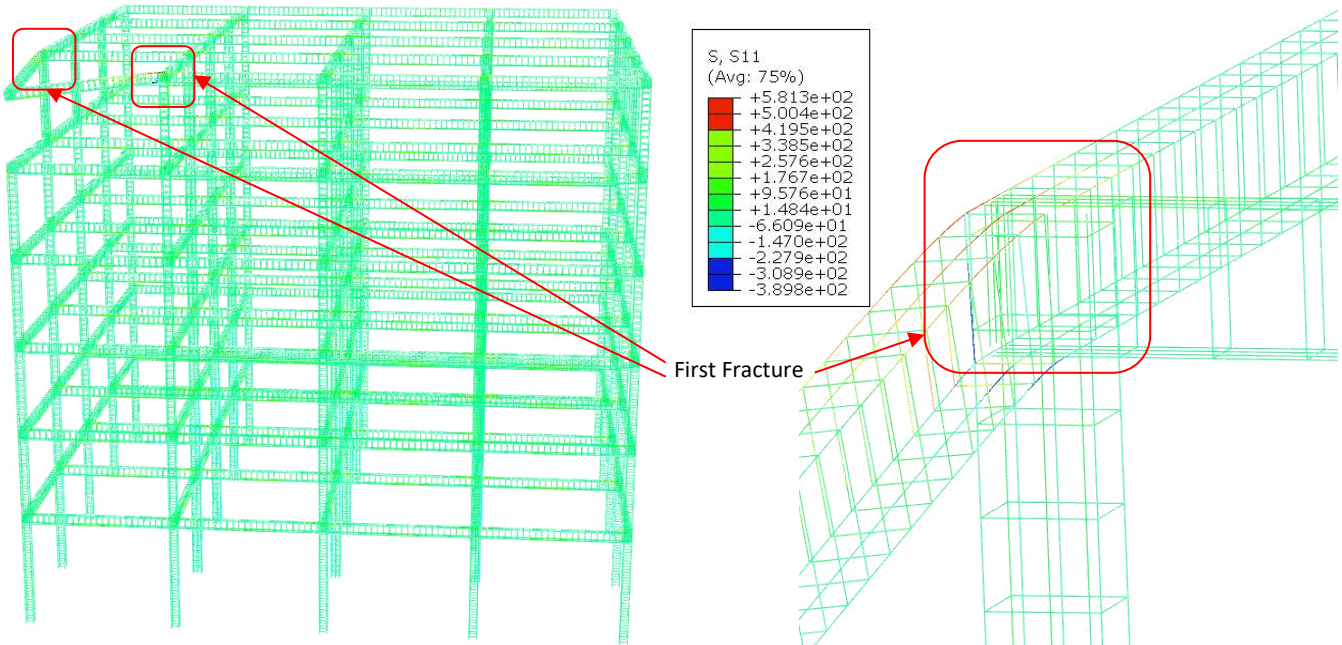


Figure 5-27: S11 Stresses in Truss Elements for BF-CC-C6 Under Pushdown Analysis at 113% Design Load at First Fracture, Full Model (Left) & Closeup on Plastic Hinge (Right)

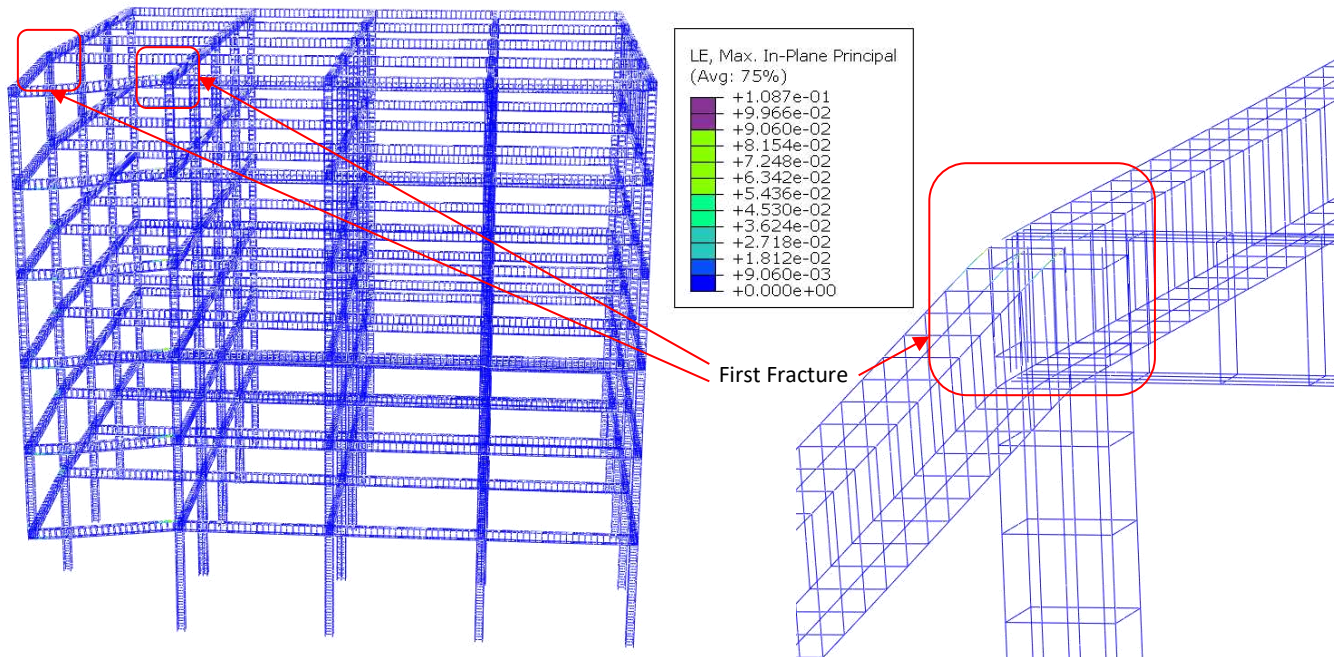


Figure 5-28: Logarithmic Strains in Truss Elements for BF-CC-C1 Under Pushdown Analysis at 155% Design Load at First Fracture, Full Model (Left) & Closeup on Plastic Hinge (Right)

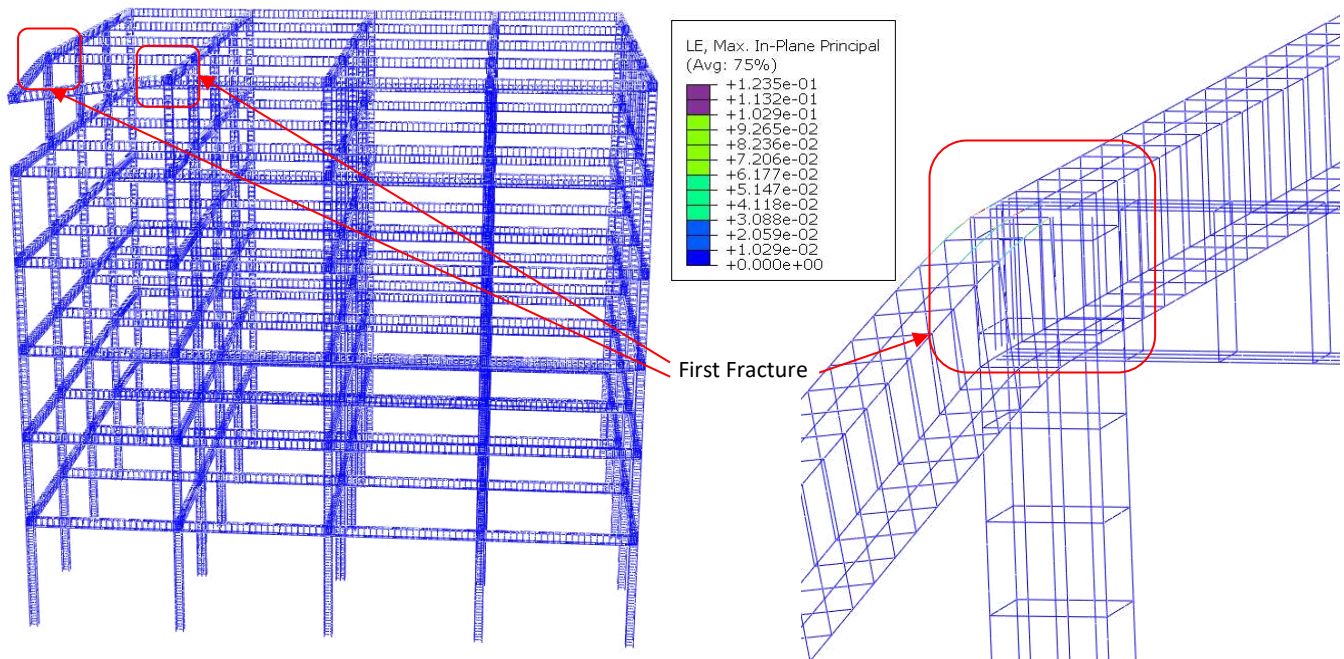


Figure 5-29: Logarithmic Strains in Truss Elements for BF-CC-C6 Under Pushdown Analysis at 113% Design Load at First Fracture, Full Model (Left) & Closeup on Plastic Hinge (Right)

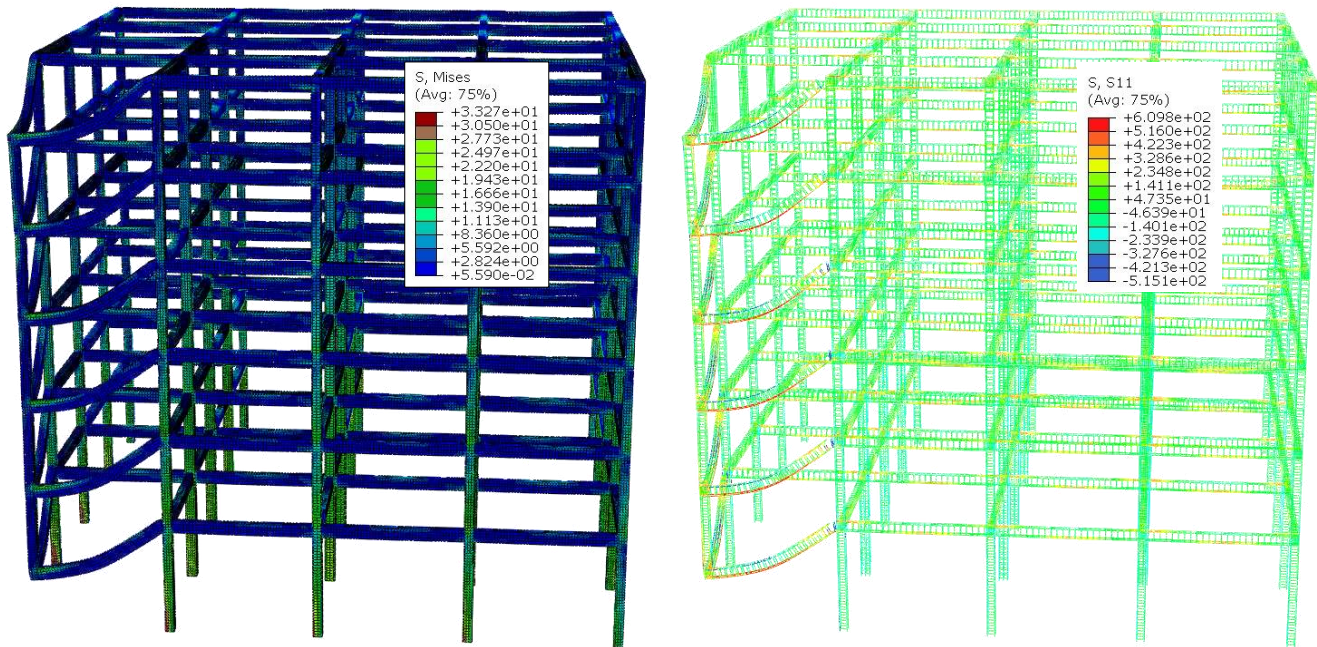


Figure 5-30: Von Mises Stresses in Solid Elements (Left) & S11 Stresses in Truss Elements (Right) for BF-CC-C1 Under Pushdown Analysis After Damage Propagation (Full Model Shown)

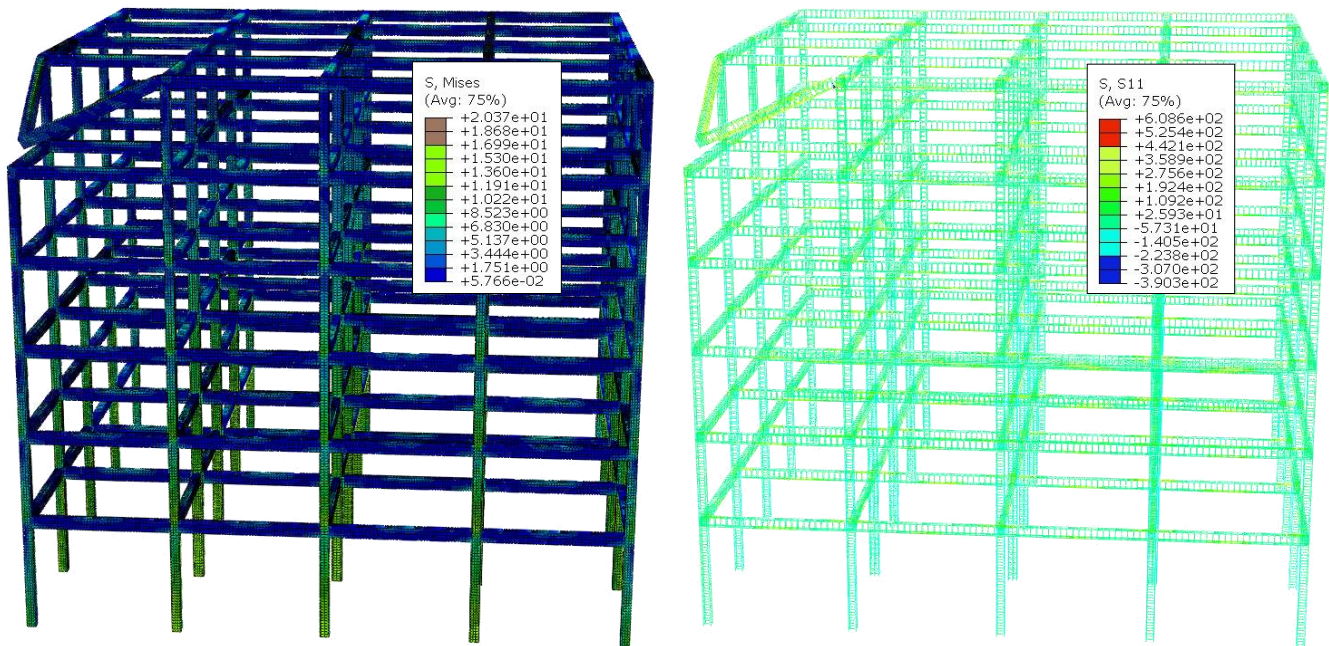


Figure 5-31: Von Mises Stresses in Solid Elements (Left) & S11 Stresses in Truss Elements (Right) for BF-CC-C6 Under Pushdown Analysis After Damage Propagation (Full Model Shown)

5.3.4.3 FULL-FRAME INTERIOR COLUMN REMOVAL RESULTS

The pushdown curves for the FF-IC models are shown in Figure 5-32, and the values of the applied load (P), displacement (u) and slope (s) at the fracture points are shown in Table 5-6.

Table 5-6: Maximum Pushdown Analysis Values for FF-IC Models

Model	FF-IC-C1	FF-IC-C2	FF-IC-C3	FF-IC-C4	FF-IC-C5	FF-IC-C6	Undamaged
P_{max}	328%	335%	340%	345%	350%	350%	365%
u_{max} (mm)	752	803	836	864	882	800	NA
s_{max}	15.04%	16.06%	16.71%	17.28%	17.65%	16.00%	NA

As evident by the pushdown curves, the responses of all six models were very similar, especially at lower displacement values where they were practically identical. This meant that, in general, each story acted by itself in resisting the applied load. This implies that the reduction of the structure to a single-story system, as has been done in previously discussed literature, is in fact an acceptable approximation. The maximum load ranged from 328% for FF-IC-C1 up to 350% for both FF-IC-C5 and FF-IC-C6, which represented a 2.32% relative standard deviation. Therefore, contrasting with the CC models, the increase in the number of floors above the removed column led to a decrease in the load-bearing capacity of the system. This is due to the fact that the failure, in this case, occurred in the columns not the beams. Therefore, the more floors above the removed column, the more redistributed load to be carried by the neighboring columns. On the other hand, the maximum displacements increased from 752 mm for FF-IC-C1 to 882 mm for FF-IC-C5 but then dropped again to 800 mm for FF-IC-C6, representing a relative standard deviation of 5.28%. In general, considering all six models, the system’s average load capacity was 341% compared to 272% in the case of the FF-CC models, representing a 25.4% difference. Although the tributary area of the adjacent/neighboring columns was the same for both systems, the FF-IC beams were subjected to lower stresses than the FF-CC beams. Due to the structural stiffness distribution, the FF-IC beams were subjected to lower bending moments at low displacements where flexural behavior was the dominant resistance mechanism. Even as displacements increased and resistance mechanisms started to shift, the stresses in the FF-IC beams were less than those in the FF-CC beams. Consequently, the FF-IC system was able to resist higher gravity loads than the FF-CC system. The FF-IC beams were able to stay intact up to the failure of the columns, which meant that although the FF-IC system had a higher load-carrying capacity, its failure was brittle. In other words, the damage was not localized, and the structure suffered a complete progressive collapse.

A closer look at Model FF-IC-C1 and Model FF-IC-C6 was considered for two points in the analysis timeline. The first point represented the first rebar fracture, and the second point was taken after damage propagation and collapse progression. Figure 5-33 and Figure 5-34 show the von Mises stresses and total displacement in solid elements at first fracture, respectively for FF-IC-C1 and FF-IC-C6. At this point, the concrete at the top of the failing

columns had started crushing. The normal stresses and strains in truss elements, at the same point, are displayed in Figure 5-35 to Figure 5-38. The first rebar fracture occurred in the first floor’s adjacent column for FF-IC-C1 and in the first floor’s diagonally opposite column for FF-IC-C6 after reaching the ultimate plastic strain of 0.12 and its corresponding true stress of 612 MPa. It should be noted that prior to fracture, the rebar started locally buckling and continued to do so as the damage progressed. Figure 5-39 and Figure 5-40 show the stresses in concrete and steel elements after damage propagation. The figures also show how more and more first-floor columns failed as the redistributed load was too much to resist, leading to the complete collapse of the first-floor columns and marking the onset of the progressive collapse of the whole building.

Lastly, comparing the results of the damaged models with the undamaged model shows that the removal of an interior column resulted in only a 4.1% to 10.1% reduction in the system's load-bearing capacity. This relatively minor reduction can be attributed to the system's robustness and the availability of alternate load redistribution paths in the case of interior column removal scenarios.

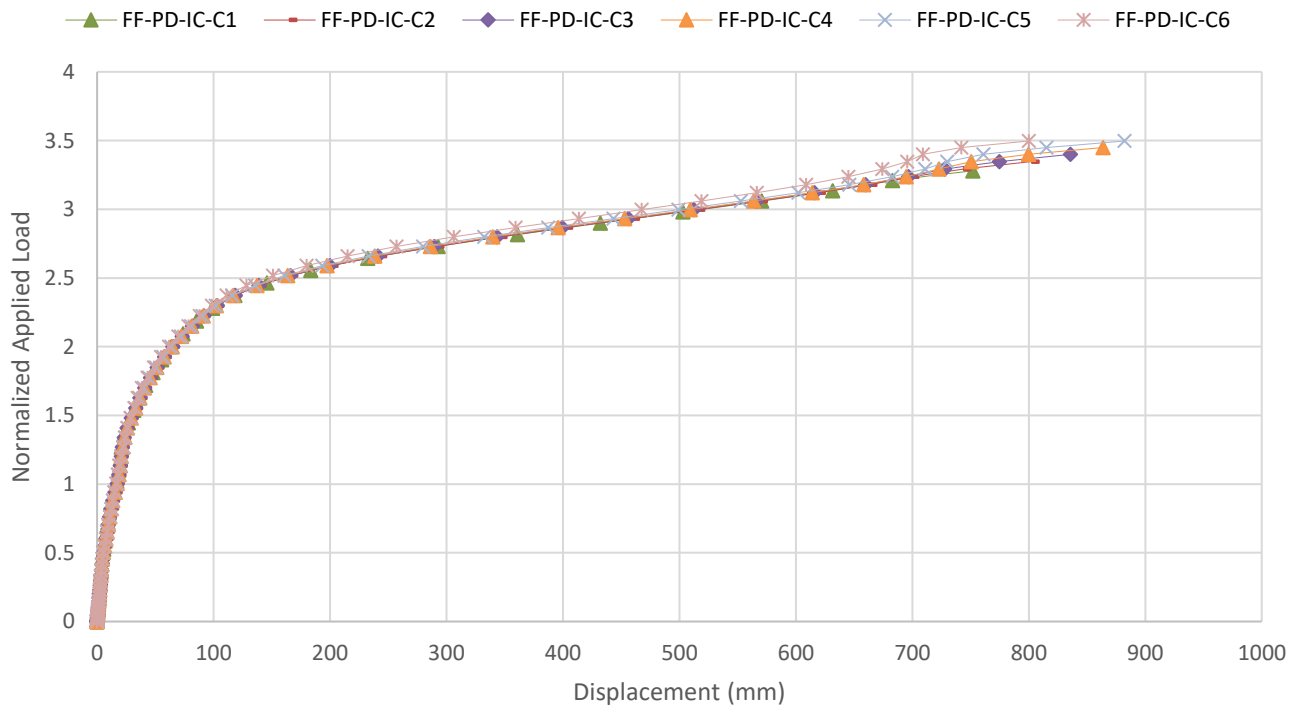


Figure 5-32: Pushdown Curves for FF-IC Models

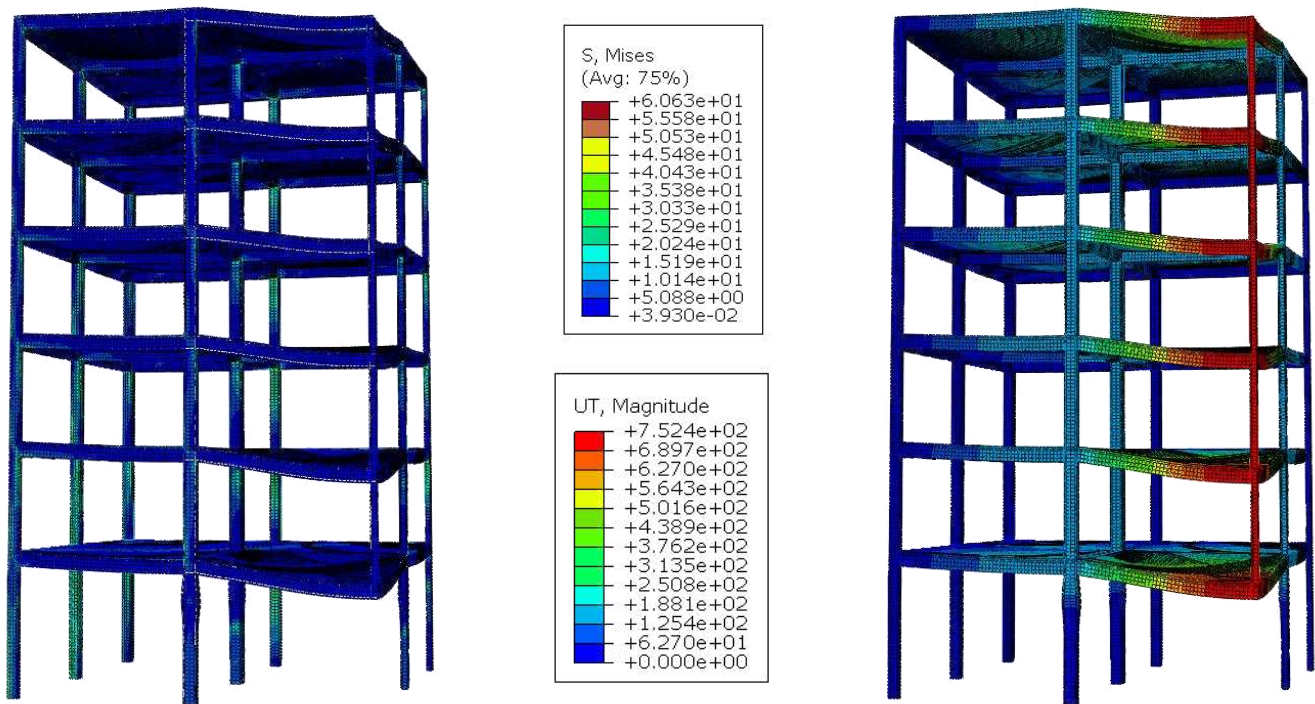


Figure 5-33: Von Mises Stresses (Left) & Total Displacement (Right) in Solid Elements for FF-IC-C1 Under Pushdown Analysis at 328% Design Load at First Fracture (Quarter Model Shown)

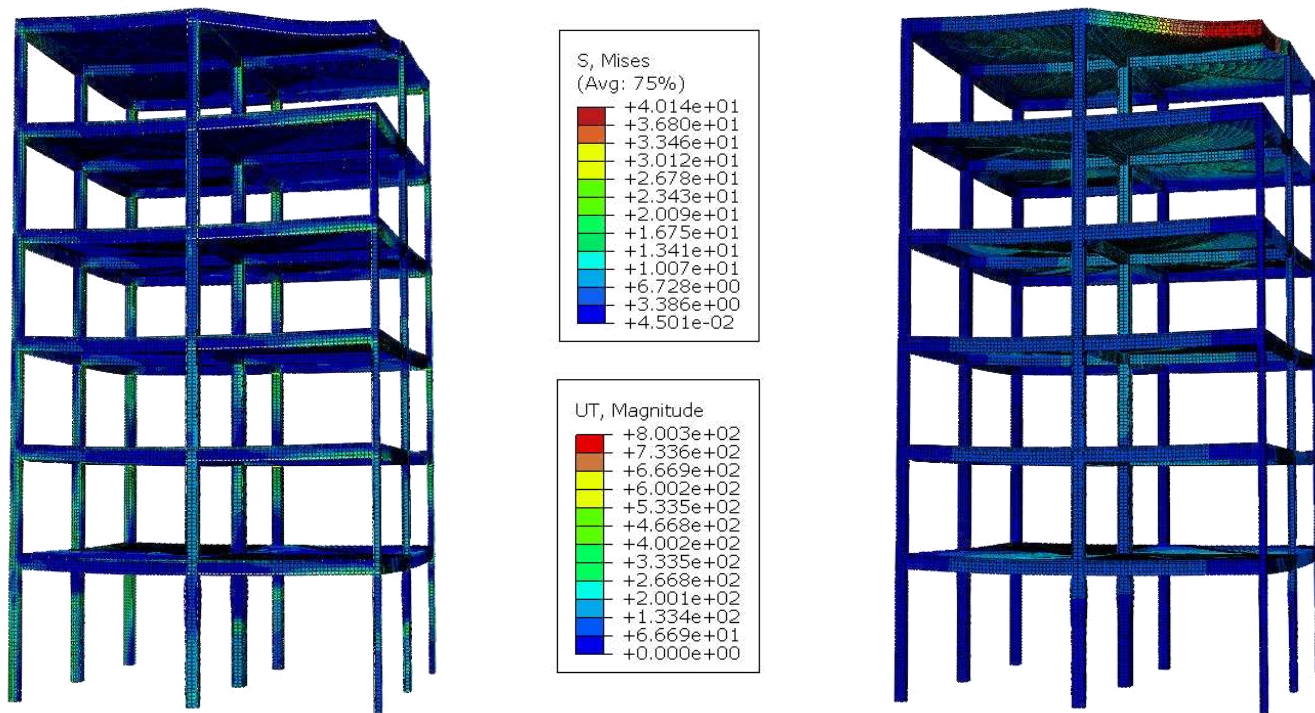


Figure 5-34: Von Mises Stresses (Left) & Total Displacement (Right) in Solid Elements for FF-IC-C6 Under Pushdown Analysis at 350% Design Load at First Fracture (Quarter Model Shown)

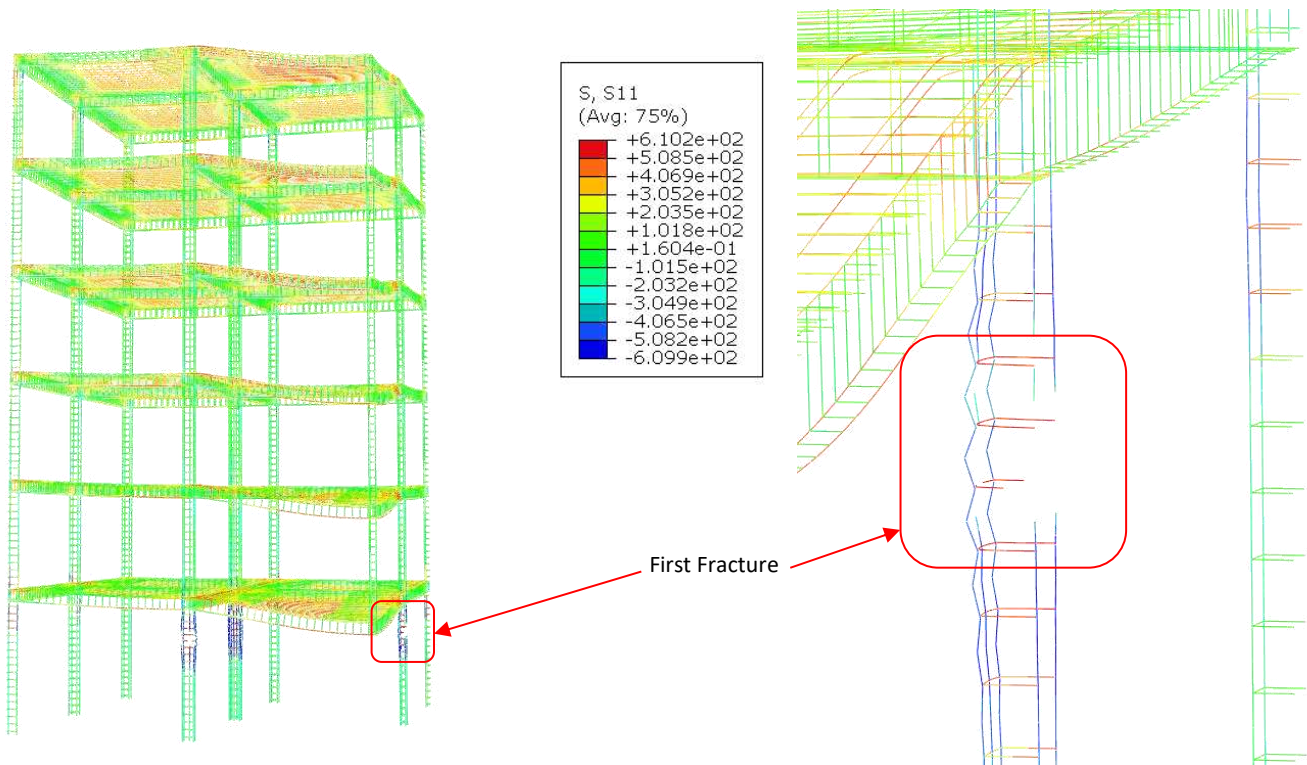


Figure 5-35: S11 Stresses in Truss Elements for FF-IC-C1 Under Pushdown Analysis at 328% Design Load at First Fracture, Quarter Model (Left) & Closeup on Plastic Hinge (Right)

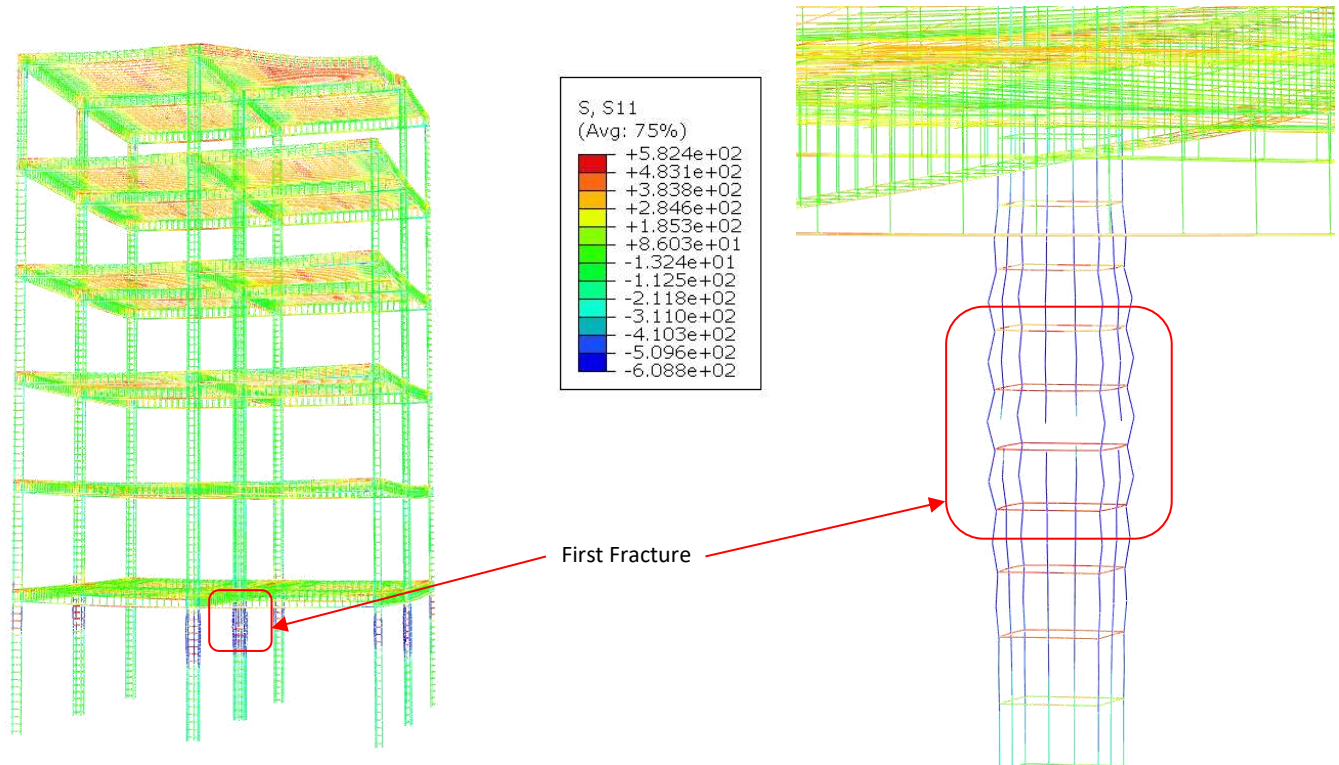


Figure 5-36: S11 Stresses in Truss Elements for FF-IC-C6 Under Pushdown Analysis at 350% Design Load at First Fracture, Quarter Model (Left) & Closeup on Plastic Hinge (Right)

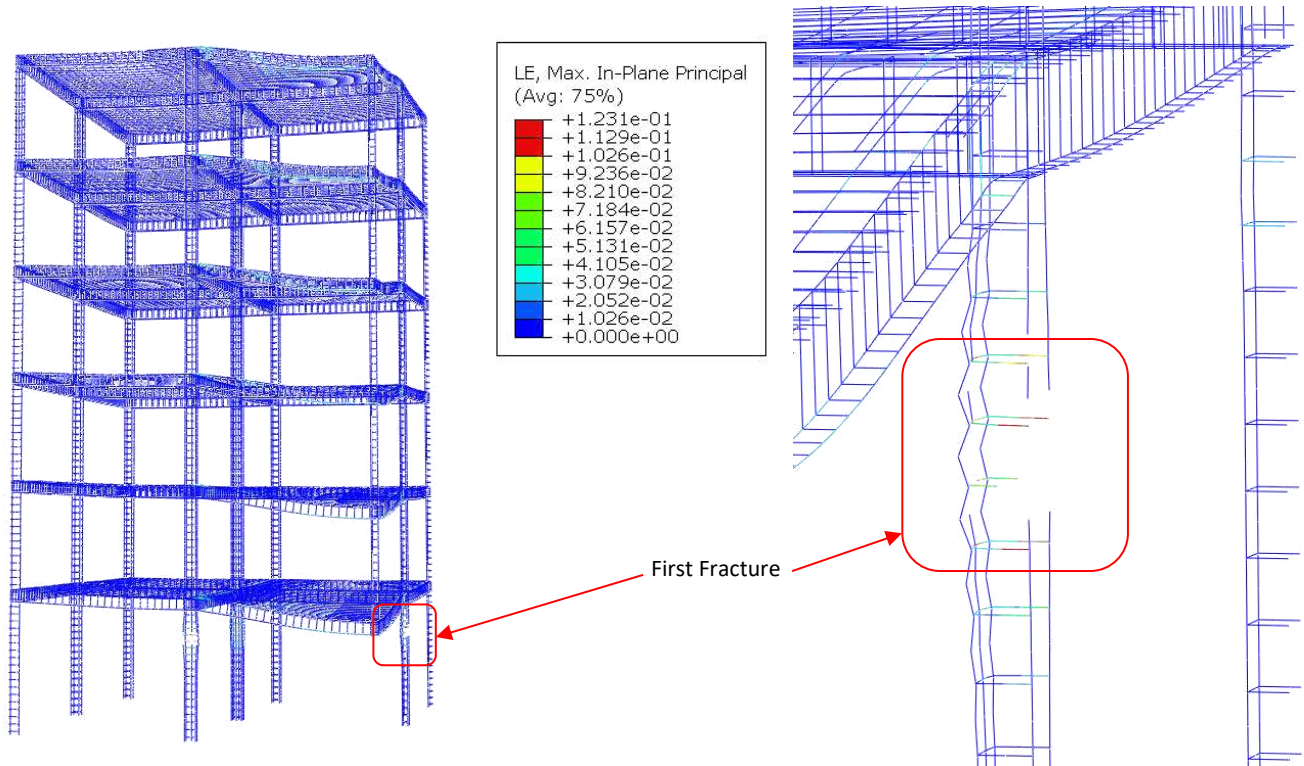


Figure 5-37: Logarithmic Strains in Truss Elements for FF-IC-C1 Under Pushdown Analysis at 328% Design Load at First Fracture, Quarter Model (Left) & Closeup on Plastic Hinge (Right)

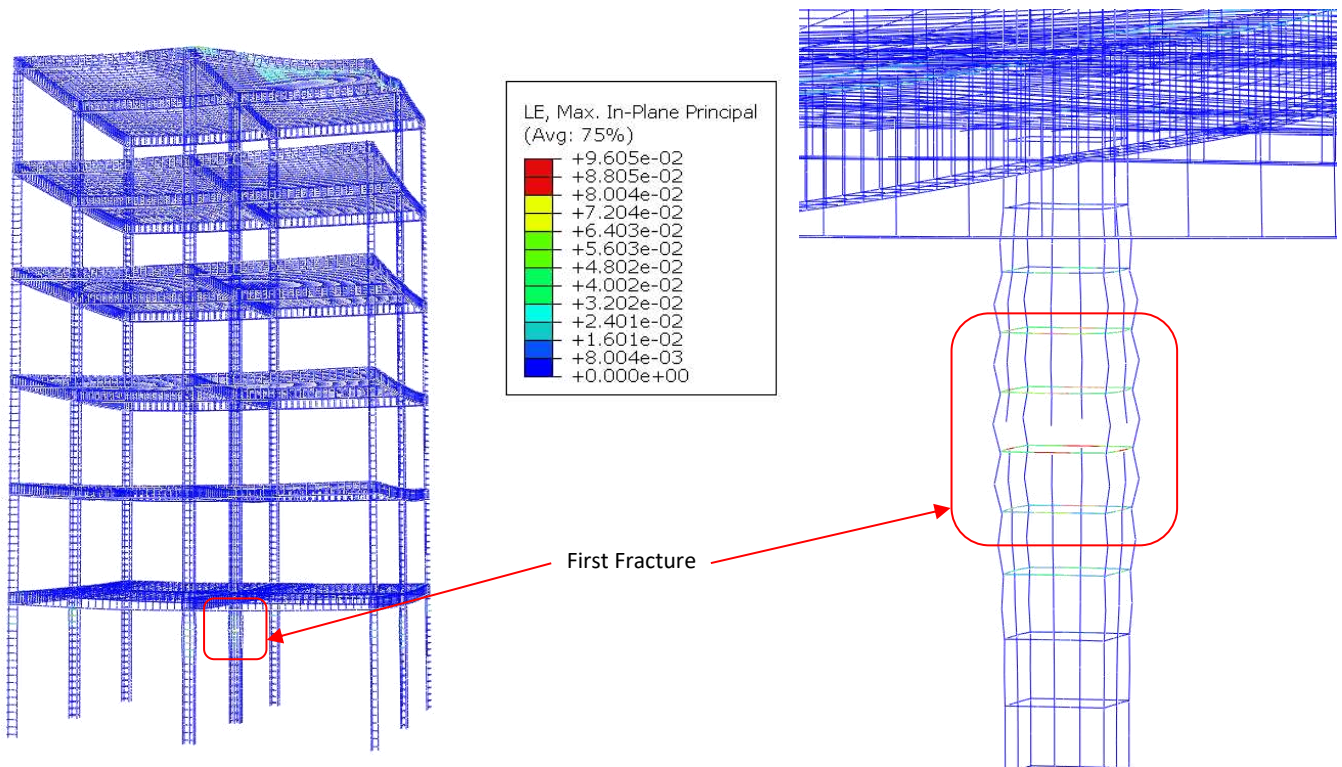


Figure 5-38: Logarithmic Strains in Truss Elements for FF-IC-C6 Under Pushdown Analysis at 350% Design Load at First Fracture, Quarter Model (Left) & Closeup on Plastic Hinge (Right)

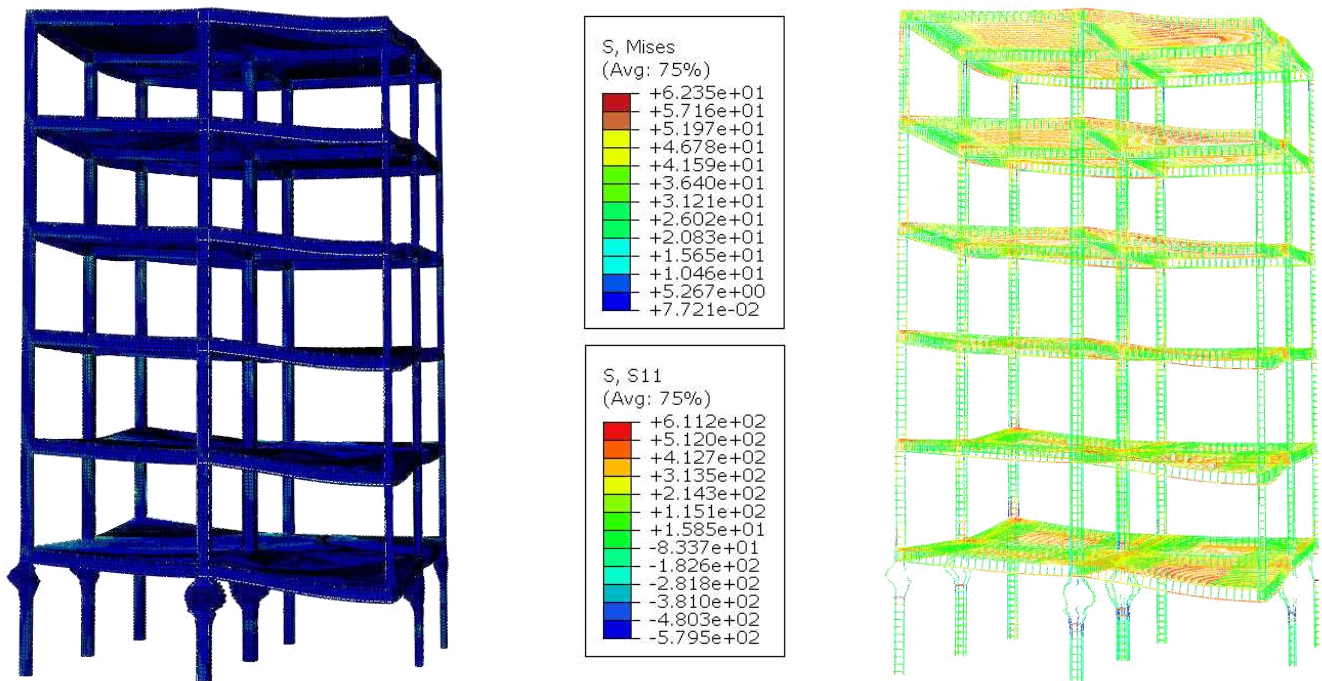


Figure 5-39: Von Mises Stresses in Solid Elements (Left) & S11 Stresses in Truss Elements (Right) for FF-IC-C1 Under Pushdown Analysis After Damage Propagation (Quarter Model Shown)

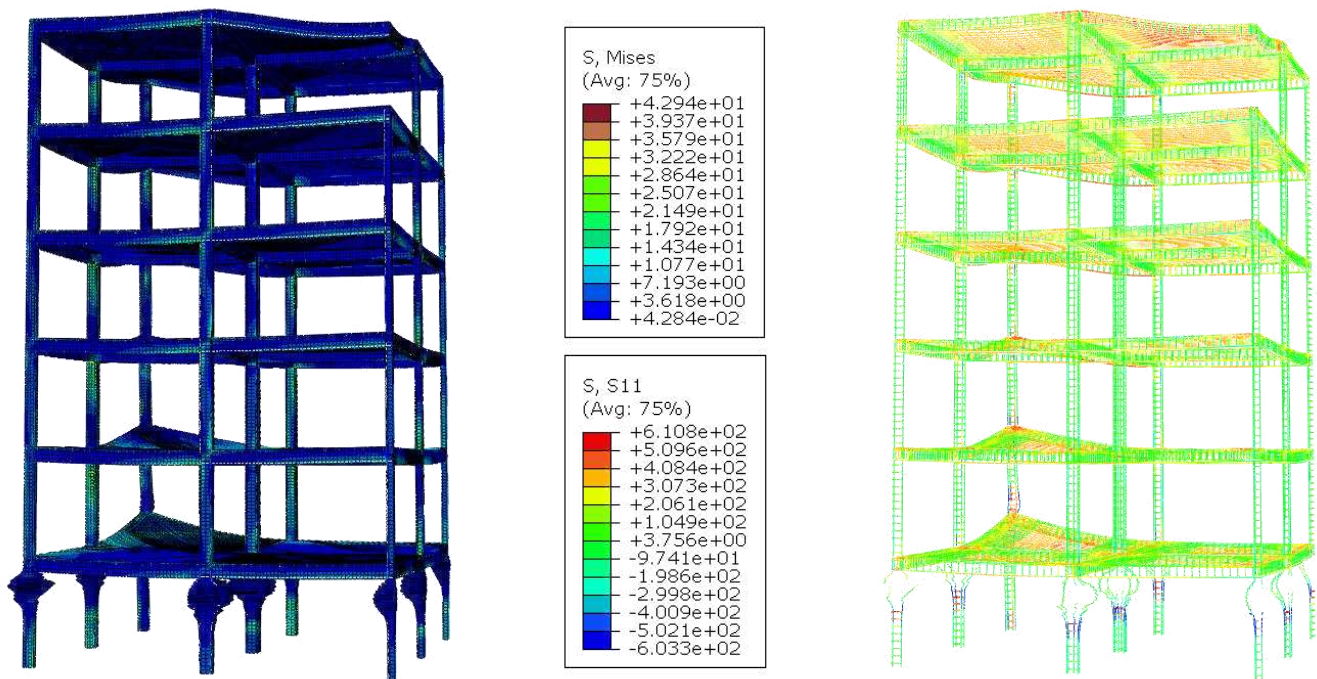


Figure 5-40: Von Mises Stresses in Solid Elements (Left) & S11 Stresses in Truss Elements (Right) for FF-IC-C6 Under Pushdown Analysis After Damage Propagation (Quarter Model Shown)

5.3.4.4 BARE-FRAME INTERIOR COLUMN REMOVAL RESULTS

The pushdown curves for the BF-IC models are shown in Figure 5-41, and the values of the applied load (P), displacement (u) and slope (s) at the fracture points are shown in Table 5-7.

Table 5-7: Maximum Pushdown Analysis Values for BF-IC Models

Model	BF-IC-C1	BF-IC-C2	BF-IC-C3	BF-IC-C4	BF-IC-C5	BF-IC-C6	Undamaged
P_{max}	141%	141%	148%	148%	152%	155%	345%
u_{max} (mm)	371	367	447	445	486	525	NA
s_{max}	7.42%	7.35%	8.93%	8.91%	9.71%	10.50%	NA

Similar to the FF-IC results, the responses of all six models were almost identical as their pushdown curves overlapped. The only apparent difference was in the failure/fracture point which seemed to increase as the number of floors above the removed column decreased. The load capacity of the system ranged from 141% for BF-IC-C1 and BF-IC-C2 to 155% for BF-IC-C6, producing a mean value of 148% and relative standard deviation of 3.57%. The vertical displacement varied from 367 mm for BF-IC-C2 to 525 mm for BF-IC-C6, resulting in an average displacement of 440 mm and relative standard deviation of 12.93%. Similar to the FF-IC models, the results imply that each floor acted separately in resisting the applied gravity loads. However, the reason models with more floors above the removed column failed first was due to the fact that the floor’s share of the own weight of the remaining upper part of the column increases as the number of floors above the removed column increases. So, for instance, in the case of Model BF-IC-C5, there is only one story above the removed column. Therefore, the own weight of the sixth-floor column shall be supported by the fifth-floor and sixth-floor beams, almost equally. So, each floor would have an additional dead load of $\frac{1}{2}$ of the weight of a single-floor column. In the case of Model BF-IC-C4, for example, there would be two stories above the removed column, sandwiched between three floors. So, each floor would receive an additional load of $\frac{2}{3}$ of a column and so on. This interpretation is based on the assumption that the relative displacement between each floor is negligible, which means that the column weight is equally distributed among the supporting floors. By examining the response, this assumption was validated and, therefore, deemed acceptable.

Further examination of Model BF-IC-C1 and Model BF-IC-C6 was carried out at two points in the analysis timeline, with the first point representing the first rebar fracture and the second point representing the partial collapse progression. The stresses and displacement in RC solid elements at first fracture are shown for BF-IC-C1 and BF-IC-C6 in Figure 5-42 and Figure 5-43, respectively. The stresses and strains in the rebar elements, at the same point, are shown in Figure 5-44 to Figure 5-47. The first rebar fracture occurred in the top longitudinal reinforcement bars of the third floor’s beam for BF-IC-C1. The rebar failed after reaching the ultimate plastic strain of 0.12 and its corresponding true stress of 612 MPa. After the initial fracture, damage progressed in all floors

above the removed column but was confined to the internal central bay. Therefore, the structure suffered a partial progressive collapse. The stresses in solid and truss elements after damage propagation are shown in Figure 5-48 and Figure 5-49.

It should be mentioned that these results highlight the difference between the bare-frame model and the full-frame model. Neglecting the effect of the slab obviously led to failure occurring in the beams and not in the columns as was the case with the full model. This could be attributed to the fact that in the case of the bare frame, all the gravity loads were supported by the rectangular beams which eventually failed as the load increased. On the other hand, with the full frame, the slab contributed to the stiffness of the beams, and therefore, the beams were able to resist the increase in gravity loads until the failure of the adjacent/neighbor columns started to occur.

Finally, comparing the results of the damaged models with the undamaged model indicates that the removal of an interior column from the bare frame altered the failure mechanism and led to a reduction in the system's load-bearing capacity ranging from 55% to 59%.

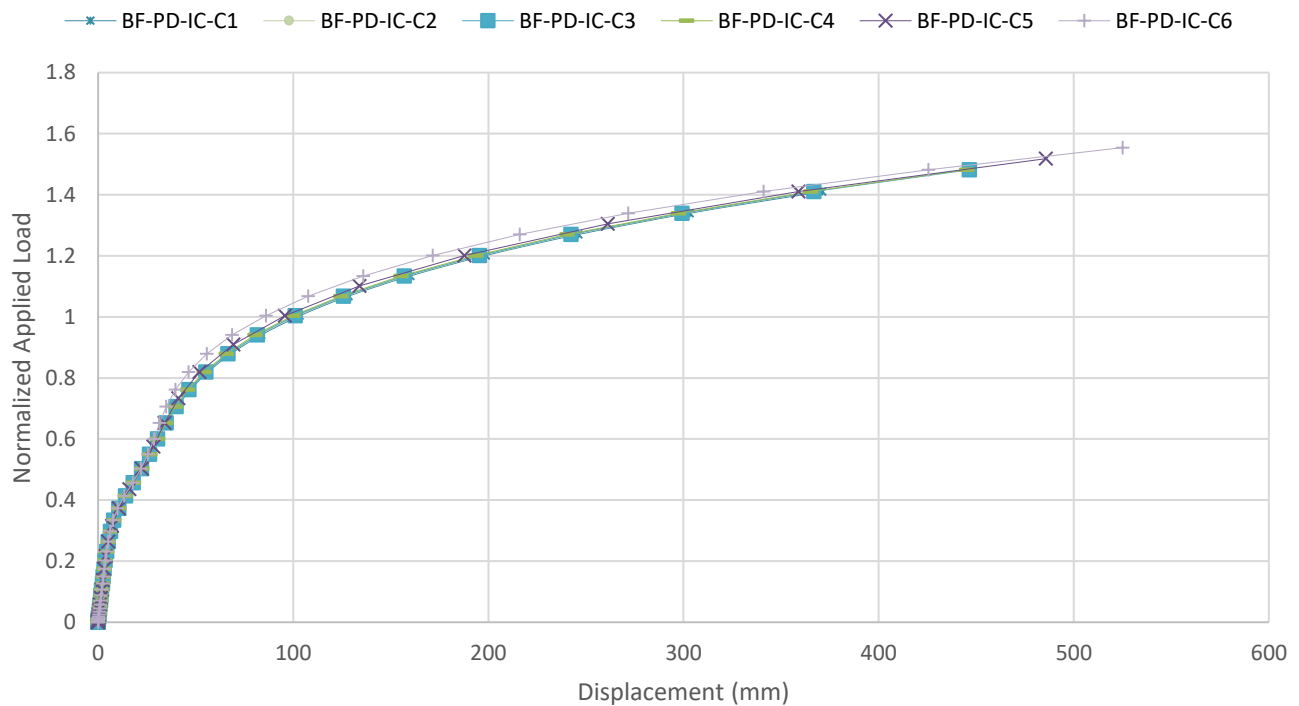


Figure 5-41: Pushdown Curves for BF-IC Models

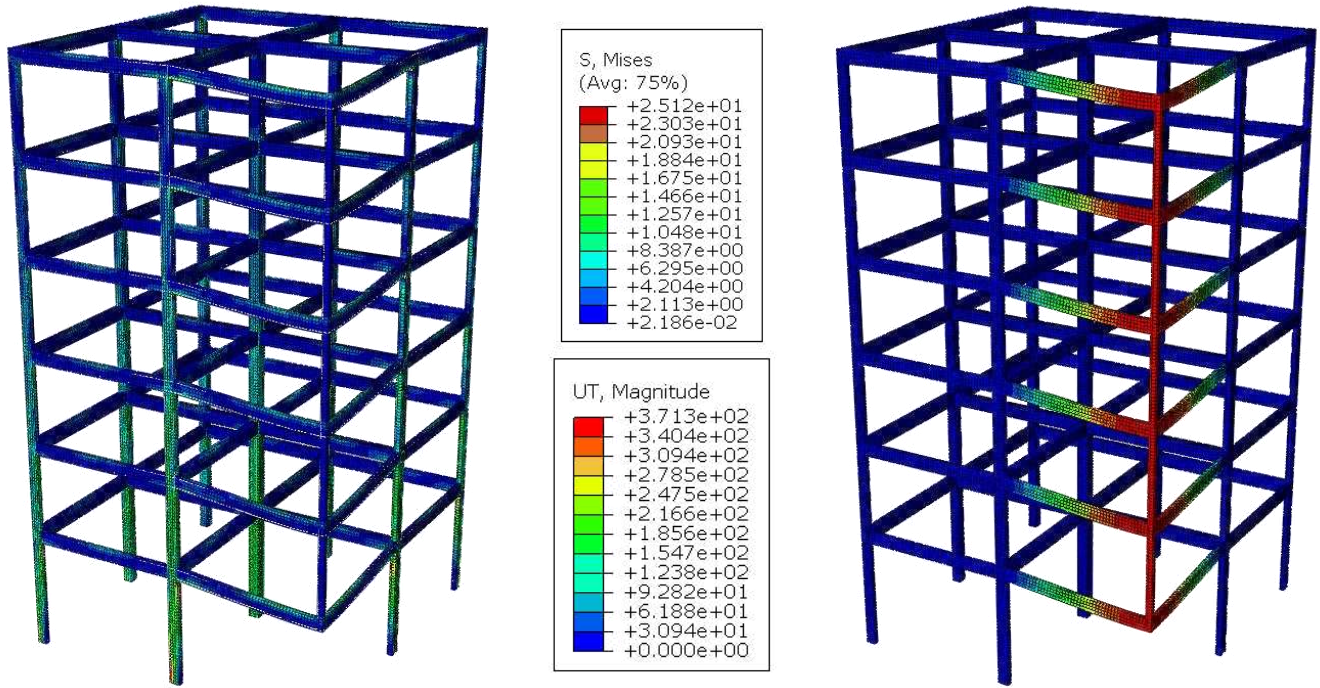


Figure 5-42: Von Mises Stresses (Left) & Total Displacement (Right) in Solid Elements for BF-IC-C1 Under Pushdown Analysis at 141% Design Load at First Fracture (Quarter Model Shown)

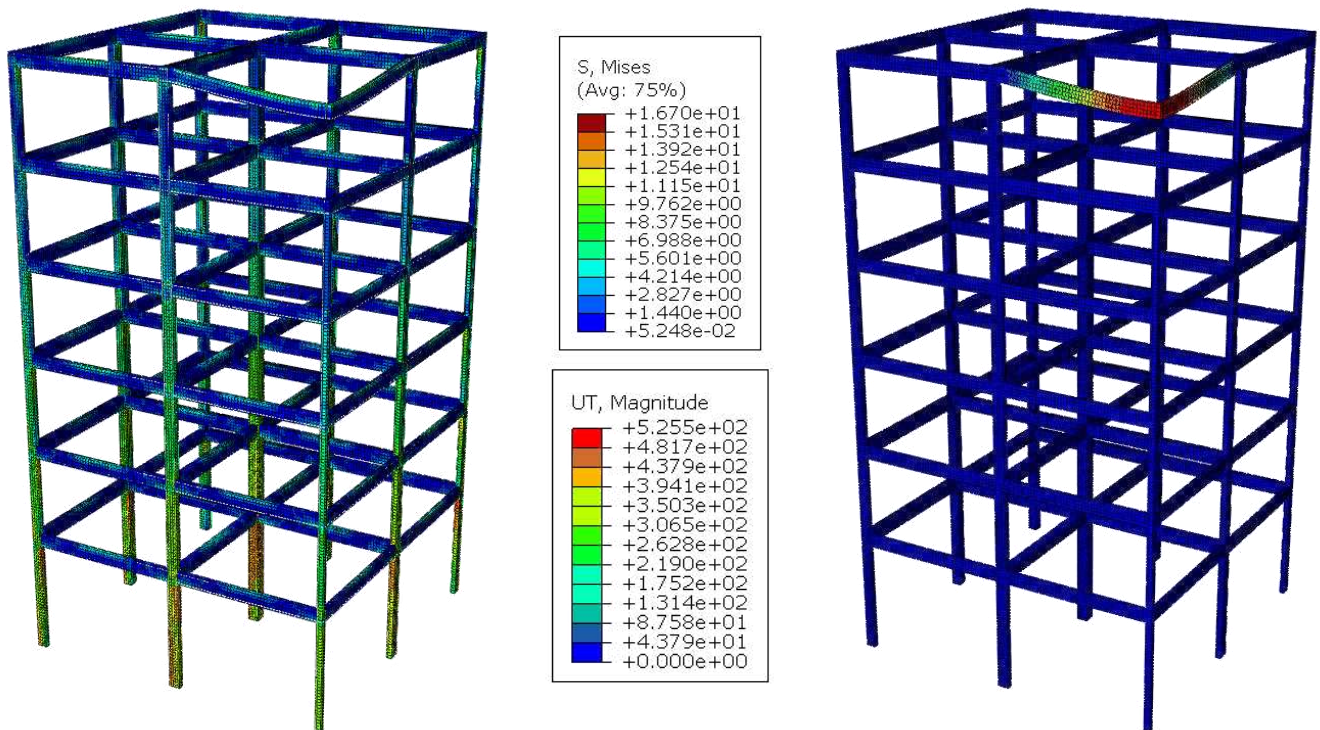


Figure 5-43: Von Mises Stresses (Left) & Total Displacement (Right) in Solid Elements for BF-IC-C6 Under Pushdown Analysis at 155% Design Load at First Fracture (Quarter Model Shown)

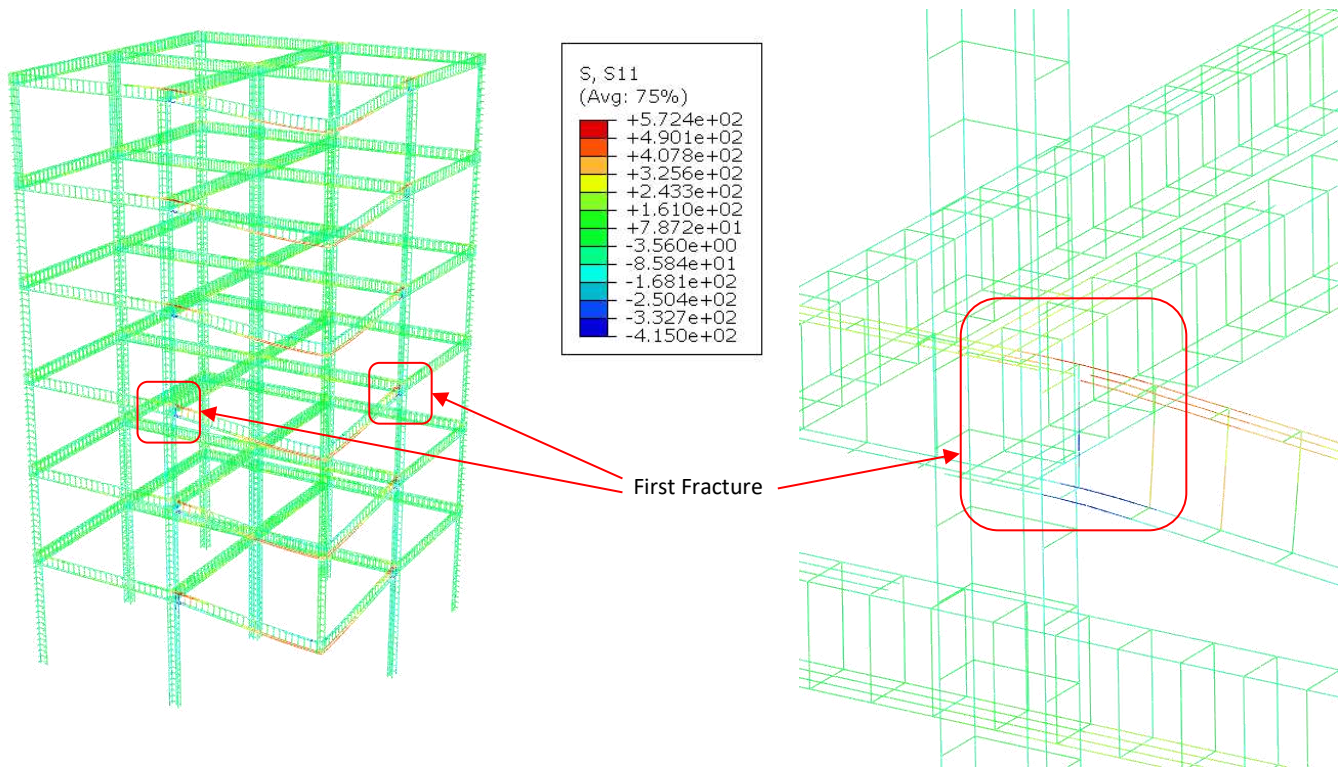


Figure 5-44: S11 Stresses in Truss Elements for BF-IC-C1 Under Pushdown Analysis at 141% Design Load at First Fracture, Quarter Model (Left) & Closeup on Plastic Hinge (Right)

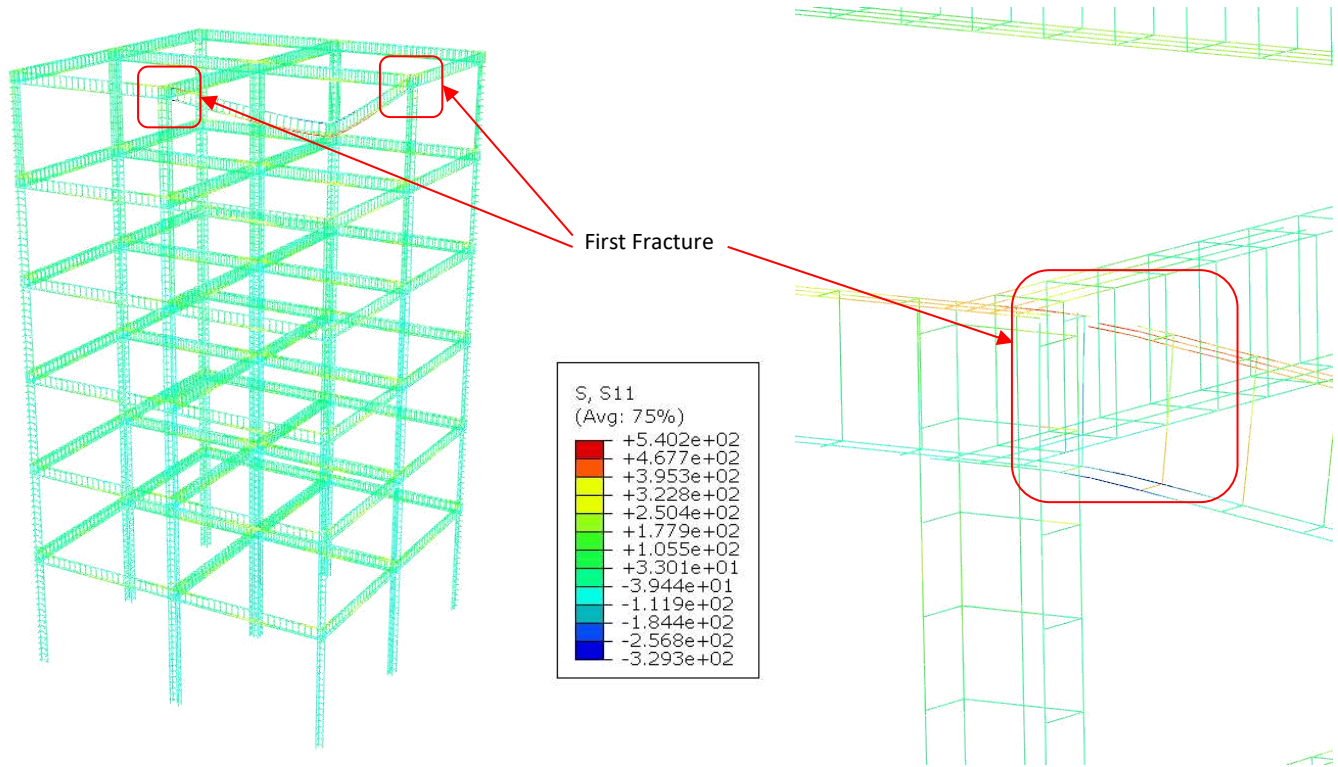


Figure 5-45: S11 Stresses in Truss Elements for BF-IC-C6 Under Pushdown Analysis at 155% Design Load at First Fracture, Quarter Model (Left) & Closeup on Plastic Hinge (Right)

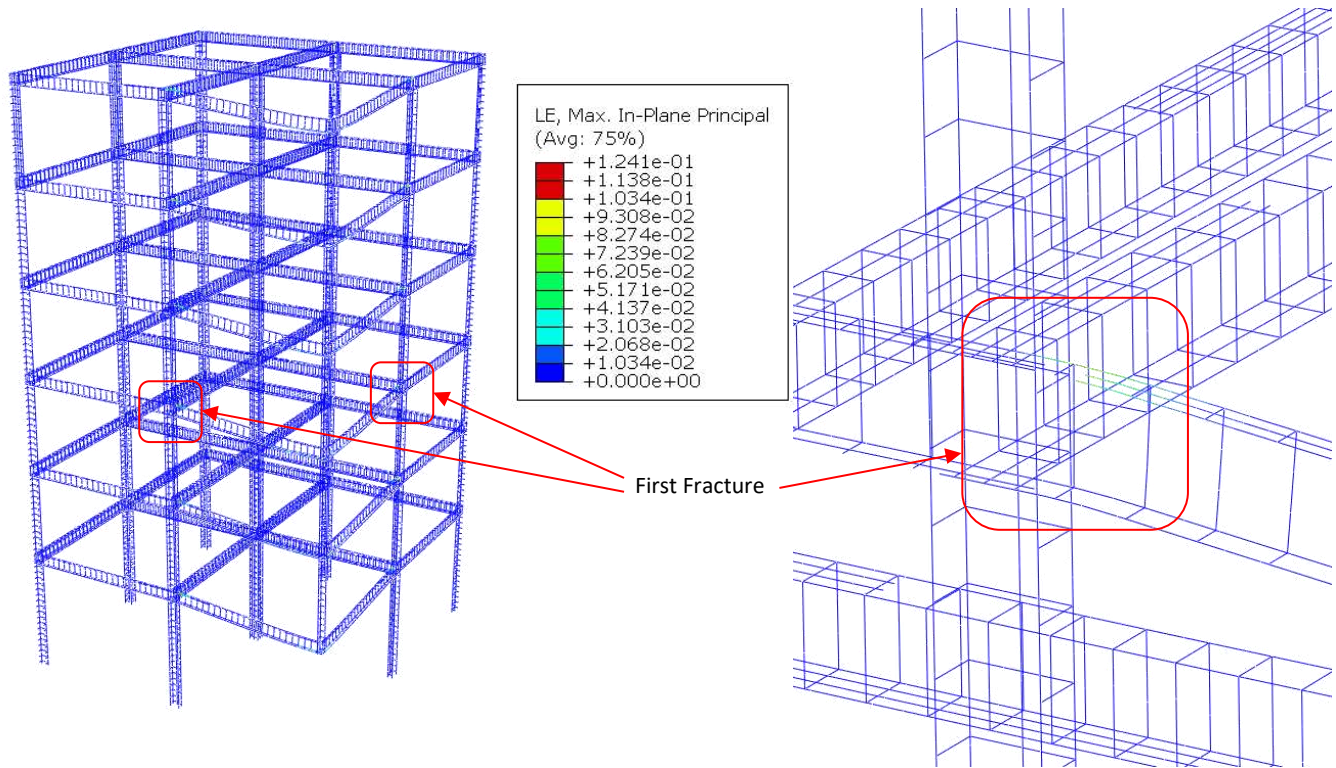


Figure 5-46: Logarithmic Strains in Truss Elements for BF-IC-C1 Under Pushdown Analysis at 141% Design Load at First Fracture, Quarter Model (Left) & Closeup on Plastic Hinge (Right)

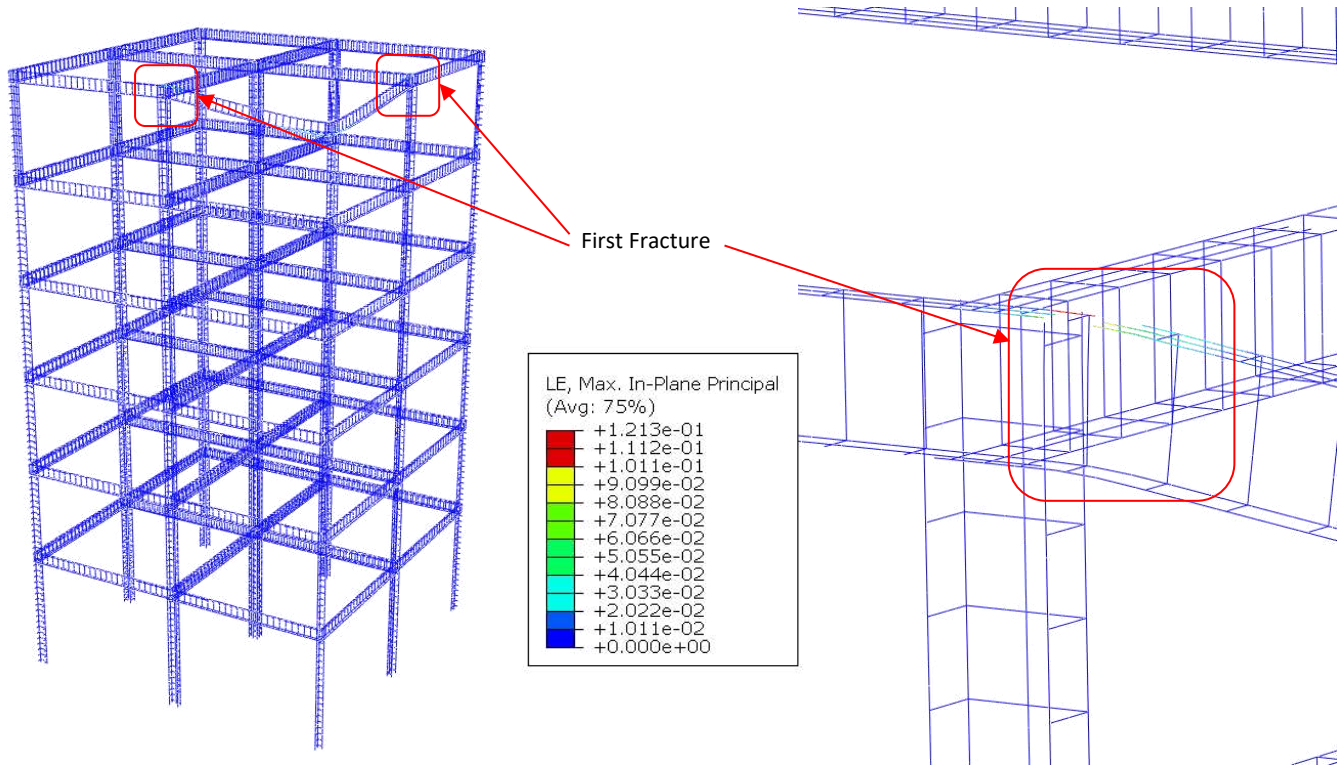


Figure 5-47: Logarithmic Strains in Truss Elements for BF-IC-C6 Under Pushdown Analysis at 155% Design Load at First Fracture, Quarter Model (Left) & Closeup on Plastic Hinge (Right)

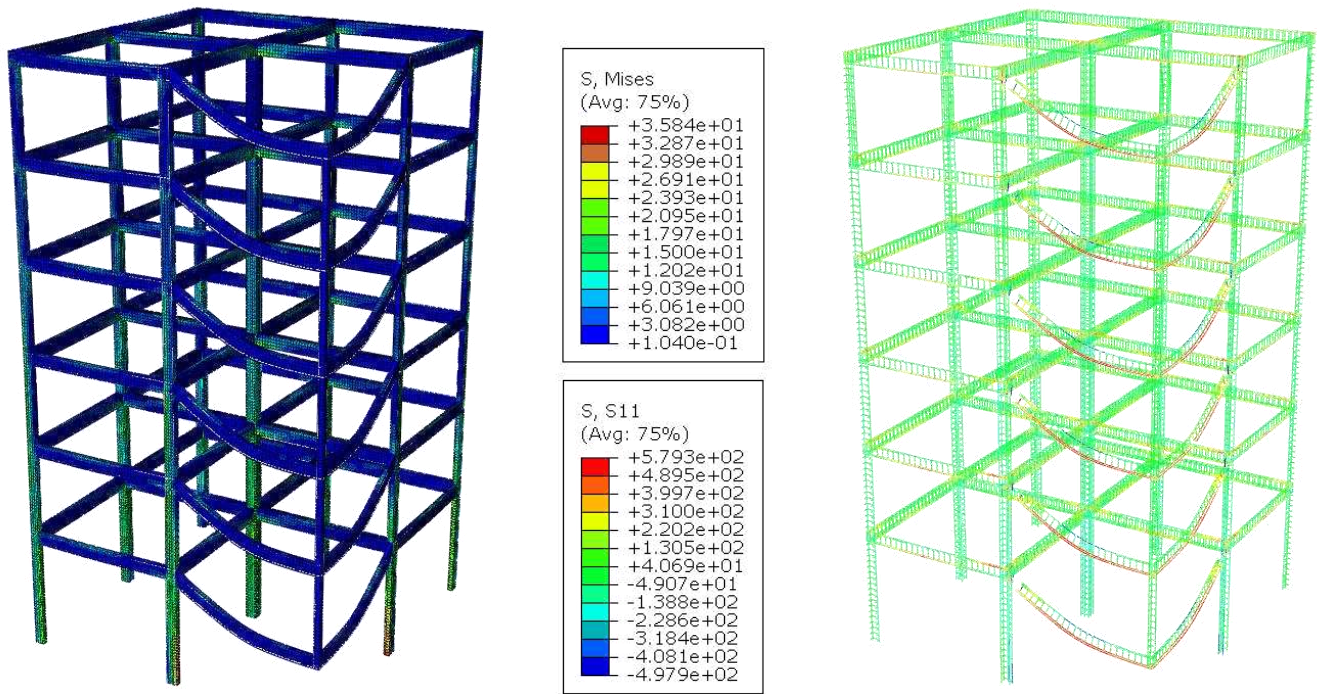


Figure 5-48: Von Mises Stresses in Solid Elements (Left) & S11 Stresses in Truss Elements (Right) for BF-IC-C1 Under Pushdown Analysis After Damage Propagation (Quarter Model Shown)

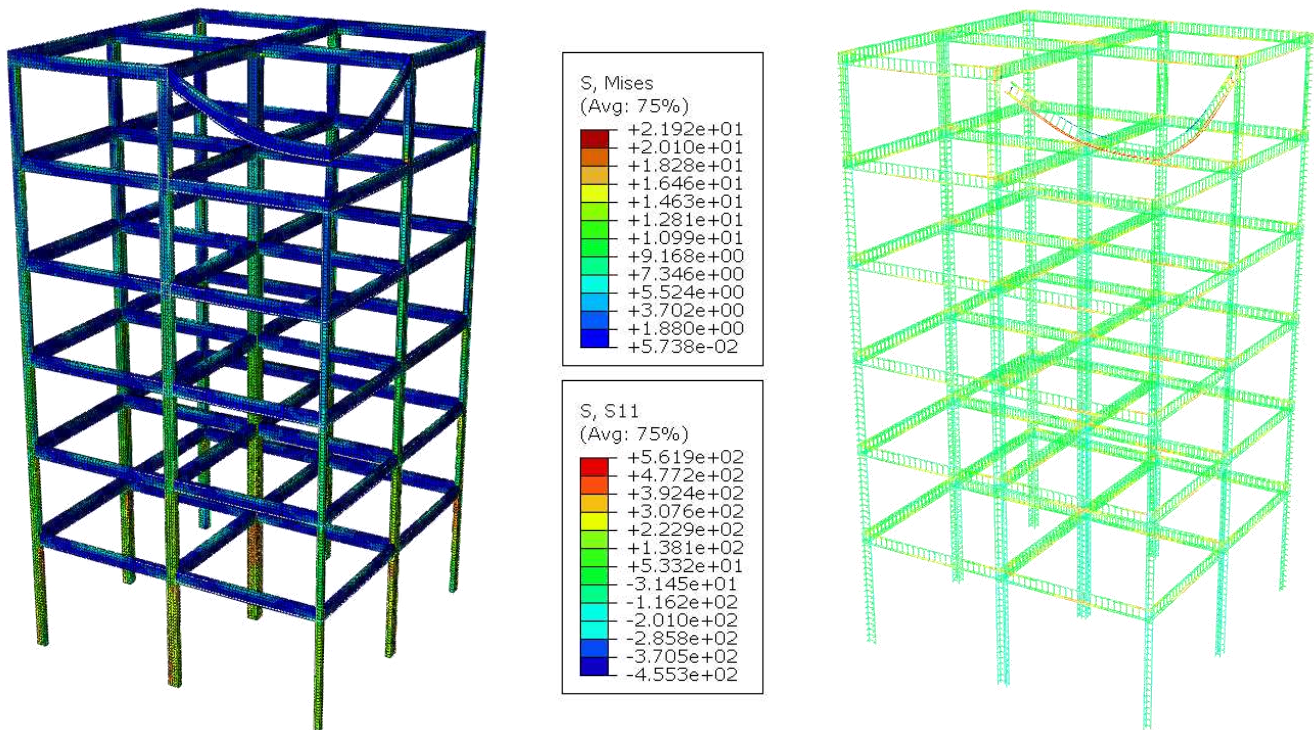


Figure 5-49: Von Mises Stresses in Solid Elements (Left) & S11 Stresses in Truss Elements (Right) for BF-IC-C6 Under Pushdown Analysis After Damage Propagation (Quarter Model Shown)

5.3.5 COLUMN LOSS ANALYSIS

The column removal simulation method described in Section 4.4.1.2 was adopted here in the analysis of the case study building. For each model and each column removal scenario, a percentage of the progressive collapse design load (1.2 D + 0.5 L) prescribed in the GSA and UFC guidelines was gradually applied to the system for a duration of 0.5 seconds. The system was then left for another 0.5 seconds, so that any transient vibrations would die out, after which the reaction forces and moments (if any) of the column in question were removed within a span of 10^{-5} seconds, which is obviously a lot less than one tenth of the period of vibration of the structure. Afterwards, the model was left to react to the extreme loading scenario for almost two more seconds.

5.3.5.1 FULL-FRAME CORNER COLUMN REMOVAL RESULTS

The corner column was removed from the model at each floor. The joint displacement at the top of the removed column is plotted against time for each model in Figure 5-50 to Figure 5-55. The applied load had been increased by 20% of the design load in each run, as shown in the graphs. By plotting the applied load percentage (normalized load) versus the maximum/permanent displacement at which the system stabilized for each loading value, the equivalent dynamic load-displacement curves or “pseudo-static” curves as dubbed in [13] shown in Figure 5-56 were created. Table 5-8 shows the values of the applied load (P), displacement (u) and slope (s) at the fracture points.

Table 5-8: Maximum Column Loss Analysis Values for FF-CC Models

Model	FF-CC-C1	FF-CC-C2	FF-CC-C3	FF-CC-C4	FF-CC-C5	FF-CC-C6
P_{max}	160%	160%	160%	160%	160%	140%
u_{max} (mm)	184	209	208	240	240	258
S_{max}	3.69%	4.17%	4.15%	4.80%	4.81%	5.15%

Model FF-CC-C1 to Model FF-CC-C5 resisted the sudden removal of the corner column up to an applied load of 160% of the design load, while the maximum load that could be resisted by Model FF-CC-C6 was found to be 140% of the design load. In general, the results showed that the response of the first five models was almost identical at load levels below 100%. However, at higher load levels, as the number of floors above the removed column decreased, the deformation increased. The maximum displacement varied from 184 mm in the case of FF-CC-C1 to 240 mm in the case of FF-CC-C4 and FF-CC-C5. On the other hand, as Model FF-CC-C6 exhibited lower load capacity (140%), it also reached a higher displacement than the rest of the models (258 mm). This observation may be attributed to the lack of Vierendeel action, as the top floor deformed alone as a cantilever in Model FF-CC-C6. Overall, the permanent displacement of the system seemed to decrease at the same load level as the

number of floors above the removed column increased due to the diaphragm effect. Systems with less floors above exhibited more flexible behavior at high load levels than systems with higher floors above.

To shed light on the progressive collapse of the systems, the applied load level at which the structure failed was examined. As done in Section 5.3.4, two models representing the two extremes of the response were chosen for this assessment, Model BF-CC-C1 under 180% load level and Model BF-CC-C6 under 160% load level. Two points in the analysis timeline were studied. The first point corresponded to the first rebar fracture while the second one represented a point within the damage propagation phase before the structure partially collapsed. The von Mises stresses and total displacement in the RC solid elements at first fracture are shown in Figure 5-57 and Figure 5-58 for FF-CC-C1 and FF-CC-C6, respectively. The normal stresses and strains in the rebar truss elements, at the same point, are shown in Figure 5-59 to Figure 5-62. The zones where the rebar first fractured are also shown in the figures. So, the first rebar fracture occurred in the top longitudinal reinforcement steel bars of the third floor’s beam for FF-CC-C1 while it happened in the top bars of the sixth floor’s beam for FF-CC-C6. Following the first fracture, damage progressed to the adjacent rebar and to the rest of the floors above the removed column. However, the damage was localized to the external corner bay as the structure suffered a partial progressive collapse. The stresses in the RC solid and rebar truss elements after damage propagation are shown in Figure 5-63 and Figure 5-64.

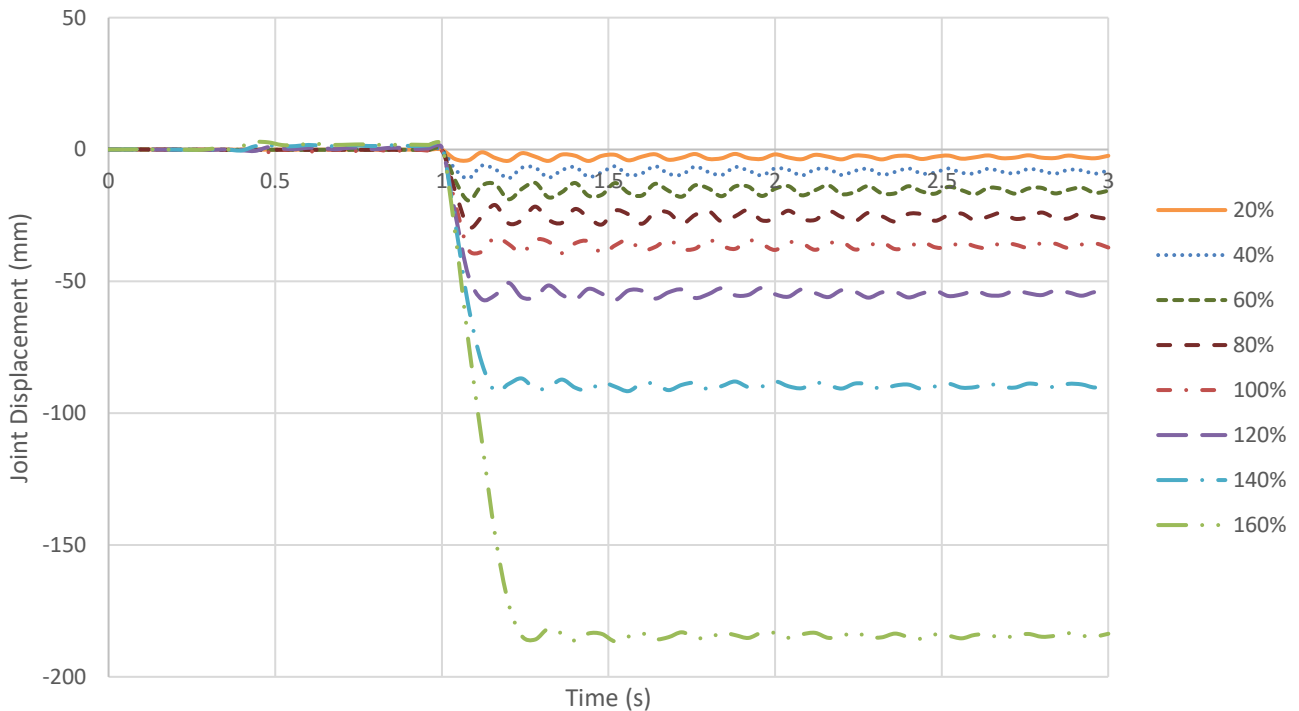


Figure 5-50: Joint Displacements for FF-CC-C1 Subjected to Sudden Column Loss Under Different Load Values

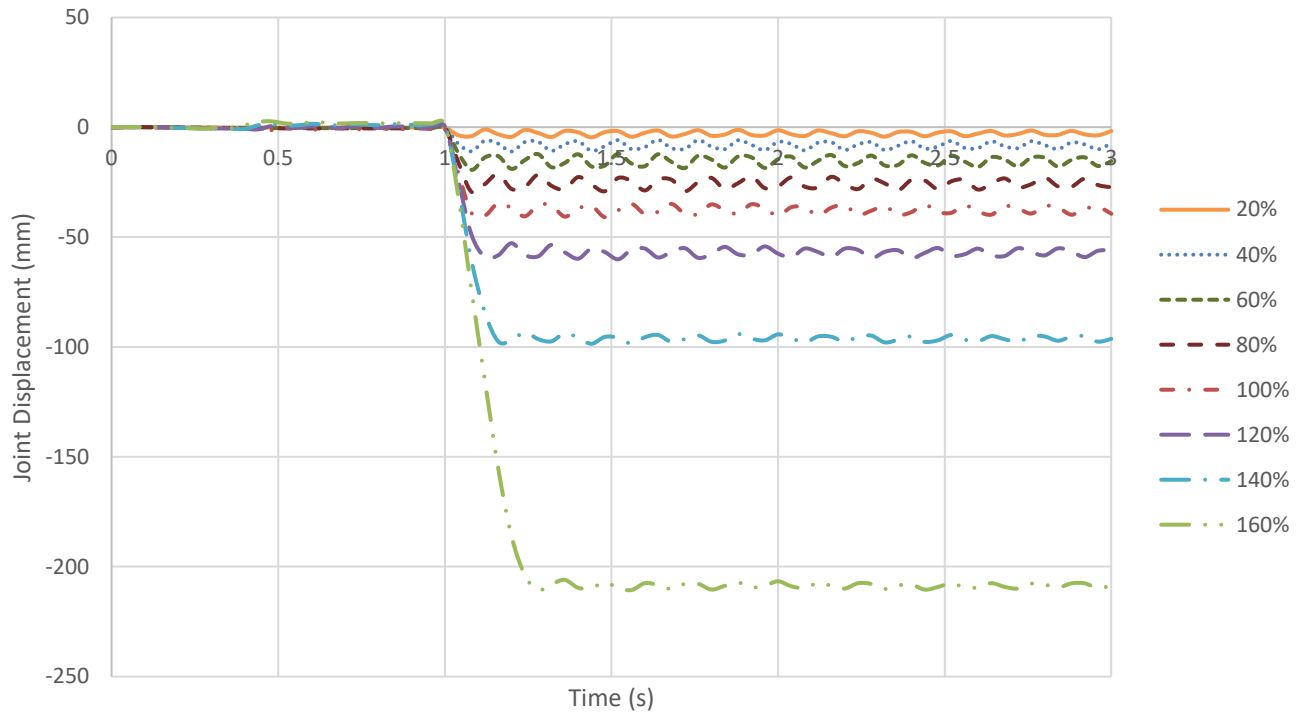


Figure 5-51: Joint Displacements for FF-CC-C2 Subjected to Sudden Column Loss Under Different Load Values

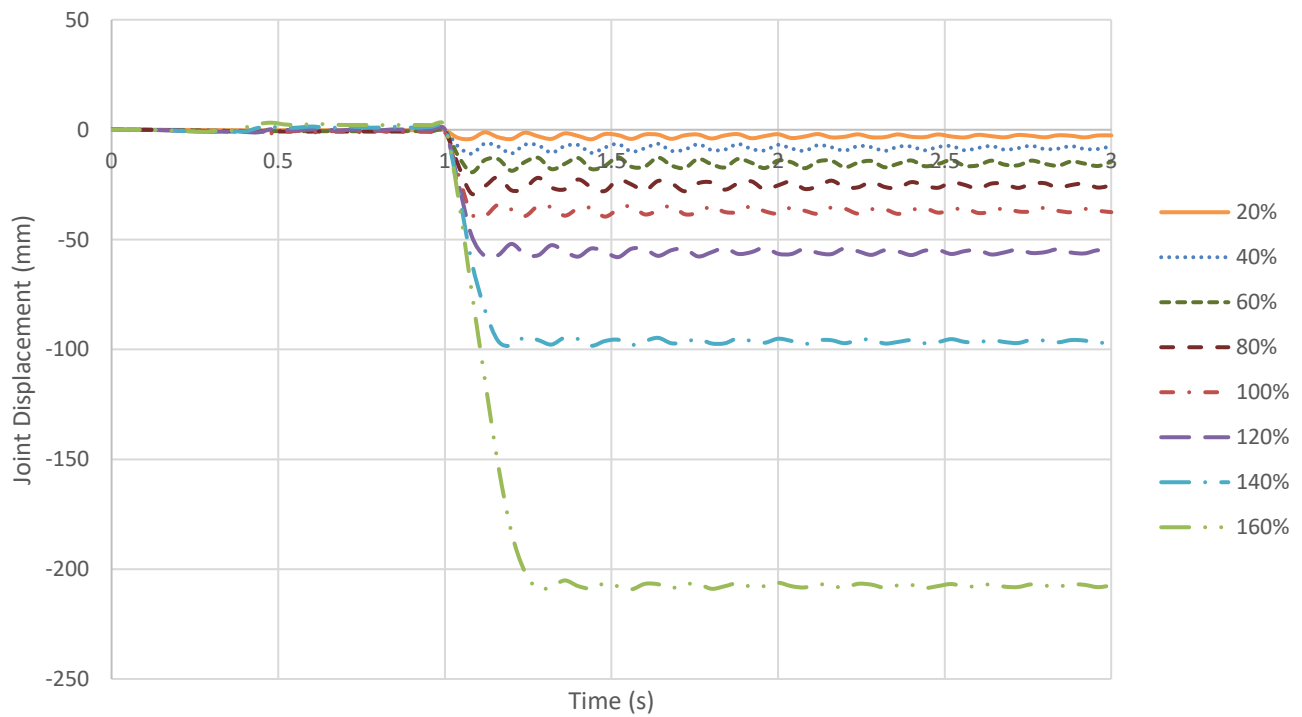


Figure 5-52: Joint Displacements for FF-CC-C3 Subjected to Sudden Column Loss Under Different Load Values

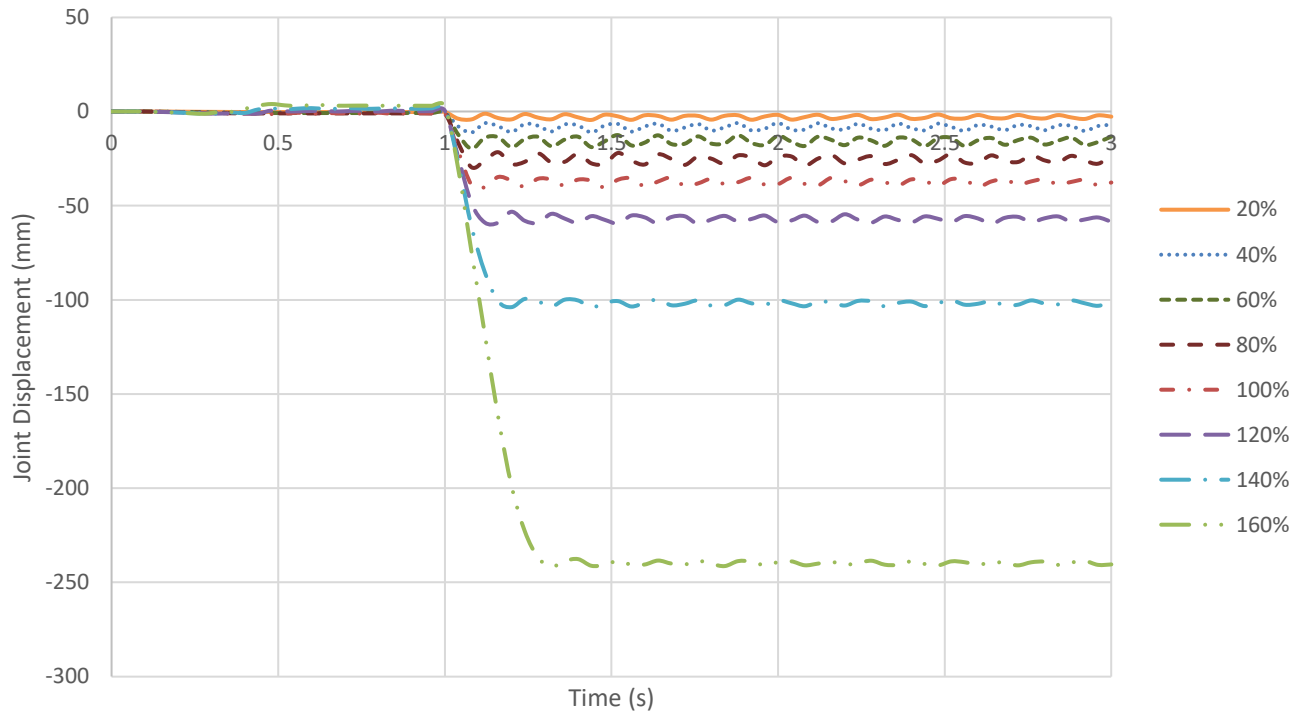


Figure 5-53: Joint Displacements for FF-CC-C4 Subjected to Sudden Column Loss Under Different Load Values

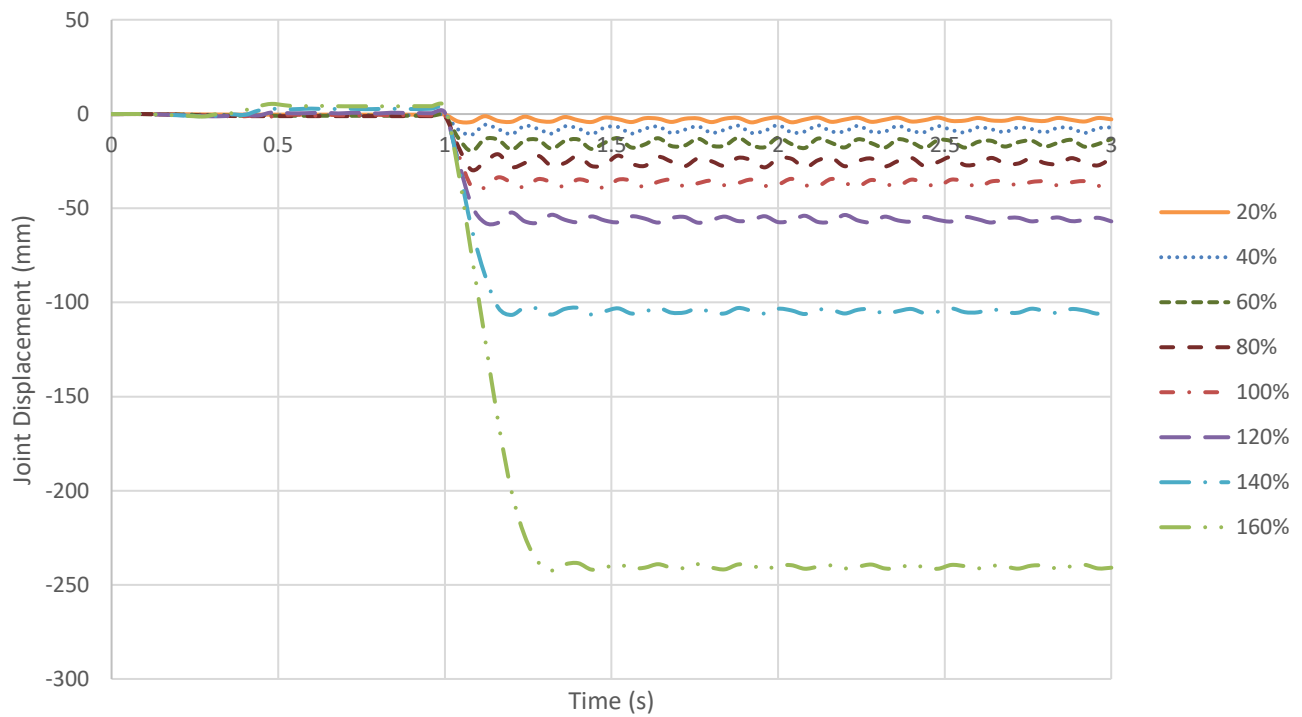


Figure 5-54: Joint Displacements for FF-CC-C5 Subjected to Sudden Column Loss Under Different Load Values

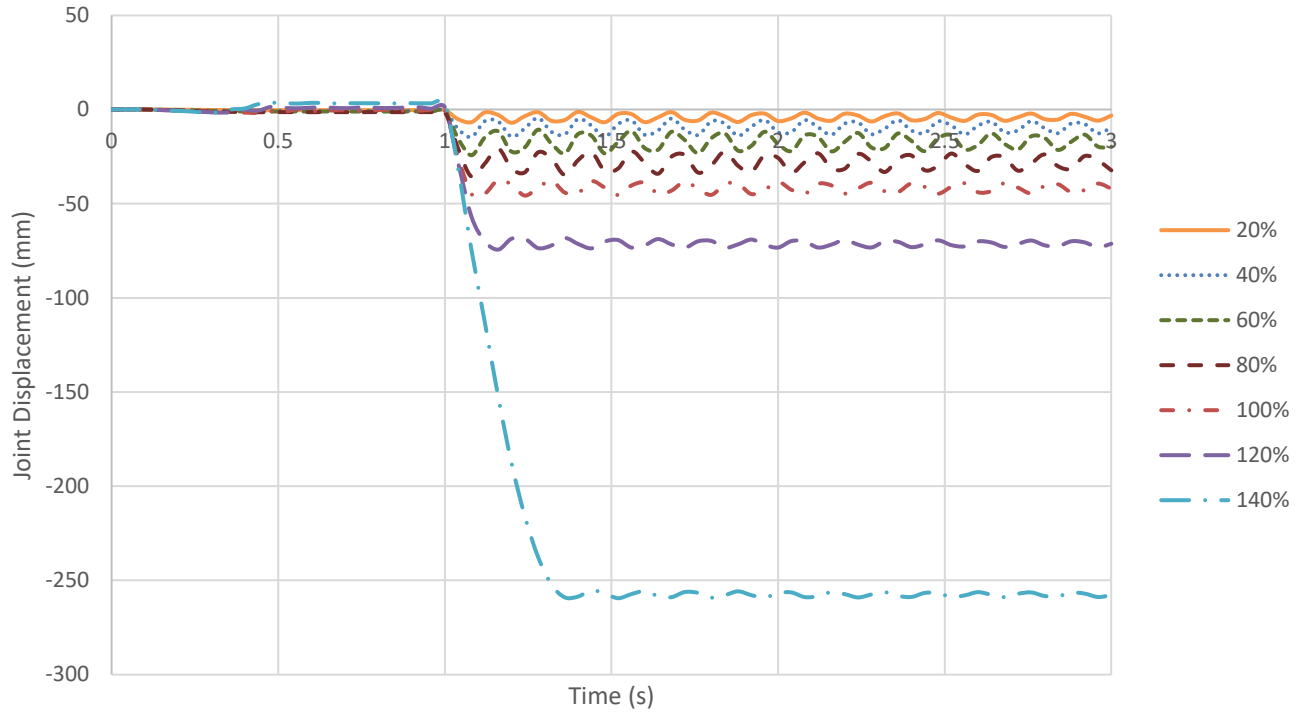


Figure 5-55: Joint Displacements for FF-CC-C6 Subjected to Sudden Column Loss Under Different Load Values

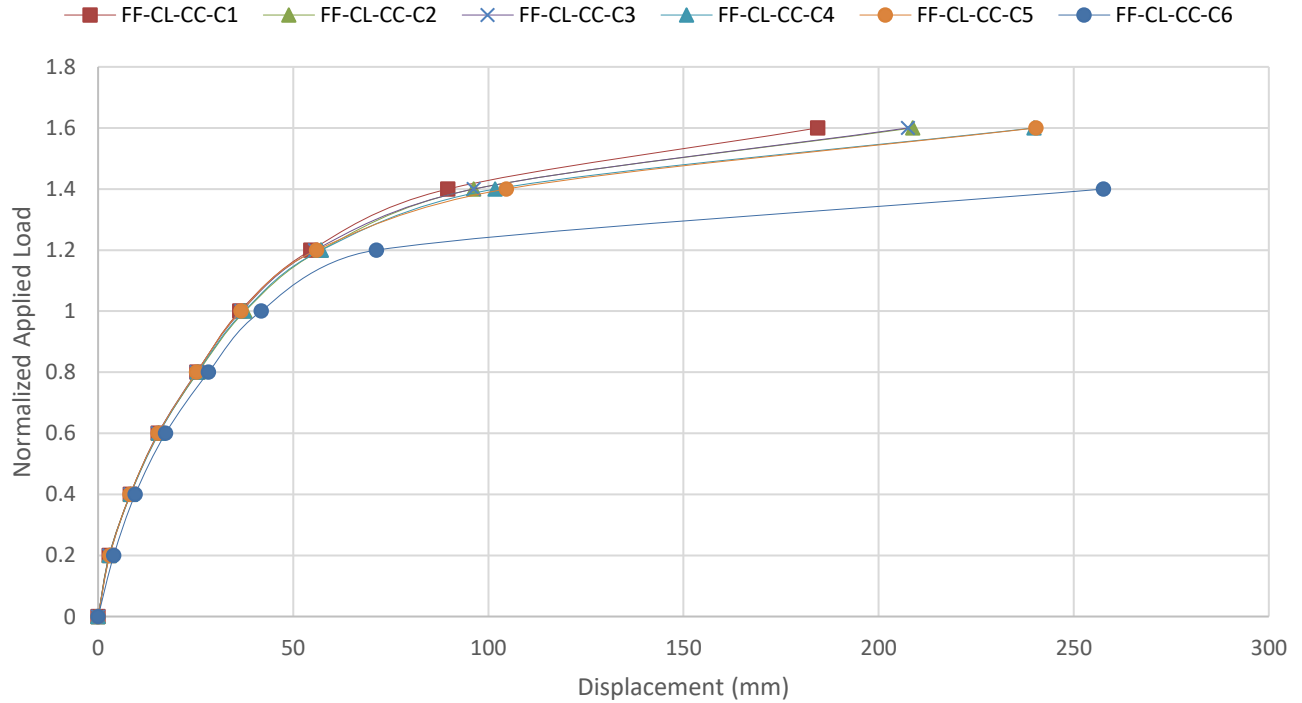


Figure 5-56: Pseudo-Static Curves for FF Due to the Sudden Loss of CC at Each Floor

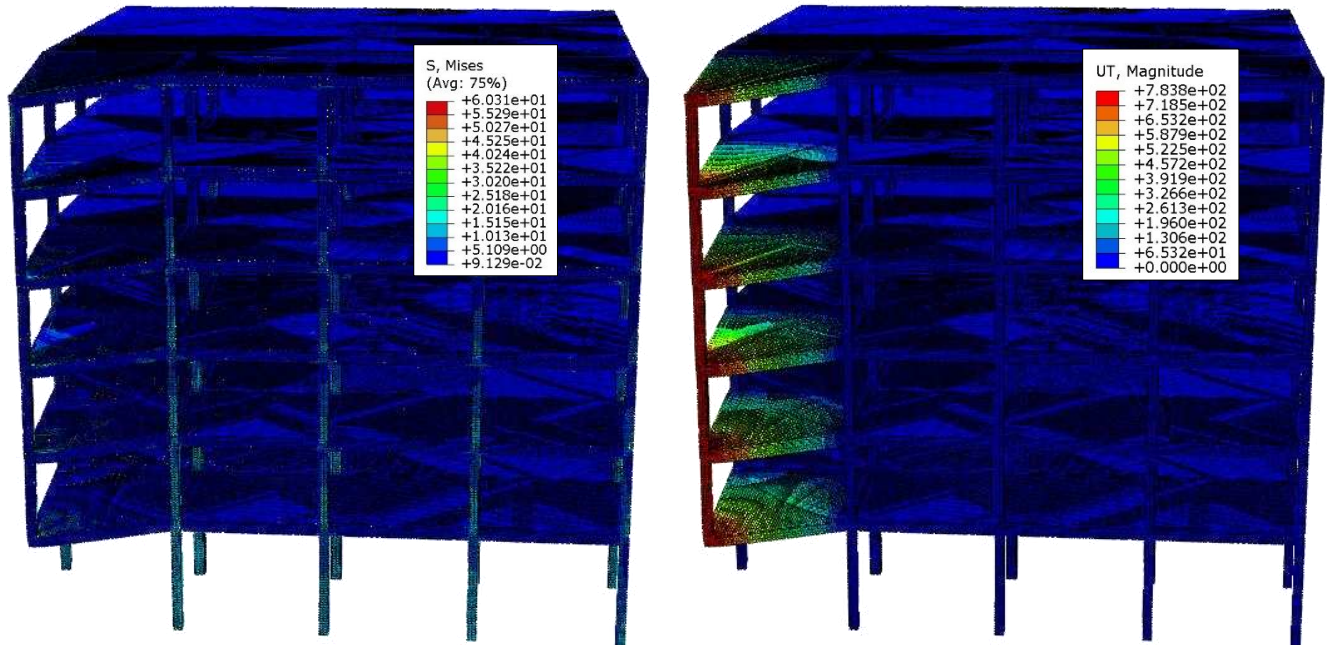


Figure 5-57: Von Mises Stresses (Left) & Total Displacement (Right) in Solid Elements for FF-CC-C1 Under Sudden Column Loss at 180% Design Load at First Fracture (Full Model Shown)

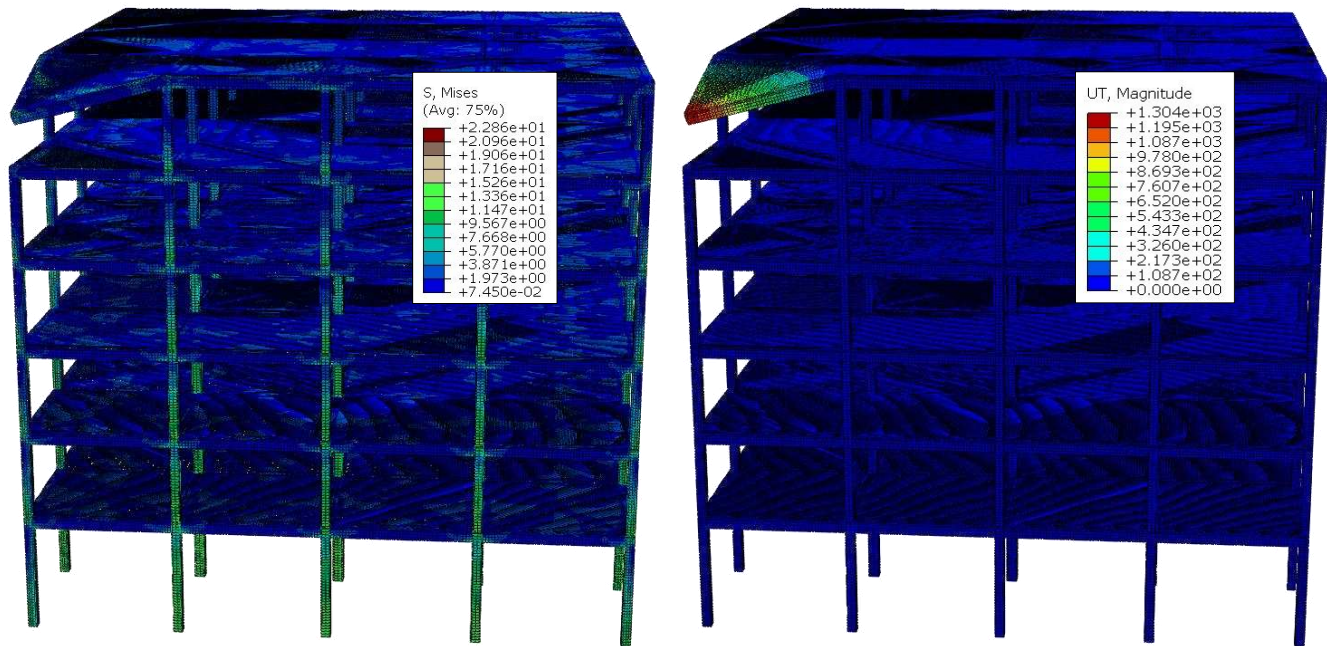


Figure 5-58: Von Mises Stresses (Left) & Total Displacement (Right) in Solid Elements for FF-CC-C6 Under Sudden Column Loss at 160% Design Load at First Fracture (Full Model Shown)

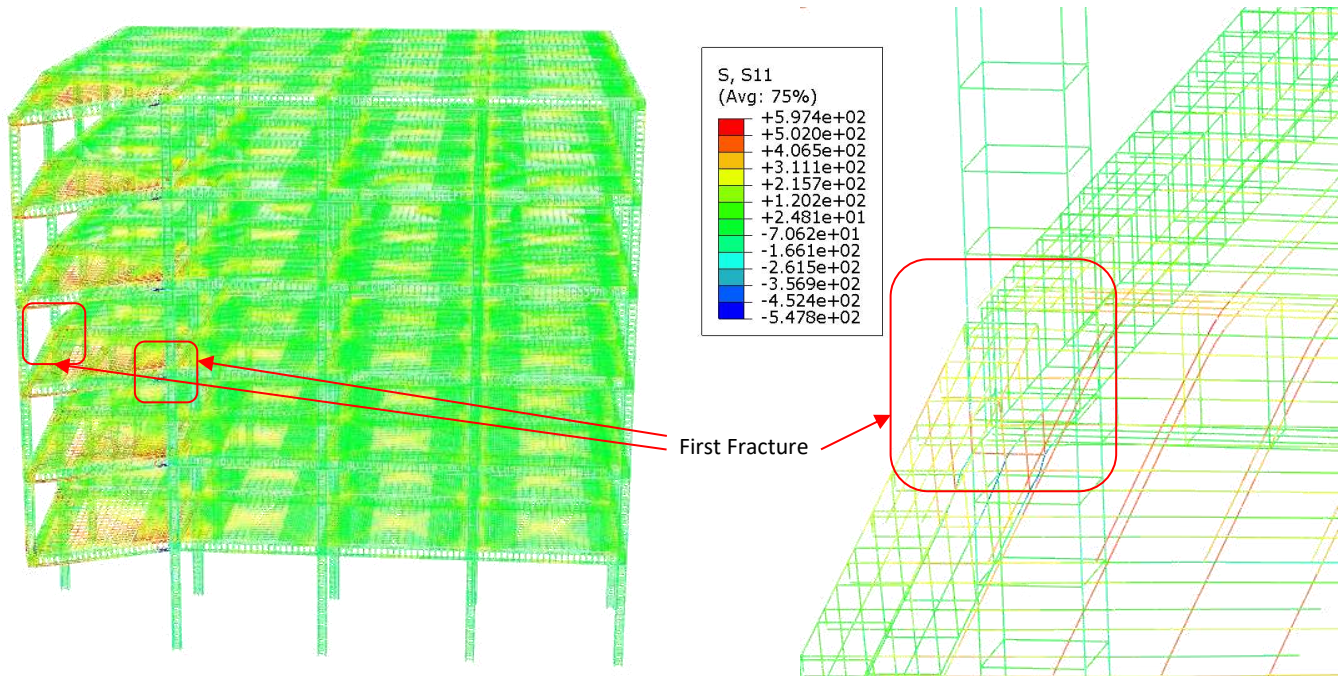


Figure 5-59: S11 Stresses in Truss Elements for FF-CC-C1 Under Sudden Column Loss at 180% Design Load at First Fracture, Full Model (Left) & Closeup on Plastic Hinge (Right)

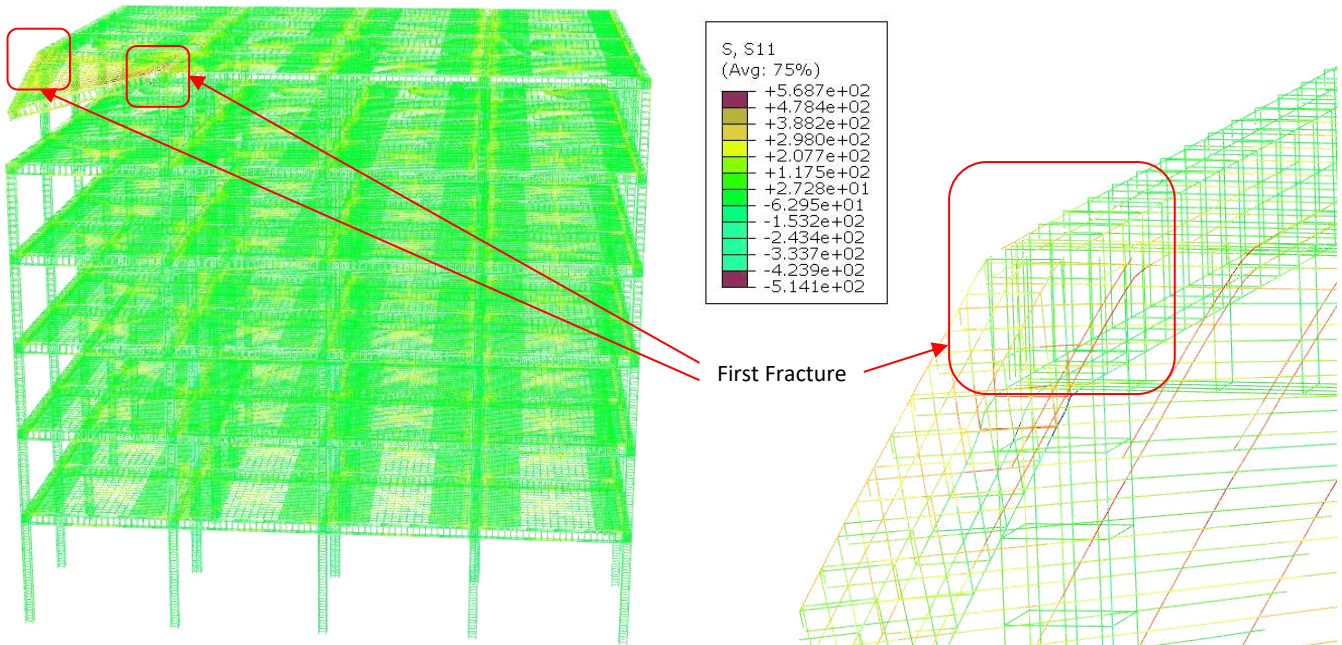


Figure 5-60: S11 Stresses in Truss Elements for FF-CC-C6 Under Sudden Column Loss at 160% Design Load at First Fracture, Full Model (Left) & Closeup on Plastic Hinge (Right)

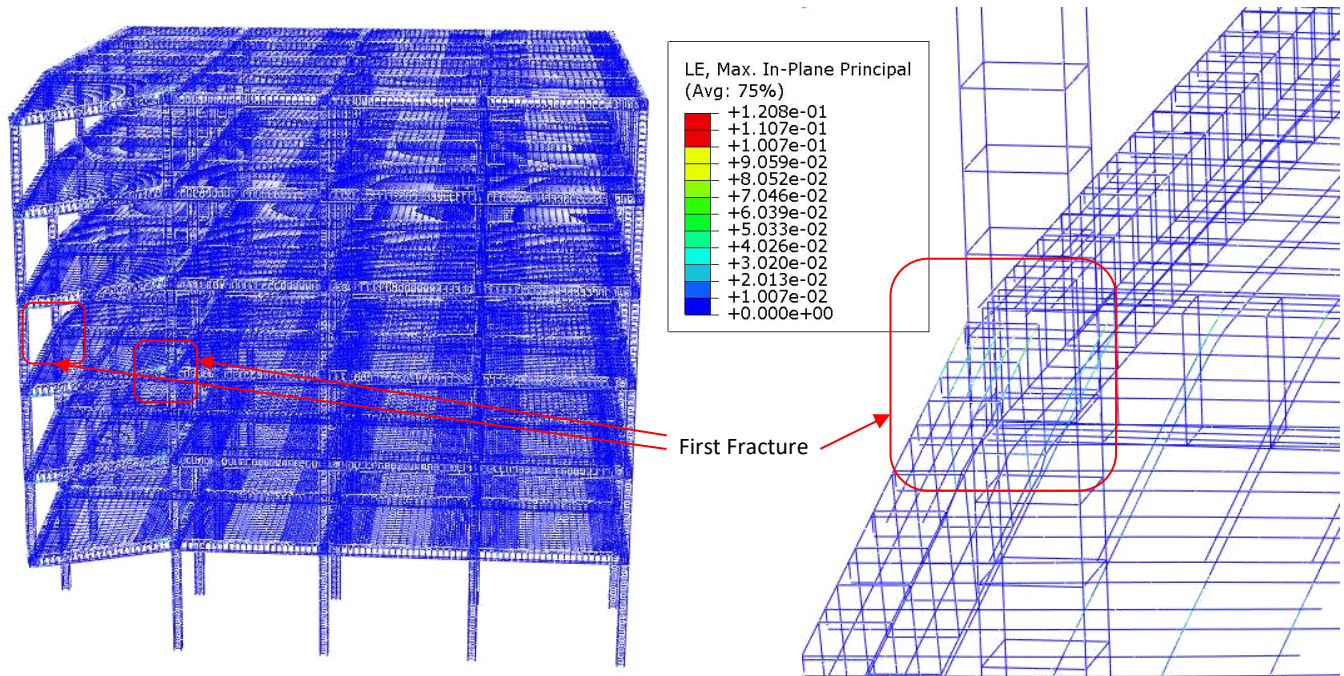


Figure 5-61: Logarithmic Strains in Truss Elements for FF-CC-C1 Under Sudden Column Loss at 180% Design Load at First Fracture, Full Model (Left) & Closeup on Plastic Hinge (Right)

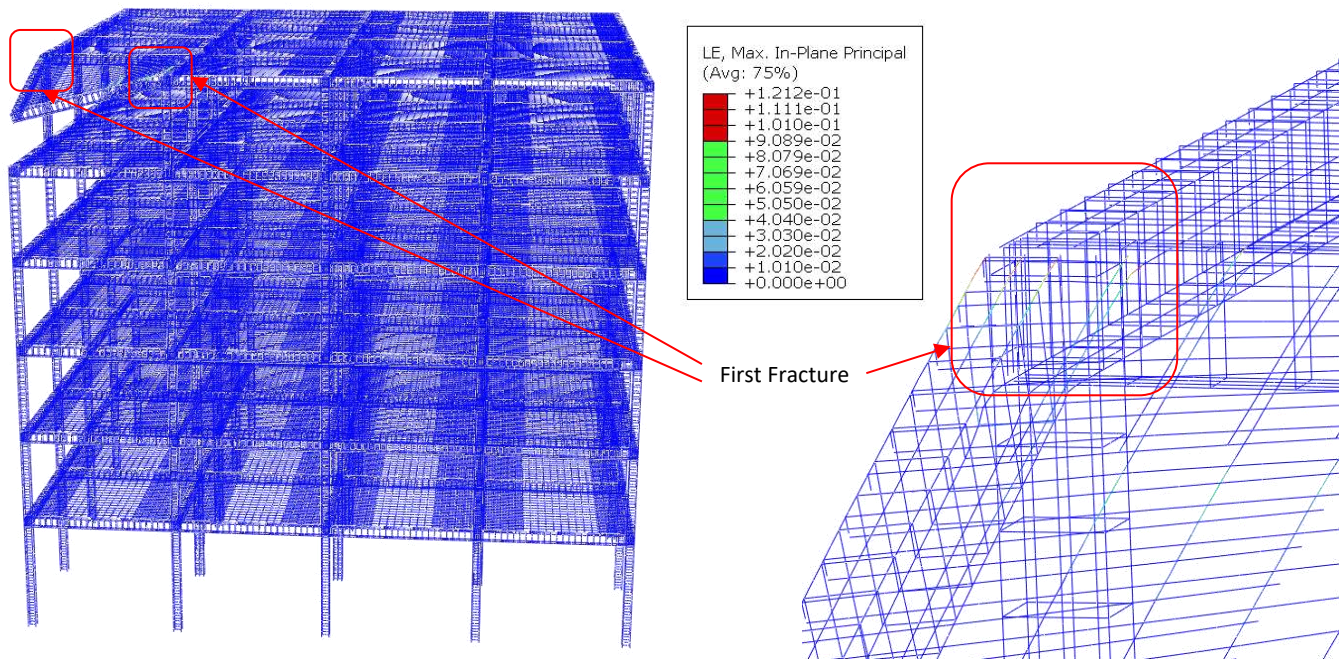


Figure 5-62: Logarithmic Strains in Truss Elements for FF-CC-C6 Under Sudden Column Loss at 160% Design Load at First Fracture, Full Model (Left) & Closeup on Plastic Hinge (Right)

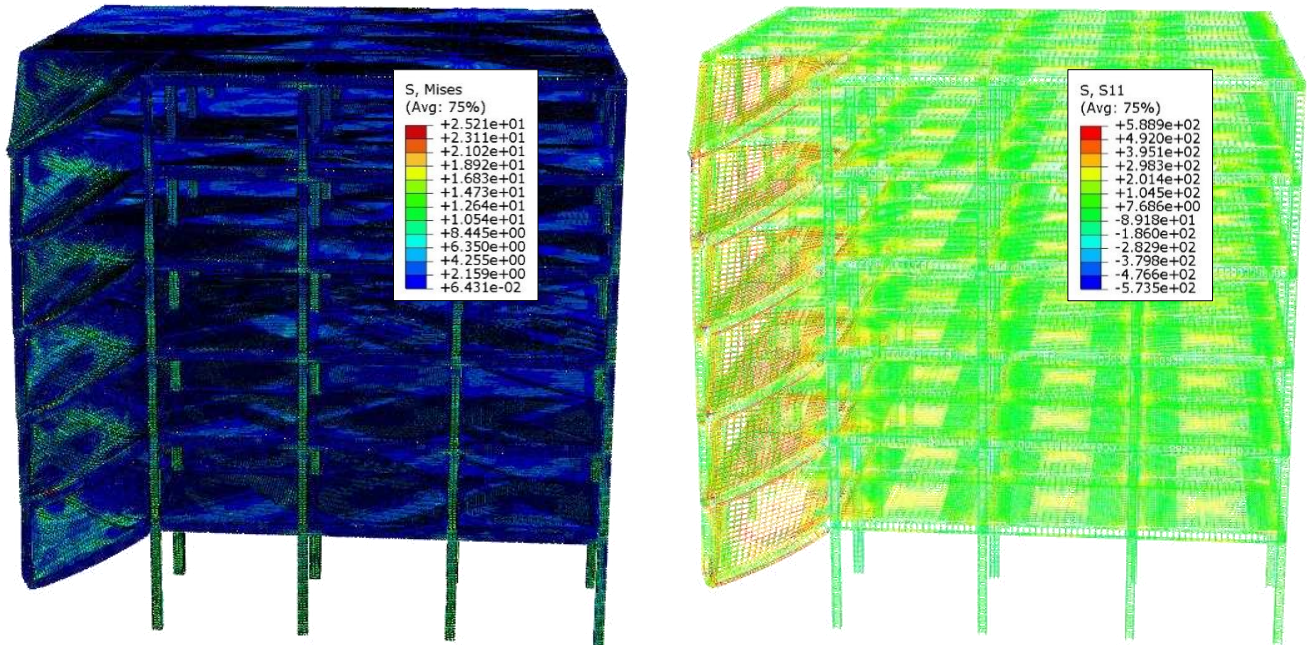


Figure 5-63: Von Mises Stresses in Solid Elements (Left) & S11 Stresses in Truss Elements (Right) for FF-CC-C1 Under Sudden Column Loss at 180% Design Load After Damage Propagation (Full Model Shown)

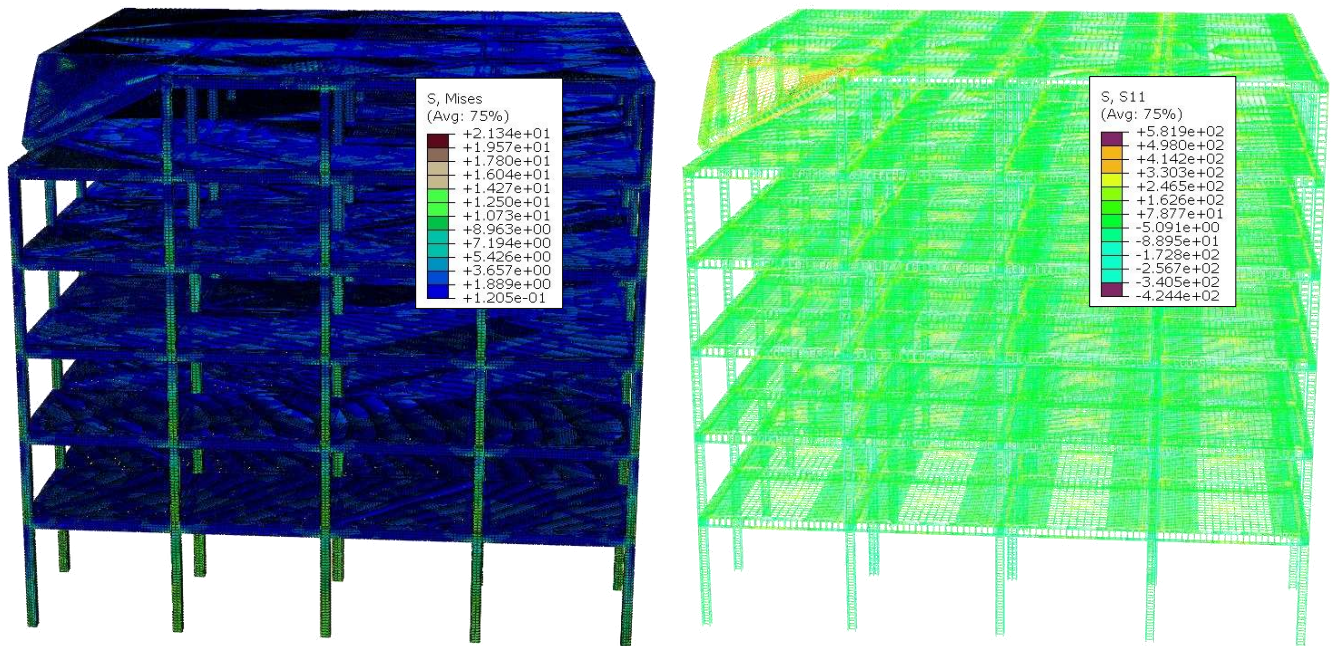


Figure 5-64: Von Mises Stresses in Solid Elements (Left) & S11 Stresses in Truss Elements (Right) for FF-CC-C6 Under Sudden Column Loss at 160% Design Load After Damage Propagation (Full Model Shown)

5.3.5.2 BARE-FRAME CORNER COLUMN REMOVAL RESULTS

Similar to the FF-CC models, the results of the BF-CC models are shown in the following figures. First, the joint displacement at the top of the removed column is plotted against time in Figure 5-65 to Figure 5-70 for different loading values for each model. The equivalent dynamic load-displacement curves or pseudo-static curves are shown in Figure 5-71, while the values of the applied load (P), displacement (u) and slope (s) at the fracture points are listed in Table 5-9.

Table 5-9: Maximum Column Loss Analysis Values for BF-CC Models

Model	BF-CC-C1	BF-CC-C2	BF-CC-C3	BF-CC-C4	BF-CC-C5	BF-CC-C6
P_{max}	80%	80%	80%	70%	70%	50%
U_{max} (mm)	322	375	480	243	323	590
S_{max}	6.44%	7.51%	9.59%	4.86%	6.45%	11.80%

The first three models, Model BF-CC-C1 to Model BF-CC-C3, reached a maximum load level of 80% with the deformation increasing as the number of floors above increased. The displacement of BF-CC-C1 reached 322 mm, while BF-CC-C2 and BF-CC-C3 reached 375 mm and 480 mm, respectively. The following two models, Model BF-CC-C4 and Model BF-CC-C5, both reached a maximum load of 70% with the deformation of the former reaching 243 mm and that of the latter reaching 323 mm. Lastly, Model BF-CC-C6 reached a maximum load of 50% and a corresponding displacement of 590 mm. The results show that, in general, as the number of floors above the removed column decreased, the maximum load capacity of the system decreased, and the permanent deflection increased. Again, the more vertically stacked closed beam-column loops the better the overall nonlinear response of the system. Hence, Model BF-CC-C6 demonstrated the weakest response as there was only one floor above the removed column and, therefore, no Vierendeel action.

A more in-depth look at the collapse progression at the failure load levels was considered in this study. Model BF-CC-C1 and Model BF-CC-C6 were selected as they represent the two ends of the spectrum in terms of nonlinear behavior. The failure load levels for the two chosen models were 80% and 50% respectively for BF-CC-C1 and BF-CC-C6. Two different points in time for each analysis were considered. The first point corresponds to the first rebar fracture which triggered a damage progression within which the second point was chosen. The von Mises stresses in the RC solid elements at first fracture along with the total displacement are shown in Figure 5-72 and Figure 5-73 respectively for BF-CC-C1 and BF-CC-C6. The stresses and strains in the rebar truss elements, at the same point, are shown in Figure 5-74 to Figure 5-77. The first rebar fracture for BF-CC-C1 happened in the top longitudinal reinforcement of the fourth floor’s beam. Triggered by the first fracture, damage progressed in the system until it partially collapsed. The damage was localized and confined to the external corner bay. The von

Mises stresses in RC solid and rebar truss elements at the second chosen point, after damage propagation, are displayed in Figure 5-78 and Figure 5-79.

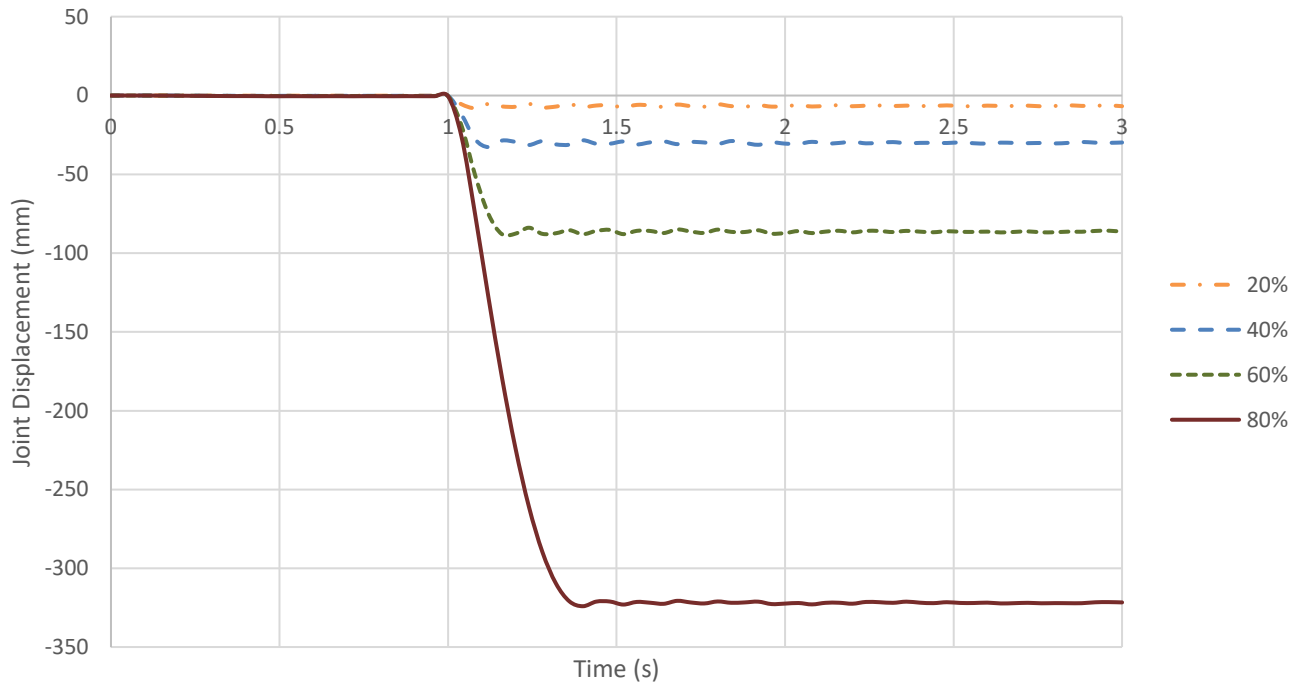


Figure 5-65: Joint Displacements for BF-CC-C1 Subjected to Sudden Column Loss Under Different Load Values

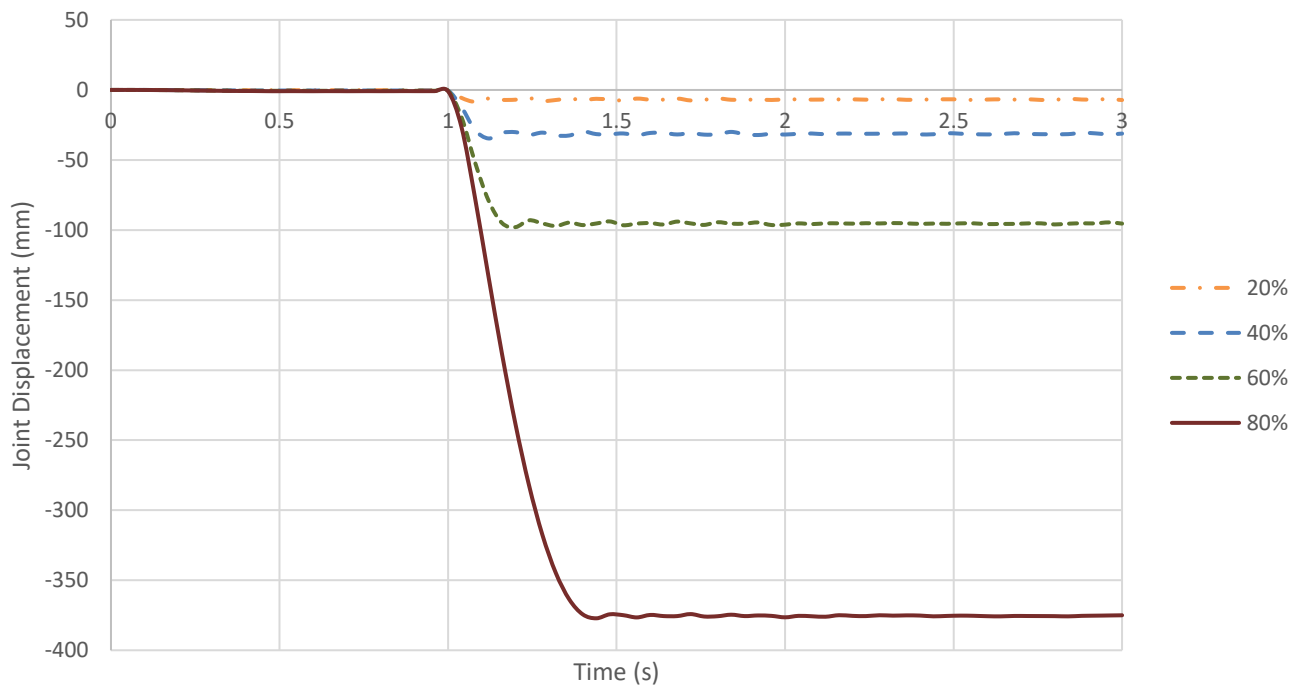


Figure 5-66: Joint Displacements for BF-CC-C2 Subjected to Sudden Column Loss Under Different Load Values

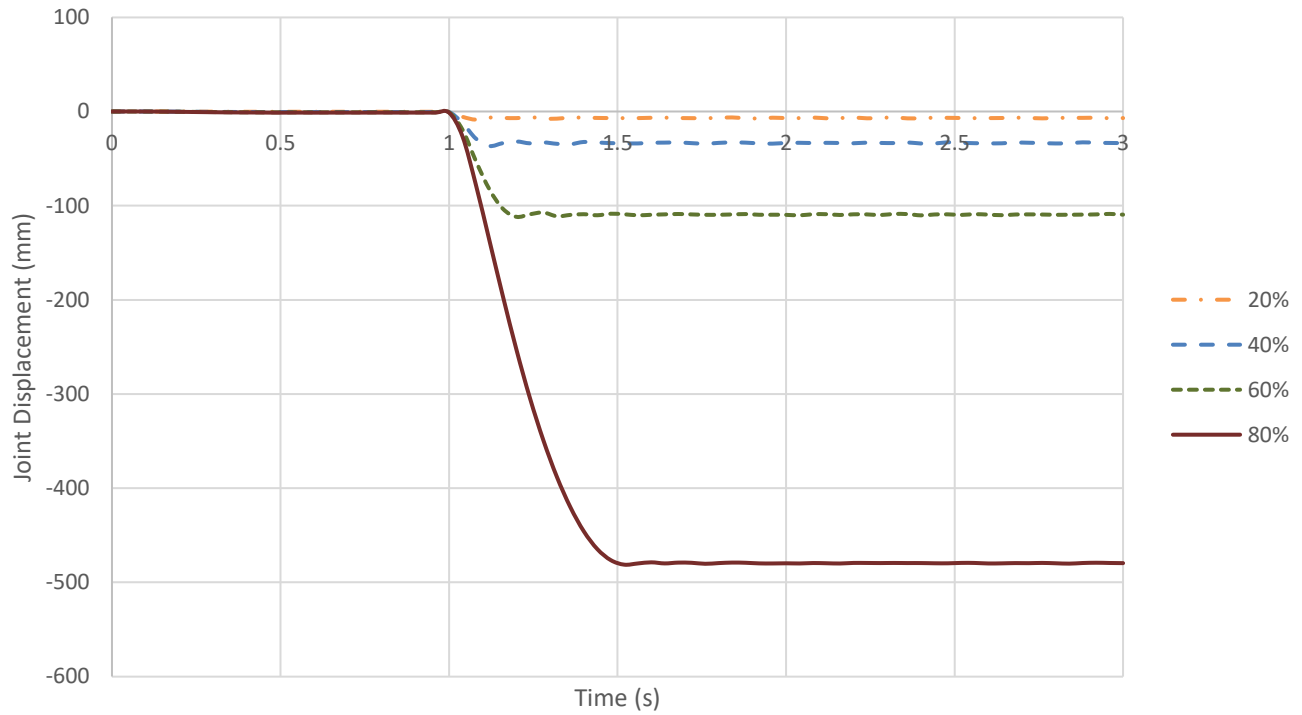


Figure 5-67: Joint Displacements for BF-CC-C3 Subjected to Sudden Column Loss Under Different Load Values

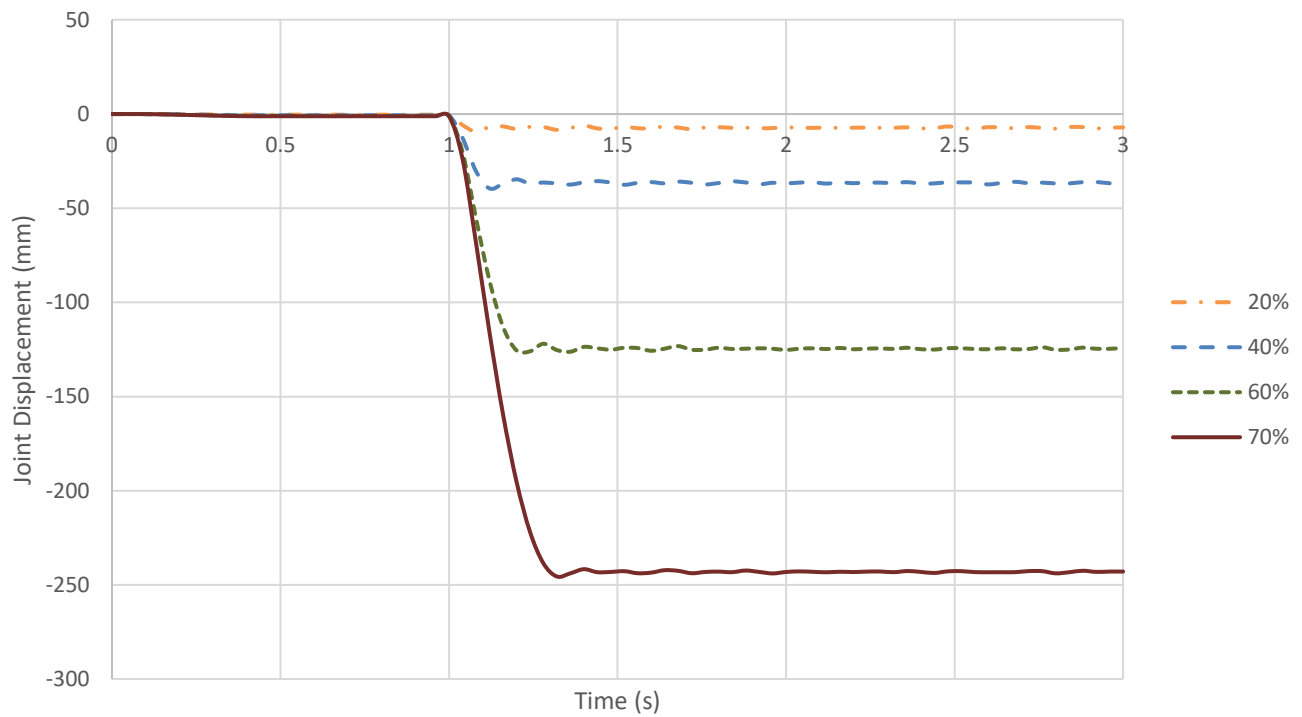


Figure 5-68: Joint Displacements for BF-CC-C4 Subjected to Sudden Column Loss Under Different Load Values

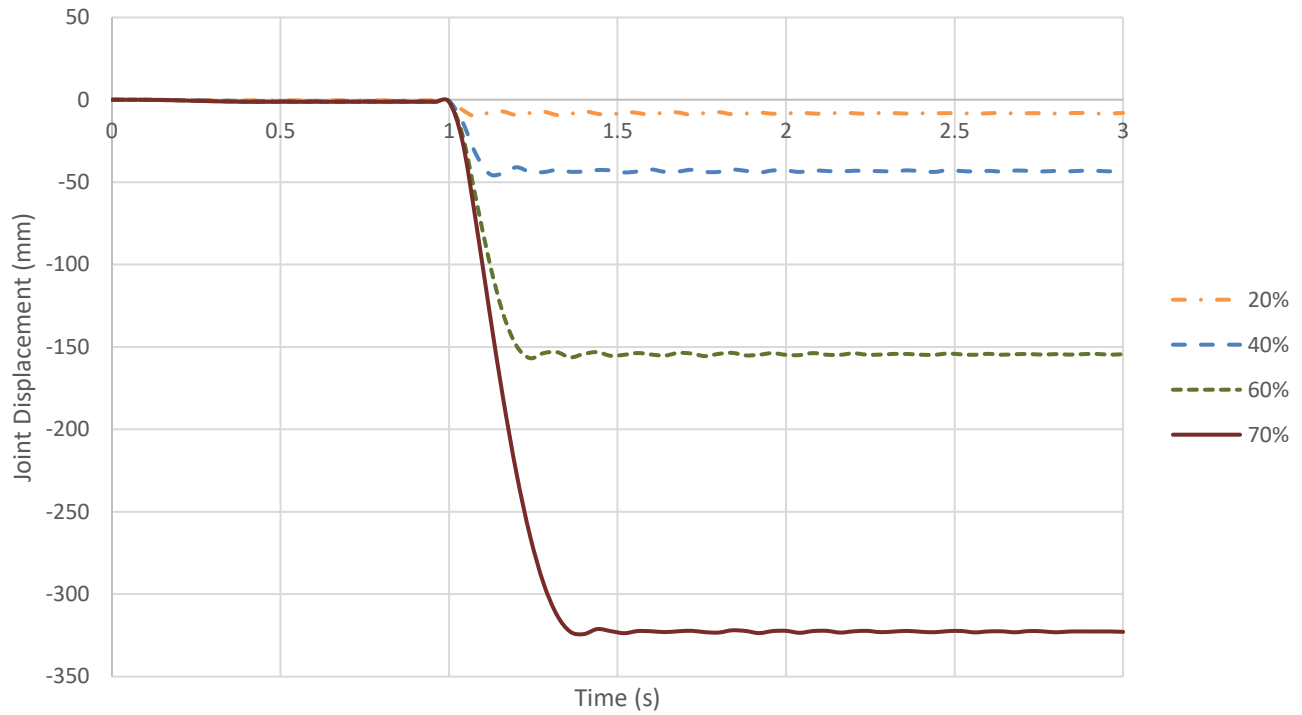


Figure 5-69: Joint Displacements for BF-CC-C5 Subjected to Sudden Column Loss Under Different Load Values

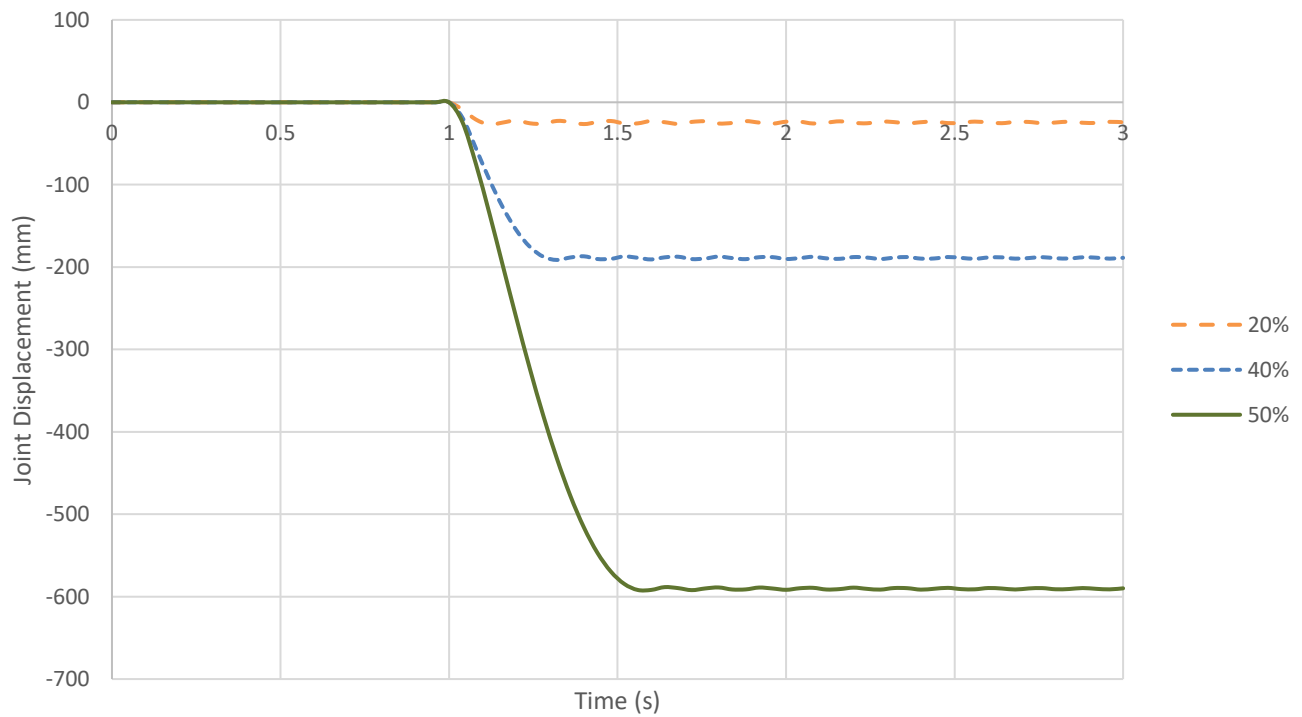


Figure 5-70: Joint Displacements for BF-CC-C6 Subjected to Sudden Column Loss Under Different Load Values

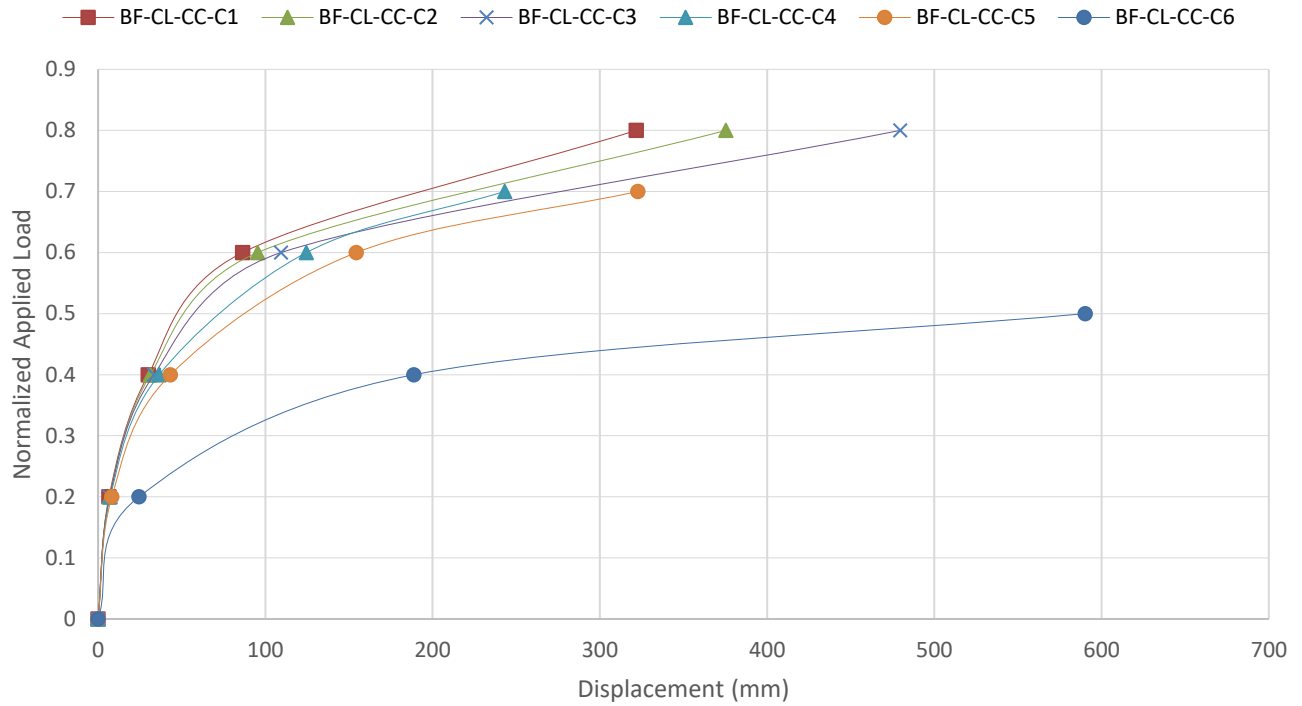


Figure 5-71: Pseudo-Static Curves for BF Due to the Sudden Loss of CC at Each Floor

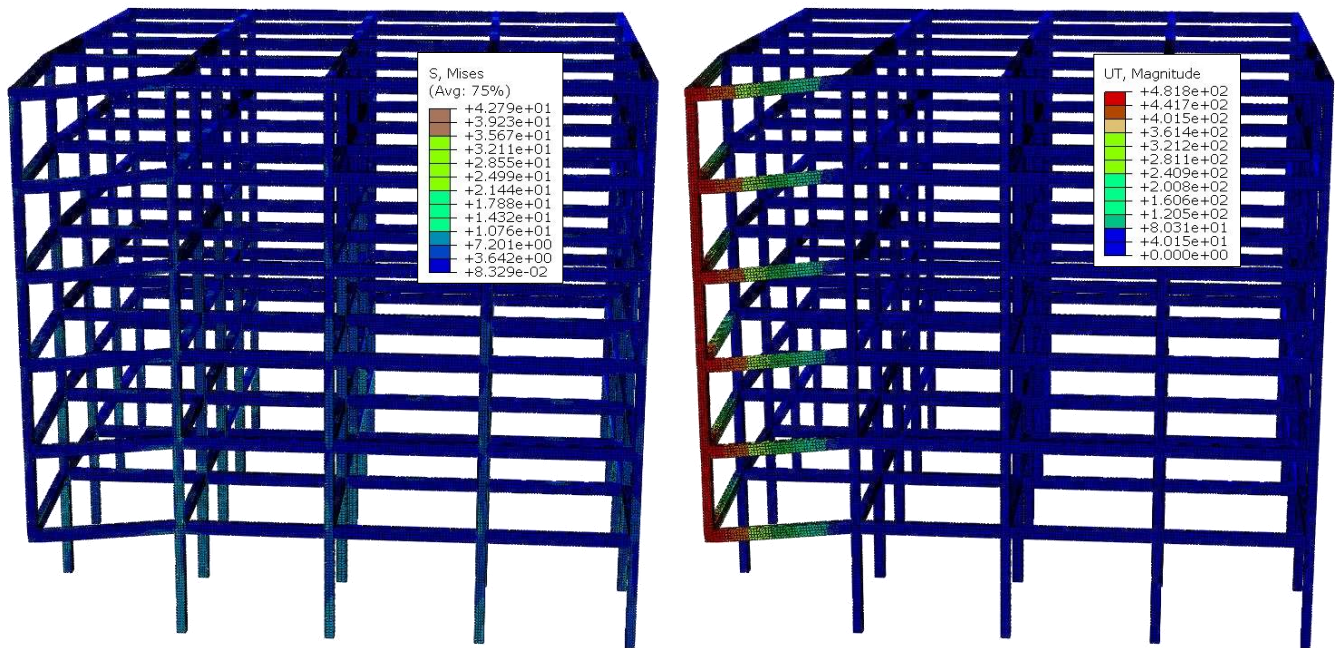


Figure 5-72: Von Mises Stresses (Left) & Total Displacement (Right) in Solid Elements for BF-CC-C1 Under Sudden Column Loss at 100% Design Load at First Fracture (Full Model Shown)



Figure 5-73: Von Mises Stresses (Left) & Total Displacement (Right) in Solid Elements for BF-CC-C6 Under Sudden Column Loss at 60% Design Load at First Fracture (Full Model Shown)

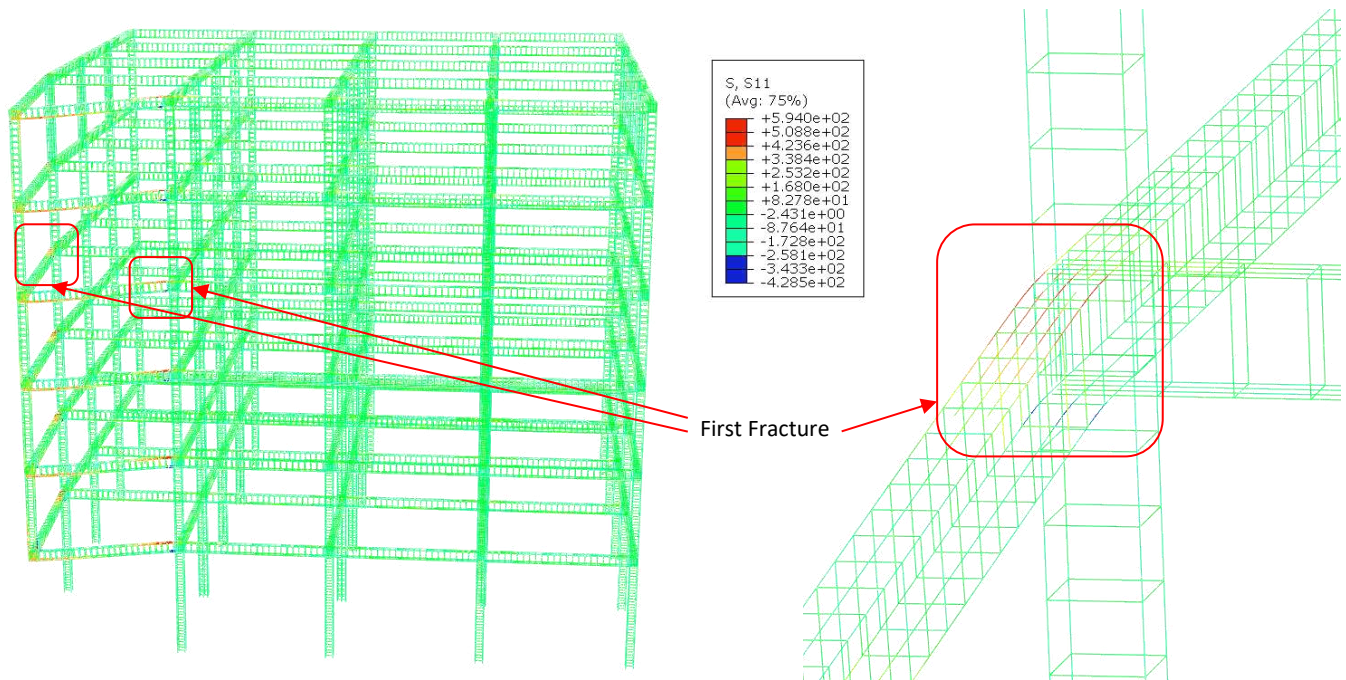


Figure 5-74: S11 Stresses in Truss Elements for BF-CC-C1 Under Sudden Column Loss at 100% Design Load at First Fracture, Full Model (Left) & Closeup on Plastic Hinge (Right)

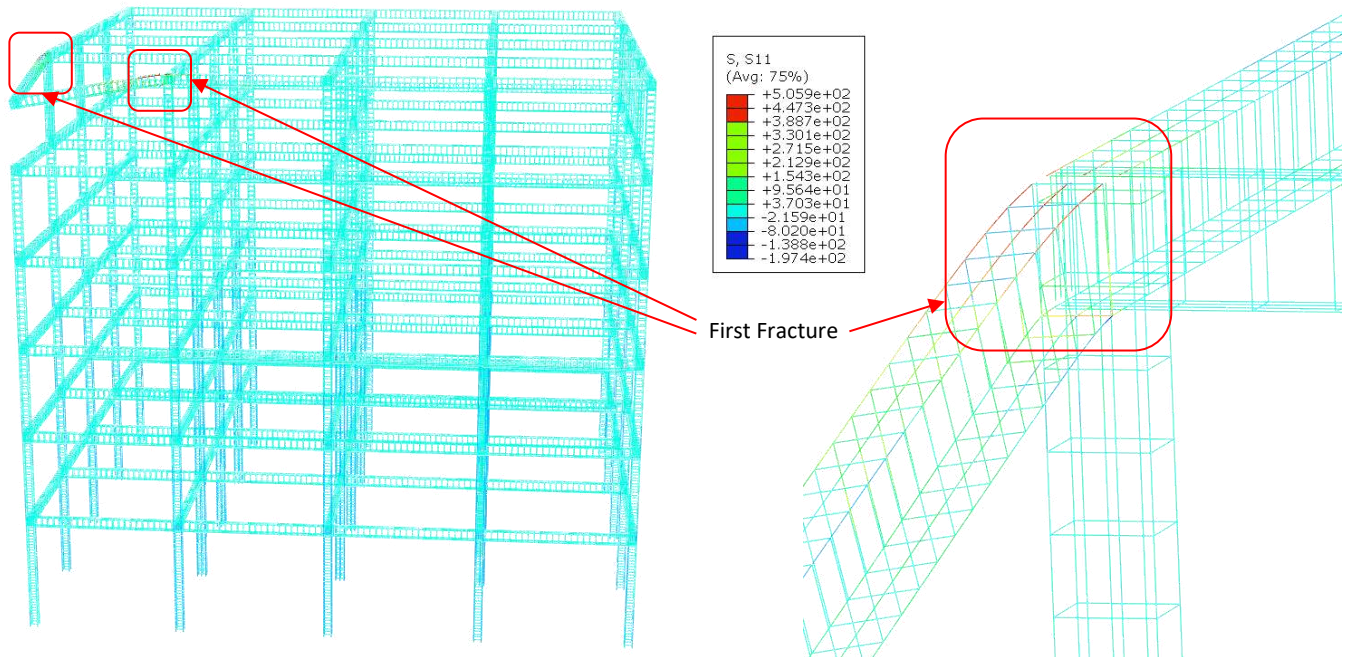


Figure 5-75: S11 Stresses in Truss Elements for BF-CC-C6 Under Sudden Column Loss at 60% Design Load at First Fracture, Full Model (Left) & Closeup on Plastic Hinge (Right)

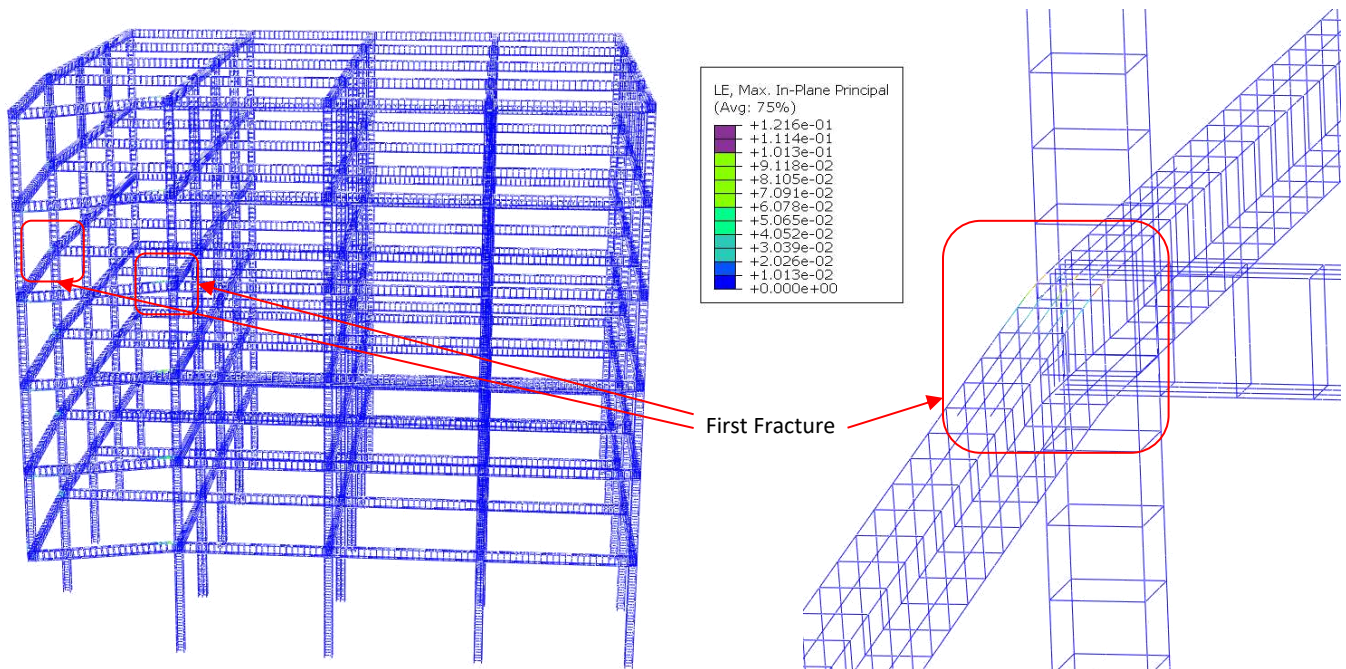


Figure 5-76: Logarithmic Strains in Truss Elements for BF-CC-C1 Under Sudden Column Loss at 100% Design Load at First Fracture, Full Model (Left) & Closeup on Plastic Hinge (Right)

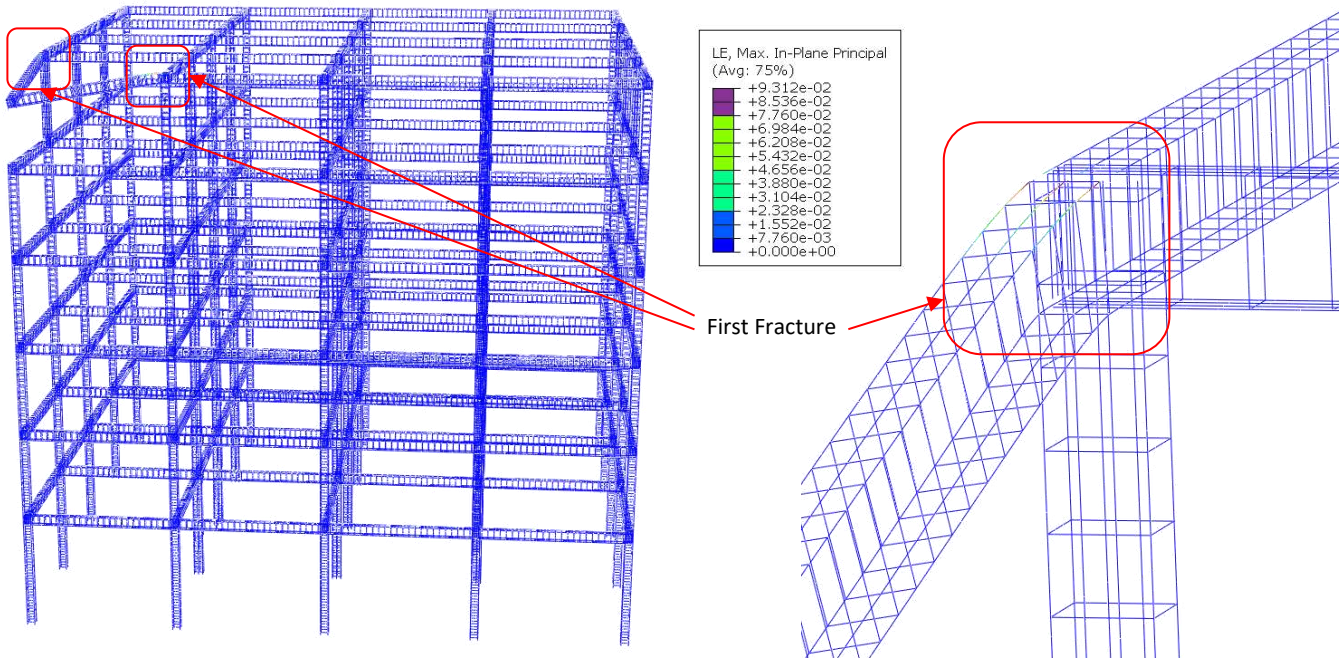


Figure 5-77: Logarithmic Strains in Truss Elements for BF-CC-C6 Under Sudden Column Loss at 60% Design Load at First Fracture, Full Model (Left) & Closeup on Plastic Hinge (Right)

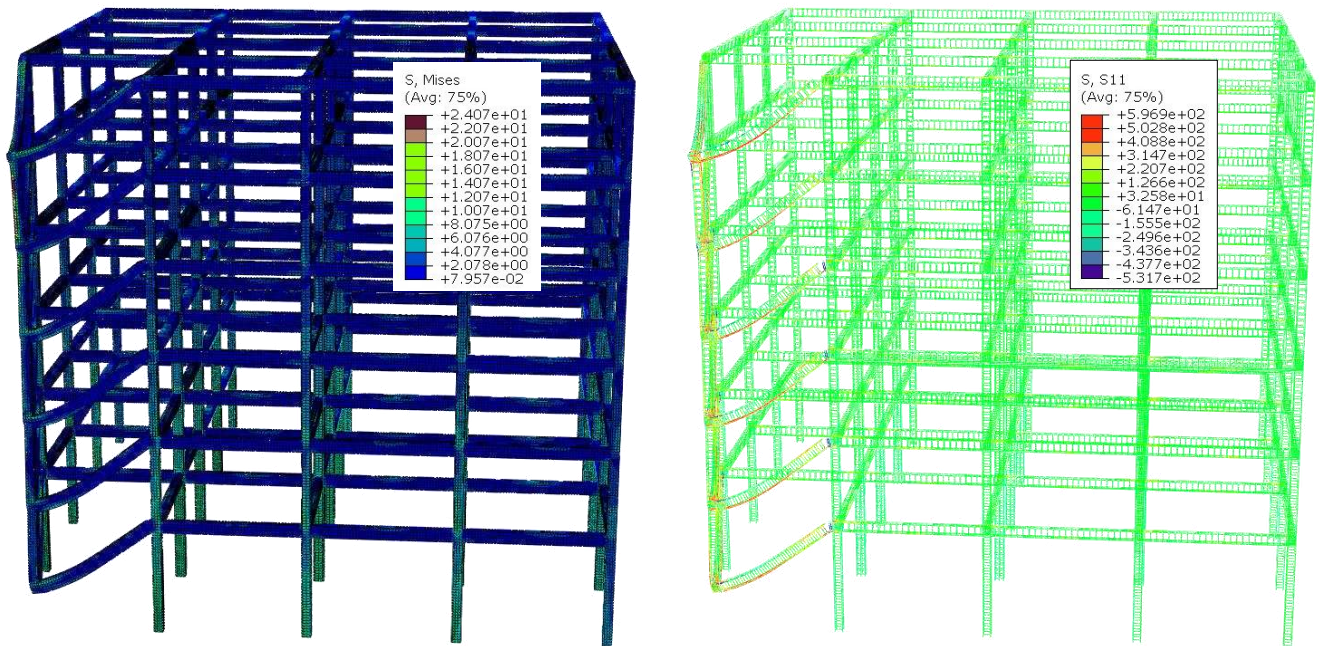


Figure 5-78: Von Mises Stresses in Solid Elements (Left) & S11 Stresses in Truss Elements (Right) for BF-CC-C1 Under Sudden Column Loss at 100% Design Load After Damage Propagation (Full Model Shown)

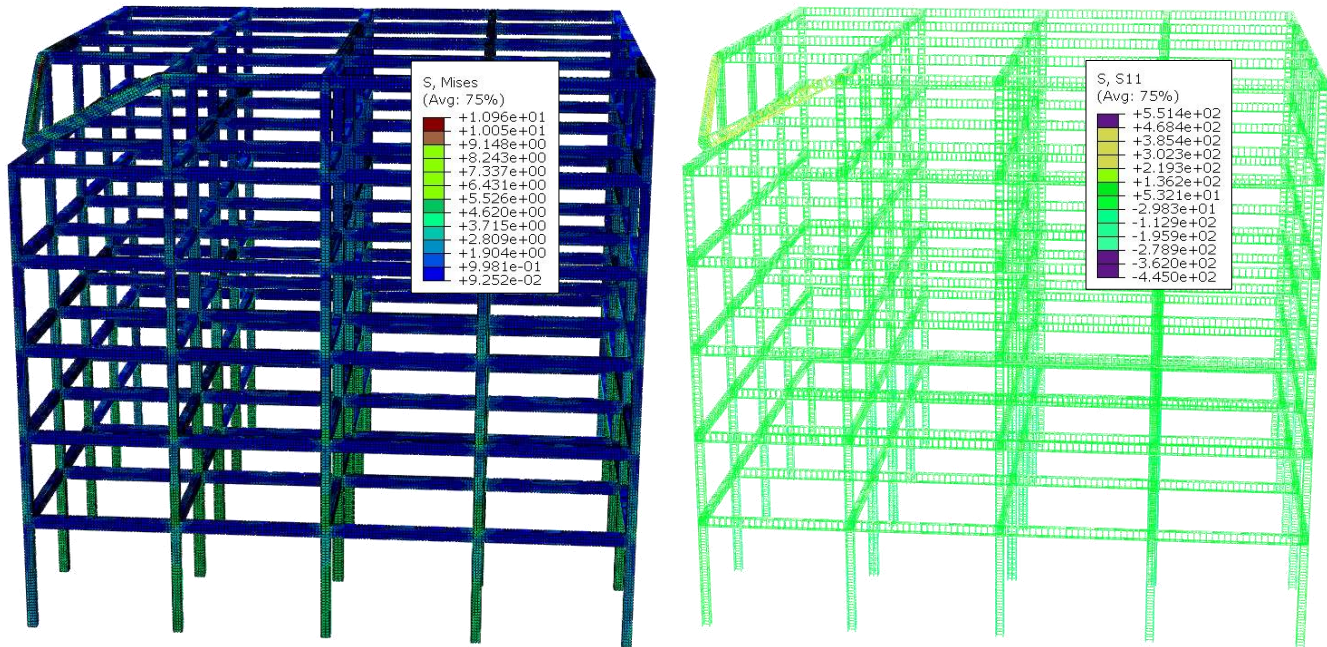


Figure 5-79: Von Mises Stresses in Solid Elements (Left) & S11 Stresses in Truss Elements (Right) for BF-CC-C6 Under Sudden Column Loss at 60% Design Load After Damage Propagation (Full Model Shown)

5.3.5.3 FULL-FRAME INTERIOR COLUMN REMOVAL RESULTS

Figure 5-80 to Figure 5-85 show the joint displacement at the top of the removed column plotted against time for different loading values. The equivalent dynamic load-displacement curves are shown in Figure 5-86, and the values of the applied load (P), displacement (u) and slope (s) at the fracture points are displayed in Table 5-10.

Table 5-10: Maximum Column Loss Analysis Values for FF-IC Models

Model	FF-IC-C1	FF-IC-C2	FF-IC-C3	FF-IC-C4	FF-IC-C5	FF-IC-C6
P_{max}	260%	280%	280%	280%	300%	300%
u_{max} (mm)	657	735	730	726	789	751
s_{max}	13.13%	14.71%	14.60%	14.51%	15.78%	15.02%

Similar to the pushdown analysis results, the responses of all six models were very close. Again, this implies that each story generally acted by itself in resisting the applied load, and therefore, the reduction of the system to a single-story is acceptable. The maximum load varied from 260% for FF-IC-C1 up to 300% for both FF-IC-C5 and FF-IC-C6, representing a 4.85% relative standard deviation. So, similar to the pushdown case and unlike the CC models, the increase in the number of floors above the removed column led to a decrease in the load-bearing capacity of the system. Again, this was attributed to the fact that the failure occurred in the columns, not the beams, which were subjected to more redistributed loads as the number of floors above the removed column increased. The pattern for the maximum displacements was not as evident, though. The lowest maximum displacement was 657 mm for FF-IC-C1, the highest was 789 mm for FF-IC-C5, and the relative standard deviation

was 5.4%. The system’s average load capacity, considering all six models, was 283% compared to 157% in the case of the FF-CC models, which represents an 80.9% difference. As explained when discussing the pushdown analysis results, the difference in results between the FF-IC and FF-CC models mainly arose from the difference in structural stiffness, even though the tributary area of the adjacent/neighbors columns was the same for both systems. At the same loading level, the FF-IC beams were subjected to lower stresses than the FF-CC beams. This helped the system reach higher loading levels without collapse. However, along with the fact that the slab contributed to the stiffness of the beams, it led to the failure of the columns before the beams. Which, in turn, led to the complete progressive collapse of the building.

Looking at Model FF-IC-C1 and Model FF-IC-C6, two points in the analysis timeline were examined. The first point represented the first rebar fracture, and the second point represented the damage propagation phase. The von Mises stresses and total displacement in the RC solid elements at first fracture, respectively for FF-IC-C1 and FF-IC-C6, are displayed in Figure 5-87 and Figure 5-88. The normal stresses and strains in truss elements, at the same point, are shown in Figure 5-89 to Figure 5-92. The first rebar fracture happened in the first floor’s adjacent column for FF-IC-C1 and FF-IC-C6 after reaching the ultimate plastic strain of 0.12 and its corresponding true stress of 612 MPa. The stresses in concrete and steel elements after damage propagation are shown in Figure 5-93 and Figure 5-94. It can be seen from the figures that almost all columns failed as both models suffered a complete progressive collapse.

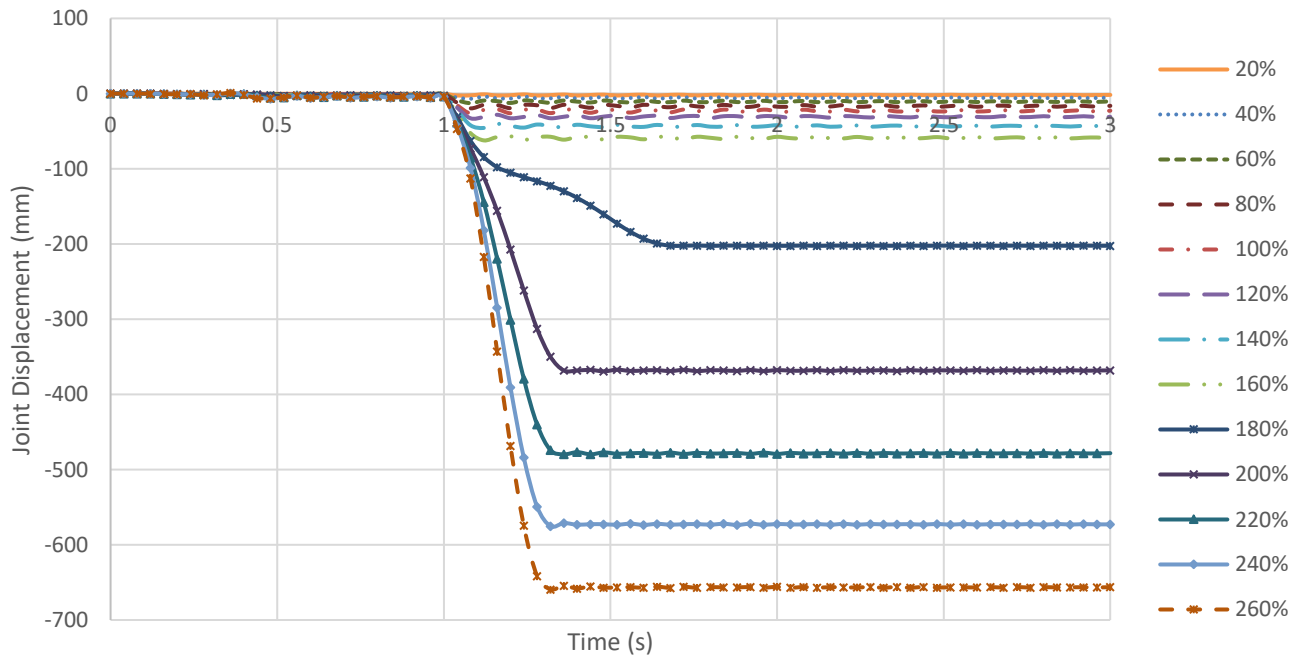


Figure 5-80: Joint Displacements for FF-IC-C1 Subjected to Sudden Column Loss Under Different Load Values

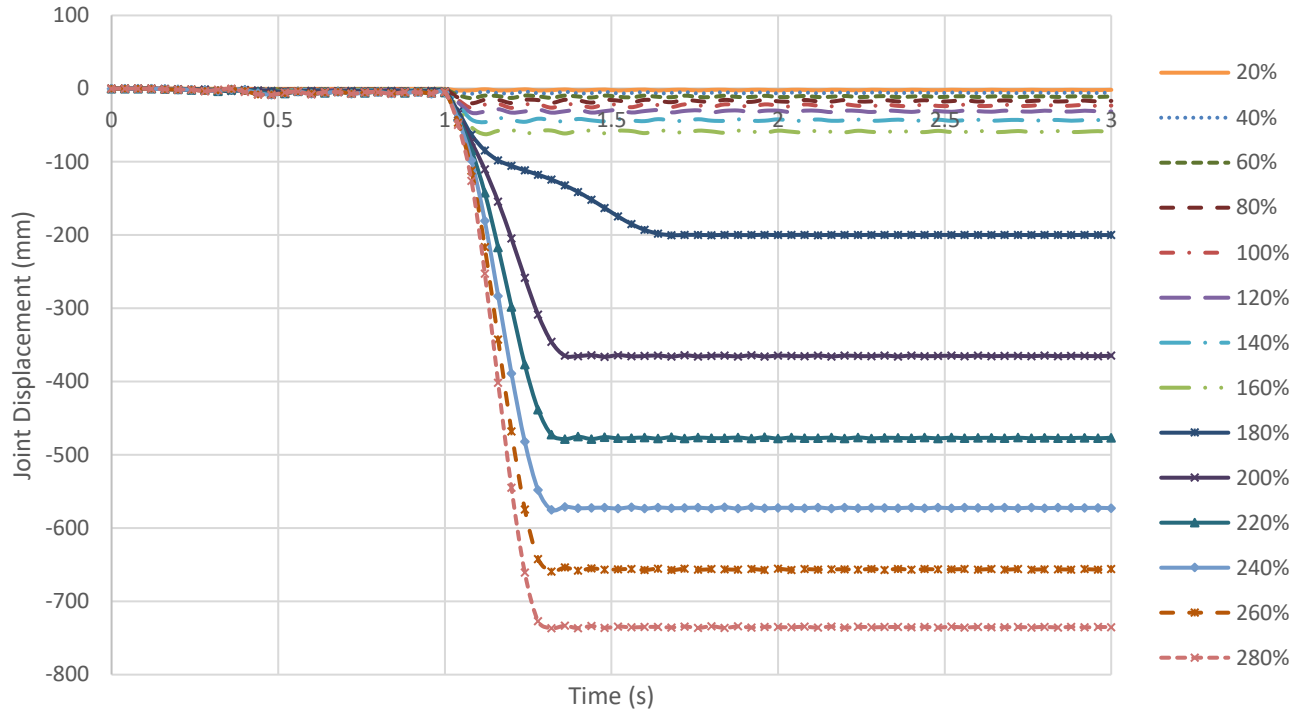


Figure 5-81: Joint Displacements for FF-IC-C2 Subjected to Sudden Column Loss Under Different Load Values

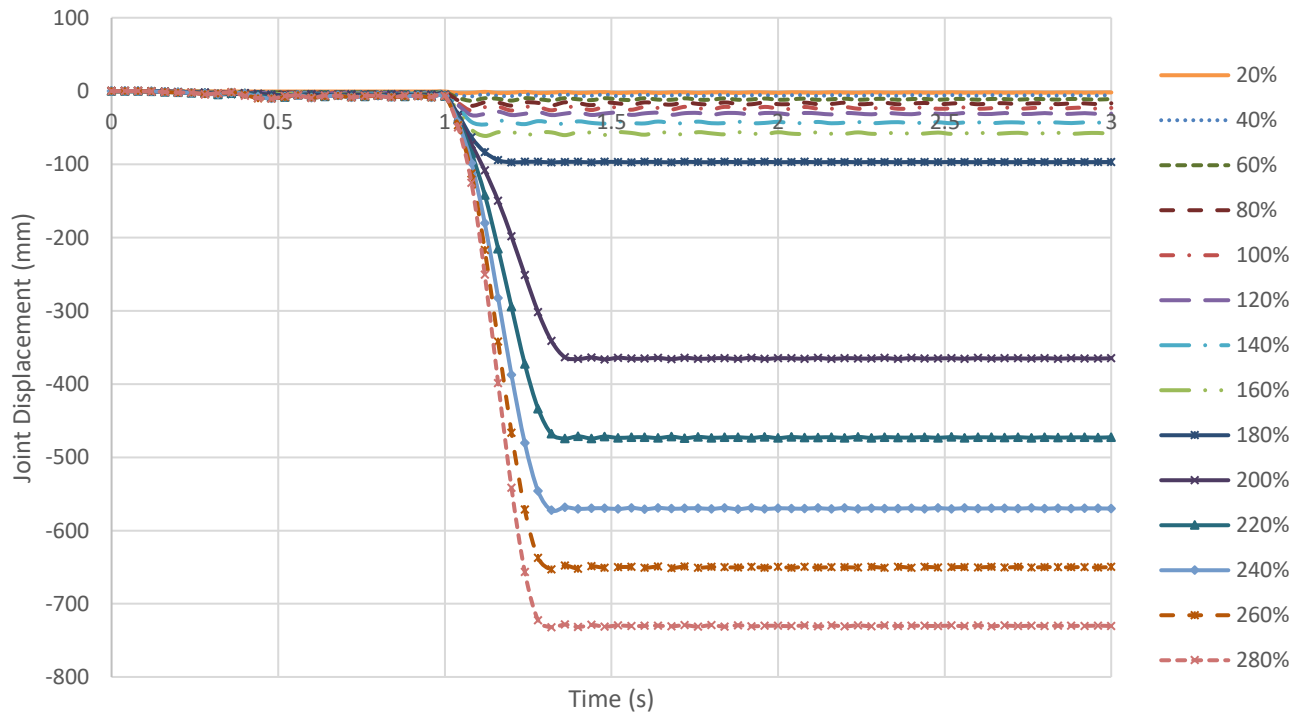


Figure 5-82: Joint Displacements for FF-IC-C3 Subjected to Sudden Column Loss Under Different Load Values

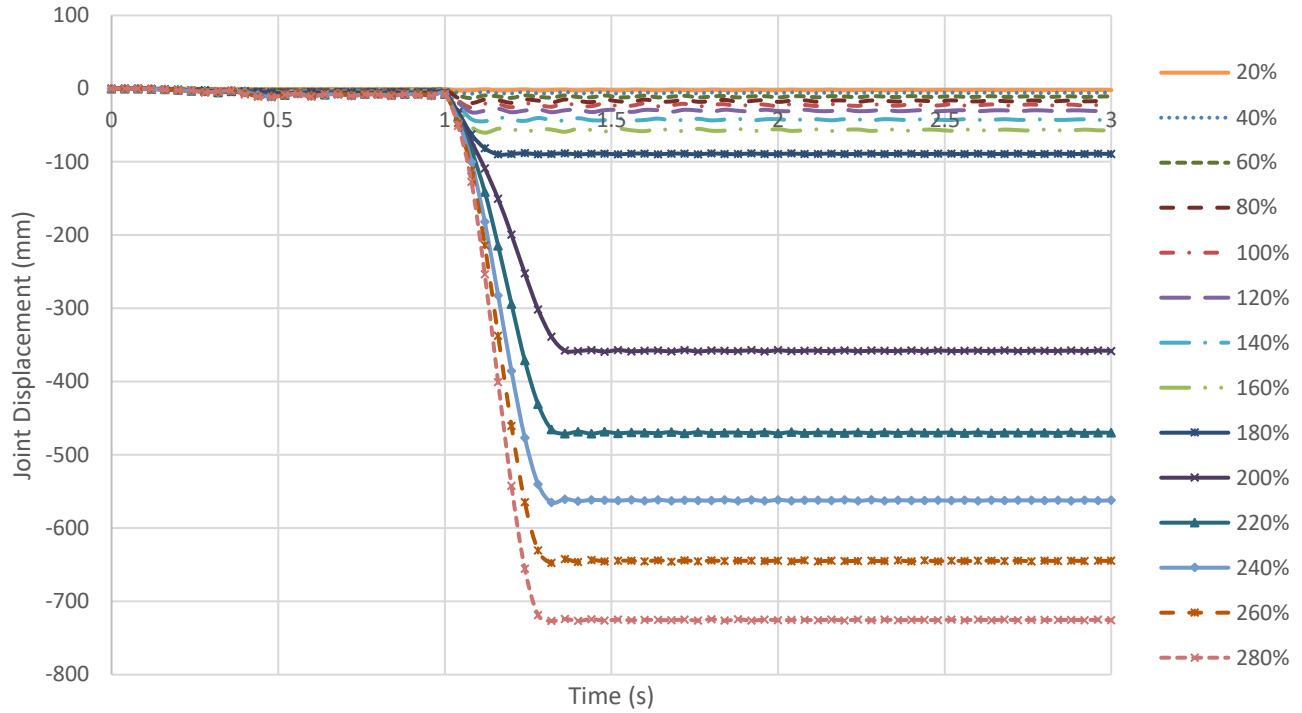


Figure 5-83: Joint Displacements for FF-IC-C4 Subjected to Sudden Column Loss Under Different Load Values

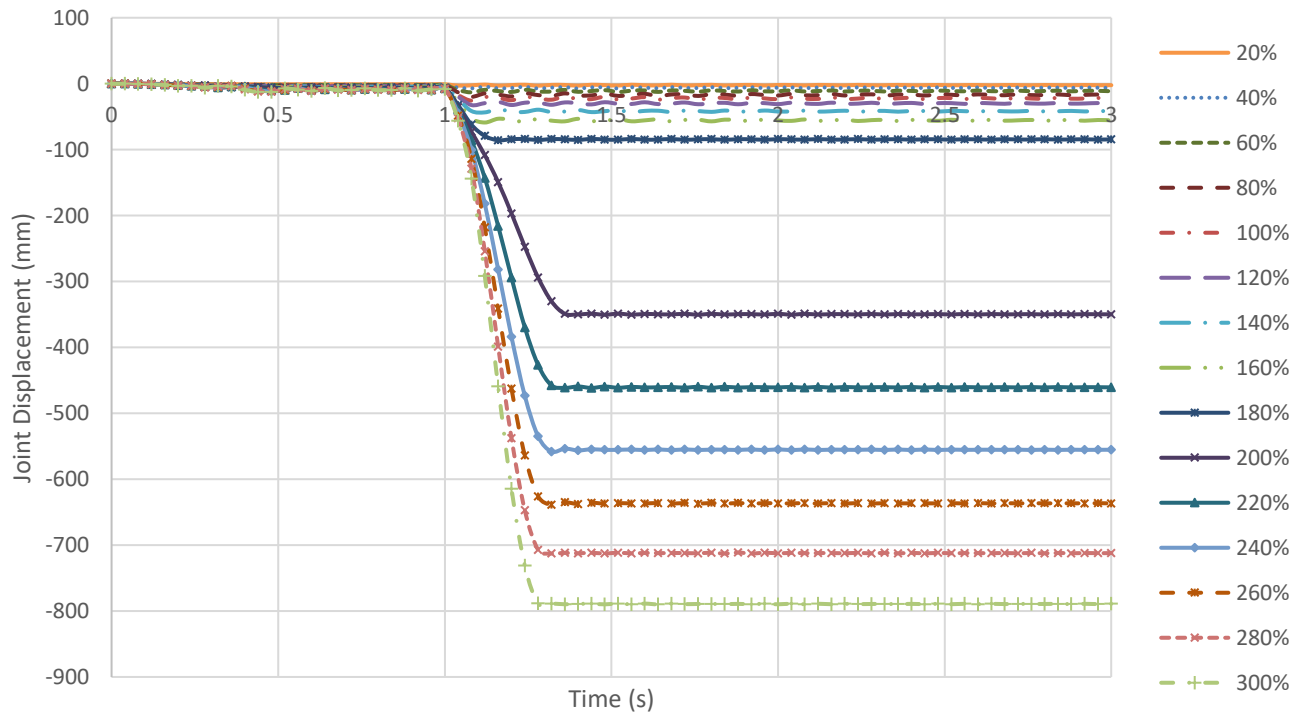


Figure 5-84: Joint Displacements for FF-IC-C5 Subjected to Sudden Column Loss Under Different Load Values

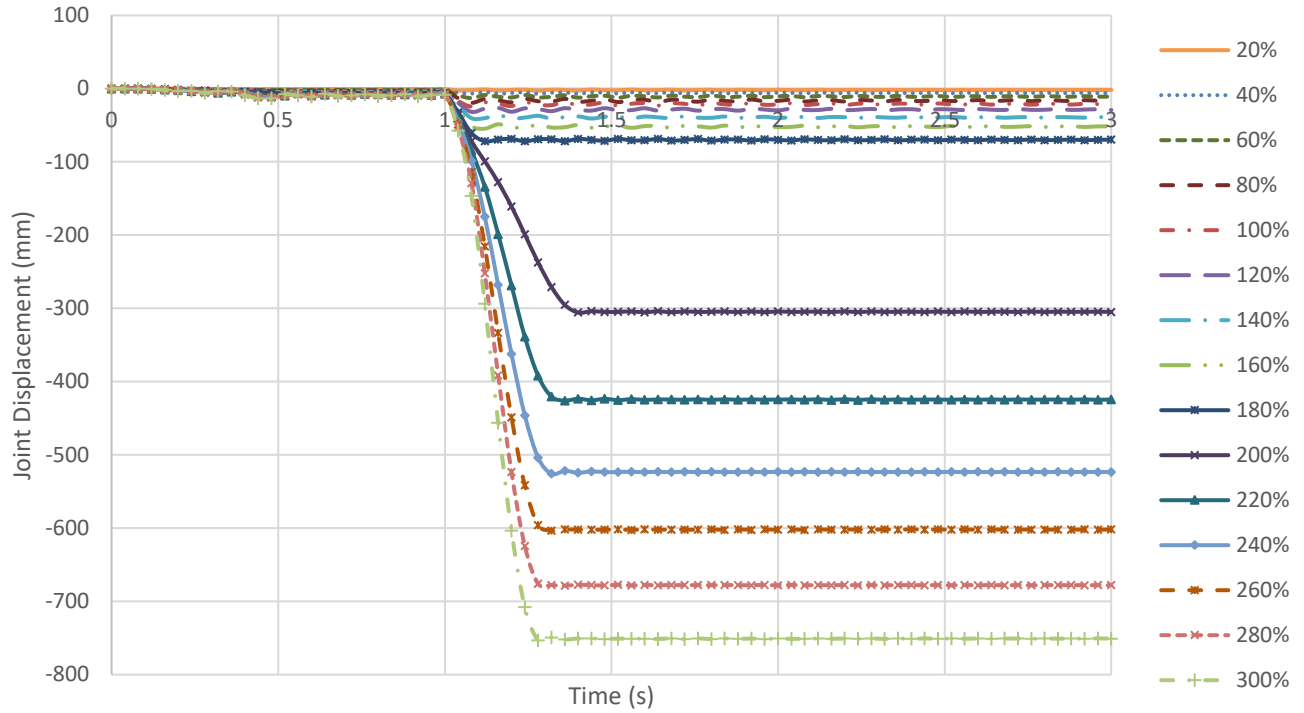


Figure 5-85: Joint Displacements for FF-IC-C6 Subjected to Sudden Column Loss Under Different Load Values

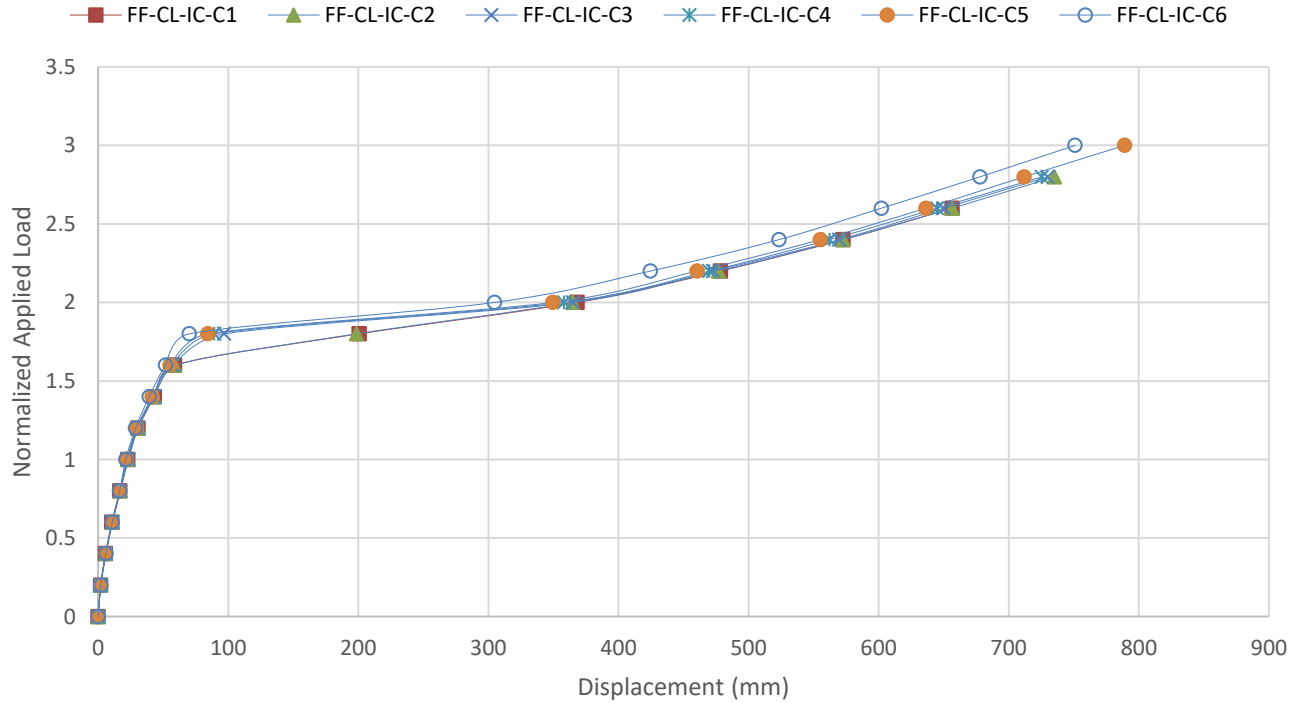


Figure 5-86: Pseudo-Static Curves for FF Due to the Sudden Loss of IC at Each Floor

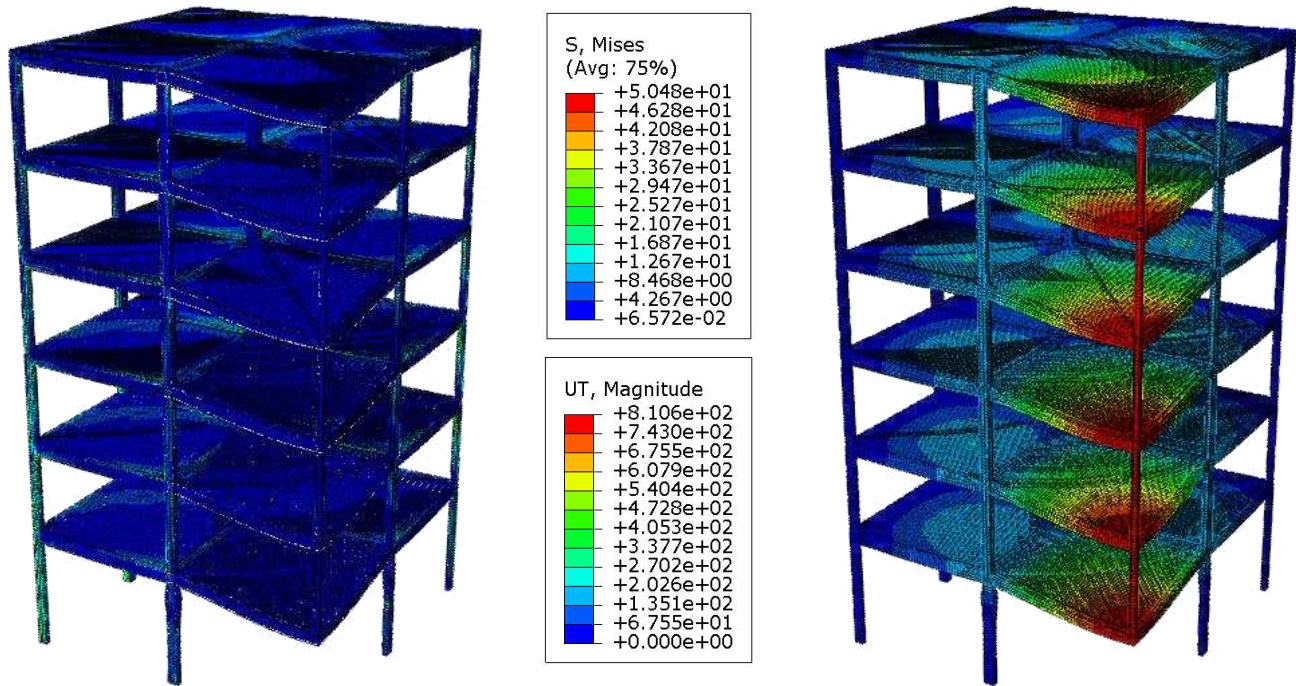


Figure 5-87: Von Mises Stresses (Left) & Total Displacement (Right) in Solid Elements for FF-IC-C1 Under Sudden Column Loss at 280% Design Load at First Fracture (Quarter Model Shown)

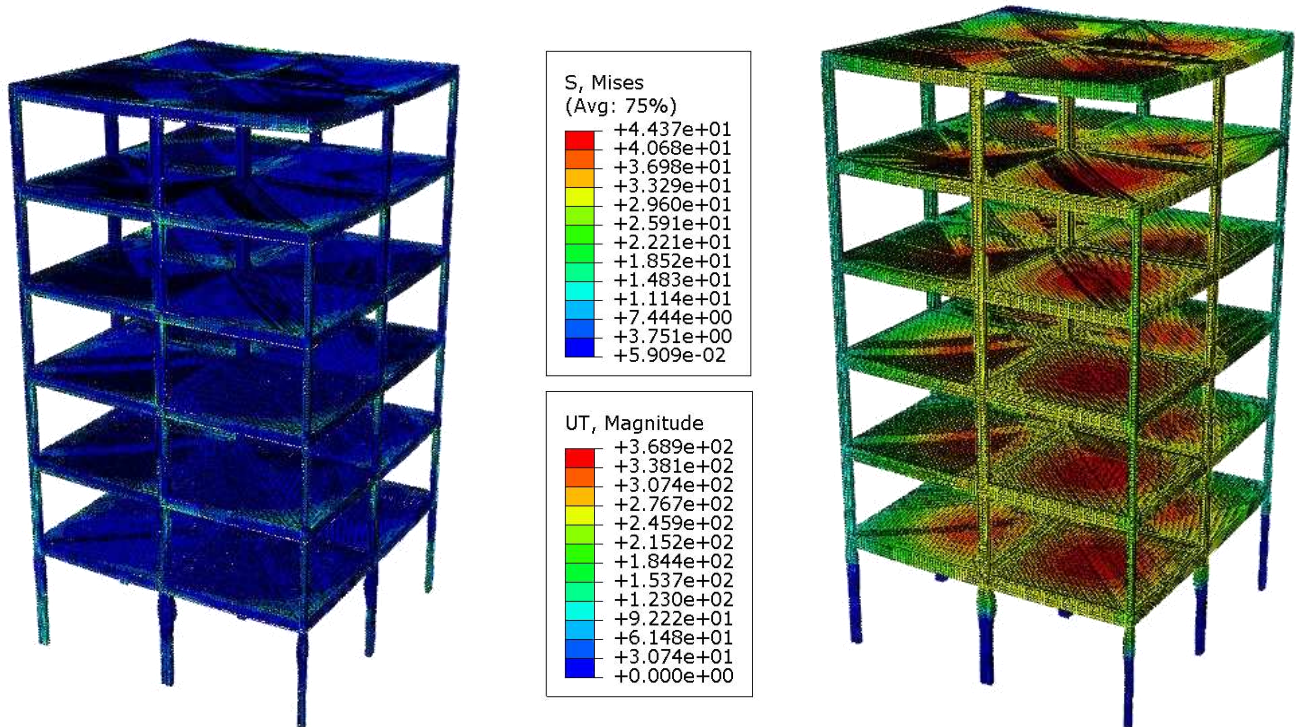


Figure 5-88: Von Mises Stresses (Left) & Total Displacement (Right) in Solid Elements for FF-IC-C6 Under Sudden Column Loss at 320% Design Load at First Fracture (Quarter Model Shown)

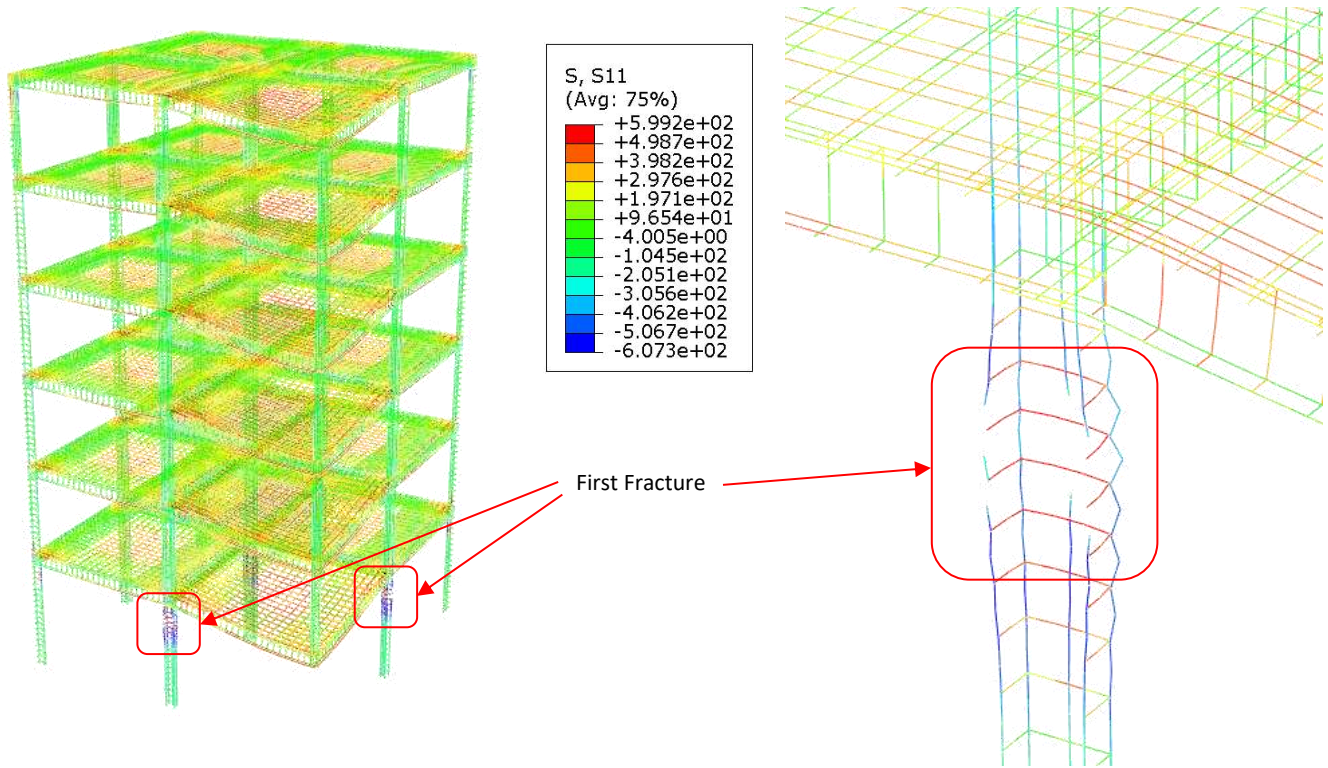


Figure 5-89: S11 Stresses in Truss Elements for FF-IC-C1 Under Sudden Column Loss at 280% Design Load at First Fracture, Quarter Model (Left) & Closeup on Plastic Hinge (Right)

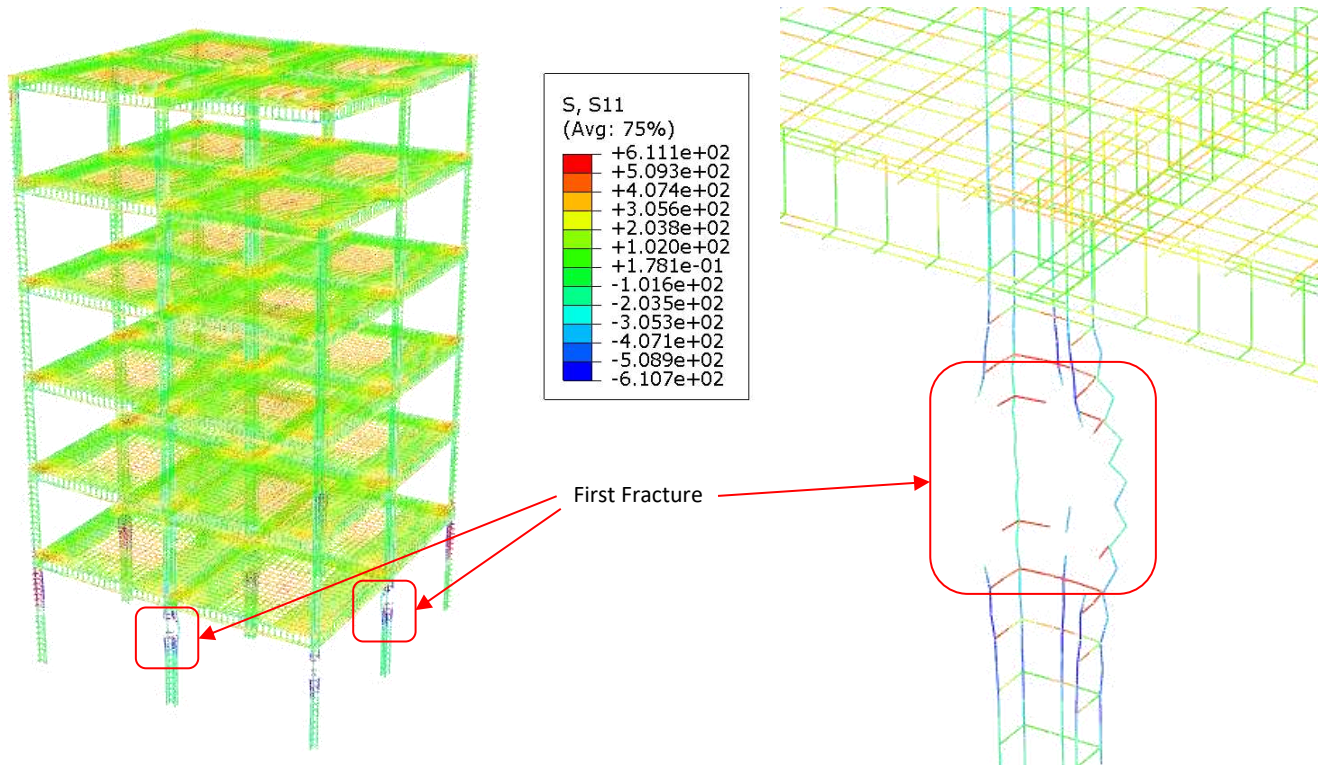


Figure 5-90: S11 Stresses in Truss Elements for FF-IC-C6 Under Sudden Column Loss at 320% Design Load at First Fracture, Quarter Model (Left) & Closeup on Plastic Hinge (Right)

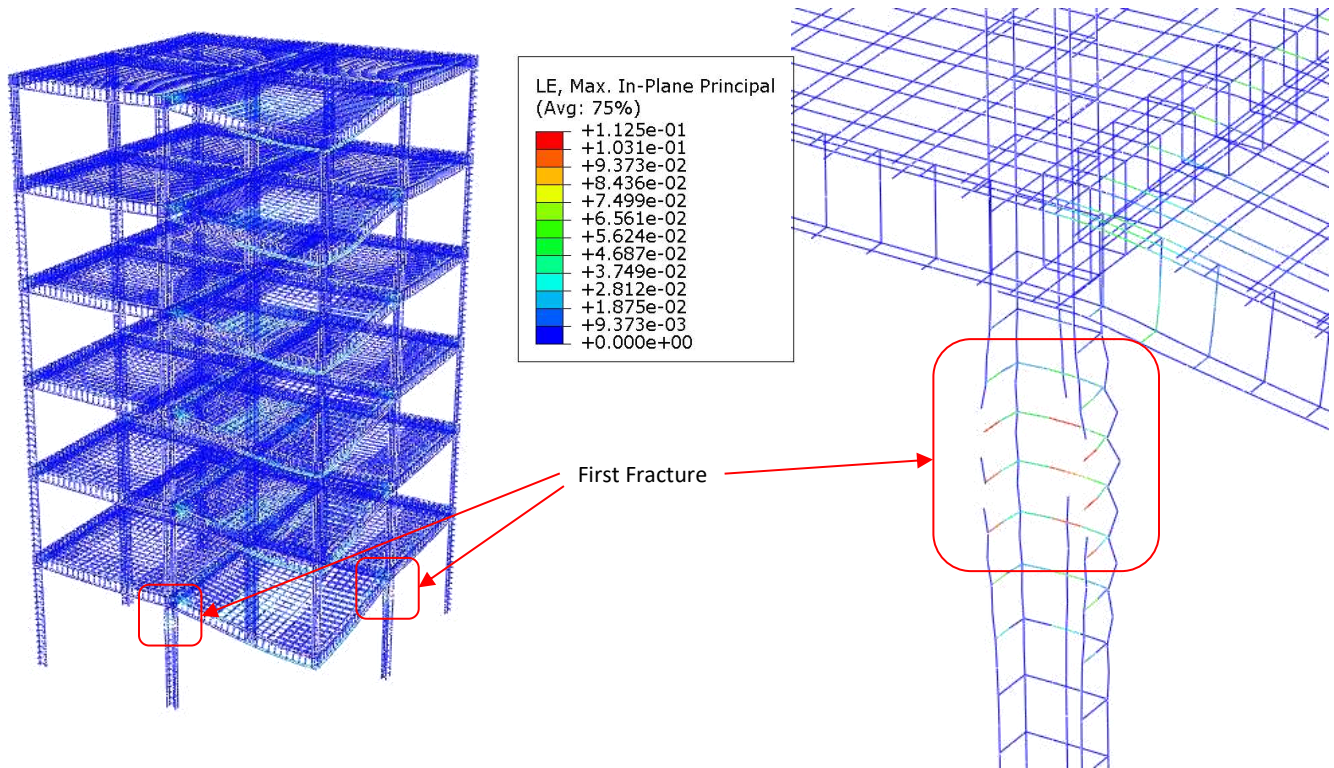


Figure 5-91: Logarithmic Strains in Truss Elements for FF-IC-C1 Under Sudden Column Loss at 280% Design Load at First Fracture, Quarter Model (Left) & Closeup on Plastic Hinge (Right)

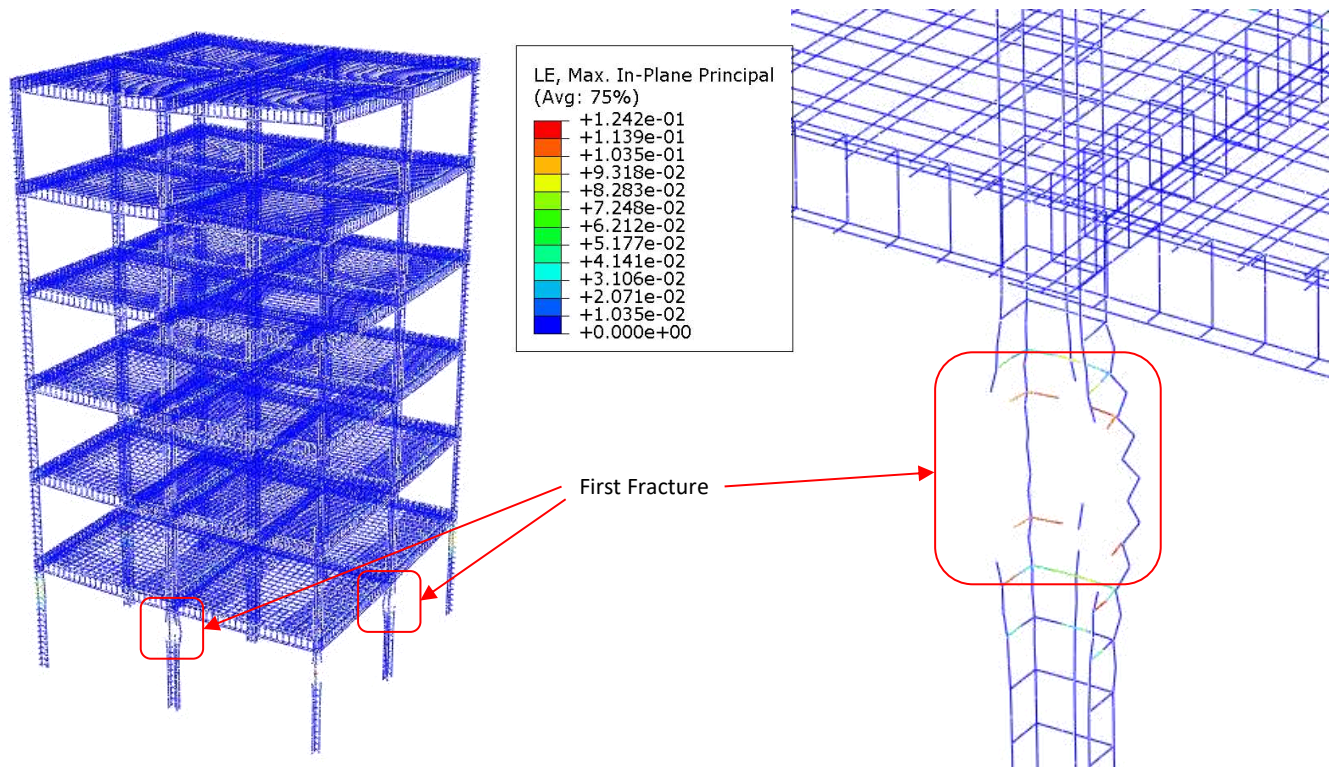


Figure 5-92: Logarithmic Strains in Truss Elements for FF-IC-C6 Under Sudden Column Loss at 320% Design Load at First Fracture, Quarter Model (Left) & Closeup on Plastic Hinge (Right)

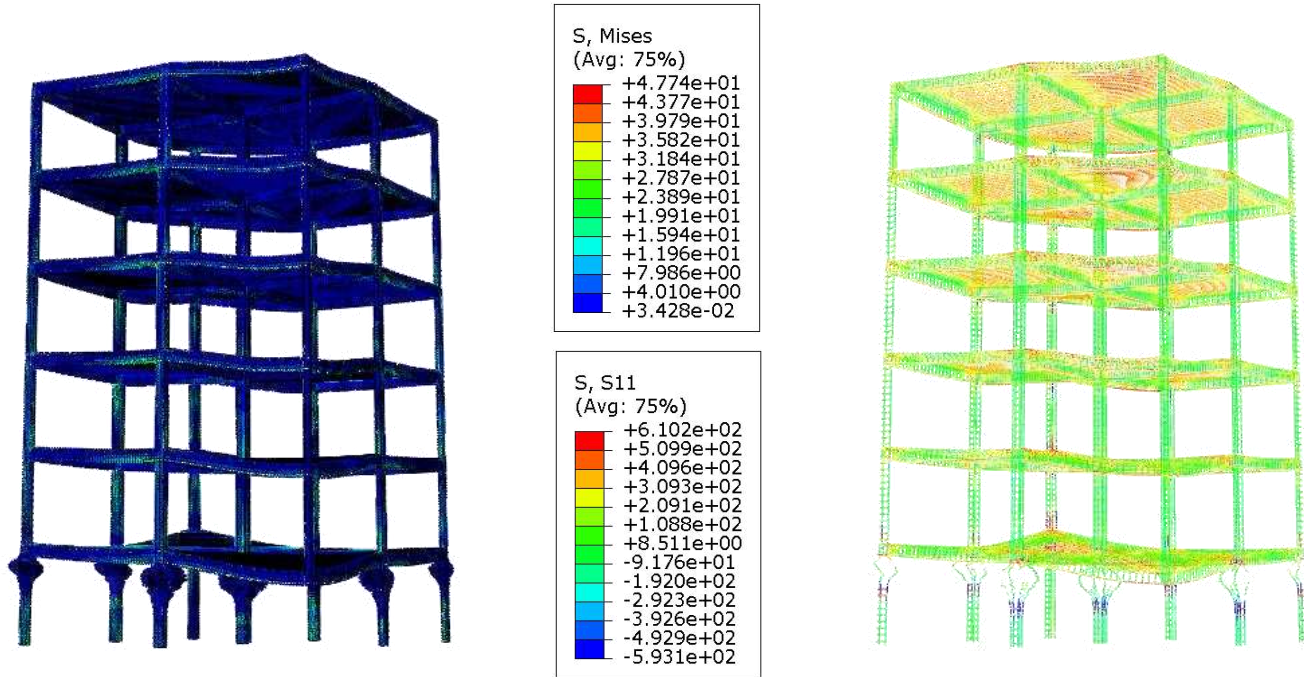


Figure 5-93: Von Mises Stresses in Solid Elements (Left) & S11 Stresses in Truss Elements (Right) for FF-IC-C1 Under Sudden Column Loss at 280% Design Load After Damage Propagation (Quarter Model Shown)

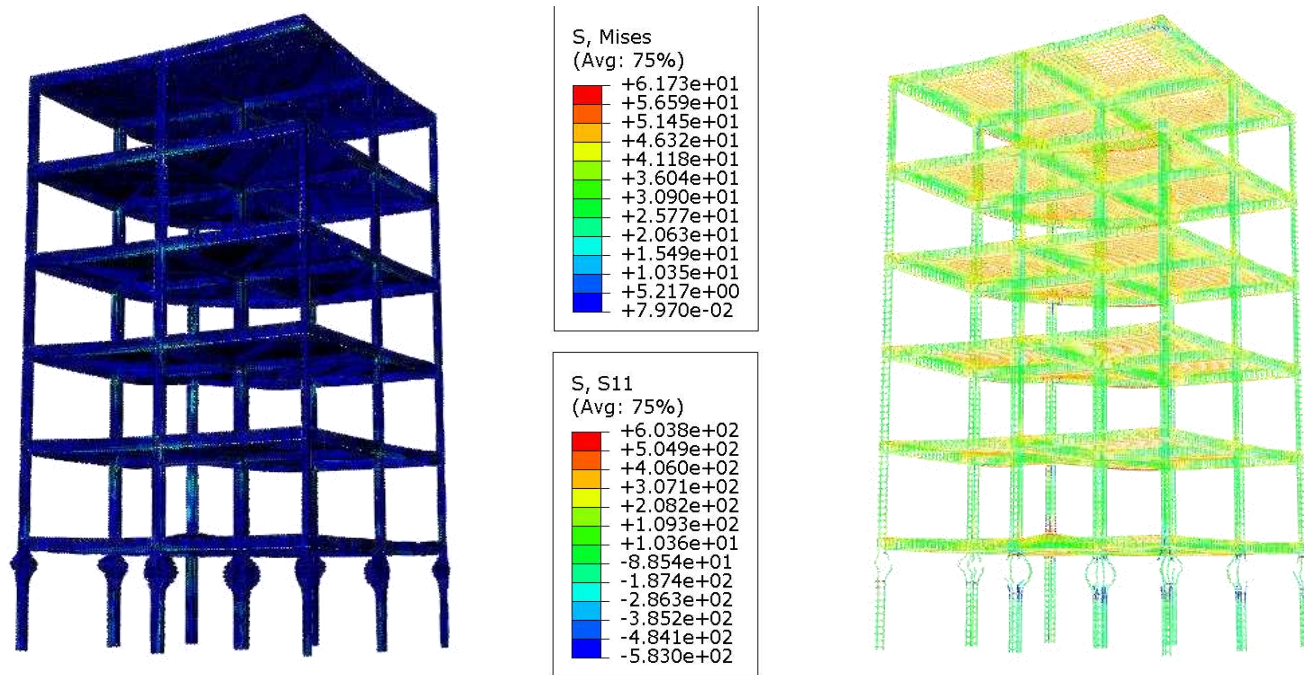


Figure 5-94: Von Mises Stresses in Solid Elements (Left) & S11 Stresses in Truss Elements (Right) for FF-IC-C6 Under Sudden Column Loss at 320% Design Load After Damage Propagation (Quarter Model Shown)

5.3.5.4 BARE-FRAME INTERIOR COLUMN REMOVAL RESULTS

The joint displacement at the top of the removed column is plotted against time in Figure 5-95 to Figure 5-100 for different loading values for each model. The pseudo-static curves are displayed in Figure 5-101 and the values of the applied load (P), displacement (u) and slope (s) at the fracture points are presented in Table 5-11.

Table 5-11: Maximum Column Loss Analysis Values for BF-IC Models

Model	BF-IC-C1	BF-IC-C2	BF-IC-C3	BF-IC-C4	BF-IC-C5	BF-IC-C6
P_{max}	80%	80%	80%	80%	80%	80%
u_{max} (mm)	312	300	291	274	242	174
s_{max}	6.24%	6.00%	5.82%	5.48%	4.84%	3.47%

All six models exhibited the same load-resisting capacity as they all reached a maximum load level of 80%. The maximum deformation of the system, on the other hand, decreased as the number of floors above the removed column increased. Model BF-IC-C1 displayed the maximum deformation at 312 mm, while BF-IC-C6 showed the minimum deformation at 174 mm for a relative standard deviation of 17.61%.

A deeper look at Model BF-IC-C1 and Model BF-IC-C6 was taken at first rebar fracture and after damage propagation during the partial progressive collapse of the system. The von Mises stresses in the RC solid elements and the total displacement at first fracture are shown in Figure 5-102 and Figure 5-103 respectively for BF-IC-C1 and BF-IC-C6. The stresses and strains in the rebar truss elements, at the same point, are shown in Figure 5-104 to Figure 5-107. The first rebar fracture for BF-CC-C1 occurred in the top longitudinal reinforcement of the first floor’s beam. This first fracture led to the propagation of damage as the system partially collapsed. The damage was localized and confined to the internal central bay. The von Mises stresses in RC solid and rebar truss elements after damage propagation, at the second chosen point, are presented in Figure 5-108 and Figure 5-109.

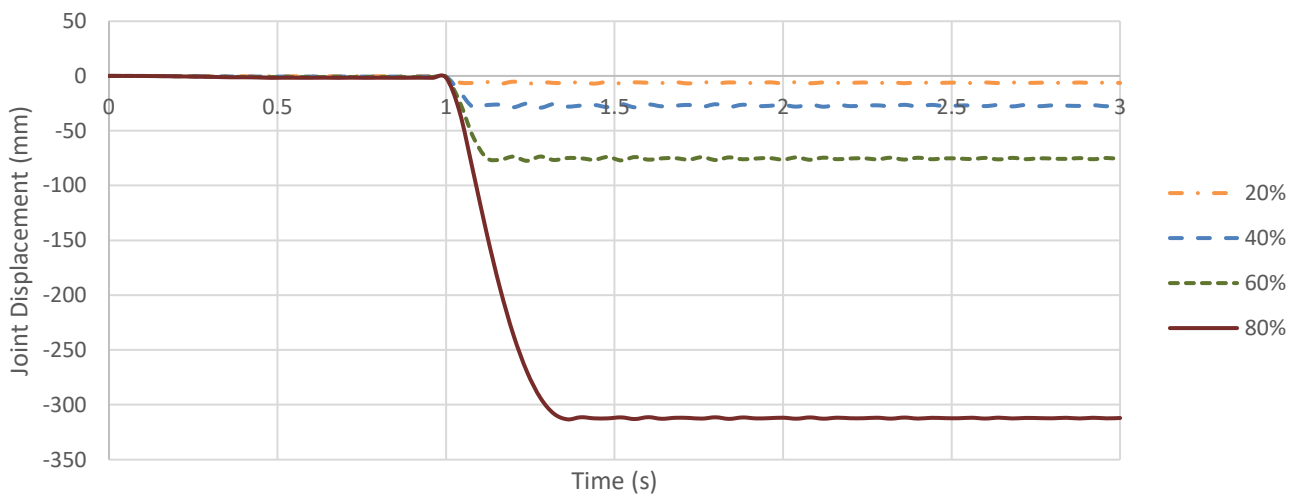


Figure 5-95: Joint Displacements for BF-IC-C1 Subjected to Sudden Column Loss Under Different Load Values

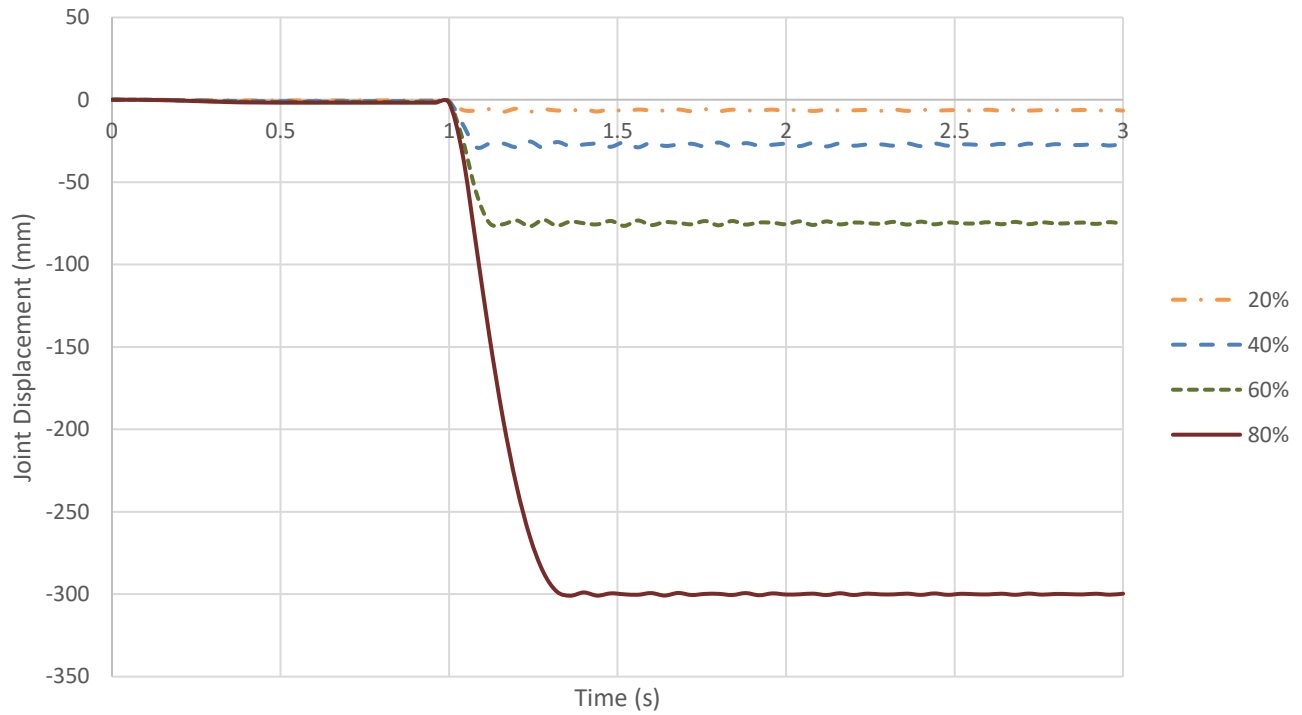


Figure 5-96: Joint Displacements for BF-IC-C2 Subjected to Sudden Column Loss Under Different Load Values

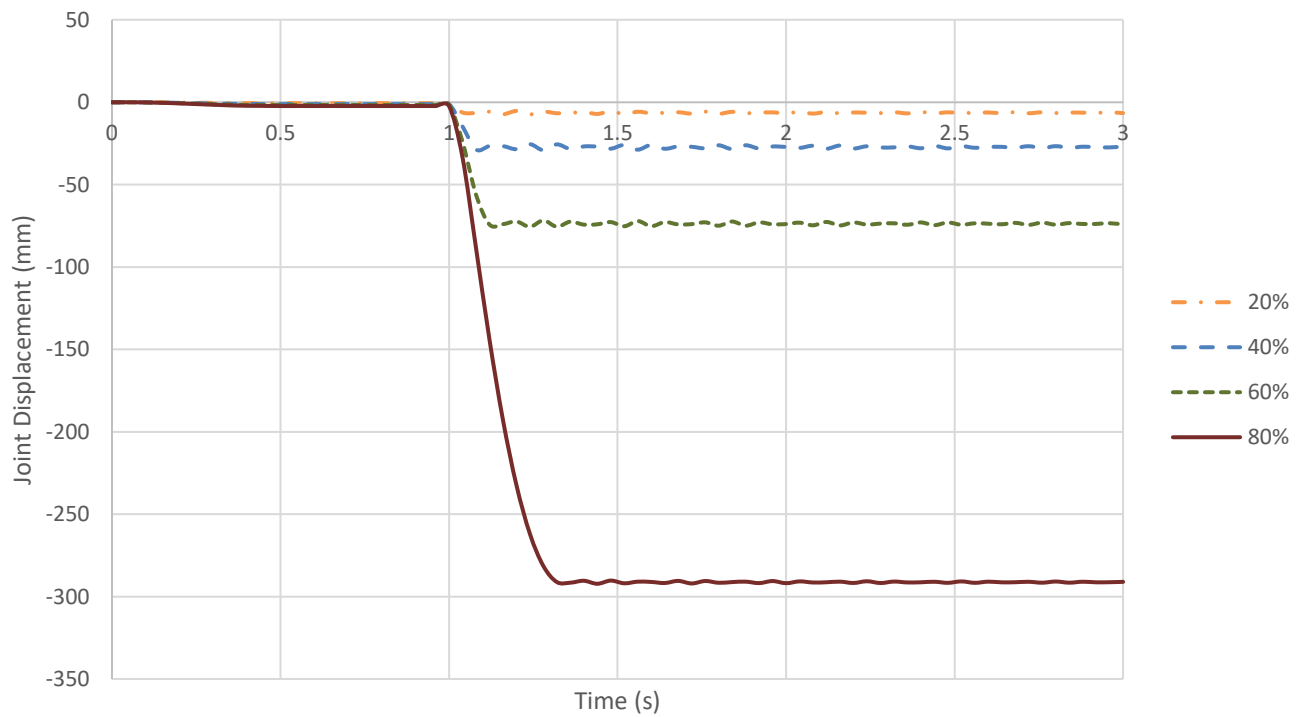


Figure 5-97: Joint Displacements for BF-IC-C3 Subjected to Sudden Column Loss Under Different Load Values

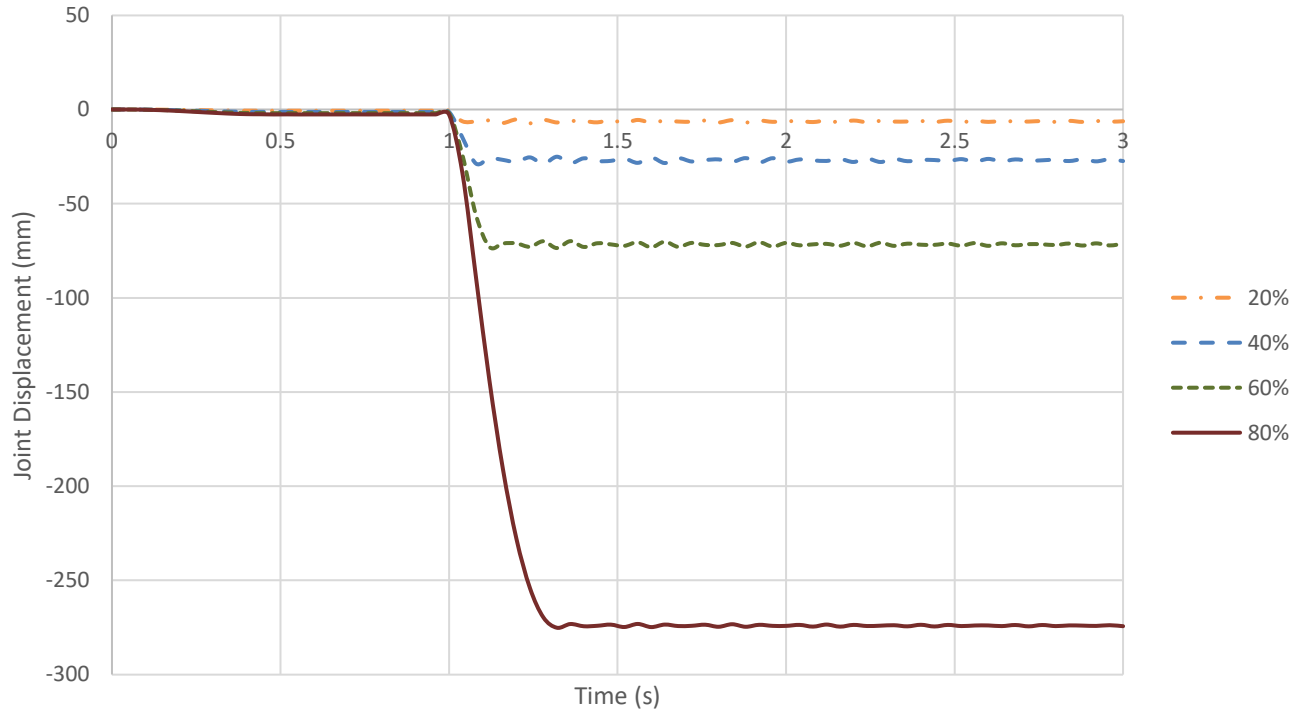


Figure 5-98: Joint Displacements for BF-IC-C4 Subjected to Sudden Column Loss Under Different Load Values

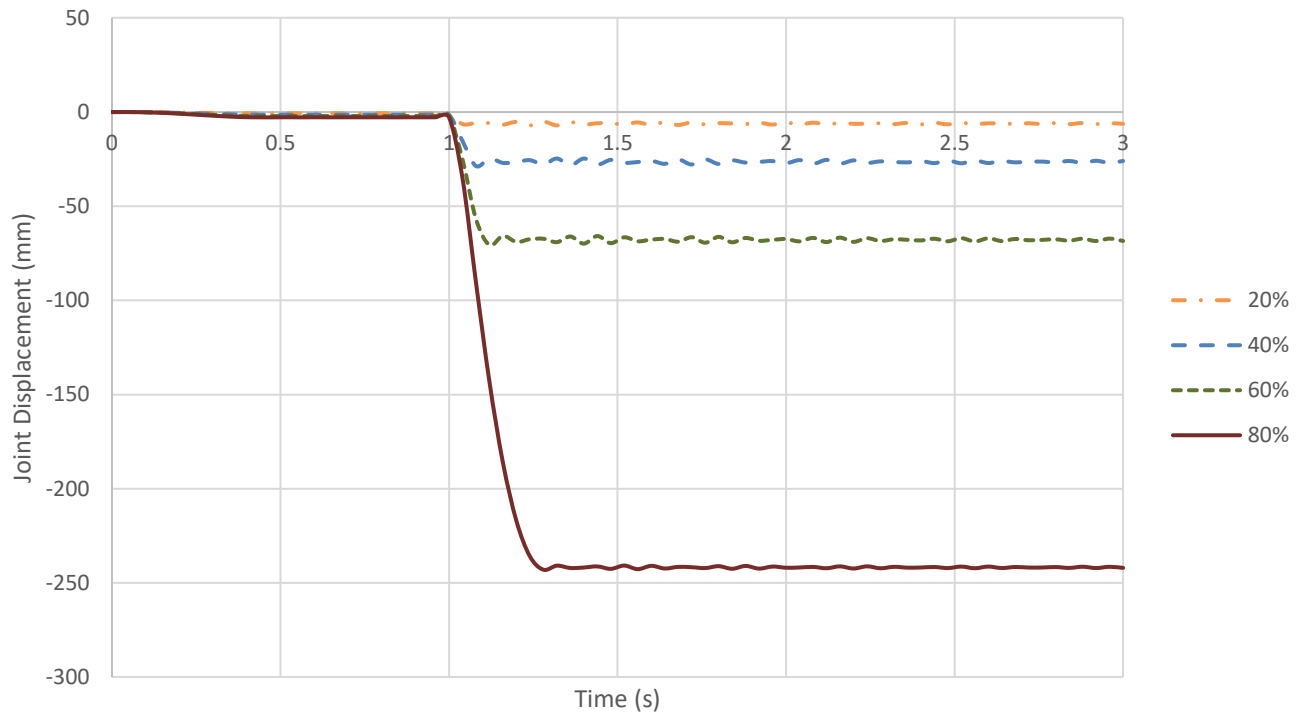


Figure 5-99: Joint Displacements for BF-IC-C5 Subjected to Sudden Column Loss Under Different Load Values

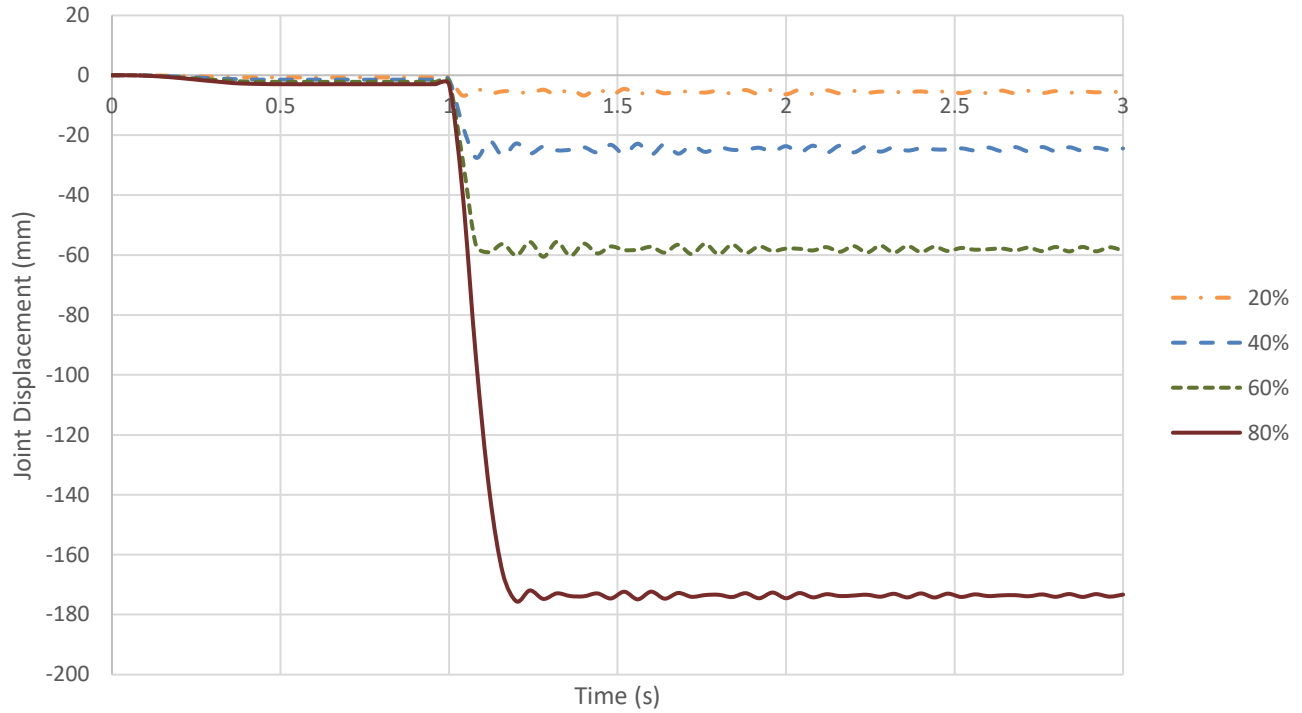


Figure 5-100: Joint Displacements for BF-IC-C6 Subjected to Sudden Column Loss Under Different Load Values

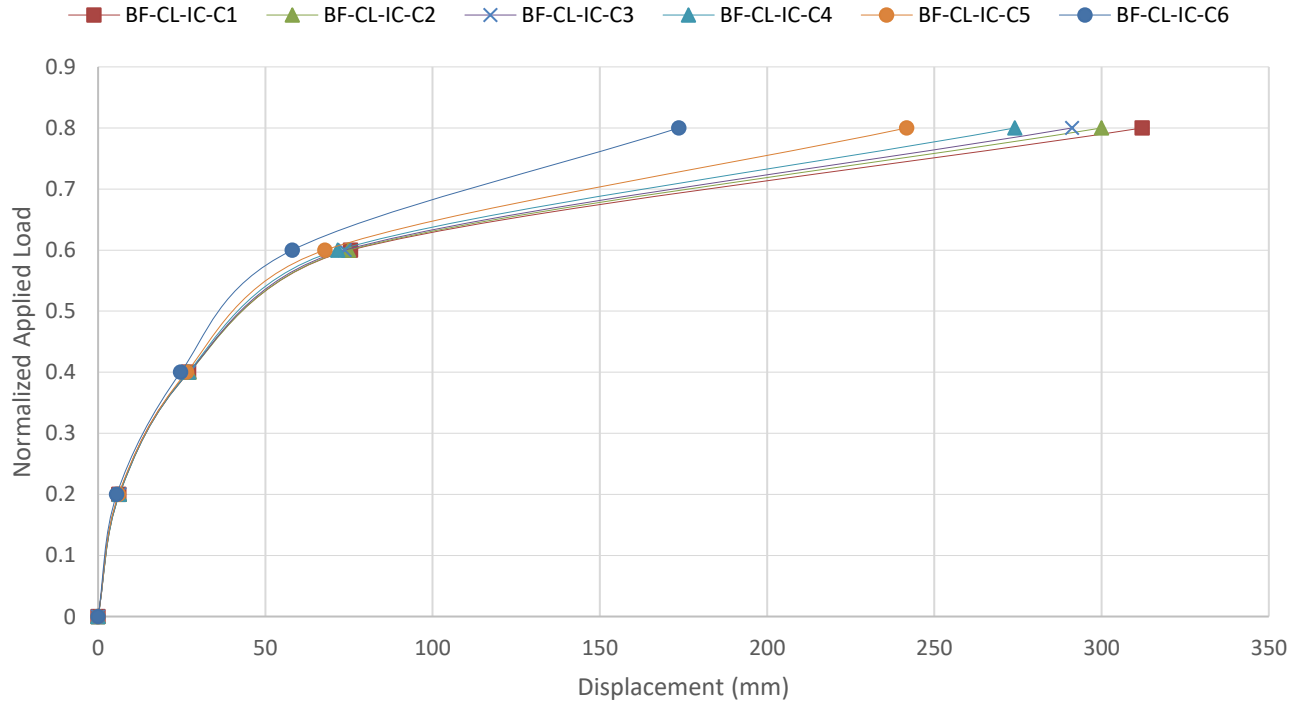


Figure 5-101: Pseudo-Static Curves for BF Due to the Sudden Loss of IC at Each Floor

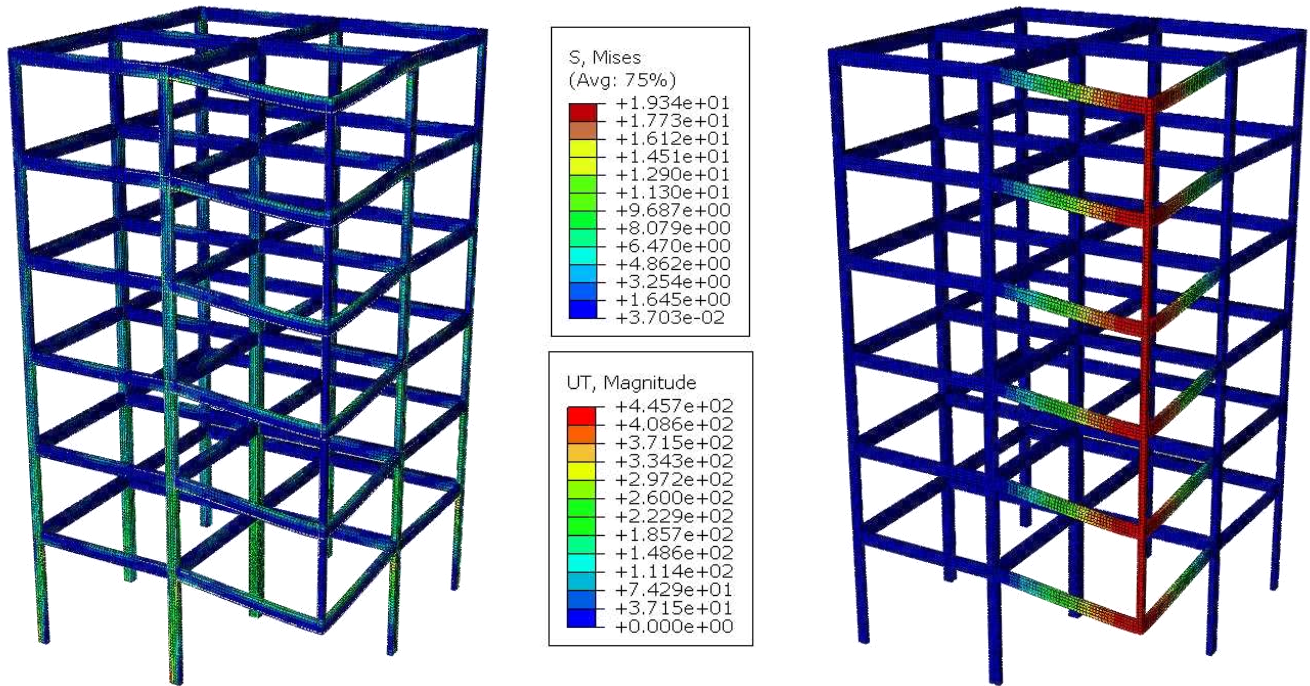


Figure 5-102: Von Mises Stresses (Left) & Total Displacement (Right) in Solid Elements for BF-IC-C1 Under Sudden Column Loss at 100% Design Load at First Fracture (Quarter Model Shown)

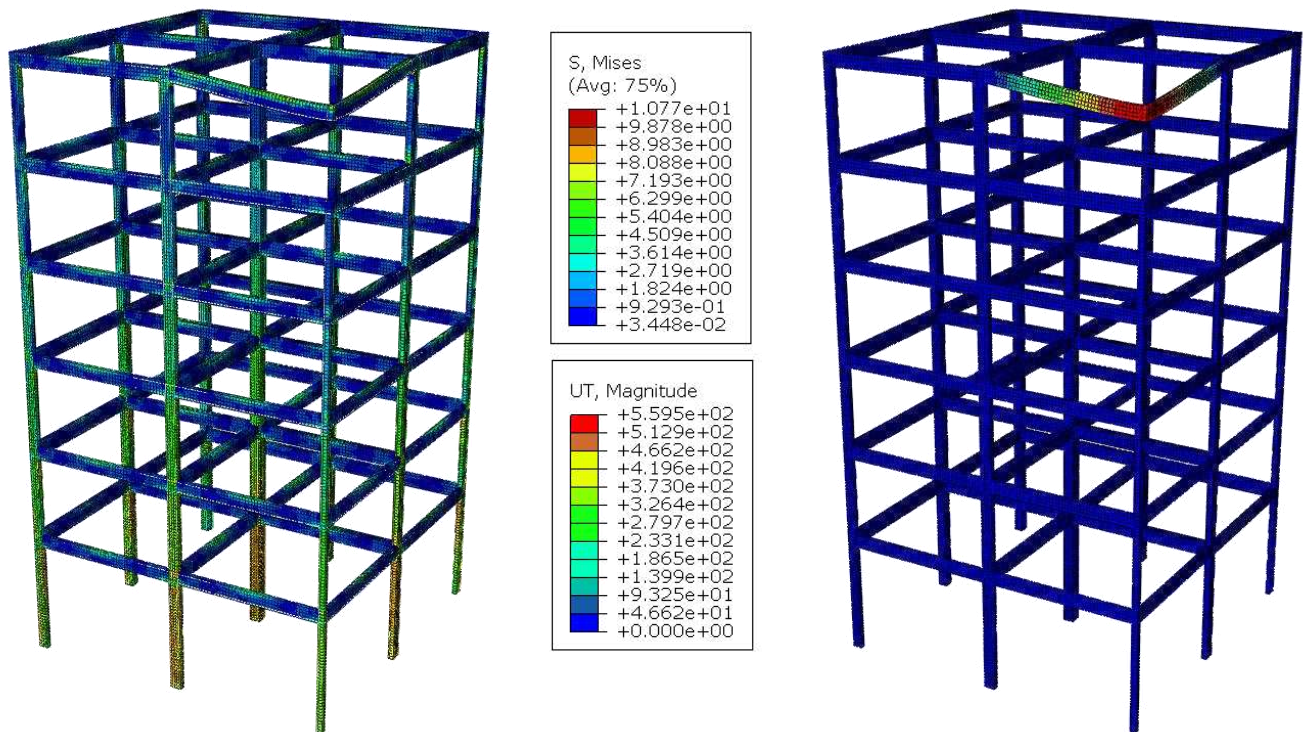


Figure 5-103: Von Mises Stresses (Left) & Total Displacement (Right) in Solid Elements for BF-IC-C6 Under Sudden Column Loss at 100% Design Load at First Fracture (Quarter Model Shown)

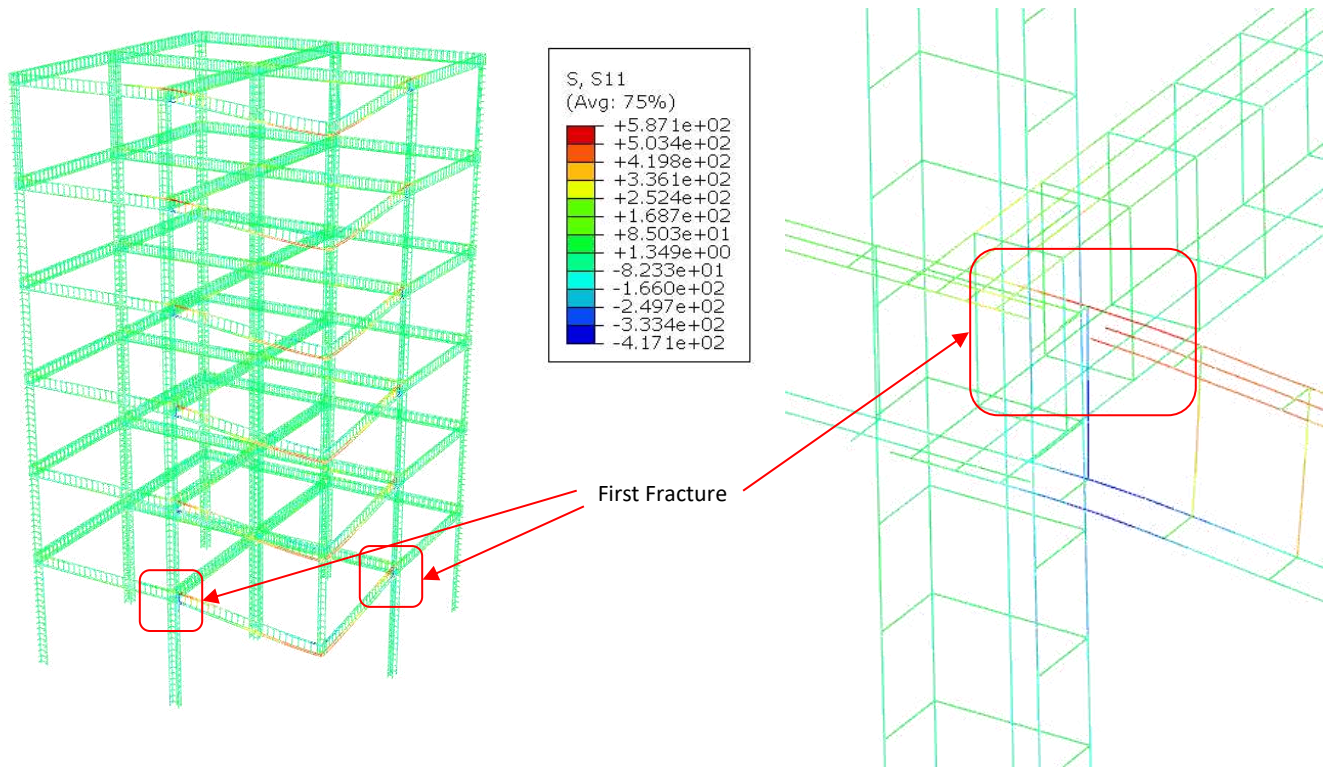


Figure 5-104: S11 Stresses in Truss Elements for BF-IC-C1 Under Sudden Column Loss at 100% Design Load at First Fracture, Quarter Model (Left) & Closeup on Plastic Hinge (Right)

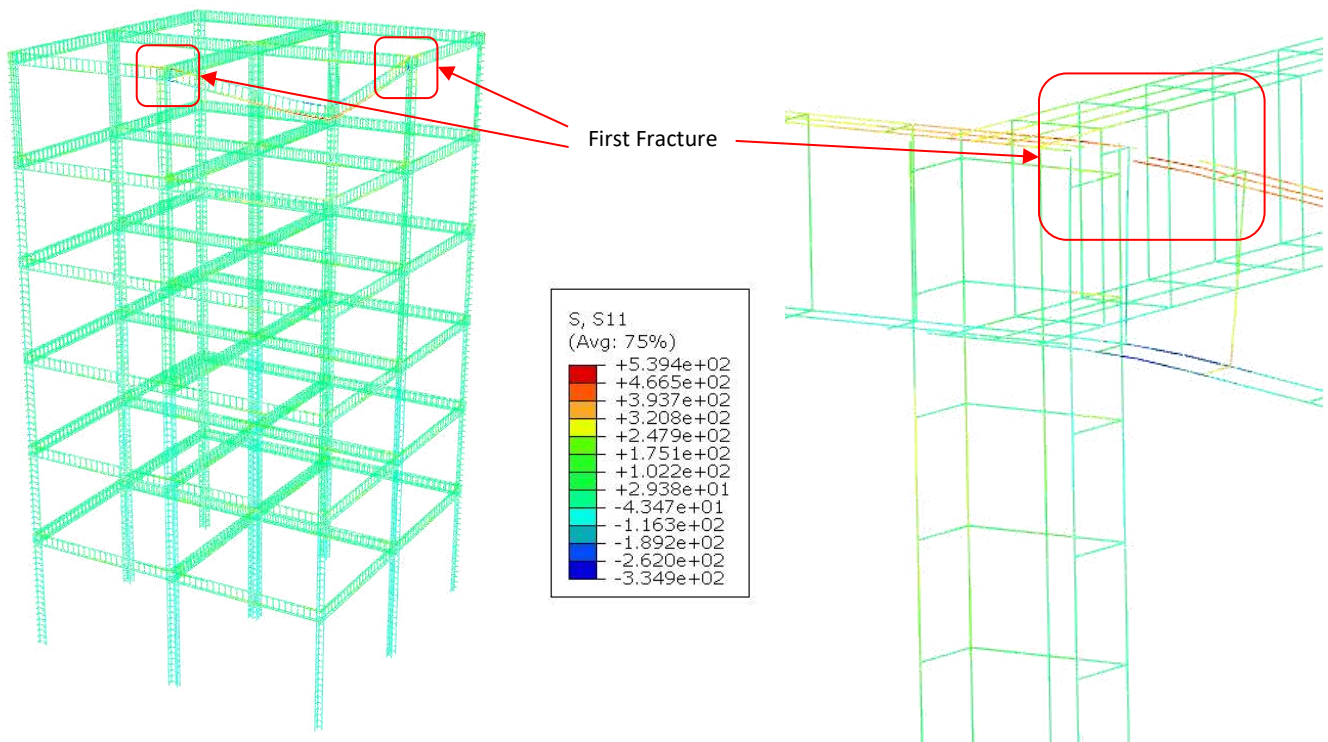


Figure 5-105: S11 Stresses in Truss Elements for BF-IC-C6 Under Sudden Column Loss at 100% Design Load at First Fracture, Quarter Model (Left) & Closeup on Plastic Hinge (Right)

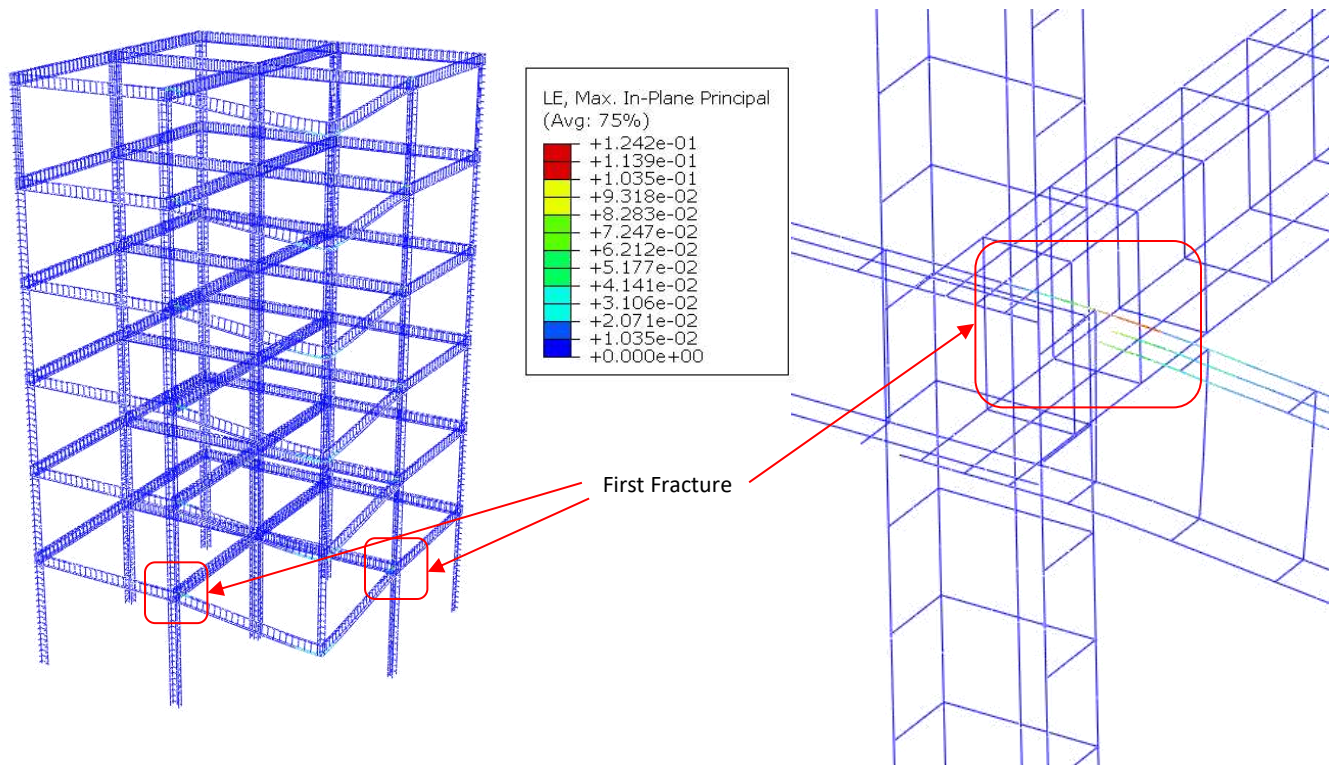


Figure 5-106: Logarithmic Strains in Truss Elements for BF-IC-C1 Under Sudden Column Loss at 100% Design Load at First Fracture, Quarter Model (Left) & Closeup on Plastic Hinge (Right)

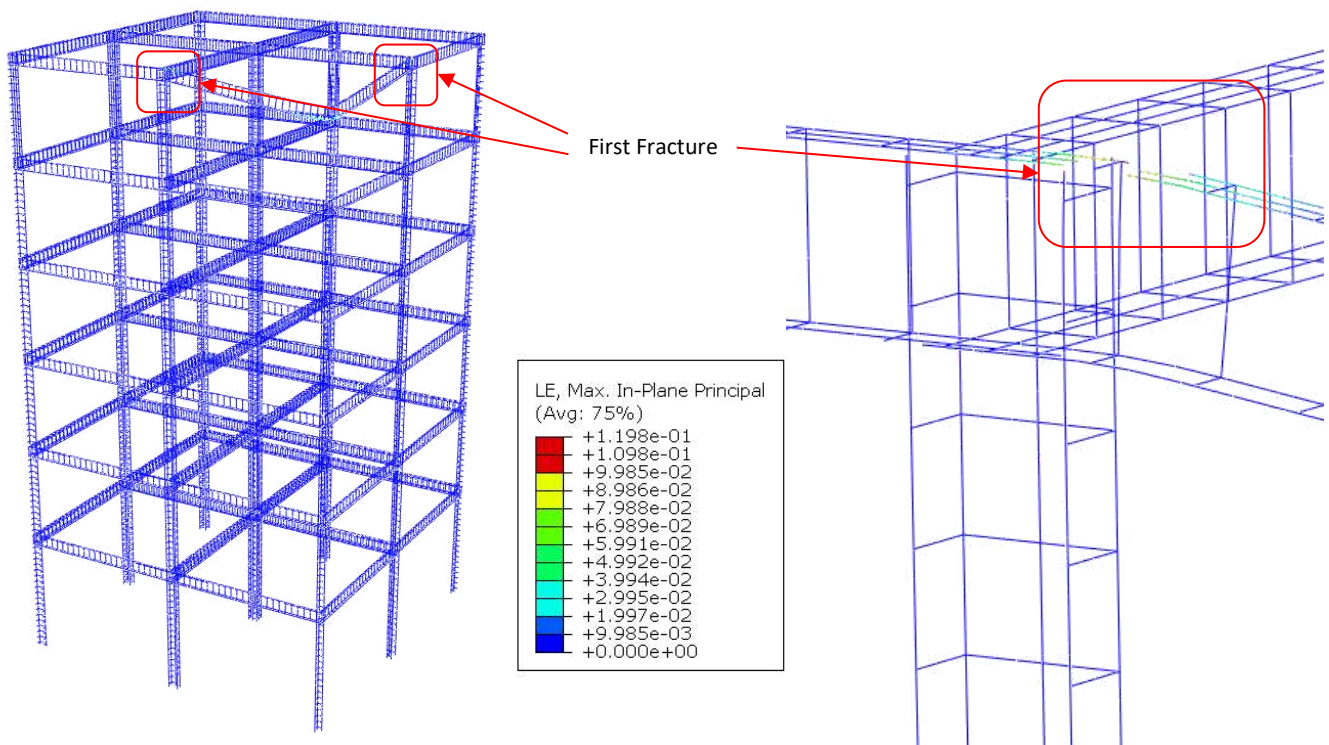


Figure 5-107: Logarithmic Strains in Truss Elements for BF-IC-C6 Under Sudden Column Loss at 100% Design Load at First Fracture, Quarter Model (Left) & Closeup on Plastic Hinge (Right)

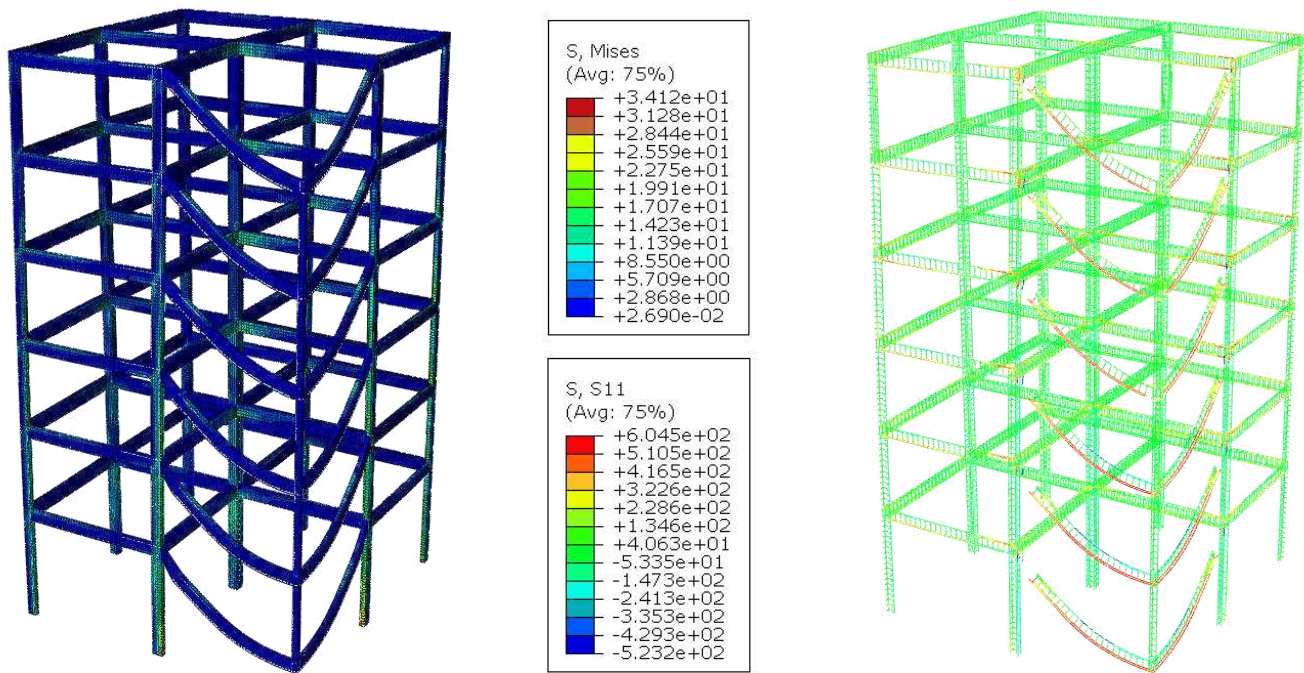


Figure 5-108: Von Mises Stresses in Solid Elements (Left) & S11 Stresses in Truss Elements (Right) for BF-IC-C1 Under Sudden Column Loss at 100% Design Load After Damage Propagation (Quarter Model Shown)

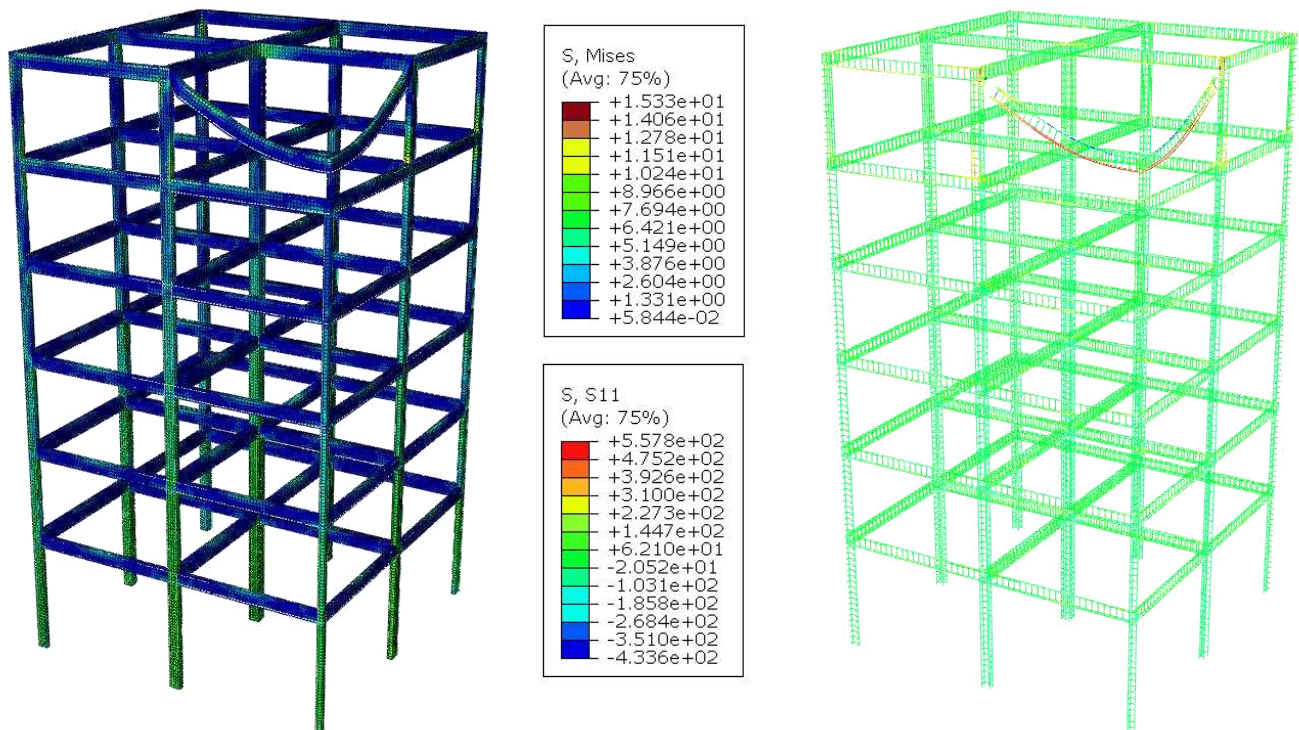


Figure 5-109: Von Mises Stresses in Solid Elements (Left) & S11 Stresses in Truss Elements (Right) for BF-IC-C6 Under Sudden Column Loss at 100% Design Load After Damage Propagation (Quarter Model Shown)

5.4 INTERPRETATION OF RESULTS

5.4.1 DYNAMIC INCREASE FACTORS

According to the GSA and UFC guidelines, the dynamic increase factors for nonlinear static procedures (NSP) are provided in Table 5-12, where θ_{pra} is the allowable plastic rotation angle as prescribed in the guidelines and θ_y is the yield rotation angle. Table 5-13 shows the calculation process followed to obtain the DIF values for the IC and CC models. It should be noted that the conjugate beam method was used to estimate the value of the yield rotation angle after simplifying (idealizing) the structural system of the beams.

As previously mentioned, one of the objectives of this study was to compute the DIF values for the case study building and compare them with the ones prescribed by the guidelines. Therefore, by dividing the normalized quasi-static force, from the pushdown analysis, by the applied dynamic force, from the column loss analysis at the same vertical displacement, the DIF values for each model were calculated. In Figure 5-110 to Figure 5-117, the dynamic load is compared with the quasi-static load, and the DIF curves are plotted against the rotation of the adjacent beam represented by the slope (s). Furthermore, the average DIF values obtained from the analysis are compared with the values prescribed by the GSA and UFC in Table 5-14. It should be noted that the same DIF values given by the guidelines are compared with the FF as well as the BF values. The results show that the prescribed DIF values are more accurate in predicting the DIF of the full-frame (FF) models. The average difference in the results of the FF-CC and FF-IC models was found to be 14.16% and 10.09%, respectively. However, the DIF values of the BF models differed significantly from the FF models, and therefore, the DIF values prescribed by the GSA and UFC are not accurate enough in predicting the DIF of the bare-frame (BF) models as the difference in the results of the BF-CC and BF-IC models was 33.66% and 25.86%, respectively.

Table 5-12: Dynamic Increase Factors for Nonlinear Static analysis [6], [7]

Material	Structure Type	Ω_N
Steel	Framed	$1.08 + 0.76/(\theta_{pra}/\theta_y + 0.83)$
Reinforced Concrete	Framed	$1.04 + 0.45/(\theta_{pra}/\theta_y + 0.48)$
	Load-Bearing Wall	2
Masonry	Load-bearing Wall	2
Wood	Load-bearing Wall	2
Cold-formed Steel	Load-bearing Wall	2

CHAPTER 5. PROGRESSIVE COLLAPSE ANALYSIS OF A MULTI-STORY CASE STUDY BUILDING

Table 5-13: Calculation of Dynamic Increase Factors According to the GSA & UFC Guidelines

Floor	Beam	ρ	ρ'	$\frac{\rho-\rho'}{\rho_{bal}}$	Trans. RFT	V		θ_{pra}	M_y	θ_y	Ω
						kN	lb/in ²				
1	External	0.74%	0.44%	0.112	NC	42.99	1.08	0.0444	65,438	0.0166	1.18
2	External	0.74%	0.44%	0.112	NC	41.81	1.05	0.0444	65,438	0.0166	1.18
3	External	0.60%	0.44%	0.062	NC	41.68	1.05	0.0469	54,446	0.0138	1.16
4	External	0.60%	0.44%	0.062	NC	41.55	1.04	0.0469	54,446	0.0138	1.16
5	External	0.44%	0.44%	0	NC	40.94	1.03	0.05	40,644	0.0103	1.12
6	External	0.44%	0.44%	0	NC	43.77	1.10	0.05	40,644	0.0103	1.12
1	Internal	0.74%	0.44%	0.112	NC	54.80	1.38	0.0444	65,438	0.0166	1.18
2	Internal	0.74%	0.44%	0.112	NC	54.41	1.37	0.0444	65,438	0.0166	1.18
3	Internal	0.74%	0.44%	0.112	NC	54.44	1.37	0.0444	65,438	0.0166	1.18
4	Internal	0.74%	0.44%	0.112	NC	54.45	1.37	0.0444	65,438	0.0166	1.18
5	Internal	0.74%	0.44%	0.112	NC	54.13	1.36	0.0444	65,438	0.0166	1.18
6	Internal	0.74%	0.44%	0.112	NC	55.26	1.39	0.0444	65,438	0.0166	1.18

Table 5-14: Comparison of DIF Values Obtained from the Analysis with Guideline-Prescribed Values

Model	DIF		Difference
	Avg.	GSA/UFC	
FF-CC-C1	1.33	1.18	11.00%
FF-CC-C2	1.34	1.18	11.71%
FF-CC-C3	1.34	1.16	13.67%
FF-CC-C4	1.35	1.16	14.47%
FF-CC-C5	1.34	1.12	15.95%
FF-CC-C6	1.37	1.12	18.17%
BF-CC-C1	1.67	1.18	29.02%
BF-CC-C2	1.70	1.18	30.54%
BF-CC-C3	1.77	1.16	34.56%
BF-CC-C4	1.63	1.16	28.95%
BF-CC-C5	1.68	1.12	32.99%
BF-CC-C6	2.08	1.12	45.88%
FF-IC-C1	1.36	1.18	13.16%
FF-IC-C2	1.35	1.18	12.14%
FF-IC-C3	1.32	1.18	10.16%
FF-IC-C4	1.28	1.18	7.46%
FF-IC-C5	1.30	1.18	9.21%
FF-IC-C6	1.29	1.18	8.41%
BF-IC-C1	1.64	1.18	27.90%
BF-IC-C2	1.63	1.18	27.23%
BF-IC-C3	1.62	1.18	26.89%
BF-IC-C4	1.60	1.18	26.31%
BF-IC-C5	1.57	1.18	24.77%
BF-IC-C6	1.52	1.18	22.07%

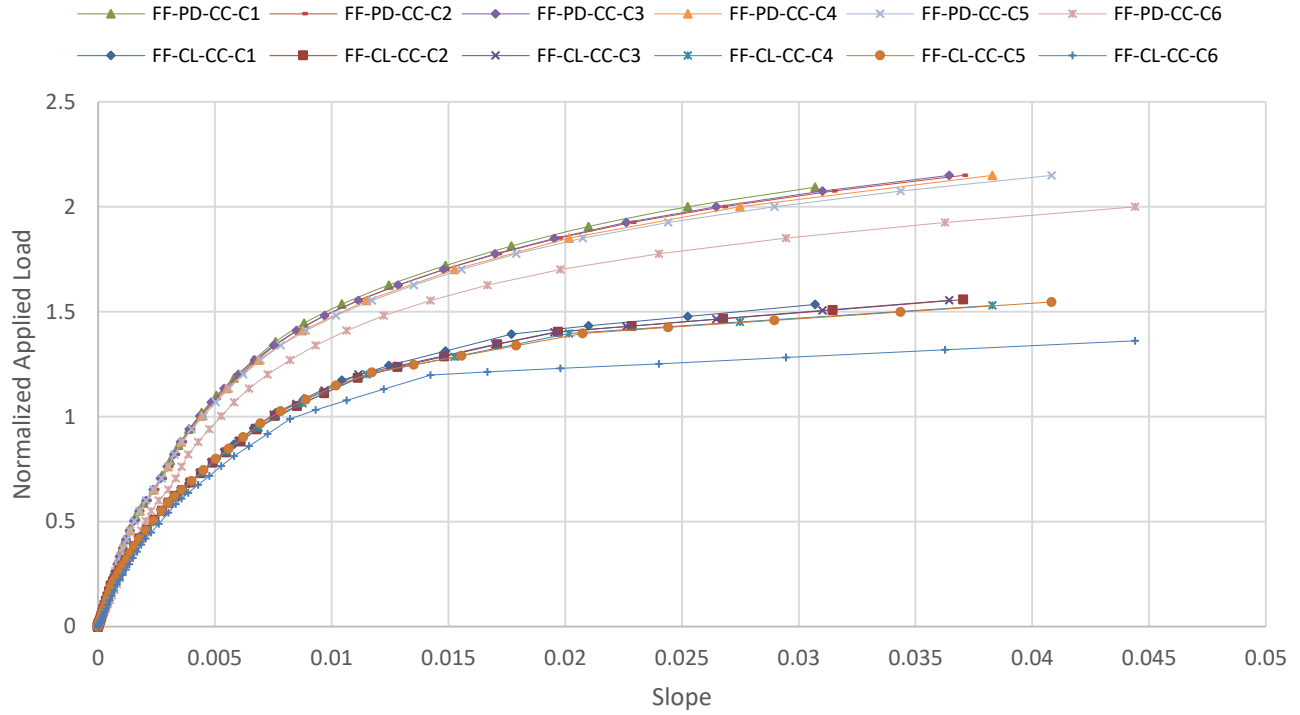


Figure 5-110: Normalized Applied Load vs. Slope for FF-CC Models

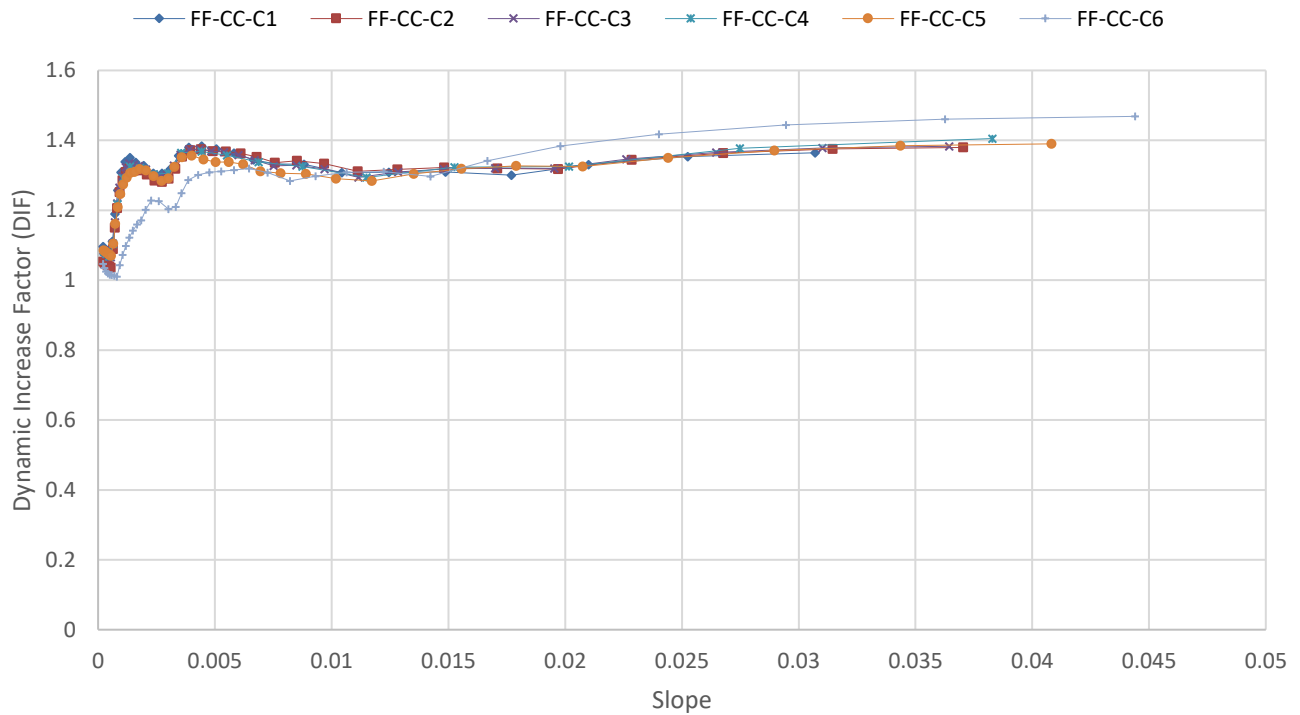


Figure 5-111: Dynamic Increase Factor for FF-CC Models

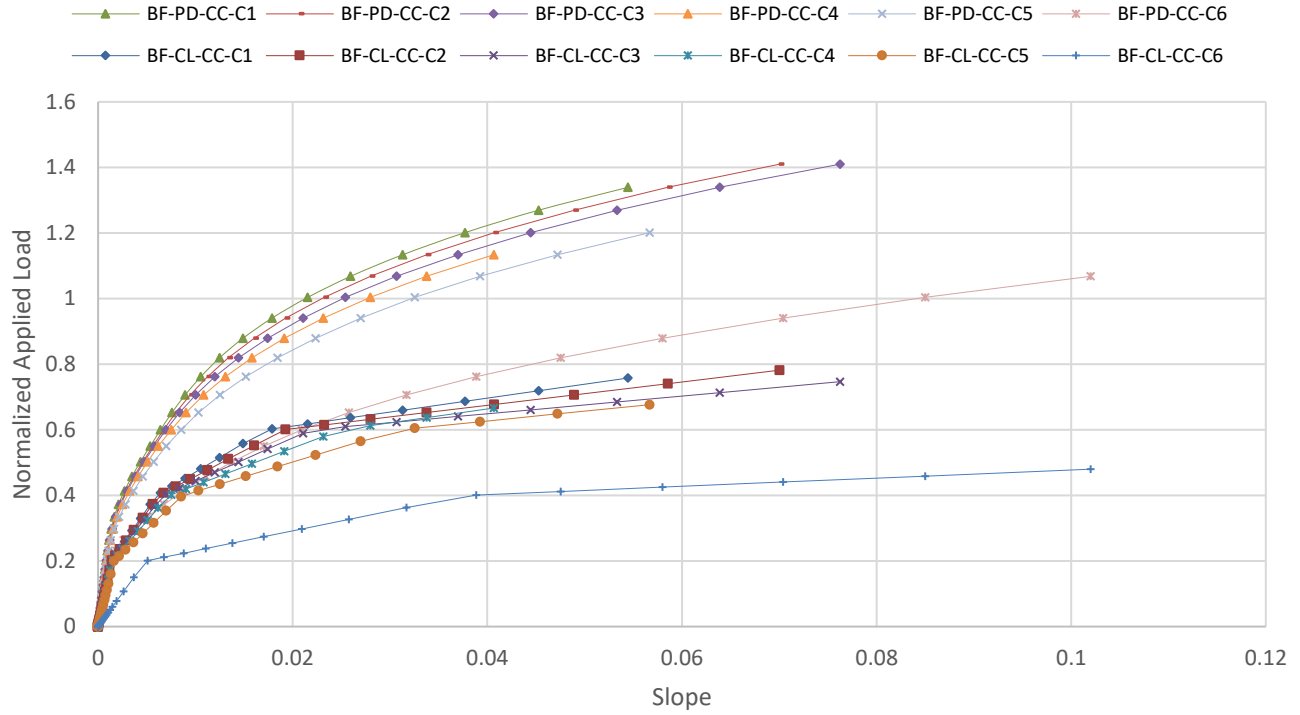


Figure 5-112: Normalized Applied Load vs. Slope for BF-CC Models

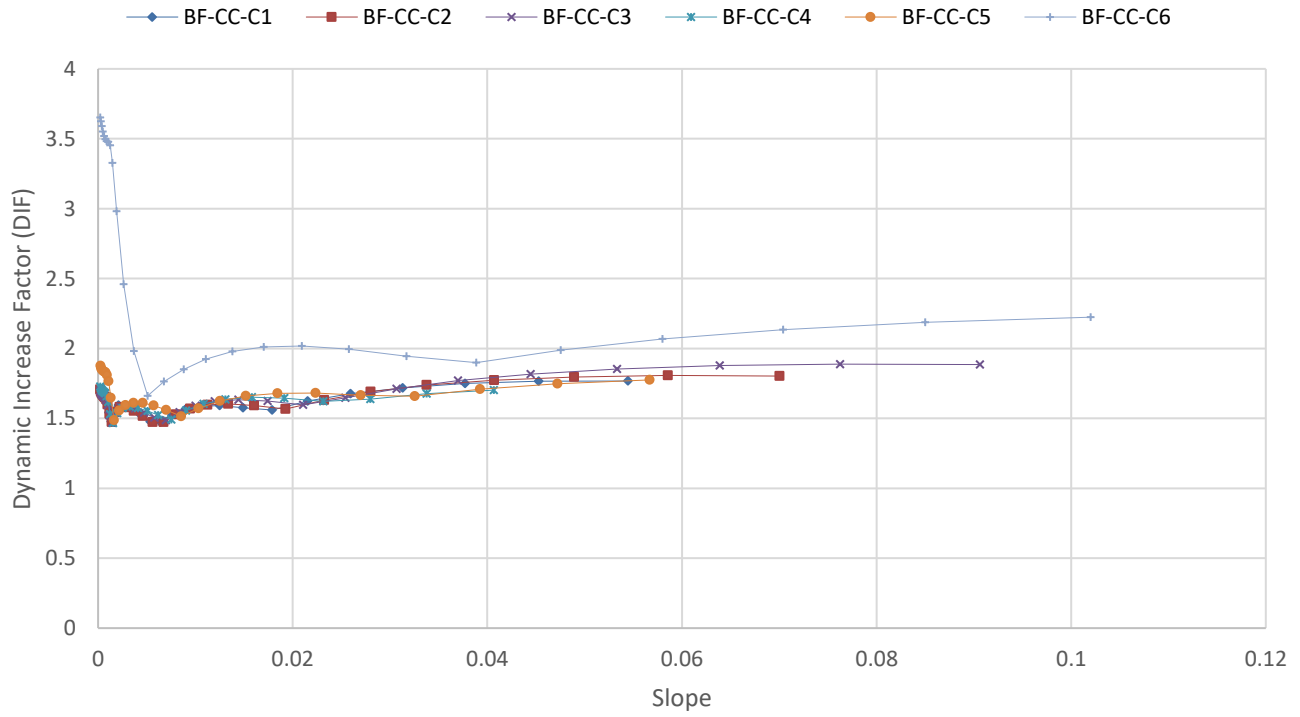


Figure 5-113: Dynamic Increase Factor for BF-CC Models

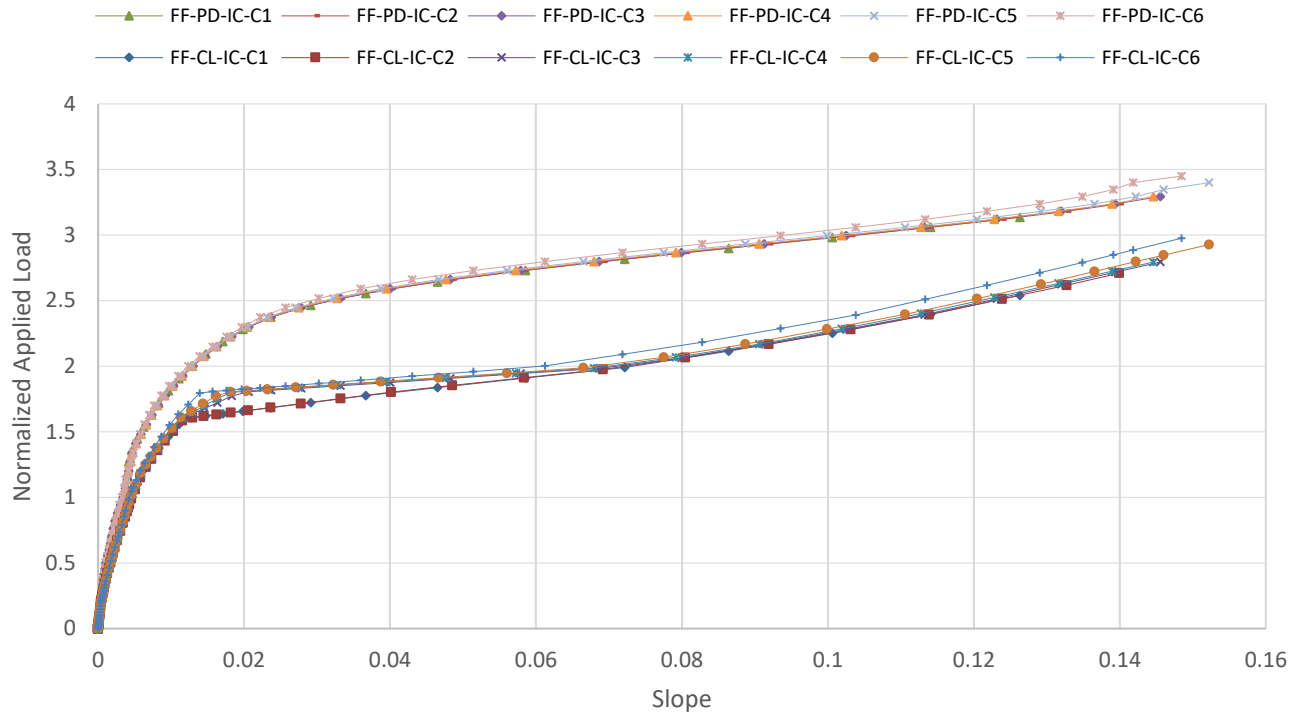


Figure 5-114: Normalized Applied Load vs. Slope for FF-IC Models

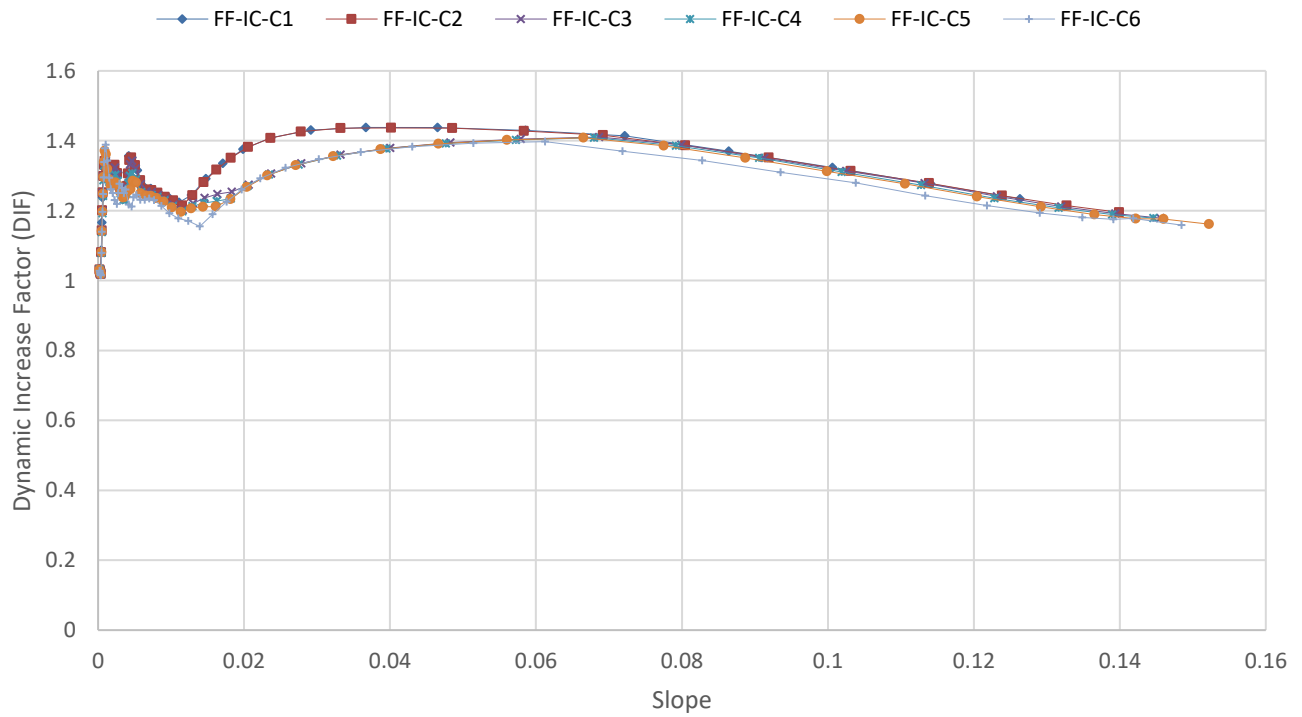


Figure 5-115: Dynamic Increase Factor for FF-IC Models

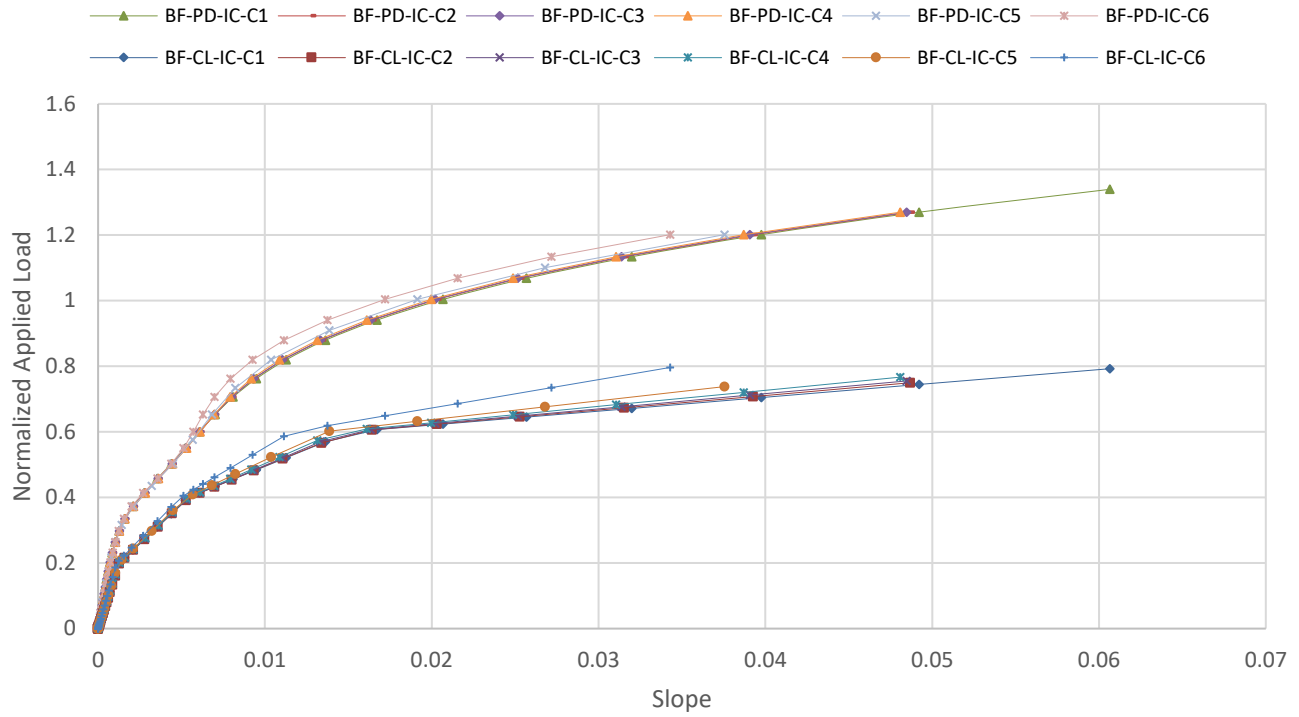


Figure 5-116: Normalized Applied Load vs. Slope for BF-IC Models

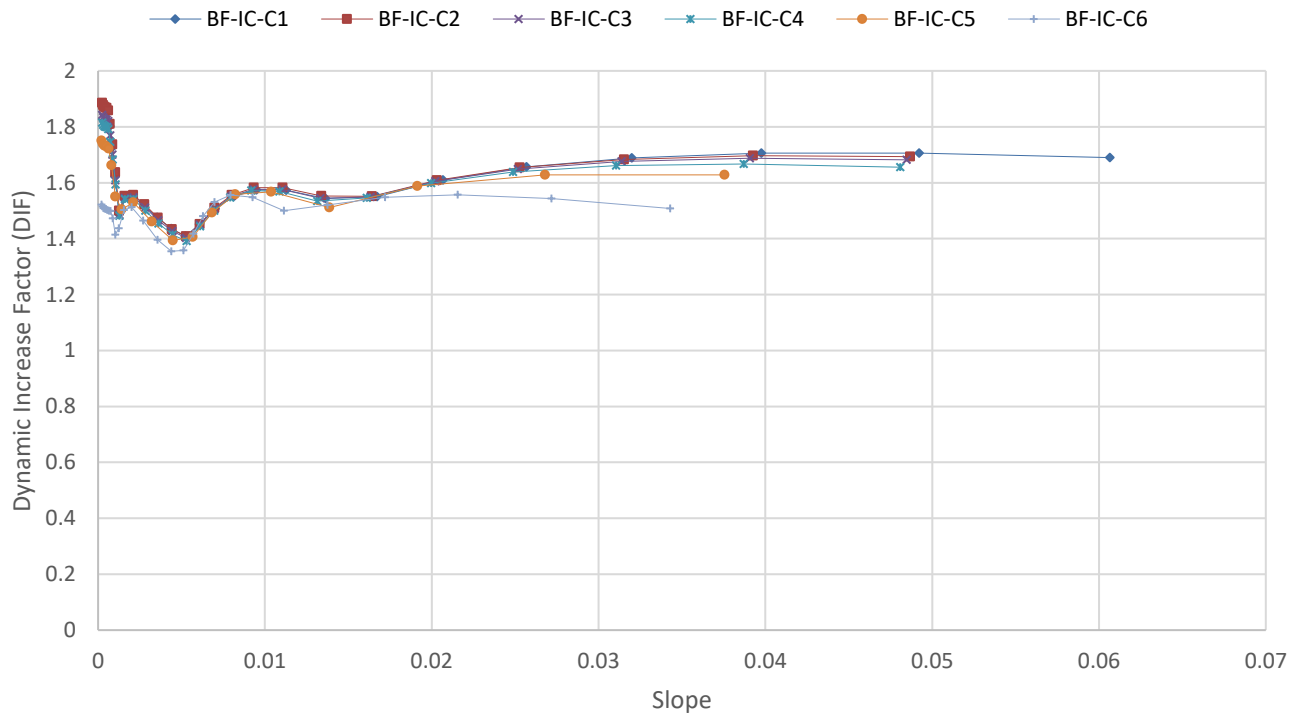


Figure 5-117: Dynamic Increase Factor for BF-IC Models

5.4.2 SLAB EFFECT

Another objective of this study was to quantify the effect of the slab on the progressive collapse as it is often overlooked in order to simplify the analysis. However, the increase in resistance brought on by the membrane action of the slab should not be neglected as it is quite substantial. In this research, a simple metric referred to as Slab Effect Factor (SEF), is proposed and used to evaluate the slab contribution to the response of the system. By dividing the force applied on the FF models by the force applied on the BF models at the same displacement, the SEF values were computed.

Figure 5-120 to Figure 5-125 show a comparison between the normalized applied load for the FF models and the BF models, as well as the SEF values, plotted against the slope, for the CC and IC models in the case of PD and CL analyses. Furthermore, Table 5-15 shows the average SEF values for each model and analysis type. Two values for the overall SEF average of all floors were also calculated. One value was computed by averaging the values from all six floors (Average₆), while the other excluded the sixth floor and only used the results from the first five floors (Average₅), as the C6 models did not capture the multi-story effect on the response, if any.

The SEF Average₅ values for the CC models were found to be 1.87 and 2.61, respectively for PD and CL analyses. As for the IC models, the SEF Average₅ values were found to be 2.14 and 2.60 for PD and CL analyses, respectively. These results show how significant the membrane action of the slab is on the response and how inaccurate and incomplete the analysis is when discounting and neglecting it. Another thing to be observed is that the effect of the slab is more pronounced when conducting dynamic analysis as opposed to quasi-static analysis. In other words, the membrane action improves the system's response in supporting inertial forces. This improvement reaches 39.6% and 21.5%, respectively for the CC and IC models.

Another way to quantify the slab effect is to simply compare the failure load in each case regardless of the corresponding displacement. In other words, this simplified slab effect factor (S-SEF) would be equal to the ratio between the maximum FF load and the maximum BF load for each column removal scenario and analysis type. Using this method, each analysis case would have a single S-SEF value as listed in Table 5-16 where the average values are also calculated and displayed. The values of the S-SEF are different from those of the SEF. In some cases, both values are close, in others, not so much. However, both metrics highlight the contribution of the slab to the structural resistance of the system, albeit in slightly different ways.

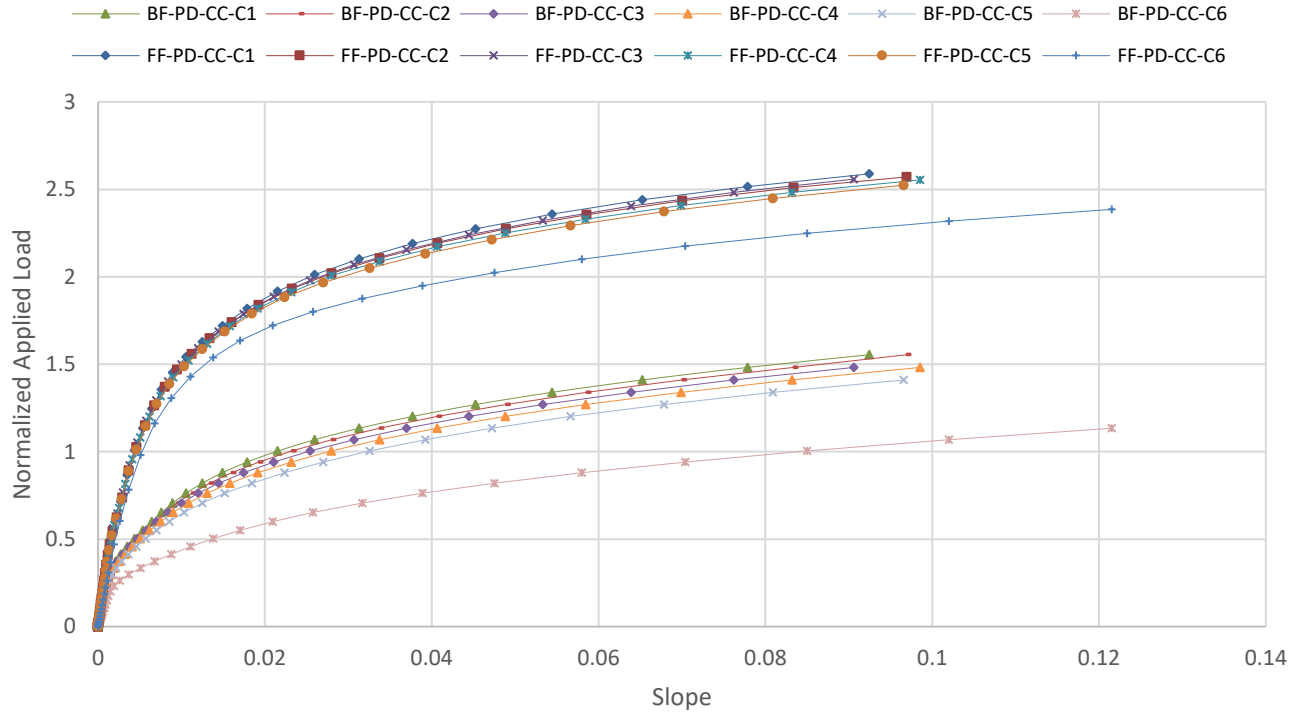


Figure 5-118: Normalized Applied Load vs. Slope for PD-CC Models

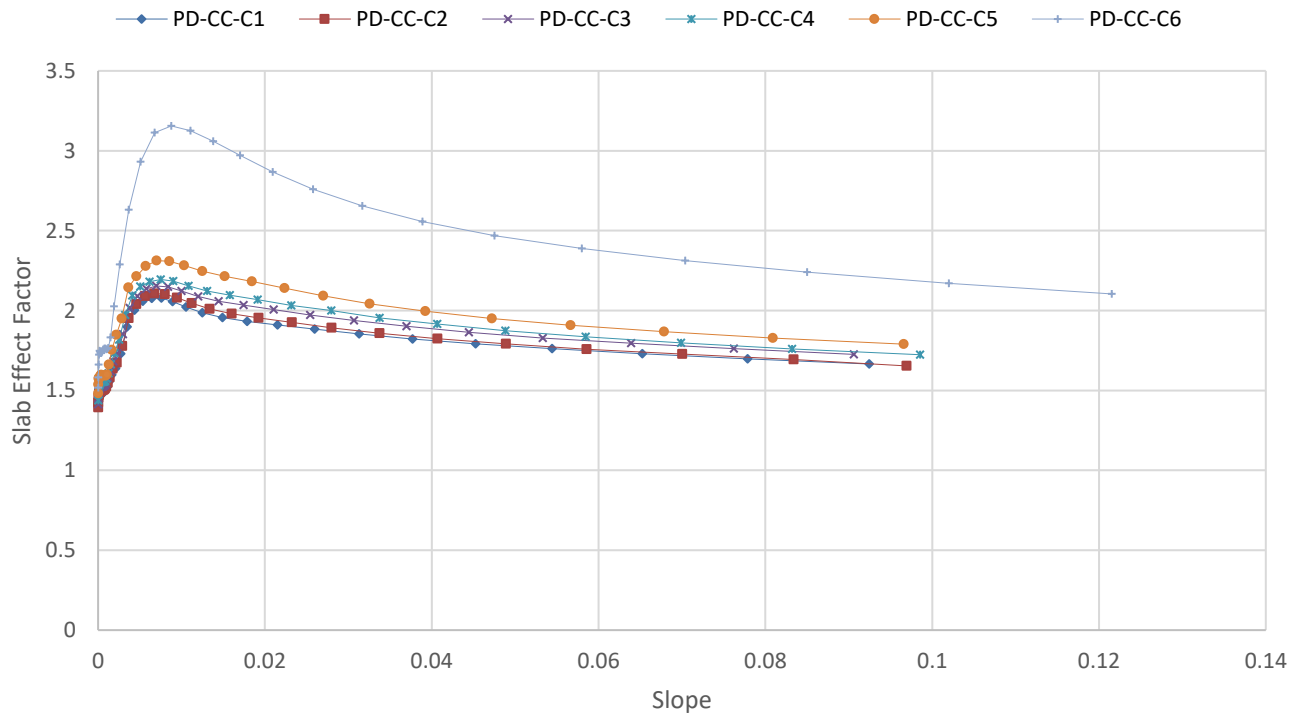


Figure 5-119: Slab Effect Factor for PD-CC Models

CHAPTER 5. PROGRESSIVE COLLAPSE ANALYSIS OF A MULTI-STORY CASE STUDY BUILDING

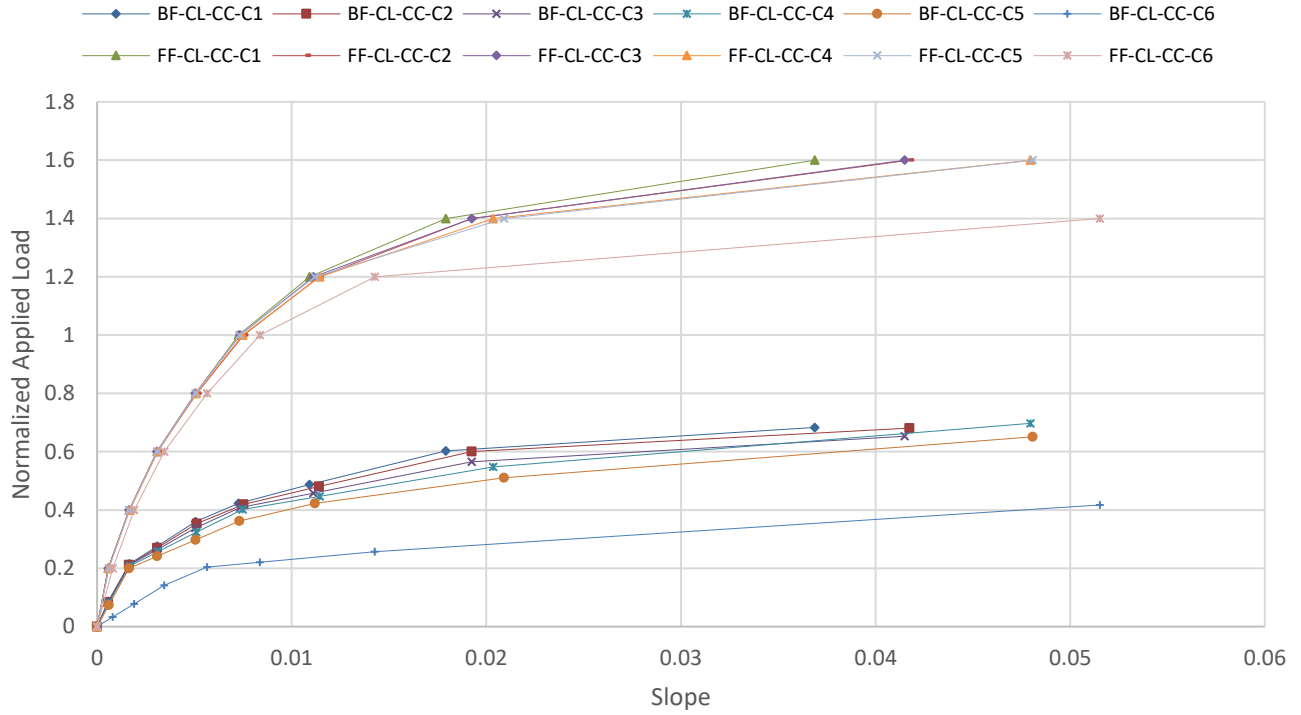


Figure 5-120: Normalized Applied Load vs. Slope for CL-CC Models

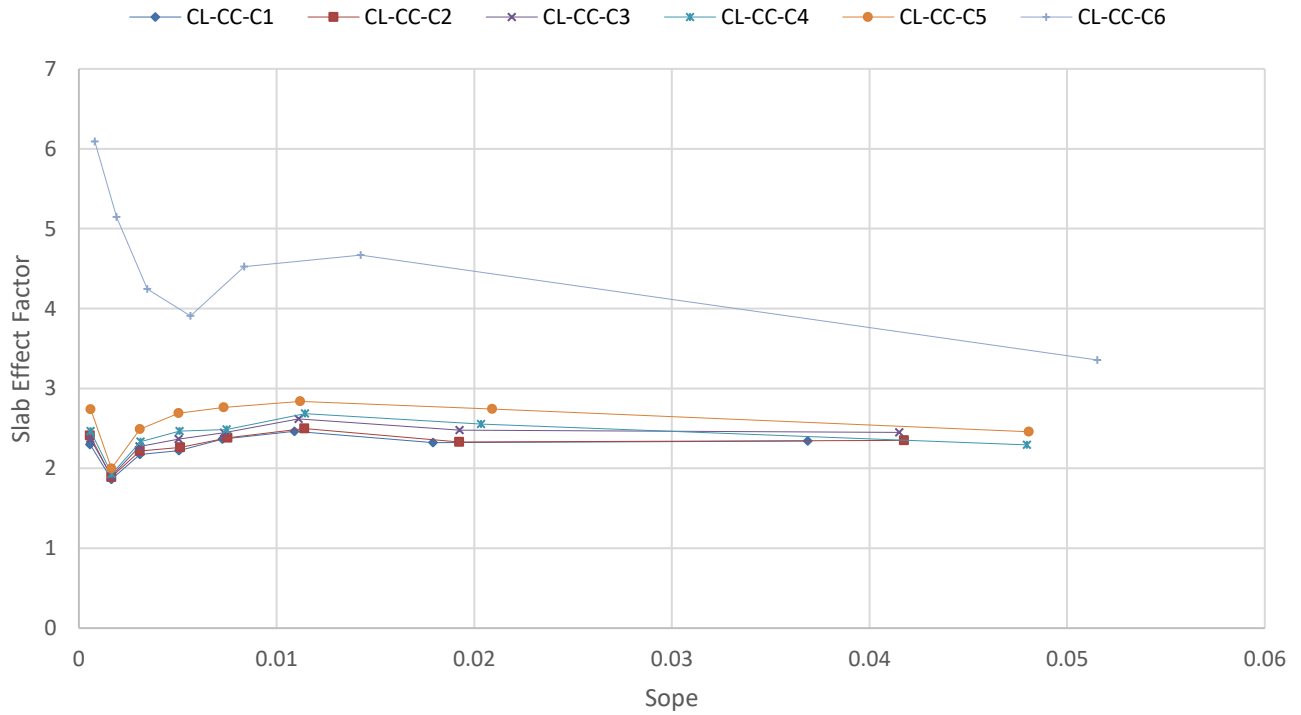


Figure 5-121: Slab Effect Factor for CL-CC Models

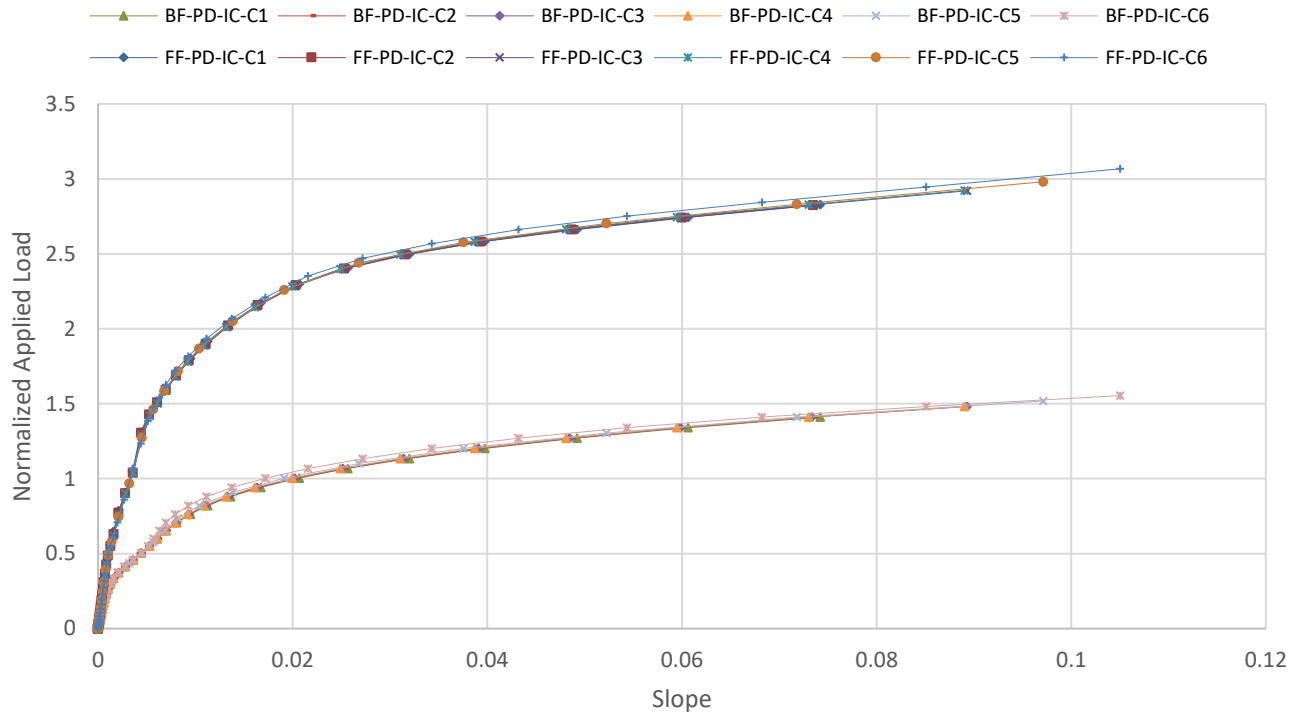


Figure 5-122: Normalized Applied Load vs. Slope for PD-IC Models

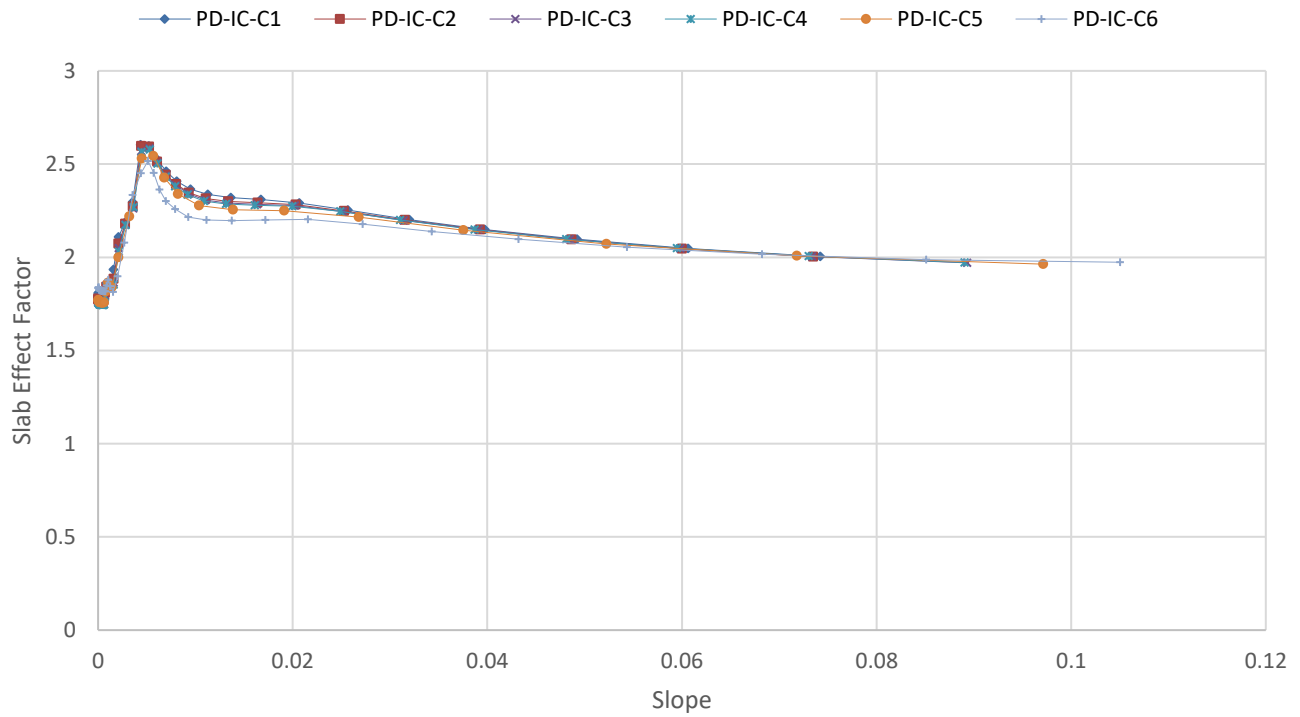


Figure 5-123: Slab Effect Factor for PD-IC Models

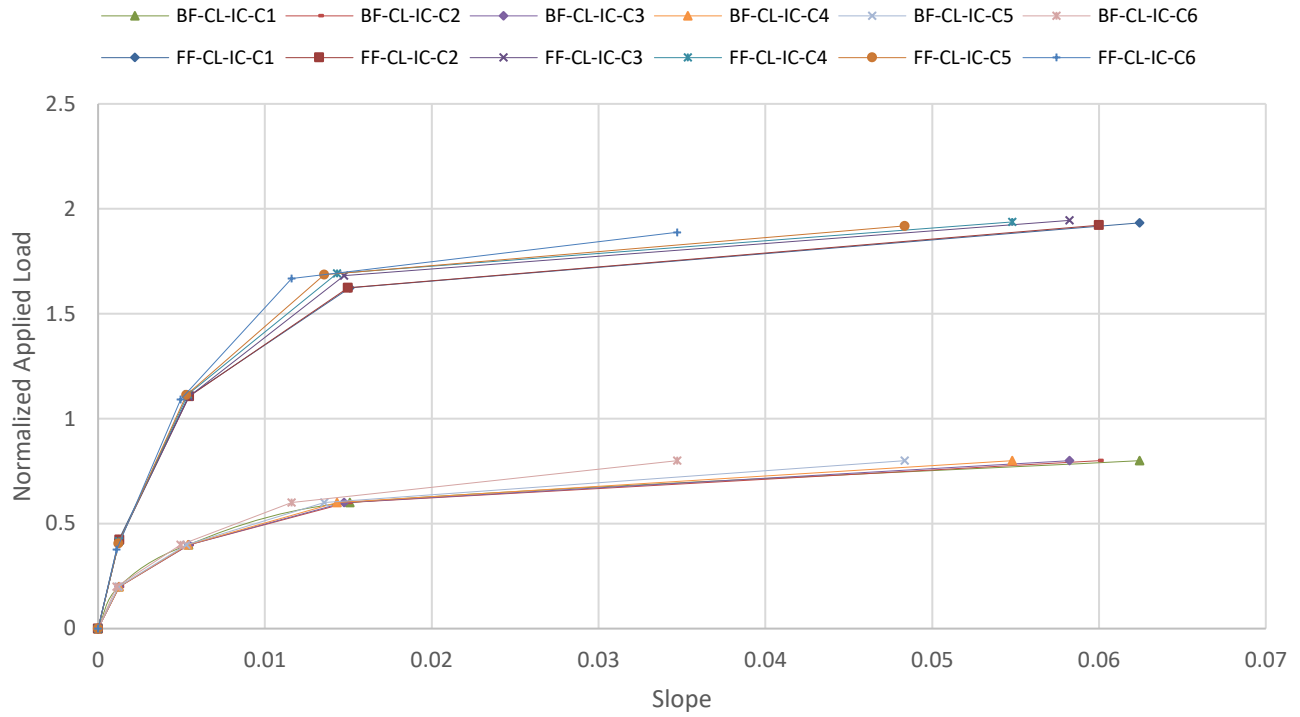


Figure 5-124: Normalized Applied Load vs. Slope for CL-IC Models

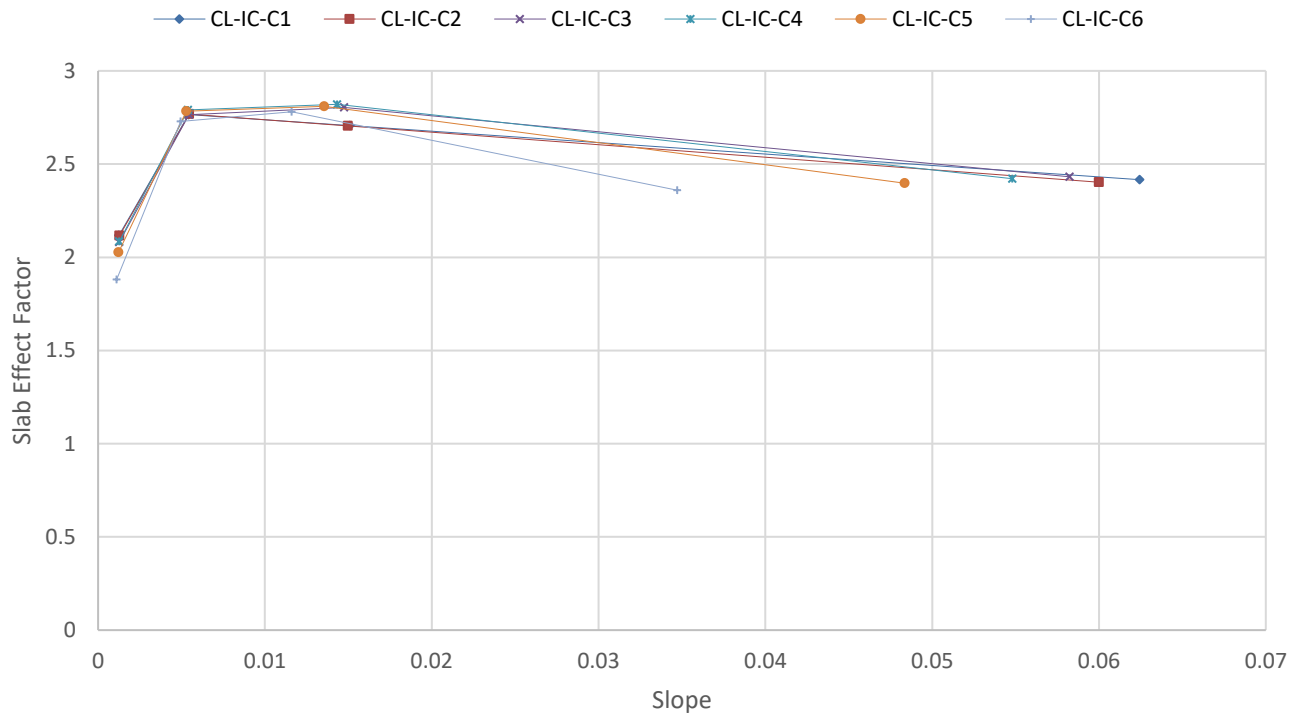


Figure 5-125: Slab Effect Factor for CL-IC Models

Table 5-15: Average Slab Effect Factor Values

Model	Analysis Type	SEF		
		Average	Average ₅ *	Average ₆ **
CC-C1	PD	1.80	1.87	1.96
CC-C2		1.81		
CC-C3		1.88		
CC-C4		1.89		
CC-C5		1.95		
CC-C6		2.44		
CC-C1	CL	3.13	2.61	2.87
CC-C2		2.34		
CC-C3		2.45		
CC-C4		2.46		
CC-C5		2.65		
CC-C6		4.17		
IC-C1	PD	2.17	2.14	2.13
IC-C2		2.17		
IC-C3		2.13		
IC-C4		2.13		
IC-C5		2.09		
IC-C6		2.08		
IC-C1	CL	2.58	2.60	2.60
IC-C2		2.57		
IC-C3		2.62		
IC-C4		2.63		
IC-C5		2.61		
IC-C6		2.57		

* Average is taken for the first 5 floors only, excluding the 6th floor's result.

** Average is taken for all 6 floors.

Table 5-16: Average Simplified Slab Effect Factor Values

Model	Analysis Type	S-SEF		
		Single Value	Average ₅ *	Average ₆ **
CC-C1	PD	1.81	1.84	1.91
CC-C2		1.76		
CC-C3		1.84		
CC-C4		1.84		
CC-C5		1.94		
CC-C6		2.28		
CC-C1	CL	2.00	2.11	2.23
CC-C2		2.00		
CC-C3		2.00		
CC-C4		2.29		
CC-C5		2.29		
CC-C6		2.80		
IC-C1	PD	2.33	2.33	2.31
IC-C2		2.37		
IC-C3		2.29		
IC-C4		2.33		
IC-C5		2.30		
IC-C6		2.25		
IC-C1	CL	3.25	3.50	3.54
IC-C2		3.50		
IC-C3		3.50		
IC-C4		3.50		
IC-C5		3.75		
IC-C6		3.75		

* Average is taken for the first 5 floors only, excluding the 6th floor's result.

** Average is taken for all 6 floors.

5.4.3 COLUMN LOCATION EFFECT

There is no doubt that the location of the removed column plays a part in the progressive collapse response of the structure. To quantify this effect, the force applied on the IC models is divided by that applied on the CC models at the same displacement. The resulting ratio is referred to herein as the Column Location Effect (CLE). The average CLE values for each frame and type of analysis are presented in Table 5-17. It should be noted that the results of the C6 models have been excluded, so the average values are based on the first 5 stories. In general, the numbers confirm the fact that the removal of the corner column is more critical than the removal of the interior column, a logical result that was always expected. However, the difference in load capacity between both cases is not as significant as one might have anticipated. This may be partially attributed to the fact that the corner column is part of the building’s lateral load-resisting system, which leads to more robust dimensioning and detailing of the frame as a whole. Consequently, following column removal, the remaining structure exhibits improved capacity to resist redistributed loads. For full frames, the IC models were able to support 19% and 24% more applied load than the CC models, in the case of PD and CL analyses, respectively. This difference is even less pronounced for bare-frame models as the increase in system load capacity from CC to IC models is 5% and 10% in the case of PD and CL analyses, respectively. It should also be noted that the difference between both column removal scenarios, IC and CC, increases in the case of dynamic analysis or when inertial forces are present.

Table 5-17: Average CLE Values

Frame Type	FF	FF	BF	BF
Analysis Type	PD	CL	PD	CL
CLE Averages ₅	1.19	1.24	1.05	1.10

5.5 MODEL REDUCTION

As demonstrated in Section 5.3.4, the pushdown curves of all six BF-IC models were almost identical. Similar observations were made for the pushdown curves of the FF-IC models as well. The only noticeable difference was the failure points which were slightly shifted from one another. However, by and large, the results were very close, which implied that each floor practically acted independently as the Vierendeel action had little to no effect on the system’s behavior, unlike what was observed in the case of the CC models. Therefore, to confirm this conclusion, two reduced BF models were created and subjected to load-control pushdown analysis, and the results were compared together with the original models. The first model was a single-story structure while the second model was a single-story 2D frame as illustrated in Figure 5-126 and Figure 5-127, respectively. Similar to the original models, only a quarter of the structure was modeled making use of the existing symmetry of the building. The columns were fixed at their bases to account for the stiffness provided by the story below. Table 5-18 shows

the maximum values obtained from the pushdown analysis for both reduced models as well as the BF-IC-C6 and the average values of all six floors and first five floors. First of all, the load-carrying capacity of the reduced models corresponding to the first rebar fracture, was found to be the same at 152% of the design load which was very close to the capacity of BF-IC-C6 which was 155% as well as both average capacity values. On the other hand, the maximum/corresponding displacement was found to be 443 mm and 446 mm respectively for the single-story and the single-frame models. Although not identical, the displacement values are within 4.3% of each other and are comparable to the average values. The displacement of 525 mm of the BF-IC-C6 model may be partially attributed to the fact that it includes the cumulative displacements of the adjacent columns at all six floors. The pushdown curves for the reduced models along with the BF-IC-C6 model are presented in Figure 5-128.

Moreover, as done in Sections 5.3.4 and 5.3.5, two points in the analysis timeline were further examined. The first point corresponded to the first rebar fracture, while the second point was after the damage had progressed. Figure 5-129 to Figure 5-134 show the stresses, strains and displacements in the solid and truss elements of both reduced models. The main things to note from the results were that the fracture occurred in the same location (i.e., the top rebar of the beam at the connection with the adjacent column) as in the original full-story models, after reaching the maximum plastic strain of 0.12. The other thing is that the damage was confined to the beams directly connected to the removed column, which again, was similar to the analysis of the full-story models. Based on these results and observations, it can be concluded that the reduction of the full-story model to a single-story or even a single-story-frame model was an acceptable approximation in the case of BF-IC models. The results confirmed the logical and intuitive hypothesis that due to the regularity and symmetry of the building, each of the beams directly connected to the removed column acted independently in supporting half of the applied load.

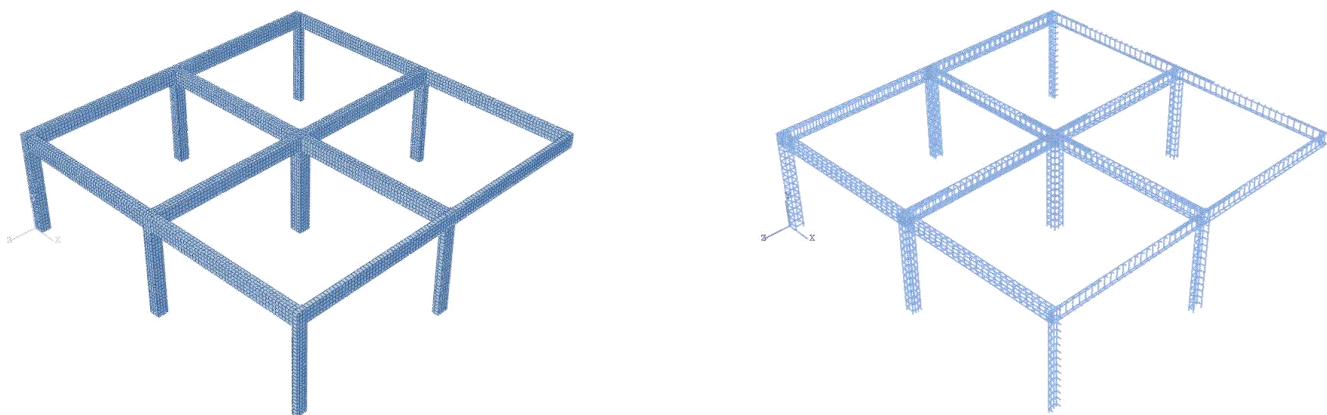


Figure 5-126: Single-Story Reduced BF-IC Abaqus Quarter Model Showing Meshed Solid Elements (Left) & Embedded Rebar (Right)

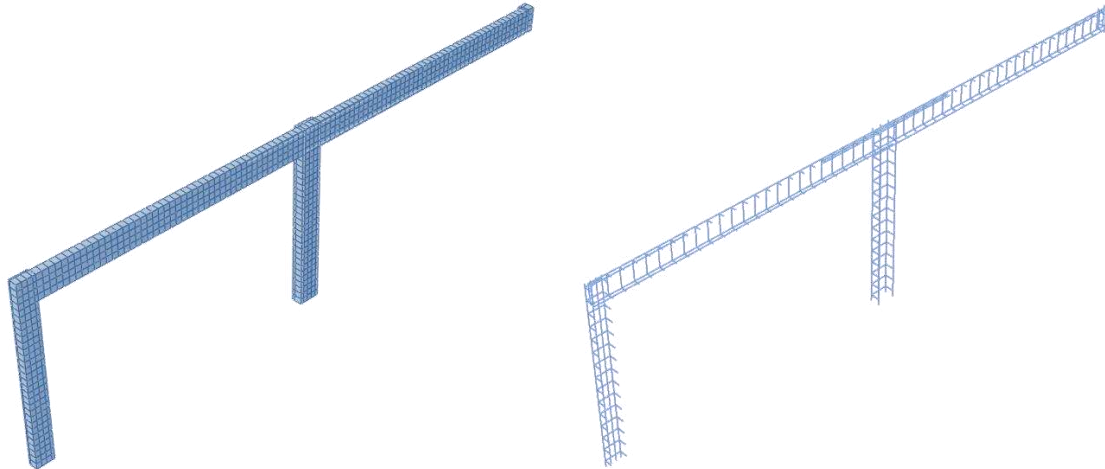


Figure 5-127: Single-Frame Reduced BF-IC Abaqus Quarter Model Showing Meshed Solid Elements (Left) & Embedded Rebar (Right)

Table 5-18: Maximum Pushdown Analysis Values for Original & Reduced BF-IC Models

Model	BF-IC-Avg.5	BF-IC-Avg.6	BF-IC-C6	BF-IC-1ST	BF-IC-1FR
P_{max}	146%	148%	155%	152%	152%
U_{max} (mm)	423	440	525	443	462
S_{max}	8.46%	8.80%	10.50%	8.86%	9.24%

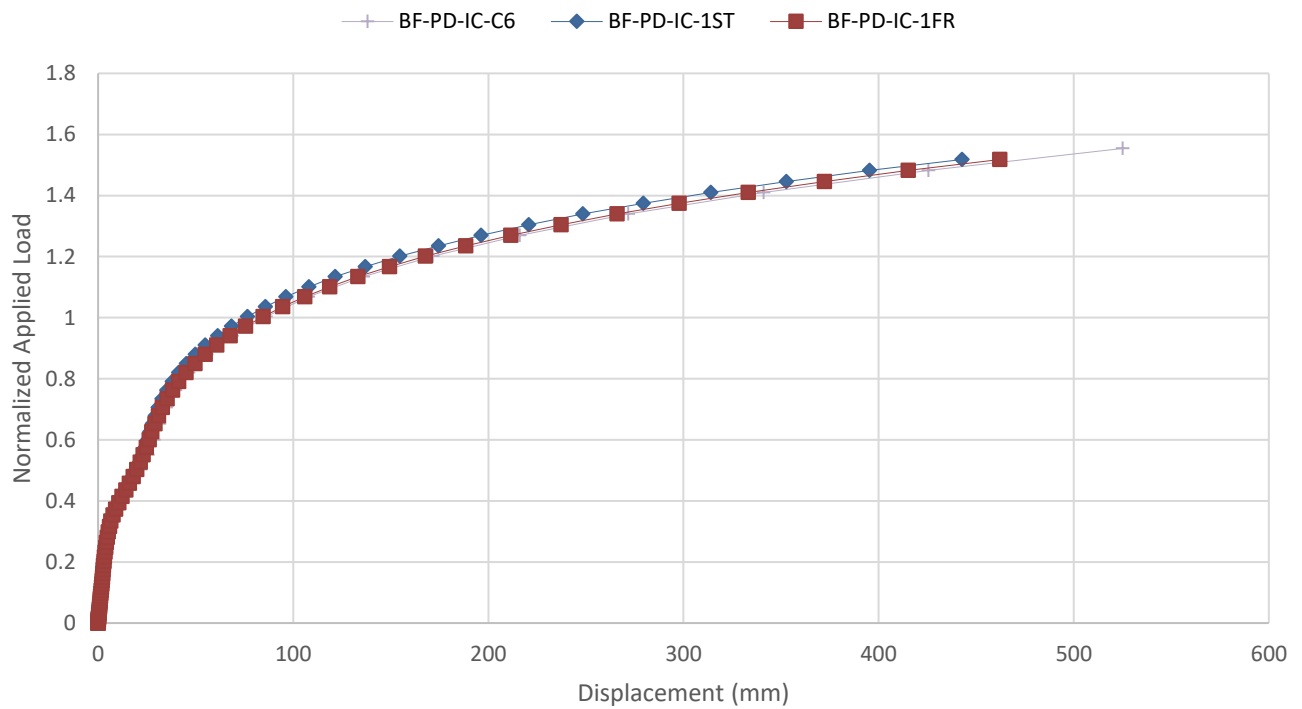


Figure 5-128: Pushdown Curves for BF-PD-IC-C6 & Reduced BF-IC Models

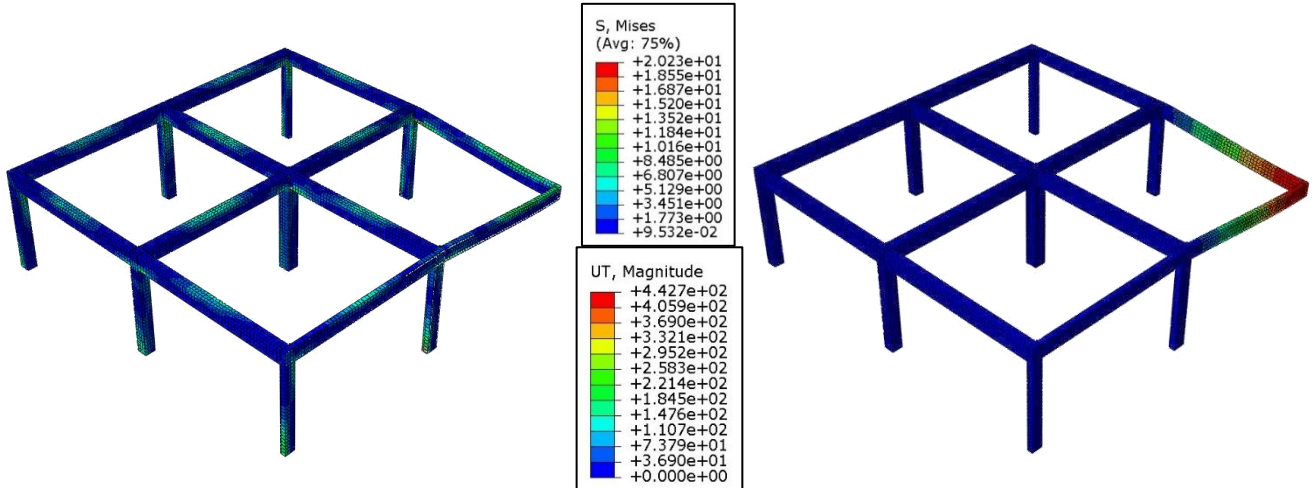


Figure 5-129: Von Mises Stresses (Left) & Total Displacement (Right) in Solid Elements for Single-Story Reduced BF-IC Model Under Pushdown Analysis at 152% Design Load at First Fracture (Quarter Model Shown)

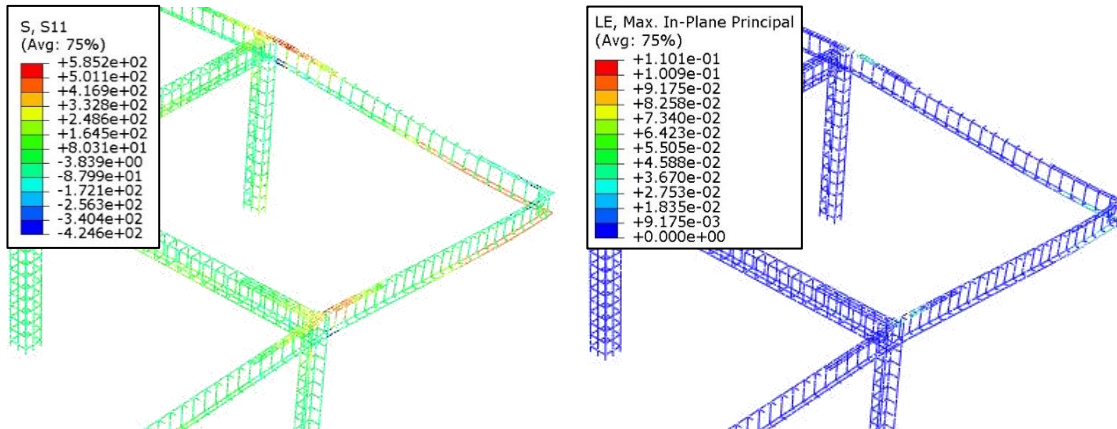


Figure 5-130: S11 Stresses (Left) & Logarithmic Strains (Right) in Truss Elements for the Single-Story Reduced BF-IC Model Under Pushdown Analysis at 152% Design Load at First Fracture

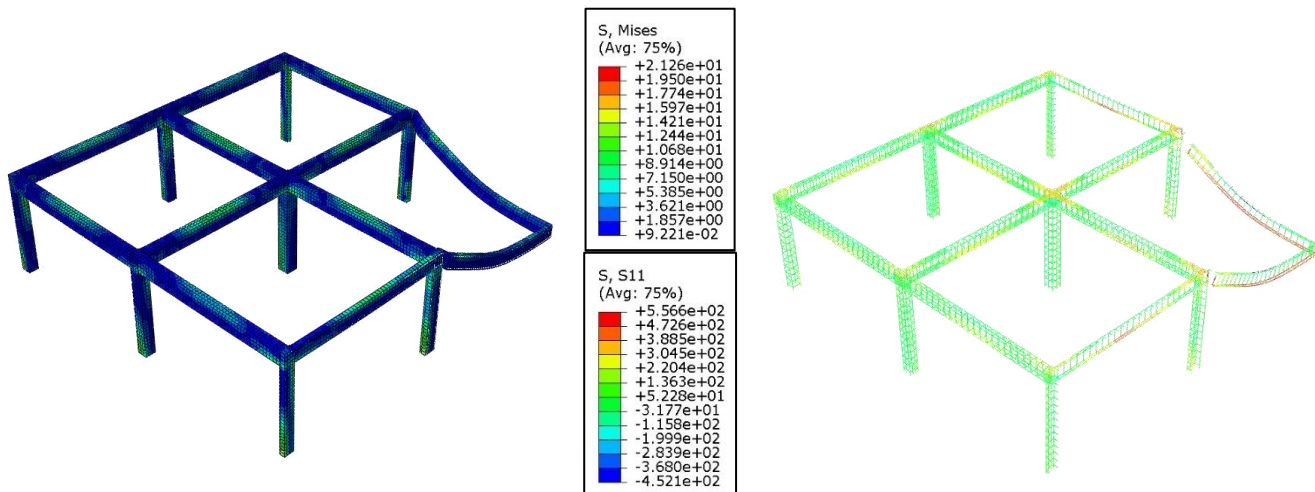


Figure 5-131: Von Mises Stresses in Solid Elements (Left) & S11 Stresses in Truss Elements (Right) for the Single-Story Reduced BF-IC Model Under Pushdown Analysis After Damage Propagation (Quarter Model Shown)

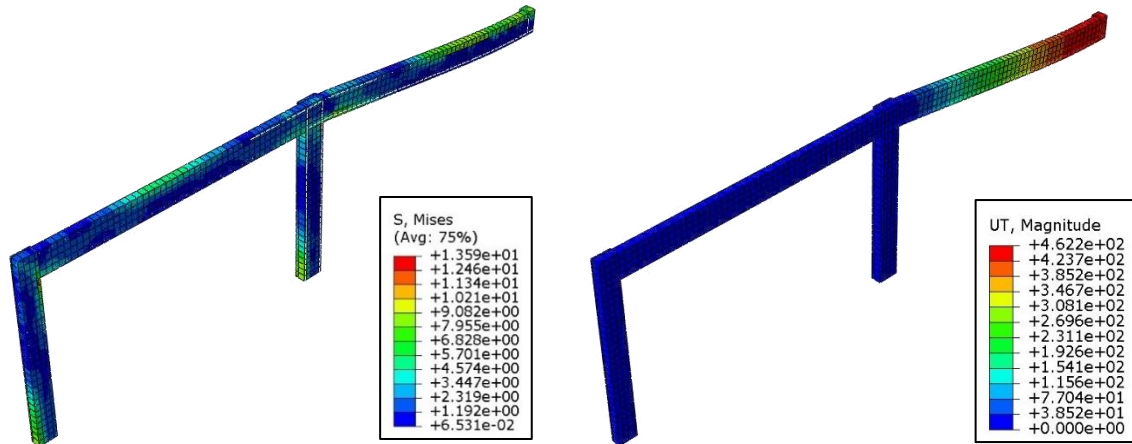


Figure 5-132: Von Mises Stresses (Left) & Total Displacement (Right) in Solid Elements for Single-Frame Reduced BF-IC Model Under Pushdown Analysis at 152% Design Load at First Fracture (Quarter Model Shown)

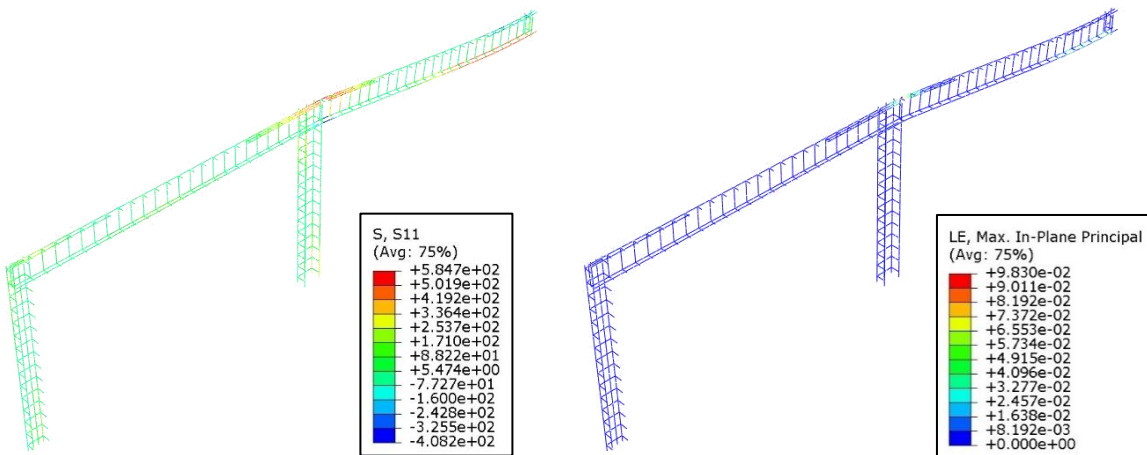


Figure 5-133: S11 Stresses (Left) & Logarithmic Strains (Right) in Truss Elements for the Single-Frame Reduced BF-IC Model Under Pushdown Analysis at 152% Design Load at First Fracture

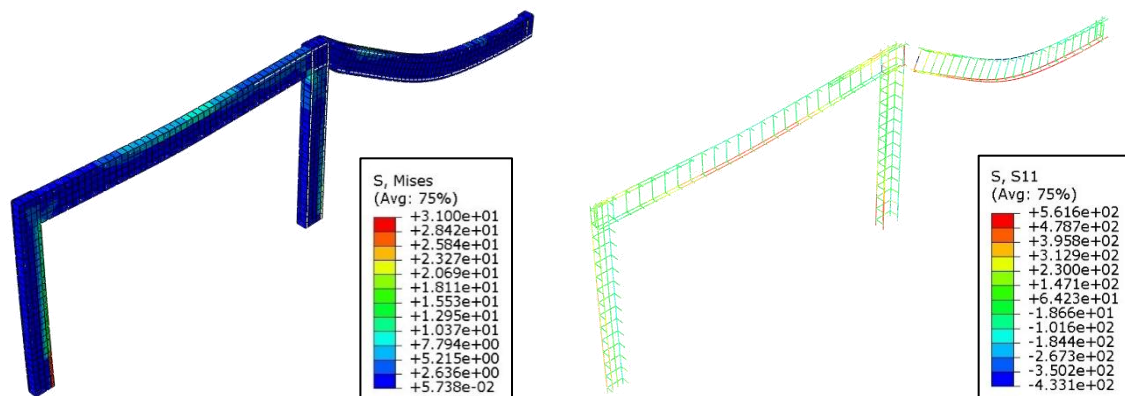


Figure 5-134: Von Mises Stresses in Solid Elements (Left) & S11 Stresses in Truss Elements (Right) for the Single-Frame Reduced BF-IC Model Under Pushdown Analysis After Damage Propagation (Quarter Model Shown)

5.6 DISPLACEMENT-CONTROL PUSHDOWN CURVES

5.6.1 REDUCED SYSTEM PUSHDOWN

As mentioned before, the pushdown curves in Section 5.3.4 were generated using load-control loading and, therefore, are unable to predict the post-peak softening part of the nonlinear response. Instead, the curves exhibit snap-through as previously explained in Section 2.4.1. In this section, an approximate technique is proposed to modify the pushdown curves in order to account for the declining arch action phase as well as the onset of catenary behavior. First, however, a comparison was made between load-control and displacement-control pushdown curves to better understand the differences between both types of curves. To obtain a valid comparison, though, the loading was concentrated at a single point, and no other loads were considered in the analysis, including the self-weight of the system. The chosen model for this study was the reduced single-story 2D bare-frame model from Section 5.5. The concentrated force, in the case of load-control, or the displacement, in the case of displacement-control, was applied at the removed interior column middle joint. The resulting displacement-control pushdown curve, however, was not horizontally restrained enough to produce a post-peak softening response under concentrated point loading. Therefore, the frame was horizontally restrained by pinning the exterior beam-column joint and reanalyzed. The resulting pushdown curve is compared with the original (unrestrained) one in Figure 5-135.

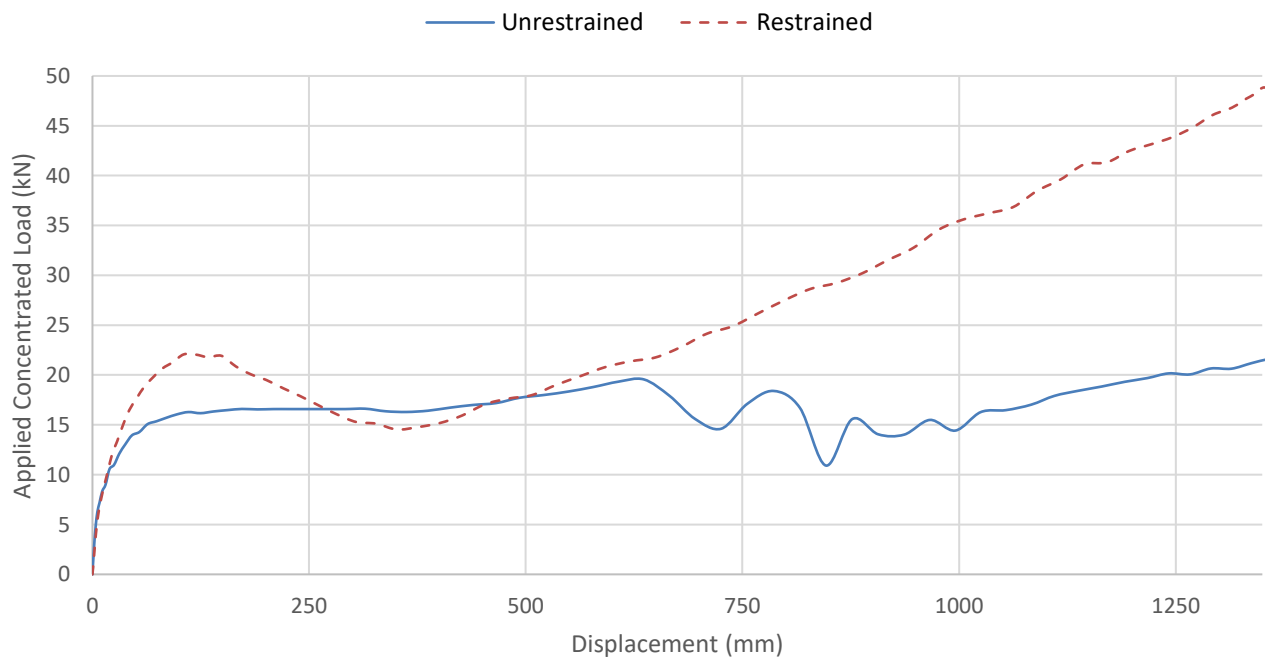


Figure 5-135: Pushdown Curves for Single-Frame Reduced BF-IC Horizontally Unrestrained & Restrained Models Subjected to Concentrated Monotonic Downward Displacement

As evident from the results, the horizontal restraint drastically improves the response of the system. The flexural/arch peak was around 16.6 kN before restraining the horizontal movement, which then led to an increase of around 33% in the peak resistance at a value of 22 kN. Although the load-carrying capacity of the horizontally restrained system did in fact drop below that of the unrestrained system for a short period of time within the displacement range of 282 mm to 453 mm before rising above it again, the overall capacity of the system significantly improved after restraining the horizontal movement of the beams. The maximum load capacity of the system reached 48.6 kN under catenary behavior at a corresponding displacement of 1357 mm, which was 111% times higher than the capacity of the unrestrained system of 23 kN corresponding to a 1452 mm displacement.

Next, a load-control pushdown analysis was conducted using a monotonic concentrated force at the removed column joint, on the horizontally restrained system. As illustrated in Figure 5-136, the resulting curve overlapped with the displacement-control curve up to the first limit point and again after reaching a deflection of 1250 mm or a slope of 0.25. The response, however, differed considerably between those two mentioned points. While this variation was anticipated, as previously discussed in Section 2.4.1, the behavior of the system during the transition phase and in part of the catenary stage was not exactly as expected. The predicted snap-through behavior did not occur in the same usual manner previously explained. Instead of directly skipping the transition phase and the first part of the catenary stage and joining the rising curve in the catenary phase at a load value slightly higher than the flexural/arch peak value, the slope of the force-displacement curve decreased significantly after reaching the first limit point but crossed the rising displacement-control curve and continued beyond it up to a displacement of around 1250 mm, at which point the load capacity increased rapidly, and the curve became almost vertical until finally joining the displacement-control curve. In other words, instead of bypassing the softening stage and snapping through to the rising catenary branch by moving almost horizontally, the force-control curve moved somewhat horizontally then almost vertically then rejoined the other curve. Another peculiar thing was the fact that it took several points to cross over to the rising catenary branch, instead of just one point as forecasted. Further investigation is needed to understand the reasons behind this behavior. Nevertheless, in general, the results highlight the main differences between both types of curves.

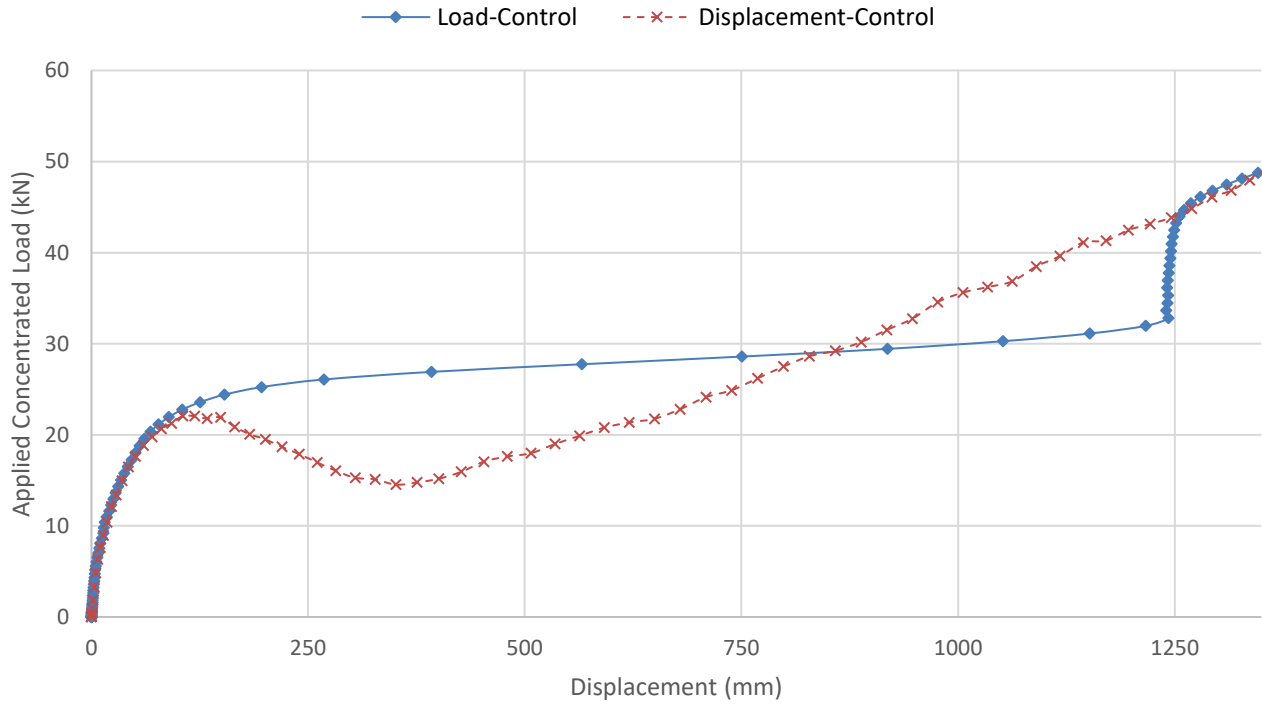


Figure 5-136: Pushdown Curves for Single-Frame Reduced BF-IC Horizontally Restrained Model Subjected to Load-Control & Displacement-Control Loading

5.6.2 ENERGY BALANCE APPROACH

As previously mentioned in Section 1.4.1.2, a method based on the principle of conservation of energy was proposed in [13] and further discussed in [85] to predict the dynamic response of structural systems subjected to column loss using their nonlinear static response. The sudden removal of a column is equivalent to the sudden application of the gravity load that was supported by that column. The external work done by this dynamic gravity load is equal to the internal strain energy absorbed by the system at the maximum dynamic deformation response (u_d) after vibration has subsided and equilibrium has been reached. Furthermore, the loss of a column will most likely result in large deformations, and the dynamic response will be dominated by a single deformation mode. Consequently, the maximum dynamic deformation (u_d) can be estimated accurately enough from the nonlinear static response of the structure under amplified static loading ($\lambda_d P_0$). Figure 5-137 shows two levels of suddenly applied gravity loading, P_1 and P_2 , and their corresponding maximum dynamic displacement, $u_{d,1}$ and $u_{d,2}$, respectively. Therefore, at any analysis point (n), according to the previously discussed energy balance concept, the following may be deduced:

$$W_n = P_n u_{d,n}$$

$$U_n = \int_0^{u_{d,n}} \lambda_n P_n du$$

$$\rightarrow P_n u_{d,n} = \int_0^{u_{d,n}} \lambda_n P_n du$$

where P_n = Suddenly applied gravity load at analysis point n ,

$u_{d,n}$ = Corresponding maximum dynamic displacement at analysis point n ,

W_n = Work done by external forces at analysis point n ,

U_n = Strain energy absorbed by the system at analysis point n ,

λ_n = Ratio between the nonlinear static force and the dynamic force corresponding to $u_{d,n}$ (i.e., dynamic increase factor) at analysis point n .

Therefore, the hatched rectangular area representing the external work done by the applied gravity load P_n equals the hatched area under the nonlinear static curve, which represents the strain energy absorbed due to nonlinear dynamic deformation. Given the nonlinear static response curve, at any point n , the displacement $u_{d,n}$ may be easily used to calculate the applied gravity load P_n . By varying the values of $u_{d,n}$ and recording each corresponding P_n , the curve depicted in Figure 5-138 can be plotted. As discussed in Section 5.3.5, this kind of curve is referred to as the pseudo-static response and directly relates the suddenly applied gravity load to the maximum dynamic displacement.

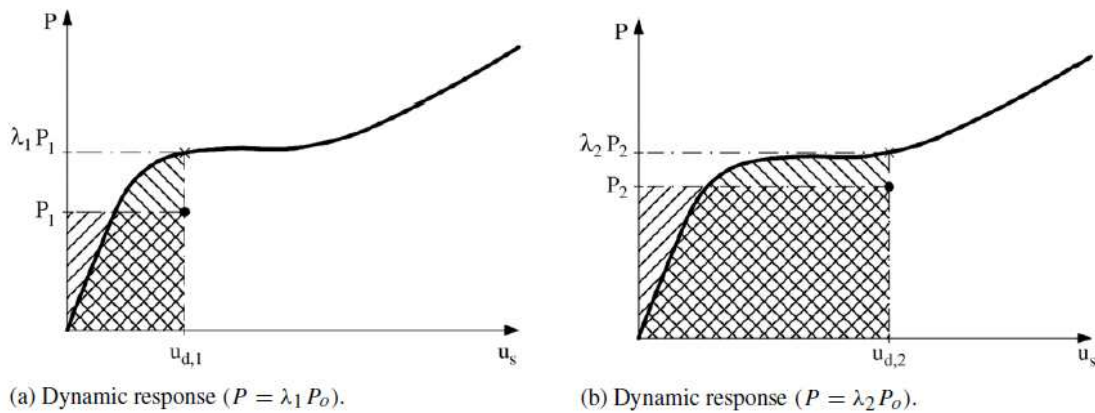


Figure 5-137: Dynamic Response at Two Various Levels of Suddenly Applied Gravity Loading [13]

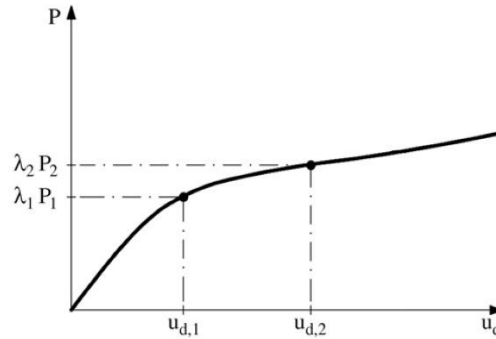


Figure 5-138: Pseudo-Static Response [13]

To test the validity of the proposed method, the pseudo-static response was generated for the horizontally restrained single-frame reduced BF-IC model using dynamic column removal analysis. It is worth noting that since the applied load is concentrated at a single point, at the removed column location, the simulation of the column removal becomes very straightforward. Simply by suddenly applying the value of the (dynamic) force at the point of application, the column removal scenario may be accurately depicted. In this situation, the two methods explained earlier in Section 0 become the same. This is because the force is directly applied to the column, therefore, the reaction of the column is equal to the force. So, the sudden removal of the column is equivalent to the sudden application of the force. Then using the proposed method, two pseudo-static curves were generated from the displacement-control and load-control pushdown curves. The curves were compared together (Figure 5-139), and a few things were concluded. The generated curves and the original one were very similar up to a deflection of around 150 mm or a slope of 3%. Then the curve generated from the load-control pushdown curve started to deviate from the other two curves. On the other hand, the curve generated from the displacement-control pushdown curve seemed to match the original curve better. The main difference is that the DC-PD-generated curve began softening after reaching a displacement of 220 mm. However, the original pseudo-static curve jumped (snapped) between the two highlighted points on the graph. This snap-through effect occurred between a displacement of 181 mm and 720 mm, which corresponded to an applied concentrated force of 18.8 kN and 18.9 kN, respectively. This behavior is attributed to the fact that up to 18.8 kN, the system is in equilibrium under the flexural/arch mechanism. However, at 18.9 kN, the system had to move into the catenary stage to find equilibrium, as the system's maximum load-carrying capacity in the compressive arch stage was exceeded. However, it may be concluded that the pseudo-static response curve generated from the displacement-control pushdown curve gives an acceptable approximation of the actual dynamic response, especially since the maximum difference between both curves was found to be under 9% at a displacement of 453 mm and 1090 mm. It should

be noted, though, that the generated curve must be adjusted so as to not allow any softening of the response (i.e., negative stiffness).

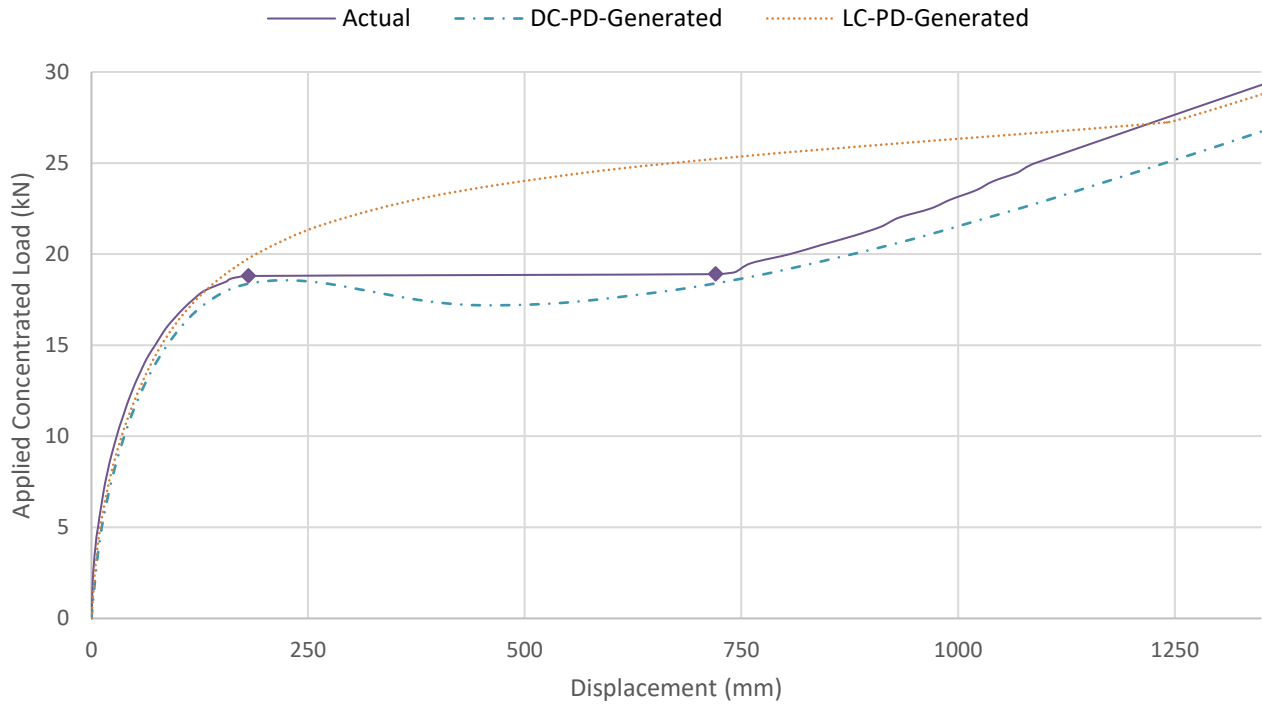


Figure 5-139: Actual vs. Generated Pseudo Static Curves for Single-Frame Reduced BF-IC Horizontally Restrained Model

5.6.3 REVERSE ENERGY BALANCE APPROACH

Based on the previous conclusion, the described energy balance method may, in theory, be used in reverse to derive the displacement-control pushdown curves. Therefore, given the actual pseudo-static response shown in Figure 5-139, an attempt was made to predict the corresponding nonlinear static curve. To obtain the pushdown load values at any given displacement, the original equation mentioned in Section 5.6.2 was differentiated with respect to the displacement u , leading to the following expression:

$$\lambda_n P_n = P_n + \frac{dP_n}{du} u_{d,n}$$

By applying the reverse equation to the actual dynamic response values, the curve shown in Figure 5-140 was created. However, as evident from the graph, the curve is only accurate up to the limit point, beyond which it deviates significantly and cannot be used as a means to predict the nonlinear static behavior of the system. This, of course, is due primarily to the fact that, as previously shown in Figure 5-139, the differences between the actual pseudo-static curve and the one generated from the displacement-control pushdown curve were minor up to the

limit point and then began increasing after that. The energy balance method is an approximate method, and therefore, its reverse implementation might produce incorrect results. Another thing to be noticed is the fact that the produced (reverse) pushdown curve is coarse and not smooth containing noise, especially as the displacement increases. This may be partly attributed to the fact that the curve is treated as linear between its main points, which each represents a column loss scenario with a different applied load. Adding more points by running more analysis cases might help improve the quality of the curve and make it smoother. Overall, while the method did not produce the required quality, it can be seen that the resulting curve follows a somewhat similar pattern as the original one, it just needs smoothing.

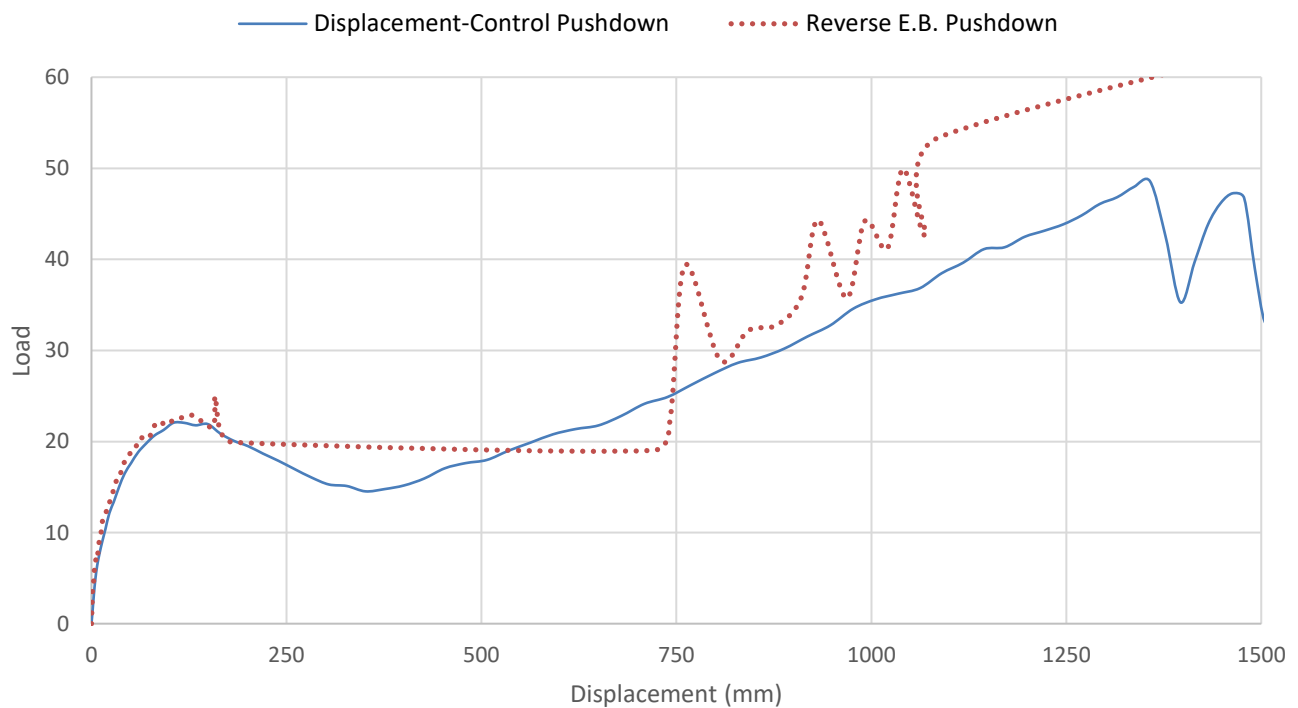


Figure 5-140: Pushdown Curve Generated from Reverse Energy Balance Method vs. Displacement-Control Pushdown Curve for Single-Frame Reduced BF-IC Horizontally Restrained Model

5.6.4 METHOD IMPLEMENTATION ON CASE STUDY

Since the pushdown curves generated in Section 5.3.4 were load-control curves, they did not show the first limit point of the nonlinear static response. Therefore, the reverse energy balance approach was used to estimate the limit point and the start of the transition phase. The actual pseudo-static curves reported in Section 5.3.5 were used to predict the nonlinear static curves. This was done for the full-frame and bare-frame models under corner column and interior column removal for C3 and C6. The reason C3 and C6 were chosen is because the first represents an intermediate floor with multi-story or Vierendeel effect, while the latter represents a single story

without any such effects. However, in order to calculate the pushdown load values, more points were needed as the curves produced by the available points were very coarse and noisy. So, additional column loss analysis was conducted on the mentioned models and the refined pseudo-static curves are shown in Figure 5-141. Then, by implementing the reverse energy balance method, approximate displacement-control pushdown curves were generated and compared with the previous load-control pushdown curves from Section 5.3.4 in Figure 5-142 to Figure 5-149. It should be noted that not all curves behaved as expected. It was anticipated that both curves, displacement-control and load-control, would have an almost identical first branch up to the limit point, beyond which they would start to deviate as previously explained. However, this was not the case in many of the generated curves. Again, this was mainly attributed to the fact that the energy balance method is approximate, and as the behavior of the structure becomes more complicated, the accuracy of the method is expected to drop. Finally, a comparison was made between the average DIF values (λ) deduced from the projected curves and the original ones calculated in Section 5.4.1, as shown in Table 5-19. The values were also compared with the GSA/UFC prescribed DIFs. It can be seen that the DIF values of the displacement-control projected curves for the bare-frame models are more consistent with the full-frame models, as the maximum variation between both models in terms of DIF was found to be 5.5%. This of course is contrasted with the DIF values obtained from the load-control pushdown where the bare frame results were too high compared to the full frame results, reaching a maximum difference of 51.8%.

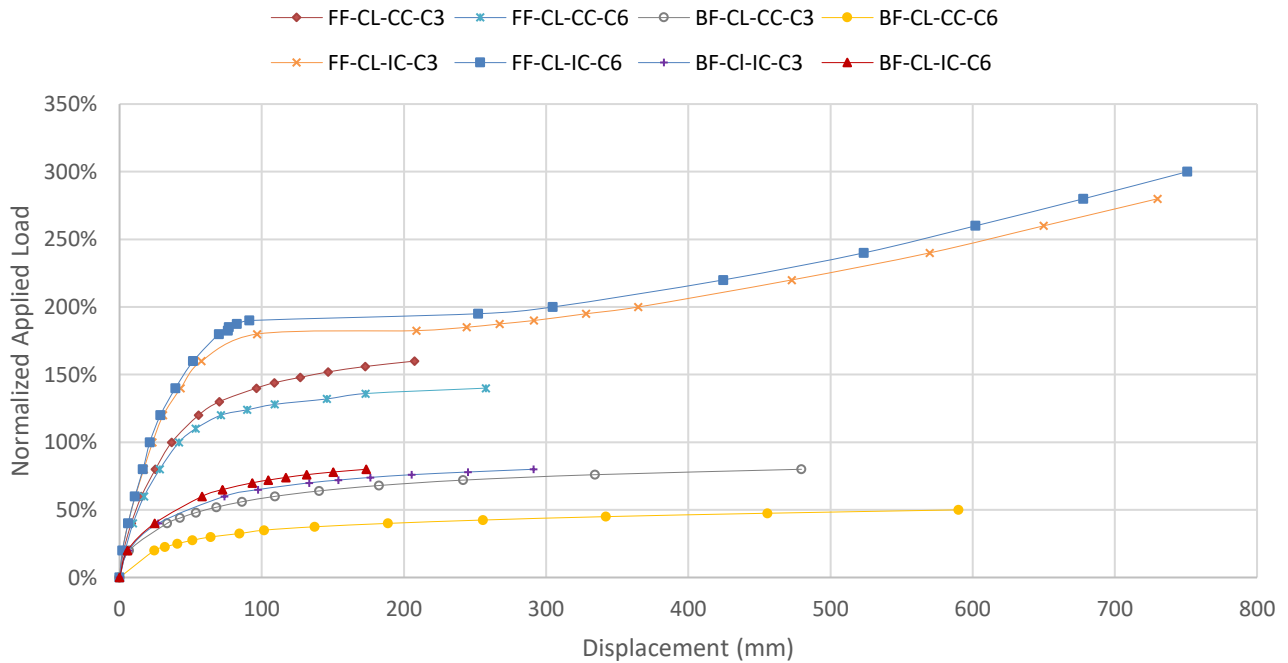


Figure 5-141: Refined Pseudo-Static Curves

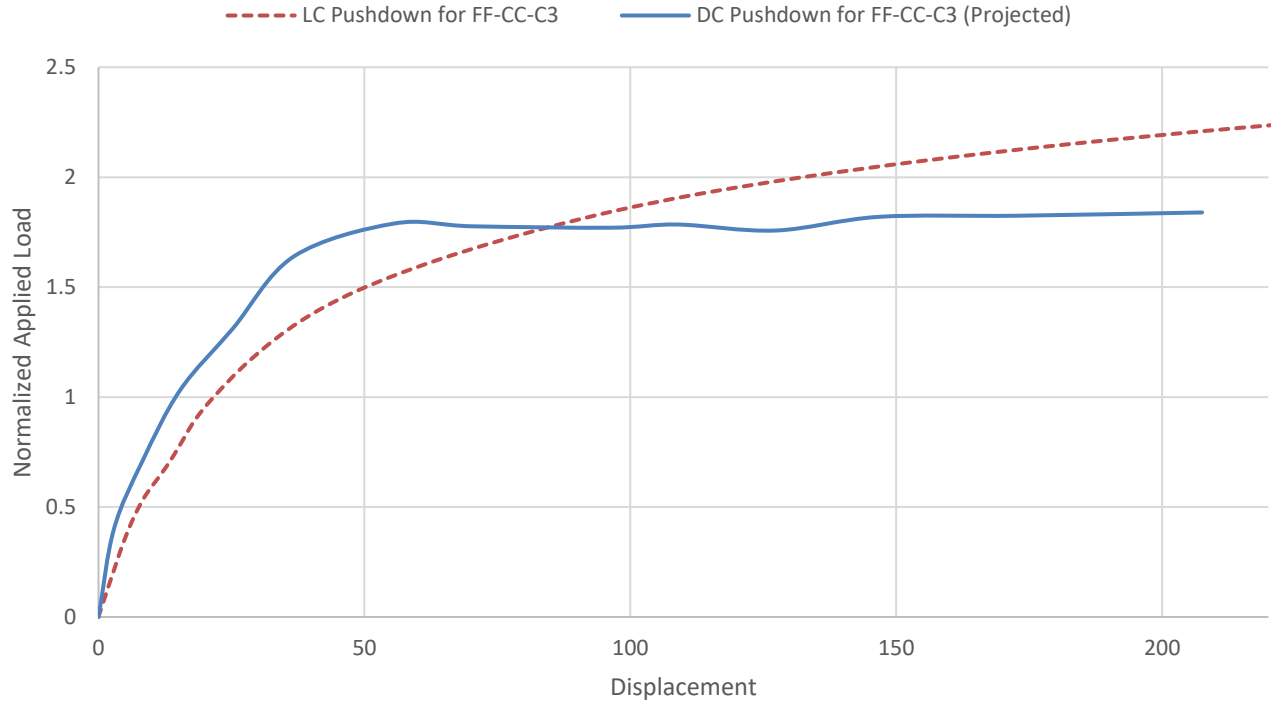


Figure 5-142: Load-Control vs. Displacement-Control (Projected) Pushdown Curves for FF-CC-C3

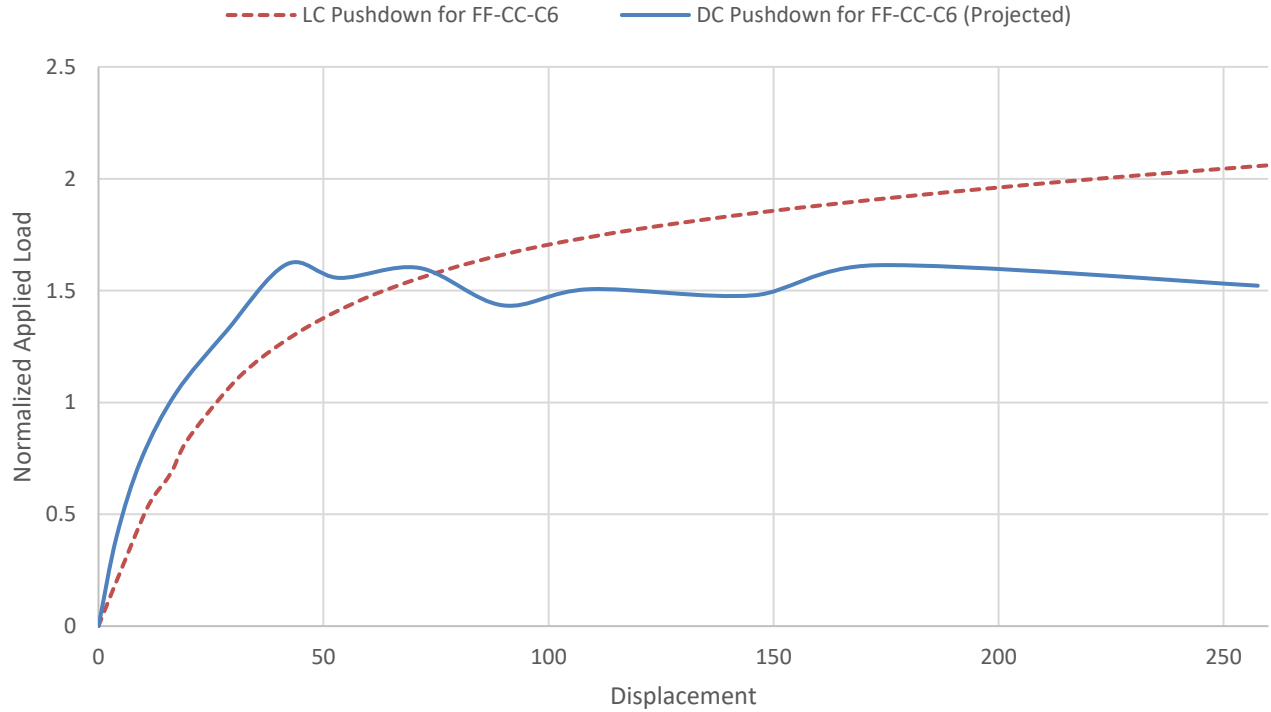


Figure 5-143: Load-Control vs. Displacement-Control (Projected) Pushdown Curves for FF-CC-C6

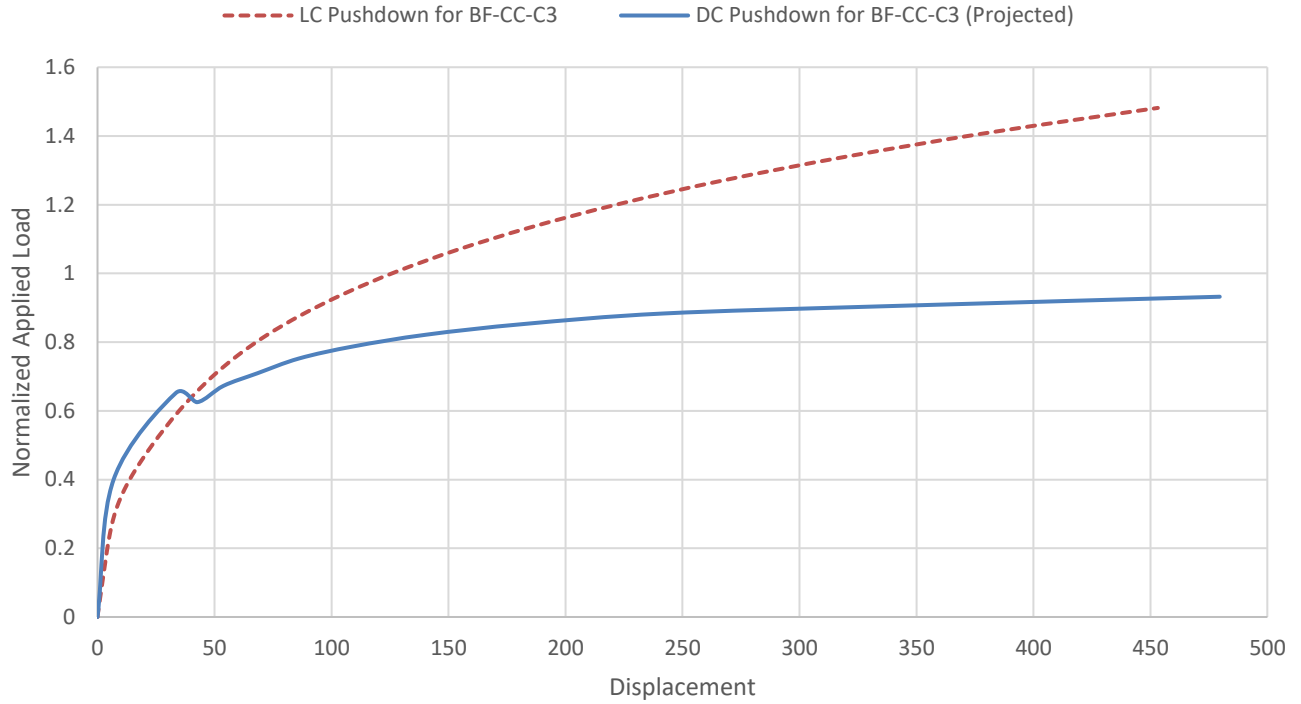


Figure 5-144: Load-Control vs. Displacement-Control (Projected) Pushdown Curves for BF-CC-C3

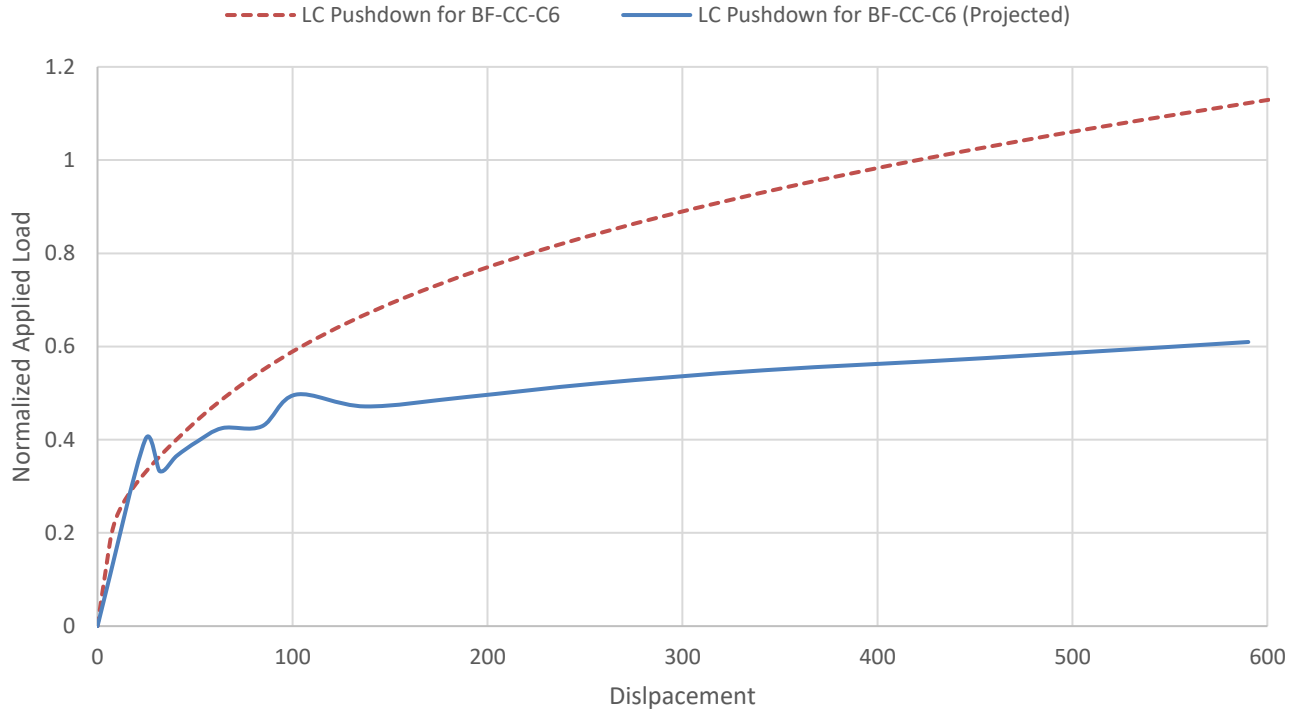


Figure 5-145: Load-Control vs. Displacement-Control (Projected) Pushdown Curves for BF-CC-C6

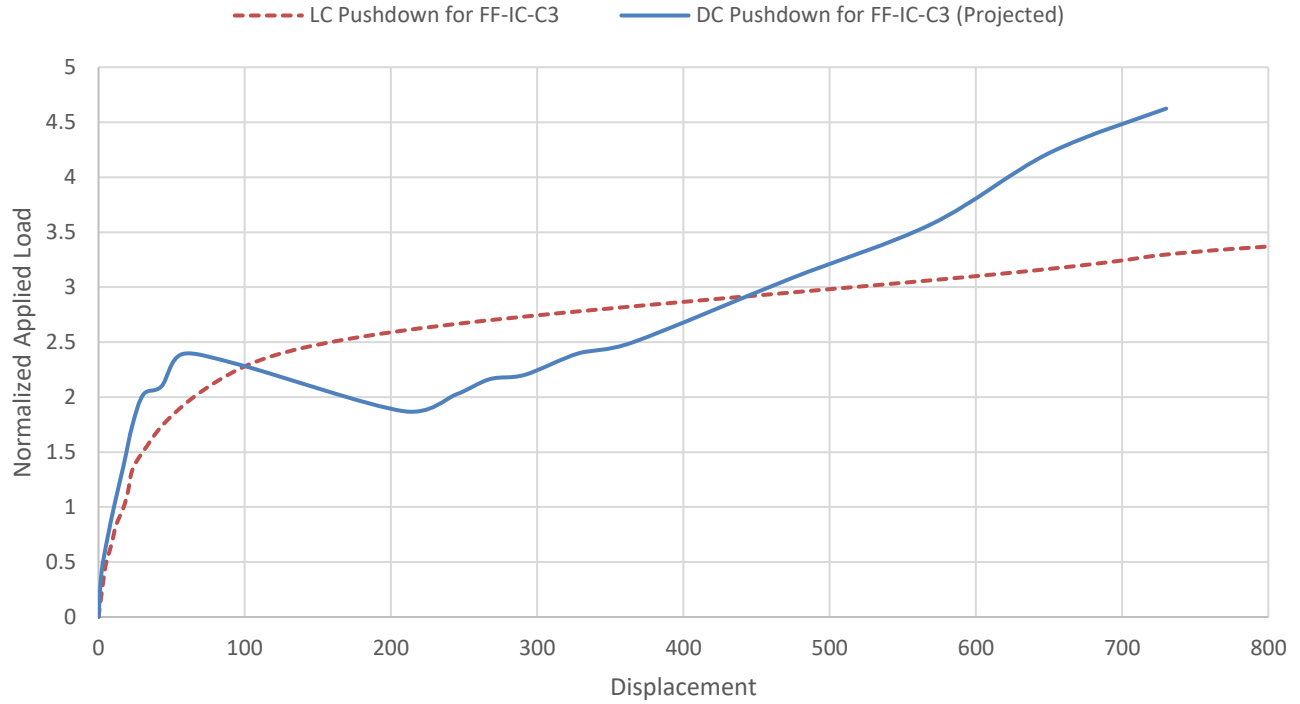


Figure 5-146: Load-Control vs. Displacement-Control (Projected) Pushdown Curves for FF-IC-C3

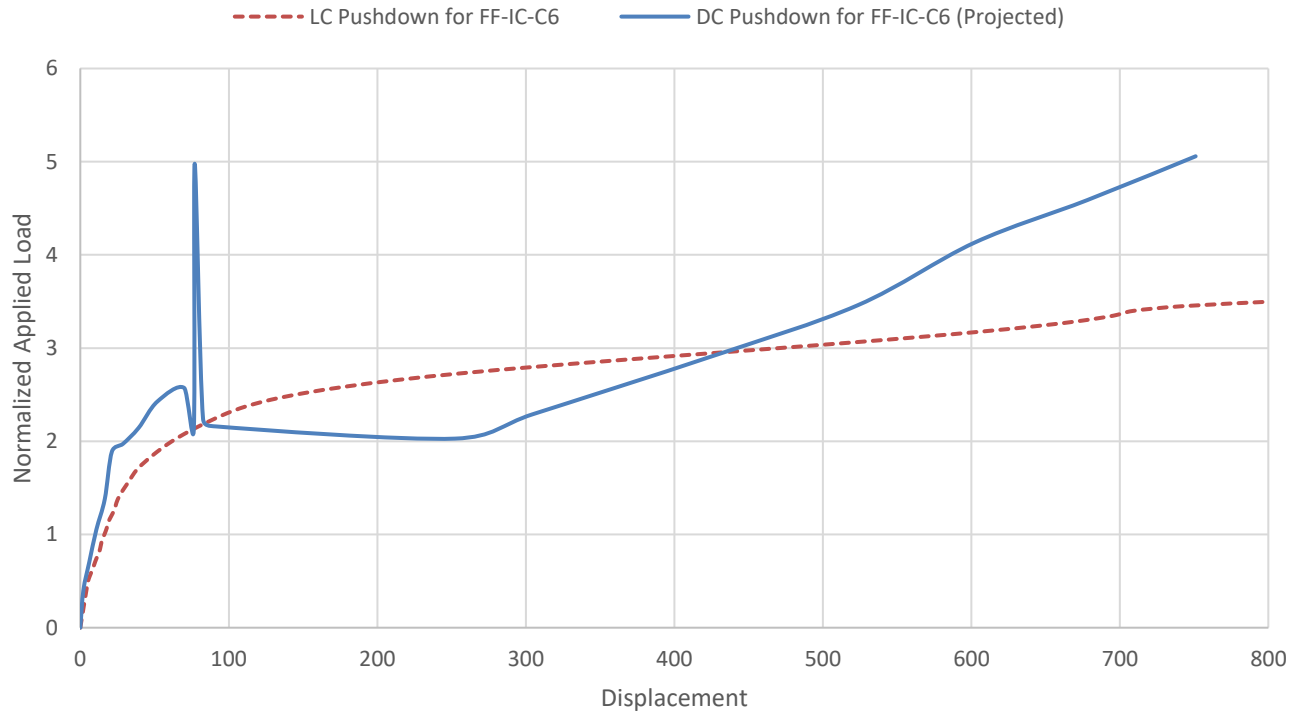


Figure 5-147: Load-Control vs. Displacement-Control (Projected) Pushdown Curves for FF-IC-C6

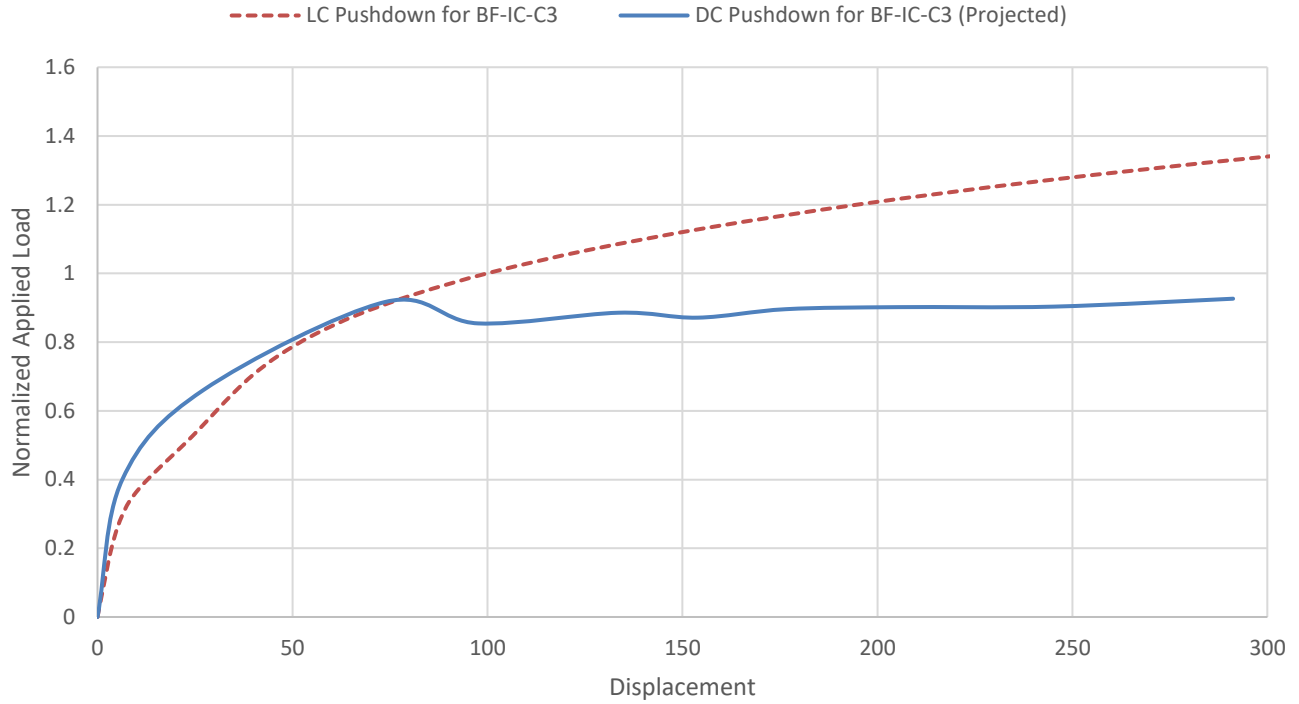


Figure 5-148: Load-Control vs. Displacement-Control (Projected) Pushdown Curves for BF-IC-C3

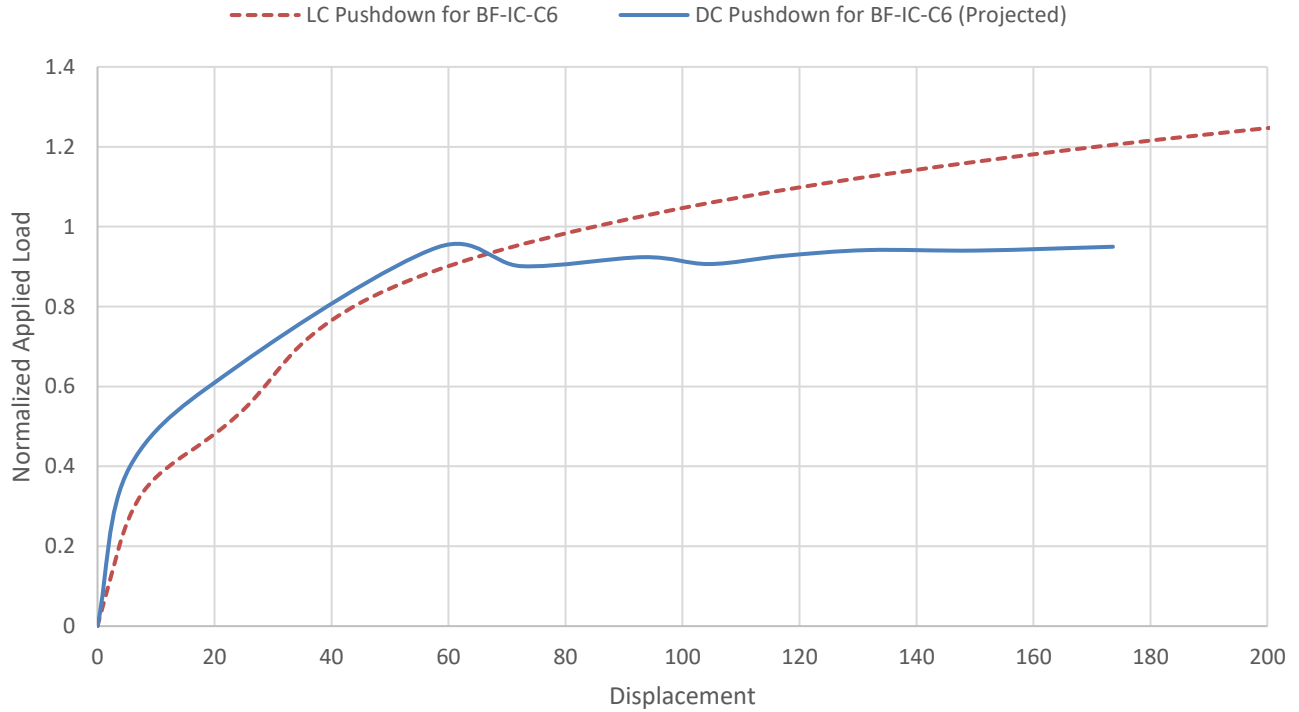


Figure 5-149: Load-Control vs. Displacement-Control (Projected) Pushdown Curves for BF-IC-C6

Table 5-19: Comparison of DIF Values

PD Type	Model							
	FF-CC-C3	FF-CC-C6	BF-CC-C3	BF-CC-C6	FF-IC-C3	FF-IC-C6	BF-IC-C3	BF-IC-C6
Load-Control	1.34	1.37	1.77	2.08	1.32	1.29	1.62	1.52
Displacement-Control	1.34	1.27	1.27	1.25	1.36	1.36	1.33	1.40
GSA/UFC	1.16	1.12	1.16	1.12	1.18	1.18	1.18	1.18

5.7 SUMMARY & CONCLUSIONS

This chapter presented a comprehensive nonlinear analysis of a six-story reinforced concrete (RC) case study building subjected to sudden column removal scenarios. The building was analyzed under both static and dynamic conditions using full-frame and bare-frame models, with interior and corner column removal considered at each story. The key findings and observations may be summarized as follows:

- The removal of columns from the first five stories produced similar results, especially in the case of the IC models. The sixth floor’s results were generally different and tended to deviate from the other five floors. This was most evident in the case of the CC models and may be attributed to the lack of Vierendeel action in the sixth-floor models, which had a great effect on the response. It should be noted, though, that the Vierendeel action was not that critical to the response of the IC models, as each floor practically acted independently. So, to get a more meaningful comparison of the results, the average load capacity of the first five floors has been computed and plotted in Figure 5-150. Of course, the pseudo-static force was used in the case of CL analysis.

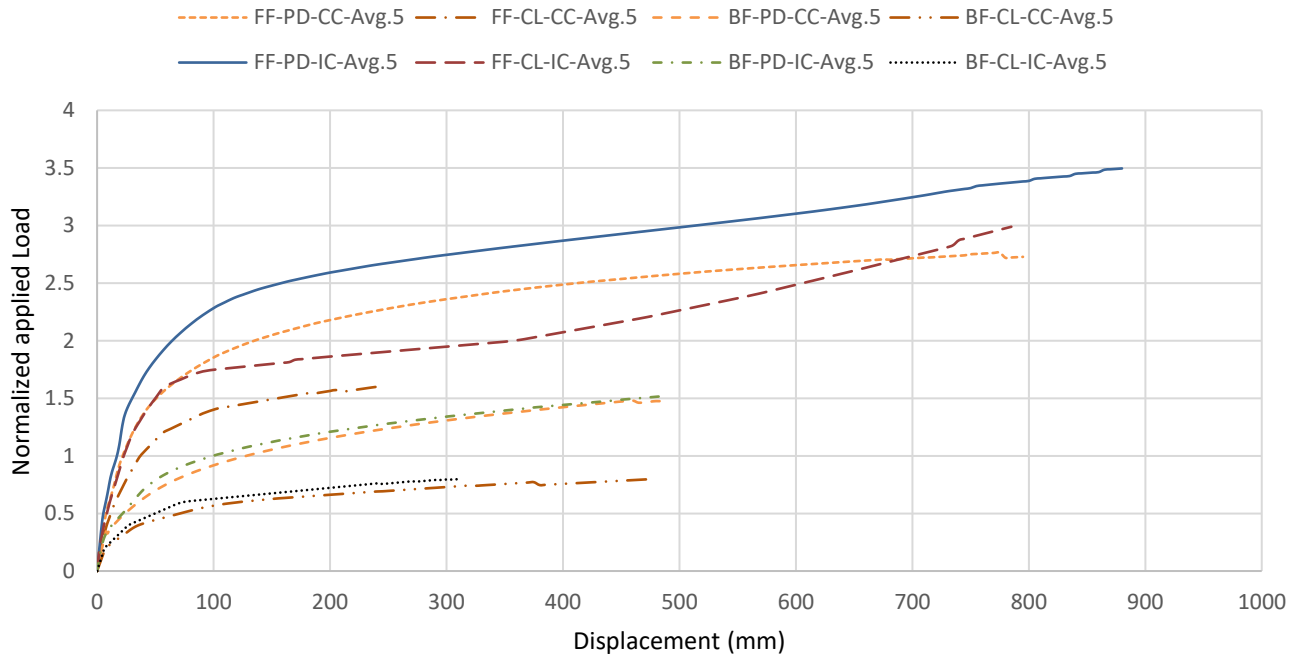


Figure 5-150: Average Normalized Load-Displacement Curves for All Models

- The most accurate depiction of column removal scenarios is achieved using nonlinear dynamic analysis on full-frame models, where the slab membrane effect is accounted for. Therefore, it can be confidently concluded that the case study building is well designed against progressive collapse according to the APM. This is because the (average) failure load or loading capacity of the system well exceeded the progressive collapse design load combination (1.2 D + 0.5 L) for interior and corner column removal scenarios. In fact, the average loading capacity obtained from the pushdown analysis on bare-frame models was also higher than the prescribed design load. The only case where the building failed to reach the target design load level was in the case of bare frames under dynamic column loss. This, of course, is an extreme case where the inertial forces are considered while the membrane action is neglected. Table 5-20 summarizes the average load capacities of all model systems along with their corresponding displacements and safety status.

Table 5-20: Average Load Capacities & Corresponding Displacements

Frame Type	Analysis Type	Removed Column	Normalized Load Capacity	Absolute Load Capacity* (kPa)	Corresponding Displacement (mm)	Safety Status According to APM	Type of Progressive Collapse
FF	PD	CC	2.77	15.57	775	Safe	Full
FF	CL	CC	1.60	9.00	240	Safe	Full
BF	PD	CC	1.48	8.33	460	Safe	Partial
BF	CL	CC	0.80	4.49	475	Unsafe	Partial
FF	PD	IC	3.50	19.68	880	Safe	Partial
FF	CL	IC	2.99	16.83	785	Safe	Partial
BF	PD	IC	1.52	8.54	485	Safe	Partial
BF	CL	IC	0.80	4.49	310	Unsafe	Partial

* Total applied slab load including finishing and live loads as well as own weight of slab.

- Under the maximum applied (failure) load, the full-frame models subjected to the removal of their interior columns suffered a full progressive collapse as the redistributed loads resulting from the failure of the beams connected to the removed columns were too much to resist by the adjacent columns at the first-floor/ground-floor level. These columns, in turn, failed, which caused the columns adjacent to them to fail as well. In the end, all the columns in the first/ground floor failed, and the whole structure collapsed. On the other hand, the other models suffered a partial progressive collapse, where the beams and slabs connected to the removed columns collapsed along with those located in the stories above. So, the damage in these cases was localized to the bay or panel in question. Of course, the impact of this collapse on the immediate bottom floor was not studied and may have led to further collapse of the structure. The type of collapse of each model is summarized in Table 5-20.

- An arbitrary visual comparison is made between the dynamic response of the bare frame (BF) and full frame (FF) for the IC and CC models in Figure 5-151. This comparison is done for the C1 models under sudden column loss at 40% design load level. Obviously, these results were shown in the previous sections, however, the aim here is to gauge an idea on how different the dynamic responses of the models are. So, the figure confirms the fact that under a constant load, FF models exhibit significantly less deformation than BF models, and that IC models suffer slightly less deformation than CC models.

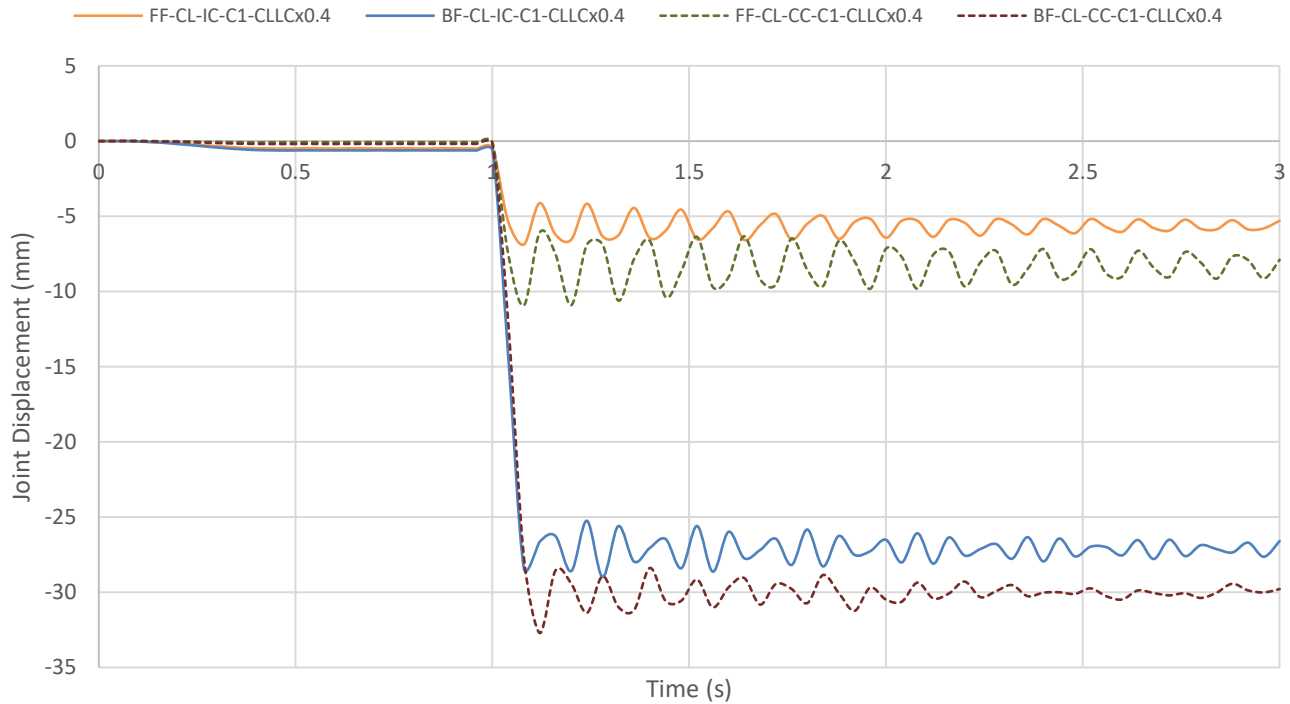


Figure 5-151: Joint Displacements for C1 Models Under Sudden Column Loss at 40% Design Load

- Dynamic Increase Factors were calculated to assess the amplification of demands on structural elements resulting from the dynamic nature of sudden column removal. Average DIF values of approximately 1.33 for full-frame models and 1.67 for bare-frame models were obtained, both exceeding the reference value of 1.17 recommended by the GSA and UFC guidelines, indicating a more critical dynamic response in the case study building.
- The influence of slab action on structural robustness was quantified by comparing the responses of full-frame and bare-frame models. Load-carrying capacity improvements ranging from 87% to 114% under quasi-static analysis and from 160% to 187% under dynamic analysis were observed, emphasizing the critical role of slab membrane action in enhancing resistance to progressive collapse, particularly under dynamic loading.

- The Column Location Effect, defined as the ratio between the load capacities of interior and corner column removal scenarios, was used to assess the influence of column position on collapse resistance. IC models exhibited 19% to 24% higher capacity than CC models in full-frame analyses and 5% to 10% higher in bare-frame models, with the disparity increasing under dynamic loading.
- The nearly identical pushdown curves across all BF-IC models confirmed that each floor behaved independently due to the absence of Vierendeel action. This was validated by comparing the full-story results with two reduced models: a single-story model and a 2D frame model. Both produced nearly the same load capacity and failure mode. Fracture occurred at the same location, and damage remained confined to the directly connected beams, confirming that model reduction to a single story or frame is a valid and accurate approximation for BF-IC scenarios. Although not explicitly analyzed, a similar single-story reduction is expected to hold for FF-IC models due to the system's symmetry and limited inter-story interaction.
- To overcome the limitations of load-control pushdown analysis in capturing post-peak softening and the onset of catenary behavior, an approximate transformation based on energy conservation was proposed to generate equivalent displacement-control pushdown curves using the pseudo-static curves. This approach was implemented on the case study's full-frame and bare-frame models under interior and corner column removal for floors C3 and C6, representing respectively an intermediate level with multi-story interaction and a top floor with single-story behavior.

6. SIMPLIFIED METHOD FOR FLEXURAL/ARCH CAPACITY ESTIMATION UNDER COLUMN LOSS

6.1 INTRODUCTION

As previously discussed in Section 2.6, there are several resistance mechanisms employed by the structural elements to redistribute the excess forces occurring from an extreme loading event. The first two mechanisms to be mobilized by the system, almost simultaneously, are the flexural resistance and compressive action. For beams, the compressive action is referred to as compressive arch action, while for slabs, it is called compressive membrane action. As explained earlier, the compressive action enhances the flexural resistance and allows the structure to reach higher capacities than those considered in the original design. It is, therefore, of high importance to be able to easily assess this improved load capacity to aid in the progressive collapse design process. Several researchers have already come up with analytical and theoretical methods to predict the flexural/arch capacity of RC beams, as in [24], [54], [86] and [87]. However, in this research, a simplified theoretical method based on the structural system proposed in [88], was developed not only to predict the peak flexural/arch resistance, but the whole response leading up to it. It should be mentioned, however, that there exists in literature a few methods that attempt to predict the complete behavior of the system under middle column loss such as the procedure proposed in [89].

6.2 METHOD DEVELOPMENT

6.2.1 ASSUMPTIONS

Referring to Figure 6-1, the main assumptions considered in this method could be summarized as follows:

- The system is symmetric about the vertical axis passing through the removed column. Therefore, only half the system may be modeled with symmetry boundary conditions imposed on the intermediate joint to restrain the in-plane rotation as well as the horizontal displacement.
- A lumped plasticity model is adopted to represent the behavior of the beam since only the beam ends undergo substantial plastic deformations, especially during the initial flexural/arch phase where displacement levels are still relatively low compared to later stages. Therefore, the beam stiffness is considered to be constant throughout its whole length, while a nonlinear rotational spring is placed at each end to represent the plastic hinges. It should be noted that concrete resistance in tension is neglected, and so the cracked area and second moment of area are considered when calculating the beam's stiffness values along its length.

- A spring is placed at the beam's end to account for the stiffness provided by the adjacent beam and/or column(s). The effect of the removed column on these adjacent structural elements during the initial phase of the response, the stage in question, is somewhat limited. Therefore, it is safe to assume that their response is linearly elastic.
- The vertical displacement at the adjacent column joint may be completely neglected since it is significantly smaller than the displacement at the removed column.
- At the beginning of the flexural/arch phase, the beam may be considered to be slightly inclined upwards in order for the compressive axial force to develop. The value of this upward distance (D) is calibrated using experimental studies found in literature.

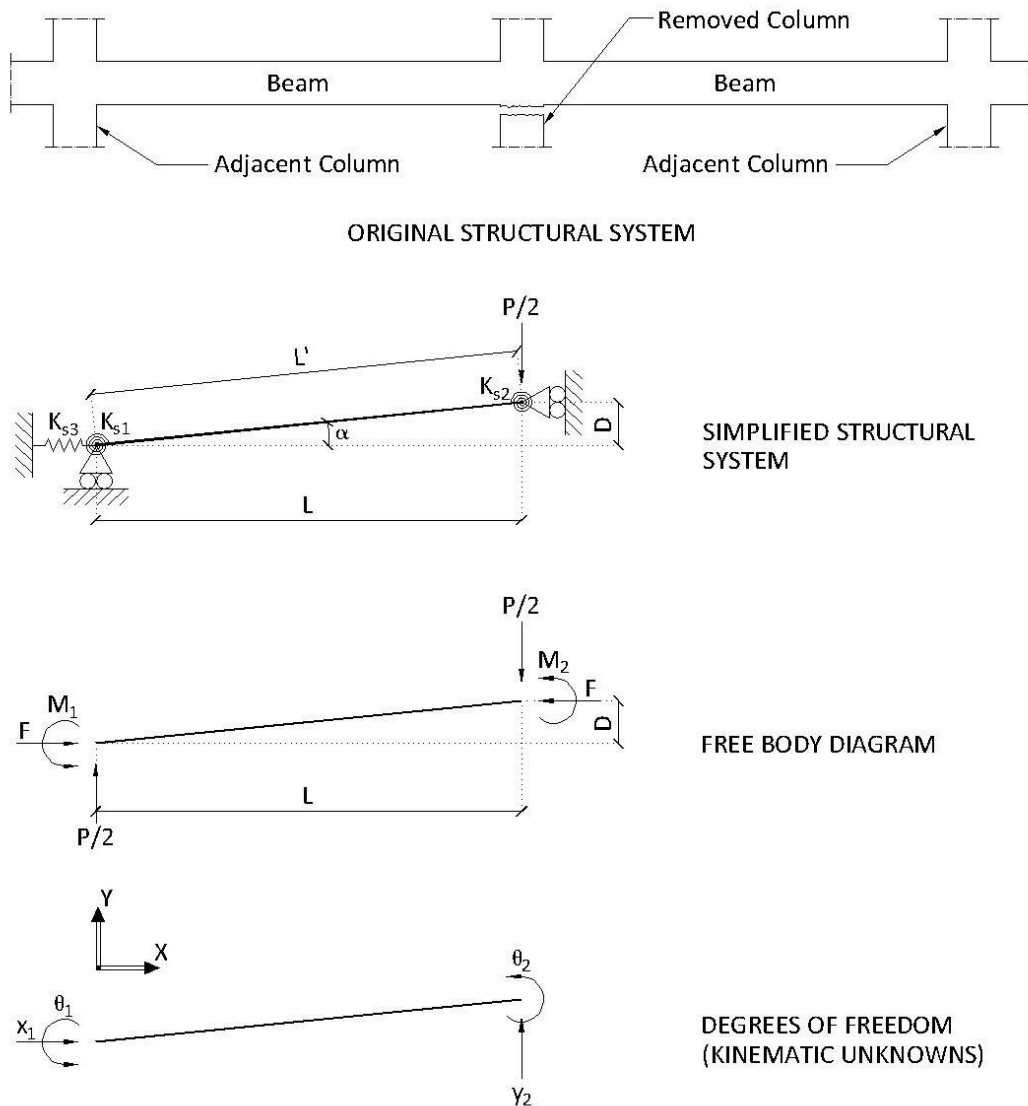


Figure 6-1: Idealization of the Structural System at the Beginning of the Flexural/Arch Phase

6.2.2 DESCRIPTION OF METHOD

Based on the assumptions mentioned in Section 6.2.1 and Figure 6-1, the following expressions may be deduced:

$$L' = \sqrt{L^2 + D^2}$$

$$\cos \alpha = \frac{L}{L'}, \quad \sin \alpha = \frac{D}{L'}$$

where L = Horizontal length of beam = Distance between the edge of the beam at the adjacent column and the centerline of the interior (removed) column = Half of the clear span of the double-span beam,

L' = Inclined length of beam,

α = Angle of inclination.

By rotating the local stiffness matrix of the beam (K_{bl}) using the transformation matrix (T), the global stiffness matrix of the beam (K_{bg}) may be calculated as follows:

$$[K_{bg}] = [T]^T \cdot [K_{bl}] \cdot [T]$$

$$[K_{bg}] = \begin{bmatrix} c & -s & 0 & 0 & 0 & 0 \\ s & c & 0 & 0 & 0 & 0 \\ 0 & 0 & 1 & 0 & 0 & 0 \\ 0 & 0 & 0 & c & -s & 0 \\ 0 & 0 & 0 & s & c & 0 \\ 0 & 0 & 0 & 0 & 0 & 1 \end{bmatrix} \cdot \begin{bmatrix} \frac{EA}{L'} & 0 & 0 & -\frac{EA}{L'} & 0 & 0 \\ 0 & \frac{12EI}{L'^3} & \frac{6EI}{L'^2} & 0 & -\frac{12EI}{L'^3} & \frac{6EI}{L'^2} \\ 0 & \frac{6EI}{L'^2} & \frac{4EI}{L'} & 0 & -\frac{6EI}{L'^2} & \frac{2EI}{L'} \\ -\frac{EA}{L'} & 0 & 0 & \frac{EA}{L'} & 0 & 0 \\ 0 & -\frac{12EI}{L'^3} & -\frac{6EI}{L'^2} & 0 & \frac{12EI}{L'^3} & -\frac{6EI}{L'^2} \\ 0 & \frac{6EI}{L'^2} & \frac{2EI}{L'} & 0 & -\frac{6EI}{L'^2} & \frac{4EI}{L'} \end{bmatrix} \cdot \begin{bmatrix} c & s & 0 & 0 & 0 & 0 \\ -s & c & 0 & 0 & 0 & 0 \\ 0 & 0 & 1 & 0 & 0 & 0 \\ 0 & 0 & 0 & c & s & 0 \\ 0 & 0 & 0 & -s & c & 0 \\ 0 & 0 & 0 & 0 & 0 & 1 \end{bmatrix}$$

$$[K_{bg}] = \begin{bmatrix} \frac{EA}{L'} c^2 + \frac{12EI}{L'^3} s^2 & (\frac{EA}{L'} - \frac{12EI}{L'^3}) cs & -\frac{6EI}{L'^2} s & -\frac{EA}{L'} c^2 - \frac{12EI}{L'^3} s^2 & (-\frac{EA}{L'} + \frac{12EI}{L'^3}) cs & -\frac{6EI}{L'^2} s \\ (\frac{EA}{L'} - \frac{12EI}{L'^3}) cs & \frac{EA}{L'} s^2 + \frac{12EI}{L'^3} c^2 & \frac{6EI}{L'^2} c & (-\frac{EA}{L'} + \frac{12EI}{L'^3}) cs & -\frac{EA}{L'} s^2 - \frac{12EI}{L'^3} c^2 & \frac{6EI}{L'^2} c \\ -\frac{6EI}{L'^2} s & \frac{6EI}{L'^2} c & \frac{4EI}{L'} & \frac{6EI}{L'^2} s & -\frac{6EI}{L'^2} c & \frac{2EI}{L'} \\ -\frac{EA}{L'} c^2 - \frac{12EI}{L'^3} s^2 & (-\frac{EA}{L'} + \frac{12EI}{L'^3}) cs & \frac{6EI}{L'^2} s & \frac{EA}{L'} c^2 + \frac{12EI}{L'^3} s^2 & (\frac{EA}{L'} - \frac{12EI}{L'^3}) cs & \frac{6EI}{L'^2} s \\ (-\frac{EA}{L'} + \frac{12EI}{L'^3}) cs & \frac{EA}{L'} s^2 - \frac{12EI}{L'^3} c^2 & -\frac{6EI}{L'^2} c & (\frac{EA}{L'} - \frac{12EI}{L'^3}) cs & \frac{EA}{L'} s^2 + \frac{12EI}{L'^3} c^2 & -\frac{6EI}{L'^2} c \\ -\frac{6EI}{L'^2} s & \frac{6EI}{L'^2} c & \frac{2EI}{L'} & \frac{6EI}{L'^2} s & -\frac{6EI}{L'^2} c & \frac{4EI}{L'} \end{bmatrix}$$

where E = Young's modulus of concrete,

A = Effective/cracked cross-sectional area of beam,

I = Effective/cracked moment of inertia of beam,

$$c = \cos \alpha,$$

$$s = \sin \alpha.$$

Therefore, the global stiffness matrix of the whole system (K_s) becomes:

$$[K_s] = \begin{bmatrix} K_{s3} & 0 & -K_{s3} & 0 & 0 & 0 & 0 & 0 & 0 & 0 \\ 0 & K_{s1} & 0 & 0 & -K_{s1} & 0 & 0 & 0 & 0 & 0 \\ -K_{s3} & 0 & \frac{EA}{L'}c^2 + \frac{12EI}{L'^3}s^2 + K_{s3} & (\frac{EA}{L'} - \frac{12EI}{L'^3})cs & \frac{-6EI}{L'^2}s & \frac{-EA}{L'}c^2 - \frac{12EI}{L'^3}s^2 & (\frac{-EA}{L'} + \frac{12EI}{L'^3})cs & \frac{-6EI}{L'^2}s & 0 & 0 \\ 0 & 0 & (\frac{EA}{L'} - \frac{12EI}{L'^3})cs & \frac{EA}{L'}s^2 + \frac{12EI}{L'^3}c^2 & \frac{6EI}{L'^2}c & (\frac{-EA}{L'} + \frac{12EI}{L'^3})cs & \frac{-EA}{L'}s^2 - \frac{12EI}{L'^3}c^2 & \frac{6EI}{L'^2}c & 0 & 0 \\ 0 & -K_{s1} & \frac{-6EI}{L'^2}s & \frac{6EI}{L'^2}c & \frac{4EI}{L'} + K_{s1} & \frac{6EI}{L'^2}s & \frac{-6EI}{L'^2}c & \frac{2EI}{L'} & 0 & 0 \\ 0 & 0 & \frac{-EA}{L'}c^2 - \frac{12EI}{L'^3}s^2 & (\frac{-EA}{L'} + \frac{12EI}{L'^3})cs & \frac{6EI}{L'^2}s & \frac{EA}{L'}c^2 + \frac{12EI}{L'^3}s^2 & (\frac{EA}{L'} - \frac{12EI}{L'^3})cs & \frac{6EI}{L'^2}s & 0 & 0 \\ 0 & 0 & (\frac{-EA}{L'} + \frac{12EI}{L'^3})cs & \frac{-EA}{L'}s^2 - \frac{12EI}{L'^3}c^2 & \frac{-6EI}{L'^2}c & (\frac{-EA}{L'} - \frac{12EI}{L'^3})cs & \frac{EA}{L'}s^2 + \frac{12EI}{L'^3}c^2 & \frac{-6EI}{L'^2}c & 0 & 0 \\ 0 & 0 & \frac{-6EI}{L'^2}s & \frac{6EI}{L'^2}c & \frac{2EI}{L'} & \frac{6EI}{L'^2}s & \frac{-6EI}{L'^2}c & \frac{4EI}{L'} + K_{s2} & -K_{s2} & 0 \\ 0 & 0 & 0 & 0 & 0 & 0 & 0 & -K_{s2} & K_{s2} & 0 \end{bmatrix}$$

where K_{s1} = Rotational spring stiffness at adjacent column joint,

K_{s2} = Rotational spring stiffness at middle column joint,

K_{s3} = Translational spring stiffness at adjacent column joint.

So, the equations of equilibrium for the system may be expressed as follows:

$$[K_s]\{U\} = \{F\}$$

$$[K_s]\{U\} = \{P\} + \{R\}$$

where $\{U\}$ = Vector of system's nodal displacements,

$\{F\}$ = Vector of nodal forces,

$\{P\}$ = Vector of applied external forces,

$\{R\}$ = Vector of reaction forces.

The detailed equilibrium equations for the system become:

$$\begin{bmatrix}
 K_{s3} & 0 & -K_{s3} & 0 & 0 & 0 & 0 & 0 & 0 & 0 \\
 0 & K_{s1} & 0 & 0 & -K_{s1} & 0 & 0 & 0 & 0 & 0 \\
 -K_{s3} & 0 & \frac{EA}{L'}C^2 + \frac{12EI}{L'^3}S^2 + K_{s3} & (\frac{EA}{L'} - \frac{12EI}{L'^3})CS & \frac{-6EI}{L'^2}S & \frac{-EA}{L'}C^2 - \frac{12EI}{L'^3}S^2 & (\frac{-EA}{L'} + \frac{12EI}{L'^3})CS & \frac{-6EI}{L'^2}S & 0 & 0 \\
 0 & 0 & (\frac{EA}{L'} - \frac{12EI}{L'^3})CS & \frac{EA}{L'}S^2 + \frac{12EI}{L'^3}C^2 & \frac{6EI}{L'^2}C & (\frac{-EA}{L'} + \frac{12EI}{L'^3})CS & \frac{-EA}{L'}S^2 - \frac{12EI}{L'^3}C^2 & \frac{6EI}{L'^2}C & 0 & 0 \\
 0 & -K_{s1} & \frac{-6EI}{L'^2}S & \frac{6EI}{L'^2}C & \frac{4EI}{L'} + K_{s1} & \frac{6EI}{L'^2}S & \frac{-6EI}{L'^2}C & \frac{2EI}{L'} & 0 & 0 \\
 0 & 0 & \frac{-EA}{L'}C^2 - \frac{12EI}{L'^3}S^2 & (\frac{-EA}{L'} + \frac{12EI}{L'^3})CS & \frac{6EI}{L'^2}S & \frac{EA}{L'}C^2 + \frac{12EI}{L'^3}S^2 & (\frac{EA}{L'} - \frac{12EI}{L'^3})CS & \frac{6EI}{L'^2}S & 0 & 0 \\
 0 & 0 & (\frac{-EA}{L'} + \frac{12EI}{L'^3})CS & \frac{-EA}{L'}S^2 - \frac{12EI}{L'^3}C^2 & \frac{-6EI}{L'^2}C & (\frac{EA}{L'} - \frac{12EI}{L'^3})CS & \frac{EA}{L'}S^2 + \frac{12EI}{L'^3}C^2 & \frac{-6EI}{L'^2}C & 0 & 0 \\
 0 & 0 & \frac{-6EI}{L'^2}S & \frac{6EI}{L'^2}C & \frac{2EI}{L'} & \frac{6EI}{L'^2}S & \frac{-6EI}{L'^2}C & \frac{4EI}{L'} + K_{s2} & -K_{s2} & 0 \\
 0 & 0 & 0 & 0 & 0 & 0 & 0 & -K_{s2} & K_{s2} & 0
 \end{bmatrix}
 \cdot
 \begin{bmatrix}
 0 \\
 0 \\
 x_1 \\
 0 \\
 \theta_1 \\
 0 \\
 y_2 \\
 \theta_2 \\
 0
 \end{bmatrix}
 =
 \begin{bmatrix}
 0 \\
 0 \\
 0 \\
 0 \\
 0 \\
 -P/2 \\
 0 \\
 0 \\
 0
 \end{bmatrix}
 +
 \begin{bmatrix}
 F \\
 M_1 \\
 0 \\
 P/2 \\
 0 \\
 -F \\
 0 \\
 0 \\
 M_2
 \end{bmatrix}$$

Since the system is kinematically indeterminate to the fourth degree, the equilibrium equations may be reduced to the following:

$$\begin{bmatrix}
 \frac{-EA}{L'}C^2 + \frac{12EI}{L'^3}S^2 + K_{s3} & \frac{-6EI}{L'^2}S & (\frac{-EA}{L'} + \frac{12EI}{L'^3})CS & \frac{-6EI}{L'^2}S \\
 \frac{-6EI}{L'^2}S & \frac{4EI}{L'} + K_{s1} & \frac{-6EI}{L'^2}C & \frac{2EI}{L'} \\
 (\frac{-EA}{L'} + \frac{12EI}{L'^3})CS & \frac{-6EI}{L'^2}C & \frac{EA}{L'}S^2 + \frac{12EI}{L'^3}C^2 & \frac{-6EI}{L'^2}C \\
 \frac{-6EI}{L'^2}S & \frac{2EI}{L'} & \frac{-6EI}{L'^2}C & \frac{4EI}{L'} + K_{s2}
 \end{bmatrix}
 \cdot
 \begin{bmatrix}
 x_1 \\
 \theta_1 \\
 y_2 \\
 \theta_2
 \end{bmatrix}
 =
 \begin{bmatrix}
 0 \\
 0 \\
 -P/2 \\
 0
 \end{bmatrix}$$

Due to the geometric nonlinearity of the model and the material plasticity represented in the rotational springs of the plastic hinges at both ends of the beam, the system's equilibrium equations must be incrementally solved. A displacement-controlled loading approach is implemented here by assuming a small vertical downward displacement (of negative value) applied at the middle column (dy_2) and then solving the equations for dx_1 , $d\theta_1$ and $d\theta_2$. Thus, the equations can be rearranged and rewritten as follows:

$$\begin{bmatrix}
 \frac{EA}{L'}C^2 + \frac{12EI}{L'^3}S^2 + K_{s3} & \frac{-6EI}{L'^2}S & \frac{-6EI}{L'^2}S \\
 \frac{-6EI}{L'^2}S & \frac{4EI}{L'} + K_{s1} & \frac{2EI}{L'} \\
 \frac{-6EI}{L'^2}S & \frac{2EI}{L'} & \frac{4EI}{L'} + K_{s2}
 \end{bmatrix}
 \cdot
 \begin{bmatrix}
 dx_1 \\
 d\theta_1 \\
 d\theta_2
 \end{bmatrix}
 =
 dy_2
 \begin{bmatrix}
 (\frac{EA}{L'} - \frac{12EI}{L'^3})CS \\
 \frac{6EI}{L'^2}C \\
 \frac{6EI}{L'^2}C
 \end{bmatrix}$$

Therefore, the system is further reduced to three simultaneous linear equations. For each analysis step, a displacement increment (dy_2) shall be imposed on the system, and the equations must be solved iteratively to obtain the values of K_{s1} and K_{s2} that correspond to θ_1 and θ_2 , respectively, according to the moment-rotation curves. So, at any increment (n) and iteration (m), the following quantities may be defined:

$$x_{1,n} = x_{1,n-1} + dx_{1,nm}$$

$$\theta_{1,n} = \theta_{1,n-1} + d\theta_{1,nm}$$

$$\theta_{2,n} = \theta_{2,n-1} + d\theta_{2,nm}$$

$$y_{2,n} = y_{2,n-1} + dy_{2,nm}$$

where $x_{1,n}$ = Total horizontal displacement of adjacent column joint at the n^{th} step of the analysis,

$x_{1,n-1}$ = Total horizontal displacement of adjacent column joint at the $(n-1)^{\text{th}}$ step of the analysis,

$dx_{1,nm}$ = Incremental horizontal displacement of adjacent column joint at the n^{th} step and m^{th} iteration,

$\theta_{1,n}$ = Total rotation angle of adjacent column joint at the n^{th} step of the analysis,

$\theta_{1,n-1}$ = Total rotation angle of adjacent column joint at the $(n-1)^{\text{th}}$ step of the analysis,

$d\theta_{1,nm}$ = Incremental rotation angle of adjacent column joint at the n^{th} step and m^{th} iteration,

$\theta_{2,n}$ = Total rotation angle of removed column joint at the n^{th} step of the analysis,

$\theta_{2,n-1}$ = Total rotation angle of removed column joint at the $(n-1)^{\text{th}}$ step of the analysis,

$d\theta_{2,nm}$ = Incremental rotation angle of removed column joint at the n^{th} step and m^{th} iteration,

$y_{2,n}$ = Total vertical displacement of removed column joint at the n^{th} step of the analysis = $n dy_2$,

$y_{2,n-1}$ = Total vertical displacement of removed column joint at the $(n-1)^{\text{th}}$ step of the analysis = $(n-1) dy_2$,

$dy_{2,nm}$ = Incremental vertical displacement of removed column joint at the n^{th} step and m^{th} iteration = dy_2 .

Therefore, the stiffness matrix is being updated at each iteration based on the values of k_{s1} and k_{s2} as well as at the beginning of each step/increment according to the following modified values:

$$L_n = L - x_{1,n-1} = L_{n-1} - dx_{1,n-1}$$

$$L_n' = L_n / \cos \alpha_n = \sqrt{L_n^2 + D_n^2}$$

$$\alpha_n = \tan^{-1} \frac{D_n}{L_n}$$

where L_n = Horizontal length of beam at the n^{th} step of the analysis,

L_n' = Inclined length of beam at the n^{th} step of the analysis,

α_n = Angle of inclination at the n^{th} step of the analysis.

Finally, at each step of the analysis, the values of the reaction forces and the (approximate) equivalent applied vertical load necessary for equilibrium, may be calculated using the following expressions:

$$F_n = F_{n-1} - K_{s3} dx_{1,n} = -K_{s3} x_{1,n}$$

$$M_{1,n} = M_{1,n-1} - K_{s1,n} d\theta_{1,n}$$

$$M_{2,n} = M_{2,n-1} - K_{s2,n} d\theta_{2,n}$$

$$P_n = 2 \left(\frac{M_{1,n} + M_{2,n} + FD_n - w_D L_n' L_n / 2}{L_n} \right)$$

where F_n = Horizontal reaction force at the n^{th} step of the analysis,

F_{n-1} = Horizontal reaction force at the $(n-1)^{\text{th}}$ step of the analysis,

$M_{1,n}$ = Moment reaction at adjacent column joint at the n^{th} step of the analysis,

$M_{1,n-1}$ = Moment reaction at adjacent column joint at the $(n-1)^{\text{th}}$ step of the analysis,

$K_{s1,n}$ = Slope of moment-rotation curve at $\theta_{1,n}$,

$M_{2,n}$ = Moment reaction at removed column joint at the n^{th} step of the analysis,

$M_{2,n-1}$ = Moment reaction at removed column joint at the $(n-1)^{\text{th}}$ step of the analysis,

$K_{s2,n}$ = Slope of moment-rotation curve at $\theta_{2,n}$,

P_n = Approximate/equivalent applied vertical load at removed column joint at the n^{th} step of the analysis,

D_n = Vertical distance between beam ends at the n^{th} step of the analysis = $D + (n-1) d_{y2} = D_{n-1} + d_{y2}$,

w_D = Uniformly distributed dead load of beam.

L_n = Horizontal length of beam at the n^{th} step of the analysis = $L - x_{1,n-1} = L_{n-1} - dx_{1,n-1}$,

L_n' = Inclined length of beam at the n^{th} step of the analysis = $L_n / \cos \alpha_n = \sqrt{L_n^2 + D_n^2}$.

By recording the P values at each step, the load displacement curve can then be plotted. The whole procedure is summarized in Figure 6-2.

As previously mentioned, to minimize drift-off errors, small increments must be used in the analysis. However, it is important to balance increment size with computational efficiency, as very small increments can significantly increase the analysis time. Therefore, a sensitivity analysis was conducted by varying the increment size and repeating the analysis until a good convergence was achieved. The results of this study are summarized for the case of the IMF tested in [16], in Table 6-1 and Figure 6-3. The results show how the solution converges as the increment size is reduced or the number of increments is increased. For instance, only a difference of 0.4% was observed between the results of 1 mm and 0.1 mm increment sizes. In this specific case (IMF), a displacement increment of 0.5 mm was used in the analysis.

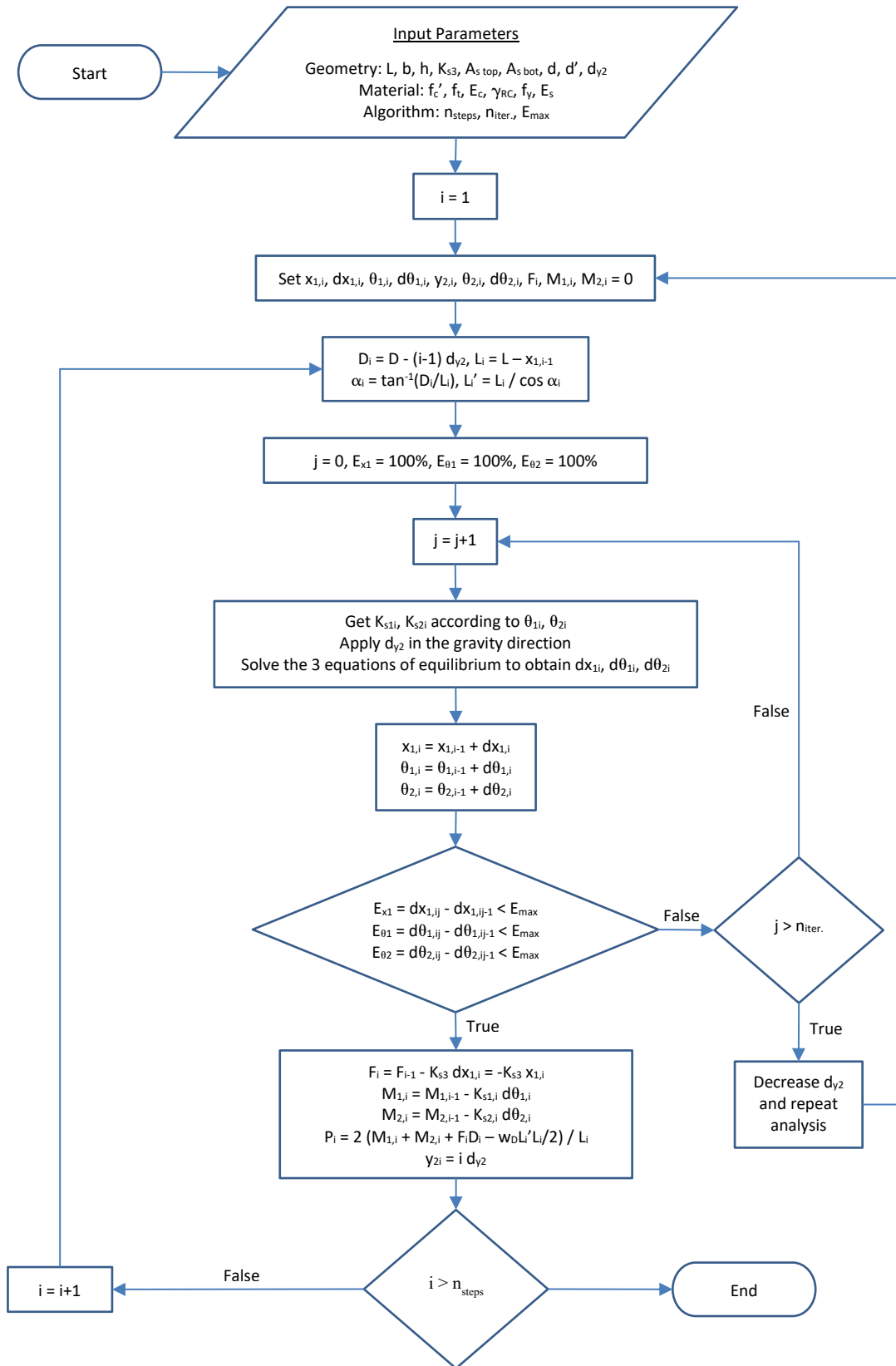


Figure 6-2: Procedure for Predicting the Initial Flexural/Arch Response

Table 6-1: Maximum Load & Corresponding Displacement for Different Increment Sizes for IMF

d_{y2} (mm)	40	20	10	4	2	1	0.5	0.25	0.1	Exp.
y_2 (mm)	160	140	150	144	146	145	144.5	144.5	144.5	127
P (kN)	199.03	219.08	269.54	283.66	284.83	287.21	287.53	288.22	288.38	296

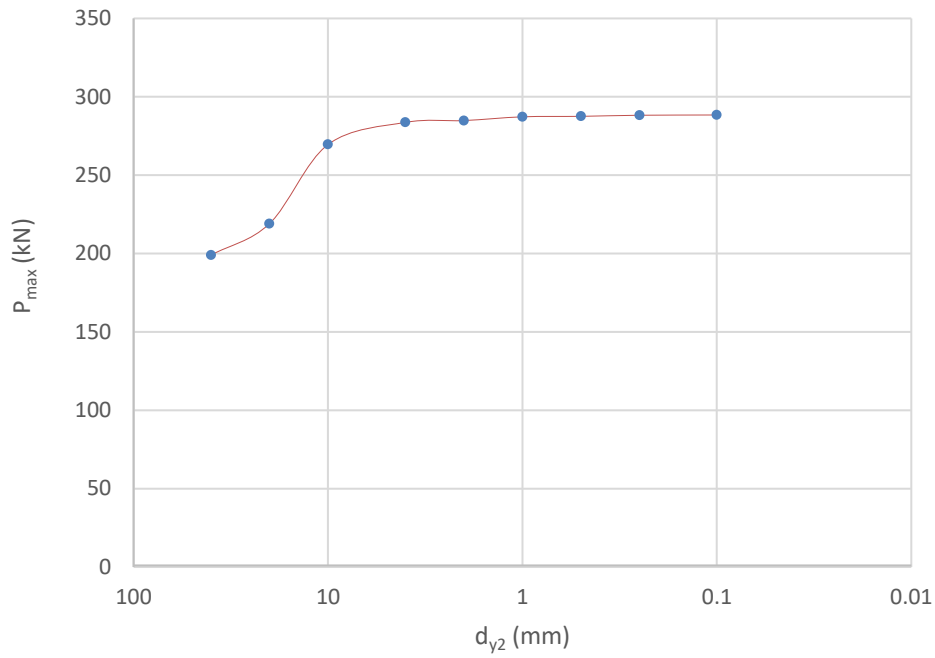


Figure 6-3: Maximum Load Sensitivity to Increment Size for IMF

6.2.3 MOMENT-ROTATION CURVES

An idealized moment-rotation curve, as shown in Figure 6-4, is used to describe the plastic behavior of the plastic hinge at each end. The curve is based on the trilinear curve described in [90]. The first point on the graph is the cracking point where the first tension cracks develop in the concrete. The cracking moment (M_{cr}) may be calculated using the following formula:

$$M_{cr} = \frac{f_t I_g}{y_t}$$

where f_t = Tensile strength of concrete,

I_g = Gross moment of inertia of beam,

y_t = Distance from the centroid of the section to the tension face.

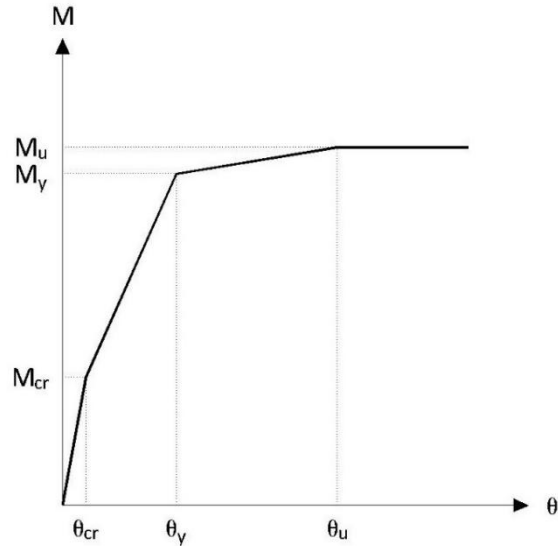


Figure 6-4: Idealized Moment-Rotation Curve at Beam Ends

The second point on the curve is the yield point where the strain in the rebar first reaches the yielding strain. The yield moment (M_y) may be computed according to first principles, as shown in Figure 6-5. Following the assumption that plane sections before bending remain plane after bending, strains must be linearly distributed along the height of the beam's cross section. Since the curvature (κ) is just the slope of the strain distribution line along the height of the beam's cross section according to the Euler-Bernoulli beam theory, the curvature must be constant for each section. Therefore, the following strain compatibility equations may be deduced, and using the stress-strain curve of the concrete, the stress distribution along the height of the section in the compression zone may be plotted. Alternatively, the equivalent stress block specified in the CSA may also be used. Finally, using the equilibrium equations, M_y may be obtained.

$$\kappa = \frac{\epsilon_c}{c} = \frac{\epsilon_s'}{c - d'} = \frac{f_y/E_s}{d-c}$$

where κ = Beam curvature at the section in question,

ϵ_c = Strain at the compression face of the section,

c = Distance from the neutral axis to the compression face,

ϵ_s' = Strain at the compression rebar,

d' = Distance from the centroid of the compression rebar to the compression face,

f_y = Yield strength of steel,

E_s = Modulus of elasticity of steel,

d = Distance from the centroid of the tension rebar to the compression face.

The third point on the curve is the ultimate point where the ultimate moment (M_u) is reached. This point corresponds to a compressive strain of -0.0035 and may also be deduced using first principles. The strain compatibility equations in this case become:

$$\kappa = \frac{0.0035}{c} = \frac{\epsilon_s'}{c - d'} = \frac{\epsilon_s}{d - c}$$

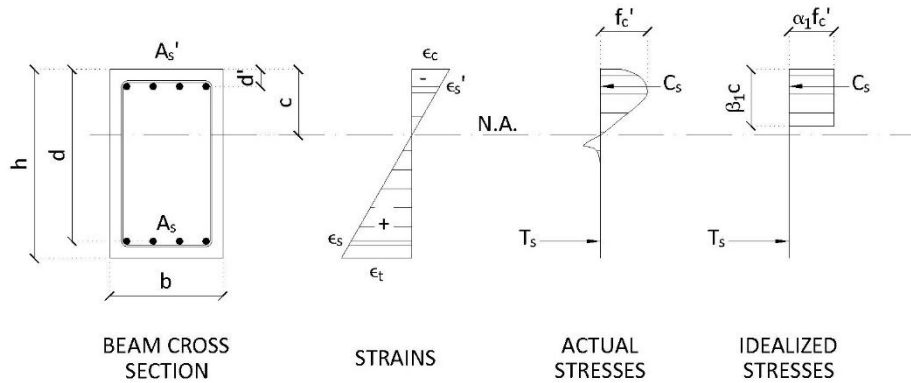


Figure 6-5: Stresses & Strains on Beam Cross Section

The corresponding rotations (θ) may then be calculated assuming a plastic hinge length (L_p) of one-half of the beam's height (h) [91], using the following expression:

$$\theta = \kappa L_p = \kappa \frac{h}{2}$$

6.2.4 D CALIBRATION

Thirty specimens from experimental studies taken from literature were used to validate the results produced by the simplified method. First, however, the value of the initial upward displacement (D), necessary for the development of the compressive arching action, had to be calibrated. To do so, the analysis was conducted using the simplified method for each case, and the value of D was altered until the error in the predicted value of the peak applied force (P_{max}) was reduced to less than 0.01%. Then, it was hypothesized that the ratio of the span of the beam to its height (L/h) would be related to and affect the value of D . Therefore, the values of D/h were plotted against L/h as shown in Figure 6-6. As postulated, a pattern emerged that could be approximated using a

linear function with a coefficient of determination (R^2) of 84.12% or a coefficient of correlation of 91.72%, expressed as follows:

$$(D/h)_{cal.} = 0.0307 (L/h) + 0.3132$$

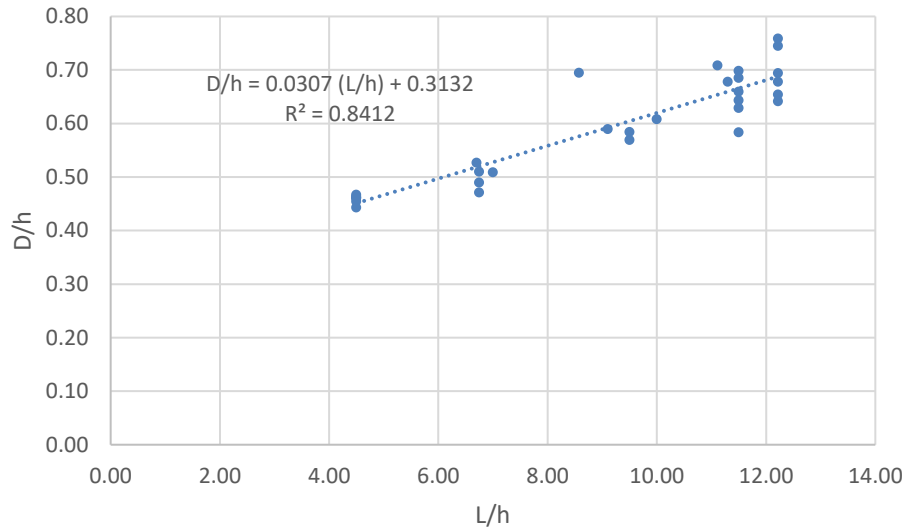


Figure 6-6: Relationship between D/h and L/h

Furthermore, the correlation curve for the values of D/h predicted by the new expression obtained from calibration and the values that produced (almost) zero error in the applied force results is plotted in Figure 6-7.

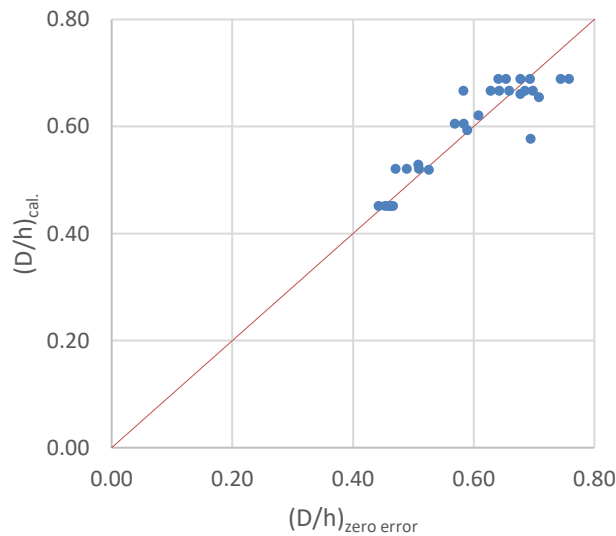


Figure 6-7: Correlation Curve for D/h Values

6.3 RESULTS

After reaching an expression for the value of D , the analysis was repeated for each of the thirty specimens, and the analytical results were compared once again with the experimental ones. This comparison is summarized in Table 6-2 where the peak resistance load and its corresponding displacement are evaluated. The assessment shows a mean value of the analytical to experimental flexural/arch load capacity ratios of 1.004, as well as a coefficient of correlation of 99.6%. On the other hand, the mean value of the analytical to experimental displacement ratios was found to be 1.023, while the coefficient of correlation was found to be 79.7%. Therefore, it could be reasoned that the method provides an acceptable technique for the approximation of the response of uniform RC beam-column sub-assemblages subjected to monotonic downward displacement. The correlation curves for the load and displacement results are shown in Figure 6-8. Moreover, to better visualize the spread in the results, the correlation curve for the normalized load capacity (k_p) is plotted in Figure 6-9. It should be noted that the correlation coefficient for the values of k_p was found to be 99.1%. The following formula was used to compute the values of k :

$$k_p = P / (f_c' b h)$$

Furthermore, the absolute error in the prediction of the peak response was calculated for each of the thirty cases and plotted in Figure 6-10 and Figure 6-11. The average absolute error was found to be 5.59% and 17.04% in predicting the maximum force and the corresponding displacement, respectively. Finally, the load-displacement curves for eighteen of the specimens were plotted in Figure 6-12 to Figure 6-16, to provide a visual comparison of the experimental and analytically predicted flexural/arch response. It should be noted, however, that this method is used for the prediction of the early response of the system up to the flexural/arch peak capacity, beyond which the results become less accurate.

CHAPTER 6. SIMPLIFIED METHOD FOR FLEXURAL/ARCH CAPACITY ESTIMATION UNDER COLUMN LOSS

Table 6-2: Comparison between Experimental & Analytical Results at Peak Flexural/Arch Resistance

Specimen	Reference	$P_{anal.}$ N	$P_{exp.}$ kN	$P_{anal.}/P_{exp.}$	$Y_{2,anal.}$ mm	$Y_{2,exp.}$ mm	$Y_{2,anal.}/Y_{2,exp.}$
IMF	[16]	287.53	296.00	0.971	144.50	127.00	1.138
SMF		746.47	903.00	0.827	161.00	112.00	1.438
P1	[24]	32.29	31.60	1.022	36.88	37.62	0.980
P2		32.10	35.50	0.904	49.88	33.36	1.495
S1	[20], [21]	40.67	41.64	0.977	71.00	78.00	0.910
S2		36.76	38.38	0.958	70.50	73.00	0.966
S3		56.54	54.47	1.038	71.25	74.40	0.958
S4		63.90	63.22	1.011	70.50	81.00	0.870
S5		74.01	70.33	1.052	70.50	74.50	0.946
S6		78.50	70.33	1.116	75.50	114.14	0.661
S7		83.27	82.82	1.005	62.75	74.40	0.843
S8		119.50	121.34	0.985	55.00	45.90	1.198
A1	[22]	161.73	168.00	0.963	57.38	48.00	1.195
A2		211.14	221.00	0.955	57.38	56.40	1.017
A3		254.27	246.00	1.034	57.38	76.40	0.751
A4		143.46	147.00	0.976	57.63	65.00	0.887
A5		186.30	198.00	0.941	57.38	70.70	0.812
A6		223.90	226.00	0.991	57.38	69.20	0.829
B1		131.66	125.00	1.053	67.13	100.00	0.671
B2		89.58	82.90	1.081	76.88	102.00	0.754
B3		78.45	74.70	1.050	76.88	85.50	0.899
C1		70.53	60.90	1.158	44.13	33.70	1.309
C2		71.21	64.90	1.097	44.13	33.50	1.317
C3		70.85	68.60	1.033	44.13	28.70	1.537
V1		[19]	36.60	40.50	0.904	52.50	48.00
V2	35.38		35.70	0.991	52.50	44.00	1.193
V3	36.57		41.40	0.883	52.50	50.00	1.050
V4	42.33		40.10	1.056	52.75	55.00	0.959
V5	42.36		41.60	1.018	52.50	53.00	0.991
V6	42.49		39.40	1.078	52.50	52.00	1.010
Mean Value				1.004			1.023
Correlation Coefficient				0.996			0.797

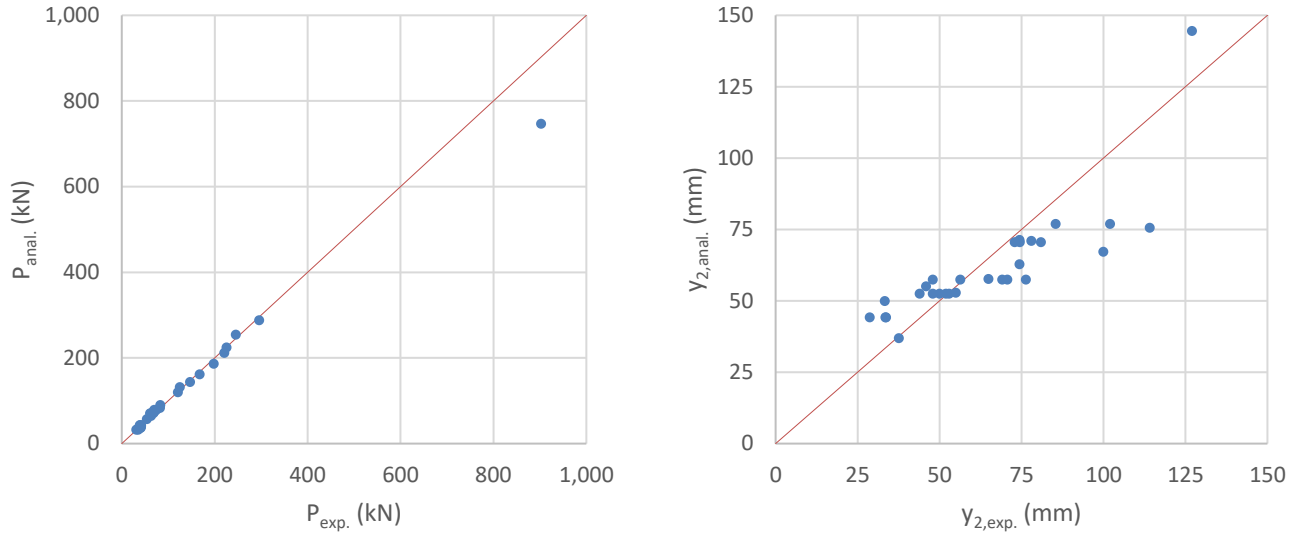


Figure 6-8: Correlation Curves for $P_{anal.}$ Values (Left) & $y_{2,anal.}$ Values (Right)

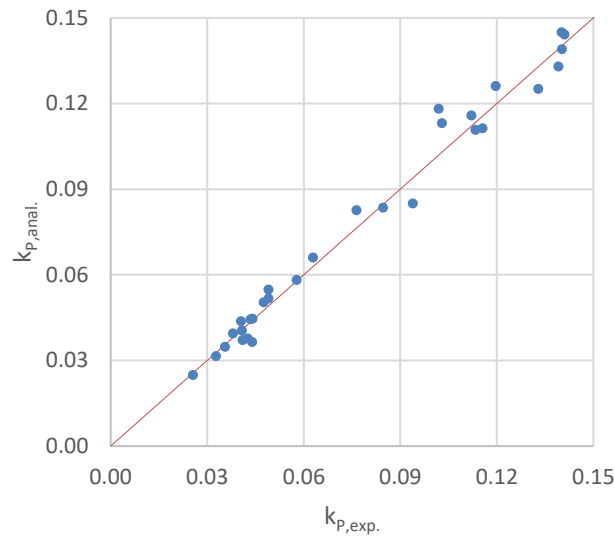


Figure 6-9: Correlation Curve for $k_{P,anal.}$ Values

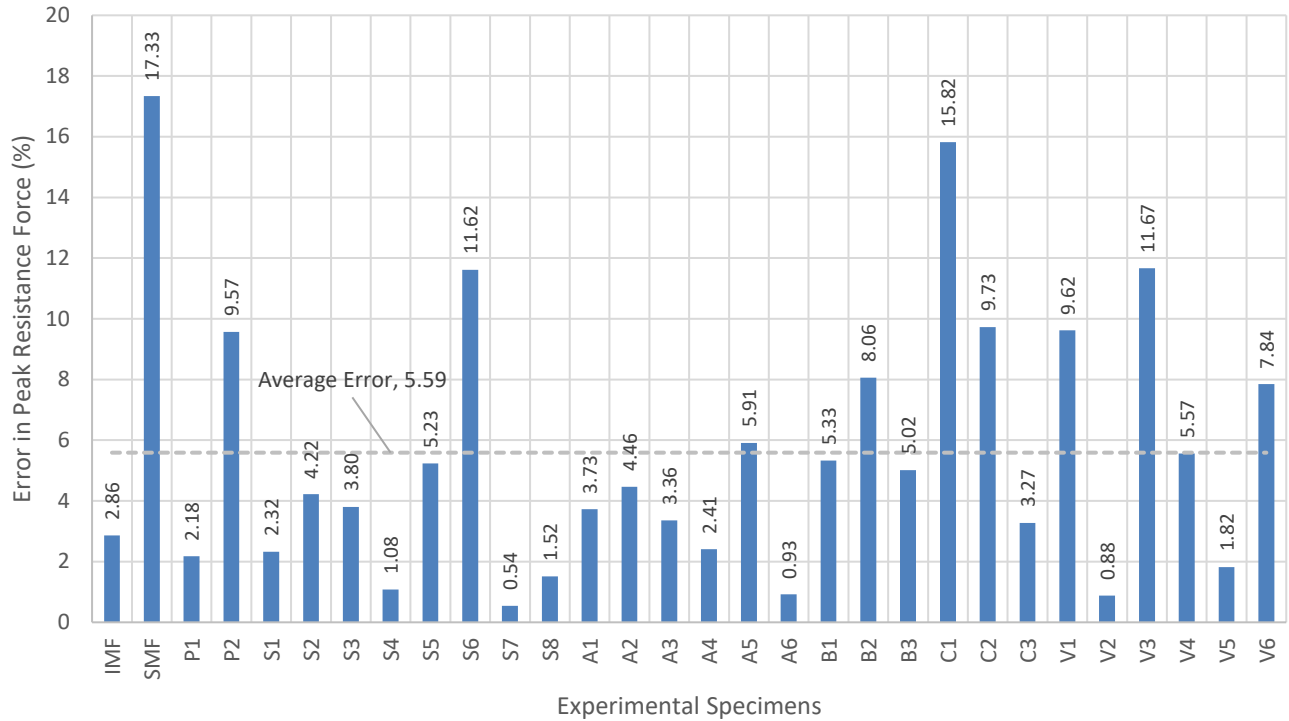


Figure 6-10: Error Percentage in P_{anal} Values

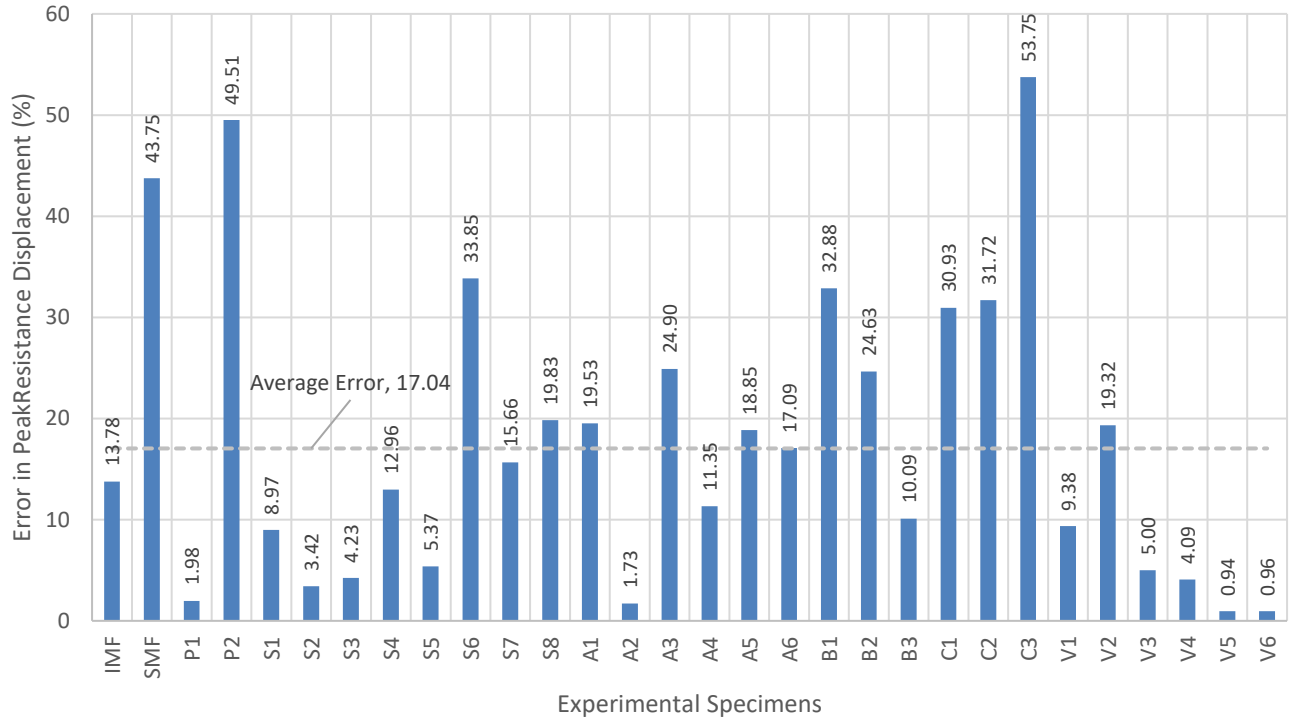


Figure 6-11: Error Percentage in $y_{2,anal}$ Values

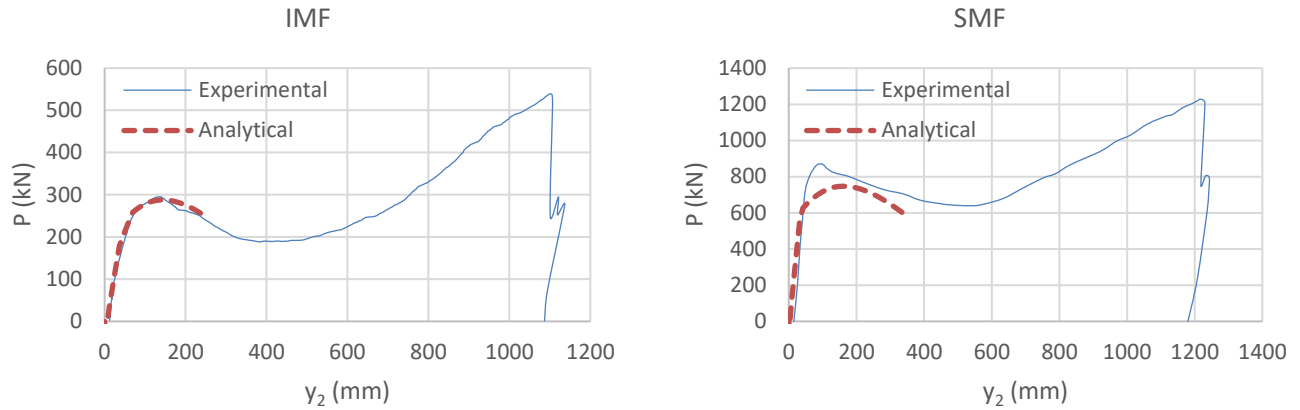


Figure 6-12: Comparison between Experimental & Analytical Load-Displacement Curves for Specimens IMF & SMF [16]

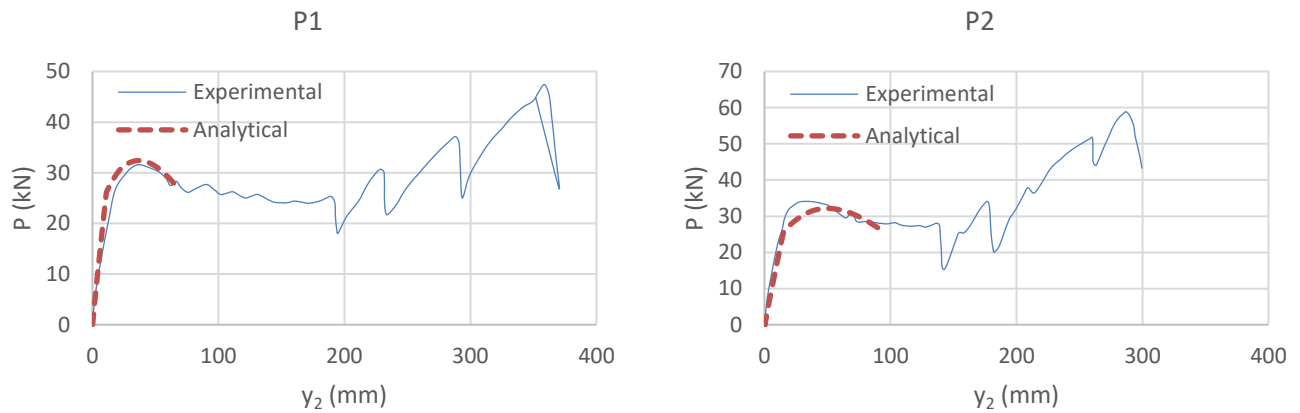


Figure 6-13: Comparison between Experimental & Analytical Load-Displacement Curves for Specimens P1 & P2 [24]

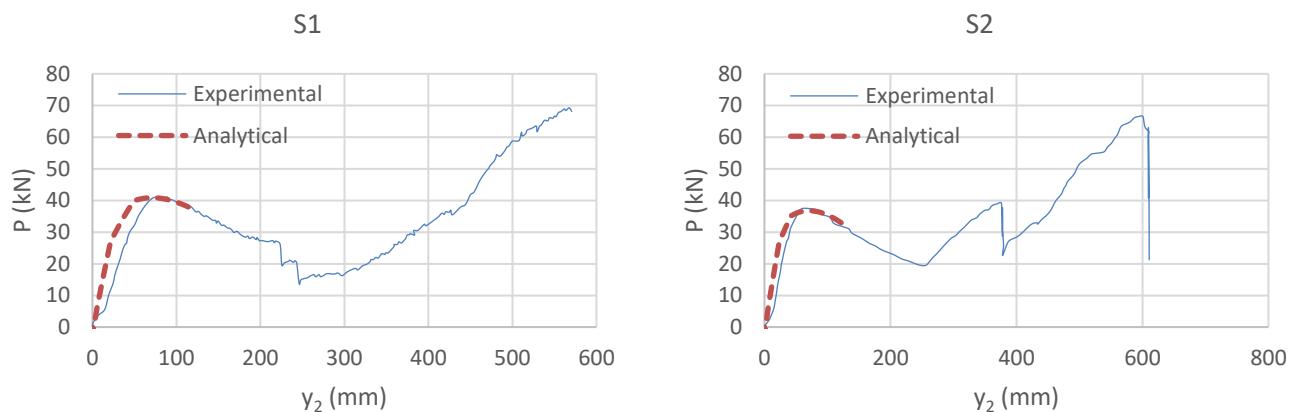


Figure 6-14: Comparison between Experimental & Analytical Load-Displacement Curves for Specimens S1 & S2 [20]

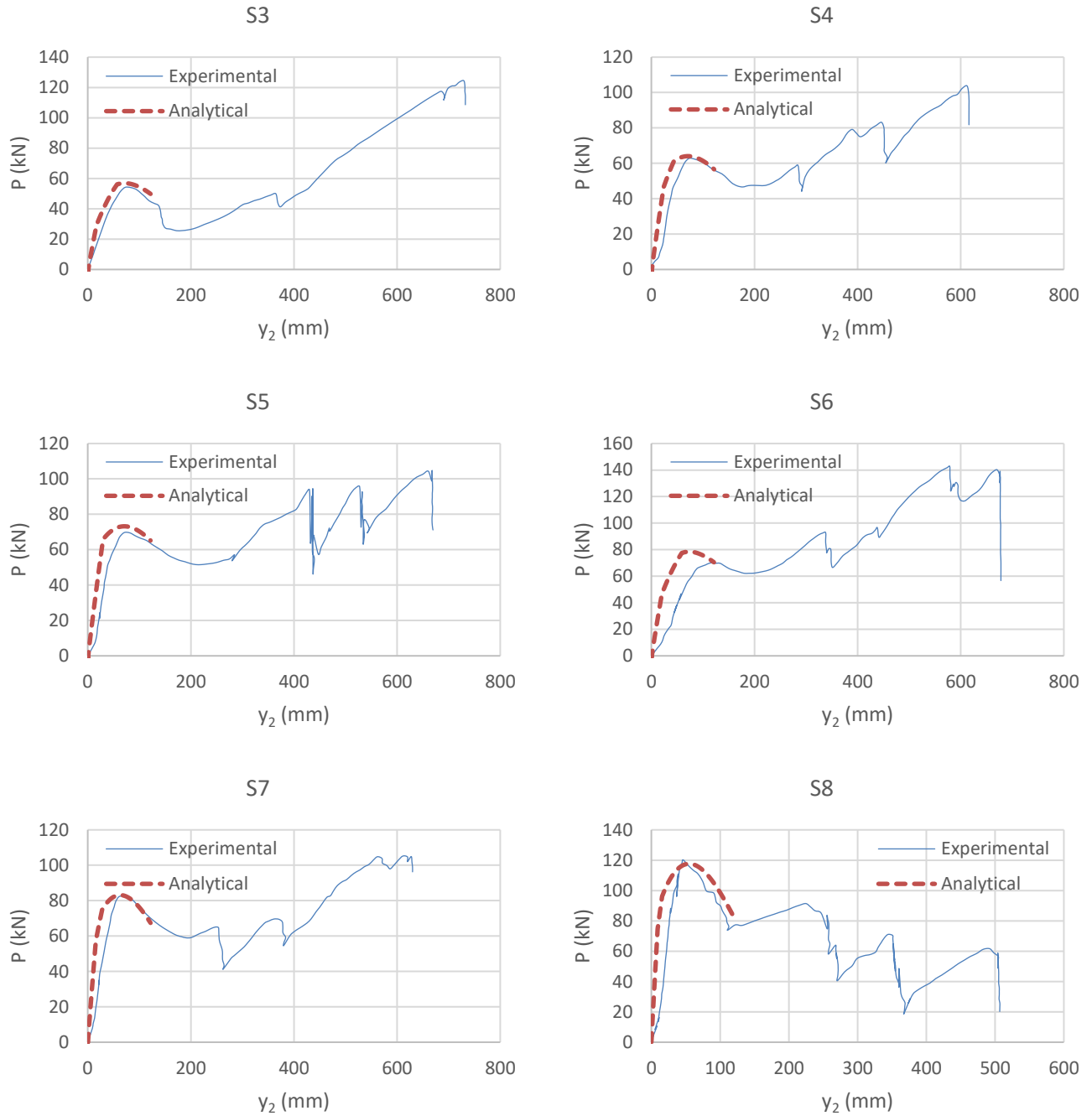


Figure 6-15: Comparison between Experimental & Analytical Load-Displacement Curves for Specimens S3 to S8 [21]

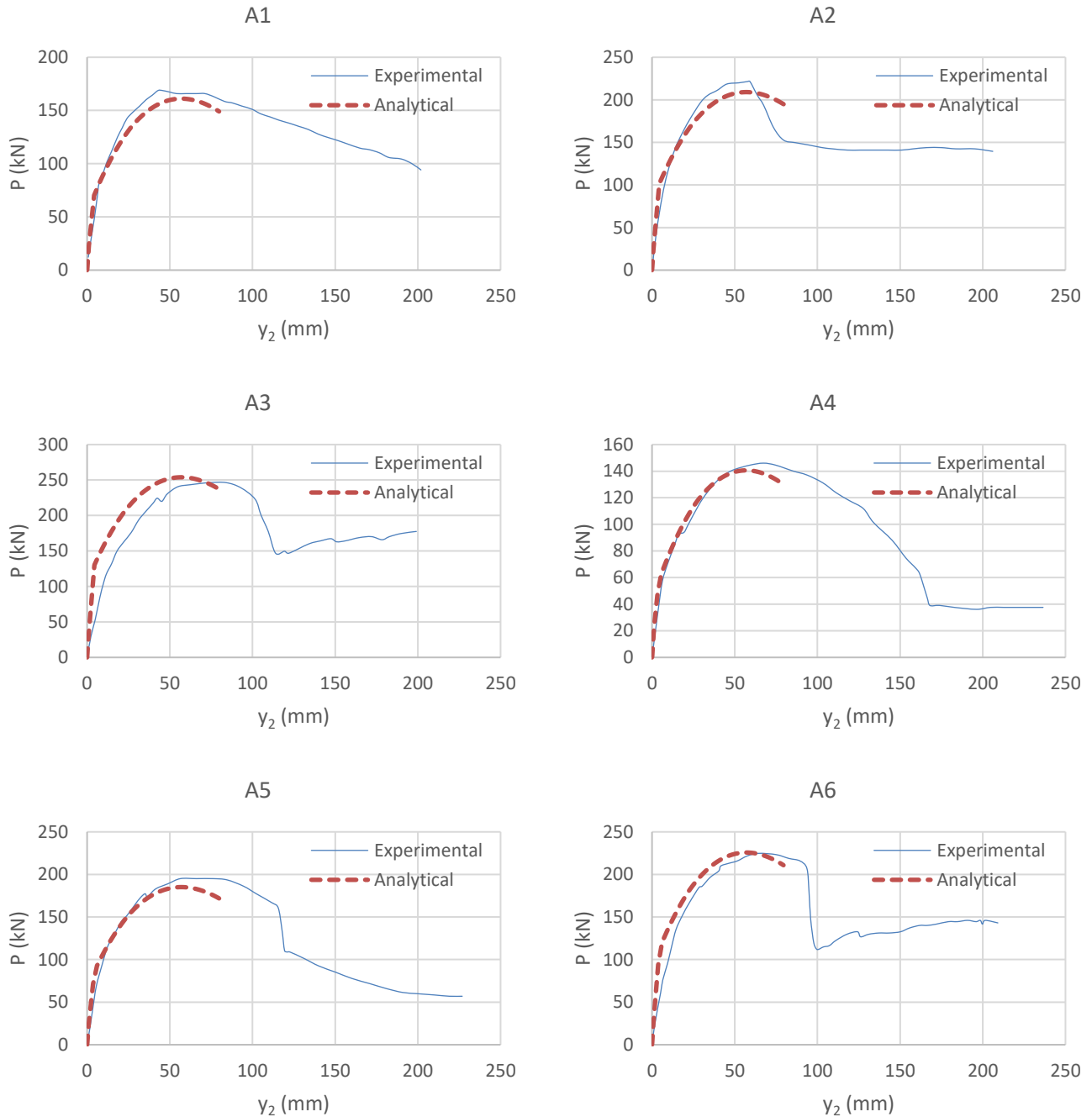


Figure 6-16: Comparison between Experimental & Analytical Load-Displacement Curves for Specimens A1 to A6 [22]

6.4 CLOSED-FORM SOLUTION

While the previously mentioned method is a lot simpler and less time consuming than detailed nonlinear analysis using Abaqus or any other FEM software, it still required the use of a spreadsheet and some coding skills to be implemented. Therefore, further simplification was attempted in order to reach a closed-form solution for

obtaining the peak flexural/arch capacity of the system. First, an expression for the corresponding displacement y_2 at peak resistance was deduced. To do so, the ratio of the analytical corresponding displacement to the beam length ($y_{2,anal.}/L$) was plotted against the value of the beam height divided by the beam length (h/L) for each specimen, as shown in Figure 6-17. A very high linear correlation of 99.9% was found between both variables, and the following expression was obtained:

$$(y_2/L)_{ECFS} = 0.1317 (h/L) + 0.0132$$

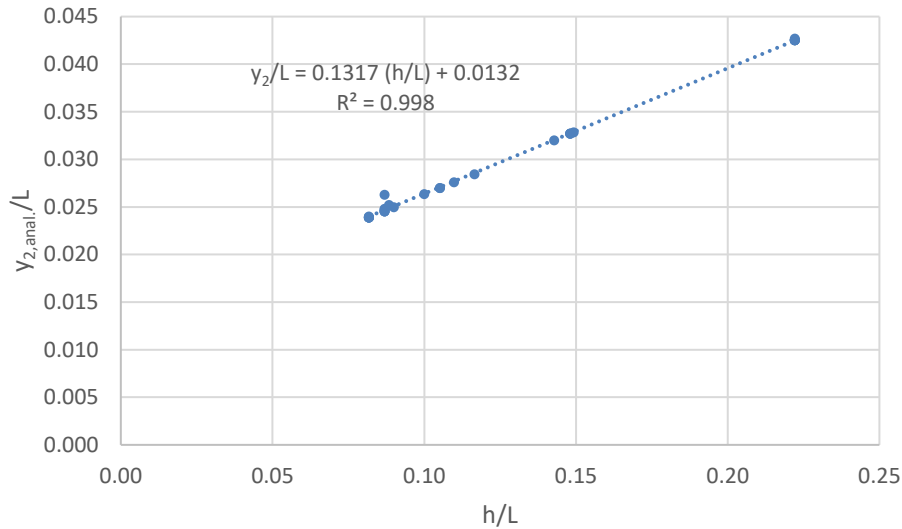


Figure 6-17: Relationship between $y_{2,anal.}/L$ & h/L

The same approach was taken to find an expression for the analytical horizontal force (F) that corresponds to the peak flexural/arch resistance load. So, the normalized horizontal force (k_F) was plotted versus the normalized applied force (k_P), which was previously calculated and compared to the experimental values. Similarly, k_F was calculated using the following equation:

$$k_F = F / (f_c' b h)$$

A good correlation was also observed between both values, as shown in Figure 6-18, where the coefficient of correlation was found to be 97.9% and the coefficient of determination was 95.81%. The linear function describing k_F then becomes:

$$k_{F,ECFS} = 5.4124 k_P - 0.0024$$

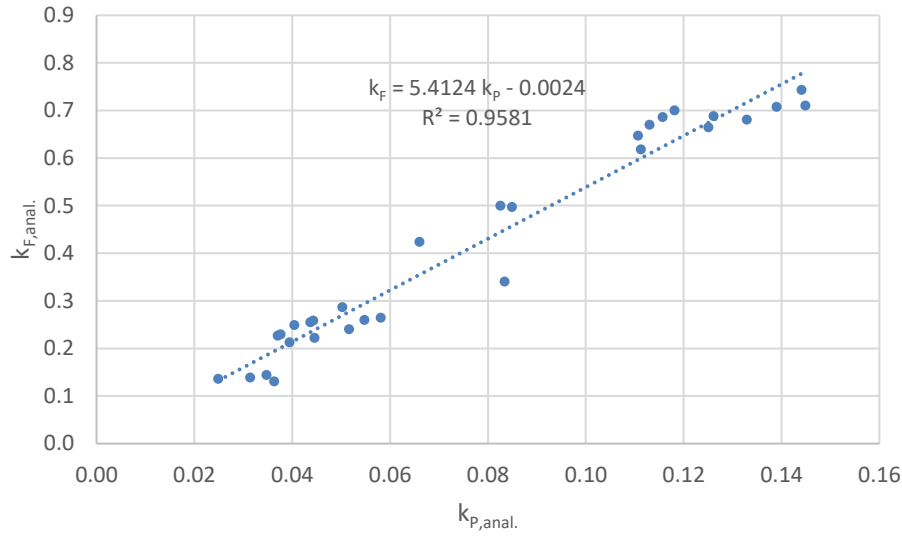


Figure 6-18: Relationship between $k_{F,anal.}$ & $k_{P,anal.}$

Finally, it was reasonable to assume that both beam ends reach their ultimate moments (M_u), or at least are very close to doing so, at the peak flexural/arch resistance. Thus, an empirical formula was derived using the following equilibrium equation:

$$P_{ECFS} = 2 \left(\frac{M_{u1} + M_{u2} + F (D - \gamma_2) - w_D L^2 / 2}{L} \right)$$

where L' was taken equal to L for simplicity. Also, the previously deduced expressions for D/h , γ_2/L and k_F were rewritten as follows:

$$D_{cal.} = 0.0307 L + 0.3132 h$$

$$\gamma_{2,ECFS} = 0.1317 h + 0.0132 L$$

$$F_{ECFS} = 5.4124 P - 0.0024 f'_c b h$$

By substituting these equations in the main equilibrium equation, the empirical closed-form solution for the load capacity of the system may be expressed as follows:

$$P_{ECFS} = \frac{M_{u1} + M_{u2} + f'_c b h \times 10^{-6} (42 L + 435.6 h) - w_D L^2 / 2}{(0.4053 L - 0.9824 h)}$$

The newly deduced formulas for P_{ECFS} and γ_2 were used to calculate the values of the peak applied load capacity and its corresponding displacement for all thirty specimens. The results were then compared with the experimental ones and those from the original analytical method. As shown in Table 6-3, the coefficient of

CHAPTER 6. SIMPLIFIED METHOD FOR FLEXURAL/ARCH CAPACITY ESTIMATION UNDER COLUMN LOSS

correlation between P_{ECFS} and $P_{anal.}$ is 99.6%, and the mean value of the ratio between them is 1.02. More importantly, the correlation coefficient between P_{ECFS} and $P_{exp.}$ is 99.7%, and the mean value of their ratio is 1.022. As for the displacement y_2 , it reached a 78.6% correlation with $y_{2,exp.}$ with a mean ratio of 1.023. The correlation curves for the applied force and the corresponding displacement, as well as the normalized force are presented in Figure 6-19 and Figure 6-20. The correlation coefficient of the normalized load was found to be 97.8%. Furthermore, the absolute error in the results of the load capacity and the corresponding displacement was found to be 8.65% and 17.23%, respectively as displayed in Figure 6-21 and Figure 6-22. Therefore, it can be concluded that the empirical closed-form expressions for the load capacity and displacement produce acceptable results that may be used in the assessment of the system’s flexural/arch response.

Table 6-3: Comparison of Empirical Results with Experimental & Analytical Results

Specimen	P_{ECFS} kN	$P_{anal.}$ kN	$P_{exp.}$ kN	$P_{ECFS}/P_{anal.}$	$P_{ECFS}/P_{exp.}$	$y_{2,ECFS}$ mm	$y_{2,exp.}$ mm	$y_{2,ECFS}/y_{2,exp.}$
IMF	286.80	287.53	296.00	0.997	0.969	142.68	127.00	1.123
SMF	938.95	746.47	903.00	1.258	1.040	161.74	112.00	1.444
P1	33.39	32.29	31.60	1.034	1.057	36.92	37.62	0.981
P2	30.53	32.10	35.50	0.951	0.860	50.11	33.36	1.502
S1	46.10	40.67	41.64	1.134	1.107	70.88	78.00	0.909
S2	40.46	36.76	38.38	1.101	1.054	70.88	73.00	0.971
S3	56.93	56.54	54.47	1.007	1.045	70.88	74.40	0.953
S4	66.62	63.90	63.22	1.043	1.054	70.88	81.00	0.875
S5	78.97	74.01	70.33	1.067	1.123	70.88	74.50	0.951
S6	85.87	78.50	70.33	1.094	1.221	70.88	114.14	0.621
S7	92.72	83.27	82.82	1.113	1.120	62.96	74.40	0.846
S8	147.36	119.50	121.34	1.233	1.214	55.04	45.90	1.199
A1	157.34	161.73	168.00	0.973	0.937	57.33	48.00	1.194
A2	232.08	211.14	221.00	1.099	1.050	57.33	56.40	1.016
A3	303.09	254.27	246.00	1.192	1.232	57.33	76.40	0.750
A4	128.77	143.46	147.00	0.898	0.876	57.33	65.00	0.882
A5	194.49	186.30	198.00	1.044	0.982	57.33	70.70	0.811
A6	253.68	223.90	226.00	1.133	1.122	57.33	69.20	0.828
B1	131.23	131.66	125.00	0.997	1.050	67.23	100.00	0.672
B2	82.59	89.58	82.90	0.922	0.996	77.13	102.00	0.756
B3	68.94	78.45	74.70	0.879	0.923	77.13	85.50	0.902
C1	65.42	70.53	60.90	0.928	1.074	44.16	33.70	1.310
C2	65.81	71.21	64.90	0.924	1.014	44.16	33.50	1.318
C3	65.60	70.85	68.60	0.926	0.956	44.16	28.70	1.539
V1	33.87	36.60	40.50	0.925	0.836	52.75	48.00	1.099
V2	32.56	35.38	35.70	0.920	0.912	52.75	44.00	1.199
V3	33.80	36.57	41.40	0.924	0.816	52.75	50.00	1.055
V4	41.05	42.33	40.10	0.970	1.024	52.75	55.00	0.959
V5	40.48	42.36	41.60	0.956	0.973	52.75	53.00	0.995
V6	40.58	42.49	39.40	0.955	1.030	52.75	52.00	1.014
Mean Value				1.020	1.022			1.023
Correlation Coefficient				0.996	0.997			0.786

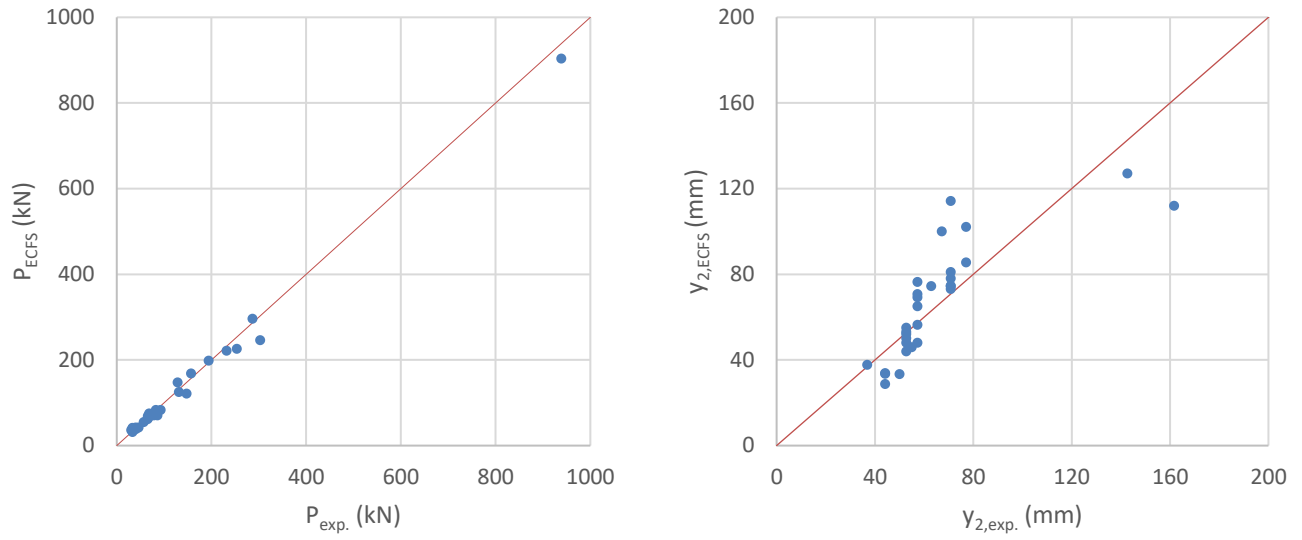


Figure 6-19: Correlation Curves for P_{ECFS} Values (Left) & $y_{2,ECFS}$ Values (Right)

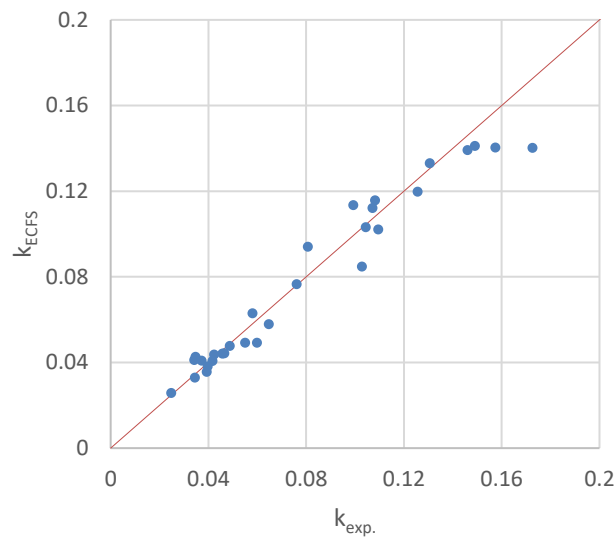


Figure 6-20: Correlation Curve for $k_{p,ECFS}$ Values

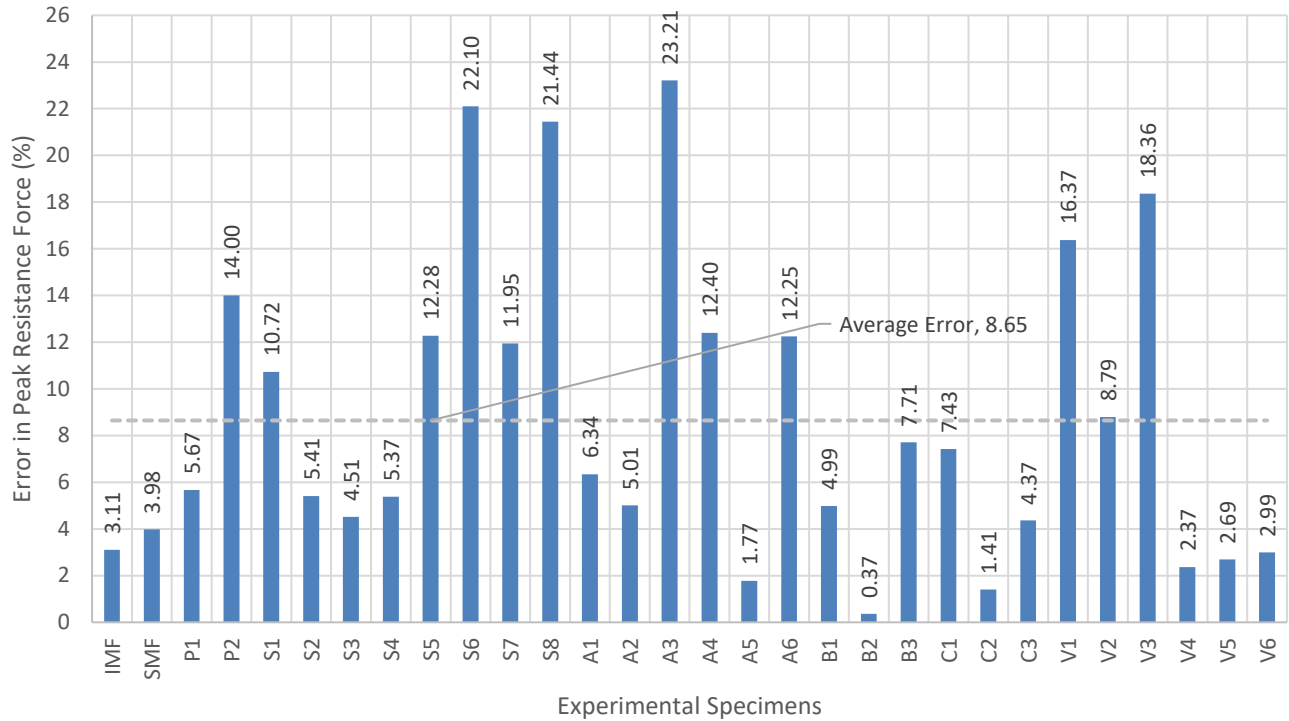


Figure 6-21: Error Percentage in P_{ECFS} Values

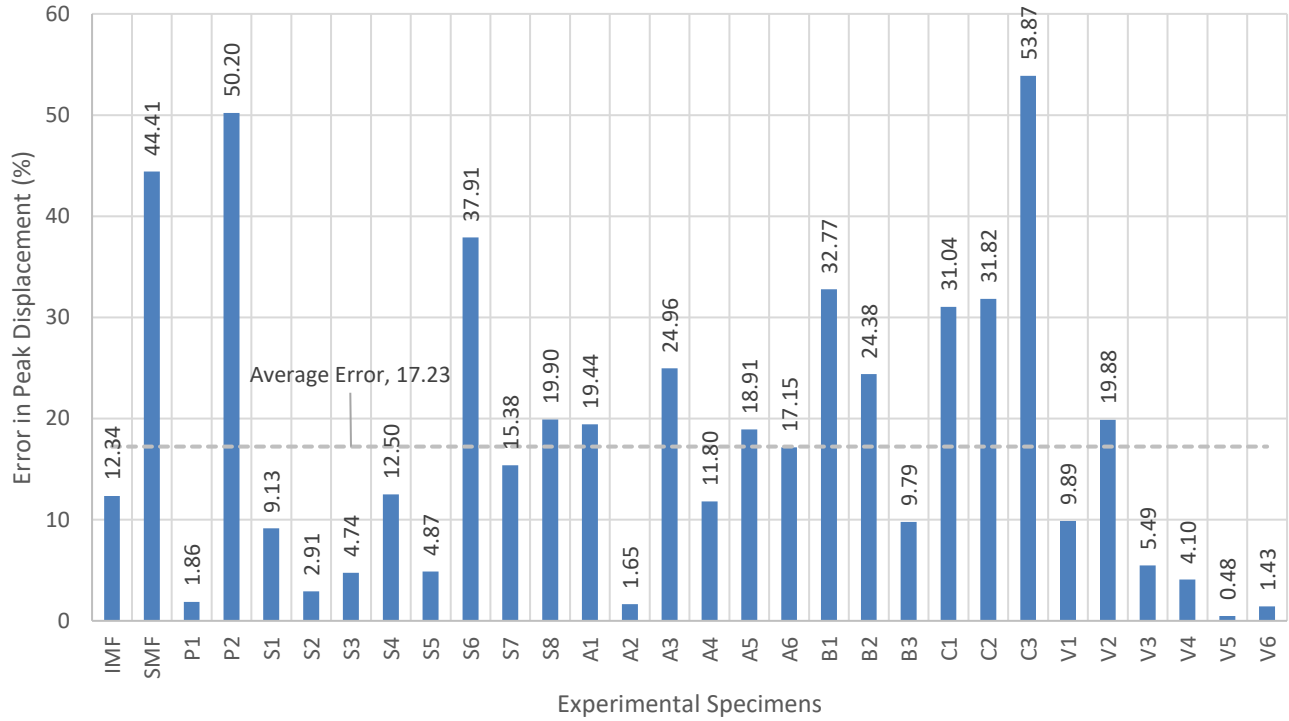


Figure 6-22: Error Percentage in $y_{2,ECFS}$ Values

6.5 TRIANGULAR DISTRIBUTED LOAD

6.5.1.1 METHOD ADAPTATION

While the developed method was found useful in predicting the nonlinear quasi-static compressive arch response of 2D double-span systems subjected to a concentrated force at the middle joint, this loading case may not be as frequent in real life. While the distributed dead load was accounted for in the developed method, its effect was minor, and it was fully applied to the structure before the application of the concentrated force. However, in most real-life scenarios, the applied load is distributed on the system. For instance, in a regular structure such as the six-story case study designed and analyzed herein, both floor beams directly connected to the removed column are subjected to a distributed load that may be approximated to a triangular load as shown in Figure 6-23. Each beam carries half of the slab load, and no concentrated force is applied on either beam. The only concentrated force that may be accounted for in this case is part of the own weight of the top column to be shared with the top-floor system. Nevertheless, this load is small enough that it may be neglected. Therefore, the simplified structural system along with the free body diagram may be modified as illustrated in Figure 6-24.

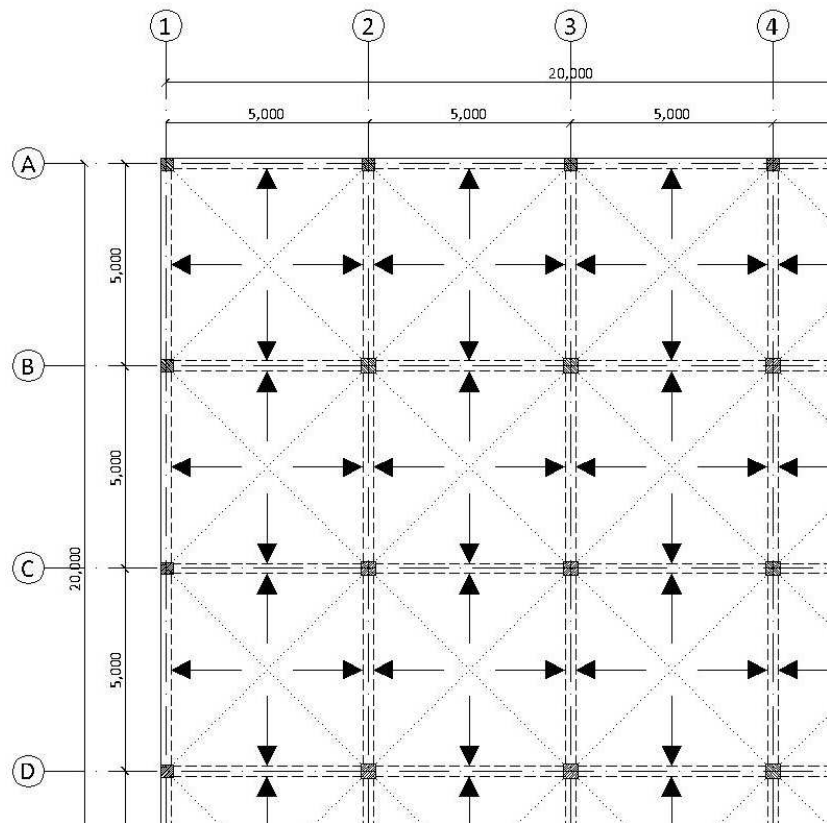


Figure 6-23: Slab Load Distribution on Beams (Partial Floor Plan Shown)

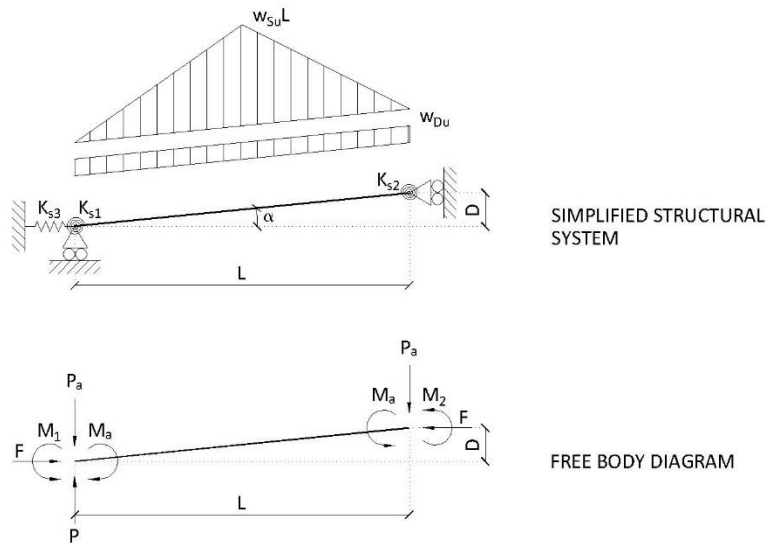


Figure 6-24: Modified Structural System & Free Body Diagram

Consequently, in order to apply the developed method, a couple of tweaks need to be made to account for this new type of applied loading. First, the load vector has to be modified, and so the equilibrium equations become:

$$\begin{bmatrix} \frac{EA}{L'} C^2 + \frac{12EI}{L'^3} S^2 + K_{s3} & \frac{-6EI}{L'^2} S & \left(\frac{-EA}{L'} + \frac{12EI}{L'^3} \right) CS & \frac{-6EI}{L'^2} S \\ \frac{-6EI}{L'^2} S & \frac{4EI}{L'} + K_{s1} & \frac{-6EI}{L'^2} C & \frac{2EI}{L'} \\ \left(\frac{-EA}{L'} + \frac{12EI}{L'^3} \right) CS & \frac{-6EI}{L'^2} C & \frac{EA}{L'} S^2 + \frac{12EI}{L'^3} C^2 & \frac{-6EI}{L'^2} C \\ \frac{-6EI}{L'^2} S & \frac{2EI}{L'} & \frac{-6EI}{L'^2} C & \frac{4EI}{L'} + K_{s2} \end{bmatrix} \cdot \begin{bmatrix} x_1 \\ \theta_1 \\ y_2 \\ \theta_2 \end{bmatrix} = \begin{bmatrix} 0 \\ -M_a \\ -P_a \\ M_a \end{bmatrix} = \begin{bmatrix} 0 \\ -\left(\frac{5w_{su}L}{8} + w_{Du} \right) \frac{L^2/c}{12} \\ -\left(\frac{w_{su}L}{2} + w_{Du} \right) \frac{L/c}{2} \\ \left(\frac{5w_{su}L}{8} + w_{Du} \right) \frac{L^2/c}{12} \end{bmatrix}$$

where P_a = Fixed-end vertical force applied at both joints,

M_a = Fixed-end Moment applied at both joints,

w_{su} = Factored distributed slab load,

w_{Du} = Factored distributed dead load of beam.

Next, because the applied load is distributed along the length of the beam, force-control loading is preferred to the displacement-control loading scheme used in Section 6.2. So, the applied fixed-end forces and moments ($\{P\}$) are incrementally imposed on the structure using the following expression:

$$\{dP\} = d\lambda \{P\}$$

where $\{dP\}$ = Vector of incrementally applied forces and moments at each step of the analysis,

$d\lambda$ = Incremental load factor.

The equilibrium equations at each increment/step may then be expressed as:

$$\begin{bmatrix} \frac{EA}{L'} C^2 + \frac{12EI}{L'^3} S^2 + K_{s3} & \frac{-6EI}{L'^2} S & \left(\frac{-EA}{L'} + \frac{12EI}{L'^3} \right) CS & \frac{-6EI}{L'^2} S \\ \frac{-6EI}{L'^2} S & \frac{4EI}{L'} + K_{s1} & \frac{-6EI}{L'^2} C & \frac{2EI}{L'} \\ \left(\frac{-EA}{L'} + \frac{12EI}{L'^3} \right) CS & \frac{-6EI}{L'^2} C & \frac{EA}{L'} S^2 + \frac{12EI}{L'^3} C^2 & \frac{-6EI}{L'^2} C \\ \frac{-6EI}{L'^2} S & \frac{2EI}{L'} & \frac{-6EI}{L'^2} C & \frac{4EI}{L'} + K_{s2} \end{bmatrix} \cdot \begin{bmatrix} dx_1 \\ d\theta_1 \\ dy_2 \\ d\theta_2 \end{bmatrix} = d\lambda \begin{bmatrix} 0 \\ -\left(\frac{5w_{Su}L}{8} + w_{Du} \right) \frac{L^2/c}{12} \\ -\left(\frac{w_{Su}L}{2} + w_{Du} \right) \frac{L/c}{2} \\ \left(\frac{5w_{Su}L}{8} + w_{Du} \right) \frac{L^2/c}{12} \end{bmatrix}$$

At each step of the analysis, an incremental load vector ($\{dP\}$) shall be applied to the system. The equations must then be solved iteratively to determine the values of K_{s1} and K_{s2} that correspond to θ_1 and θ_2 , respectively, based on the moment-rotation curves. After obtaining the incremental nodal displacements, the incremental nodal forces/moments as well as the cumulative displacements and forces/moments may be calculated using the same equations specified in Section 6.2.2, at any analysis step or increment (n). Finally, by taking the moments about point 1, the normalized equivalent force at increment n ($P_{norm,n}$) applied at point 2, may be calculated using the following expression:

$$P_{norm,n} = \left(\frac{M_{1,n} + M_{2,n} + FD_n}{L_n} \right) / \left(\left(\frac{w_{Su}L_n}{2} + w_{Du} \right) \frac{L_n / \cos \alpha_n}{2} \right)$$

6.5.1.2 CASE STUDY RESULTS COMPARISON

To test the validity of the triangular distributed load method, the case study model was evaluated and compared with the results previously obtained from the numerical analysis. The approximate displacement-control pushdown curves developed in Section 5.6 were used in the comparison shown in Figure 6-25. The approximate method produced acceptable results as the accuracy of the predicted peak flexural/arch resistance compared to the numerical results were 14.73% and 10.02% for models BF-IC-C3 and BF-IC-C6, respectively.

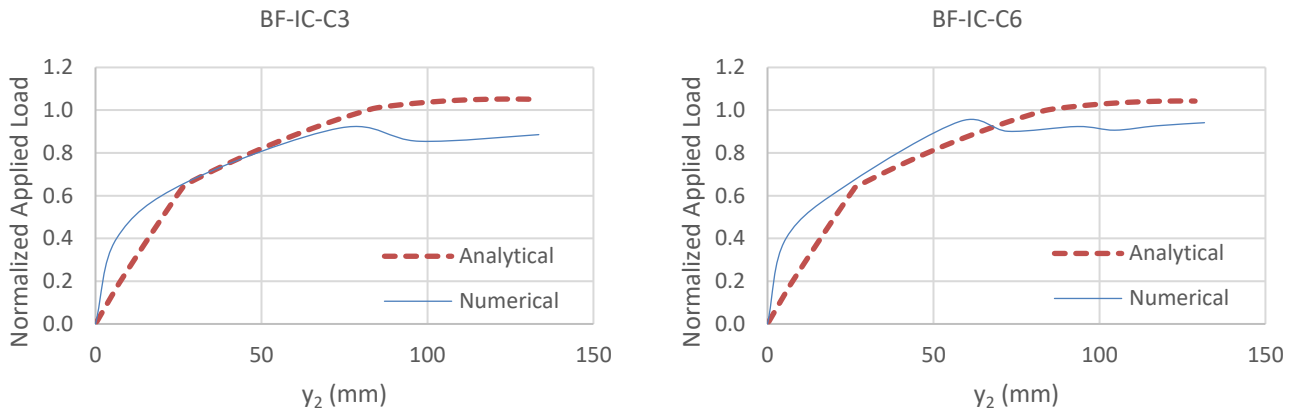


Figure 6-25: Comparison between Numerical & Analytical Load-Displacement Curves for Models BF-IC-C3 and BF-IC-C6

6.6 SUMMARY & CONCLUSIONS

A simplified analytical method was developed in this study to estimate the initial flexural/arch resistance of reinforced concrete beams subjected to column removal scenarios. The method is based on idealizing the structure as a double-span beam with lumped plasticity concentrated at the ends and incorporating geometric nonlinearity through an incremental iterative solution. Key simplifying assumptions include perfect symmetry, elastic behavior of adjacent elements, and neglecting concrete tension strength. Calibration against thirty experimental specimens showed that the method predicted the peak load with an average absolute error of 5.6% and the corresponding displacement with an average error of 17.0%.

To further enhance usability, an empirical closed-form solution was developed to directly estimate the peak flexural/arch load and corresponding displacement. This approach achieved a correlation coefficient of 99.7% for peak load prediction compared to experimental results, with an average absolute error of 8.7%.

Additionally, the method was adapted to account for triangularly distributed slab loading rather than concentrated point loads, improving its applicability to real-world floor systems. Validation against case study models demonstrated that the adapted method predicted the peak flexural/arch resistance with approximately 10-15% accuracy.

Overall, the proposed method provides a practical and efficient tool for preliminary evaluation of RC frames' progressive collapse resistance during the flexural/arch phase following column removal, balancing simplicity, speed and reasonable accuracy.

7. CONCLUSIONS

7.1 SUMMARY

This thesis presented an in-depth investigation into the progressive collapse resistance of regular reinforced concrete (RC) framed structures, focusing on various configurations, loading scenarios and analytical methods. Through a series of nonlinear static and dynamic analyses, using the Alternate Path Method (APM), various column removal scenarios were explored. The differences in structural response between interior (IC) and corner (CC) column removals were studied. By analyzing full-frame (FF) and bare-frame (BF) models, the contribution of the slabs to the structural response was quantified. The role of load distribution (concentrated versus distributed loads) and the impact of modeling strategies, including single-story and single-frame model reductions, were also examined. The research also aimed to address the limitations of current dynamic increase factors (DIFs) and develop a more nuanced understanding of the progressive collapse resistance mechanisms. Finally, a simplified method for the prediction of the flexural/arch response was developed.

7.2 RESEARCH CONTRIBUTIONS

This study makes several contributions to the field of progressive collapse analysis of reinforced concrete (RC) structures:

- It presents a detailed nonlinear simulation of a full-scale, multi-story RC building in which concrete and reinforcement were explicitly modeled. Such comprehensive modeling is rarely found in the literature, which typically focuses on simplified representations or sub-assemblies.
- The influence of floor slabs and membrane action was quantified through systematic comparison between full-frame and bare-frame models under both static and dynamic column loss scenarios. A dedicated metric, the Slab Effect Factor (SEF), was introduced to capture the relative enhancement in load capacity attributable to slab action.
- The variation of Dynamic Increase Factors (DIFs) across the structural response was investigated, revealing that the use of constant, guideline-prescribed values can significantly underestimate dynamic effects—particularly in bare-frame models. The study provided displacement-based DIFs for different structural configurations, offering a more accurate and context-sensitive approach for assessing dynamic demand in progressive collapse scenarios.
- The impact of column removal location was assessed using a new metric, the Column Location Effect (CLE), which captures the relative difference in load capacity between interior and corner column removal cases.

CHAPTER 7. CONCLUSIONS

- The study also examined the effect of modeling simplifications. Single-story and even 2D frame reductions were validated in specific cases, while their limitations were highlighted for others, particularly under corner column loss.
- A simplified analytical method was developed to estimate the peak flexural/arch response of RC frames. The method, grounded in first principles and simplified assumptions, was calibrated against both experimental data and high-fidelity numerical models, demonstrating strong agreement with full-scale results.

These contributions address gaps in current research by providing validated insights into the collapse behavior of detailed multi-story RC systems, advancing both practical modeling techniques and theoretical understanding.

7.3 KEY FINDINGS OF THE THESIS

7.3.1 KEY FINDINGS FROM THE CASE STUDY ANALYSES

This section summarizes the key findings obtained from the numerical simulations and comparative analyses of the case study structural models.

7.3.1.1 LOAD-CARRYING CAPACITY & FAILURE MECHANISM

In general, in the case of interior column (IC) removal, the failure mechanism of the full frame (FF) differed from that of the bare frame (BF). The former reached a maximum normalized load-carrying capacity of 350% in the case of quasi-static pushdown analysis and 300% in the case of dynamic column loss analysis. On the other hand, the latter reached a maximum load of 155% and 80% in the case of pushdown and column loss, respectively. Nevertheless, the full frame suffered a complete progressive collapse as the failure occurred in the columns of the first floor and not in the beams which were strengthened by the existence of the floor slabs. Conversely, the bare frame only suffered a partial progressive collapse as the damage was localized to the bay/panel above the removed column.

In the case of corner column (CC) removal, both FF and BF models suffered a partial progressive collapse, and the maximum load capacity of the former was found to be 282% and 160% respectively in the case of pushdown and dynamic column loss analyses. The latter reached 155% and 80% under pushdown and dynamic column loss analyses, respectively.

7.3.1.2 INFLUENCE OF COLUMN REMOVAL FLOOR & VIERENDEEL ACTION

The response of the structure to the loss of an interior column (IC) was almost the same regardless of the floor from which the column was removed. The maximum load-carrying capacity of the structure did slightly increase

CHAPTER 7. CONCLUSIONS

as the number of floors above the removed column decreased, though. This is attributed to the fact that, in the case of the full frame, the failure occurred in the neighboring/adjacent columns which were subjected to more redistributed load as the number of floors above the removed column increase. On the other hand, in the bare frame case, while the failure did occur in the beams due to the lack of membrane action, the systems with more floors above the removed column attained a higher load-bearing capacity due to the increase in the concentrated force per floor which resulted from the own weight of the remaining columns above the removed one. Therefore, it can be concluded that, to a great extent, each floor acted separately. This means that, in the case of IC removal, the Vierendeel effect is negligible. It also means that single-story reduction is an acceptable modeling technique in this case. Even 2D single-frame reduction proved appropriate, provided the building is regular and the spans in both horizontal directions are equal.

On the other hand, the Vierendeel action played a noteworthy role in the response of building models subjected to the removal of the corner column (CC). In general, systems with more floors above the removed column exhibited a slightly higher load-carrying capacity than systems with less floors above. However, the difference was significant in the case of the removal of the corner column of the last (top) floor. This is attributed to the lack of Vierendeel action as the system was effectively a single-story cantilever. Therefore, single-story or single-frame model reduction may not be an accurate modeling approach.

In short, the removal of columns from the lower floors was more critical for IC removal scenarios, while the opposite was observed in the case of CC removal scenarios.

7.3.1.3 CONTRIBUTION OF FLOOR SLABS & MEMBRANE ACTION

The results of the analysis clearly illustrate that the inclusion of slabs in the full-frame models plays a critical role in enhancing progressive collapse resistance. Slabs contributed significantly through membrane action, which enabled more effective load redistribution following the removal of key columns. Two metrics proposed in Section 5.4.2 emphasized the influence of the slab on the response as it more than doubled the load-carrying capacity of the structure in most cases. Also, it was noted that the slab's contribution was a bit higher in the case of dynamic analysis when compared to quasi-static (pushdown) analysis.

7.3.1.4 EFFECT OF REMOVED COLUMN LOCATION

The location of the removed column (IC vs. CC) had an obvious impact on the structural response. Interior columns, being part of a more redundant load path, allowed for better redistribution of forces, as reflected by the higher load-carrying capacities in both FF-IC and BF-IC models. On the other hand, corner column removal led to lower

CHAPTER 7. CONCLUSIONS

load capacities due to the more localized nature of the load transfer. As defined earlier, the Column Location Effect (CLE) quantified the difference in load capacity between IC and CC removal scenarios. The results showed that this difference was not as pronounced as one might expect. One possible explanation is that the corner column belongs to the building's lateral load-resisting system and, therefore, the entire frame was designed and detailed accordingly which enhanced the ability of the system to absorb and redistribute loads following the column's removal. In full-frame models, IC models support 19% and 24% more load in PD and CL analyses, respectively, than CC models. This gap is even narrower in bare-frame models, with IC models carrying 5% more load in PD analyses and 10% more in CL analyses compared to CC models. This highlights that the distinction between interior and corner column removal scenarios becomes more accentuated under dynamic analysis conditions.

7.3.1.5 INFLUENCE OF LOAD TYPE

Another observation made was the differences in failure mechanisms between concentrated and distributed loads. For distributed loads, failure generally initiated at the ends of double-span beams, where the supports experienced higher shear and moment demands. In contrast, concentrated loads led to failure at midspan, where bending moments were greatest. This difference is important for understanding how load distribution affects the initiation and progression of collapse, and it has significant implications for designing RC structures with improved collapse resistance under different loading conditions.

7.3.1.6 DYNAMIC INCREASE FACTORS

The dynamic increase factors were calculated and compared to the GSA/UFC-prescribed values and were found to be a bit higher in the case of full frames and much higher in the case of bare frames. The average DIF in the case of corner column removal scenarios was found to be 1.35 and 1.75 for full-frame and bare-frame models, respectively, as opposed to the average prescribed value of 1.15. On the other hand, in the case of interior column removal scenarios, the average DIF was 1.32 and 1.60 respectively for full-frame and bare-frame models, while the average prescribed value was 1.18. As shown in Section 5.4.1, the DIF values varied across different points in the response, indicating that the use of an average DIF introduces an approximation.

The (displacement-control) DIF values deduced in Section 5.6.4 showed more consistency in the sense that the bare frame values were not that high and were close to the full frame values. The average values were 1.30, 1.26, 1.36 and 1.36 for the FF-CC, BF-CC, FF-IC and BF-IC models, respectively.

CHAPTER 7. CONCLUSIONS

7.3.1.7 DISPLACEMENTS AT PEAK CAPACITY & FAILURE

According to thirty experimental specimens, the average displacement at which the peak flexural/arch resistance occurred was about 3% of the single beam span. Based on the projected pushdown curves of Section 5.6.4, the numerical models of the case study reached the same peak at deflection values around an average relative displacement of 1.2%.

The majority of the analyzed models failed in the catenary phase. Under pushdown analysis, the failure of the FF-CC and FF-IC models occurred at a mean relative (normalized) displacement of 16%, while the BF-CC and BF-IC failed at a displacement of 10% and 9%, respectively. As for the dynamic column loss analysis, the FF-CC and FF-IC models reached a maximum displacement of 4% and 15%, respectively, while the BF-CC and BF-IC reached a displacement of 8% and 5%. However, it should be reiterated that the term failure is used to refer to the first rebar fracture in the structure which usually triggers the partial or full progressive collapse of the system.

7.3.2 KEY FINDINGS FROM THE SIMPLIFIED ANALYTICAL METHOD

The simplified analytical method was evaluated through calibration against experimental data from previous studies and benchmarked against detailed finite element results. It predicted the peak flexural/arch capacity of RC sub-assemblages with coefficients of correlation of 99.6% and 79.7% for peak load and corresponding deflection, respectively, with average errors of 5.59% and 17.04%.

When applied to the case study bare-frame models with interior column removal from the third and sixth floors (BF-IC-C3 and BF-IC-C6), the method yielded prediction errors of 14.73% and 10.02%, respectively, relative to detailed simulation results. These outcomes characterize the accuracy of the approach within the context of this study.

7.4 LIMITATIONS & FUTURE RESEARCH

While this research helps expand the current knowledge and understanding of progressive collapse behavior of RC framed structures by studying their nonlinear behavior and response to extreme loading conditions, limitations to the adopted approach must also be acknowledged. The following are some of these limitations along with future research recommendations:

CHAPTER 7. CONCLUSIONS

7.4.1 BUILDING CONFIGURATION & PROPERTIES

The first obvious limitation is the fact that this study was conducted on regular RC structures with equal spans in both horizontal directions. Therefore, more building configurations with different aspect ratios as well as irregular structures need to be examined.

Moreover, the span to depth ratio of the beams, the thickness of the slabs, the reinforcement ratio of the beams and slabs, the characteristic strength of concrete, the yield strength of steel, etc. were all constant for all the models of the study. So, a parametric study where these values are varied is recommended as it would be of great use for the understanding of the progressive collapse behavior of the structures.

It should be noted that while flat slab and flat plate systems are commonly used in Canada, in the present study, the slab and beam system has been considered. This system is presumably more robust in progressive collapse scenarios, and the benchmark studies available have a similar structural system suitable for verifying the numerical models. However, in the future, a similar study should also be conducted on flat slab and flat plate systems to improve our understanding of their progressive collapse behavior.

7.4.2 STRUCTURAL RESPONSE EVALUATION CRITERION

While the displacement capacity of the numerical models was discussed, the main focus in this study for evaluating the structural response was on the load capacity.

7.4.3 DIF LIMITATION

In this study, DIF values were averaged throughout the entire load-displacement response, which simplifies the dynamic behavior by not considering variations at each displacement stage. In reality, the DIF may fluctuate based on the stiffness degradation, structural ductility and energy absorption mechanisms, meaning that a single value may oversimplify the dynamic demands at critical moments of the collapse.

7.4.4 BOND SLIP

Under large deformations such as those encountered under extreme loading conditions, bond slip may play a role in the response of the system. While it was not modeled in this research, it is recommended to take it into account in future research.

7.4.5 NON-STRUCTURAL ELEMENTS

Non-structural components, such as infill walls or cladding, were not considered in this study. However, under extreme loading conditions, these elements can affect the overall stiffness and collapse progression of RC structures and should be considered for a more comprehensive analysis.

7.4.6 APM LIMITATION

The use of the APM as a means of representing extreme loading conditions and assessing the progressive collapse response of structures is somewhat arbitrary as discussed earlier in this thesis. Therefore, it could be argued that the behavior of the structure due to the APM loading case only shows its response due to said method and does not guarantee the prediction of its response due to other extreme loading cases. Such cases may be the loss or even partial damage of more than one column at a time.

7.4.7 SIMPLIFIED METHOD IMPROVEMENT

While the simplified method developed in this study showed promising results, future research could focus on further refining this method to improve its accuracy for a wider range of structural configurations and loading scenarios. This would enhance its applicability in practical engineering design.

7.4.8 THE NEED FOR MORE EXPERIMENTAL STUDIES

The study relied heavily on numerical simulations and validation against experimental data from literature. However, more full-scale experimental tests on RC frames subjected to progressive collapse scenarios are still needed to provide critical data to validate numerical simulations and simplified methods. Experimental validation would strengthen the reliability of the findings and offer valuable insights into real-world structural behavior.

REFERENCES

- [1] M. Byfield, W. Mudalige, C. Morison and E. Stoddart, "A Review of Progressive Collapse Research and Regulations," *Structures and Buildings*, vol. 167, no. SB8, pp. 447-456, 2013.
- [2] M. Minkjan, "The Downfall of British Modernist Architecture," *Failed Architecture*, 13 June 2013. [Online]. Available: <https://failedarchitecture.com/the-downfall-of-british-modernist-architecture/>. [Accessed 28 April 2025].
- [3] C. I. Colliers (Knowledge Leader, "How the Murrah Building Bombing Changed Federal Facilities Security," Knowledge Leader (Colliers), 19 April 2018. [Online]. Available: <https://knowledge-leader.colliers.com/editor/how-the-murrah-building-bombing-changed-federal-facilities-security/>. [Accessed 28 April 2025].
- [4] H. Tagel-Din and N. A. Rahman, "Simulation of the Alfred P. Murrah Federal Building Collapse due to Blast Loads," in *Building Integration Solutions (Architectural Engineering Conference, AEI 2006)*, Omaha, 2006.
- [5] E. Brunesi, R. Nascimbene, F. Parisi and N. Augenti, "Progressive Collapse Fragility of Reinforced Concrete Framed Structures Through Incremental Dynamic Analysis," *Engineering Structures*, vol. 104, pp. 65-79, 2015.
- [6] General Service Administration (GSA), *Alternate Path Analysis & Design Guidelines for Progressive Collapse Resistance*, Washington, DC, 2013.
- [7] Department of Defense (DOD), *United Facilities Criteria (UFC): Design of Buildings to Resist Progressive Collapse*, UFC 4-023-03, Washington, DC, 2009.
- [8] H. M. Elsanadedy, T. H. Almusallam, Y. R. Alharbi, Y. A. Al-Salloum and H. Abbas, "Progressive Collapse Potential of a Typical Steel Building Due to Blast Attacks," *Journal of Constructional Steel Research*, vol. 101, pp. 143-157, 2014.

REFERENCES

- [9] Y. A. Al-Salloum, T. H. Almusallam, M. Y. Khawaji, T. Ngo, H. M. Elsanadedy and H. Abbas, "Progressive Collapse Analysis of RC Buildings Against Internal Blast," *Advances in Structural Engineering*, vol. 18, no. 12, pp. 2181-2192, 2015.
- [10] S. Gerasimidis and J. Sideri, "A New Partial-Distributed Damage Method for Progressive Collapse Analysis of Steel Frames," *Journal of Constructional Steel Research*, vol. 119, pp. 233-245, 2016.
- [11] Department of Defense (DOD), United Facilities Criteria (UFC): Structural Engineering, UFC 3-301-01, Washington, DC, 2013.
- [12] A. A. Khalil, "Enhanced Modeling of Steel Structures for Progressive Collapse Analysis Using the Applied Element Method," *Journal of Performance of Constructed Facilities*, vol. 26, no. 6, pp. 766-779, 2012.
- [13] B. A. Izzuddin, A. Y. Vlassis and D. A. Nethercot, "Progressive Collapse of Multi-Storey Buildings Due to Sudden Column Loss - Part I: Simplified Assessment Framework," *Engineering Structures*, vol. 30, pp. 1308-1318, 2008.
- [14] W. Yi, F. Yi and Y. Zhou, "Experimental Studies on Progressive Collapse Behavior of RC Frame Structures: Advances and Future Needs," *International Journal of Concrete Structures and Materials*, vol. 15, no. 31, pp. 1-23, 2021.
- [15] H. Jian and S. Li, "Progressive Collapse Resistance of RC Frames under a Side Column Removal Scenario: The Mechanism Explained," *International Journal of Concrete Structures and Materials*, vol. 10, no. 2, p. 237-247, 2016.
- [16] H. S. Lew, Y. Bao, S. Pujol and M. A. Sozen, "Experimental Study of Reinforced Concrete Assemblies under Column Removal Scenario," *ACI Structural Journal*, vol. 111, no. 4, pp. 881-892, 2014.
- [17] R. Ahmadi, O. Rashidian, R. Abbasnia and F. M. Nav, "Experimental and Numerical Evaluation of Progressive Collapse Behavior in Scaled RC Beam-Column Subassembly," *Shock and Vibration*, vol. 2016, no. 1, 2016.

REFERENCES

- [18] Z. Xi, Z. Zhang, W. Qin and P. Zhang, "Experiments and a Reverse-Curved Compressive Arch Model for the Progressive Collapse Resistance of Reinforced Concrete Frames," *Engineering Failure analysis*, vol. 135, 2022.
- [19] N. FarhangVesali, H. Valipour, B. Samali and S. Foster, "Development of Arching Action in Longitudinally-Restrained Reinforced Concrete Beams," *Construction and Building*, vol. 47, pp. 7-19, 2013.
- [20] J. Yu and K. H. Tan, "Experimental and Numerical Investigation on Progressive Collapse Resistance of Reinforced Concrete Beam Column Sub-Assemblages," *Engineering Structures*, vol. 55, pp. 90-106, 2013.
- [21] J. Yu and K. H. Tan, "Structural Behavior of RC Beam-Column Subassemblages under a Middle Column Removal Scenario," *Journal of Structural Engineering*, vol. 139, no. 2, pp. 233-250, 2013.
- [22] Y. Su, Y. Tian and X. Song, "Progressive Collapse Resistance of Axially-Restrained Frame Beams," *ACI Structural Journal*, vol. 106, no. 5, pp. 600-607, 2009.
- [23] X.-L. Gu, B. Zhang, X.-K. Huang and X.-L. Wang, "Experimental Investigation on Progressive Collapse Resistance of Precast Concrete Frame Structures with Different Beam-Column Connections," *Journal of Building Engineering*, vol. 56, 2022.
- [24] K. Qian, B. Li and J.-X. Ma, "Load-Carrying Mechanism to Resist Progressive Collapse of RC Buildings," *Journal of Structural Engineering*, vol. 141, no. 2, p. 04014107, 2015.
- [25] K. Qian, B. Li and Z. Zhang, "Testing and Simulation of 3D Effects on Progressive Collapse Resistance of RC Buildings," *Magazine of Concrete Research*, vol. 67, no. 4, pp. 163-178, 2015.
- [26] N. S. Lim, K. Tan and C. Lee, "Experimental Studies of 3D RC Substructures under Exterior and Corner Column Removal Scenarios," *Engineering Structures*, vol. 150, pp. 409-427, 2017.
- [27] J. M. Adam, M. Buitrago, E. Bertolesi, J. Sagaseta and J. J. Moragues, "Dynamic Performance of a Real-Scale Reinforced Concrete Building Test under a Corner-Column Failure Scenario," *Engineering Structures*, vol. 210, 2020.

REFERENCES

- [28] K. Qian and B. Li, "Dynamic Performance of RC Beam-Column Substructures Under the Scenario of the Loss of a Corner Column—Experimental Results," *Engineering Structures*, vol. 42, pp. 154-167, 2012.
- [29] K. Qian and B. Li, "Dynamic and Residual Behavior of Reinforced Concrete Floors Following Instantaneous Removal of a Column," *Engineering Structures*, vol. 148, pp. 175-184, 2017.
- [30] K. Qian, X.-Y. Chen and T. Huang, "Dynamic Response of RC Beam-Slab Substructures Following Instantaneous Removal of Columns," *Journal of Building Engineering*, vol. 45, 2022.
- [31] H.-S. Kim, J.-G. Ahn and H.-S. Ahn, "Computational Simulation of Progressive Collapse of Reinforced Concrete Rigid Frame with Reinforcement Contact Model," *Advances in Structural Engineering*, vol. 19, no. 6, pp. 982-994, 2016.
- [32] Y. Bao and S. K. Kunnath, "Simplified Progressive Collapse Simulation of RC Frame-Wall Structures," *Engineering Structures*, vol. 32, no. 10, pp. 3153-3162, 2010.
- [33] M. Talaat and K. M. Mosalam, "Modeling Progressive Collapse in Reinforced Concrete Buildings Using Direct Element Removal," *Earthquake Engineering & Structural Dynamics*, vol. 38, no. 5, pp. 609-634, 2009.
- [34] I. Leahu-Aluas and F. Abed-Meraim, "A Proposed Set of Popular Limit-Point Buckling Benchmark Problems," *Structural Engineering and Mechanics*, vol. 38, no. 6, pp. 767-802, 2011.
- [35] B. A. Memon and X.-z. Su, "Arc-Length Technique for Nonlinear Finite Element Analysis," *Zhejiang University SCIENCE*, vol. 5, no. 5, pp. 618-628, 2004.
- [36] M. A. M. Torkamani and M. Sonmez, "Solution Techniques for Nonlinear Equilibrium Equations," in *Structures Congress 2008: 18th Analysis and Computation Specialty Conference*, Vancouver, 2008.
- [37] E. Masoero, F. K. Wittel, H. J. Herrmann and B. M. Chiaia, "Progressive Collapse Mechanisms of Brittle and Ductile Framed Structures," *Journal of Engineering Mechanics*, vol. 136, no. 8, pp. 987-995, 2010.
- [38] X. Lu, X. Lin and L. Ye, "Simulation of Structural Collapse with Coupled Finite Element-Discrete Element Method," in *Computational Structural Engineering*, Shanghai, 2009.

REFERENCES

- [39] K. Meguro and H. Tagel-Din, "A New Simplified and Efficient Technique for Fracture Behavior Analysis of Concrete Structures," in *Fracture Mechanics of Concrete Structures (FraMCoS-3)*, Gifu, 1998.
- [40] K. Meguro and H. Tagel-Din, "Applied Element Method for Structural Analysis: Theory and Application for Linear Materials," *Structural Engineering / Earthquake Engineering*, vol. 17, pp. 21-35, 2000.
- [41] H.-S. Kim and H.-H. Wee, "Separation Strain for Progressive Collapse Analysis of Reinforced Concrete Building Using Applied Element Method," *Advances in Structural Engineering*, vol. 19, no. 3, pp. 437-448, 2016.
- [42] H. Tagel-Din and K. Meguro, "Nonlinear Simulation of RC Structures Using Applied Element Method," *Structural Engineering / Earthquake Engineering*, vol. 17, pp. 137-148, 2000.
- [43] V. Gohel, P. V. Patel and D. Joshi, "Analysis of Frame using Applied Element Method (AEM)," in *Chemical, Civil and Mechanical Engineering Tracks of 3rd Nirma University International Conference on Engineering (NUiCONE 2012)*, Ahmedabad, 2012.
- [44] A. Shakeri and K. Bargi, "Use of Applied Element Method for Structural Analysis," *KSCE Journal of Civil Engineering*, vol. 19, no. 5, pp. 1375-1384, 2015.
- [45] K. Meguro and H. Tagel-Din, "Applied Element Simulation of RC Structures Under Cyclic Loading," *Journal of Structural Engineering*, vol. 127, no. 11, pp. 1295-1305, 2001.
- [46] K. Meguro and H. S. Tagel-Din, "Applied Element Method Used for Large Displacement Structural Analysis," *Journal of Natural Disaster Science*, vol. 24, no. 1, pp. 25-34, 2002.
- [47] Reuters, "Oklahoma City victims remembered 20 years after bombing," Reuters, 19 April 2015. [Online]. Available: <https://www.reuters.com/article/world/uk/oklahoma-city-victims-remembered-20-years-after-bombing-idUSKBN0NA0EW/>. [Accessed 28 April 2025].
- [48] S. J. Mirvalad, "Robustness and Retrofit Strategies for Seismically-Designed Multistory Steel Frame Buildings Prone to Progressive Collapse," Montreal, 2013.

REFERENCES

- [49] Z. X. Fang and H. T. Fan, "Redundancy of Structural Systems in the Context of Structural Safety," in *The Twelfth East Asia-Pacific Conference on Structural Engineering and Construction (EASEC 12)*, Hong Kong, 2011.
- [50] F. Rouhani, "Developing a Plastic Hinge Model for RC Beams Prone to Progressive Collapse," Montreal, 2015.
- [51] M. Adom-Asamoah and N. O. Ankamah, "Effect of Design Ductility on the Progressive Collapse Potential of RC Frame Structures Designed to Eurocode 8," *American Journal of Civil Engineering*, vol. 4, no. 2, pp. 40-49, 2016.
- [52] E. Brunesi, R. Nascimbene and F. Parisi, "Progressive Collapse Fragility Models of RC Framed Buildings Based on Pushdown Analysis," in *European Congress on Computational Methods in Applied Sciences and Engineering (ECCOMAS 2016)*, Crete Island, 2016.
- [53] L. A. Bredean and M. D. Botez, "The Influence of Beams Design and the Slabs Effect on the Progressive Collapse Resisting Mechanisms Development for RC Framed Structures," *Engineering Failure Analysis*, vol. 91, pp. 527-542, 2018.
- [54] R. Abbasnia and F. M. Nav, "A Theoretical Method for Calculating the Compressive Arch Capacity of RC Beams Against Progressive Collapse," *Structural Concrete*, vol. 17, no. 1, pp. 21-31, 2016.
- [55] M. B. Parlpour, A. Budak and O. A. Düzgün, "Investigation of Progressive Collapse Resistance Mechanism in Reinforced Concrete Beam–Column Assembly," *Iranian Journal of Science and Technology, Transactions of Civil Engineering*, vol. 45, pp. 505-512, 2021.
- [56] C. G. Bailey, "Membrane Action of Slab/Beam Composite Floor Systems in Fire," *Engineering Structures*, vol. 26, no. 12, pp. 1691-1703, 2004.
- [57] K. Du, D. Yan, J. Bai, H. Chen, N. Teng and J. Sun, "Progressive-Collapse Test of Slab Effects on Reinforced Concrete Spatial Frame Substructures," *Magazine of Concrete Research*, vol. 73, no. 21, pp. 1081-1099, 2021.

REFERENCES

- [58] X. Lu, K. Lin, Y. Li, H. Guan, P. Ren and Y. Zhou, "Experimental Investigation of RC Beam-Slab Substructures Against Progressive Collapse Subject to an Edge-Column-Removal Scenario," *Engineering Structures*, vol. 149, pp. 91-103, 2017.
- [59] Y. Zeng, Y. Li, M. Sun, M. Noori and X. Wei, "Dynamic Progressive Collapse Response of 3D Monolithic Precast Concrete Frame Structures Considering Slab Effects," *Structures*, vol. 60, 2024.
- [60] Y. Wang, B. Zhang, X.-L. Gu and F. Lin, "Experimental and Numerical Investigation on Progressive Collapse Resistance of RC Frame Structures Considering Transverse Beam and Slab Effects," *Journal of Building Engineering*, vol. 47, 2022.
- [61] J. Yu, L. Luo and Y. Li, "Numerical Study of Progressive Collapse Resistance of RC Beam-Slab Substructures Under Perimeter Column Removal Scenarios," *Engineering Structures*, vol. 159, pp. 14-27, 2018.
- [62] S. Amiri, H. Saffari and J. Mashhadi, "Assessment of Dynamic Increase Factor for Progressive Collapse Analysis of RC Structures," *Engineering Failure Analysis*, vol. 84, pp. 300-310, 2018.
- [63] M. Ferraioli, "Dynamic Increase Factor for Nonlinear Static Analysis of RC Frame Buildings Against Progressive Collapse," *International Journal of Civil Engineering*, vol. 17, pp. 281-303, 2019.
- [64] International Code Council (ICC), International Building Code, Falls Church, VA, 2003.
- [65] American Society of Civil Engineers (ASCE), Minimum Design Loads for Buildings and Other Structures (SEI/ASCE 7-02), Reston, VA, 2002.
- [66] American Concrete Institute (ACI), Building Code Requirements for Structural Concrete (ACI 318-02) and Commentary (318R-02), Farmington Hills, MI, 2002.
- [67] ACI Committee 318 and American Concrete Institute, Building Code Requirements for Structural Concrete (ACI 318-19) : An ACI Standard; Commentary on Building Code Requirements for Structural Concrete (ACI 318R-19), Farmington Hills: American Concrete Institute, 2019.

REFERENCES

- [68] Canadian Commission on Building and Fire Codes, National Building Code of Canada: 2015, Ottawa: National Research Council of Canada, 2015.
- [69] Canadian Standards Association, A23.3-14 Design of Concrete Structures, Toronto: CSA Group, 2014.
- [70] Cement Association of Canada and Canadian Standards Association, Concrete Design Handbook - 4th Edition, Ottawa: Cement Association of Canada, 2016.
- [71] N. Usefi, F. M. Nav and R. Abbasnia, "Finite Element Analysis of RC Elements in Progressive Collapse Scenario," *GRAĐEVINAR*, vol. 68, no. 12, pp. 1009-1022, 2016.
- [72] Y. Bao, H. S. Lew and S. K. Kunnath, "Modeling of Reinforced Concrete Assemblies under Column-Removal Scenario," *Journal of Structural Engineering*, vol. 140, no. 1, pp. (04013026-1)-(04013026-13), 2014.
- [73] Dassault Systèmes Simulia Corp., ABAQUS 6.14: Analysis User's Guide, Providence, 2014.
- [74] L. Qingfu, G. Wei and K. Yihang, "Parameter Calculation and Verification of Concrete Plastic Damage Model of ABAQUS," in *International Conference on Architecture, Civil and Hydraulic Engineering (ACHE2019)*, Guangzhou, 2020.
- [75] B. Alfarah, F. López-Almansa and S. Oller, "New Methodology for Calculating Damage Variables Evolution in Plastic Damage Model for RC Structures," *Engineering Structures*, vol. 132, pp. 70-86, 2017.
- [76] M. Hafezolghorani, F. Hejazi, R. Vaghei, M. S. Bin Jaafar and K. Karimzade, "Simplified Damage Plasticity Model for Concrete," *Structural Engineering International*, vol. 27, no. 1, pp. 68-78, 2017.
- [77] T. Yu, J. Teng, Y. Wong and S. Dong, "Finite Element Modeling of Confined Concrete-II: Plastic-Damage Model," *Engineering Structures*, vol. 32, no. 3, pp. 680-691, 2010.
- [78] L. Hsu and C.-T. Hsu, "Complete Stress-Strain Behaviour of High-Strength Concrete Under Compression," *Magazine of Concrete Research*, vol. 46, no. 169, pp. 301-312, 1994.

REFERENCES

- [79] R. Nayal and H. A. Rasheed, "Tension Stiffening Model for Concrete Beams Reinforced with Steel and FRP Bars," *Journal of Materials in Civil Engineering*, vol. 18, no. 6, pp. 831-841, 2006.
- [80] B. Wahalathantri, D. Thambiratnam, T. Chan and S. Fawzia, "A Material Model for Flexural Crack Simulation in Reinforced Concrete Elements Using ABAQUS," in *Proceedings of the First International Conference on Engineering, Designing and Developing the Built Environment for Sustainable Wellbeing*, Brisbane, 2011.
- [81] A. Demir, H. Ozturk, K. Edip, M. Stojmanovska and A. Bogdanovic, "Effect of Viscosity Parameter on the Numerical Simulation of Reinforced Concrete Deep Beam Behavior," *The Online Journal of Science and Technology*, vol. 8, no. 3, pp. 50-56, 2018.
- [82] W. Ramberg and W. R. Osgood, "Description of Stress–Strain Curves by Three Parameters (Technical Note No. 902)," National Advisory Committee for Aeronautics, Washington DC, 1945.
- [83] Dassault Systèmes Simulia Corp., ABAQUS 2016: Getting Started with ABAQUS/CAE, 2015.
- [84] D. Stephen, D. Lam, J. Forth, J. Ye and K. Daniel Tsavdaridis, "An Evaluation of Modelling Approaches and Column Removal Time on Progressive Collapse of Building," *Journal of Constructional Steel Research*, vol. 153, pp. 243-253, 2019.
- [85] P. M. Stylianidis, D. A. Nethercot, B. A. Izzudin and A. Y. Elghazouli, "Modelling of Beam Response for Progressive Collapse Analysis," *Structures*, vol. 3, pp. 137-152, 2015.
- [86] X. Lu, K. Lin, C. Li and Y. Li, "New Analytical Calculation Models for Compressive Arch Action in Reinforced Concrete Structures," *Engineering Structures*, vol. 168, pp. 721-735, 2018.
- [87] I. Azim, J. Yang, M. F. Iqbal, M. F. Javed, S. Nazar, F. Wang and Q.-f. Liu, "Semi-analytical Model for Compressive Arch Action Capacity of RC Frame Structures," *Structures*, vol. 27, pp. 1231-1245, 2020.
- [88] P. Stylianidis, D. Nethercot, B. Izzuddin and A. Elghazouli, "Study of the Mechanics of Progressive Collapse with Simplified Beam Models," *Engineering Structures*, vol. 117, pp. 287-304, 2016.

REFERENCES

- [89] Y. Gan, J. Chen, H. Zeng and D. Zeng, "Whole-Process Analytical Model on Progressive Collapse Response of Reinforced Concrete Structures under Middle Column Loss," *Engineering Structures*, vol. 302, 2024.
- [90] R. Park and T. Paulay, *Reinforced Concrete Structures*, New York: J. Wiley & Sons, 1975.
- [91] A. C. Birely, L. N. Lowes and D. E. Lehman, "A Model for the Practical Nonlinear Analysis of Reinforced-Concrete Frames Including Joint Flexibility," *Engineering Structures*, vol. 34, pp. 455-465, 2012.

APPENDIX A. SOFTWARE VALIDATION INPUT & RESULTS

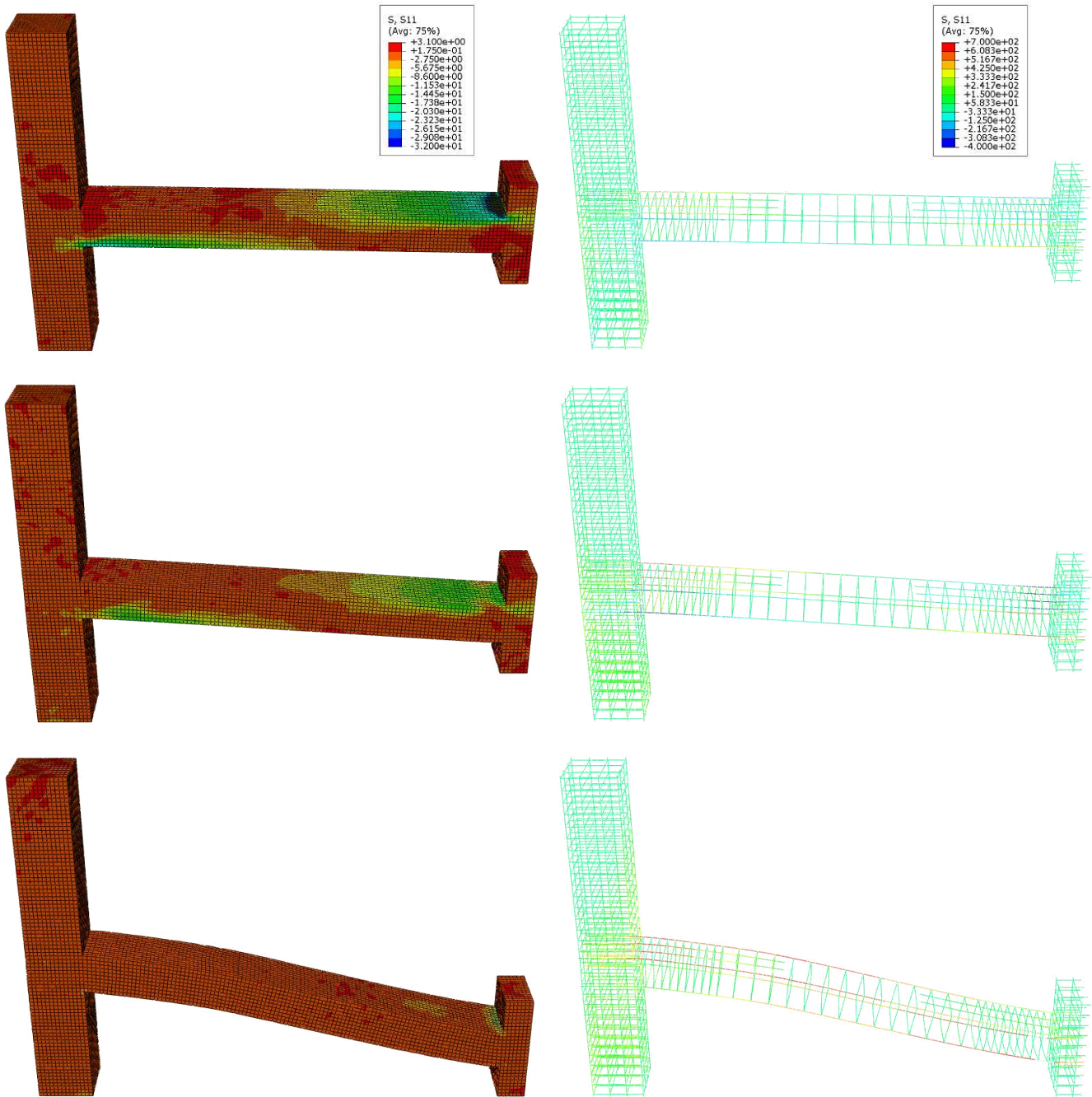


Figure A-1: Normal Stresses in Concrete in X-Direction (Left) & Rebar (Right) for IMF During Rising Arch Action, Declining Arch Action & Catenary Action

APPENDIX A: SOFTWARE VALIDATION INPUT & RESULTS

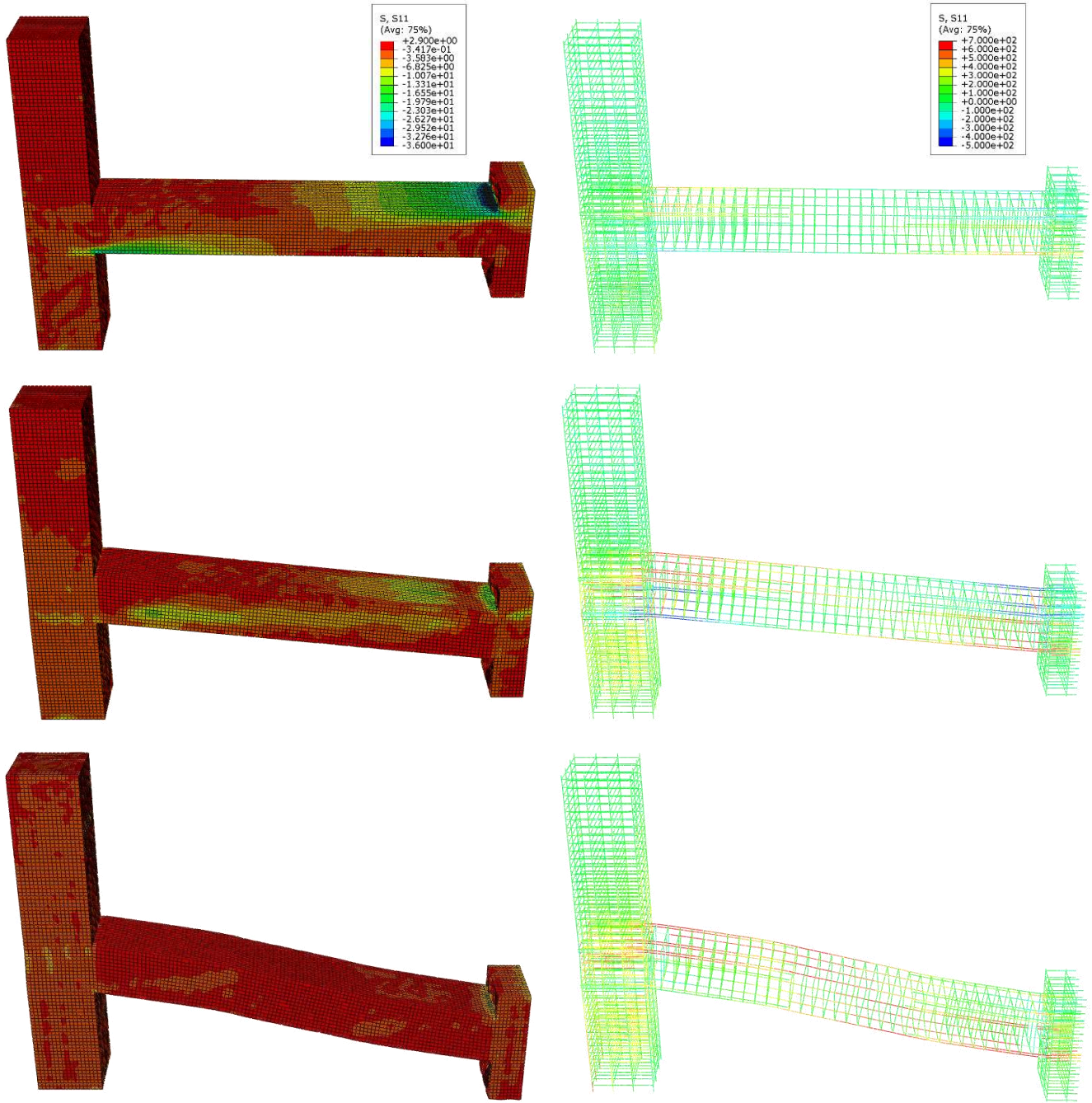


Figure A-2: Normal Stresses in Concrete in X-Direction (Left) & Rebar (Right) for SMF During Rising Arch Action, Declining Arch Action & Catenary Action

APPENDIX A: SOFTWARE VALIDATION INPUT & RESULTS

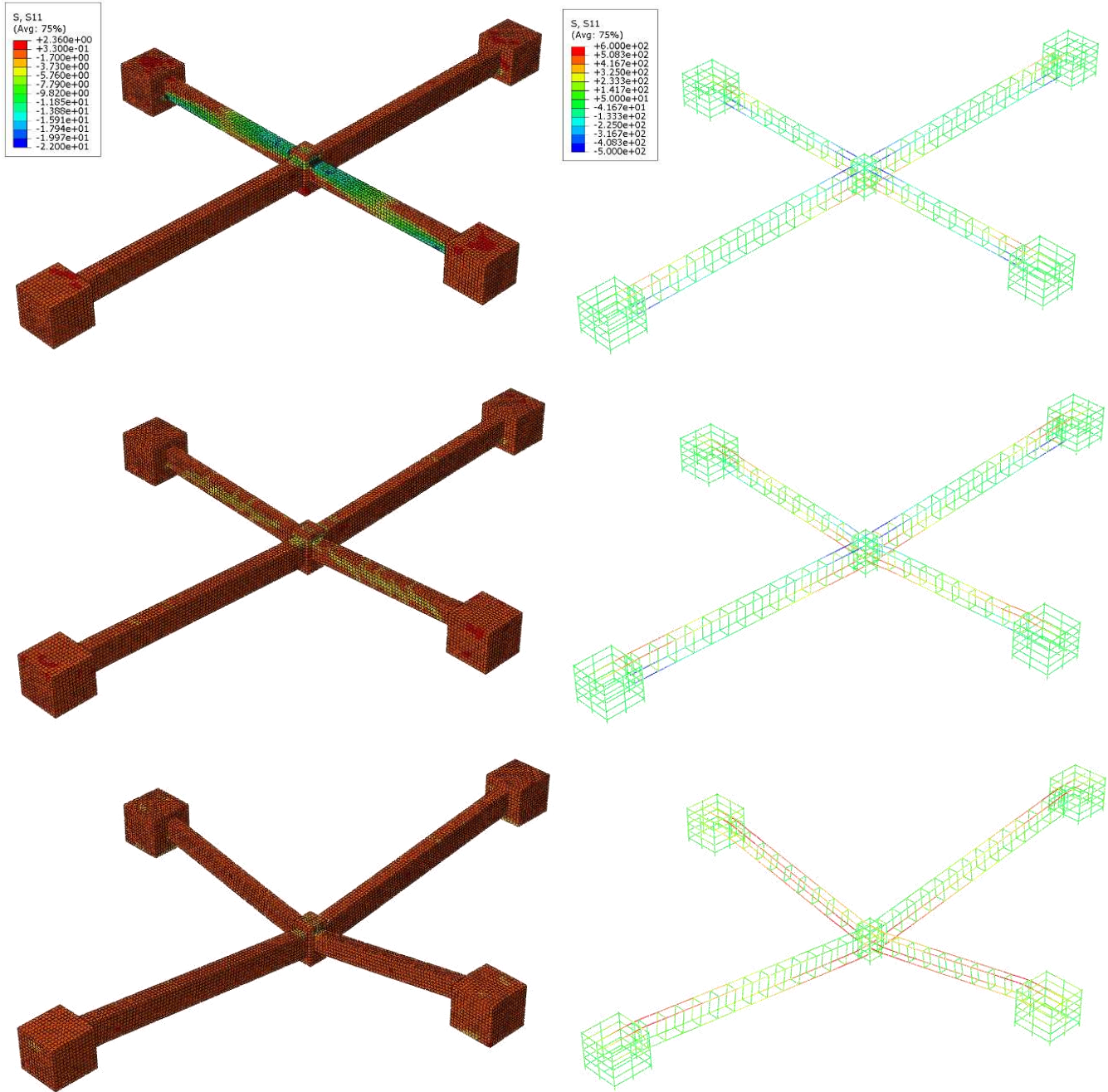


Figure A-3: Normal Stresses in Concrete in X-Direction (Left) & Rebar (Right) for T1 During Rising Arch Action, Declining Arch Action & Catenary Action

APPENDIX A: SOFTWARE VALIDATION INPUT & RESULTS

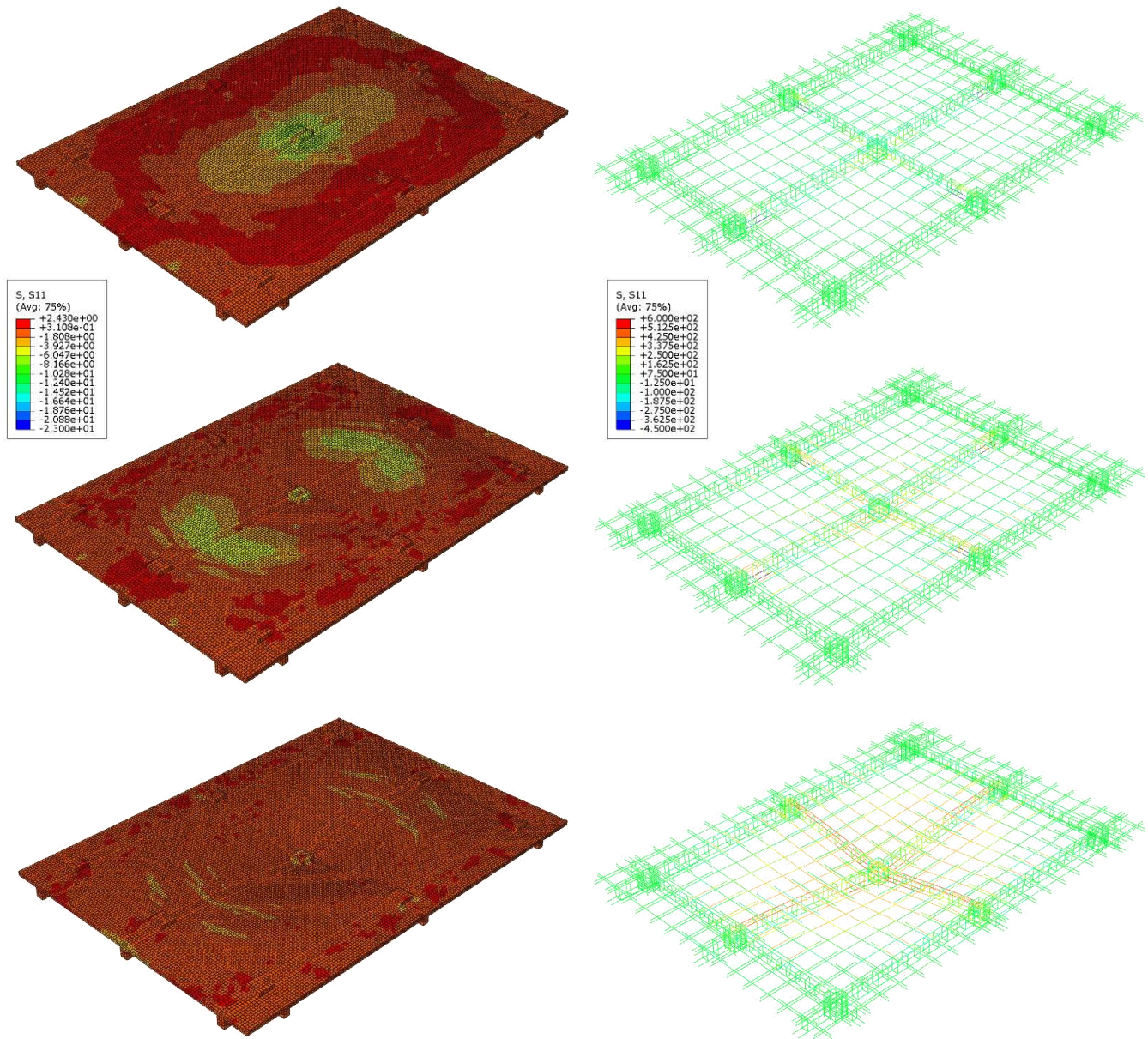


Figure A-4: Normal Stresses in Concrete in X-Direction (Left) & Rebar (Right) for S1 During Rising Arch Action, Declining Arch Action & Catenary Action

APPENDIX A: SOFTWARE VALIDATION INPUT & RESULTS

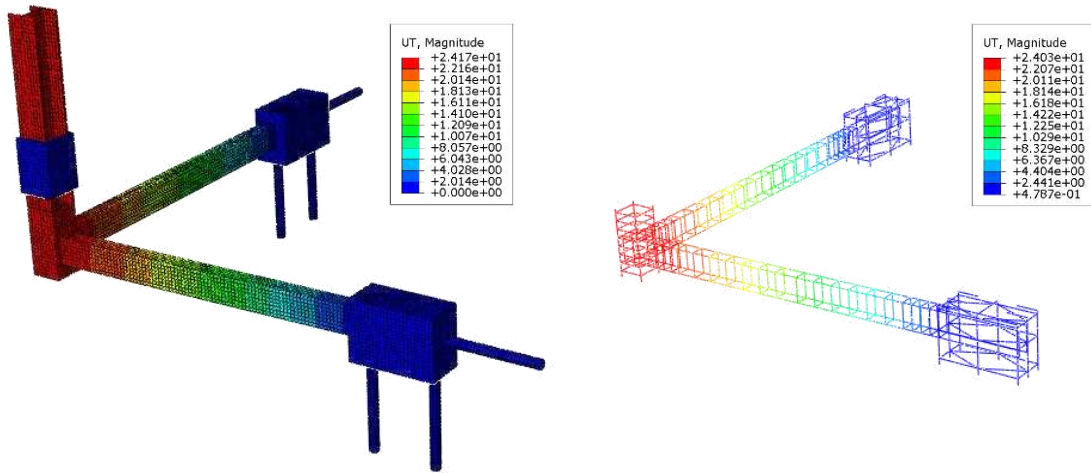


Figure A-5: Total Displacement in Solid Elements (Left) & Truss Elements (Right) in DF2 at the End of the Analysis

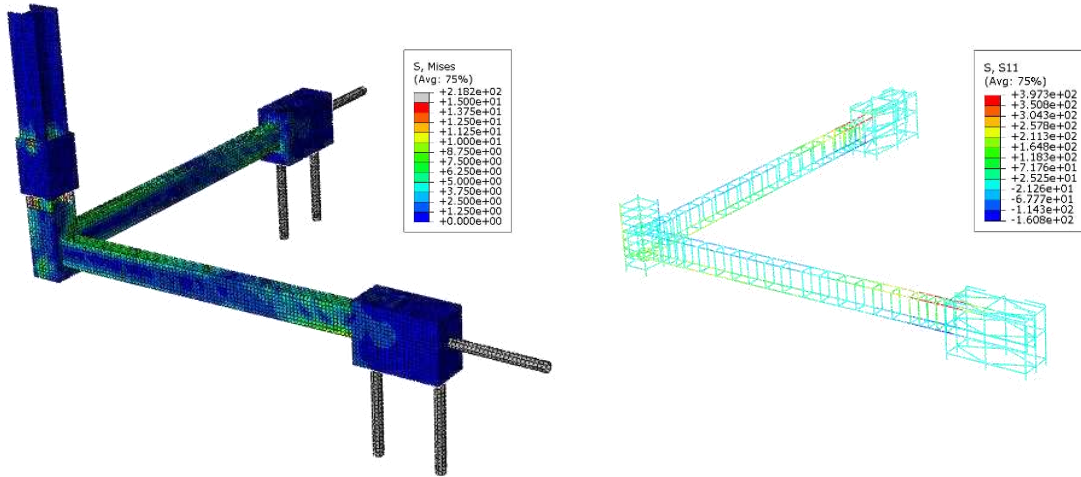


Figure A-6: Von Mises Stresses in Solid Elements (Left) & S11 Stresses in Truss Elements (Right) in DF2 at the End of the Analysis

APPENDIX A: SOFTWARE VALIDATION INPUT & RESULTS

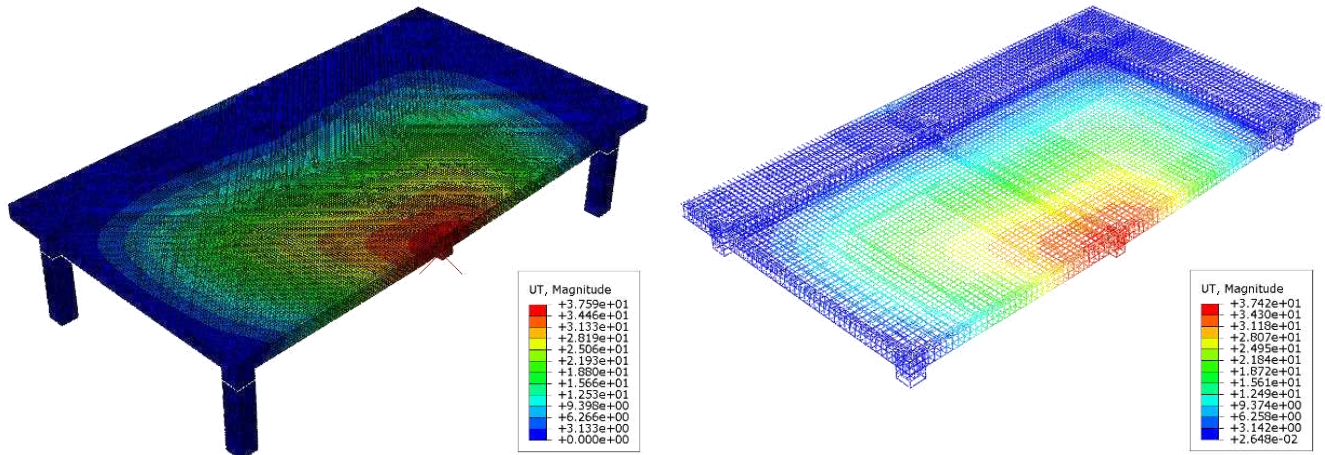


Figure A-7: Total Displacement in Solid Elements (Left) & Truss Elements (Right) in D-0.91 at the End of the Analysis

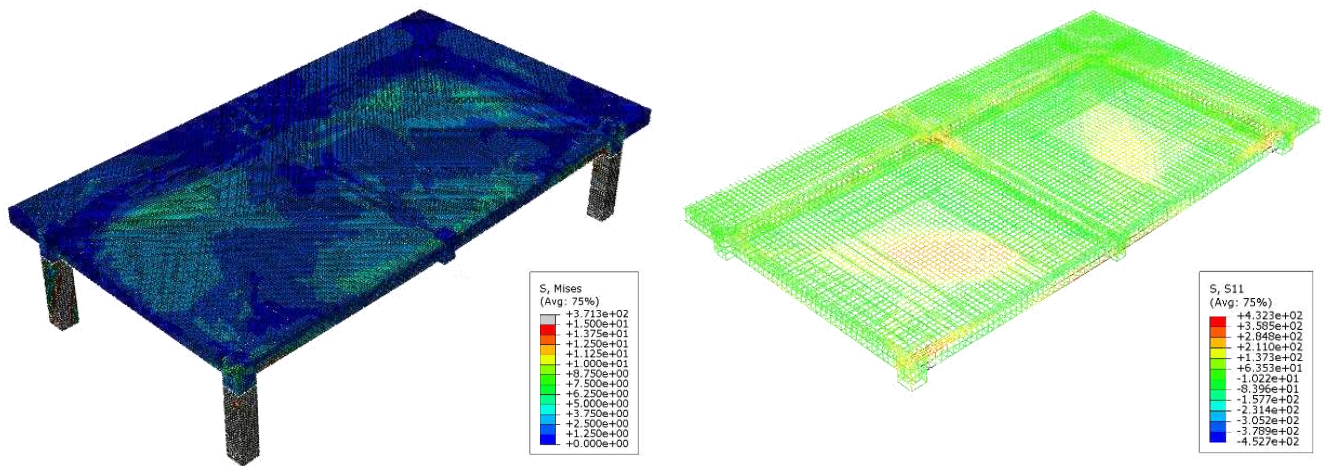


Figure A-8: Von Mises Stresses in Solid Elements (Left) & S11 Stresses in Truss Elements (Right) in D-0.91 at the End of the Analysis

APPENDIX B. RESULTS OF ANALYSIS & DESIGN OF BUILDING IN SAP2000

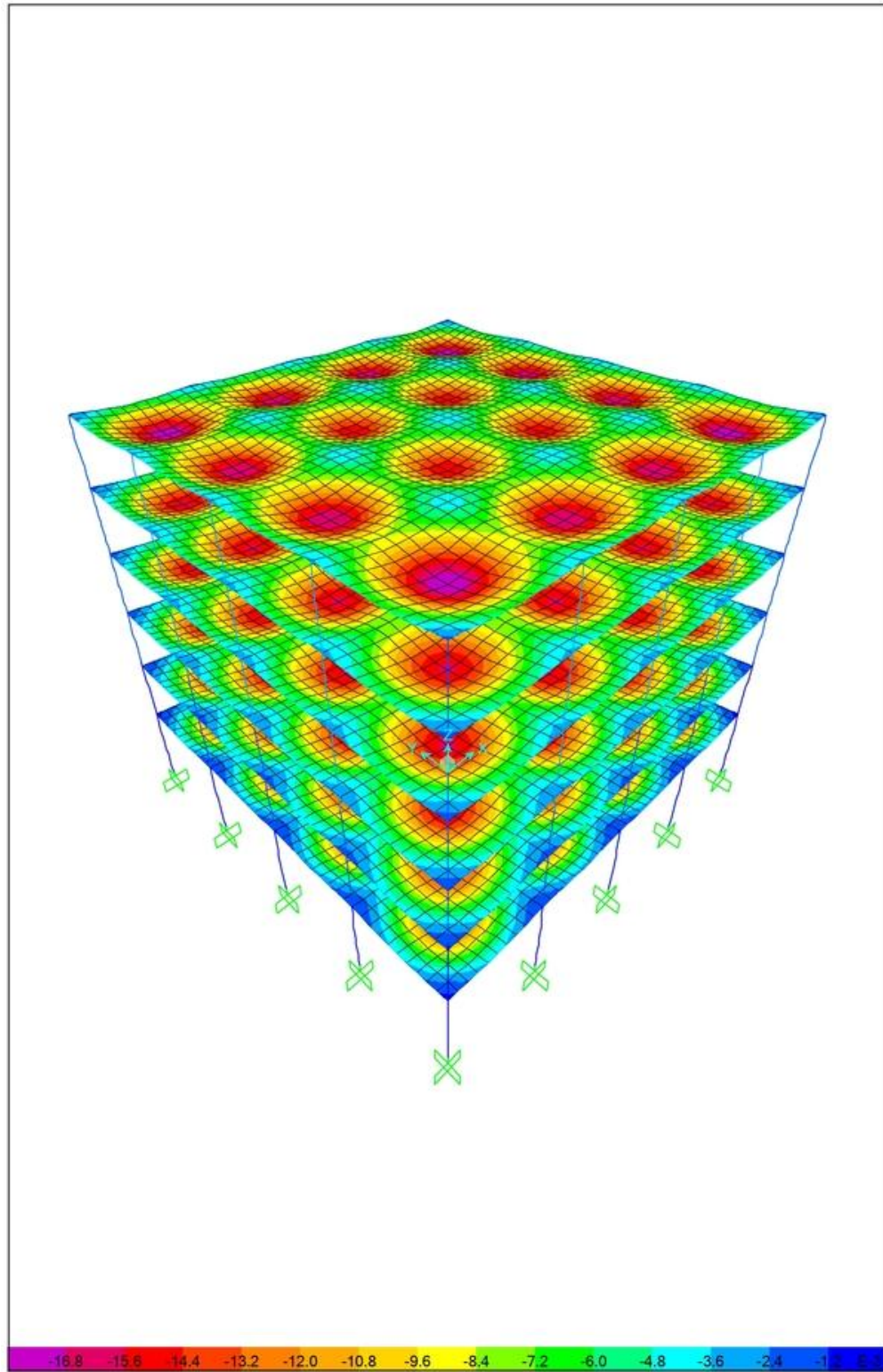


Figure B-1: Deformed Shape (Scale Factor = 50) Due to Service Loads (mm)

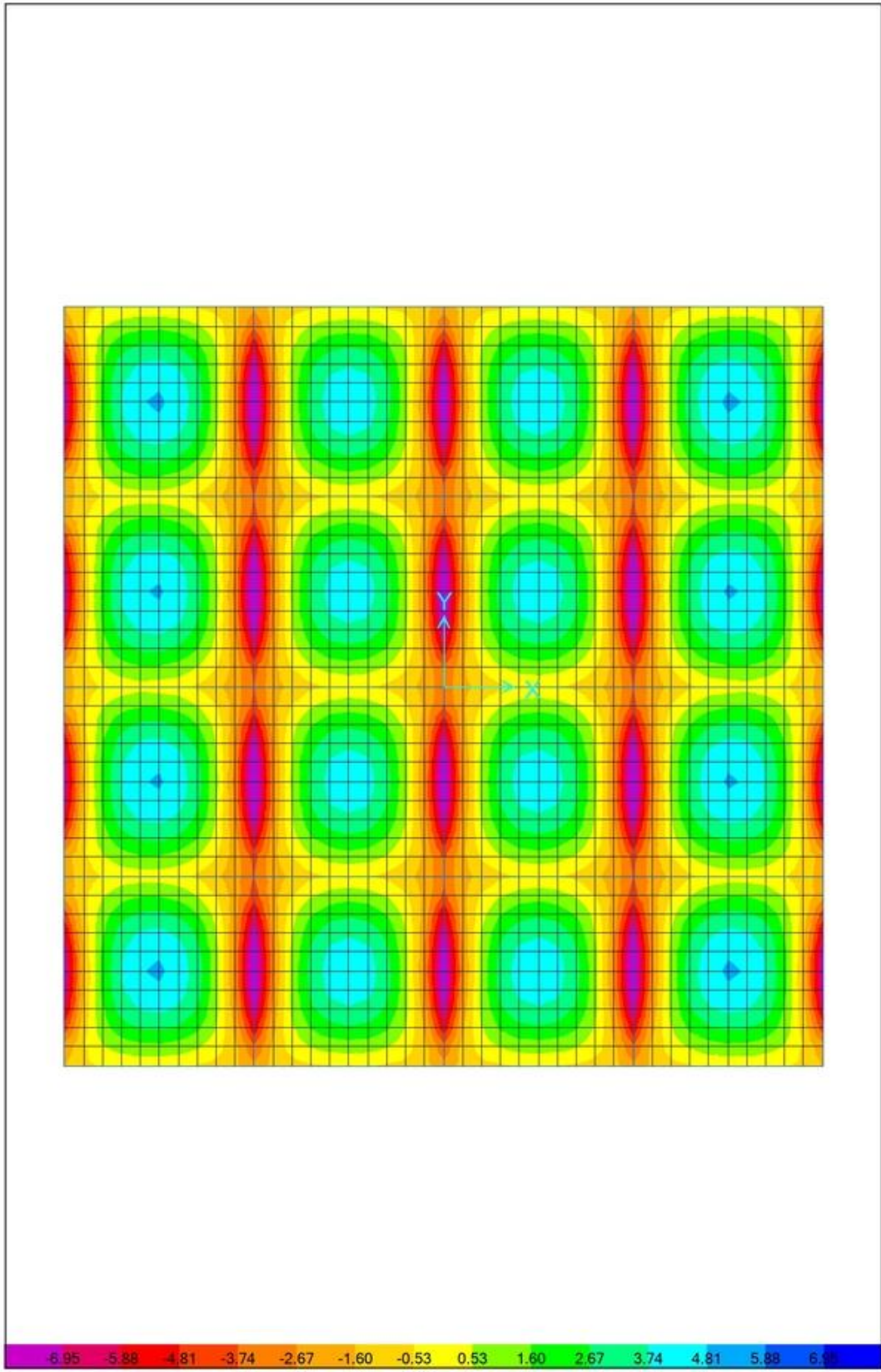
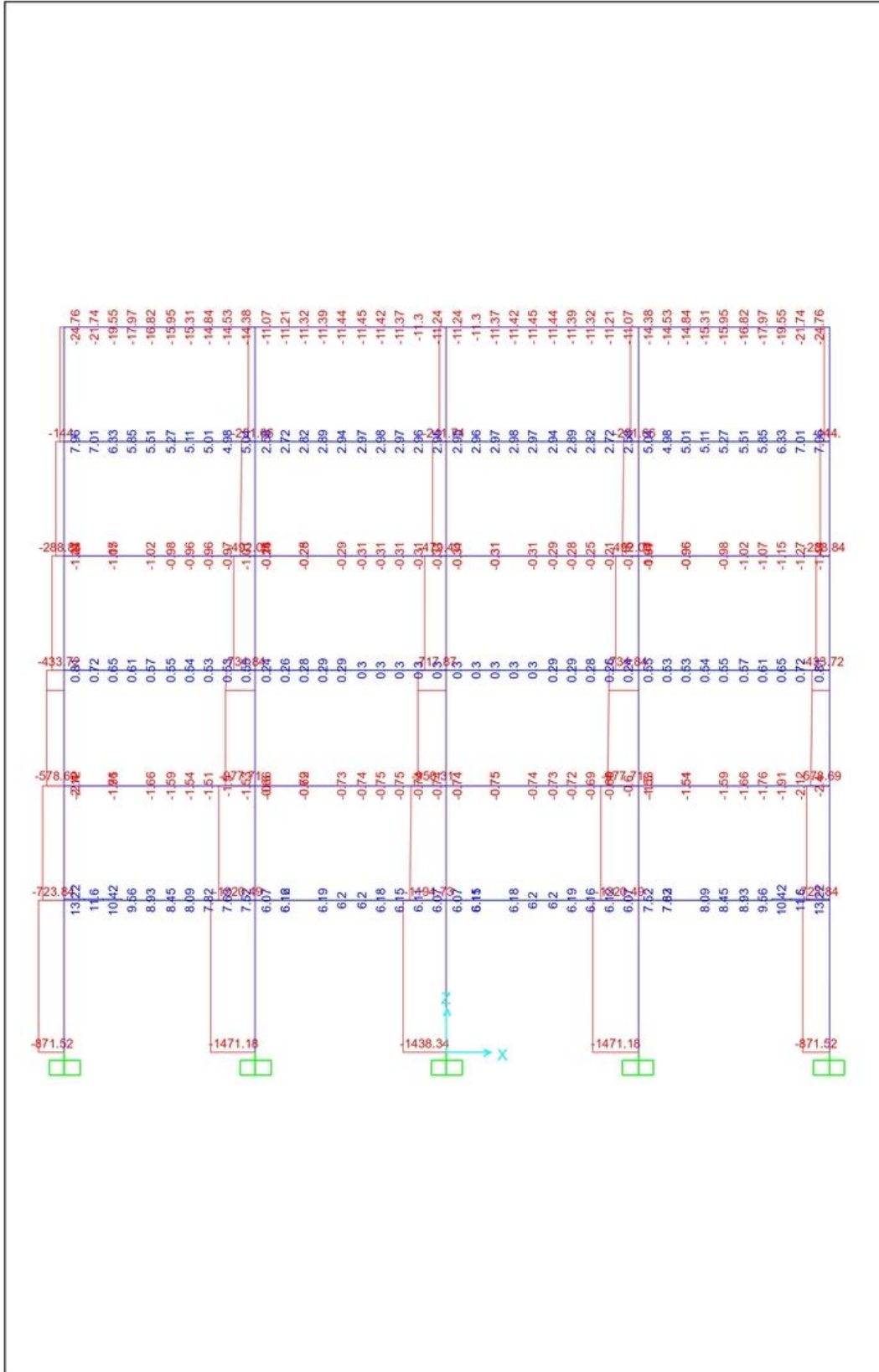


Figure B-2: Bending Moments in X-Direction in Typical Slab Due to Combo 1 (kN.mm)

APPENDIX B: RESULTS OF ANALYSIS & DESIGN OF BUILDING IN SAP2000



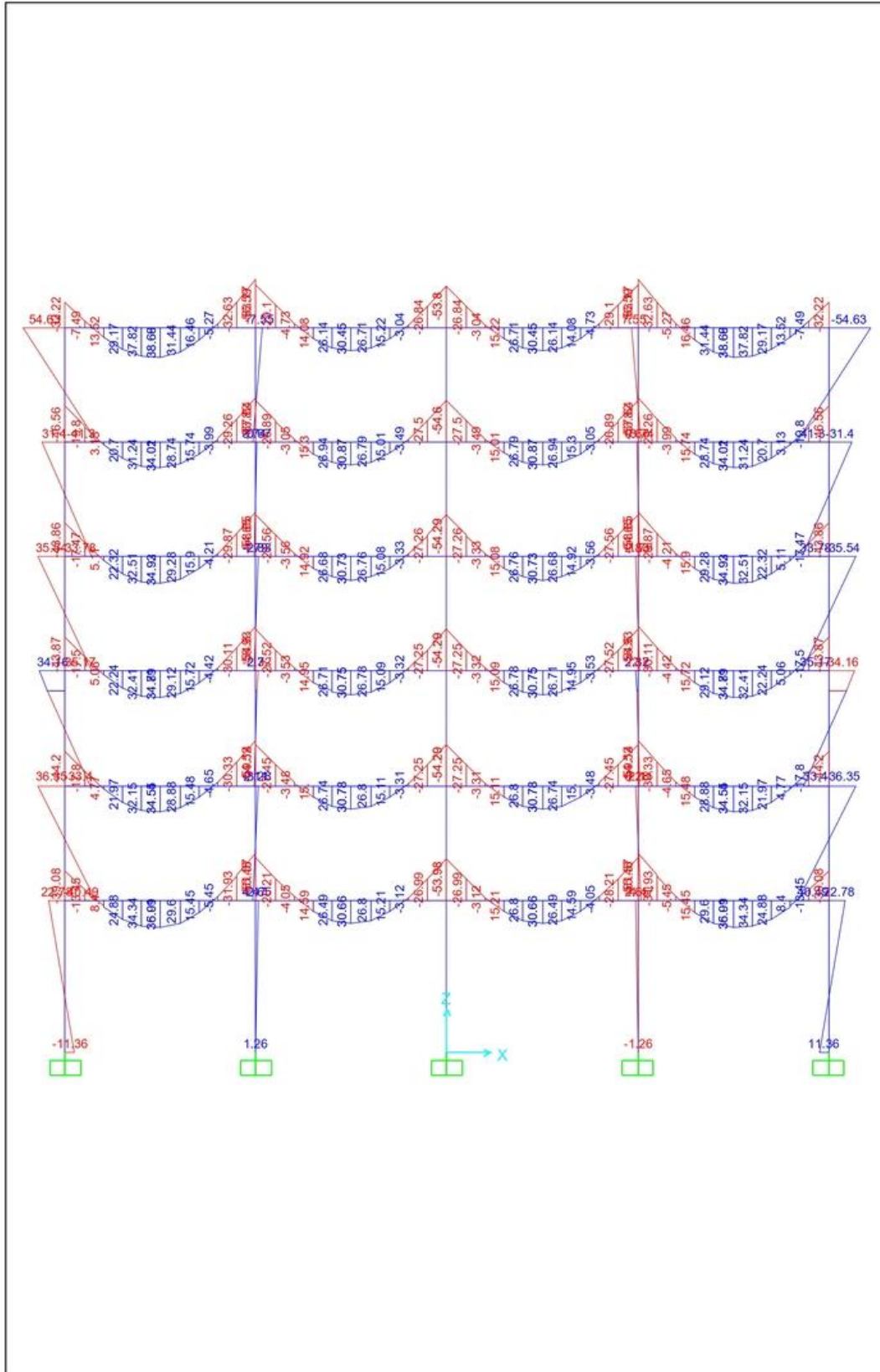


Figure B-5: In-Plane Bending Moments in Interior Frames Due to Combo 1 (kN.mm)

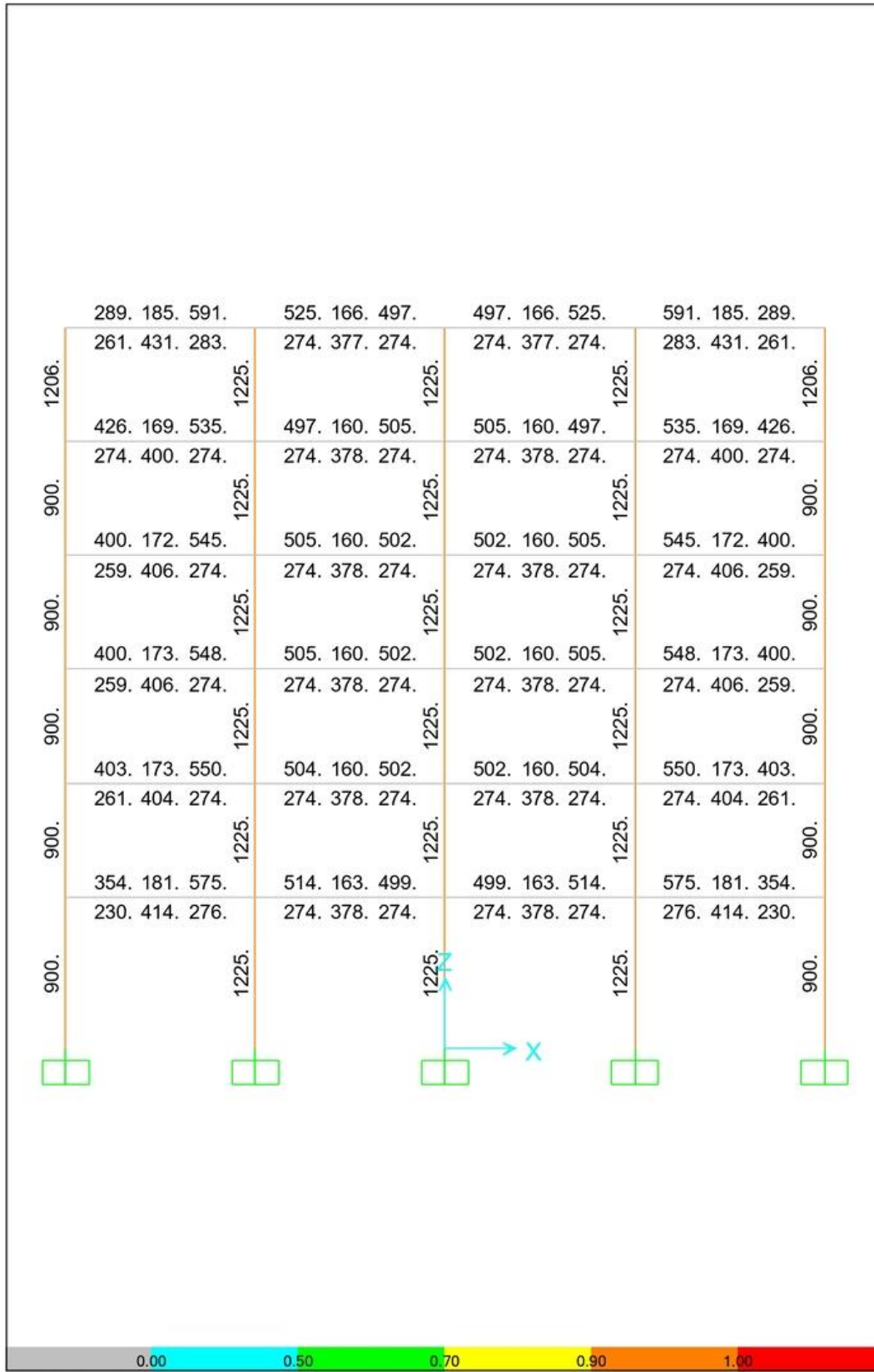


Figure B-6: Required Reinforcing Area in Interior Frames According to CSA A23.3-14 [69] (mm^2)

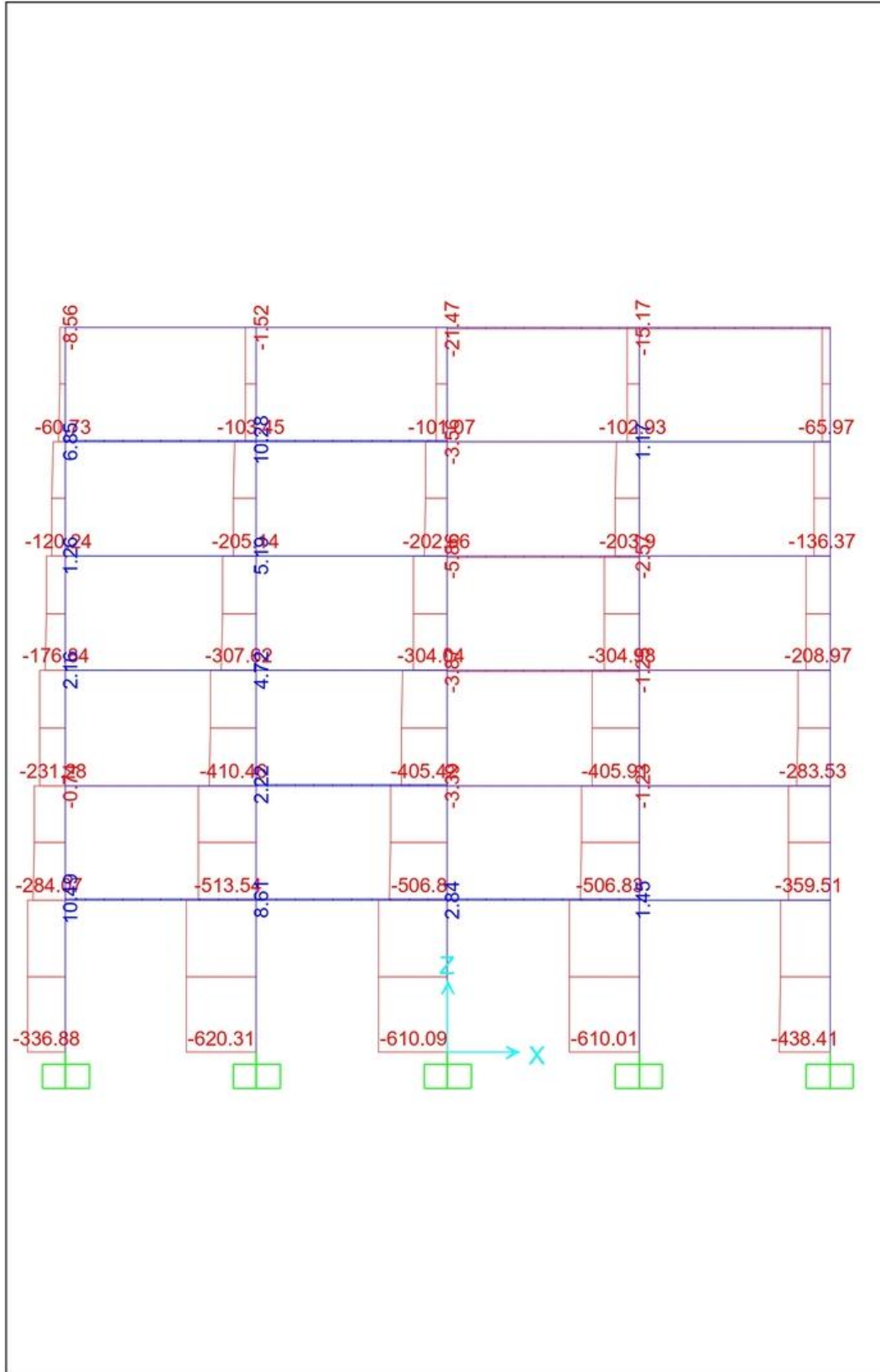


Figure B-8: Axial Forces in Exterior Frames Due to Combo 2 (kN)

APPENDIX B: RESULTS OF ANALYSIS & DESIGN OF BUILDING IN SAP2000

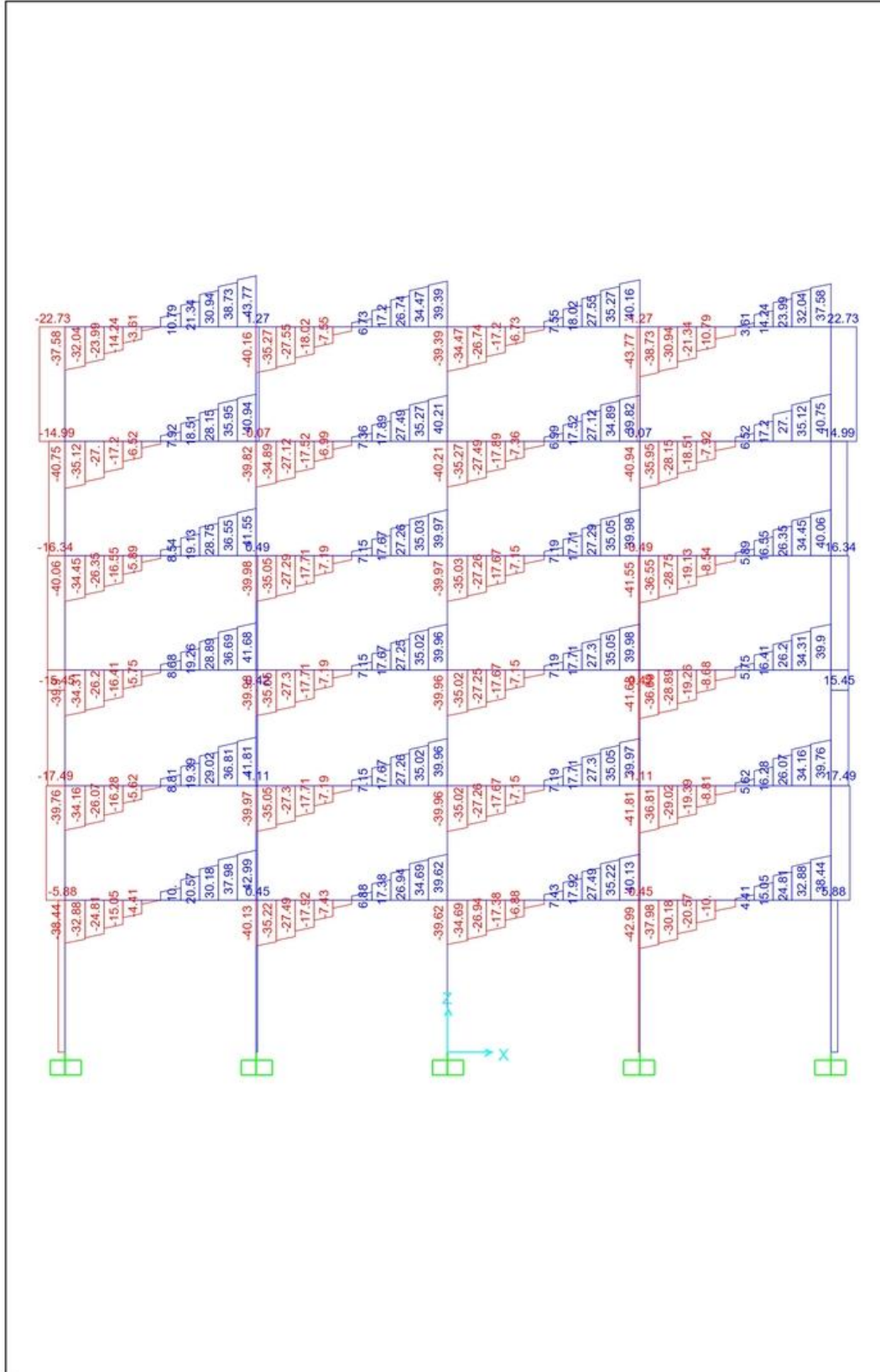


Figure B-9: In-Plane Shear Forces in Exterior Frames Due to Combo 1 (kN)

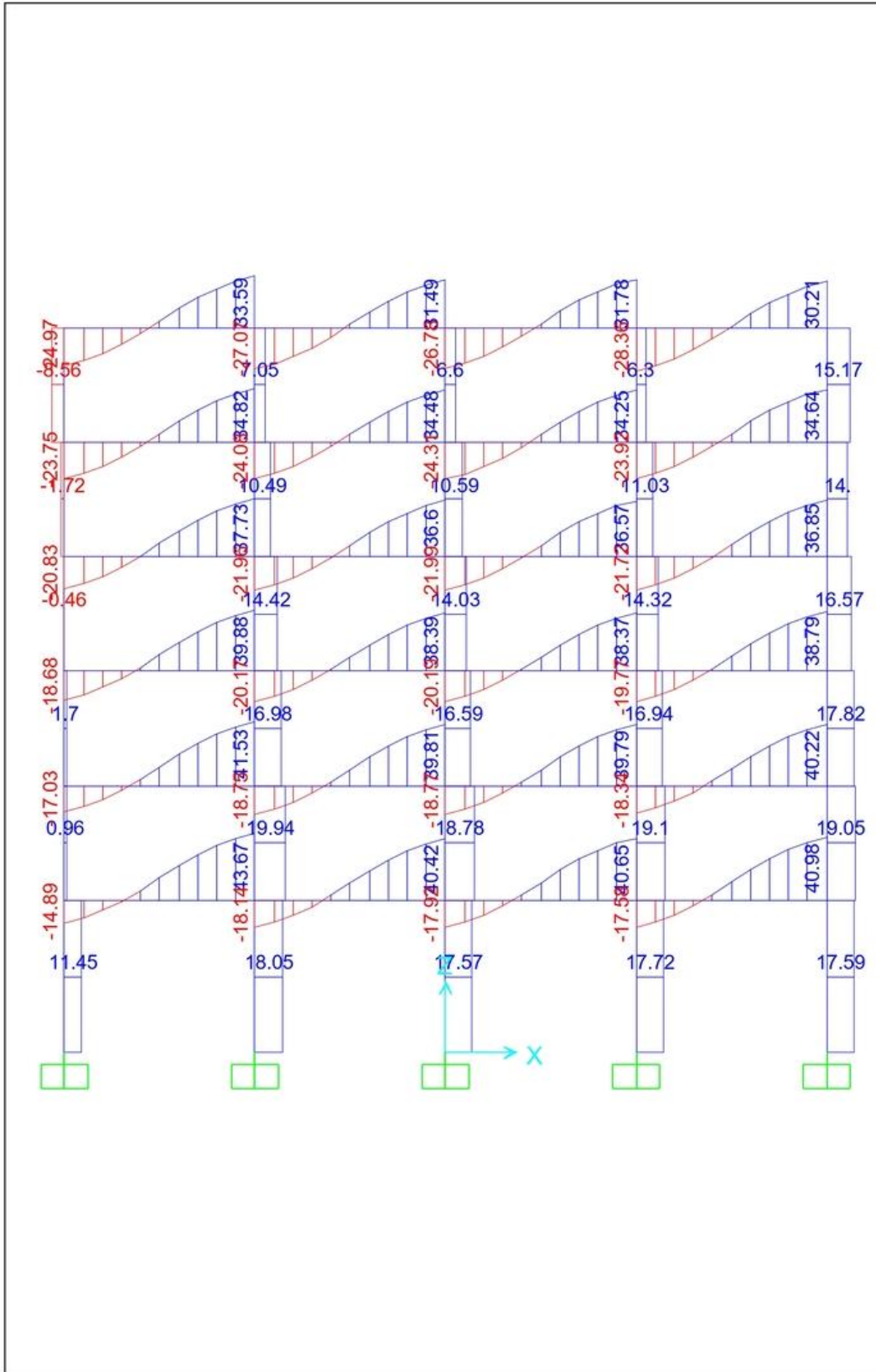


Figure B-10: In-Plane Shear Forces in Exterior Frames Due to Combo 2 (kN)

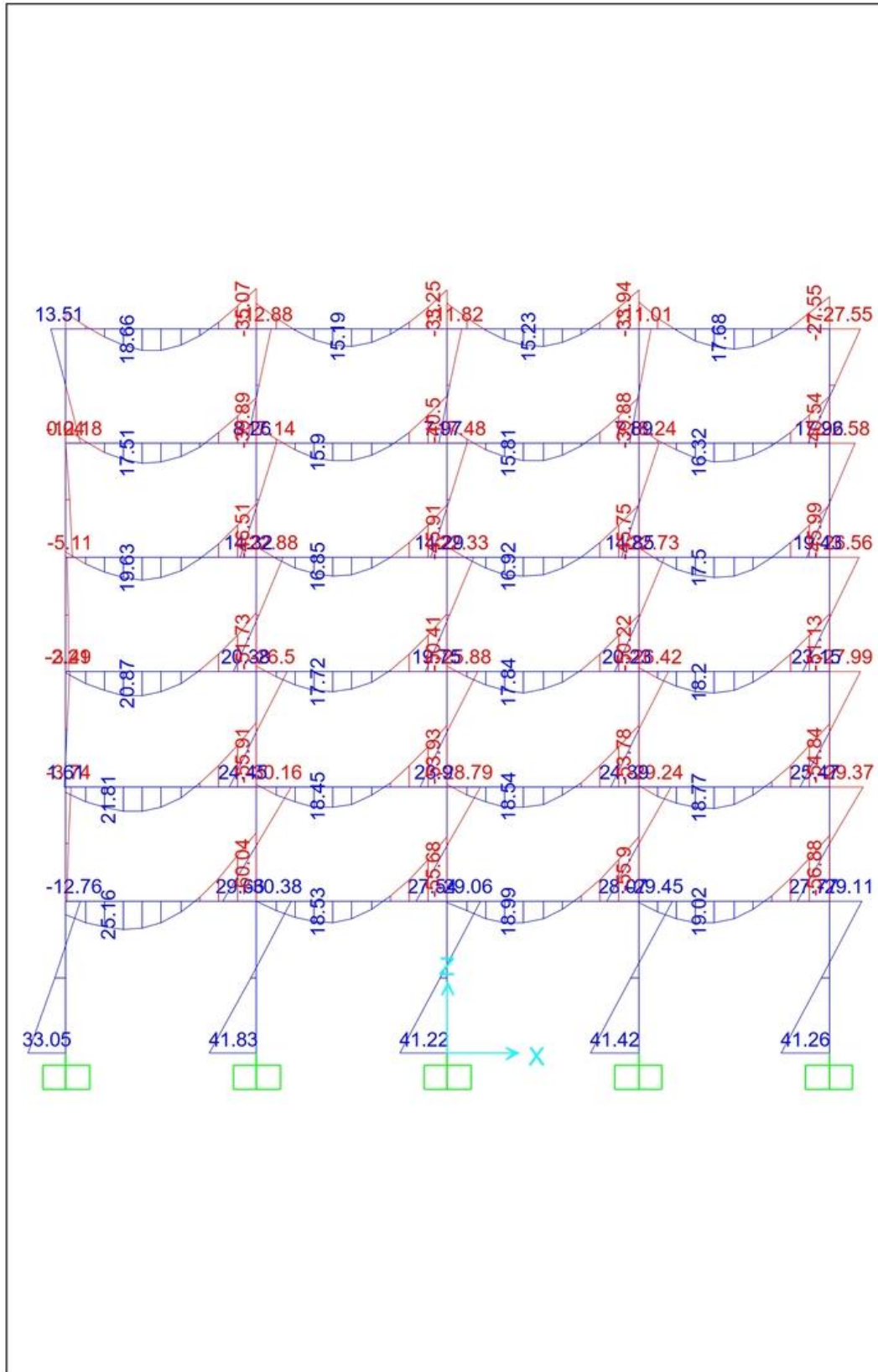


Figure B-12: In-Plane Bending Moments in Exterior Frames Due to Combo 2 (kN.mm)

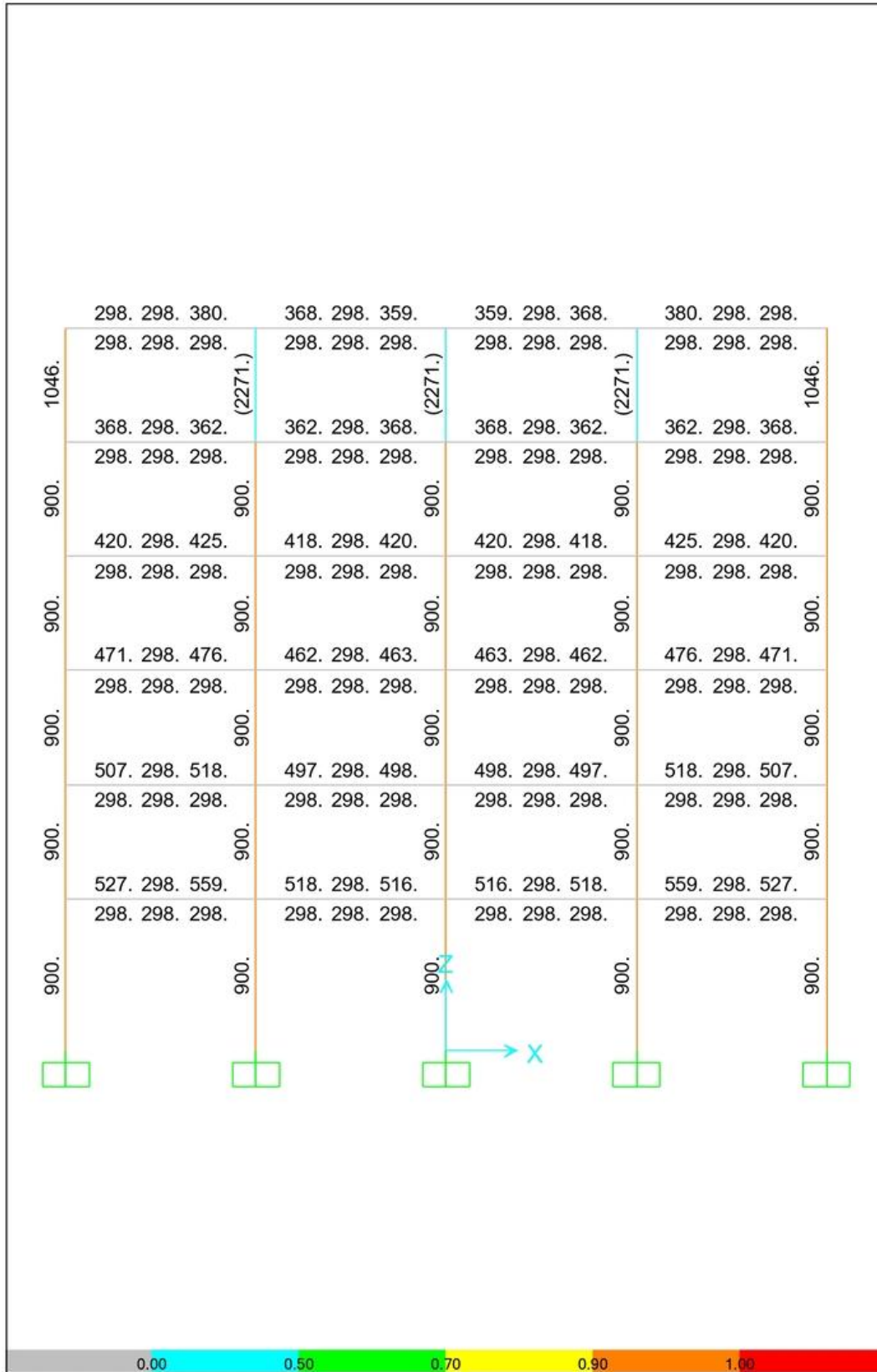


Figure B-13: Reinforcing Area in Exterior Frames According to CSA A23.3-14 [69] (mm²)

APPENDIX C. CASE STUDY DAMAGED MODELS

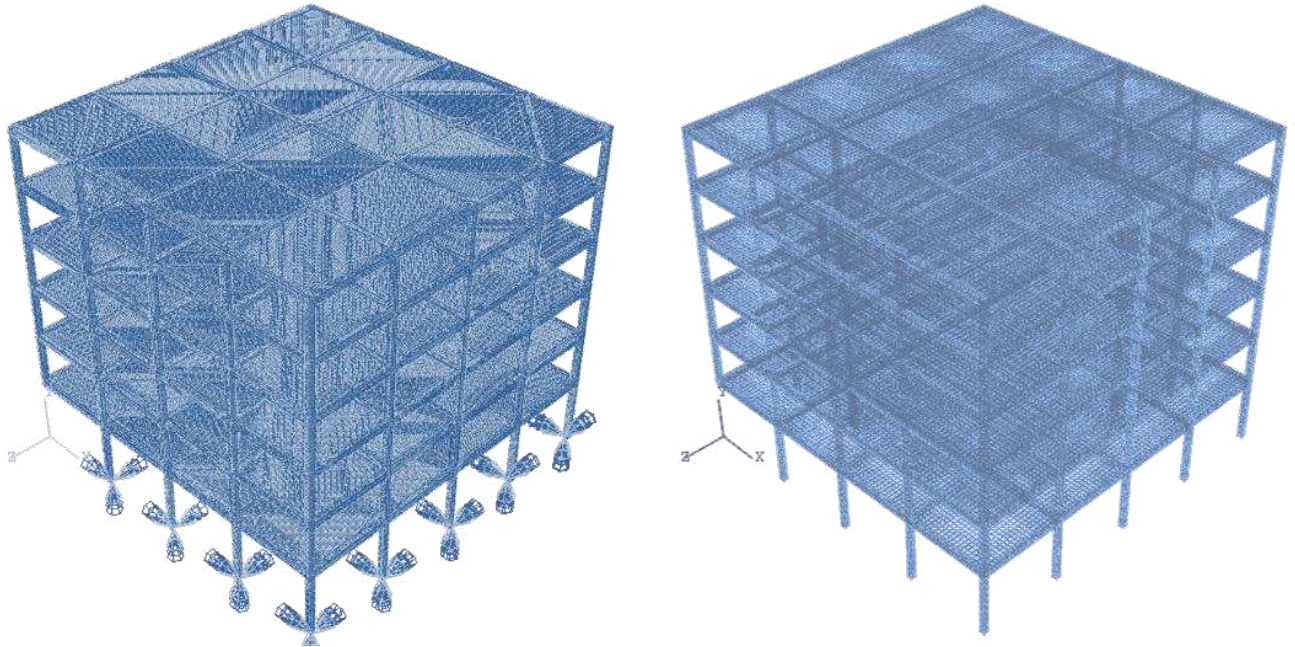


Figure C-1: Abaqus Model for FF-CC-C1 Showing Meshed Solid Elements with Restraints (Left) & Embedded Rebar (Right)

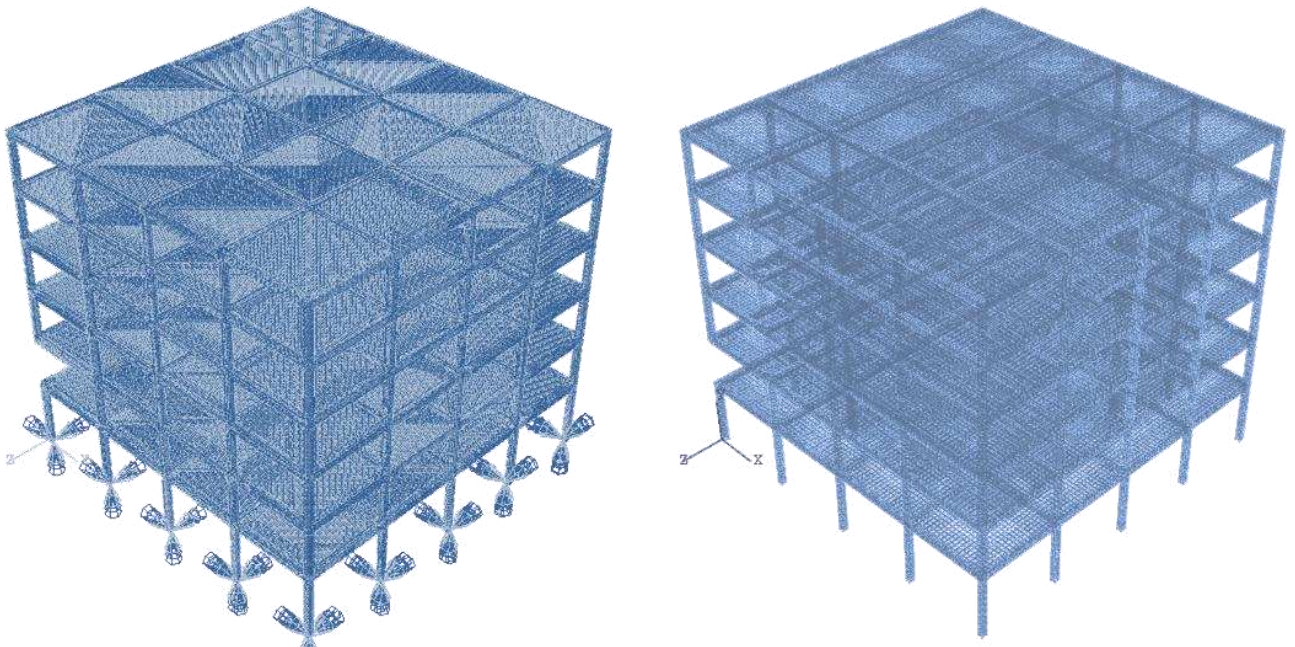


Figure C-2: Abaqus Model for FF-CC-C2 Showing Meshed Solid Elements with Restraints (Left) & Embedded Rebar (Right)

APPENDIX C: CASE STUDY DAMAGED MODELS

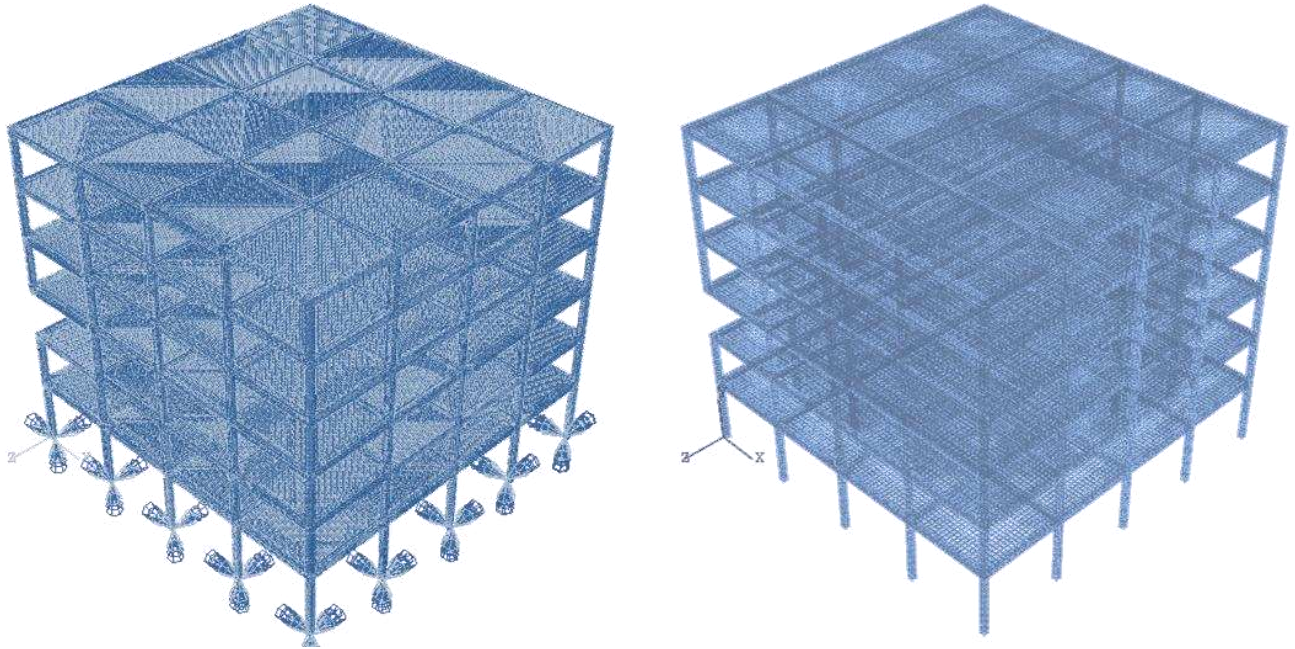


Figure C-3: Abaqus Model for FF-CC-C3 Showing Meshed Solid Elements with Restraints (Left) & Embedded Rebar (Right)

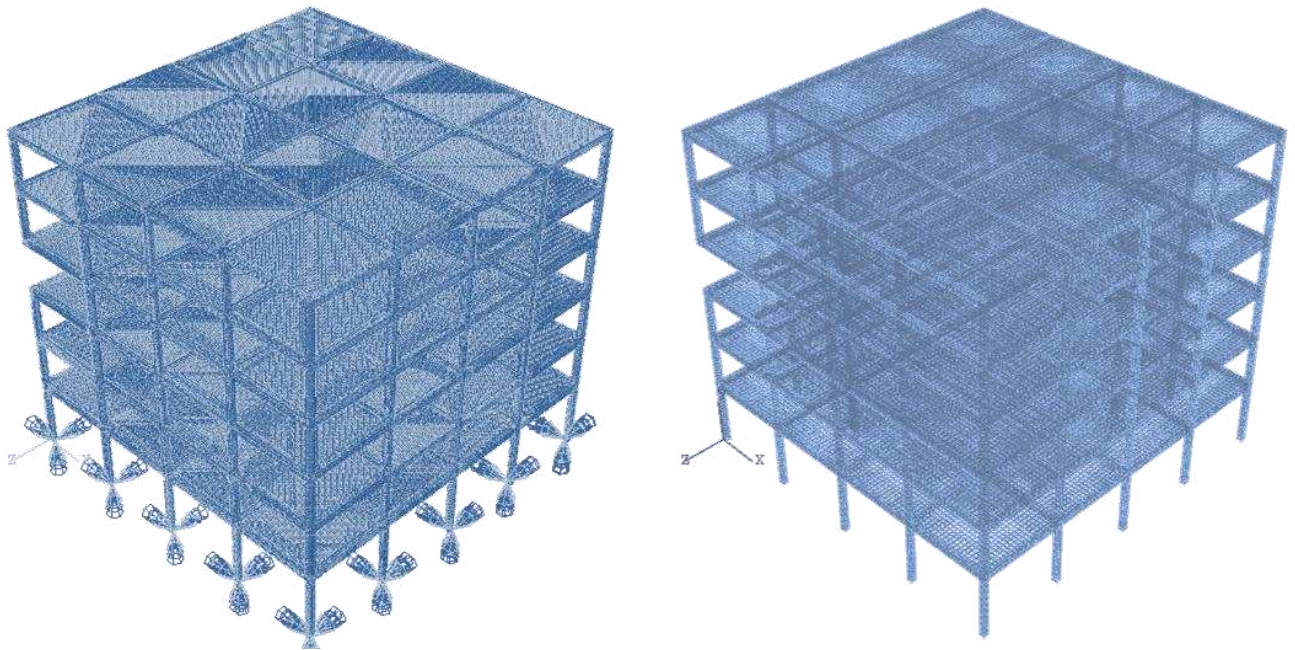


Figure C-4: Abaqus Model for FF-CC-C4 Showing Meshed Solid Elements with Restraints (Left) & Embedded Rebar (Right)

APPENDIX C: CASE STUDY DAMAGED MODELS

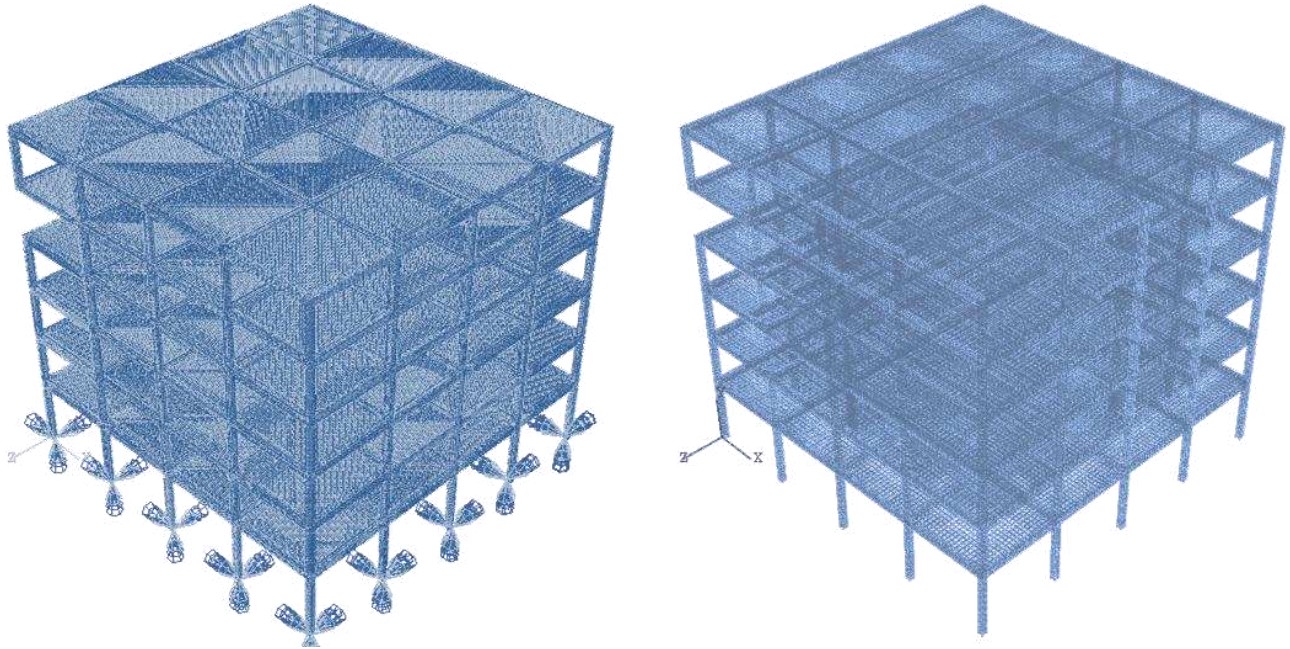


Figure C-5: Abaqus Model for FF-CC-C5 Showing Meshed Solid Elements with Restraints (Left) & Embedded Rebar (Right)

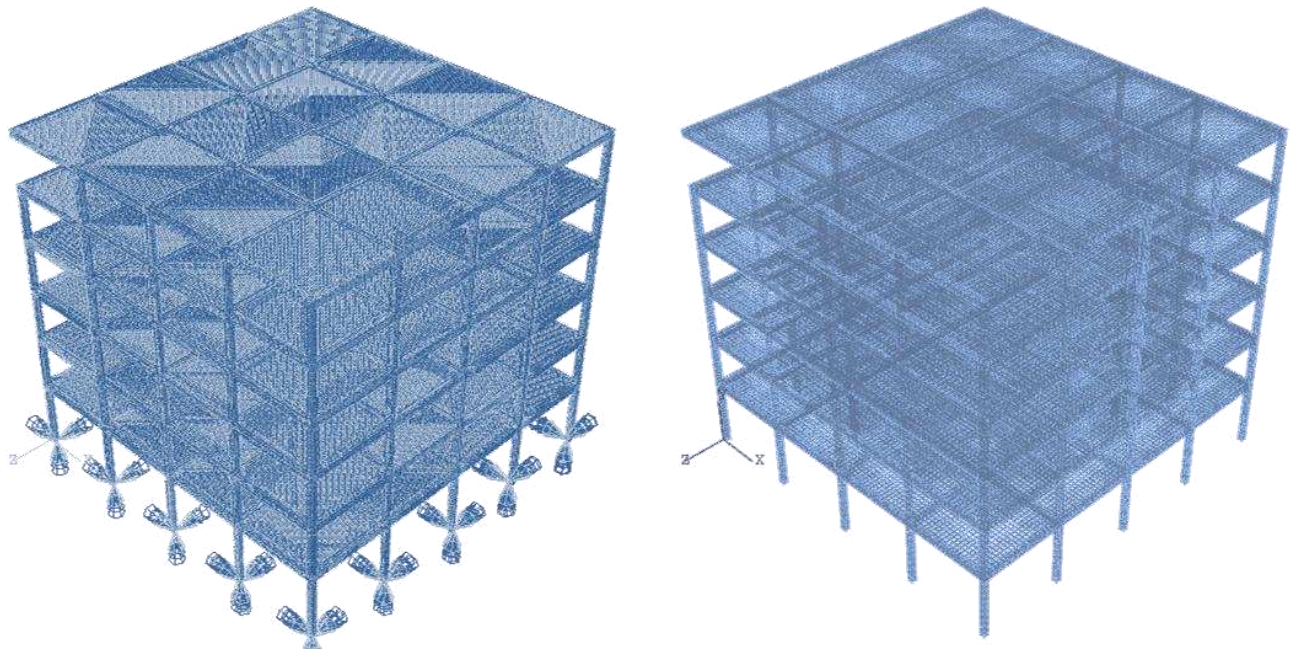


Figure C-6: Abaqus Model for FF-CC-C6 Showing Meshed Solid Elements with Restraints (Left) & Embedded Rebar (Right)

APPENDIX C: CASE STUDY DAMAGED MODELS

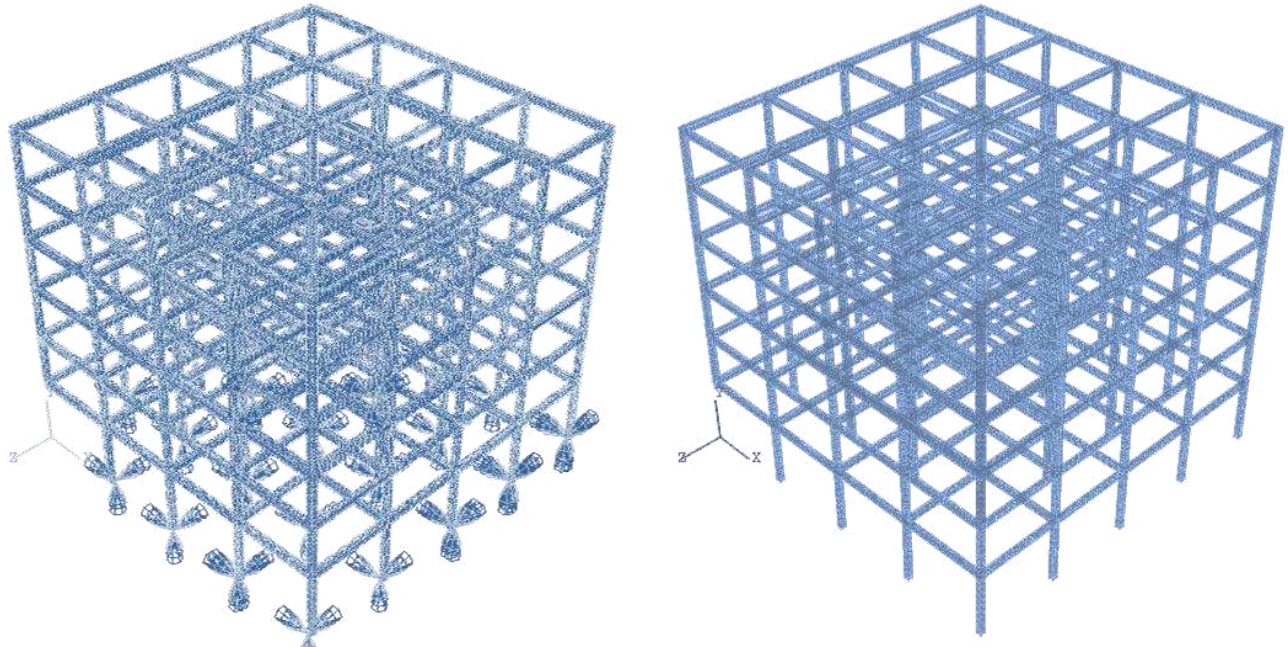


Figure C-7: Abaqus Model for BF-CC-C1 Showing Meshed Solid Elements with Restraints (Left) & Embedded Rebar (Right)

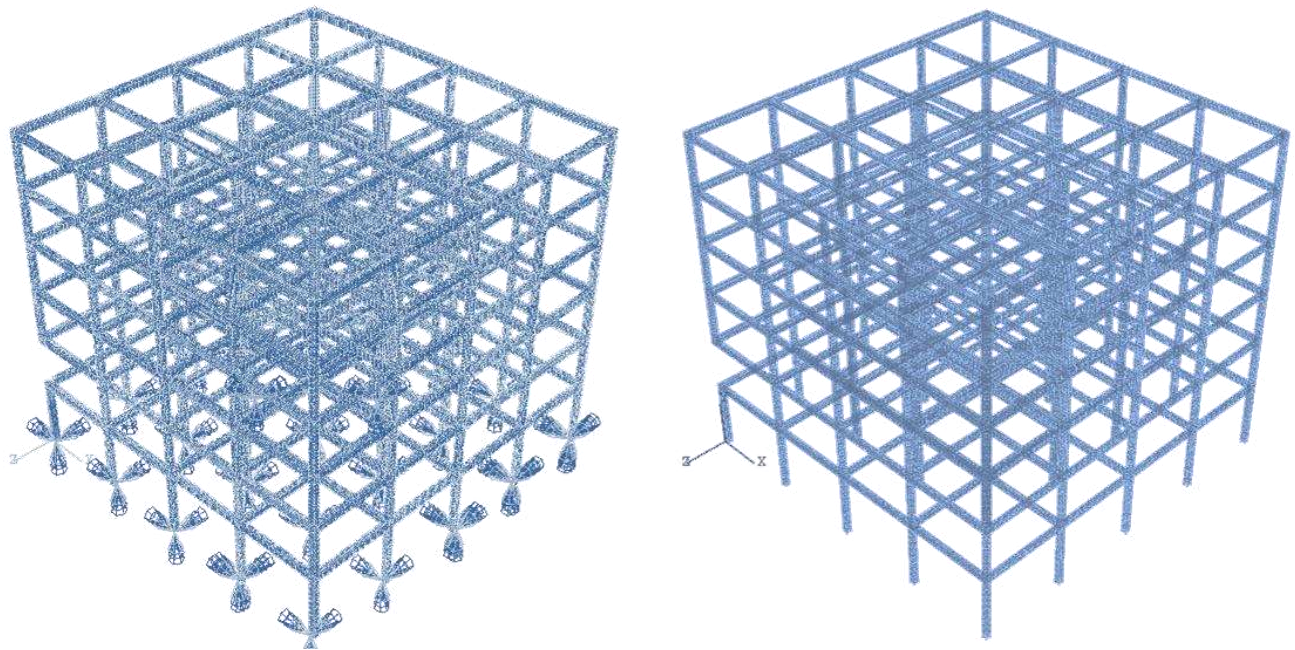


Figure C-8: Abaqus Model for BF-CC-C2 Showing Meshed Solid Elements with Restraints (Left) & Embedded Rebar (Right)

APPENDIX C: CASE STUDY DAMAGED MODELS

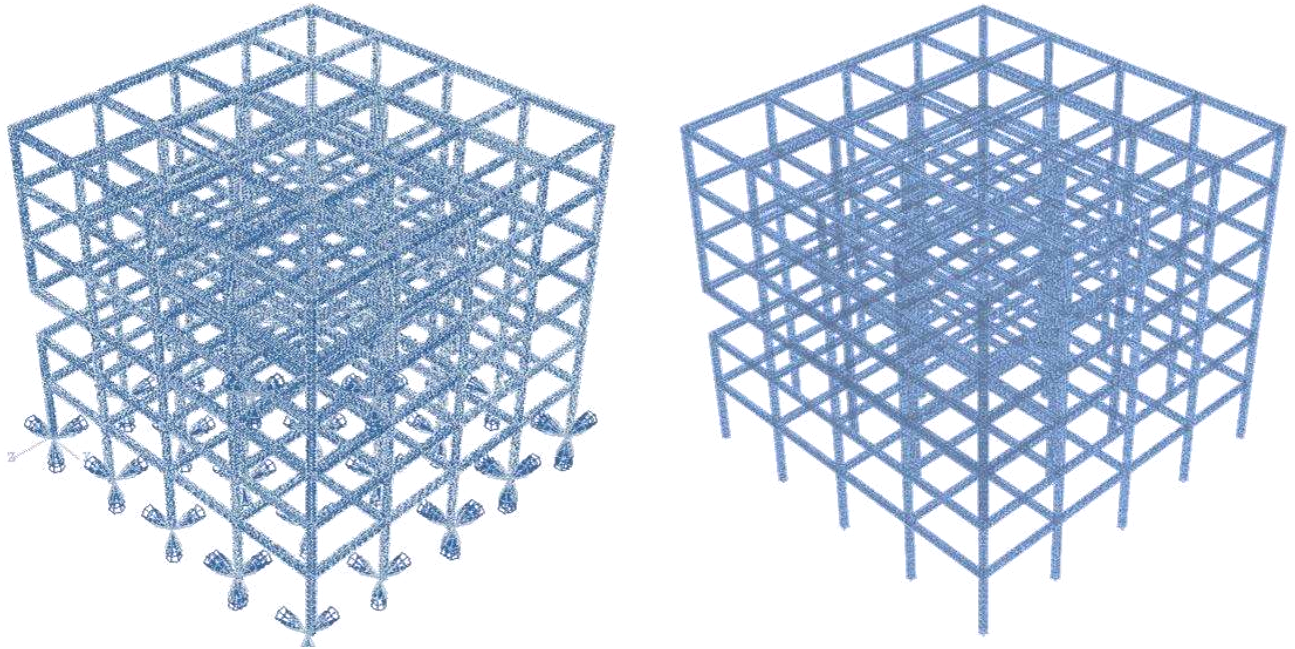


Figure C-9: Abaqus Model for BF-CC-C3 Showing Meshed Solid Elements with Restraints (Left) & Embedded Rebar (Right)

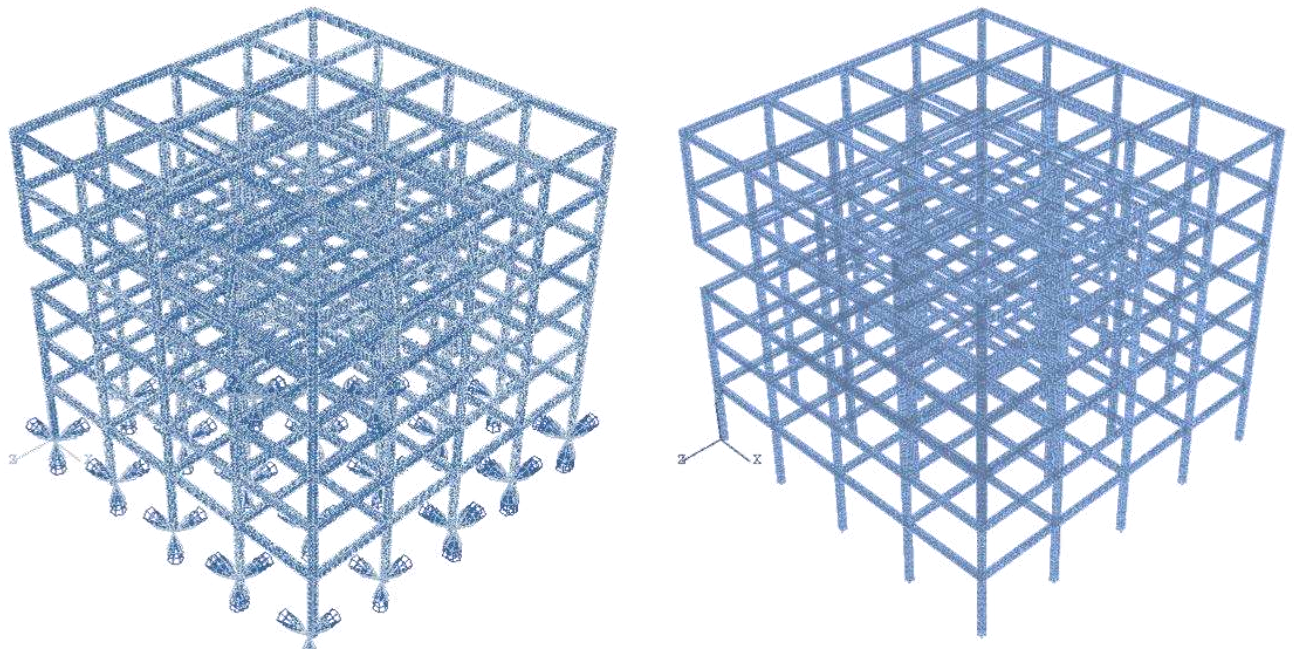


Figure C-10: Abaqus Model for BF-CC-C4 Showing Meshed Solid Elements with Restraints (Left) & Embedded Rebar (Right)

APPENDIX C: CASE STUDY DAMAGED MODELS

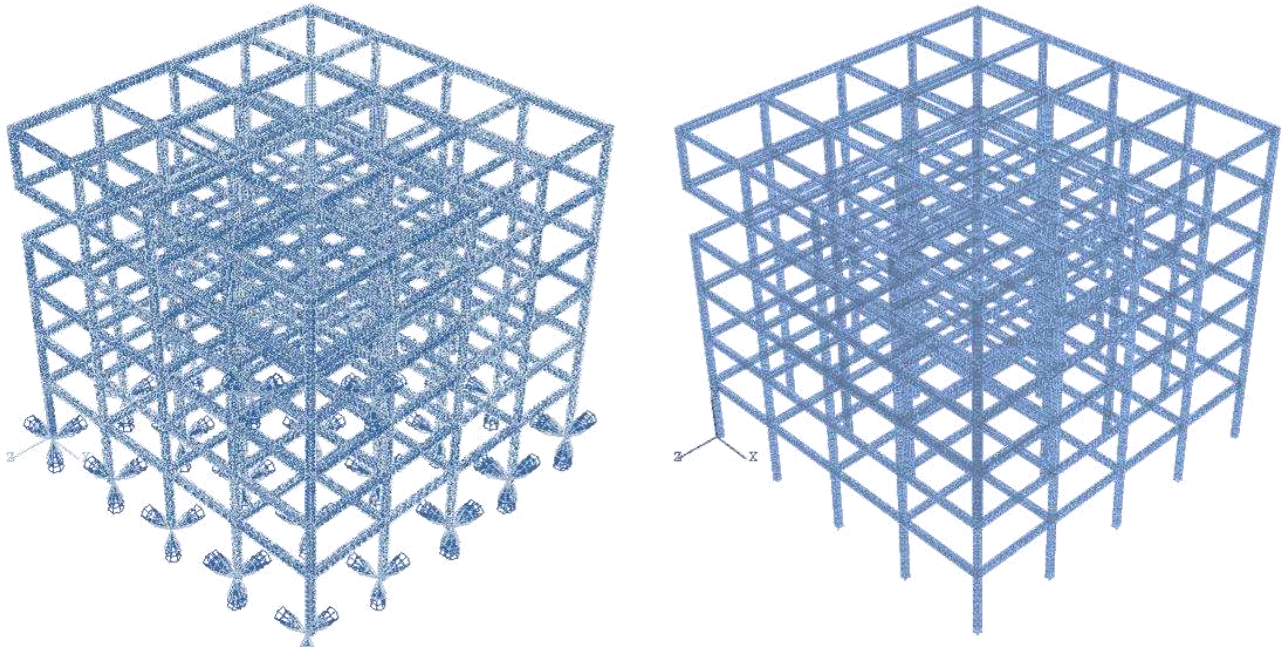


Figure C-11: Abaqus Model for BF-CC-C5 Showing Meshed Solid Elements with Restraints (Left) & Embedded Rebar (Right)

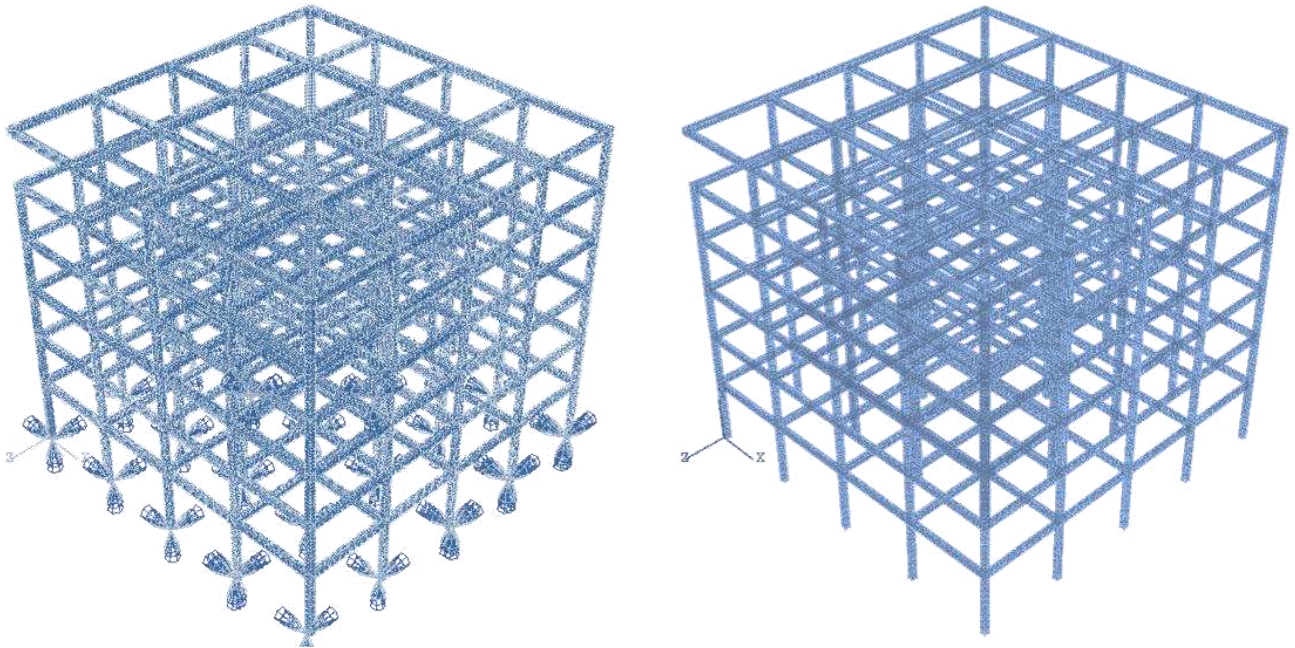


Figure C-12: Abaqus Model for BF-CC-C6 Showing Meshed Solid Elements with Restraints (Left) & Embedded Rebar (Right)

APPENDIX C: CASE STUDY DAMAGED MODELS

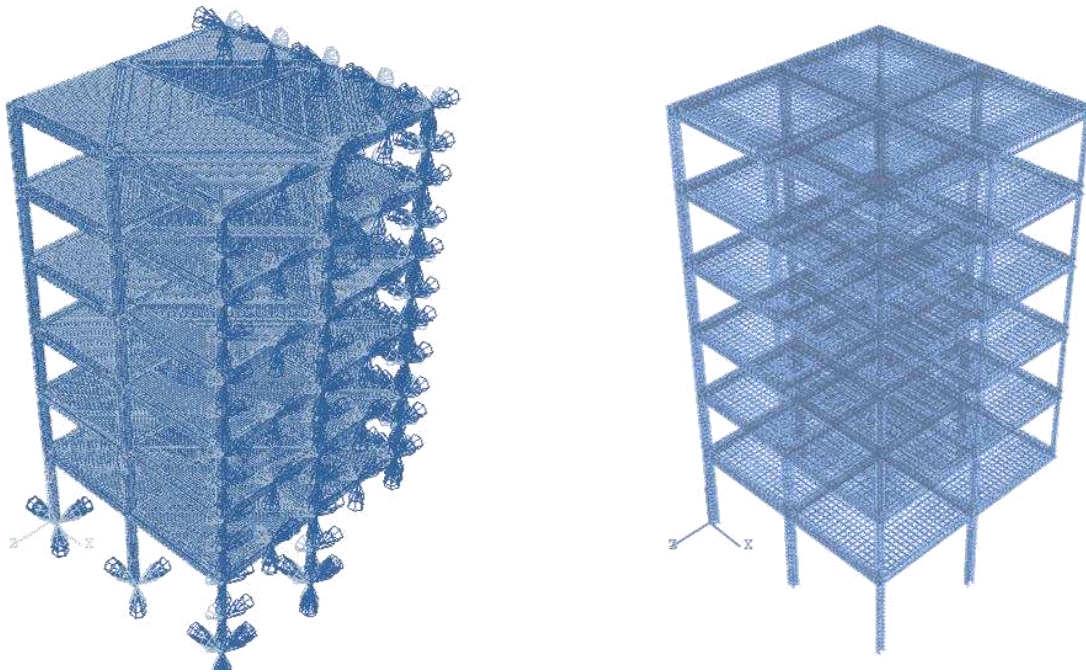


Figure C-13: Abaqus Model for FF-IC-C1 Showing Meshed Solid Elements with Restraints (Left) & Embedded Rebar (Right)

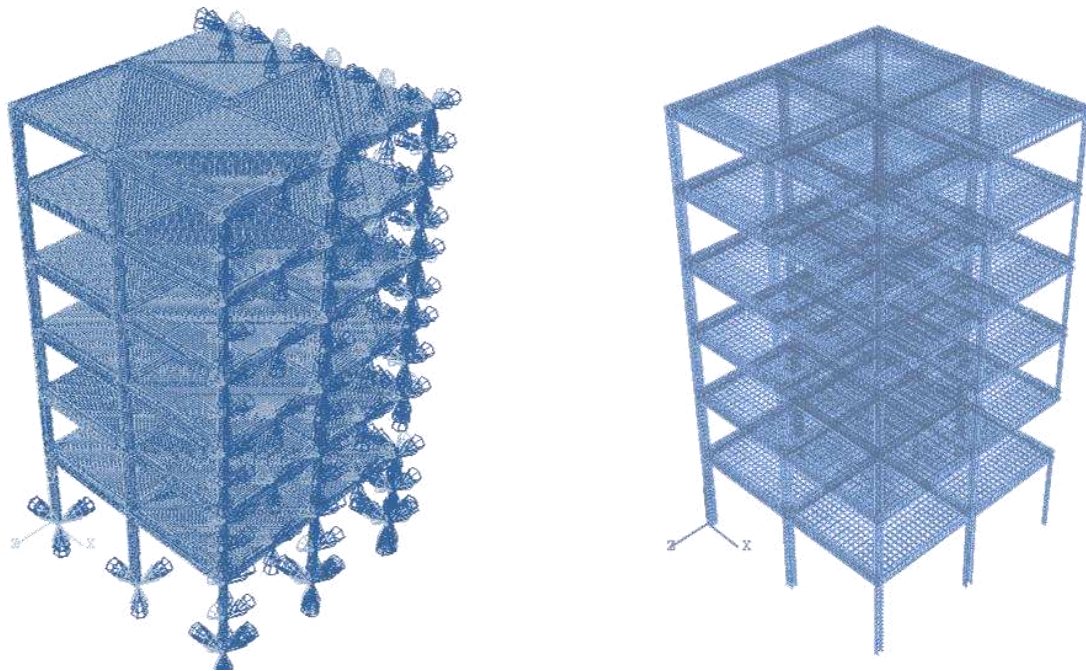


Figure C-14: Abaqus Model for FF-IC-C2 Showing Meshed Solid Elements with Restraints (Left) & Embedded Rebar (Right)

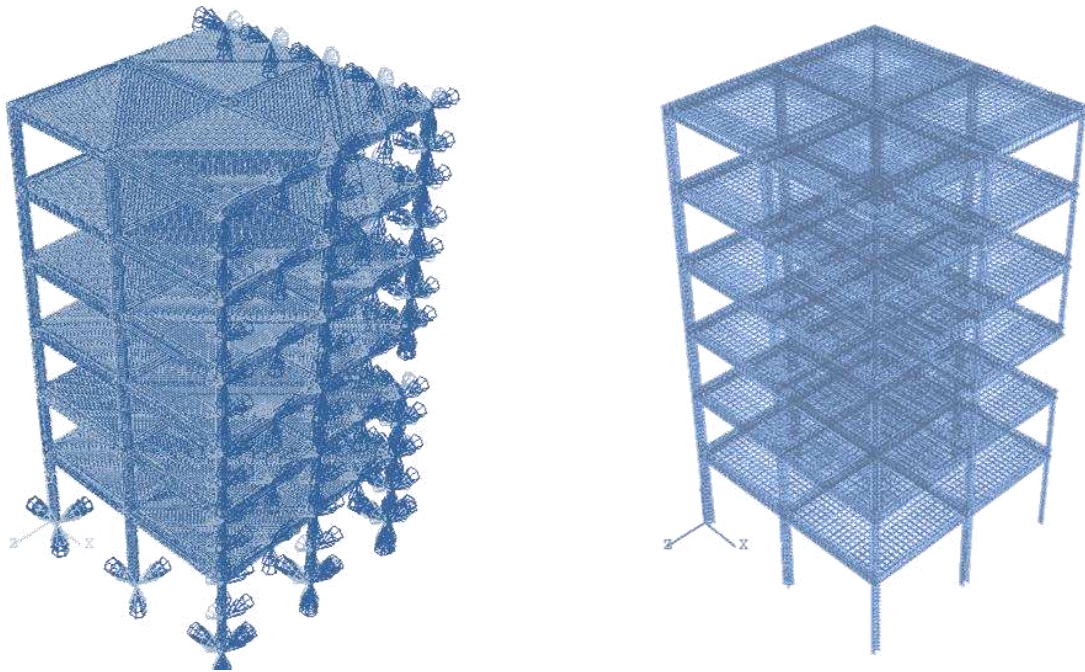


Figure C-15: Abaqus Model for FF-IC-C3 Showing Meshed Solid Elements with Restraints (Left) & Embedded Rebar (Right)

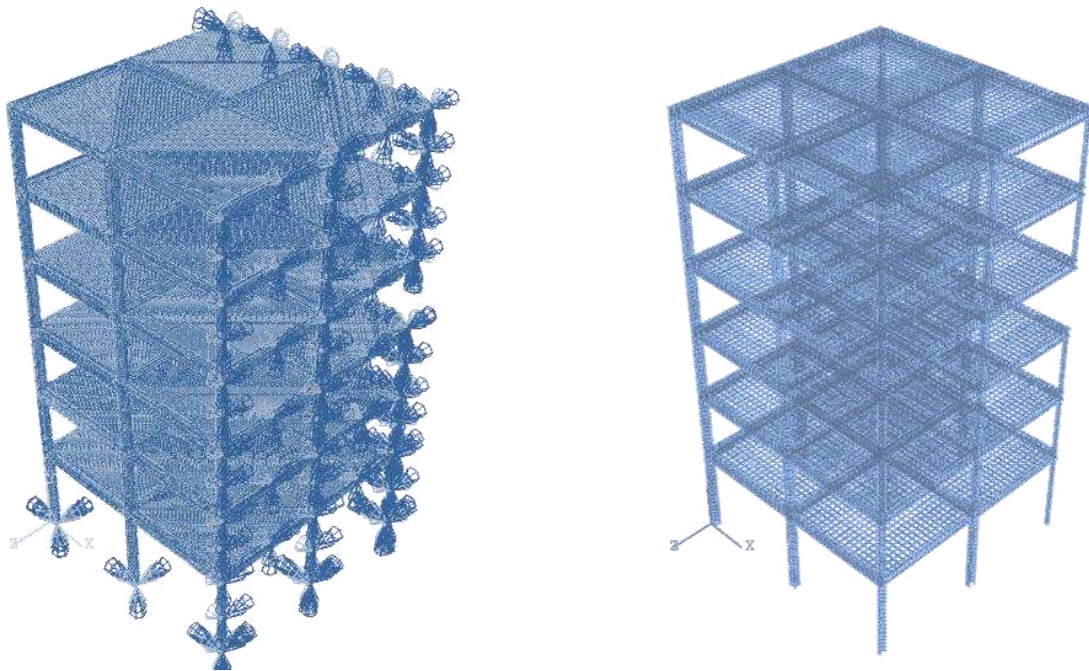


Figure C-16: Abaqus Model for FF-IC-C4 Showing Meshed Solid Elements with Restraints (Left) & Embedded Rebar (Right)

APPENDIX C: CASE STUDY DAMAGED MODELS

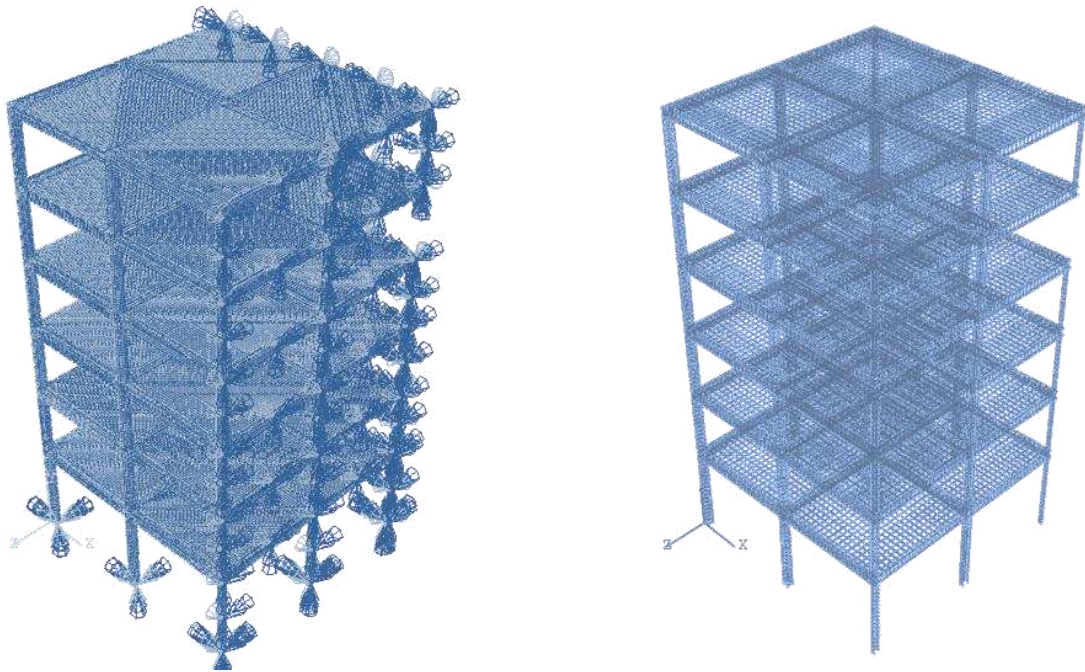


Figure C-17: Abaqus Model for FF-IC-C5 Showing Meshed Solid Elements with Restraints (Left) & Embedded Rebar (Right)

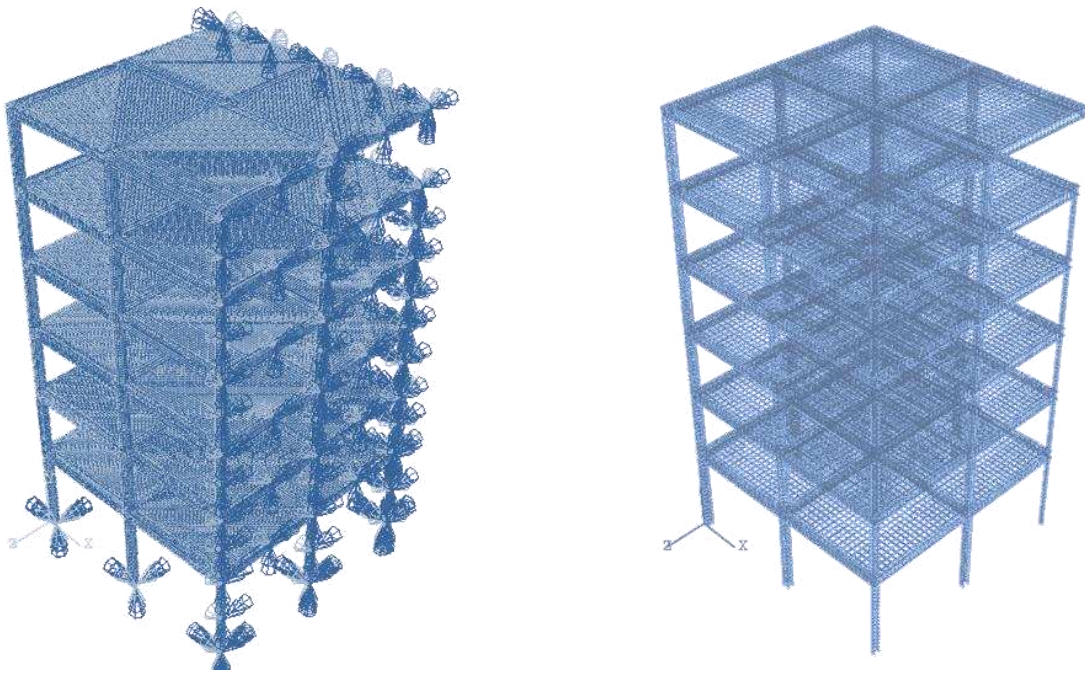


Figure C-18: Abaqus Model for FF-IC-C6 Showing Meshed Solid Elements with Restraints (Left) & Embedded Rebar (Right)

APPENDIX C: CASE STUDY DAMAGED MODELS

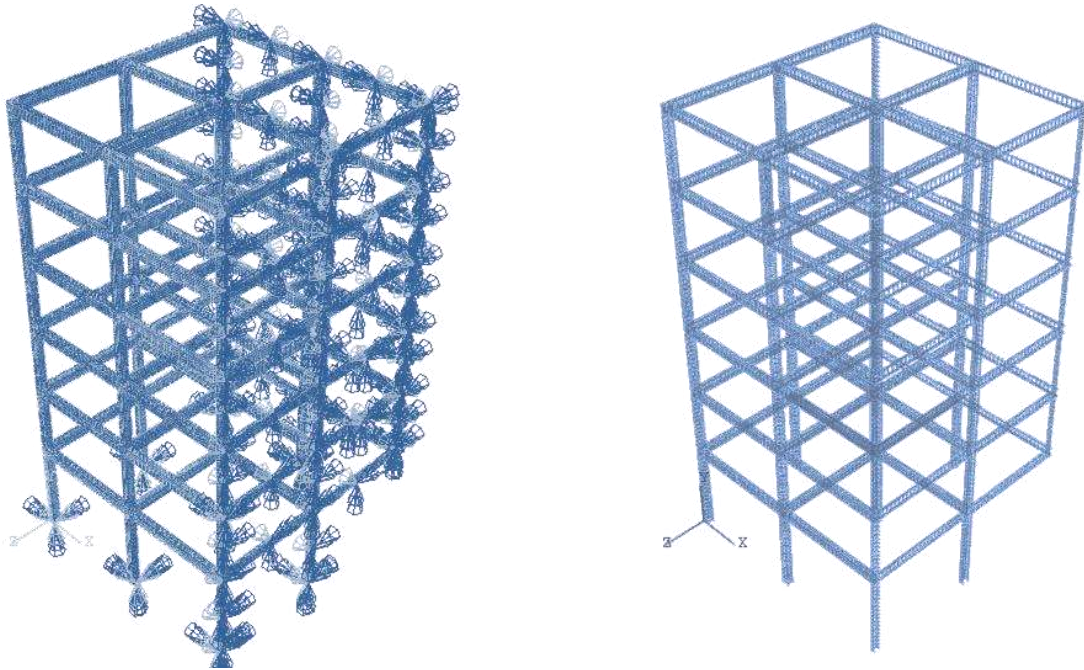


Figure C-19: Abaqus Model for BF-IC-C1 Showing Meshed Solid Elements with Restraints (Left) & Embedded Rebar (Right)

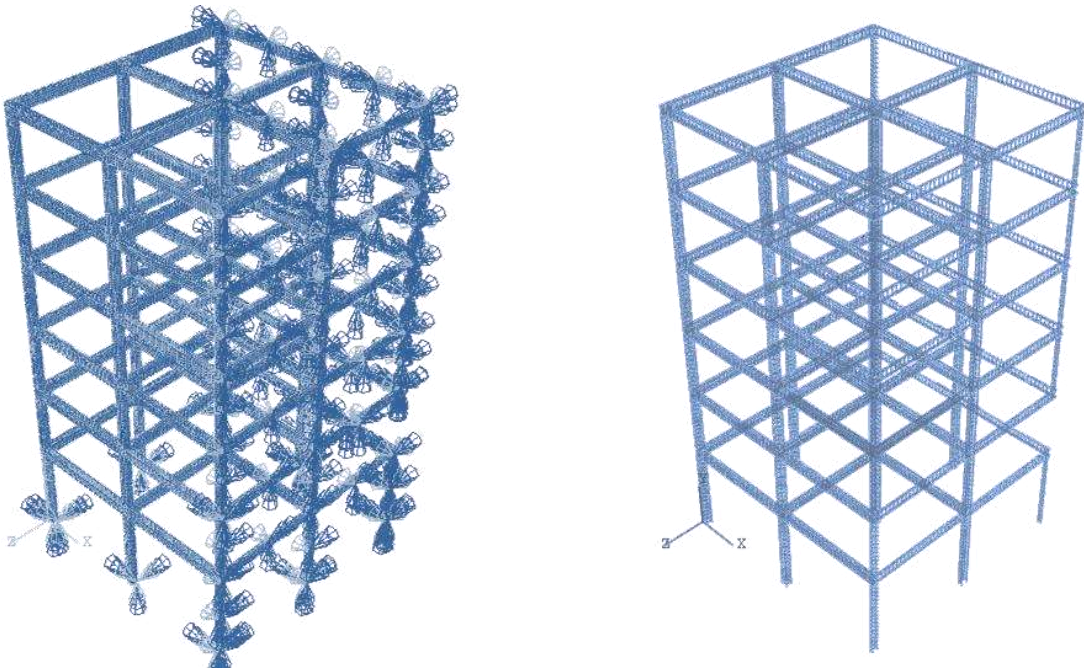


Figure C-20: Abaqus Model for BF-IC-C2 Showing Meshed Solid Elements with Restraints (Left) & Embedded Rebar (Right)

APPENDIX C: CASE STUDY DAMAGED MODELS

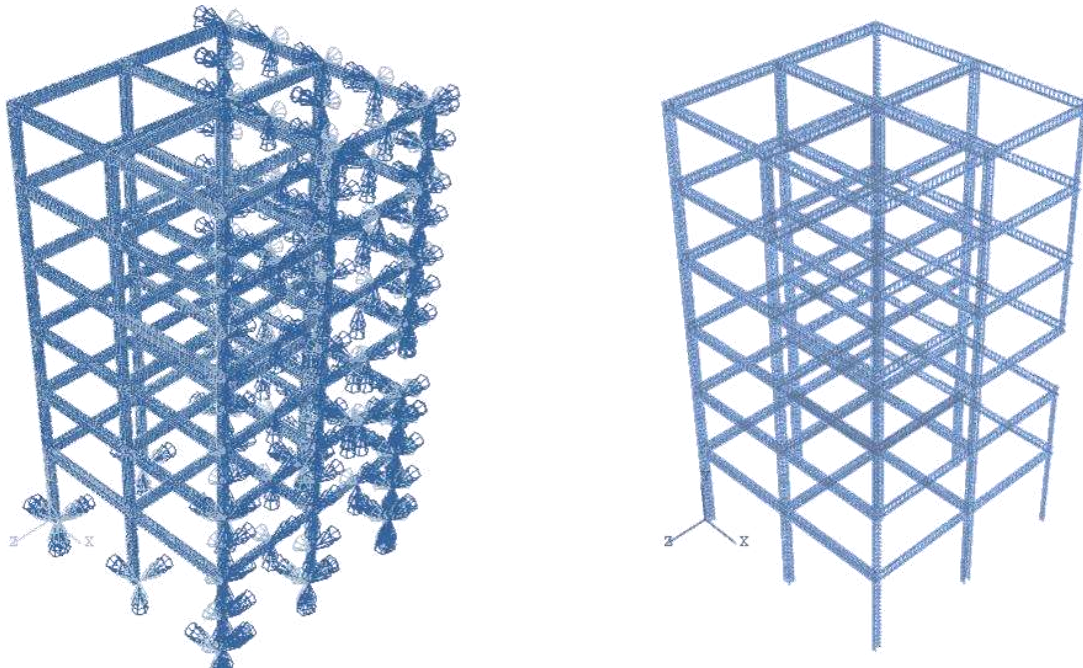


Figure C-21: Abaqus Model for BF-IC-C3 Showing Meshed Solid Elements with Restraints (Left) & Embedded Rebar (Right)

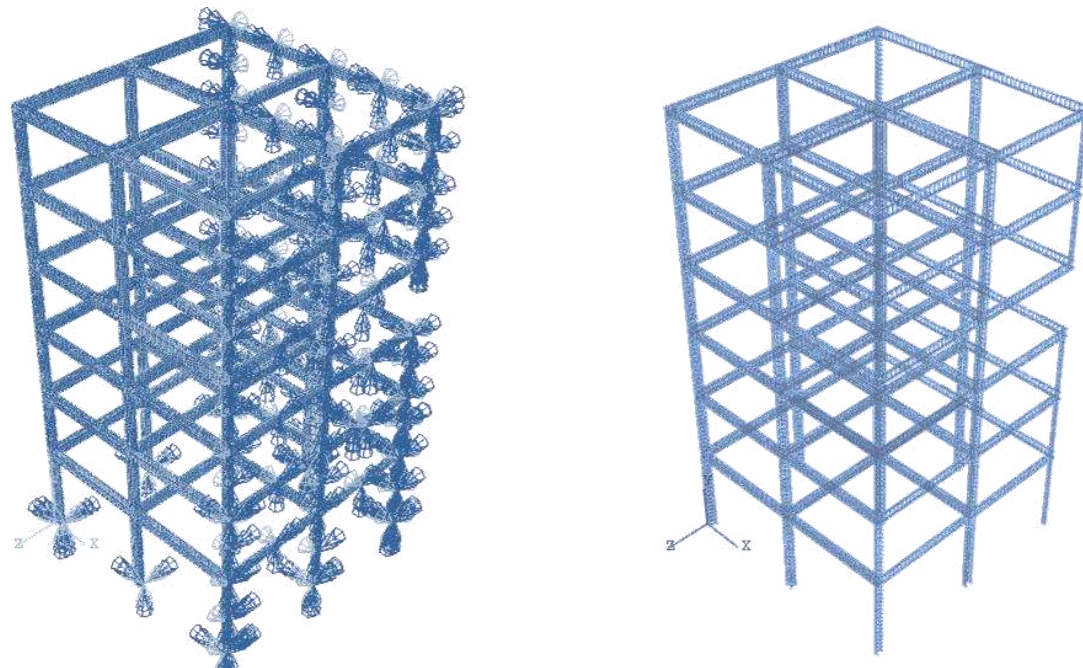


Figure C-22: Abaqus Model for BF-IC-C4 Showing Meshed Solid Elements with Restraints (Left) & Embedded Rebar (Right)

APPENDIX C: CASE STUDY DAMAGED MODELS

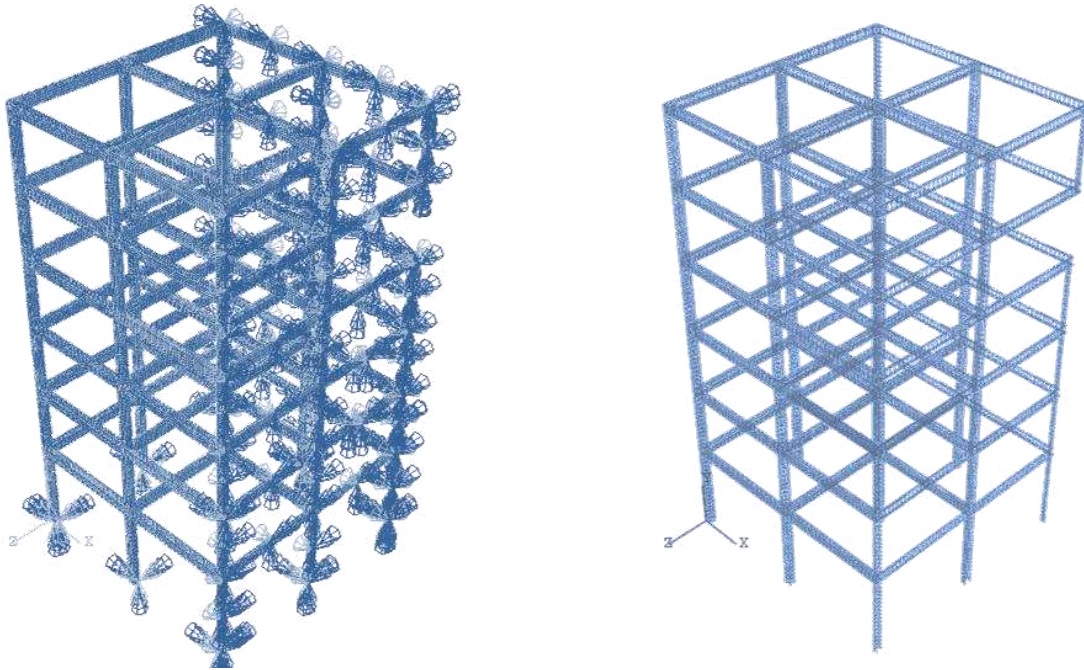


Figure C-23: Abaqus Model for BF-IC-C5 Showing Meshed Solid Elements with Restraints (Left) & Embedded Rebar (Right)

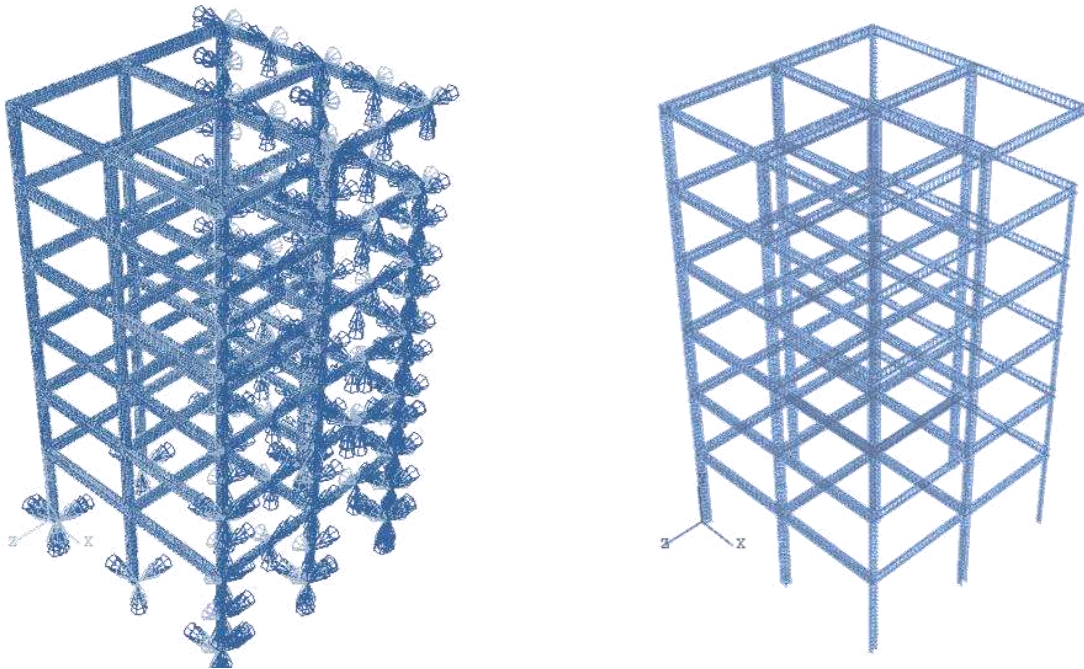


Figure C-24: Abaqus Model for BF-IC-C6 Showing Meshed Solid Elements with Restraints (Left) & Embedded Rebar (Right)